



*catalysts*

# Photocatalysis in the Wastewater Treatment

---

Edited by

Gassan Hodaifa and Rafael Borja

Printed Edition of the Special Issue Published in *Catalysts*

# **Photocatalysis in the Wastewater Treatment**





# Photocatalysis in the Wastewater Treatment

Editors

**Gassan Hodaifa**

**Rafael Borja**

MDPI • Basel • Beijing • Wuhan • Barcelona • Belgrade • Manchester • Tokyo • Cluj • Tianjin



### *Editors*

Gassan Hodaifa  
Molecular Biology and  
Biochemical Engineering  
Department/Chemical  
Engineering Area  
Pablo de Olavide University  
Sevilla  
Spain

Rafael Borja  
Biotecnología de los  
Alimentos  
Instituto de la Grasa (CSIC,  
Spanish National Research  
Council)  
Sevilla  
Spain

### *Editorial Office*

MDPI  
St. Alban-Anlage 66  
4052 Basel, Switzerland

This is a reprint of articles from the Special Issue published online in the open access journal *Catalysts* (ISSN 2073-4344) (available at: [www.mdpi.com/journal/catalysts/special-issues/photocatal.wastewater](http://www.mdpi.com/journal/catalysts/special-issues/photocatal.wastewater)).

For citation purposes, cite each article independently as indicated on the article page online and as indicated below:

LastName, A.A.; LastName, B.B.; LastName, C.C. Article Title. *Journal Name* **Year**, Volume Number, Page Range.

**ISBN 978-3-0365-6393-0 (Hbk)**

**ISBN 978-3-0365-6392-3 (PDF)**

© 2023 by the authors. Articles in this book are Open Access and distributed under the Creative Commons Attribution (CC BY) license, which allows users to download, copy and build upon published articles, as long as the author and publisher are properly credited, which ensures maximum dissemination and a wider impact of our publications.

The book as a whole is distributed by MDPI under the terms and conditions of the Creative Commons license CC BY-NC-ND.



# Contents

About the Editors . . . . .	vii
Preface to "Photocatalysis in the Wastewater Treatment" . . . . .	ix
<b>Guihua Dong, Bing Chen, Bo Liu, Stanislav R. Stoyanov, Yiqi Cao and Min Yang et al.</b> UV Stimulated Manganese Dioxide for the Persulfate Catalytic Degradation of Bisphenol A Reprinted from: <i>Catalysts</i> <b>2021</b> , <i>11</i> , 502, doi:10.3390/catal11040502 . . . . .	1
<b>Jingbang Sun, Ni Han, Yan Gu, Xiaowang Lu, Liang Si and Qinfang Zhang</b> Hole Doping to Enhance the Photocatalytic Activity of Bi <sub>4</sub> NbO <sub>8</sub> Cl Reprinted from: <i>Catalysts</i> <b>2020</b> , <i>10</i> , 1425, doi:10.3390/catal10121425 . . . . .	15
<b>Hongji Li, Yu Zhang, Jiaqi Diao, Mengmeng Qiang and Zhe Chen</b> Synthesis and Photocatalytic Activity of Hierarchical Zn-ZSM-5 Structures Reprinted from: <i>Catalysts</i> <b>2021</b> , <i>11</i> , 797, doi:10.3390/catal11070797 . . . . .	27
<b>Stefano Alberti, Irene Basciu, Marco Voccianti and Maurizio Ferretti</b> Experimental and Physico-Chemical Comparison of ZnO Nanoparticles' Activity for Photocatalytic Applications in Wastewater Treatment Reprinted from: <i>Catalysts</i> <b>2021</b> , <i>11</i> , 678, doi:10.3390/catal11060678 . . . . .	43
<b>Xin Zhong, Yihong Cai, Heping Bai, Wei Huang and Binxue Zhou</b> Visible Light Driven Spherical CuBi <sub>2</sub> O <sub>4</sub> with Surface Oxygen Vacancy Enhanced Photocatalytic Activity: Catalyst Fabrication, Performance, and Reaction Mechanism Reprinted from: <i>Catalysts</i> <b>2020</b> , <i>10</i> , 945, doi:10.3390/catal10080945 . . . . .	57
<b>Saule Mergenbayeva, Timur Sh. Atabaev and Stavros G. Pouloupoulos</b> Ti <sub>2</sub> O <sub>3</sub> /TiO <sub>2</sub> -Assisted Solar Photocatalytic Degradation of 4-tert-Butylphenol in Water Reprinted from: <i>Catalysts</i> <b>2021</b> , <i>11</i> , 1379, doi:10.3390/catal11111379 . . . . .	73
<b>Jianhua Song, Dedong Zeng, Yu Xie, Fayun Zhang, Shenli Rao and Fahui Wang et al.</b> Preparation of CdS Nanoparticles-TiO <sub>2</sub> Nanorod Heterojunction and Their High-Performance Photocatalytic Activity Reprinted from: <i>Catalysts</i> <b>2020</b> , <i>10</i> , 441, doi:10.3390/catal10040441 . . . . .	93
<b>Ivana Grčić, Andreja Gajović, Milivoj Plodinec, Kristina Šimunković, Hrvoje Ivanković and Marc-Georg Willinger</b> Enhanced Visible-Light Driven Photocatalytic Activity of Ag@TiO <sub>2</sub> Photocatalyst Prepared in Chitosan Matrix Reprinted from: <i>Catalysts</i> <b>2020</b> , <i>10</i> , 763, doi:10.3390/catal10070763 . . . . .	107
<b>Khelil Bouziane Errahmani, Ouassila Benhabiles, Sohbi Bellebia, Zohra Bengharez, Mattheus Goosen and Hacene Mahmoudi</b> Photocatalytic Nanocomposite Polymer-TiO <sub>2</sub> Membranes for Pollutant Removal from Wastewater Reprinted from: <i>Catalysts</i> <b>2021</b> , <i>11</i> , 402, doi:10.3390/catal11030402 . . . . .	125
<b>Gassan Hodaifa, Cristina Agabo García and Rafael Borja</b> Study of Catalysts' Influence on Photocatalysis/ Photodegradation of Olive Oil Mill Wastewater. Determination of the Optimum Working Conditions Reprinted from: <i>Catalysts</i> <b>2020</b> , <i>10</i> , 554, doi:10.3390/catal10050554 . . . . .	141

<b>Natalia Villota, Cristian Ferreiro, Hussein Ahmad Qulatein, Jose María Lomas, Luis Miguel Camarero and José Ignacio Lombraña</b> Colour Changes during the Carbamazepine Oxidation by Photo-Fenton Reprinted from: <i>Catalysts</i> <b>2021</b> , <i>11</i> , 386, doi:10.3390/catal11030386 . . . . .	<b>159</b>
<b>Lariana Negrão Beraldo de Almeida, Tatiana Gulminie Josué, Othavio Henrique Lupepsa Nogueira, Daniele Toniolo Dias, Angelo Marcelo Tusset and Onélia Aparecida Andreo dos Santos et al.</b> Quarry Residue: Treatment of Industrial Effluent Containing Dye Reprinted from: <i>Catalysts</i> <b>2021</b> , <i>11</i> , 852, doi:10.3390/catal11070852 . . . . .	<b>173</b>
<b>Syed Nabeel Ahmed and Waseem Haider</b> Enhanced Photocatalytic Activity of ZnO-Graphene Oxide Nanocomposite by Electron Scavenging Reprinted from: <i>Catalysts</i> <b>2021</b> , <i>11</i> , 187, doi:10.3390/catal11020187 . . . . .	<b>187</b>

# About the Editors

## Gassan Hodaifa

Gassan Hodaifa (H-Index 24 in Web of Science) is a Food Engineer (Univ. De Albaath, Syria), Chemical Engineer (Univ. Of Granada) and Doctor, University of Jaén in Doctoral Program: Biotechnology and Agri-Food Engineering. His research began in 1997 with a predoctoral fellowship for work carried out in Spain, and he joined the research group “Bioprocesses TEP-138 (J. Andalucía)” and worked in the fields of Microalgae, Treatment of Wastewaters, Chemical Oxidation, Membrane Technology, Adsorption, Pesticide Removal, Olive Oil Processing, Enzyme Biotechnology and Nematode Biotechnology. He participated in 27 research projects (8 as IP), 4 of which were European (1 PRIMA Project and 3 in collaboration with M.A.P.A. and the INFAOLIVA and UNAPROLIVA companies), with which he signed 16 research contracts (4 as IP). Two contracts were as an Adviser for the Mega Japanese Company “Asahi Kasei Corporation”, six projects were financed by J. Andalucía (two of them as IP), five projects were with the National Research Plan, one was a project of Madrid Community, and the rest were with companies. His research work includes 64 published articles, 56 articles published in *JCR* (31 in Q1, 18 in Q2, and 7 in Q3; of these articles, more than 10 were published in collaboration with authors from different countries on all continents; total articles in Open Access Journals: 6), 4 articles in journals with impact factors, and 5 other articles in outreach magazines to society. Two patents for the water purification of olive oil mill wastewater, 2 books, 46 book chapters with prestigious publishers such as Academic Press (Elsevier), CRC Press, Taylor and Francis Group, Springer International Publishing AG etc. He published, as an Editor-in-Chief, two Special Issues in *J. Chemistry* and *Catalysts* both from *JCR*. He has participated in 125 Congresses. He is currently a member of 15 Editorial Boards of International Journals such as *Catalysts*, *Heliyon*, etc.

## Rafael Borja

Rafael Borja is Doctor (PhD) in Chemical Sciences. Since 1986 he has been working as a researcher at the Instituto de la Grasa (CSIC, Spanish National Research Council) in Seville, after obtaining an FPI grant funded by the Andalusian Government for the Doctoral Thesis. San Alberto Magno Prize for Doctoral Theses awarded by the National Association of Spanish Chemists (ANQUE), Delegation of Andalusia in 1991. During the period September 1992 - September 1994, he made a postdoctoral stay at the “Environmental Technology Centre” belonging to the “Department of Chemical Engineering” of the “University of Manchester - Institute of Science and Technology (UMIST)” of Manchester, United Kingdom. In 1997 he obtained the position of Tenured Scientist of the CSIC, developing since then several lines of research related to the use and treatment of wastewaters and solid wastes from agro-food industries. In 2008 he obtained the position of Research Scientist at the CSIC. He has directed 6 Doctoral Theses and is a co-author of 8 patents. He has published 302 articles in different scientific journals included in the “Science Citation Index (SCI)”. According to the database Scopus he has an index h of 56 (January 2023). According to this same database, it has a total number of 10,483 citations (January 2023).

He has been the principal investigator of 12 projects funded by the R&D National Plan and by the European Union, as well as several R&D contracts developed at the Instituto de la Grasa (CSIC) in Seville. He currently is a member of the Editorial Board of the scientific journals “Process Biochemistry” (Elsevier), “Catalysts” (MDPI) and “Emerging Science Journal (Ital Publication)”. During the period 2013-2015 he was vice-president of the association “International



Association of the Mediterranean Agro-industrial Wastes (IAMAW)“located in Perugia, Italy, and from 2016 to 2019 he was a member of the “Audit Committee“of this Association.

# Preface to "Photocatalysis in the Wastewater Treatment"

The modernization of our society and the great technological advances in the agro-food, chemical, pharmaceutical and biotechnological sectors have allowed the establishment of large industries over the last fifty years. Most of these industries are characterized by the high consumption of drinking water, which is transformed into wastewater during these industrial processes. Unfortunately, a large part of this wastewater is difficult to treat due to the presence of a high organic load, persistent compounds, toxic and inhibitory compounds, etc. This fact has presented a challenge to conventional urban wastewater treatment plants (CUWTPs), which are increasingly unable to meet the standards set by local, national, or international legislation. On the other hand, in the last decade, climate change has been evident due to the significant carbon footprint and the hydraulic footprint these industries have. Additionally, drinking water is scarce in many countries.

The use of photocatalysis for wastewater treatment is an important area of research that is not yet fully exploited at an industrial level and has significant potential in the disposal of many industrial effluents, particularly the effluents that are difficult to treat using conventional treatment processes. This reprint outlines the latest advances in the field of wastewater treatment through photocatalysis. In this sense, we mention treatments based on photolysis,  $\text{TiO}_2$ /solar light, oxidants/ultraviolet irradiation, oxidants/catalyst/ultraviolet irradiation, etc. In addition, this reprint describes catalyst manufacturing methods and reaction mechanisms.

This reprint is addressed to all readers interested in the manufacture of catalysts and photooxidation-based treatment processes, whether academics or professionals. Finally, the editors would like to thank the authors who have participated in the writing of this reprint, which will be of great interest at the industrial, academic and research levels.



**Gassan Hodaifa and Rafael Borja**  
*Editors*





## Article

# UV Stimulated Manganese Dioxide for the Persulfate Catalytic Degradation of Bisphenol A

Guihua Dong <sup>1</sup>, Bing Chen <sup>1,\*</sup> , Bo Liu <sup>1</sup>, Stanislav R. Stoyanov <sup>2,\*</sup>, Yiqi Cao <sup>1</sup>, Min Yang <sup>1</sup> and Baiyu Zhang <sup>1</sup> 

<sup>1</sup> Northern Region Persistent Organic Pollution Control (NRPOP) Laboratory, Faculty of Engineering and Applied Science, Memorial University of Newfoundland, St. John's, NL A1B 3X5, Canada; gdong@mun.ca (G.D.); bl4184@mun.ca (B.L.); yiqic@mun.ca (Y.C.); min.yang@mun.ca (M.Y.); bzhang@mun.ca (B.Z.)

<sup>2</sup> Natural Resources Canada, CanmetENERGY Devon, 1 Oil Patch Drive, Devon, AB T9G 1A8, Canada

\* Correspondence: bchen@mun.ca (B.C.); stanislav.stoyanov@canada.ca (S.R.S.)

**Abstract:** One of the most commonly produced industrial chemicals worldwide, bisphenol A (BPA), is used as a precursor in plastics, resins, paints, and many other materials. It has been proved that BPA can cause long-term adverse effects on ecosystems and human health due to its toxicity as an endocrine disruptor. In this study, we developed an integrated MnO<sub>2</sub>/UV/persulfate (PS) process for use in BPA photocatalytic degradation from water and examined the reaction mechanisms, degradation pathways, and toxicity reduction. Comparative tests using MnO<sub>2</sub>, PS, UV, UV/MnO<sub>2</sub>, MnO<sub>2</sub>/PS, and UV/PS processes were conducted under the same conditions to investigate the mechanism of BPA catalytic degradation by the proposed MnO<sub>2</sub>/UV/PS process. The best performance was observed in the MnO<sub>2</sub>/UV/PS process in which BPA was completely removed in 30 min with a reduction rate of over 90% for total organic carbon after 2 h. This process also showed a stable removal efficiency with a large variation of pH levels (3.6 to 10.0). Kinetic analysis suggested that <sup>1</sup>O<sub>2</sub> and SO<sub>4</sub><sup>•−</sup> played more critical roles than •OH for BPA degradation. Infrared spectra showed that UV irradiation could stimulate the generation of −OH groups on the MnO<sub>2</sub> photocatalyst surface, facilitating the PS catalytic degradation of BPA in this process. The degradation pathways were further proposed in five steps, and thirteen intermediates were identified by gas chromatography-mass spectrometry. The acute toxicity was analyzed during the treatment, showing a slight increase (by 3.3%) in the first 30 min and then a decrease by four-fold over 2 h. These findings help elucidate the mechanism and pathways of BPA degradation and provide an effective PS catalytic strategy.

**Keywords:** BPA; UV stimulated MnO<sub>2</sub>; photocatalytic degradation; synergistic effect; pathways; toxicity

**Citation:** Dong, G.; Chen, B.; Liu, B.; Stoyanov, S.R.; Cao, Y.; Yang, M.; Zhang, B. UV Stimulated Manganese Dioxide for the Persulfate Catalytic Degradation of Bisphenol A. *Catalysts* **2021**, *11*, 502. <https://doi.org/10.3390/catal11040502>

Academic Editors: Gassan Hodaifa and Rafael Borja

Received: 24 March 2021

Accepted: 14 April 2021

Published: 16 April 2021

**Publisher's Note:** MDPI stays neutral with regard to jurisdictional claims in published maps and institutional affiliations.



**Copyright:** © 2021 by the authors. Licensee MDPI, Basel, Switzerland. This article is an open access article distributed under the terms and conditions of the Creative Commons Attribution (CC BY) license (<https://creativecommons.org/licenses/by/4.0/>).

## 1. Introduction

Bisphenol A (BPA) is a high-production-volume industrial chemical used as a precursor in synthetic polycarbonate plastics and epoxy resins, as well as many consumer products, including food containers, paper products, toys, medical equipment, and electronics [1]. Growing evidence has shown the long-term negative effects of BPA on aquatic life and human health [2,3]. Several studies have reported on the potential adverse effects of BPA exposure to humans during critical stages of neonatal or early development [3,4]. Meanwhile, BPA was ubiquitously detected in river water and soil at microgram levels [5,6]. Moreover, the highest BPA concentrations were found in landfill leachate in Japan (up to 17.2 mg/L) and Germany (4.2–25 mg/L) [7–9]. Growing concerns have been raised on the associated environmental risks caused by BPA as both a sole emerging contaminant and co-contaminant [10–12], leading to urgent demands for effective remediating techniques towards contaminated waters.

Advanced oxidation processes (AOPs) based on the production of hydroxyl radical (•OH), which acts as a powerful oxidant, have been regarded as highly promising for the

degradation of BPA [13,14]. Persulfate-based AOPs have drawn considerable attention in recent years due to their high efficiency for generating sulfate radical ( $\text{SO}_4^{\bullet-}$ ), which has more positive redox potential (2.6–3.1 V) than  $\bullet\text{OH}$  (1.9–2.7 V), to degrade recalcitrant organic pollutants [15,16]. Persulfate (PS) is one of the main precursors for the generation of  $\text{SO}_4^{\bullet-}$  [17,18]. PS can be activated by transition metal catalysts (such as iron oxides and manganese oxides), nonmetal catalysts, ultraviolet (UV) and visible light, ultrasound, alkaline, heat, and strong oxidants to produce  $\text{SO}_4^{\bullet-}$  and other radicals for the removal of organic pollutants [19,20].

Synergistic PS catalytic activation was recently demonstrated with enhanced contaminants removal. Most attention has been paid to the applications of transition metals or their oxides (e.g., iron, copper, and cobalt) and UV as hybrid activators for PS catalytic activation [21–23]. In fact, manganese dioxide ( $\text{MnO}_2$ ) is widely used as a catalyst or activator in various heterogeneous reaction systems due to its high natural abundance, low toxicity, and low environmental impacts [24–26].  $\text{MnO}_2$  is a promising candidate for photocatalyst application due to its narrow bandgap (1–2 eV) and ability to absorb light under solar energy [27]. However, to our best knowledge, synergistic use of  $\text{MnO}_2$  and UV has never been applied for PS activation. Recently, Eslami et al. [28] confirmed that the synergistic use of  $\text{MnO}_2$  and UV is a promising hybrid activator for peroxymonosulfate (PMS) activation. Accordingly, there are many distinctive differences during activation of PS and PMS, especially in reactivity toward radicals and responses to different pH levels [29]. Furthermore, the synergistic mechanism for PS catalytic activation, especially the interactions between  $\text{MnO}_2$  and UV, remains unknown and deserves further investigation.

In this study, we first developed an enhanced  $\text{MnO}_2$ /UV/PS process for the efficient removal and mineralization of BPA. The optimum activation performance of UV irradiation and  $\text{MnO}_2$  in various conditions was examined in detail. The enhanced BPA degradation mechanism in the hybrid catalytic process was then explored using quenching studies for reactive oxygen species (ROS). More importantly, the effect of UV irradiation on the  $\text{MnO}_2$  surface in this process was substantially investigated. Moreover, the complex BPA degradation mechanism was presented in terms of the predominant reaction pathways, supported by intermediates identified using gas chromatography-mass spectrometry (GC-MS). Finally, the acute toxicity due to the BPA removal through the  $\text{MnO}_2$ /UV/PS process was evaluated.

## 2. Results and Discussion

### 2.1. Degradation and Mineralization of BPA

To evaluate and compare the BPA degradation and mineralization performance of the  $\text{MnO}_2$ /UV/PS process with those of its component processes, seven different processes (namely PS,  $\text{MnO}_2$ , UV, UV/ $\text{MnO}_2$ ,  $\text{MnO}_2$ /PS, UV/PS, and  $\text{MnO}_2$ /UV/PS) were tested (Figure 1).

The PS process alone had no effect on BPA removal, while only 3.6% of BPA could be removed by the  $\text{MnO}_2$  process after 2 h (Figure 1a). Lin et al. [30] reported the relatively high efficacy of BPA removal from a 4.4  $\mu\text{M}$  solution using a high concentration of 800  $\mu\text{M}$   $\text{MnO}_2$  over 10 min. The low BPA removal efficiency of our  $\text{MnO}_2$  process might be due to its relatively low concentration of  $\text{MnO}_2$  compared to BPA. The individual applications of  $\text{MnO}_2$  and PS were ineffective, presumably due to slow (or no) free radical generation and negligible absorption capacity of  $\text{MnO}_2$  in this study. Both UV and UV/ $\text{MnO}_2$  processes degraded 75.0% and 85.0% of BPA in 2 h, respectively. In the  $\text{MnO}_2$ /PS process, the removal efficiency of 87.8% was observed after 2 h, whereas the UV-activated PS process could effectively remove all BPA in 45 min. The synergistic PS catalytic activation by  $\text{MnO}_2$ /UV could entirely remove BPA within 30 min. Both the UV/PS and  $\text{MnO}_2$ /UV/PS processes had better performances than the  $\text{MnO}_2$ /PS process, and the concurrent presence of UV and  $\text{MnO}_2$  further enhanced the PS catalytic activation, and consequently, the BPA degradation.

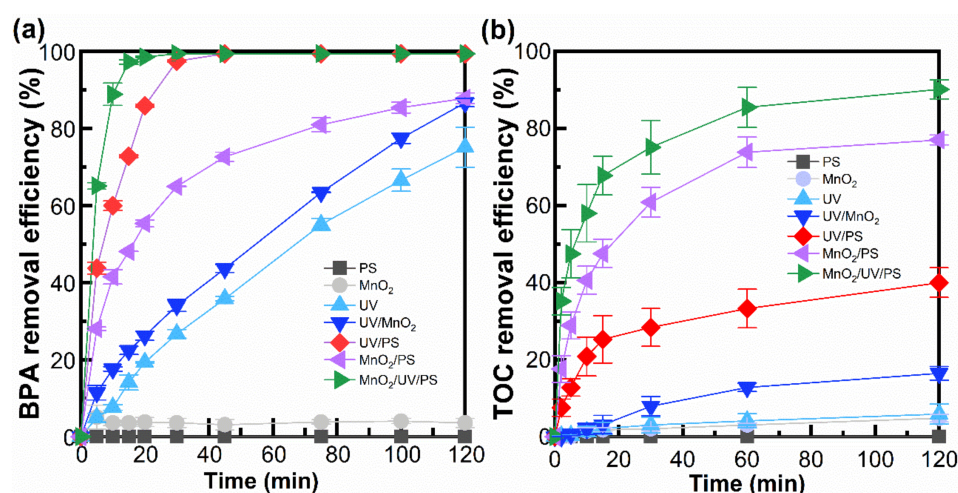


**Figure 1.** BPA (a) and TOC (b) removal over time using the PS,  $\text{MnO}_2$ , UV, UV/ $\text{MnO}_2$ ,  $\text{MnO}_2$ /PS, UV/PS, and  $\text{MnO}_2$ /UV/PS processes. Conditions at  $t = 0$  min:  $[\text{BPA}] = 30$  mg/L,  $[\text{PS}] = 1$  mM,  $[\text{MnO}_2] = 0.25$  g/L,  $\text{pH} = 6.5$ ,  $T = 22\text{--}25$  °C.

A TOC analyzer was employed to explore the mineralization of BPA in the above-noted seven processes. Figure 1b shows that the TOC removal efficiencies of these seven processes were quite different. The TOC removal efficiencies of the PS,  $\text{MnO}_2$ , and UV processes after 2 h of treatment were 0%, 4.8%, and 5.8%, respectively, indicating the sole processes could barely mineralize BPA from the aqueous phase. The TOC removal efficiency in the UV/ $\text{MnO}_2$  process was enhanced to 16.4%, which implied the combination of UV irradiation and  $\text{MnO}_2$  had a positive effect on BPA mineralization. The  $\text{MnO}_2$ /PS process further increased the removal efficiency to 77.0%. Huang and Zhang [31] suggested that  $\text{MnO}_2$  activated PS could promote the generation of radicals (such as  $\text{SO}_4^{\bullet-}$  and  $\bullet\text{OH}$ ) to remove organic pollutants. The results of the UV/PS process showed that BPA could be removed entirely in 45 min, but the TOC value remained high, even after 2 h of treatment (40.0% of the mineralization rate). PS residuals in the  $\text{MnO}_2$ /PS, UV/PS, and  $\text{MnO}_2$ /UV/PS processes (Figure S1) suggested the UV irradiation was the main factor in the acceleration of PS decomposition. Meanwhile, the  $\text{MnO}_2$ /PS process showed high effectiveness in the BPA mineralization. Remarkably, the  $\text{MnO}_2$ /UV/PS process could achieve more than 90.0% of TOC removal efficiency in 2 h, which demonstrated that PS activation by the combination of UV and  $\text{MnO}_2$  could effectively improve the BPA and TOC removal from water.

## 2.2. Effects of $\text{MnO}_2$ Dosages, PS Concentrations, and pH Levels on BPA Degradation

We further evaluated the effects of the  $\text{MnO}_2$  dosages, PS concentrations, and pH levels on BPA degradation using the  $\text{MnO}_2$ /UV/PS process within 30 min. Figure 2a shows that the extent of BPA degradation was gradually promoted with the increased  $\text{MnO}_2$  dosages (0.05–0.30 g/L) due to the availability of more surface sites for PS activation. Complete BPA degradation was observed with a  $\text{MnO}_2$  dosage of 0.25 g/L; further increasing dosages slightly improved degradation. The effects of PS concentrations were then evaluated under the conditions of 0.25 g/L  $\text{MnO}_2$  and UV irradiation (Figure 2b). Compared with the effect of  $\text{MnO}_2$ , increasing PS concentration enhanced BPA degradation to a greater extent, leading to a complete BPA removal at 1 mM PS. The further increase of PS dosages only promoted the removal rate slightly, indicating that the concentration of 1 mM was sufficient for BPA degradation. Therefore, 0.25 g/L  $\text{MnO}_2$  and 1 mM PS was optimized for the efficient degradation of BPA in our study.

As can be seen, BPA could be effectively degraded with an efficiency of over 80% in a wide range of pH levels (3.6 to 10.0) (Figure 2c). The degradation rate was relatively low under acidic conditions (pH 3.6 and 5.0). The lowest reaction rate occurred at pH 5.0. According to the reports by Criquet and Leitner [32], this phenomenon was caused by



the increased consumption of  $\text{SO}_4^{\bullet-}$  by acetic acid in buffer at pH 5.0 compared to other pH levels. At pH 6.5, the improved BPA degradation was achieved comparing with acidic conditions. At pH 8.0 and 10.0, a slight improvement of BPA degradation could be due to the additional PS activation by alkaline conditions [33]. Lee, Von Gunten, and Kim [29] suggested that the main oxidants may change from  $\text{SO}_4^{\bullet-}$  to  $\bullet\text{OH}$  under alkaline conditions, leading to the abatement of organics that persisted in PS activation. From Figure 2d, the PS decomposition rate can be seen to have gradually increased along with the increased pH value. In contrast, the contaminant degradation was significant in acidic (pH 4.0) conditions, and decreased at neutral (pH 7.0) and alkaline (pH 10.0) conditions in the PMS activation process [28]. The high efficiency of the  $\text{MnO}_2$ /UV/PS oxidation process in a wide range of pH levels (pH from 3.6 to 10.0) suggests its robust capacity in treating wastewater with broad pH ranges.

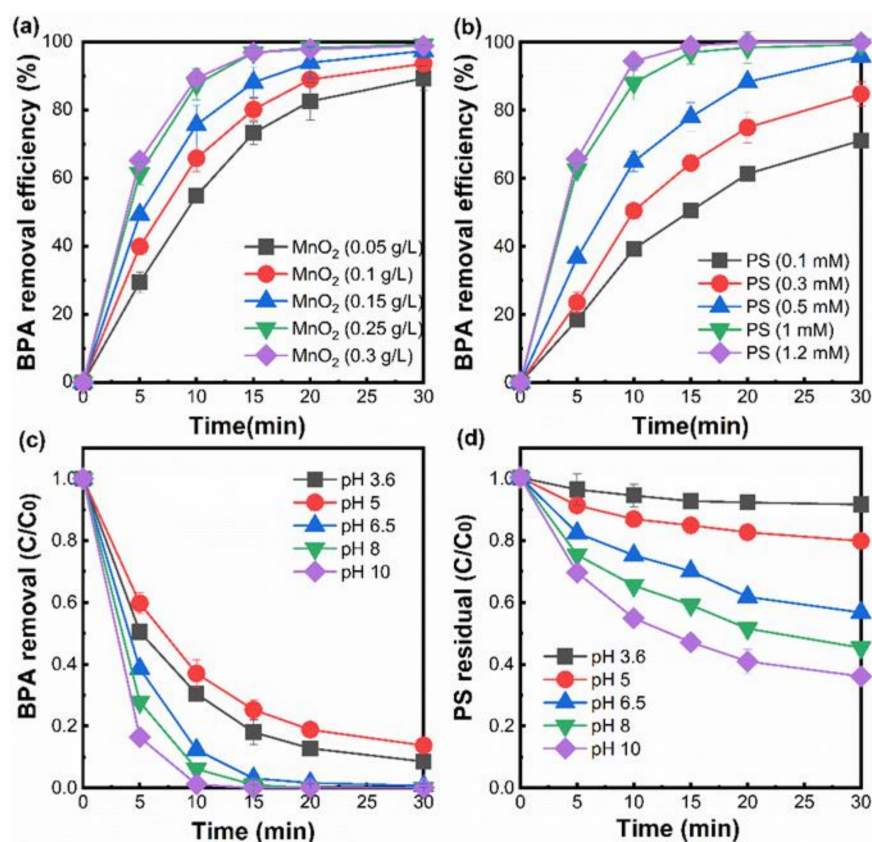


**Figure 2.** Effects of (a)  $\text{MnO}_2$  dosages, (b) PS concentration, and (c) pH level on BPA removal, and PS residual in different pH levels (d). Conditions at  $t = 0$  min: [BPA] = 30 mg/L, pH in (a) and (b) = 6.5, [PS] in (a) and (c) = 1 mM,  $[\text{MnO}_2]$  in (b) and (c) = 0.25 g/L.

### 2.3. Kinetic Evaluation and Reaction Mechanism Analysis

#### 2.3.1. Synergistic Effect of $\text{MnO}_2$ and UV

Batch tests of three processes ( $\text{MnO}_2$ /PS, UV/PS, and  $\text{MnO}_2$ /UV/PS) were implemented for 30 min to explore the synergistic effect of  $\text{MnO}_2$  and UV as the hybrid catalyst of PS. The pseudo-first-order kinetic behaviors of the three processes are shown in Figure 3. The rate constants of both the  $\text{MnO}_2$ /PS process ( $k_{\text{MnO}_2/\text{PS}} = 0.0334 \text{ min}^{-1}$ ) and the UV/PS process ( $k_{\text{UV/PS}} = 0.1177 \text{ min}^{-1}$ ) were found to be lower than that of the  $\text{MnO}_2$ /UV/PS process ( $k_{\text{MnO}_2/\text{UV/PS}} = 0.2196 \text{ min}^{-1}$ ). The degree of synergy between  $\text{MnO}_2$  and UV as the hybrid catalyst was calculated from the rate constants according to Equation (1) [34]. The calculated degree of synergy value (%S) of 31.2% for the hybrid  $\text{MnO}_2$ /UV/PS process reflected the synergistic PS catalytic activation by  $\text{MnO}_2$  and UV, which accelerated BPA removal beyond the sum of the rates achieved by the independent  $\text{MnO}_2$ /PS and UV/PS

processes. To explore the mechanism of the  $\text{MnO}_2/\text{UV}/\text{PS}$  process, quenching experiments were conducted as discussed in the following section.

$$\%S = \frac{k_{\text{MnO}_2/\text{UV}/\text{PS}} - (k_{\text{MnO}_2/\text{PS}} + k_{\text{UV}/\text{PS}})}{k_{\text{MnO}_2/\text{UV}/\text{PS}}} \times 100 \quad (1)$$

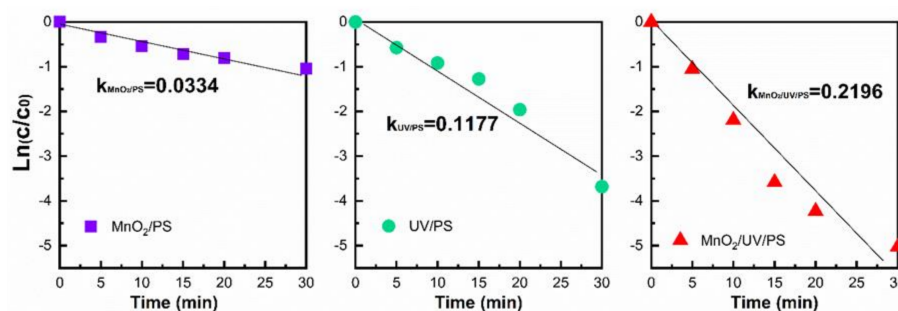
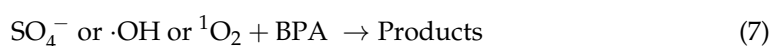
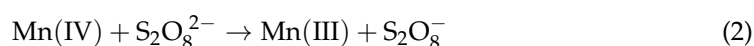


**Figure 3.** BPA degradation using  $\text{MnO}_2/\text{PS}$ ,  $\text{UV}/\text{PS}$ , and  $\text{MnO}_2/\text{UV}/\text{PS}$  processes over 30 min.  $k$  = rate constant of pseudo-first-order kinetics. Conditions at  $t = 0$  min:  $[\text{BPA}] = 30$  mg/L,  $[\text{PS}] = 1$  mM,  $[\text{MnO}_2] = 0.25$  g/L,  $\text{pH} = 6.5$ .

### 2.3.2. Contribution of ROS ( $\bullet\text{OH}$ , $\text{SO}_4^{\bullet-}$ , and $^1\text{O}_2$ )

To elucidate the ROS involved in the  $\text{MnO}_2/\text{PS}$ ,  $\text{UV}/\text{PS}$ , and  $\text{MnO}_2/\text{UV}/\text{PS}$  processes for BPA catalytic degradation, quenching experiments using MeOH, TBA, and FFA were carried out. The  $\text{UV}/\text{MnO}_2$  process was also tested as a control. The MeOH could rapidly react with both  $\text{SO}_4^{\bullet-}$  ( $k = 2.5 \times 10^7 \text{ M}^{-1}\text{s}^{-1}$ ) and  $\bullet\text{OH}$  ( $k = 9.7 \times 10^8 \text{ M}^{-1}\text{s}^{-1}$ ), and TBA could rapidly quench  $\bullet\text{OH}$  with a rate constant in the range of  $3.8\text{--}7.6 \times 10^8 \text{ M}^{-1}\text{s}^{-1}$  [25]. As the rate constant for TBA quenching of  $\bullet\text{OH}$  was 1000 times higher than that with  $\text{SO}_4^{\bullet-}$ , it was frequently employed as a  $\bullet\text{OH}$  scavenger [28]. The FFA was confirmed to effectively quench singlet oxygen ( $^1\text{O}_2$ ) with a rate constant of  $1.2 \times 10^8 \text{ M}^{-1}\text{s}^{-1}$  [35,36]. Therefore, in this study, MeOH (1 M), TBA (1 M), and FFA (5 mM) were used to distinguish between  $\text{SO}_4^{\bullet-}$ ,  $\bullet\text{OH}$ , and  $^1\text{O}_2$ , respectively. All the scavenger concentrations were excessive according to previous studies [37]. The dynamic performance of the above four BPA catalytic degradation processes was evaluated in the same conditions.

The control test showed that only limited  $^1\text{O}_2$  and  $\bullet\text{OH}$  could be generated in the  $\text{UV}/\text{MnO}_2$  process to degrade BPA (Figure S2). In the  $\text{MnO}_2/\text{PS}$  process (Figure 4a), FFA slightly inhibited BPA degradation by decreasing BPA removal efficiency from 65.0% to 62.0%, while a 55.0% removal rate was observed with TBA; however, MeOH showed the strongest inhibition effect by decreasing the BPA removal efficiency to 40.0%, indicating that  $\text{SO}_4^{\bullet-}$  had a significant contribution in the  $\text{MnO}_2/\text{PS}$  process. Several chemical reactions likely occurred, resulting in the generation of ROS. Initially, the  $\text{SO}_4^{\bullet-}$  species could be generated according to Equations (2) and (3) [38]. Subsequently, more radicals were produced by the chain reactions initiated by  $\text{SO}_4^{\bullet-}$ , producing  $\bullet\text{OH}$  and  $^1\text{O}_2$  species (Equations (4)–(6)) [37,39]. The quenching experiments proved that the ROS would attack and degrade BPA (Equation (7)).



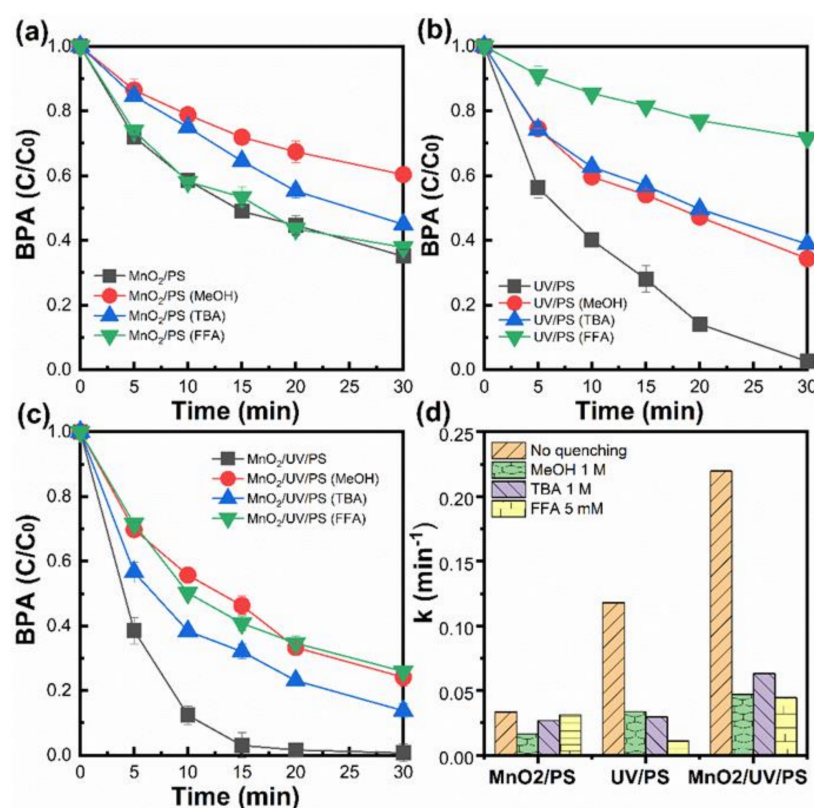


**Figure 4.** Effects of radical inhibitors on BPA concentrations over 30 min for (a) MnO<sub>2</sub>/PS, (b) UV/PS, and (c) MnO<sub>2</sub>/UV/PS processes, and (d) the effects these inhibitors have on the process rate constants. Initial conditions: [BPA] = 30 mg/L, pH = 6.5, [PS] = 1 mM, [MnO<sub>2</sub>] = 0.25 g/L. When an inhibitor is used, initial [MeOH] = 1 M or [TBA] = 1 M or [FFA] = 5 mM.

As shown in Figure 4b, the removal efficiency of BPA in the UV/PS process decreased from 97.0% to 66.0%, 61.0%, and 28.0% after MeOH, TBA, and FFA were added, respectively. These results indicate that SO<sub>4</sub><sup>•−</sup>, •OH, and <sup>1</sup>O<sub>2</sub> were generated, and the <sup>1</sup>O<sub>2</sub> species played a crucial role, followed by SO<sub>4</sub><sup>•−</sup> and •OH. Unlike in the MnO<sub>2</sub>/PS process, upon irradiation with UV light, the peroxy acid O–O bond reportedly underwent a cleavage reaction and generated two equivalents of SO<sub>4</sub><sup>•−</sup> (Equation (7)) [40]. Consequently, ROS such as •OH and <sup>1</sup>O<sub>2</sub> were converted through Equations (4) and (6) [37,39] and further reacted with BPA. Wang et al. [41] confirmed that <sup>1</sup>O<sub>2</sub> was generated under UV irradiation but that this reaction had little effect on the mineralization of organic species. Our study confirmed that the UV/PS process achieved a high BPA removal rate, albeit a lower TOC removal rate (Figure 1b), in agreement with Wang, Teng, Hu, Wu, Huang, Luo, and Christie [41].



The BPA removal efficiency of the MnO<sub>2</sub>/UV/PS process decreased from 100.0% to 76.0%, 86.0%, and 74.0% in the presence of MeOH, TBA, and FFA, respectively (Figure 4c). These findings indicate that plenty of SO<sub>4</sub><sup>•−</sup>, •OH, and <sup>1</sup>O<sub>2</sub> species were generated to decompose BPA (Figure 4d). Among these ROS, <sup>1</sup>O<sub>2</sub> and SO<sub>4</sub><sup>•−</sup> played more critical roles than •OH. The above reactions (Equations (2)–(8)) may also occur in the synergistic process. Given that <sup>1</sup>O<sub>2</sub> had little effect on the mineralization rate of organics, more robust degradation and mineralization occurred when SO<sub>4</sub><sup>•−</sup> attacked the BPA. The detailed parameters before and after quenching experiments are displayed in Table S1. To better understand the interaction between UV irradiation and MnO<sub>2</sub>, more characterization analyses of MnO<sub>2</sub> are discussed below.

#### 2.4. Infrared Spectra of MnO<sub>2</sub> and Mn Leaching in Different Processes

The ATR-FTIR spectra of the MnO<sub>2</sub> particles (Figure 5a) contained several distinct peaks with different changes after 2 h of treatment with the MnO<sub>2</sub>, UV/MnO<sub>2</sub>, MnO<sub>2</sub>/PS, and MnO<sub>2</sub>/UV/PS processes. The bands at around 720 and 650 cm<sup>-1</sup> were assigned to the Mn–O stretching and bending vibrations within a MnO<sub>6</sub> octahedral coordination environment [42,43]. The interactions between manganese and other factors (e.g., UV, persulfate, and BPA) were revealed in the range of 2500 to 1000 cm<sup>-1</sup> [42]. The band at around 1120 cm<sup>-1</sup> could be assigned to vibrations of Mn–OH bonds [44]. A blue-shift of about 52 cm<sup>-1</sup> was observed in both UV/MnO<sub>2</sub> and MnO<sub>2</sub>/UV/PS processes, indicating UV irradiation could affect the bond between Mn and OH. Two bands at around 1653 and 1546 cm<sup>-1</sup> represented the vibrations related to the interactions between Mn centers with OH and related surface groups [45]. A blue shift of about 48 cm<sup>-1</sup> at the peak position 1546 cm<sup>-1</sup> was observed in the MnO<sub>2</sub>/PS and MnO<sub>2</sub>/UV/PS processes, which suggests that PS might affect the MnO<sub>2</sub> surface. A new peak appeared at around 3380 cm<sup>-1</sup>, which only occurred in the MnO<sub>2</sub>/UV/PS process, attributing to the single bond –OH stretching vibration on the MnO<sub>2</sub> surface. For heterogeneous catalytic reactions, the degradation of organics mostly occurred on the surface of the catalyst. The –OH groups on the surface of metal oxides would enhance peroxide activation since they could make a bridge between peroxides and metal oxide surfaces [46,47]. Therefore, the generated –OH groups on the MnO<sub>2</sub> surface might improve BPA degradation in MnO<sub>2</sub>/UV/PS process.

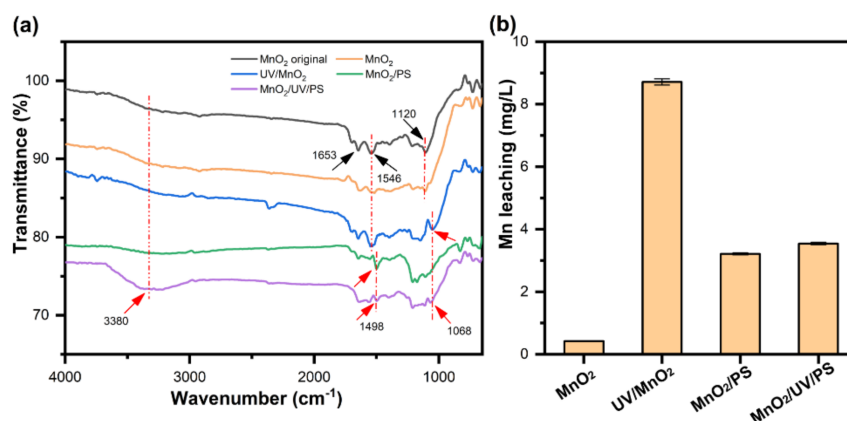


**Figure 5.** ATR-FTIR spectra of MnO<sub>2</sub> particles (a) and the concentration of Mn leaching (b) after 2 h treatment via MnO<sub>2</sub> only, UV/MnO<sub>2</sub>, MnO<sub>2</sub>/PS, and MnO<sub>2</sub>/UV/PS processes.

The ICP-OES was further applied to identify Mn leaching after 2 h of treatment in MnO<sub>2</sub>, UV/MnO<sub>2</sub>, MnO<sub>2</sub>/PS, and MnO<sub>2</sub>/UV/PS processes (Figure 5b). Limited Mn leaching in the MnO<sub>2</sub> process indicates that only a small amount of MnO<sub>2</sub> might be involved in BPA oxidation, which is consistent with the results of the BPA degradation experiments (Figure 1). In contrast, in the UV/MnO<sub>2</sub> process, the Mn leaching was significantly increased to 8.71 mg/L. Therefore, UV irradiation could stimulate the surface of MnO<sub>2</sub> to produce more Mn ions. The Mn leaching (3.21 mg/L) was relatively moderate in the MnO<sub>2</sub>/PS process. Intriguingly, compared with the MnO<sub>2</sub>/PS process, only 0.30 mg/L of Mn leaching was increased in the MnO<sub>2</sub>/UV/PS process. In the UV/MnO<sub>2</sub> process, high Mn leaching had little effect on BPA mineralization (Figure 1b). Fortunately, in the UV/MnO<sub>2</sub>/PS process, Mn leaching was greatly reduced, and BPA mineralization was significantly increased. When PS was present, UV irradiation might promote the formation of –OH groups on the surface of MnO<sub>2</sub> to protect the structure of MnO<sub>2</sub> and decrease Mn leaching.

A relatively high concentration of Mn leaching was observed in our study, mainly due to the long reaction time (2 h) for organic mineralization (e.g., over 90.0% TOC removed). Relatively low concentrations of Mn leaching were reported given the short reaction time (less than 1 h), in which thorough mineralization of organics was not consid-



ered [28,47,48]. In future research, we aim to investigate methods to decrease Mn leaching while maintaining high organic mineralization.

### 2.5. Reusability of $\text{MnO}_2$

To test the reusability of the photocatalyst,  $\text{MnO}_2$  particles were recovered and reused five times with the same initial conditions in the  $\text{MnO}_2/\text{PS}$  and  $\text{MnO}_2/\text{UV}/\text{PS}$  processes. As shown in Figure 6, the removal rate of BPA in the  $\text{MnO}_2/\text{UV}/\text{PS}$  process was 100.0% in the first three recycles and only decreased by 12.0% after five recycles; however, the removal rate of BPA continuously decreased from the initial 65.0% to 34.0% in the  $\text{MnO}_2/\text{PS}$  process. The  $\text{MnO}_2$  particles in the  $\text{MnO}_2/\text{UV}/\text{PS}$  process showed excellent stability for BPA degradation; this may be because the surface hydroxyl groups were generated under UV irradiation, which was confirmed by the ATR-FTIR results (Figure 5a). The recovered  $\text{MnO}_2$  particles had obvious agglomeration from the fourth cycle, leading to decreased surface contact with PS and reduced BPA removal. In addition, both XRD (Figure S3) and SEM (Figure S4) results manifested no significant change of the crystal structure, and morphology of  $\text{MnO}_2$  was observed after reactions in the  $\text{MnO}_2/\text{UV}/\text{PS}$  process.

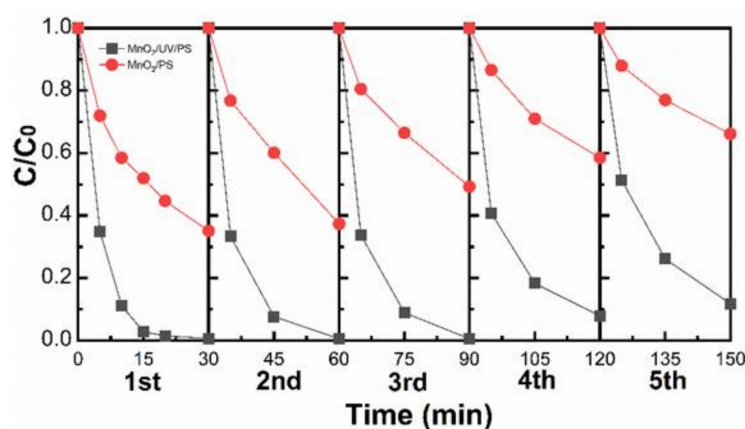


Figure 6.  $\text{MnO}_2$  recycles in  $\text{MnO}_2/\text{PS}$  and  $\text{MnO}_2/\text{UV}/\text{PS}$  processes.

### 2.6. Proposed Degradation Products and Pathways

To determine the BPA catalytic degradation pathways and intermediates under the  $\text{MnO}_2/\text{UV}/\text{PS}$  process, the reaction solutions (after 5, 15, 30, 60, 90, and 120 min) were subjected to a GC-MS analysis after extraction and derivatization. As shown in Table S2, 13 products were identified as their silylated derivatives, some of which had been proposed in previous studies. The fragment ions for both BPA and intermediates are given in Figure S5. Some degradation products may have remained unidentified in this study, as not all components could be effectively extracted into methylene chloride.

Based on the intermediates identified by GC-MS, BPA catalytic degradation via the  $\text{MnO}_2/\text{UV}/\text{PS}$  process, we propose that they occur in five steps (Figure 7). Both charge and spin densities, calculated using density functional theory, indicate that the 1, 2, 4, 6, and 7 positions of BPA (shown in red in Figure 7 top) were the most susceptible to free radical attacks [30,49]. In the first step, attacks at positions 2 and 6 were considered, and the BPA oxidative condensation through C–C and ether bridges between two phenyl rings led to the formation of dimers, such as P12 and P13. Previous studies confirmed that such condensation reactions commonly occurred upon the oxidation of phenolic compounds [50,51]. It is worth noting that these dimers were very unstable and gradually decomposed as the reaction proceeded (Figure S6). In the second step, it was presumed that the free radicals attacked both BPA and the dimers formed in the first step at positions 1, 4, and 7. The rupture of phenolic C–O and O–H bonds and the C–C bond (between phenyl and isopropyl groups) led to the formation of three active species containing phenol moieties of BPA, labeled BPA-1, BPA-2, and BPA-3. In the third step, we propose that a variety of rearrangement reactions occurred among these active species. For instance,

the coupling reaction between BPA-1 and BPA-2 would generate P11. The BPA-2 was further oxidized, subsequently recombining with another molecule of BPA directly at the position of 2 to create the ether P10. The generation of P8 was formed by hydroxylation that occurred when water molecules attacked the aromatic ring through electrophilic action [52]. Meanwhile, multiple BPA intermediates were considered to undergo coupling and deprotonation reactions to generate P9. In the fourth step, the carbocation of BPA-3 could trigger a suite of oxidation, substitution, or elimination reactions to yield P1, P2, P3, P4, and P5. In detail, the BPA-3 was subject to deprotonation to give P4 or substitution by hydroxyl, yielding P2. The elimination reaction of P2 produced P3. The BPA-3 could be subject to ketonization, generating P5, or elimination reaction, producing P1. Subsequently, the fifth step would take place with the cleavage of the phenyl rings by a free radical attack. Long-chain carboxylic acids would be produced during this step by the combination of fragments (P6 and P7) [51,53]. Finally, these long-chain compounds would continue to be converted into small molecules, such as oxalic and malonic acids [54], and ultimately into carbon dioxide and water.

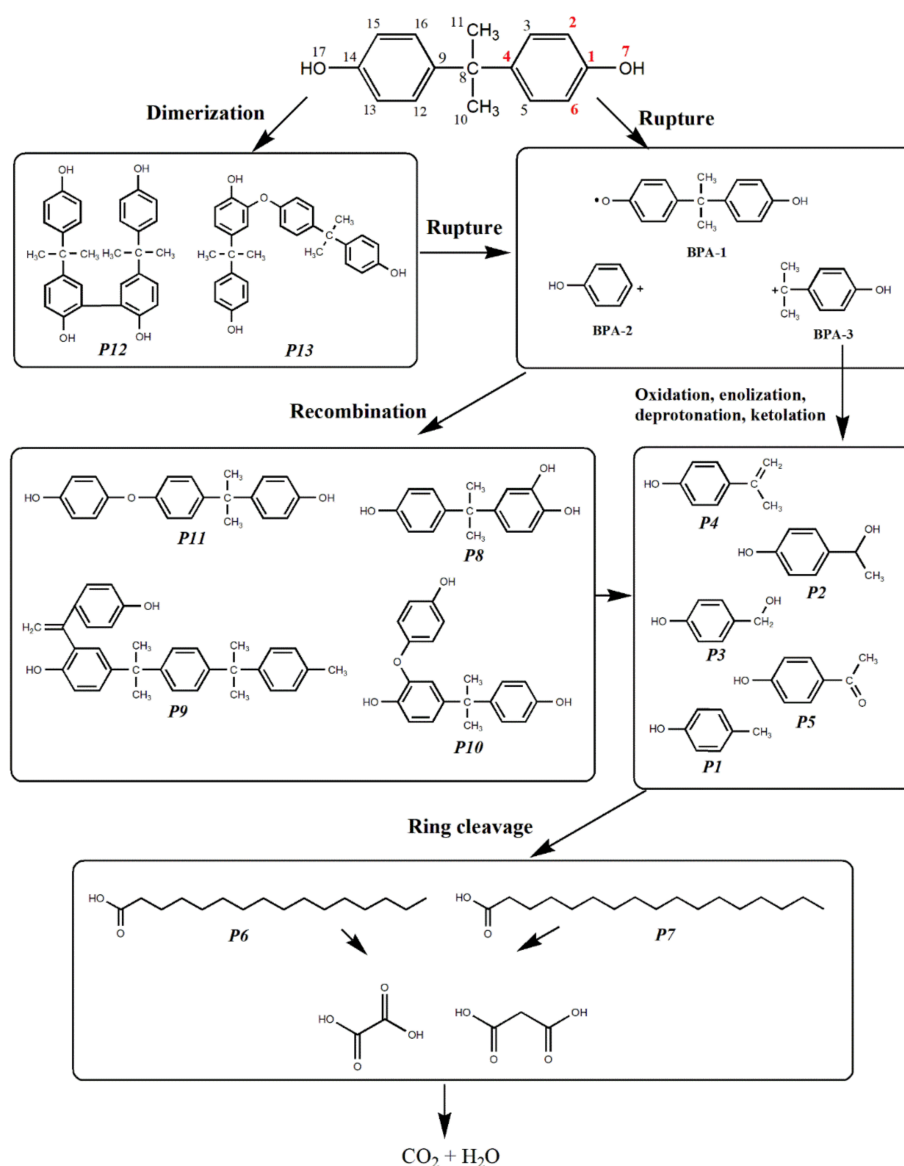


**Figure 7.** Proposed main BPA degradation pathways with steps leading to the intermediates identified using GC-MS (Table S2) under the MnO<sub>2</sub>/UV/PS process.

### 2.7. Acute Toxicity Evaluation

The toxicity of the BPA solution in the  $\text{MnO}_2$ /UV/PS process was monitored over 2 h with and without a buffer (pH 6.5). The estimated  $\text{EC}_{50}$  value of the initial BPA solution was 2.06 mg/L in the present study, which is lower than previous reports (3.46–7.7 mg/L) [55,56]; this may be because the  $\text{MnO}_2$  and PS were present in our initial BPA sample, causing the increased toxicity. Given these influencing factors, we evaluated a relative trend of the toxicity changes in the reaction process. Moreover, the samples were diluted four-fold before testing to concentrations that help provide a consistent instrumental response.

As shown in Figure 8, the  $\text{EC}_{50}$  value increased from 17.5% to 75.0% within 30 min, and then gradually decreased to 27.7% after 2 h without buffer. In the unbuffered process, the pH decreased from 6.5 for the initial BPA solution to 5.5 after 30 min, and to 2.9 after 120 min. Considering that luminescent bacterial metabolism is inhibited by overly acidic environments, as the pH value of the reaction mixture decreased, the increase in toxicity was observed by declining bioluminescence. In order to discern the effect of pH on the toxicity determination, a phosphate buffer was used to maintain the pH of the reaction mixture at 6.5. We observed that the  $\text{EC}_{50}$  value decreased slightly by 3.3% after the first 30 min of the process, followed by a substantial four-fold increase by 82.5% after 2 h. In the above discussion and Figure 1, we confirmed that the concentration of BPA and TOC of the reaction mixture decreased rapidly, especially in the first 30 min; therefore, we conclude that the increased toxicity observed in the first 30 min could be caused by some BPA degradation intermediates. Figure S6 shows that the intermediates were observed after the first 30 min of the process and that most of these gradually degraded at process times of between 30 and 120 min. These results are consistent with the toxicity test.

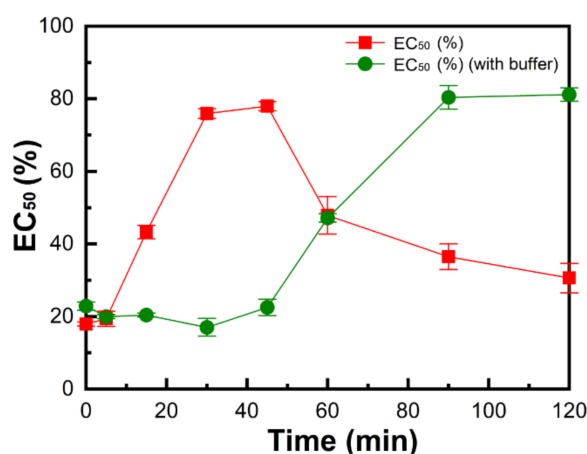


**Figure 8.**  $\text{EC}_{50}$  of  $\text{MnO}_2$ /UV/PS process mixtures determined after four-fold dilution with the Microtox® Basic test. Initial conditions: [BPA] = 30 mg/L, [PS] = 1 mM, [ $\text{MnO}_2$ ] = 0.25 g/L, with (out) phosphate buffer, pH = 6.5.

## 3. Materials and Methods

### 3.1. Chemicals and Reagents

BPA (2, 2-bis (4-hydroxyphenyl) propane, purity > 99%),  $\text{MnO}_2$  (particle size = 10  $\mu\text{m}$ ), sodium persulfate (PS, purity > 99%), methanol (MeOH), tert-butyl alcohol (TBA), furfuryl alcohol (FFA), sodium acetate, acetic acid, sodium monohydrogen phosphate, disodium hydrogen phosphate, sodium carbonate, bicarbonate, toluene, and phosphoric acid were purchased from Sigma-Aldrich (Oakville, ON, Canada). N, O-bis(trimethylsilyl)trifluoroacetamide with trimethylchlorosilane (BSTFA + TMCS) for gas chromatography derivatization, LiChropur™, containing 1% TMCS, 99% (excluding TMCS) was purchased from Sigma-Aldrich (Oakville, ON, Canada), as well.

### 3.2. Degradation Experiments

All degradation experiments were conducted in 200 mL glass bottles placed on a room temperature shaker (280 r/min) (Figure S7). A 30 mg/L sample of the BPA solution prepared with deionized water was placed in each glass bottle. PS (1 mM) and  $\text{MnO}_2$  (0.25 g/L) were added into each glass bottle. A UV-254 nm (UVP 90-0012-01 Model) source (Krackeler Scientific, Albany, NY, USA) was used to treat the solutions. The UV lamp was inserted into the glass bottle and protected by a quartz tube. The tinfoil was wrapped outside the glass bottle to ensure that the experiment was carried out safely (Figure S7). In the evaluation of the impact of solution pH, different buffers were adopted using sodium acetate and acetic acid for pH 3.6 and 5.0, sodium dihydrogen phosphate and disodium hydrogen phosphate for pH 6.5 and 8.0, and sodium carbonate and bicarbonate for pH 10.0.

### 3.3. Analysis of Water Samples

The water samples were collected by syringe and first filtered through 0.22  $\mu\text{m}$  membrane filters, and the BPA concentrations were analyzed using a high-performance liquid chromatography (HPLC) instrument with a C18 column (Agilent 1260 Infinity II, Mississauga, ON, Canada). An acetonitrile/water (50:50, v/v) mixture was used as a mixed mobile phase at a flow rate of 1 mL/min. The detection wavelength was 276 nm. Under these conditions, the BPA peak in the chromatogram corresponds to an elution time of 6.24 min. The total organic carbon (TOC) concentrations were measured by the burning oxidation-non-dispersive infrared absorption method using a Shimadzu TOC-L analyzer (Shimadzu, Tokyo, Japan). Phosphoric acid was added into the samples before measuring TOC to maintain the solution pH < 1. The pH was measured using a pH meter (EL20, Mettler Toledo®, Mississauga, ON, Canada). The PS concentrations were detected following a modified spectrophotometric method [57] (Text S1). The leached Mn concentrations in different processes were measured using an inductively coupled plasma optical emission spectrometer (ICP-OES, LabX, Midland, ON, Canada).

### 3.4. Characterization and Recovery of $\text{MnO}_2$

The surface functional groups of  $\text{MnO}_2$  before and after degradation reaction in  $\text{MnO}_2$ , UV/ $\text{MnO}_2$ ,  $\text{MnO}_2$ /PS, and  $\text{MnO}_2$ /UV/PS processes were characterized using Fourier-transform infrared spectroscopy with attenuated total reflectance (ATR-FTIR). Other characterization methods (XRD and SEM) are listed in the supplementary materials (Text S2). Based on the XRD results, the  $\text{MnO}_2$  used in this study is consistent with the phase of  $\beta$ - $\text{MnO}_2$ ; this phase had the highest efficiency on PS activation [37].  $\text{MnO}_2$  particles were recovered and dried in a vacuum oven (Fisherbrand Isotemp Model 281A, Fisher Scientific, Ottawa, ON, Canada, set at 60 °C, 12 h).

### 3.5. Intermediates Analysis

To analyze the BPA degradation intermediates in the  $\text{MnO}_2$ /UV/PS process, the reaction solutions (at 0, 5, 15, 30, 60, 90, and 120 min) were analyzed using Agilent 7890 GC coupled with an Agilent 5975 MS (Agilent technologies, Mississauga, ON, Canada). The details of BPA extraction, derivatization, and GC-MS analysis methods were based on previous studies [30,58,59] (Text S3).

### 3.6. Toxicity Evaluation

Acute toxicity tests of the  $\text{MnO}_2$ /UV/PS-treated samples were carried out using a Microtox® Model 500 (M500) analyzer, whose primary indicator is the luminous bacterium *Vibrio fischeri*. The acute toxicity test relies on bacterial luminescence via cellular respiration. Inhibition of cellular activity (caused by exposure to toxins, acidic or alkaline conditions, etc.) decreases the respiratory rate, leading to a corresponding decrease in luminosity. The pH range of 6.0–8.5 is recommended to be the standard since *V. fischeri* is pH-sensitive [60]. The toxicity testing of BPA and its intermediates were conducted both with and without phosphate buffer (pH = 6.5). In addition to BPA, the presence



of MnO<sub>2</sub> particles, PS, etc., would affect the light-emitting bacteria, so each sample was diluted before testing. To ensure consistency, the first sample was quickly obtained in the presence of MnO<sub>2</sub> and PS. Therefore, the measured effective concentration that was given the half-maximal response (EC<sub>50</sub>) of the original BPA might differ from the value given in the literature [55,56].

#### 4. Conclusions

This study proposed an integrated MnO<sub>2</sub>/UV-activated PS process for BPA catalytic degradation and demonstrated that the synergistic use of MnO<sub>2</sub> and UV is a more powerful hybrid catalyst of PS in this AOP. The mineralization of the MnO<sub>2</sub>/UV/PS process was significantly improved in comparison with MnO<sub>2</sub> or UV as a single catalyst. This process also showed a stable removal efficiency with a large variation of pH levels (3.6 to 10.0). The presence of SO<sub>4</sub><sup>•−</sup> and <sup>1</sup>O<sub>2</sub> was the key to the more rapid decomposition of BPA. Infrared spectra showed that UV irradiation could stimulate the generation of –OH groups on the MnO<sub>2</sub> surface, facilitating the PS activation in this process. The degradation pathways consisting of 5 steps and 13 intermediates were further investigated using GC-MS. The acute toxicity of reaction mixtures during the process was evaluated, which confirmed the overall reduction by the proposed method. These findings indicated that the combination of MnO<sub>2</sub> with UV improved PS catalytic activation as a more promising means of treating persistent and emerging organic pollutants. Our current research includes controlling the Mn leaching and applying other water matrixes (like real wastewater) to evaluate the feasibility of this process.

**Supplementary Materials:** The supplementary data, figures, and tables are provided in Supplementary Materials. The following are available online at <https://www.mdpi.com/article/10.3390/catal11040502/s1>.

**Author Contributions:** Conceptualization, G.D. and B.C.; methodology, G.D. and B.L.; resources, G.D., Y.C. and M.Y.; writing—original draft preparation, G.D.; writing—review and editing, G.D., B.L., S.R.S. and B.C.; supervision, B.C., S.R.S. and B.Z.; project administration, B.C. All authors have read and agreed to the published version of the manuscript.

**Funding:** This research received no external funding.

**Data Availability Statement:** The raw data supporting the conclusions of this article will be made available by the authors, without undue reservation, to any qualified researcher.

**Acknowledgments:** This research was supported by the Natural Sciences and Engineering Research Council of Canada (NSERC) and the Canada Foundation for Innovation (CFI), as well as the NSERC Collaborative Research and Training Experience (CREATE) Program and PEOPLE Network. S.R.S. acknowledged the support of the Government of Canada's Program of Energy Research and Development (PERD). The authors acknowledge Lindsay J. Hounjet, Natural Resources Canada, and CanmetENERGY Devon, for their valuable comments.

**Conflicts of Interest:** The authors declare no conflict of interest.

**Copyright Statement:** © Her Majesty the Queen in Right of Canada, as represented by the Minister of Natural Resources Canada, 2021.

#### References

1. Ouada, S.B.; Ali, R.B.; Leboulanger, C.; Ouada, H.B.; Sayadi, S. Effect of Bisphenol A on the extremophilic microalgal strain *Picocystis* sp. (Chlorophyta) and its high BPA removal ability. *Ecotoxicol. Environ. Saf.* **2018**, *158*, 1–8. [CrossRef] [PubMed]
2. Santangeli, S.; Maradonna, F.; Gioacchini, G.; Cobellis, G.; Piccinetti, C.C.; Dalla Valle, L.; Carnevali, O. BPA-induced deregulation of epigenetic patterns: Effects on female zebrafish reproduction. *Sci. Rep.* **2016**, *6*, 1–11. [CrossRef] [PubMed]
3. Newbold, R.R.; Jefferson, W.N.; Padilla-Banks, E. Long-term adverse effects of neonatal exposure to bisphenol A on the murine female reproductive tract. *Reprod. Toxicol.* **2007**, *24*, 253–258. [CrossRef] [PubMed]
4. Monje, L.; Varayoud, J.; Muñoz-de-Toro, M.; Luque, E.H.; Ramos, J.G. Exposure of neonatal female rats to bisphenol A disrupts hypothalamic LHRH pre-mRNA processing and estrogen receptor alpha expression in nuclei controlling estrous cyclicity. *Reprod. Toxicol.* **2010**, *30*, 625–634. [CrossRef] [PubMed]

5. Huang, Y.; Wong, C.; Zheng, J.; Bouwman, H.; Barra, R.; Wahlström, B.; Neretin, L.; Wong, M.H. Bisphenol A (BPA) in China: A review of sources, environmental levels, and potential human health impacts. *Environ. Int.* **2012**, *42*, 91–99. [CrossRef]
6. Kwak, J.I.; Moon, J.; Kim, D.; Cui, R.; An, Y.-J. Determination of the soil hazardous concentrations of bisphenol A using the species sensitivity approach. *J. Hazard. Mater.* **2018**, *344*, 390–397. [CrossRef]
7. Yamamoto, T.; Yasuhara, A.; Shiraishi, H.; Nakasugi, O. Bisphenol A in hazardous waste landfill leachates. *Chemosphere* **2001**, *42*, 415–418. [CrossRef]
8. Schwarzbauer, J.; Heim, S.; Brinker, S.; Littke, R. Occurrence and alteration of organic contaminants in seepage and leakage water from a waste deposit landfill. *Water Res.* **2002**, *36*, 2275–2287. [CrossRef]
9. Xiao, C.; Wang, L.; Zhou, Q.; Huang, X. Hazards of bisphenol A (BPA) exposure: A systematic review of plant toxicology studies. *J. Hazard. Mater.* **2020**, *384*, 121488. [CrossRef]
10. Haffner, D.; Schecter, A. Persistent organic pollutants (POPs): A primer for practicing clinicians. *Curr. Environ. Health Rep.* **2014**, *1*, 123–131. [CrossRef]
11. McBean, E. Removal of emerging contaminants: The next water revolution. *J. Environ. Inform. Lett.* **2019**, *1*, 1–7. [CrossRef]
12. Cao, Y.; Yu, M.; Dong, G.; Chen, B.; Zhang, B. Digital PCR as an emerging tool for monitoring of microbial biodegradation. *Molecules* **2020**, *25*, 706. [CrossRef] [PubMed]
13. Ghernaout, D.; Elboughdiri, N. Advanced oxidation processes for wastewater treatment: Facts and future trends. *Open Access Libr. J.* **2020**, *7*, 1–15. [CrossRef]
14. Liu, B.; Chen, B.; Zhang, B.; Song, X.; Zeng, G.; Lee, K. Photocatalytic ozonation of offshore produced water by TiO<sub>2</sub> nanotube arrays coupled with UV-LED irradiation. *J. Hazard. Mater.* **2021**, *402*, 123456. [CrossRef] [PubMed]
15. Oh, W.-D.; Dong, Z.; Lim, T.-T. Generation of sulfate radical through heterogeneous catalysis for organic contaminants removal: Current development, challenges and prospects. *Appl. Catal. B Environ.* **2016**, *194*, 169–201. [CrossRef]
16. Lin, Y.-T.; Chiu, Y.-T.; Ciou, C.; Liang, C. Natural organic activator quercetin for persulfate oxidative degradation of halogenated hydrocarbons. *Environ. Sci. Water Res. Technol.* **2019**, *5*, 1064–1071. [CrossRef]
17. Zhao, Q.; Mao, Q.; Zhou, Y.; Wei, J.; Liu, X.; Yang, J.; Luo, L.; Zhang, J.; Chen, H.; Chen, H. Metal-free carbon materials-catalyzed sulfate radical-based advanced oxidation processes: A review on heterogeneous catalysts and applications. *Chemosphere* **2017**, *189*, 224–238. [CrossRef] [PubMed]
18. Li, R.; Hu, H.; Ma, Y.; Liu, X.; Zhang, L.; Zhou, S.; Deng, B.; Lin, H.; Zhang, H. Persulfate enhanced photocatalytic degradation of bisphenol A over wasted batteries-derived ZnFe<sub>2</sub>O<sub>4</sub> under visible light. *J. Clean. Prod.* **2020**, *276*, 124246. [CrossRef]
19. Wang, J.; Wang, S. Activation of persulfate (PS) and peroxymonosulfate (PMS) and application for the degradation of emerging contaminants. *Chem. Eng. J.* **2018**, *334*, 1502–1517. [CrossRef]
20. Petala, A.; Arvaniti, O.S.; Christofili, M.; Safakas, A.; Frontistis, Z.; Mantzavinos, D. Lanthanum Nickel Oxide: An Effective Heterogeneous Activator of Sodium Persulfate for Antibiotics Elimination. *Catalysts* **2020**, *10*, 1373. [CrossRef]
21. Pan, Y.; Zhang, Y.; Zhou, M.; Cai, J.; Tian, Y. Enhanced removal of emerging contaminants using persulfate activated by UV and pre-magnetized FeO. *Chem. Eng. J.* **2019**, *361*, 908–918. [CrossRef]
22. Wang, B.; Fu, T.; An, B.; Liu, Y. UV light-assisted persulfate activation by CuO-Cu<sub>2</sub>O for the degradation of sulfamerazine. *Sep. Purif. Technol.* **2020**, *251*, 117321. [CrossRef]
23. Pan, X.; Yan, L.; Li, C.; Qu, R.; Wang, Z. Degradation of UV-filter benzophenone-3 in aqueous solution using persulfate catalyzed by cobalt ferrite. *Chem. Eng. J.* **2017**, *326*, 1197–1209. [CrossRef]
24. Dong, G.; Huang, L.; Wu, X.; Wang, C.; Liu, Y.; Liu, G.; Wang, L.; Liu, X.; Xia, H. Effect and mechanism analysis of MnO<sub>2</sub> on permeable reactive barrier (PRB) system for the removal of tetracycline. *Chemosphere* **2018**, *193*, 702–710. [CrossRef]
25. Huang, J.; Dai, Y.; Singewald, K.; Liu, C.-C.; Saxena, S.; Zhang, H. Effects of MnO<sub>2</sub> of different structures on activation of peroxymonosulfate for bisphenol A degradation under acidic conditions. *Chem. Eng. J.* **2019**, *370*, 906–915. [CrossRef]
26. Mazloomi, S.; Nasser, S.; Nabizadeh, R.; Yaghmaei, K.; Alimohammadi, K.; Nazmara, S.; Mahvi, A.H. Remediation of fuel oil contaminated soils by activated persulfate in the presence of MnO<sub>2</sub>. *Soil Water Res.* **2016**, *11*, 131–138. [CrossRef]
27. Chiam, S.-L.; Pung, S.-Y.; Yeoh, F.-Y. Recent developments in MnO<sub>2</sub>-based photocatalysts for organic dye removal: A review. *Environ. Sci. Pollut. Res.* **2020**, *27*, 5759–5778. [CrossRef]
28. Eslami, A.; Hashemi, M.; Ghanbari, F. Degradation of 4-chlorophenol using catalyzed peroxymonosulfate with nano-MnO<sub>2</sub>/UV irradiation: Toxicity assessment and evaluation for industrial wastewater treatment. *J. Clean. Prod.* **2018**, *195*, 1389–1397. [CrossRef]
29. Lee, J.; Von Gunten, U.; Kim, J.-H. Persulfate-based advanced oxidation: Critical assessment of opportunities and roadblocks. *Environ. Sci. Technol.* **2020**, *54*, 3064–3081. [CrossRef]
30. Lin, K.; Liu, W.; Gan, J. Oxidative removal of bisphenol A by manganese dioxide: Efficacy, products, and pathways. *Environ. Sci. Technol.* **2009**, *43*, 3860–3864. [CrossRef] [PubMed]
31. Huang, J.; Zhang, H. Mn-based catalysts for sulfate radical-based advanced oxidation processes: A review. *Environ. Int.* **2019**, *133*, 105141. [CrossRef]
32. Criquet, J.; Leitner, N.K.V. Degradation of acetic acid with sulfate radical generated by persulfate ions photolysis. *Chemosphere* **2009**, *77*, 194–200. [CrossRef]
33. Lominchar, M.; Santos, A.; De Miguel, E.; Romero, A. Remediation of aged diesel contaminated soil by alkaline activated persulfate. *Sci. Total Environ.* **2018**, *622*, 41–48. [CrossRef] [PubMed]

34. Frontistis, Z.; Daskalaki, V.M.; Hapeshi, E.; Drosou, C.; Fatta-Kassinos, D.; Xekoukoulotakis, N.P.; Mantzavinos, D. Photocatalytic (UV-A/TiO<sub>2</sub>) degradation of 17 $\alpha$ -ethynylestradiol in environmental matrices: Experimental studies and artificial neural network modeling. *J. Photochem. Photobiol. A Chem.* **2012**, *240*, 33–41. [CrossRef]
35. Zhou, Y.; Jiang, J.; Gao, Y.; Ma, J.; Pang, S.-Y.; Li, J.; Lu, X.-T.; Yuan, L.-P. Activation of peroxymonosulfate by benzoquinone: A novel nonradical oxidation process. *Environ. Sci. Technol.* **2015**, *49*, 12941–12950. [CrossRef]
36. Li, C.; Wu, J.; Peng, W.; Fang, Z.; Liu, J. Peroxymonosulfate activation for efficient sulfamethoxazole degradation by Fe<sub>3</sub>O<sub>4</sub>/ $\beta$ -FeOOH nanocomposites: Coexistence of radical and non-radical reactions. *Chem. Eng. J.* **2019**, *356*, 904–914. [CrossRef]
37. Zhu, S.; Li, X.; Kang, J.; Duan, X.; Wang, S. Persulfate activation on crystallographic manganese oxides: Mechanism of singlet oxygen evolution for nonradical selective degradation of aqueous contaminants. *Environ. Sci. Technol.* **2018**, *53*, 307–315. [CrossRef]
38. Zhao, Y.; Zhao, Y.; Zhou, R.; Mao, Y.; Tang, W.; Ren, H. Insights into the degradation of 2,4-dichlorophenol in aqueous solution by  $\alpha$ -MnO<sub>2</sub> nanowire activated persulfate: Catalytic performance and kinetic modeling. *RSC Adv.* **2016**, *6*, 35441–35448. [CrossRef]
39. Lu, X.; Shao, Y.; Gao, N.; Chen, J.; Zhang, Y.; Xiang, H.; Guo, Y. Degradation of diclofenac by UV-activated persulfate process: Kinetic studies, degradation pathways and toxicity assessments. *Ecotoxicol. Environ. Saf.* **2017**, *141*, 139–147. [CrossRef] [PubMed]
40. Liu, Y.; He, X.; Fu, Y.; Dionysiou, D.D. Kinetics and mechanism investigation on the destruction of oxytetracycline by UV-254 nm activation of persulfate. *J. Hazard. Mater.* **2016**, *305*, 229–239. [CrossRef]
41. Wang, A.; Teng, Y.; Hu, X.; Wu, L.; Huang, Y.; Luo, Y.; Christie, P. Photodegradation of diphenylarsinic acid by UV-C light: Implication for its remediation. *J. Hazard. Mater.* **2016**, *308*, 199–207. [CrossRef]
42. Ananth, M.; Pethkar, S.; Dakshinamurthi, K. Distortion of MnO<sub>6</sub> octahedra and electrochemical activity of Nstutite-based MnO<sub>2</sub> polymorphs for alkaline electrolytes—An FTIR study. *J. Power Sources* **1998**, *75*, 278–282. [CrossRef]
43. Xie, J.; Chen, L.; Zhou, W.-F.; Au, C.-T.; Yin, S.-F. Selective oxidation of p-chlorotoluene to p-chlorobenzaldehyde over metal-modified OMS-2 molecular sieves. *J. Mol. Catal. A Chem.* **2016**, *425*, 110–115. [CrossRef]
44. Liu, R.; Liu, H.; Qiang, Z.; Qu, J.; Li, G.; Wang, D. Effects of calcium ions on surface characteristics and adsorptive properties of hydrous manganese dioxide. *J. Colloid Interface Sci.* **2009**, *331*, 275–280. [CrossRef] [PubMed]
45. Khan, A.; Liao, Z.; Liu, Y.; Jawad, A.; Iftikhar, J.; Chen, Z. Synergistic degradation of phenols using peroxymonosulfate activated by CuO-Co<sub>3</sub>O<sub>4</sub>@ MnO<sub>2</sub> nanocatalyst. *J. Hazard. Mater.* **2017**, *329*, 262–271. [CrossRef] [PubMed]
46. Ren, Y.; Lin, L.; Ma, J.; Yang, J.; Feng, J.; Fan, Z. Sulfate radicals induced from peroxymonosulfate by magnetic ferrosphenel MFe<sub>2</sub>O<sub>4</sub> (M= Co, Cu, Mn, and Zn) as heterogeneous catalysts in the water. *Appl. Catal. B Environ.* **2015**, *165*, 572–578. [CrossRef]
47. Dong, Z.; Zhang, Q.; Chen, B.-Y.; Hong, J. Oxidation of bisphenol A by persulfate via Fe<sub>3</sub>O<sub>4</sub>- $\alpha$ -MnO<sub>2</sub> nanoflower-like catalyst: Mechanism and efficiency. *Chem. Eng. J.* **2019**, *357*, 337–347. [CrossRef]
48. Huang, G.-X.; Wang, C.-Y.; Yang, C.-W.; Guo, P.-C.; Yu, H.-Q. Degradation of bisphenol A by peroxymonosulfate catalytically activated with Mn<sub>1.8</sub>Fe<sub>1.2</sub>O<sub>4</sub> nanospheres: Synergism between Mn and Fe. *Environ. Sci. Technol.* **2017**, *51*, 12611–12618. [CrossRef]
49. Yao, J.; Qu, R.; Wang, X.; Sharma, V.K.; Shad, A.; Dar, A.A.; Wang, Z. Visible light and fulvic acid assisted generation of Mn (III) to oxidize bisphenol A: The effect of tetrabromobisphenol A. *Water Res.* **2020**, *169*, 115273. [CrossRef]
50. Zhang, H.; Huang, C.-H. Reactivity and transformation of antibacterial N-oxides in the presence of manganese oxide. *Environ. Sci. Technol.* **2005**, *39*, 593–601. [CrossRef]
51. de Freitas, E.N.; Bubna, G.A.; Brugnari, T.; Kato, C.G.; Nolli, M.; Rauen, T.G.; Moreira, R.D.; Peralta, R.A.; Bracht, A.; de Souza, C.G. Removal of bisphenol A by laccases from *Pleurotus ostreatus* and *Pleurotus pulmonarius* and evaluation of ecotoxicity of degradation products. *Chem. Eng. J.* **2017**, *330*, 1361–1369. [CrossRef]
52. Lin, J.; Hu, Y.; Wang, L.; Liang, D.; Ruan, X.; Shao, S. M88/PS/Vis system for degradation of bisphenol A: Environmental factors, degradation pathways, and toxicity evaluation. *Chem. Eng. J.* **2020**, *382*, 122931. [CrossRef]
53. Molkenthin, M.; Olmez-Hanci, T.; Jekel, M.R.; Arslan-Alaton, I. Photo-Fenton-like treatment of BPA: Effect of UV light source and water matrix on toxicity and transformation products. *Water Res.* **2013**, *47*, 5052–5064. [CrossRef] [PubMed]
54. Kusvuran, E.; Yildirim, D. Degradation of bisphenol A by ozonation and determination of degradation intermediates by gas chromatography–mass spectrometry and liquid chromatography–mass spectrometry. *Chem. Eng. J.* **2013**, *220*, 6–14. [CrossRef]
55. Chiang, K.; Lim, T.M.; Tsen, L.; Lee, C.C. Photocatalytic degradation and mineralization of bisphenol A by TiO<sub>2</sub> and platinized TiO<sub>2</sub>. *Appl. Catal. A Gen.* **2004**, *261*, 225–237. [CrossRef]
56. Tobajas, M.; Verdugo, V.; Polo, A.M.; Rodriguez, J.J.; Mohedano, A.F. Assessment of toxicity and biodegradability on activated sludge of priority and emerging pollutants. *Environ. Technol.* **2016**, *37*, 713–721. [CrossRef] [PubMed]
57. Lee, H.; Lee, H.-J.; Jeong, J.; Lee, J.; Park, N.-B.; Lee, C. Activation of persulfates by carbon nanotubes: Oxidation of organic compounds by nonradical mechanism. *Chem. Eng. J.* **2015**, *266*, 28–33. [CrossRef]
58. Sharma, J.; Mishra, I.; Dionysiou, D.D.; Kumar, V. Oxidative removal of Bisphenol A by UV-C/peroxymonosulfate (PMS): Kinetics, influence of co-existing chemicals and degradation pathway. *Chem. Eng. J.* **2015**, *276*, 193–204. [CrossRef]
59. Cao, Y.; Zhang, B.; Zhu, Z.; Song, X.; Cai, Q.; Chen, B.; Dong, G.; Ye, X. Microbial eco-physiological strategies for salinity-mediated crude oil biodegradation. *Sci. Total Environ.* **2020**, *727*, 138723. [CrossRef]
60. Johnson, B.T. Microtox<sup>®</sup> acute toxicity test. In *Small-Scale Freshwater Toxicity Investigations*; Springer: Berlin/Heidelberg, Germany, 2005; pp. 69–105.

## Article

# Hole Doping to Enhance the Photocatalytic Activity of $\text{Bi}_4\text{NbO}_8\text{Cl}$

Jingbang Sun <sup>1,†</sup>, Ni Han <sup>1,†</sup>, Yan Gu <sup>1</sup>, Xiaowang Lu <sup>1</sup>, Liang Si <sup>2</sup>  and Qinfang Zhang <sup>1,\*</sup> 

<sup>1</sup> School of Materials Science and Engineering, Yancheng Institute of Technology, Yancheng 224001, China; SunJB0604@gmail.com (J.S.); nihanycit112019@gmail.com (N.H.); ygu9705@gmail.com (Y.G.); luxiaowang@ycit.edu.cn (X.L.)

<sup>2</sup> Ningbo Institute of Materials Technology and Engineering (NIMTE), Chinese Academy of Sciences, Ningbo 315201, China; siliang@nimte.ac.cn

\* Correspondence: qfangzhang@ycit.edu.cn or qfangzhang@gmail.com

† They are contributed equally to this work.

Received: 18 November 2020; Accepted: 1 December 2020; Published: 5 December 2020

**Abstract:** An increase of carrier concentration is one of the most important routes for enhancing the catalytic performance of semiconductor photocatalysts. In this study, the Sillén–Aurivillius oxychloride  $\text{Bi}_4\text{NbO}_8\text{Cl}$  with hole doping was successfully prepared by a solid-state reaction method. X-ray powder diffraction (XRD), scanning electron microscopy (SEM), ultraviolet–visible diffuse reflectance spectra (UV–vis DRS), X-ray photoelectron spectrometry (XPS) and photoluminescence spectra (PL) were used to characterize and analyze the prepared samples. The experimental results and density functional theory calculations demonstrate that hole doping can be formed in  $\text{Bi}_4\text{NbO}_8\text{Cl}$  by inserting zinc into the niobium site, and the photocatalytic activity can be improved by introducing additional holes into  $\text{Bi}_4\text{NbO}_8\text{Cl}$ . The photogenerated hole ( $\text{h}^+$ ) is considered to be the main active species to degrade trypan blue (TB) through trapping experiments. The optimal photocatalyst of  $\text{Bi}_4\text{Nb}_{0.8}\text{Zn}_{0.2}\text{O}_8\text{Cl}$  exhibits excellent photocatalytic activity in degradation of trypan blue under visible light irradiation. Moreover, a possible photocatalytic degradation mechanism is discussed according to the experimental and analytical results.

**Keywords:**  $\text{Bi}_4\text{NbO}_8\text{Cl}$ ; hole doping; visible light; photocatalytic degradation

## 1. Introduction

Recently, environmental pollution and energy shortages have become two main challenges for human beings. In particular, the discharge of various organic wastewaters has seriously caused irreversible damage to the environment and human beings [1–3]. Among the reported remediation methods, semiconductor photocatalysis has been regarded as an effective route to eliminate contaminants. In particular, the development of visible light-driven photocatalysts has attracted increasing attention from the perspective of solar energy conversion [4,5].

In recent years, a novel bismuth-based photocatalyst  $\text{Bi}_4\text{NbO}_8\text{Cl}$  has attracted much attention. It has a layered Sillén–Aurivillius perovskite structure and consists of single-layer  $\text{NbO}_4$  perovskite blocks that are separated by  $(\text{Bi}_2\text{O}_2)_2\text{Cl}$  blocks, which is beneficial for the efficient separation and migration of the photogenerated charge carriers. Moreover, the valence band maxima (VBM) of  $\text{Bi}_4\text{NbO}_8\text{Cl}$  is mainly composed of O-2p orbital rather than Cl-3p orbits, so its VBM level is more negative than that of typical oxides [6–8]. Therefore,  $\text{Bi}_4\text{NbO}_8\text{Cl}$  is considered to be a stable visible light-response photocatalyst with narrow bandgap and which is usually applied to degrade organic pollutants. Shi et al. [9] prepared a layered Bi-based oxychloride  $\text{Bi}_4\text{NbO}_8\text{Cl}$ , and found that the visible light-driven photocatalytic activities for degrading methyl orange (MO) over different catalysts

follow the decreasing order of  $\text{Bi}_4\text{NbO}_8\text{Cl} > \text{Bi}_3\text{O}_4\text{Cl} > \text{anatase TiO}_2$ ; Sundaram et al. [10] synthesized  $\text{Bi}_4\text{NbO}_8\text{Cl}$  nanoparticles by a solution combustion method and the mineralization efficiency of Congo red dye can reach 75% in 80 min.

However, in order to further improve the photocatalytic performance of  $\text{Bi}_4\text{NbO}_8\text{Cl}$ , many methods have been developed such as semiconductor recombination [11,12], deposition of noble metals [13,14], deposition of non-noble metals [15] and metal ions doping [16]. Among these methods, transition metal ions doping is considered to be one of the most promising, which can increase carrier concentration and improve the charge carrier transport [17]. Thus, transition ion doping can effectively improve the photocatalytic performance of  $\text{Bi}_4\text{NbO}_8\text{Cl}$ . Shangguan et al. [16] utilized yttrium-doped  $\text{Bi}_4\text{NbO}_8\text{Cl}$  to synthesize  $\text{Bi}_{4-x}\text{Y}_x\text{NbO}_8\text{Cl}$  and enhance photocatalytic activity. As common dopants, doping of transition metals tungsten (W) and zinc (Zn) is considered to be an effective method to improve the photocatalytic activity of semiconductors [18,19].

However, through our investigation, there are few reports preparing tungsten- or zinc-doped  $\text{Bi}_4\text{NbO}_8\text{Cl}$  material and studying their photocatalytic performance. In this work, a series of W-doped and Zn-doped  $\text{Bi}_4\text{NbO}_8\text{Cl}$  materials with different dopant concentrations were synthesized via a solid-state reaction method. The photocatalytic activities of the W-doped and Zn-doped  $\text{Bi}_4\text{NbO}_8\text{Cl}$  materials were investigated by degradation of trypan blue (TB) under visible light. Finally, the possible hole-doping mechanism of photocatalytic degradation of TB was also discussed.

## 2. Results

### 2.1. Synthesis of $\text{Bi}_4\text{Nb}_{1-x}\text{W}_x\text{O}_8\text{Cl}$ and $\text{Bi}_4\text{Nb}_{1-x}\text{Zn}_x\text{O}_8\text{Cl}$ ( $x = 0.1, 0.2, 0.3$ ) Powder

The photocatalysts were synthesized by a solid-state reaction. Firstly, 2 mM  $\text{Bi}(\text{NO}_3)_3 \cdot 5\text{H}_2\text{O}$  was dissolved in 20 mL ethylene glycol, subsequently 10 mL KCl solution (0.2 mol/L) gradually added to obtain the precursor. After filtration and washing, the precursor was dried at 333 K for 12 h to obtain  $\text{BiOCl}$ . Secondly, the stoichiometric amount of prepared  $\text{BiOCl}$ ,  $\text{Bi}_2\text{O}_3$  (Aladdin, 99.9%),  $\text{Nb}_2\text{O}_5$  (Aladdin, 99.9%) and  $\text{WO}_3$  or  $\text{ZnO}$  powders (Aladdin, 99.9%) were adequately ground and calcined in a muffle furnace at 973 K for 24 h. Finally,  $\text{Bi}_4\text{Nb}_{1-x}\text{W}_x\text{O}_8\text{Cl}$  and  $\text{Bi}_4\text{Nb}_{1-x}\text{Zn}_x\text{O}_8\text{Cl}$  ( $x = 0.1, 0.2, 0.3$ ) series powders were prepared.  $\text{WO}_3$  or  $\text{ZnO}$  was used to replace the component of  $\text{Nb}_2\text{O}_5$ , the  $x$  value of the very small part being 0, 0.1, 0.2, 0.3, respectively. The samples with the atomic ratio of Zn to Nb (0, 1:9, 2:8, 3:7) were labeled as BNO, BNZ-1, BNZ-2 and BNZ-3, respectively. Those of W to Nb (1:9, 2:8, 3:7) were labeled as BWZ-1, BWZ-2, BWZ-3, respectively.

### 2.2. Characterization

An X-ray diffractometer (XRD) with Cu  $K\alpha$  radiation (X'Pert<sup>3</sup> Powder, PANalytical, Almelo, the Netherlands,  $\lambda = 0.15406$  nm) was used to carry out of the phase identification. The morphologies of the samples were studied by Nova a Nano 450 (FEI, Hillsboro, OR, USA) field-emission scanning electron microscope (FESEM), X-ray photoelectron spectroscopy (XPS) was performed by an ESCALAB 250xi XPS system (Thermo Fisher Scientific, Carlsbad, CA, USA). A Shimadzu UV-2550 ultraviolet UV-visible diffuse reflectance spectrum (Shimadzu, Kyoto, Japan) was used for the test of the spectral absorption curves of the samples, with a wavelength scanning range of 200–800 nm. The photoluminescence (PL) spectra were collected by a Hitachi F-4600 spectrometer (Hitachi, Tokyo, Japan).

### 2.3. Photocatalytic Activity

Photocatalytic activities of  $\text{Bi}_4\text{Nb}_{1-x}\text{W}_x\text{O}_8\text{Cl}$  and  $\text{Bi}_4\text{Nb}_{1-x}\text{Zn}_x\text{O}_8\text{Cl}$  series were evaluated by degrading TB under a 500 W Xe Lamp (420 nm cut off filter) illumination. In the study of degradation, 30 mg prepared photocatalyst was dispersed evenly in 30 mL TB solution (10 mg/mL) at room temperature. The mixture was magnetically stirred in the dark for 30 min before illumination. Then the TB solution was exposed to visible light illumination with stirring, and 3 mL suspension was collected every 15 min,

and then centrifuged at 12,000 rpm for 5 min to remove the photocatalyst. Finally, the concentration of TB was determined by a spectrophotometer.

#### 2.4. Density Functional Theory (DFT) Calculation

Here, in this paper, we studied the electronic structures of pure and doped  $\text{Bi}_4\text{NbO}_8\text{Cl}$  systems by performing first-principles calculations based on density functional theory (DFT). The Wien2k program package [20] was employed and the Perdew-Burke-Ernzerh (PBE) version of the generalised gradient approximation (GGA) [21] was adopted. We used a  $13 \times 13 \times 2$  momentum grid, and  $R_{\text{MT}}^*K_{\text{max}} = 7.0$  with a muffin-tin radius  $R_{\text{MT}} = 1.84, 2.30, 1.67$  and  $2.5$  a.u. for Nb, Bi, O and Cl atoms, respectively.

The crystal structure presented in Section 3.6 is adopted for calculations. Electron and hole doping are approximately achieved by applying virtual crystal approximation (VCA) implemented in Wien2k. We treat the valence states of W and Zn as  $6s^25d^4$  and  $4s^2$ , respectively. Considering the valence state of Nb is  $5d^14d^4$ , hence 20% W and 20% Zn doping induces 0.2 electron and 0.6 hole doping per Nb, respectively.

### 3. Discussion

#### 3.1. X-Ray Diffractogram (XRD) Patterns Analysis

The XRD patterns of the  $\text{Bi}_4\text{NbO}_8\text{Cl}$ ,  $\text{Bi}_4\text{Nb}_{1-x}\text{W}_x\text{O}_8\text{Cl}$  and  $\text{Bi}_4\text{Nb}_{1-x}\text{Zn}_x\text{O}_8\text{Cl}$  series are shown in Figure 1. As shown in Figure 1a, the diffraction peaks observed are well indexed to the  $\text{Bi}_4\text{NbO}_8\text{Cl}$  (JCPDS NO.84-0843), and no other diffraction peaks can be found. Which indicates that either W or Zn doping does not affect the crystal structure of  $\text{Bi}_4\text{NbO}_8\text{Cl}$ . It is noteworthy that the diffraction peak at about  $29.6^\circ$  slightly shifts to higher angles with the increase of dopant content (Figure 1b). This phenomenon can be attributed to the ionic radius of  $\text{Zn}^{2+}$  ( $0.74 \text{ \AA}$ ) and  $\text{W}^{6+}$  ( $0.62 \text{ \AA}$ ) both being smaller than that of  $\text{Nb}^{5+}$  ( $0.78 \text{ \AA}$ ), the incorporation of W or Zn ions in  $\text{Bi}_4\text{NbO}_8\text{Cl}$  lattice via substituting Nb ions consequently induce distortion in the crystal lattice of  $\text{Bi}_4\text{NbO}_8\text{Cl}$  [18,22,23]. This means that W or Zn elements were successfully doped to the  $\text{Bi}_4\text{NbO}_8\text{Cl}$  lattice.

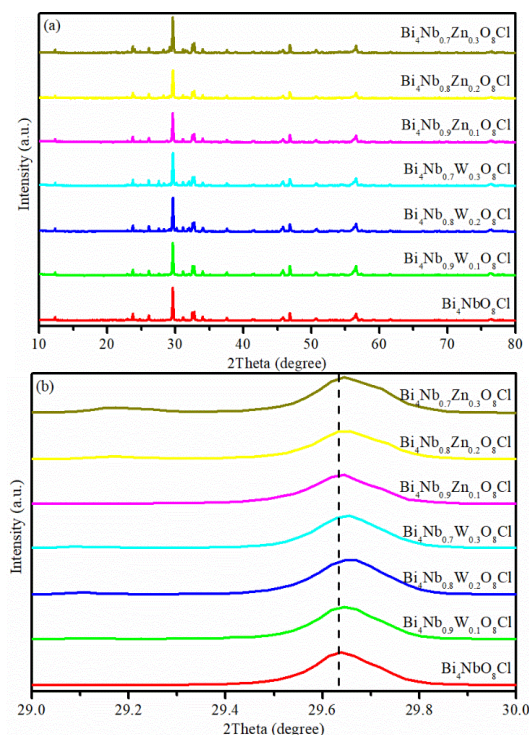


**Figure 1.** (a) X-ray diffraction (XRD) patterns of  $\text{Bi}_4\text{NbO}_8\text{Cl}$ ,  $\text{Bi}_4\text{Nb}_{1-x}\text{W}_x\text{O}_8\text{Cl}$  and  $\text{Bi}_4\text{Nb}_{1-x}\text{Zn}_x\text{O}_8\text{Cl}$  series, (b) diffraction peak positions in the range of  $2\theta = 29\text{--}30^\circ$ .

### 3.2. Scanning Electron Microscopy (SEM)

The morphologies of  $\text{Bi}_4\text{NbO}_8\text{Cl}$  and  $\text{Bi}_4\text{Nb}_{0.8}\text{Zn}_{0.2}\text{O}_8\text{Cl}$  are shown in Figure 2. It can be seen that  $\text{Bi}_4\text{NbO}_8\text{Cl}$  is composed of a large number of nanoplates (Figure 2a,b); After Zinc doping, the morphology of the sample has changed.  $\text{Bi}_4\text{Nb}_{0.8}\text{Zn}_{0.2}\text{O}_8\text{Cl}$  has a lamellar stacking structure with the thickness of about 100 nm (Figure 2a,b). The morphology of  $\text{Bi}_4\text{Nb}_{0.9}\text{Zn}_{0.1}\text{O}_8\text{Cl}$  and  $\text{Bi}_4\text{Nb}_{0.7}\text{Zn}_{0.3}\text{O}_8\text{Cl}$  are presented in Figure S1. It can be seen that the morphologies of the catalysts change little with the different amount of zinc doping.

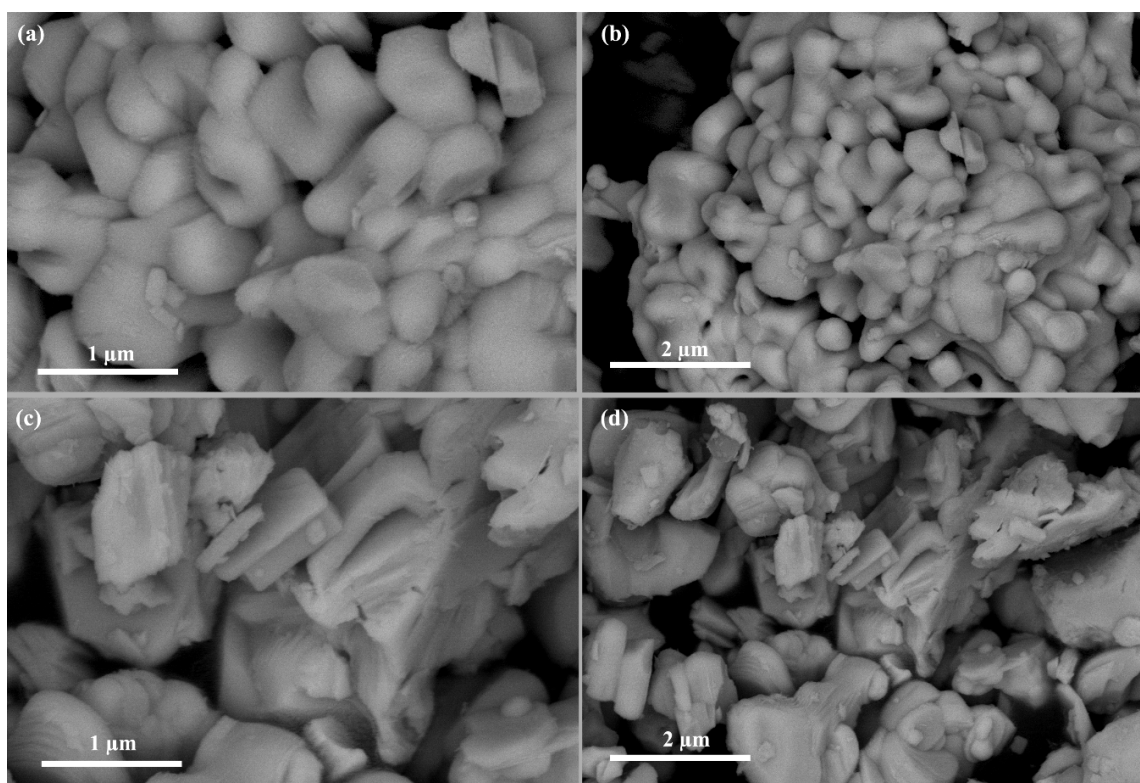


**Figure 2.** The scanning electron microscope (SEM) images of  $\text{Bi}_4\text{NbO}_8\text{Cl}$  (a,b) and  $\text{Bi}_4\text{Nb}_{0.8}\text{Zn}_{0.2}\text{O}_8\text{Cl}$  (c,d).

### 3.3. X-Ray Photoelectron Spectroscopy

The surface chemical element states of  $\text{Bi}_4\text{NbO}_8\text{Cl}$  and  $\text{Bi}_4\text{Nb}_{0.8}\text{Zn}_{0.2}\text{O}_8\text{Cl}$  were investigated by X-ray photoelectron spectroscopy. Figure 3a shows the existence of C, N, Bi, Nb and Cl element in  $\text{Bi}_4\text{NbO}_8\text{Cl}$ . Compared with  $\text{Bi}_4\text{NbO}_8\text{Cl}$ , the characteristic peak of Zn is added in the  $\text{Bi}_4\text{Nb}_{0.8}\text{Zn}_{0.2}\text{O}_8\text{Cl}$  spectrum, indicating that the Zn element has been successfully doped in  $\text{Bi}_4\text{NbO}_8\text{Cl}$ . As shown in Figure 3b,d, the Bi 4f spectrum of  $\text{Bi}_4\text{NbO}_8\text{Cl}$  with the peaks at 164.17 eV and 158.86 eV are indexed to Bi 4f<sub>7/2</sub> and Bi 4f<sub>5/2</sub>, respectively. This indicates that the valence state of Bi is trivalent [24,25]. The peaks of Nb 3d<sub>5/2</sub> and Nb 3d<sub>3/2</sub> appear at 206.23 eV and 208.98 eV for  $\text{Bi}_4\text{NbO}_8\text{Cl}$ , indicating the existence of Nb<sup>5+</sup> state (Figure 3b). However, the two peaks for  $\text{Bi}_4\text{NbO}_8\text{Cl}$  located at 198.3 eV and 199.9 eV, belonging to Cl 2p<sub>3/2</sub> and Cl 2p<sub>1/2</sub>, respectively (Figure 3c). Notably, the Bi 4f, Nb 3d and Cl 2p peaks for  $\text{Bi}_4\text{Nb}_{0.8}\text{Zn}_{0.2}\text{O}_8\text{Cl}$  all display a slight migration towards lower binding energy compared to  $\text{Bi}_4\text{NbO}_8\text{Cl}$ , suggesting that the chemical circumstances of Bi, Nb and Cl elements have changed since the zinc is doped [16,26]. The O 1s peaks for  $\text{Bi}_4\text{NbO}_8\text{Cl}$  (Figure 2d) can be divided into three peaks at 529.55 eV, 530.89 eV, and 531.32 eV, which separately belong to the crystal lattice oxygen, Bi–O bonds and Nb–O bonds. However, when the zinc is doped, the characteristic O 1s peaks change. This may be attributed to the formation of Nb–O–Zn–O bond [27]. Zinc signals are detected after Zn<sup>2+</sup> doping, as shown in Figure 3b, the peaks located at 1023.52 eV and 1046.65 eV are contributed to Zn 2p<sub>3/2</sub> and Zn 2p<sub>1/2</sub>, respectively [28].



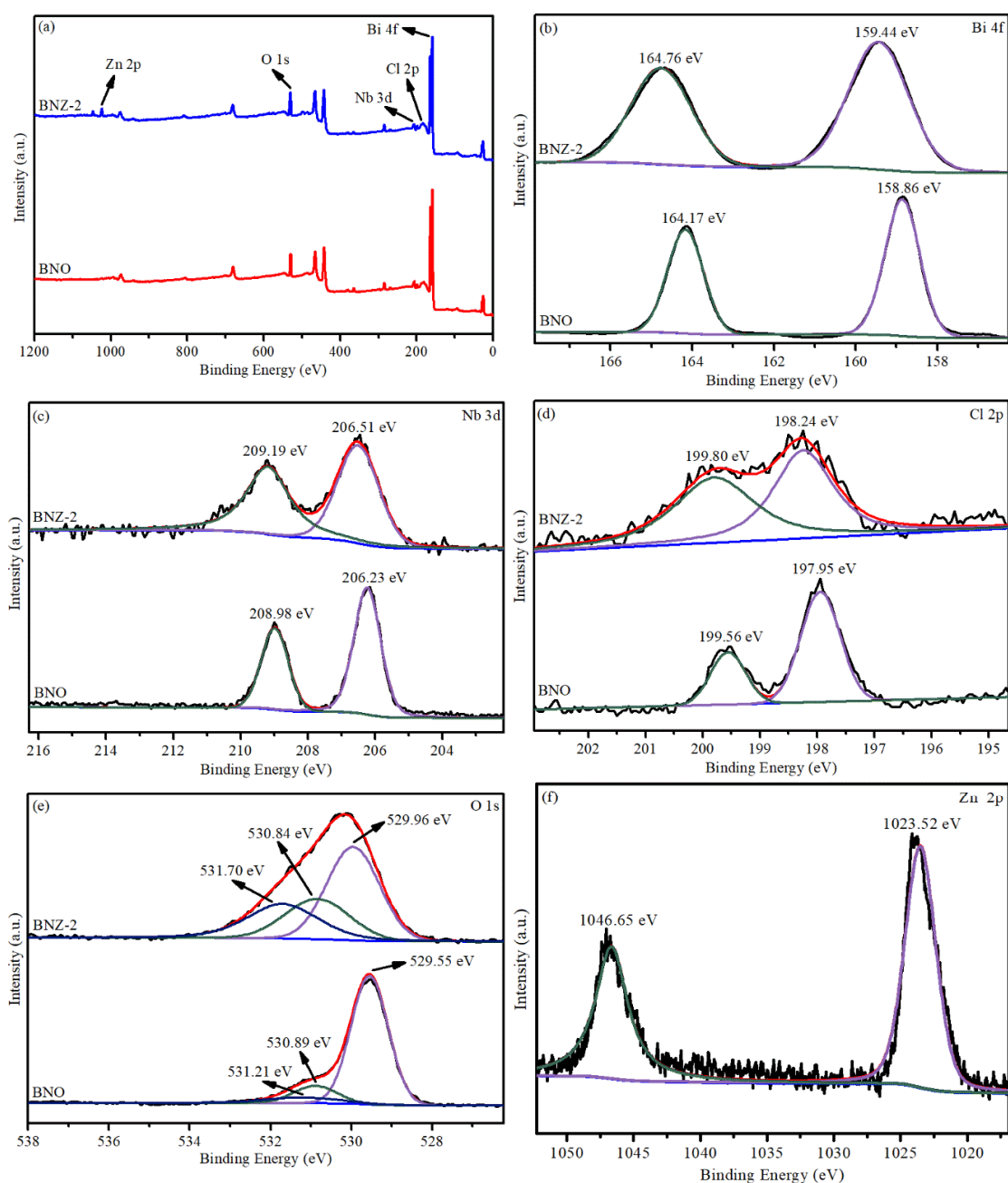


**Figure 3.** X-ray photoelectron spectrometry (XPS) spectra of  $\text{Bi}_4\text{NbO}_8\text{Cl}$  and  $\text{Bi}_4\text{Nb}_{0.8}\text{Zn}_{0.2}\text{O}_8\text{Cl}$ : (a) Survey, (b) Bi 4f, (c) Nb 3d, (d) Cl 2p (e) O 1s and (f) Zn 2p.

### 3.4. Ultraviolet–Visible (UV–Vis) Diffuse Reflectance Spectrum

Figure 4a shows the ultraviolet–visible (UV–vis) diffuse reflectance spectrum of  $\text{Bi}_4\text{NbO}_8\text{Cl}$ ,  $\text{Bi}_4\text{Nb}_{1-x}\text{W}_x\text{O}_8\text{Cl}$  and  $\text{Bi}_4\text{Nb}_{1-x}\text{Zn}_x\text{O}_8\text{Cl}$  series. It can be seen that all the photocatalysts have strong absorption in the visible light region and exhibit almost the same absorption edges with either W or Zn doping. The band gap energy ( $E_g$ ) is determined by the following equation using the data of optical absorption vs. wavelength near the band edge [29,30]:

$$\alpha h\nu = A(h\nu - E_g)^{2/n} \quad (1)$$

where  $A$  indicates a constant,  $\alpha$ ,  $h\nu$ , and  $E_g$  are respective to absorption coefficient, photon energy and band gap energy, respectively. In this work,  $n$  is 1 due to the  $\text{BiNbO}_8\text{Cl}$  being a kind of indirect



gap semiconductor [31]. The band gap energy ( $E_g$ ) value can be obtained by extrapolating the linear portion of the  $h\nu - (\alpha h\nu)^{1/2}$  curve. As shown in Figure 4b, the band gap of BNO is about 2.45 eV and there are no significant changes after either W or Zn doping, indicating that the absorption of light is caused by the band gap transition rather than the transition of the impurity energy level. The results show that a new photocatalyst with visible light response has been successfully prepared, which may provide the excellent photocatalytic activity.

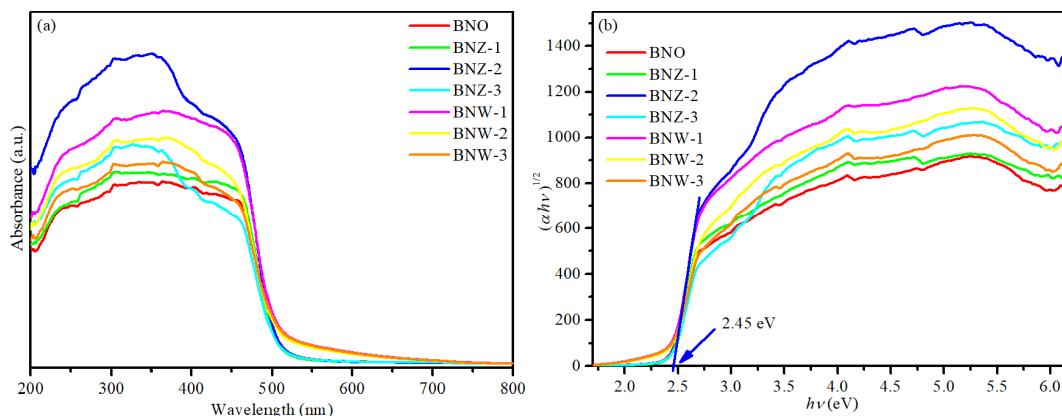


**Figure 4.** (a) Ultraviolet–visible (UV–vis) absorption spectra (b) plots of  $(\alpha h\nu)^{1/2}$  vs.  $h\nu$  of  $\text{Bi}_4\text{NbO}_8\text{Cl}$ ,  $\text{Bi}_4\text{Nb}_{1-x}\text{W}_x\text{O}_8\text{Cl}$  and  $\text{Bi}_4\text{Nb}_{1-x}\text{Zn}_x\text{O}_8\text{Cl}$  series.

### 3.5. Photocatalytic Activity

In the dye degradation experiment, TB was chosen as the dye model under visible irradiation at  $\text{pH} \approx 7$ . Figure 5a shows the degradation profiles under visible irradiation. It can be seen that the degradation ratio of BNO is about 83.5% within 90 min. However, the photocatalytic degradation efficiency of BNW-1, BNW-2 and BNW-2 are lower than that of BNO indicating that W doping could not effectively improve the degradation efficiency of TB. In contrast, it can be found that all of the Zn-doped samples show higher photocatalytic degradation abilities than the pure  $\text{Bi}_4\text{NbO}_8\text{Cl}$  photocatalyst. The BNZ-2 photocatalyst displays the highest photocatalytic activity and the removal rate can reach 96% in 90 min. The results confirm that the introduction of Zinc in  $\text{Bi}_4\text{NbO}_8\text{Cl}$  could effectively enhance photocatalytic activity.

In order to quantitatively study the reaction kinetics of the degradation process, a first-order model is used to fit the reaction data. The formula is as follows [32,33]:  $\ln(C_0/C) = kt + b$ , where  $k$  is the apparent first-order rate constant, and  $\ln(C_0/C)$  has a linear relationship with catalytic reaction time. As can be seen in Figure 5c, the pseudo first-order rate constants ( $k$ ) for BNZ-2 reaches  $0.03085 \text{ min}^{-1}$ , which is about 1.5 times as high as that of BNO ( $k = 0.02019$ ) and about 3 times that of BNW-2, respectively. Figure 5d shows the temporal evolution of the UV–visible absorption spectral changes during TB degradation process by BNZ-2 photocatalyst. As time goes on, the characteristic absorption peaks between 500 and 800 nm region have reduced gradually, which indicates that the molecular structure of organic pollutants is destroyed.

### 3.6. Computational Details

Using the first-principles methods, we calculated the band structures of  $\text{Bi}_4\text{NbO}_8\text{Cl}$  and doped systems. As the chemical valence is two for zinc and six for tungsten, this means hole doping for  $\text{Bi}_4\text{Nb}_{0.8}\text{Zn}_{0.2}\text{O}_8\text{Cl}$  and electron doping for  $\text{Bi}_4\text{Nb}_{0.8}\text{W}_{0.2}\text{O}_8\text{Cl}$  system. From the band structures in Figure 6, we can clearly see the tungsten doping will introduce the additional electron carriers, while the hole carriers will increase by zinc doping. Therefore, it is not too difficult to understand the reason why enhancement of photodegradation properties of  $\text{Bi}_4\text{Nb}_{0.8}\text{Zn}_{0.2}\text{O}_8\text{Cl}$ , in which the hole carriers play a role for the photocatalytic mechanism.

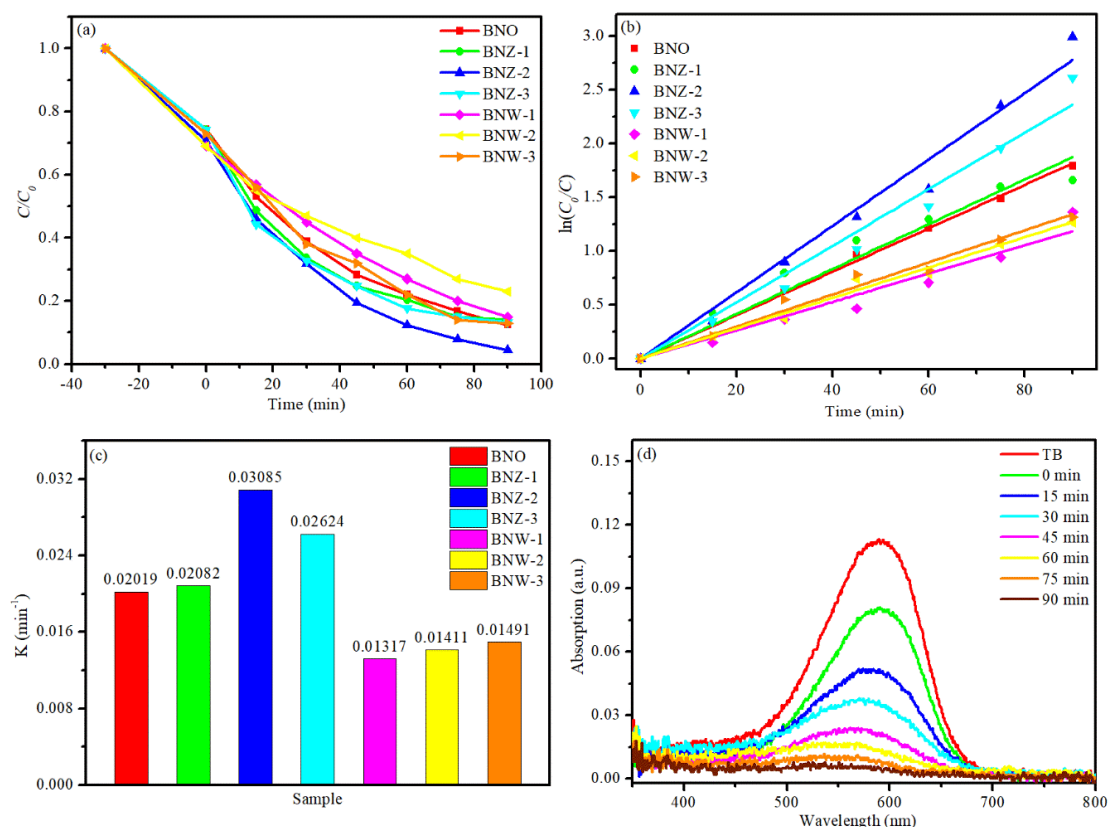


**Figure 5.** (a) Photocatalytic activity, (b) kinetic curves, (c) apparent rate constant (K), (d) UV-vis absorption spectra changes with  $\text{Bi}_4\text{Nb}_{0.8}\text{Zn}_{0.2}\text{O}_8\text{Cl}$ .

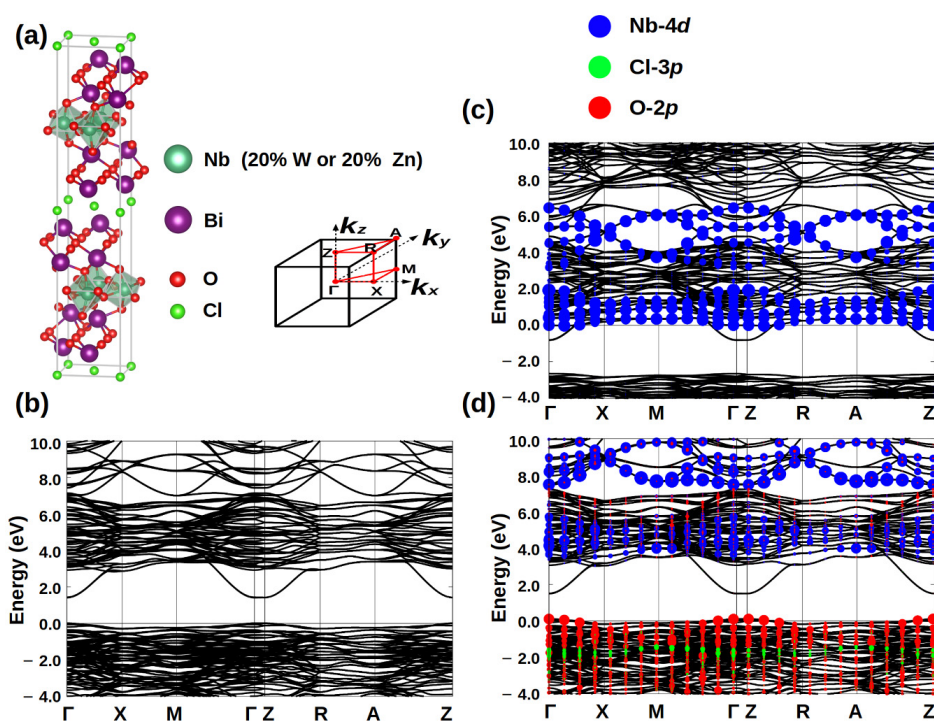


**Figure 6.** (a) Crystal structure of  $\text{Bi}_4\text{NbO}_8\text{Cl}$ , and density functional theory (DFT) band structure of undoped (b)  $\text{Bi}_4\text{NbO}_8\text{Cl}$ , 20% W doping on Nb (c), and (d) 20% Zn doping on Nb. The adopted Brillouin zone and band plotting k-path are also shown in (a). In (c,d), the orbital characters of Nb-4d, O-2p and Cl-3p are labeled by blue, red and green dots, respectively. The Fermi energy is set as 0 eV.

### 3.7. Possible Photocatalysis Mechanism

It is noteworthy that all of the W-doped  $\text{Bi}_4\text{NbO}_8\text{Cl}$  photocatalysts have lower photocatalytic activity than that of pure  $\text{Bi}_4\text{NbO}_8\text{Cl}$ . In contrast, the Zn-doped  $\text{Bi}_4\text{NbO}_8\text{Cl}$  photocatalysts have higher photocatalytic activities than that of pure  $\text{Bi}_4\text{NbO}_8\text{Cl}$ . This phenomenon can be attributed to the  $\text{Zn}^{2+}$  ions being incorporated into the  $\text{Bi}_4\text{NbO}_8\text{Cl}$  via replacing the  $\text{Nb}^{5+}$  lattice sites, and the positive charge of  $\text{Zn}^{2+}$  ion being less than that of  $\text{Nb}^{5+}$ , thus forming a negative charge center at the position of  $\text{Zn}^{2+}$ . In order to maintain the charge balance,  $\text{Zn}^{2+}$  ions will fetter the hole ( $\text{h}^+$ ) and make it difficult to move freely [34]. Therefore, the increase of the concentration of holes ( $\text{h}^+$ ) around zinc ion leads to the formation of hole doping in  $\text{Bi}_4\text{NbO}_8\text{Cl}$ , which has strong oxidation performance and is beneficial to photocatalytic degradation. In addition, hole fettering limit the effective recombination of photogenerated electrons and holes. The photoluminescence technique is used to analysis the separation efficiency of photoelectron-hole pairs. As shown in Figure 7, BNO exhibits higher emission peak than BNZ-2, indicating that the recombination of photoelectron-hole pairs is faster [35,36]. Therefore, the doping of zinc can promote the separation of photogenerated electrons and holes, improving the photocatalytic efficiency.

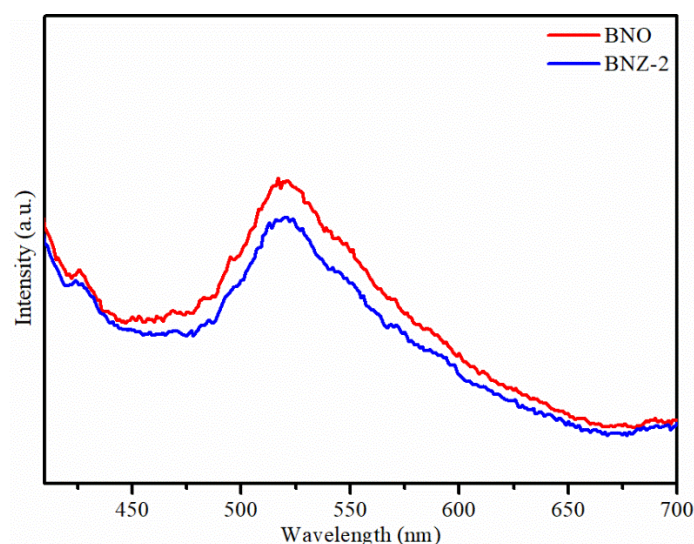


**Figure 7.** Photoluminescence spectra of  $\text{Bi}_4\text{NbO}_8\text{Cl}$  and  $\text{Bi}_4\text{Nb}_{0.8}\text{Zn}_{0.2}\text{O}_8\text{Cl}$  photocatalysts.

By contrast, the positive charge of the  $\text{W}^{6+}$  ion is greater than that of the  $\text{Nb}^{5+}$ , the  $\text{W}^{6+}$  will capture the electrons to maintain the charge balance, and forming the electrons ( $\text{e}^-$ ) doping in  $\text{Bi}_4\text{NbO}_8\text{Cl}$ . However, the  $\text{W}^{6+}$  can capture the conduction band electrons ( $\text{e}^-$ ) and hinder the formation of super oxide radicals ( $\bullet\text{O}_2^-$ ), which leads to the decrease of photocatalytic degradation efficiency [37]. Therefore, the doping of W in  $\text{Bi}_4\text{NbO}_8\text{Cl}$  leads to the decrease of photocatalytic activity. The above mechanism can be also used to understand the photocatalytic activity in  $\text{Bi}_4\text{Ti}_{0.5}\text{W}_{0.5}\text{O}_8\text{Cl}$  system, which is almost the same with  $\text{Bi}_4\text{NbO}_8\text{Cl}$  [38].

The trapping experiments were used to detect the main active species in the process of photocatalytic degradation. The *Tert*-butanol (*t*-BuOH, an  $\bullet\text{OH}$  scavenger), *p*-benzoquinone (BQ; an  $\bullet\text{O}_2^-$  scavenger), and disodium ethylenediamine tetraacetate (EDTA-2Na,  $\text{h}^+$  scavenger) were used as quenchers [39]. As shown in Figure 8a,b, after adding the *t*-BuOH, the photocatalytic degradation of TB is slightly decreased for both BNO and BNZ-2, indicating hydroxyl radicals ( $\bullet\text{OH}$ ) have little impact on the photocatalytic degradation process. When the BQ and EDTA-2Na are added, the photocatalytic degradation rate of TB decreased sharply, suggesting that the hole ( $\text{h}^+$ ) and super oxide radicals ( $\bullet\text{O}_2^-$ ) are the main active species in the TB degradation process. In contrast, it suggests that the effect of hole ( $\text{h}^+$ ) on BT degradation is more critical than that of super oxide radicals ( $\bullet\text{O}_2^-$ ) over BNZ-2 (Figure 8b).

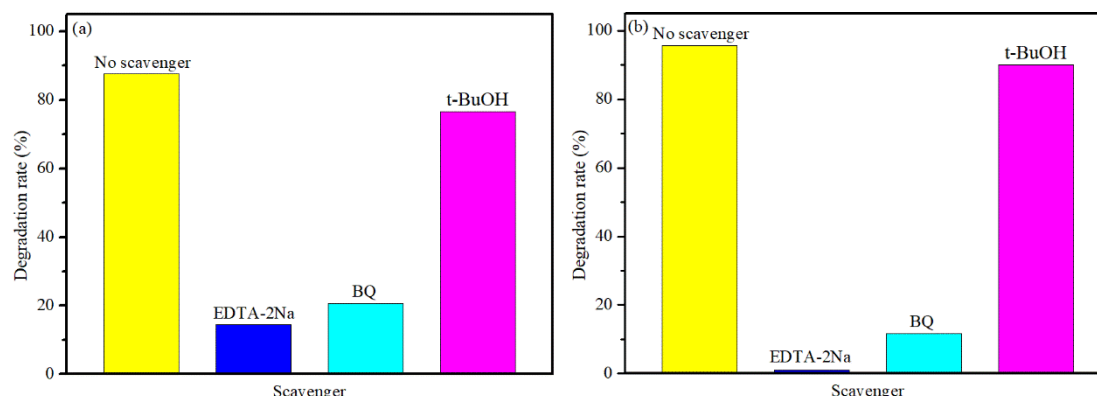
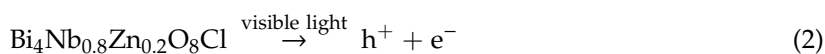


**Figure 8.** Photodegradation of trypan blue (TB) by different quenchers over Bi<sub>4</sub>NbO<sub>8</sub>Cl (a) and Bi<sub>4</sub>Nb<sub>0.8</sub>Zn<sub>0.2</sub>O<sub>8</sub>Cl (b).

Based on the above experiments and analysis, a mechanism of TB degradation by Zn-doped Bi<sub>4</sub>NbO<sub>8</sub>Cl photocatalysts under visible light is proposed. As mentioned, the Zn-doped Bi<sub>4</sub>NbO<sub>8</sub>Cl photocatalysts can be excited and generate the photogenerated electrons (e<sup>−</sup>) and holes (h<sup>+</sup>) pairs under visible light. The electrons (e<sup>−</sup>) react with adsorbed O<sub>2</sub> to generate superoxide radical (•O<sub>2</sub><sup>−</sup>), which is a strong oxidant and can degrade TB. Because of the hole (h<sup>+</sup>) doping in Bi<sub>4</sub>NbO<sub>8</sub>Cl, the hole is far more oxidative than •OH radical. Therefore, holes (h<sup>+</sup>) play a main role in the photocatalytic degradation of TB. The photogenerated holes (h<sup>+</sup>) of Zn-doped Bi<sub>4</sub>NbO<sub>8</sub>Cl can directly transform TB molecules into H<sub>2</sub>O, CO<sub>2</sub> and mineral [40]. Finally, the organic pollutants are photocatalytically degraded by this novel hole-doped photocatalyst. The possible charge carrier transfer path is as follows:



#### 4. Conclusions

A novel layered photocatalyst of Bi<sub>4</sub>NbO<sub>8</sub>Cl doped with zinc was successfully synthesized by a solid-state reaction method. It was found that the introduction of zinc ions into Bi<sub>4</sub>NbO<sub>8</sub>Cl can construct hole (h<sup>+</sup>) doping in Bi<sub>4</sub>NbO<sub>8</sub>Cl and promote the separation of photogenerated electrons. Compared to Bi<sub>4</sub>NbO<sub>8</sub>Cl, Bi<sub>4</sub>Nb<sub>1−x</sub>Zn<sub>x</sub>O<sub>8</sub>Cl (x = 0.1, 0.2, 0.3) series photocatalysts show significantly higher photocatalytic activities for trypan blue degradation. In particular, when the atomic ratio of Zn to Nb is 2:8, the photocatalyst showed the highest photocatalytic activity and the removal ratio of trypan blue could reach 96% in 90 min. Furthermore, hole (h<sup>+</sup>) was considered as the effective species in the photocatalytic degradation process. On the basis of the experimental results and density functional theory calculations, the hole carriers play a role in the photocatalytic mechanism. This material may have potential application prospects in the degradation of organic pollutants from wastewater.

**Supplementary Materials:** The following are available online at <http://www.mdpi.com/2073-4344/10/12/1425/s1>, Figure S1. SEM images of Bi<sub>4</sub>Nb<sub>0.9</sub>Zn<sub>0.1</sub>O<sub>8</sub>Cl (a) (b); Bi<sub>4</sub>Nb<sub>0.7</sub>Zn<sub>0.3</sub>O<sub>8</sub>Cl (c) (d).

**Author Contributions:** Conceptualization, X.L. and Q.Z.; Methodology, L.S. and Q.Z.; Validation, J.S., N.H. and Y.G.; Formal Analysis, N.H.; Investigation, Q.Z.; Resources, X.L. and L.S.; Data Curation, J.S. and N.H.; Writing—Original Draft Preparation, X.L. and Q.Z.; Writing—Review and Editing, L.S. and Q.Z.; Visualization, J.S., Q.Z. and N.H.; Supervision, Q.Z.; Project Administration, Q.Z.; Funding Acquisition, X.L. and Q.Z. All authors have read and agreed to the published version of the manuscript.

**Funding:** This work was supported by the Natural Science Foundation of Jiangsu Province (20KJA430004) and the Postgraduate Research and Practice Innovation Program of Jiangsu Province (SJCX20\_1239).

**Conflicts of Interest:** The authors declare no conflict of interest. The founding sponsors had no role in the design of the study; in the collection, analyses, or interpretation of data; in the writing of the manuscript; or in the decision to publish the results.

## References

1. Zangeneh, H.; Zinatizadeh, A.A.; Zinadini, S.; Feyzi, M.; Rafiee, E.; Bahnemann, D.W. A novel L-Histidine (C, N) codoped-TiO<sub>2</sub>-CdS nanocomposite for efficient visible photo-degradation of recalcitrant compounds from wastewater. *J. Hazard. Mater.* **2019**, *369*, 384–397. [CrossRef] [PubMed]
2. Li, T.T.; Zhao, L.H.; He, Y.M.; Cai, J.; Luo, M.F.; Lin, J.J. Synthesis of g-C<sub>3</sub>N<sub>4</sub>/SmVO<sub>4</sub> composite photocatalyst with improved visible light photocatalytic activities in RhB degradation. *Appl. Catal. B* **2013**, *129*, 255–263. [CrossRef]
3. Padervand, M.; Jalilian, E.; Majdani, R.; Goshadezhn, M. BiOCl/AgCl-BiOI/AgI quaternary nanocomposite for the efficient photodegradation of organic wastewaters and pathogenic bacteria under visible light. *J. Water Process. Eng.* **2019**, *29*, 100789–100796. [CrossRef]
4. Pirhashemi, M.; Habibi-Yangjeh, A.; Pouran, S.R. Review on the criteria anticipated for the fabrication of highly efficient ZnO-based visible-light-driven photocatalysts. *J. Ind. Eng. Chem.* **2018**, *62*, 1–25. [CrossRef]
5. Zhang, L.; Zhu, Y. A review of controllable synthesis and enhancement of performances of bismuth tungstate visible-light-driven photocatalysts. *Catal. Sci. Technol.* **2012**, *2*, 694–706. [CrossRef]
6. Fujito, H.; Kunioku, H.; Kato, D.; Suzuki, H.; Higashi, M.; Kageyama, H.; Abe, R. Layered Perovskite Oxychloride Bi<sub>4</sub>NbO<sub>8</sub>Cl: A Stable Visible Light Responsive Photocatalyst for Water Splitting. *J. Am. Chem. Soc.* **2016**, *138*, 2082–2085. [CrossRef]
7. You, Y.; Wang, S.; Xiao, K.; Ma, T.; Zhang, Y.; Huang, H. Z-Scheme g-C<sub>3</sub>N<sub>4</sub>/Bi<sub>4</sub>NbO<sub>8</sub>Cl Heterojunction for Enhanced Photocatalytic Hydrogen Production. *ACS Sustain. Chem. Eng.* **2018**, *6*, 16219–16227. [CrossRef]
8. Ogawa, K.; Nakada, A.; Suzuki, H.; Tomita, O.; Higashi, M.; Saeki, A.; Kageyama, H.; Abe, R. Flux Synthesis of Layered Oxyhalide Bi<sub>4</sub>NbO<sub>8</sub>Cl Photocatalyst for Efficient Z-Scheme Water Splitting under Visible Light. *ACS Appl. Mater. Interfaces* **2019**, *11*, 5642–5650. [CrossRef]
9. Lin, X.; Huang, T.; Huang, F.; Wang, W.; Shi, J. Photocatalytic activity of a Bi-based oxychloride Bi<sub>4</sub>NbO<sub>8</sub>Cl. *J. Mater. Chem.* **2007**, *17*, 2145–2150. [CrossRef]
10. Bhat, S.S.M.; Sundaram, N.G. Photocatalysis of Bi<sub>4</sub>NbO<sub>8</sub>Cl hierarchical nanostructure for degradation of dye under Solar/UV irradiation. *New J. Chem.* **2015**, *39*, 3956–3966. [CrossRef]
11. Xu, Y.; You, Y.; Huang, H.; Guo, Y.; Zhang, Y. Bi<sub>4</sub>NbO<sub>8</sub>Cl {001} nanosheets coupled with g-C<sub>3</sub>N<sub>4</sub> as 2D/2D heterojunction for photocatalytic degradation and CO<sub>2</sub> reduction. *J. Hazard. Mater.* **2019**, *381*, 121159. [CrossRef] [PubMed]
12. Qu, X.; Gao, Z.; Zhao, X.; Shi, L.; Du, F.; Song, H. Construction of p-n type Bi<sub>2</sub>O<sub>3</sub>/Bi<sub>4</sub>NbO<sub>8</sub>Cl 0D/2D heterojunction with enhanced photodegradation performance for organic pollutants. *Appl. Surf. Sci.* **2020**, *529*, 147248. [CrossRef]
13. Qu, X.; Liu, M.; Zhai, H.; Zhao, X.; Shi, L.; Du, F. Plasmonic Ag-promoted layered perovskite oxyhalide Bi<sub>4</sub>NbO<sub>8</sub>Cl for enhanced photocatalytic performance towards water decontamination. *J. Alloy. Compd.* **2019**, *810*, 151919. [CrossRef]
14. Ruan, Y.; Zhang, N.; Zhu, Y.; Zhao, W.; Xu, J.; Chen, H. Photoelectrochemical Bioanalysis Platform of Gold Nanoparticles Equipped Perovskite Bi<sub>4</sub>NbO<sub>8</sub>Cl. *Anal. Chem.* **2017**, *89*, 7869–7875. [CrossRef] [PubMed]
15. Wu, X.; Zhang, Y.; Wang, K.; Zhang, S.; Qu, X.; Shi, L.; Du, F. In-situ construction of Bi/defective Bi<sub>4</sub>NbO<sub>8</sub>Cl for non-noble metal based Mott-Schottky photocatalysts towards organic pollutants removal. *J. Hazard. Mater.* **2020**, *393*, 122408. [CrossRef] [PubMed]
16. Wei, Z.; Liu, J.; Fang, W.; Qin, Z.; Jiang, Z.; Shangguan, W. Enhanced photocatalytic hydrogen evolution using a novel in situ heterojunction yttrium-doped Bi<sub>4</sub>NbO<sub>8</sub>Cl@Nb<sub>2</sub>O<sub>5</sub>. *Int. J. Hydrog. Energy* **2018**, *43*, 14281–14292. [CrossRef]
17. Medhi, R.; Marquez, M.D.; Lee, T.R. Visible-Light-Active Doped Metal Oxide Nanoparticles: Review of their Synthesis, Properties, and Applications. *ACS Appl. Nano Mater.* **2020**, *3*, 6156–6185. [CrossRef]

18. Guo, G.; Yan, H. Zn-doped  $\text{Bi}_2\text{O}_2\text{CO}_3$ : Synthesis, characterization and photocatalytic properties. *Chem. Phys.* **2020**, *538*, 110920. [CrossRef]
19. Xu, K.; Shen, J.; Xu, D.; Li, Z.; Zhang, S.; Wu, Z.; Feng, W.; Xiao, X.; Zhang, S.; Liu, J. Molten-salt-mediated synthesis of bulk W doped BiOCl with highly enhanced visible-light photocatalytic performances. *Appl. Surf. Sci.* **2019**, *459*, 143595. [CrossRef]
20. Blaha, P.; Schwarz, K.; Madsen, G.; Kvasnicka, D.; Luitz, J. *WIEN2k, An Augmented Plane Wave Plus Local Orbitals Program for Calculating Crystal Properties*; Vienna University of Technology: Vienna, Austria, 2001.
21. Perdew, J.; Burke, K.; Ernzerhof, M. Generalized Gradient Approximation Made Simple. *Phys. Rev. Lett.* **1996**, *77*, 3865. [CrossRef]
22. Guo, J.; Liao, X.; Lee, M.; Hyett, G.; Huang, C.; Hewak, D.W.; Mailis, S.; Zhou, W.; Jiang, Z. Experimental and DFT insights of the Zn-doping effects on the visible-light photocatalytic water splitting and dye decomposition over Zn-doped BiOBr photocatalysts. *Appl. Catal. B* **2019**, *243*, 502–512. [CrossRef]
23. Truc, N.T.T.; Bach, L.G.; Hanh, N.T.; Pham, T.D.; Chi, N.T.P.L.; Tran, D.T.; Nguyen, M.V.; Nguyen, V.N. The superior photocatalytic activity of Nb doped  $\text{TiO}_2/\text{g-C}_3\text{N}_4$  direct Z-scheme system for efficient conversion of  $\text{CO}_2$  into valuable fuels. *J. Colloid Interface Sci.* **2019**, *540*, 1–8. [CrossRef] [PubMed]
24. Zhong, X.; Zhang, K.; Wu, D.; Ye, X.; Huang, W.; Zhou, B. Enhanced photocatalytic degradation of levofloxacin by Fe-doped BiOCl nanosheets under LED light irradiation. *Chem. Eng. J.* **2020**, *383*, 123148. [CrossRef]
25. Zhong, X.; Cai, Y.; Bai, H.; Huang, W.; Zhou, B. Visible Light Driven Spherical  $\text{CuBi}_2\text{O}_4$  with Surface Oxygen Vacancy Enhanced Photocatalytic Activity: Catalyst Fabrication, Performance, and Reaction Mechanism. *Catalysts* **2020**, *10*, 945. [CrossRef]
26. Wang, C.; Zhang, Y.; Wang, W.; Pei, D.; Huang, G.; Chen, J.; Zhang, X.; Yu, H. Enhanced photocatalytic degradation of bisphenol A by Co-doped BiOCl nanosheets under visible light irradiation. *Appl. Catal. B* **2018**, *121*, 320–328. [CrossRef]
27. Qu, X.; Liu, M.; Gao, Z.; Zhai, H.; Ren, W.; Shi, L.; Du, F. A novel ternary  $\text{Bi}_4\text{NbO}_8\text{Cl}/\text{BiOCl}/\text{Nb}_2\text{O}_5$  architecture via in-situ solvothermal-induced electron-trap with enhanced photocatalytic activities. *Appl. Surf. Sci.* **2020**, *506*, 1446788. [CrossRef]
28. Wang, Z.; Xu, J.; Zhou, H.; Zhang, X. Facile synthesis of Zn(II)-doped  $\text{g-C}_3\text{N}_4$  and their enhanced photocatalytic activity under visible light irradiation. *Rare Met.* **2019**, *38*, 459–467. [CrossRef]
29. Lu, X.; Li, X.; Chen, F.; Chen, Z.; Qian, J.; Zhang, Q. Biotemplating synthesis of N-doped two-dimensional  $\text{CeO}_2\text{-TiO}_2$  nanosheets with enhanced visible light photocatalytic desulfurization performance. *J. Alloy. Compd.* **2020**, *815*, 152326. [CrossRef]
30. Lu, X.; Li, X.; Qian, J.; Miao, N.; Yao, C.; Chen, Z. Synthesis and characterization of  $\text{CeO}_2/\text{TiO}_2$  nanotube arrays and enhanced photocatalytic oxidative desulfurization performance. *J. Alloy. Compd.* **2016**, *661*, 363–371. [CrossRef]
31. Gao, Z.; Qu, X. Construction of  $\text{ZnTiO}_3/\text{Bi}_4\text{NbO}_8\text{Cl}$  heterojunction with enhanced photocatalytic performance. *Nanoscale Res. Lett.* **2020**, *15*, 64. [CrossRef]
32. Li, X.; Zhu, W.; Lu, X.; Zuo, S.; Yao, C.; Ni, C. Integrated nanostructures of  $\text{CeO}_2/\text{attapulgit}/\text{g-C}_3\text{N}_4$  as efficient catalyst for photocatalytic desulfurization: Mechanism, kinetics and influencing factors. *Chem. Eng. J.* **2017**, *326*, 87–98. [CrossRef]
33. Wang, Y.; Jung, D.W. Synthesis of novel BiOCl/LiBiO<sub>3</sub> p-n heterojunction photocatalysts and their enhanced photocatalytic performance. *Solid State Sci.* **2019**, *91*, 42–48. [CrossRef]
34. Li, W.; Huang, W.; Zhou, H.; Yin, H.; Zheng, Y.; Song, X. Synthesis of  $\text{Zn}^{2+}$  doped BiOCl hierarchical nanostructures and their exceptional visible light photocatalytic properties. *J. Alloy. Compd.* **2015**, *638*, 148–154. [CrossRef]
35. Jiang, D.; Wang, T.; Xu, Q.; Li, D.; Meng, S.; Chen, M. Perovskite oxide ultrathin nanosheets/ $\text{g-C}_3\text{N}_4$  2D-2D heterojunction photocatalysts with significantly enhanced photocatalytic activity towards the photodegradation of tetracycline. *Appl. Catal. B* **2017**, *201*, 617–628. [CrossRef]
36. Gao, C.; Xue, J.; Zhang, L.; Cui, K.; Li, H.; Yu, J. Paper-Based Origami Photoelectrochemical Sensing Platform with  $\text{TiO}_2/\text{Bi}_4\text{NbO}_8\text{Cl}/\text{Co-Pi}$  Cascade Structure Enabling of Bidirectional Modulation of Charge Carrier Separation. *Anal. Chem.* **2018**, *90*, 14116–14120. [CrossRef]
37. Zou, Y.; Gong, Y.; Lin, B.; Mellott, N.P. Photodegradation of methylene blue in the visible spectrum: An efficient  $\text{W}^{6+}$  ion doped anatase titania photocatalyst via a solvothermal method. *Vacuum* **2016**, *126*, 63–69. [CrossRef]



38. Zhen, S.; Zhu, L.; Dong, Z.; Fan, L.; Wang, B.; Zhang, Q. A New Bi-Based Oxychloride  $\text{Bi}_4\text{Ti}_{0.5}\text{W}_{0.5}\text{O}_8\text{Cl}$  as a Photocatalyst. *Catal. Lett.* **2018**, *148*, 2480–2486. [CrossRef]
39. Han, N.; Xu, Q.; Beyene, G.; Zhang, Q. Enhanced photocatalytic activity over g- $\text{C}_3\text{N}_4/(\text{BiO})_2(\text{OH})_x\text{Cl}_{2-x}$  Z-scheme heterojunction. *Appl. Surf. Sci.* **2020**, *521*, 146464–146475. [CrossRef]
40. Majumdar, A.; Ghosh, U.; Pal, A. Novel 2D/2D g- $\text{C}_3\text{N}_4/\text{Bi}_4\text{NbO}_8\text{Cl}$  nano-composite for enhanced photocatalytic degradation of oxytetracycline under visible LED light irradiation. *J. Colloid Interface Sci.* **2021**, *584*, 320–331. [CrossRef]

**Publisher's Note:** MDPI stays neutral with regard to jurisdictional claims in published maps and institutional affiliations.



© 2020 by the authors. Licensee MDPI, Basel, Switzerland. This article is an open access article distributed under the terms and conditions of the Creative Commons Attribution (CC BY) license (<http://creativecommons.org/licenses/by/4.0/>).

## Article

# Synthesis and Photocatalytic Activity of Hierarchical Zn-ZSM-5 Structures

Hongji Li \*, Yu Zhang, Jiaqi Diao, Mengmeng Qiang and Zhe Chen

School of Urban Planning and Municipal Engineering, Xi'an Polytechnic University, Xi'an 710048, China; zhangyu970522@163.com (Y.Z.); djq41917030125@163.com (J.D.); qmm0620@163.com (M.Q.); chenzhe00123@163.com (Z.C.)

\* Correspondence: 20120803@xpu.edu.cn

**Abstract:** Hierarchical Zn-ZSM-5 photocatalyst structures were synthesized via a hydrothermal one-pot synthesis route using a double template. Activated attapulgite (Si-ATP) and zinc nitrate ( $\text{Zn}(\text{NO}_3)_2$ ) precursors were used as silicon and zinc sources, respectively. The structural properties, morphology, photocatalytic activity and the texture properties of the synthesized Zn-ZSM-5 photocatalysts were investigated using X-ray diffraction (XRD), scanning electron microscope (SEM), diffracted ultraviolet–visible (UV–Vis) spectrometry (DRUV–Vis) and  $\text{N}_2$  adsorption/desorption, respectively. It was found that the composites exhibit a typical MFI framework structure, a hexahedral twin structure and typical UV absorption peaks at 292 nm and 246 nm, when the Zn/Si mole ratio reaches its optimum value of 1:100. The hierarchical nanocrystals exhibit a similar Brunauer–Emmett–Teller surface area ( $309 \text{ m}^2 \text{ g}^{-1}$ ) and a high mesopore ratio (37.47%) as compared to commercial zeolites. Sub-nano-sized zinc oxide (ZnO) particles with small size moieties were implanted and isolated in the silica matrices of micro-mesoporous zeolite, which had a significant photocatalytic activity and reusability of degrading methylene blue (MB) dyeing wastewater. Using a 500 W mercury lamp with the wavelength range from 185–500 nm operating during an illumination time of 30 min, the concentration of MB decreases significantly in the presence of Zn-ZSM-5 photocatalyst leading to a 95.56% of degradation, where the ratio still remained at 94.32% after six times of reuse.

**Keywords:** hierarchical structures; Zn-ZSM-5 photocatalyst; micro-mesoporous; methylene blue

**Citation:** Li, H.; Zhang, Y.; Diao, J.; Qiang, M.; Chen, Z. Synthesis and Photocatalytic Activity of Hierarchical Zn-ZSM-5 Structures. *Catalysts* **2021**, *11*, 797. <https://doi.org/10.3390/catal11070797>

Academic Editors: Gassan Hodaifa and Rafael Borja

Received: 21 April 2021

Accepted: 29 June 2021

Published: 29 June 2021

**Publisher's Note:** MDPI stays neutral with regard to jurisdictional claims in published maps and institutional affiliations.



**Copyright:** © 2021 by the authors. Licensee MDPI, Basel, Switzerland. This article is an open access article distributed under the terms and conditions of the Creative Commons Attribution (CC BY) license (<https://creativecommons.org/licenses/by/4.0/>).

## 1. Introduction

Printing and dyeing wastewaters are a complex mixture of pollutants including some carcinogenic, teratogenic and mutagenic organic compounds derived from aromatic hydrocarbons and heterocyclic compounds. The pollutants are characterized by high chroma, high chemical oxygen demand (COD), high pH, high salinity, high hardness and low biodegradability [1,2]. Therefore, efficient methods for degrading printing and dyeing wastewater for safe disposal are urgently needed [3]. The technique of photocatalysis enables an efficient use of solar energy to degrade organic matter and has, therefore, attracted considerable research interest recently to be utilized for printing and dyeing wastewater degradation [4–6].

In this context, the semiconducting photocatalyst ZnO has become a major research target in the field of photocatalytic degradation of water pollutants, since it offers several advantages such as facile synthesis, good practicability, an environmentally-friendly nature and no secondary pollution [7–9]. Notwithstanding the efficient degradation rates reported in these publications, pristine ZnO possesses some setbacks such as a wide energy band-gap ( $E_g = 3.37 \text{ eV}$ ) and limited spectral response to ultraviolet (UV) light. At the same time, it is also prone to photochemical corrosion. Moreover, ZnO particles can easily agglomerate, resulting in a low recovery rate and poor performance in industrial applications. To overcome such disadvantages of pristine ZnO, different approaches have been followed to increase the specific surface area and to generate more reaction sites to improve the



photocatalytic activity [10–12]. In recent years, considerable research efforts have been dedicated to ZnO composite materials [13]. ZnO has been successfully combined with graphene oxide [14], single-walled carbon nanotubes [15], fullerenes [16], Ag [17] and Pd [18], which has improved its photocatalytic activity to some extent. However, these composites are limited by high cost and complicated multi-step synthesis procedures. As a possible solution, hierarchical ZSM-5 zeolite structures are widely used as carriers of adsorbents and photocatalysts due to a high specific surface area, considerable volume of the micro-mesoporous pores, good structural stability and great capability for the separation and recovery of systems [19–22].

Chen et al. [23] successfully synthesized ZnO nanorods as a matrix to fabricate noble metal (Pt, Pd, and Ru)-supported ZnO photocatalysts by a liquid phase reduction method. It was shown that the incorporation of such noble metals significantly improves the photocatalytic performance of ZnO. Yang et al. [24] reported the synthesis of ZnO/stellerite composites via a direct deposition method, where the close combination and effective dispersion of ZnO and stellerite was achieved. The bandgap was reduced significantly in the composite and enhanced adsorption was obtained leading to improved photocatalytic performance. Zahra [25] et al. showed that ZnO nanoparticles can precipitate on the surface of ZSM-5 zeolite. The resulting ZSM-5/ZnO nanocomposites were further modified by silver nanoparticles of different quantities to investigate their photocatalytic efficiency. The investigation of different models describing the dye removal kinetics, a pseudo-second-order model was found to be most promising. This led to the conclusion that zeolite is an excellent carrier of ZnO. However, only few studies have been reported on the preparation of hierarchical Zn-ZSM-5 zeolite photocatalyst structures using double templating agents and a one-step crystallization hydrothermal method, to the best of the authors' knowledge. Furthermore, few reports exist regarding the investigation of the effect of the Zn/Si molar ratio on the framework and pore structure of these synthetic composites.

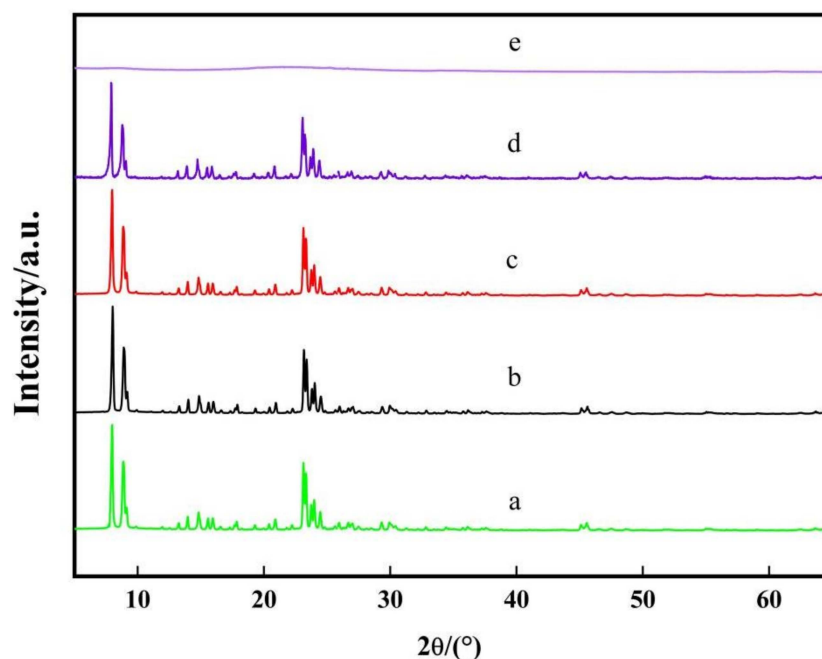
In this paper, Si-ATP and  $\text{Zn}(\text{NO}_3)_2$  were used as precursor silicon and Zn sources, respectively, to prepare hierarchical Zn-ZSM-5 zeolite photocatalyst via a hydrothermal one-pot synthesis process using a double template. The crystal structure, morphology, pore structure and photocatalytic activity of the samples were characterized by X-ray diffraction (XRD), scanning electron microscopy (SEM), diffracted ultraviolet–visible (UV–Vis) spectrometry (DRUV–Vis), and  $\text{N}_2$  adsorption/desorption and pore size distribution analysis, respectively. The effects of the pore structure and Zn/Si ratio on the photocatalytic performance of the synthesized products were investigated, and further details about the photocatalytic mechanism could be revealed.

## 2. Results and Discussion

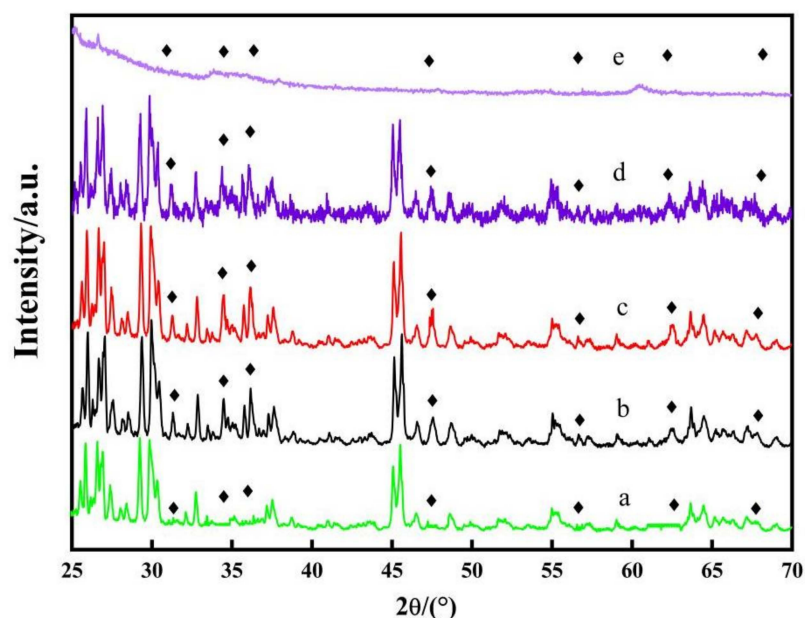
### 2.1. Characterization by X-ray Diffraction (XRD)

Figure 1 shows XRD patterns of samples with different Zn/Si ratio. Strong diffraction peaks appeared in sample a at  $2\theta = 7.9^\circ, 8.8^\circ, 23.2^\circ, 23.9^\circ$  and  $24.4^\circ$ , which is consistent with the typical MFI framework of hierarchical ZSM-5 zeolite [26]. These peaks are preserved in samples b, c and d, indicating crystalline order of the zeolite framework. However, with the increase of the Zn/Si ratio, the characteristic peak intensities of the zeolite decrease gradually, which indicates that the addition of Zn led to slight degradation of the crystallinity of the zeolite framework. An abrupt change is noted for a Zn/Si ratio of 1:25, when the diffraction peaks of ZSM-5 zeolite disappear. Only the onset of very broad peaks appear near  $20\text{--}30^\circ$  and  $60^\circ$  can be observed, which indicates that the addition of excessive Zn source hinders the crystallization of the MFI framework. In this case, the synthetic product is an amorphous crystal containing zinc. Figure 2 shows XRD patterns of samples with different Zn/Si ratio between 25–70° for further exploring the synthesis of zinc oxide in the product. Zn/Si ratios range from 1: 200 to 1: 50, and the XRD patterns of these zeolites are in good agreement with the database JCPDS card (No.36-1451),  $2\theta = 30.9^\circ, 34.4^\circ, 36.2^\circ, 47.5^\circ, 56.5^\circ, 62.8^\circ$  and  $67.9^\circ$  represents the crystal face (100) (002) (101) (102) (110) (103) and

(112) from hexahedron phase, respectively. With Zn/Si ratio increased to 1:100, the XRD pattern shows the characteristic peak intensity of ZnO is higher and sharper. The addition of excessive zinc source results in the disappearance of typical characteristic peaks of ZnO, which indicates that the crystal gradually becomes amorphous.



**Figure 1.** X-ray diffraction (XRD) patterns of pure ZSM-5 (a) and composite products with different Zn/Si ratios Zn-ZSM-5 n(Zn)/n(Si) of: (b) 1:200; (c) 1:100; (d) 1:50; (e) 1:25.



**Figure 2.** XRD (25–70°) patterns of pure ZSM-5 (a) and composite products with different Zn/Si ratios Zn-ZSM-5 n(Zn)/n(Si) of: (b) 1:200; (c) 1:100; (d) 1:50; (e) 1:25.

## 2.2. Characterization by Scanning Electron Microscopy (SEM)

SEM images collected with a  $\times 10,000$  magnification depict the sample morphology with different Zn/Si ratios (Figure 3). Obviously, sample a is a typical hexahedral ZSM-5 zeolite. When the Zn content is increased in terms of a Zn/Si ratio in the range of 1:200 to 1:50, samples b, c, and d show hexagonal twinned grains. Two hexahedrons grow

vertically and alternately, forming a plurality of faces. In addition, with the change of the Zn/Si ratio, the grain size also changes. This may be attributed to the fact that the electronegativity of  $\text{Zn}^{2+}$  in the zeolite pore structure is stronger than that of the bridging oxygen on the aluminum in the main zeolite framework [26]. This may result in a clustering phenomenon between the crystals, accompanied by an unclear angular structure of the grains. At the same time, irregular grains are formed on the twin surface, which were identified as small sub-nano ZnO clusters using UV diffuse reflectance spectroscopy. On the other hand, sample e is flocculent and amorphous, and contains a considerable amount of impurities, indicating that the addition of excessive zinc would impede the growth of the hexahedron crystalline structure of zeolite ZSM-5.

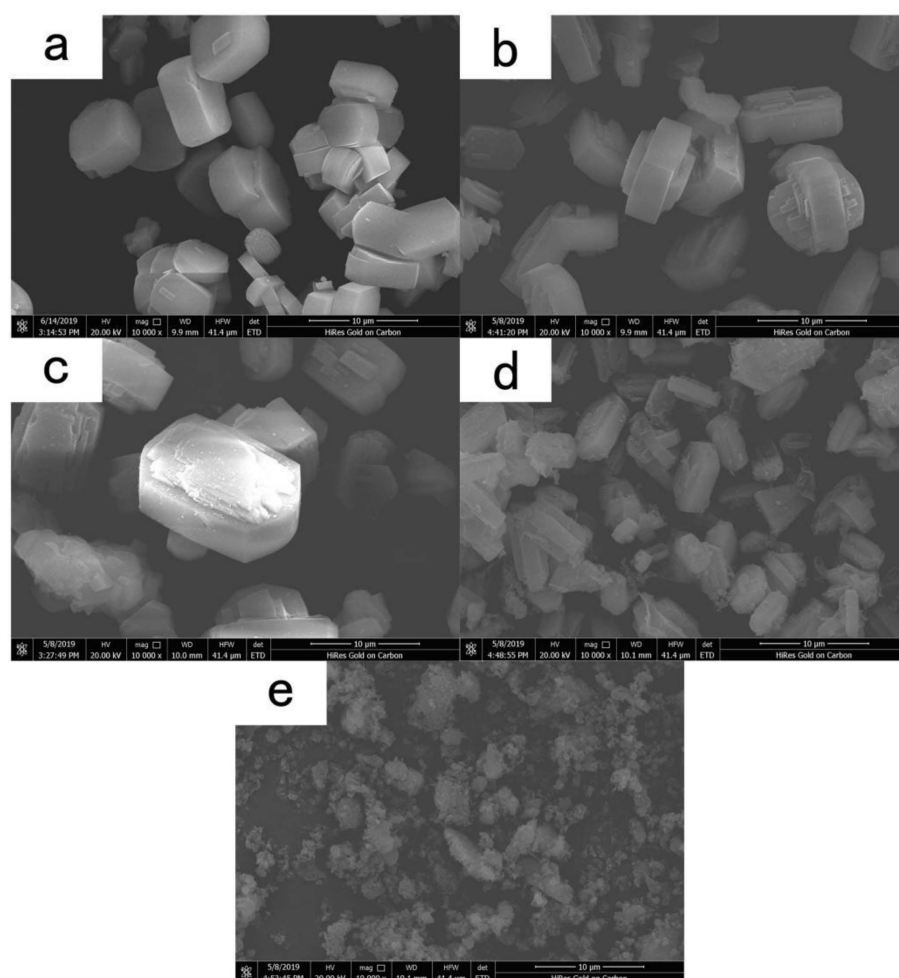


**Figure 3.** SEM morphology of pure ZSM-5 (a) and composite products with different Zn/Si ratios Zn-ZSM-5 n(Zn)/n(Si) of: (b) 1:200; (c) 1:100; (d) 1:50; (e) 1:25.

### 2.3. Diffracted Ultraviolet–Visible (UV–Vis) Spectra

The diffuse reflectance UV–visible spectra demonstrate the photo-response activity of the photocatalysts with different Zn/Si ratios, as shown in Figure 4. When the Zn/Si ratio is within the range of 1:200 to 1:50, Zn species may be highly dispersed in the ZSM-5 zeolite framework, since they display absorption peaks at 292 nm and 246 nm. The absorption peak near 292 nm may be attributed to the small sub-nano ZnO clusters, and the absorption peak at 246 nm may be attributed to the characteristic peak of strong interaction between the small sub-nano ZnO cluster and zeolite [27]. For less Zn content in terms of a of Zn/Si ratio of 1:200 in sample b, the content of small sub-nano ZnO clusters in the sample b may be low. This in turn may lead to a quantum size effect, and concomitantly a peak blue-shifting at 246 nm is observed. When the Zn content increases to a Zn/Si ratio of

1:100, the intensity of the absorption peak increases significantly and red shifts can be detected, indicating that the sample now exhibits an expanded response range to light and the photocatalytic activity increases. When the Zn content further increases to a Zn/Si ratio of 1:50, the overlap of electronic wave functions is enlarged due to the formation of more sub-nano ZnO clusters, which may result in the increase of internal stress in the particles. Therefore, the energy band gap is narrowed. As a result, the UV absorption peak of the sample d is decreased and blue shifts were observed. According to the XRD and SEM results, an excessive Zn content may impede the formation of the main zeolite structure, leading to the appearance of amorphous crystals, and more importantly there are no groups or products with UV absorption activity present in the structure. For the determination of the bandgap value of the composite products with different Zn/Si ratios Zn-ZSM-5, the Tauc's method fitted with the data, the values of the band gap energy were that 3.36 eV, which was determined as for a neat semiconductor with ZnO from Figure 5.

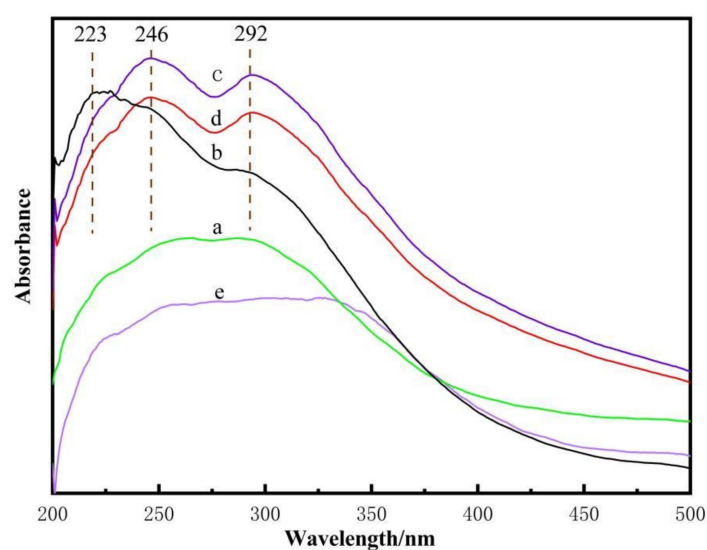


**Figure 4.** Diffuse reflectance ultraviolet–visible (UV–Vis) spectra of pure ZSM-5 (a) and composite products with different Zn/Si ratios Zn-ZSM-5 n(Zn)/n(Si) of: (b) 1:200; (c) 1:100; (d) 1:50; (e) 1:25.

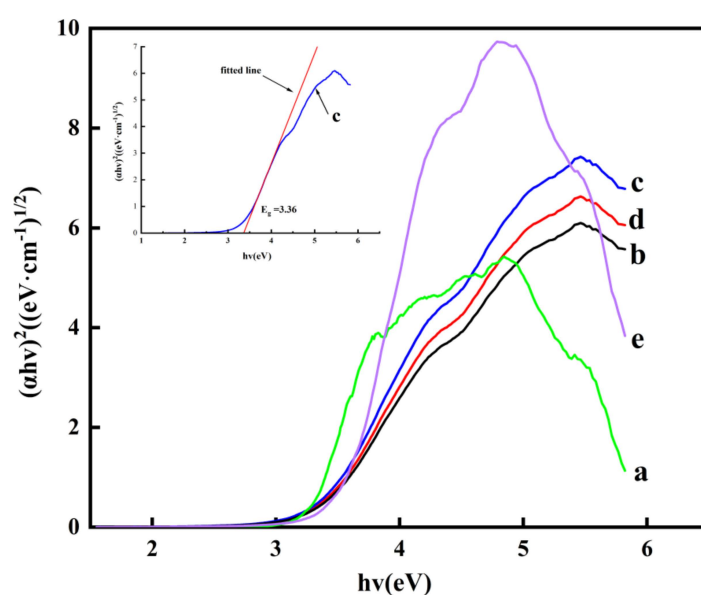


**Figure 5.** Tauc plots of pure ZSM-5 (a) and composite products with different Zn/Si ratios Zn-ZSM5 n(Zn)/n(Si) of: (b) 1:200; (c) 1:100; (d) 1:50; (e) 1:25. The determinations of  $E_g$  for measurements c are shown as insets.

#### 2.4. Specific Surface Area and Pore Size

Figure 6 shows the  $N_2$  adsorption–desorption isotherms of pure ZSM-5 and various composites with different Zn/Si ratios. H4-type hysteresis loops were observed in samples a–d, indicating that the mesoporous channels were uniform upon the addition of Zn to a certain extent, and the curves can be classified as type IV adsorption/desorption isotherms [28,29]. In the case of Zn excess, H3-type hysteresis loops appear in sample e, indicating that the shape and size of the channels have become uneven, which confirms that excessive Zn doping affects the crystal formation. Figure 7 shows the pore size distribution of hierarchical zeolite with different Zn contents. It can be seen from Table 1 that the pore structure and specific surface area change with the increase of the Zn content. For a Zn/Si ratio in the range from 1:200 to 1:50, the small sub-nano ZnO clusters affect the pore structure and especially the decrease of small-sized pores is significant. Furthermore, with the increase of the Zn content, the specific surface area shows a significant downward trend, which further demonstrates that sub-nano ZnO clusters with photocatalytic activity enter the surface and pores of the hierarchical zeolite. The pore size of 3.48 nm for pure ZSM-5 zeolite decreased to 2.26 nm with the introduction of Zn at a Zn/Si ratio of 1:100. This may be explained by the filling of the pores in the zeolite structure by sub-nanometer ZnO. When the Zn content continues to increase from a Zn/Si ratio of 1:100 to 1:50, the changes of specific surface area and pore size are no longer significant. This indicates that a Zn/Si ratio of 1:100 leads to a good pore structure and structural stability. When more Zn is added ( $n(\text{Zn})/n(\text{Si}) > 1:50$ ), the excessive Zn will affect the formation of the zeolite framework as mentioned above, and the number of intergranular pores and macropores increase. The specific surface area drops suddenly and the total pore volume increases, which may be related to the fact that the original zeolite structure is no longer stable. Hierarchical ZSM-5 zeolite has good adsorption performance, which is beneficial to the enrichment of photocatalytic fillers entering the mesoporous zeolite. When the position of photocatalytic active groups is in the environment with relatively high substrate concentration, the photocatalytic reaction rate can be improved. Therefore, zeolite loses its stable structure when the material loses its structural stability.

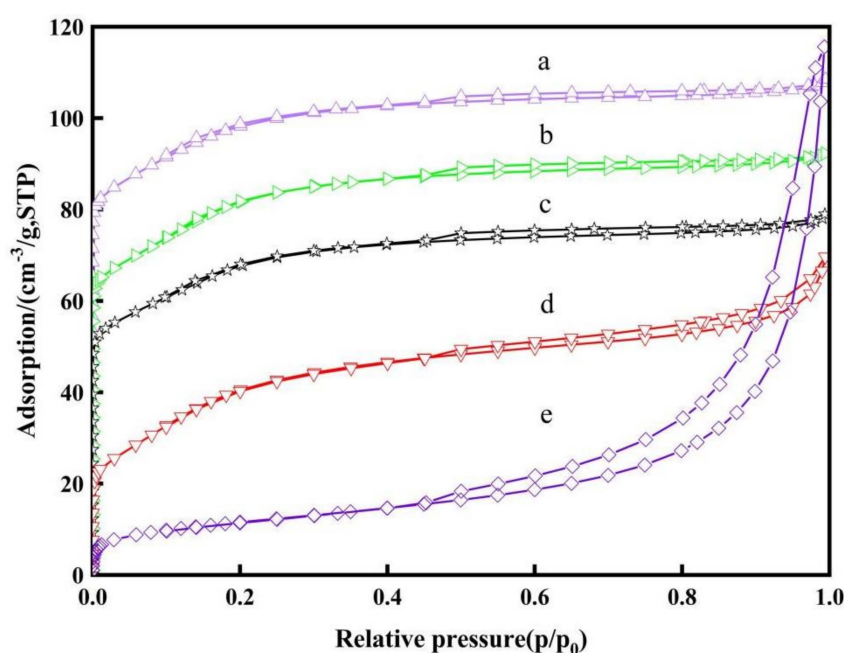


**Figure 6.**  $N_2$  adsorption-desorption isotherms of pure ZSM-5 (a) and composite products with different Zn/Si ratios Zn–ZSM-5  $n(\text{Zn})/n(\text{Si})$  of: (b) 1:200; (c) 1:100; (d) 1:50; (e) 1:25.

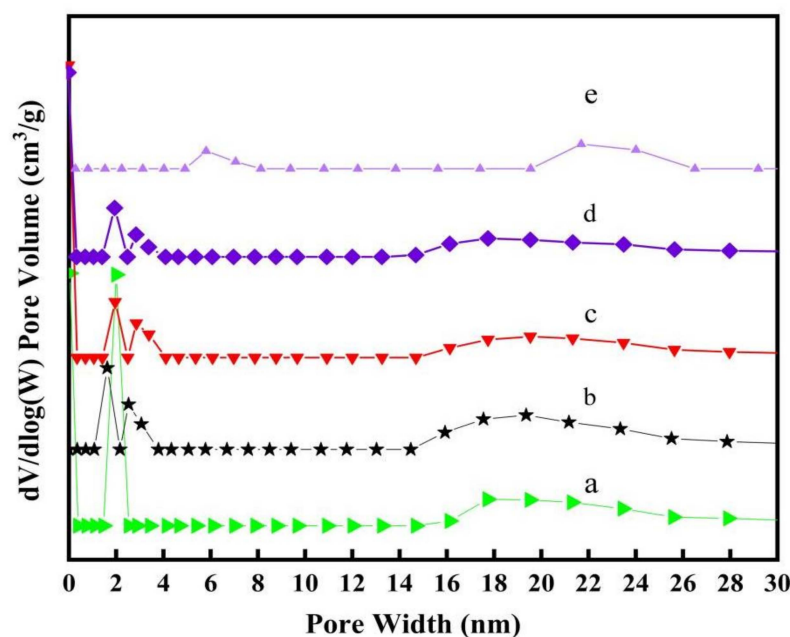


**Figure 7.** Pore size distribution of pure ZSM-5 (a) and composite products with different Zn/Si ratios Zn-ZSM-5 n(Zn)/n(Si) of: (b) 1:200; (c) 1:100; (d) 1:50; (e) 1:25.

**Table 1.** Textural properties of ZSM-5 and products with different Zn/Si ratios.

Sample	$S_{BET}/(m^2/g)$	$V_{tot}/(cm^3/g)$	$V_{mes}/(cm^3/g)$	$V_{mes}/V_{tot}$ (%)	Pore Size/(nm)
a	333	0.19	0.093	48.83	3.48
b	319	0.18	0.072	39.67	2.73
c	309	0.18	0.068	37.47	2.46
d	308	0.16	0.055	33.41	2.26
e	120	0.54	0.497	91.78	14.46

### 3. Photocatalytic Performance

#### 3.1. Photocatalytic Performances of Samples with Different Zn/Si Ratios

For the study of photocatalytic performance, the hierarchical Zn-ZSM-5 zeolite photocatalysts with different Zn/Si ratio were added to the MB solutions to perform photocatalytic reactions. The results are shown in Figure 8. In the dark reaction stage of 0–30 min, all samples were in the adsorption stage. After 30–60 min, the adsorption equilibrium state is reached. Under illumination for 0–10 min, the degradation rate curve showed a sharp decrease, followed by a gradual line flattening. For a Zn/Si ratio between 1:200 and 1:100, the photocatalytic degradation efficiency is significantly improved, while the photocatalytic degradation efficiency decreases when the ratio of Zn/Si is between 1:100 to 1:50. This implies that the optimal Zn/Si ratio is achieved at 1:100 in sample c. When the Zn content further increases to a Zn/Si ratio of 1:25 in sample e, the photocatalytic degradation efficiency was lower than that of the unmodified ZSM-5 zeolite. This is due to the instability of the zeolite structure as mentioned above. To summarize, in the case that the amount of Zn added is insufficient, the quantity of photocatalytic reaction sites determines the reaction rate. That is to say, the more Zn that is added, the better the photocatalytic performance of hierarchical Zn-containing zeolite will be. On the other hand, when Zn is added in excess, too many sub-nanometer ZnO clusters will affect the stability of the ZSM-5 zeolite framework structure and the synthesis of hierarchical Zn-containing zeolite basically fails and the structure cannot be used as a photocatalyst. The extra sub-nanometer ZnO clusters of sub- $NaNO_2$  may enter the pores and occupy the adsorption channel of MB, thus affecting the adsorption process. Additionally, the occupation of pores will also



affect the entry of dye molecules and the discharge of reaction intermediates, thus affecting the whole reaction process. Therefore, the deterioration of the photocatalytic activity, since the photocatalytic reactions take place on the surface of sub-nano ZnO clusters within the mesopores. Photocatalytic reactions will take place on the surface of sub-nano ZnO clusters with photocatalytic activity. An appropriate amount of Zn will increase the number of reactive groups without causing pore blockage and significant improvements in photocatalytic degradation can be achieved.

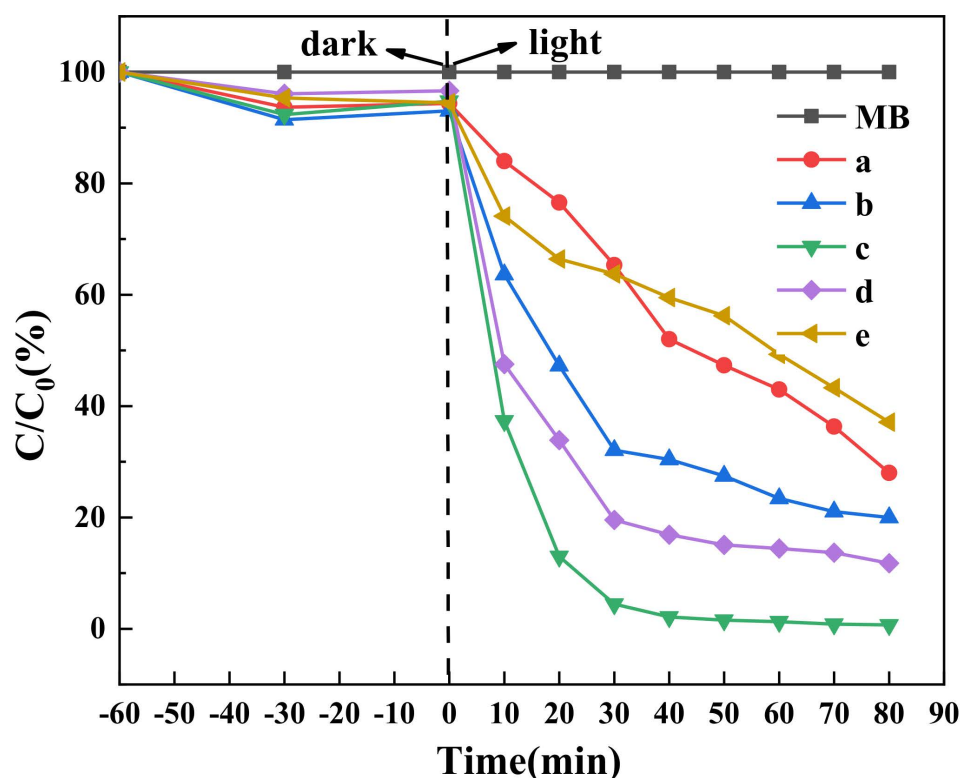


**Figure 8.** Photocatalytic effect of pure ZSM-5 (a) and composite products with different Zn/Si ratios Zn-ZSM-5 n(Zn)/n(Si) of: (b) 1:200; (c) 1:100; (d) 1:50; (e) 1:25. Experimental condition: V = 100 mL, T = 5 °C; catalyst dose, 0.2 g/L; initial concentration of pollutant, 50 mg/L; initial concentration of oxidant = 0.8 mmol/L; pH = 7.

### 3.2. Effects of Solution System on Photocatalytic Degradation

For Figure 9, under the illumination of 60 min, the photocatalytic degradation rate of the hierarchical Zn-ZSM-5 zeolite was 63.26%, and the hierarchical ZSM-5 zeolite with 0.1 mL of 30% (mass fraction) H<sub>2</sub>O<sub>2</sub> solution is 61.44%. Meanwhile, after turning on the light, the reaction rate of dropping H<sub>2</sub>O<sub>2</sub> solution is basically unaffected. This is because H<sub>2</sub>O<sub>2</sub>, as an electron trapping agent, can inhibit the recombination of photogenerated electron-hole pairs. Hydroxyl radical ( $\cdot$ OH) was generated through a series of reactions after captured electrons by H<sub>2</sub>O<sub>2</sub>. The obtained  $\cdot$ OH are well dispersed in the photocatalytic system, so that photocatalytic degradation of MB solution could be continuously performed. In addition, the bond energy of oxygen–oxygen bonds in H<sub>2</sub>O<sub>2</sub> is 142 kJ/mol. When the wavelength of light source is less than 800 nm, the light utilization efficiency increases and more hydroxyl groups are generated.

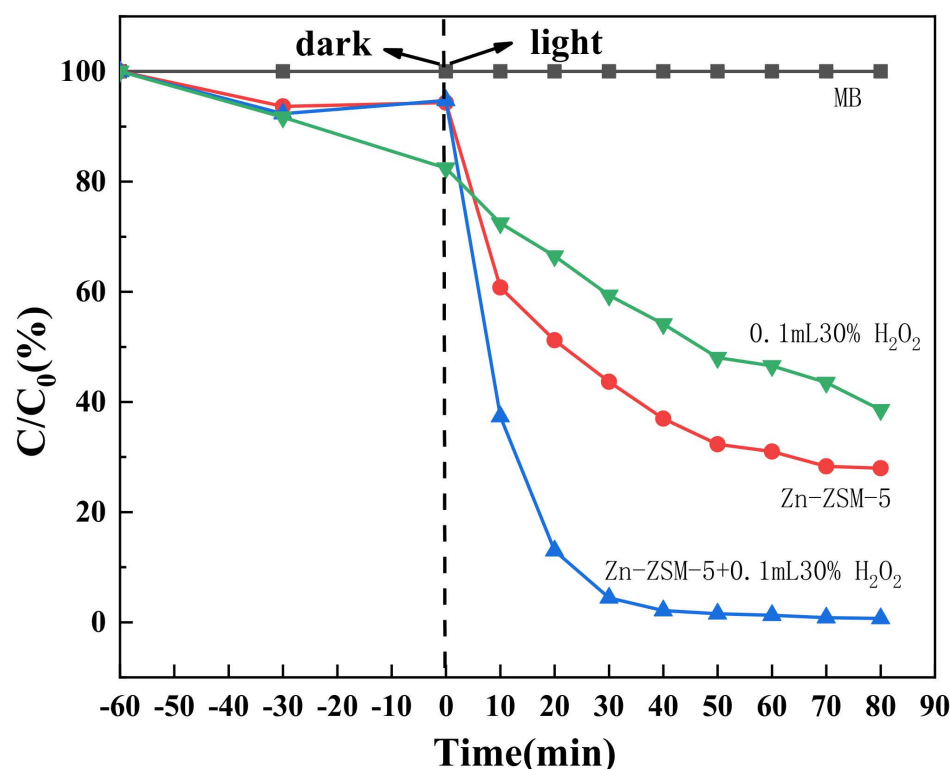


Figure 9. Effect of solution system on photocatalytic activity.

### 3.3. Photodegradation Kinetics of Hierarchical Zn-ZSM-5 Photocatalyst Structures

Under UV–visible light, the photodegradation kinetics of hierarchical Zn-ZSM-5 photocatalyst structures with different ratio of Zn/Si,  $n(\text{Zn})/n(\text{Si})$  of: (b) 1:200; (c) 1:100; (d) 1:50, are described by pseudo-first order rate constant (Equation (1)), which illustrates that the reactions take place at a solid–liquid interface.

$$\ln(C/C_0) = -k \cdot t \quad (1)$$

In here,  $k$  is the apparent first-order rate constant for the MB degradation. Figure 10 shows the plot of natural logarithm of the normalized concentration  $[\ln(C/C_0)]$  as a function of irradiation time ( $t$ ) for the photodegradation of MB in the presence of hierarchical Zn-ZSM-5 photocatalyst structures. As can be seen in Figures 10 and 11, all the data fitted well to a straight line passing through the origin. The linear relationship suggests that the degradation reaction is pseudo-first-order. The obtained first-order rate constants ( $k$ ) for the degradation of MB in the presence of hierarchical Zn-ZSM-5 photocatalyst structures with 1:100 ratio of Zn/Si had the fastest kinetics. Our kinetic results indicate that hierarchical Zn-ZSM-5 photocatalyst structures with 1:100 ratio of Zn/Si have a fast degradation rate of MB and show perfect photocatalytic performance. Therefore, apart from being a sorbent and a supporting platform, ZSM-5 also enhances the photocatalytic properties of ZnO. This excellent photocatalytic activity can be explained by two main processes: (1) direct adsorption of MB onto micro-mesoporous Zn-ZSM-5 zeolite, and (2) photodegradation of the adsorbed dye on the catalytic surface of Zn-ZSM-5 zeolite under UV-irradiation. The photocatalytic degradation can be enhanced by increasing the amount of dye adsorbed onto the adsorbent. Based on the above, the role of Zn-ZSM-5 zeolite is imperative in photocatalytic degradation due to its porous structure and high surface area, which provides more accessible adsorption sites. A control experiment for the photodegradation of MB (10 mg/L, 10 mL) by Zn-ZSM-5 zeolite (10 mg) is also conducted. However, no appreciable change in absorbance of the MB solution is observed even after 12 h. Zn-ZSM-5 zeolite has significantly high specific surface area, porosity and particle size as compared to traditional microporous ZSM-5 zeolite, which therefore lead to ZnO dispersion and



high MB adsorption. The importance of the adsorption step to photocatalysis is further revealed in this result. During the photocatalytic degradation, the color of MB solution disappeared as the solution exposed to UV light, which can be ascribed to the destruction of the chromophore.

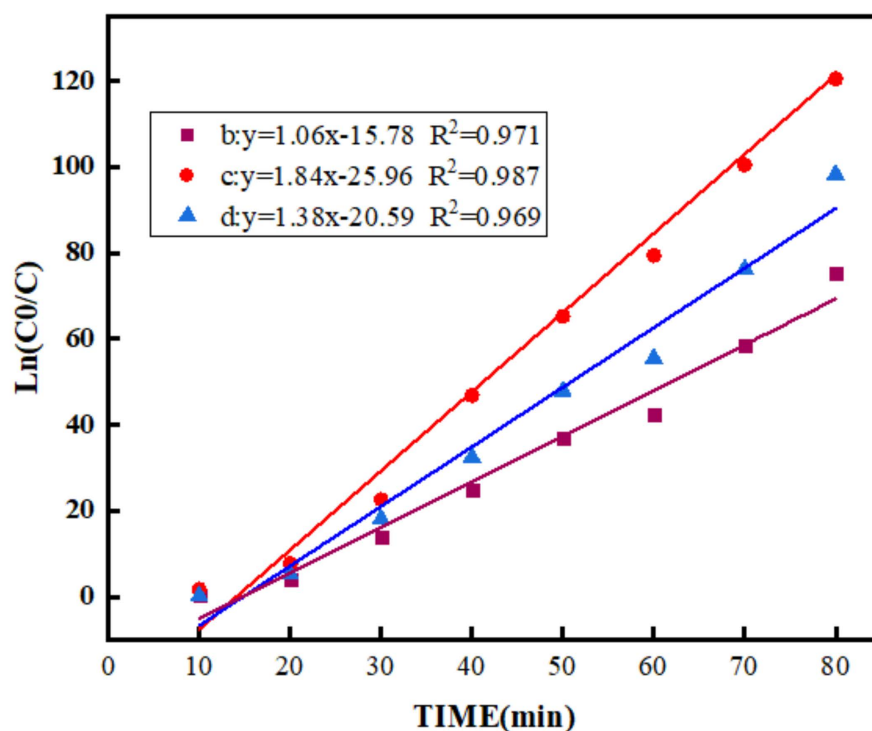


**Figure 10.** First-order kinetics of hierarchical Zn-ZSM-5 photocatalyst structures with different Zn/Si ratios Zn-ZSM-5 n(Zn)/n(Si) of: (b) 1:200; (c) 1:100; (d) 1:50.

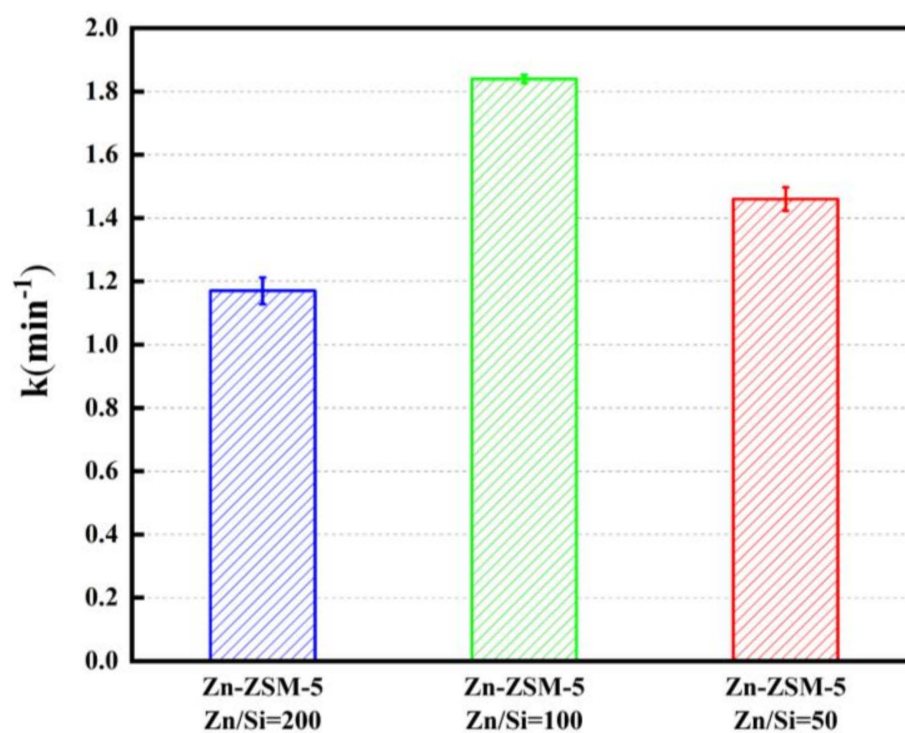


**Figure 11.** Photocatalysis kinetic constants of the evaluated conditions.

### 3.4. Reusability

In order to test the reusability of the material further, the recycling experiments are conducted under the same conditions, the result showed in Figure 12. The photocatalytic activity of hierarchical Zn-ZSM-5 (Zn/Si = 1:100) still reaches 94.32% after being reused for 6 times. Due to their morphology, some particles may not be recovered by suffering from the repeated mechanical external forces such as stirring, suction filtration and calcination, which may lead to the observed slight decrease of the photocatalytic performance of the zeolite after repeated operations. It should be stated though that the repeated use has only a moderate impact on the material. Under 500 W light irradiation, the optimal Zn-ZSM-5 zeolite (Zn/Si ratio = 1:100) exhibits a photocatalytic degradation rate of MB of 95.56% and 99.28% after 30 min and at the end of the reaction, respectively. In addition, the Zn-ZSM-5 zeolite photocatalyst has excellent photocatalytic stability and, more important the degradation rate after six cycles still exhibited a high value of 94.32%.

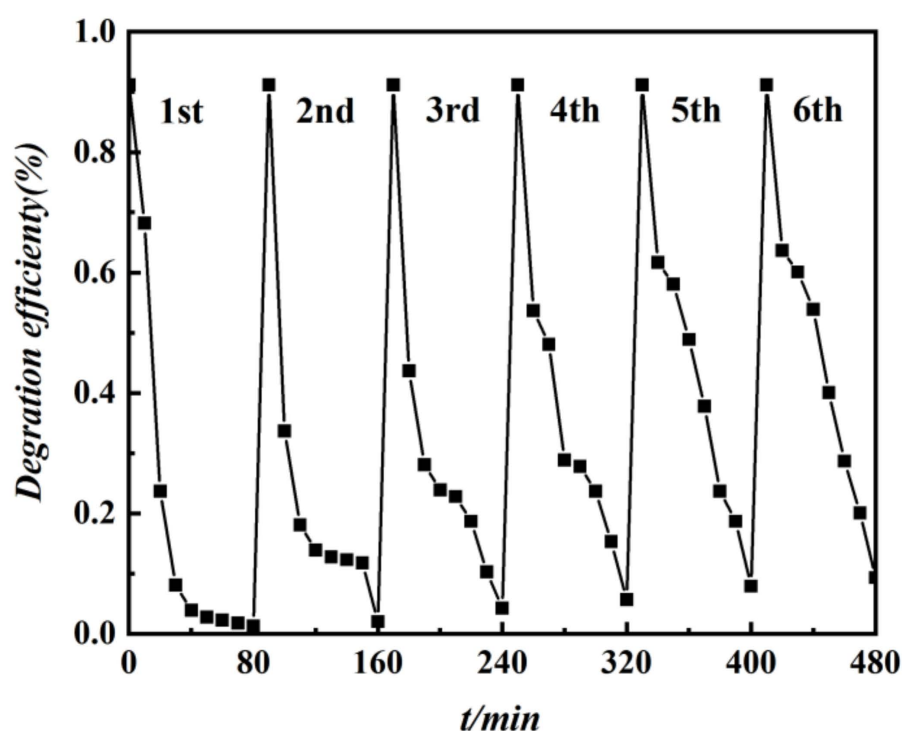


**Figure 12.** Regeneration and reusability of the photocatalyst in different cycles.

### 3.5. X-Ray Photoelectron Spectroscopy (XPS) Analysis of Reused Samples

To confirm the expected compositions of the last reused Zn-ZSM-5 samples, compared with pure ZSM-5, all peaks (O 1s, Zn 2p, Al 2p, Si 2s and Si 2p) relevant to this study are identified, as shown in Figure 13a and Table 2. The full-range X-ray photoelectron spectroscopy (XPS) spectra results seen in Figure 1 qualitatively revealed the existence of Si 2s, Si 2p, Al 2p and O 1s in pure ZSM-5, with atomic percent accounts for 9.45%, 11.69%, 1.15% and 40.50%, respectively. High-resolution XPS spectra of Zn-ZSM-5 samples (n(Zn)/n(Si) of 1:100), which reveals not only the existence of Si 2s, Si 2p, Al 2p and O 1s, with atomic percent accounts for 9.65%, 12.23%, 1.16% and 42.88%, but also the existence of Zn 2p, with atomic percent accounts for 0.61%. Thus, it can be concluded that the partial metal cations of Zn is located in the framework of Zn-ZSM-5 samples. Figure 13b shows that the peak of Zn 2p XPS spectra in Zn-ZSM-5 samples appears three bonding environments, which are Zn-OH<sup>+</sup> (1023.5 eV), ZnO (1021.7 eV), Zn 2p 3/2 (1021.4 eV) [30]. Among of them, the higher binding energy of zinc species (1023.5 eV) is mainly due to the formation of Zn-OH<sup>+</sup> with the framework of ZSM-5 zeolite, the binding energy of zinc species between 1021.7 eV and 1021.4 eV comes from the sub-nano-sized ZnO particles with small size moieties in micro-mesoporous zeolite [19].

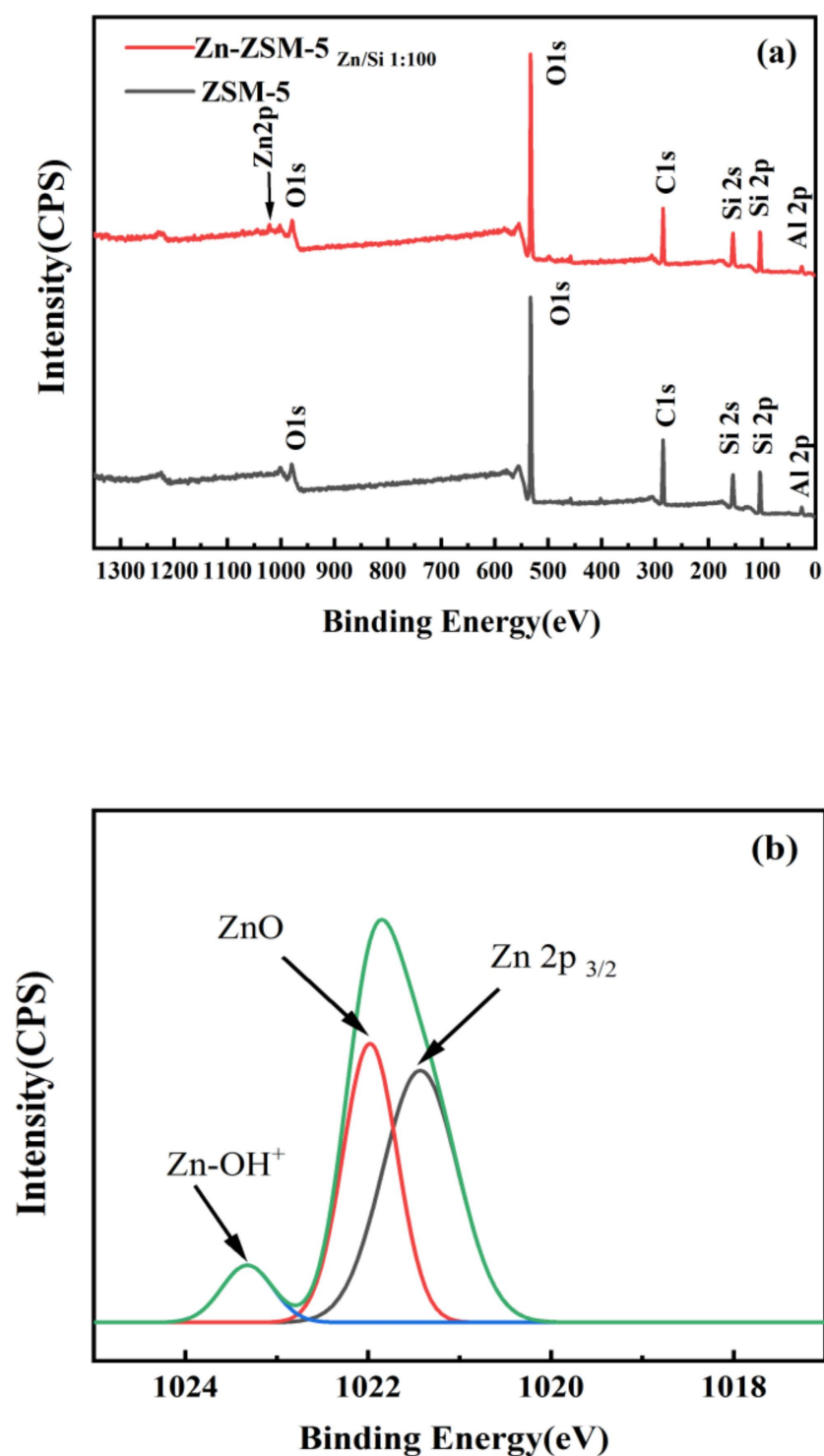


**Figure 13.** X-ray photoelectron spectroscopy (XPS) survey spectra of (a) pure ZSM-5 and Zn-ZSM-5 (Zn/Si = 1:100) and (b) Zn 2p in Zn-ZSM-5 composite products (n(Zn)/n(Si) of 1:100).

**Table 2.** Atomic percent accounts of pure ZSM-5 and Zn-ZSM-5 from XPS survey spectra (Unit: %).

Sample	O1s	Zn2p	C1s	Si2s	Si2p	Al2p
ZSM-5	40.5	0.00	37.20	9.45	11.69	1.15
Zn-ZSM-5	42.88	0.61	33.46	9.65	12.23	1.16

## 4. Experimental

### 4.1. Synthesis of Hierarchical Zn-ZSM-5 Composite Photocatalysts

Alkali-modified attapulgite [31] and 9% (mass fraction) hydrochloric acid were transferred into a hydrothermal crystallization kettle in the solid-liquid ratio of 1:8, followed by hydration at 180 °C for 12 h. The solution was centrifuged, rinsed and dried to obtain a zeolite precursor Si-ATP.

Accurately weighed amounts of 0.055 g NaAlO<sub>2</sub>, 0.118 g polyethylene oxide–polypropylene oxide–polyethylene (PEO-PPO-PEO, short for P123) as mesoporous template, 0.55 g tetrapropylammonium bromide (TPABr) microporous template and various amounts of Zn(NO<sub>3</sub>)<sub>2</sub> were mixed and dissolved in 5.20 mL of deionized water. Next, 0.8 g Si-ATP and 2.1 mL NaOH solution (1 mol/L) were added and stirred in a water bath at 60 °C for 2 h to obtain the initial gel. Next, the samples were transferred to a hydrothermal PTFE crystallization reactor, which was sealed and crystallization was carried out at 180 °C for 36 h in a conventional oven (DZF-603, Shanghai Jinghong Experimental Equipment Co., Ltd.). After carrying out the reaction process, the reaction was allowed to cool down naturally to room. All of the synthesized products were washed by centrifuging repeatedly with distilled deionized water, and subsequently dried at 80 °C for 6 h in ambient condition, then calcination in a muffle furnace at 550 °C for 5 h to remove the template agent, leading to the final product. The amount of Zn(NO<sub>3</sub>)<sub>2</sub> was adjusted to 5 different values of 0, 1.98, 3.96, 7.92 and 15.84 mg to obtain pure ZSM-5 zeolite and Zn-ZSM-5 composites with Zn/Si ratios of 1:200, 1:100, 1:50 and 1:25, respectively. The samples were named as sample a, b, c, d and e, respectively.

### 4.2. Sample Characterization

An X-ray diffractometer (Shimadzu, Tokyo, Japan) was used to analyze the crystallography of the synthesized samples. The morphology was tested by SEM using an FEI Quanta-450-FEG (FEI Company, Hillsboro, OR, USA). The light response of the samples was evaluated by an Evolution 220 dual-beam UV–Vis spectrophotometer (Thermo Fisher Scientific Company, Waltham, MA, USA). The N<sub>2</sub> adsorption-desorption isotherms of the samples were measured using a Micromeritics ASAP 2020 PlusHD88 (New York, NY, USA) equipment. The total pore volume was obtained by converting the nitrogen adsorption capacity into the volume of liquid nitrogen at the relative pressure ( $P/P_0$ ) of 0.95.

### 4.3. Photocatalytic Degradation Evaluation

Tests of the photocatalytic activity of the synthesized Zn-ZSM-5 zeolite photocatalyst were carried out under UV radiation. First, 50.00 mg of methylene blue dye as the target pollutant were dissolved in 1.00 L deionized (DI) water and heated to 60 °C for 8 h to simulate dyeing wastewater. For each degradation solution, 20 mg of sample and 0.1 mL of 30% (mass fraction) H<sub>2</sub>O<sub>2</sub> solution were added into 100 mL of the methylene blue solution, and the mix was transferred to the photocatalytic reactor. Under dark conditions, the adsorption equilibrium was achieved by magnetic stirring for 60 min. After turning on a 500 W mercury light source, 5 mL of degradation solution was taken out every 10 min. The solution was firstly filtered through a microporous membrane ( $d = 0.45 \mu\text{m}$ ) and the absorbance of the solution at the methylene blue (MB) maximum absorption wavelength of  $\lambda = 664 \text{ nm}$  was measured by an UV–visible spectrophotometer (UV757CRT, Shanghai Precision Scientific Instrument Co., Ltd. China).

### 4.4. Repeatability Experiment of Photocatalytic Degradation

Collecting and setting the suspension of photocatalyst particles until 48 h, then the filtrate was filtered to colorless. The acquired photocatalytic material is put into muffle furnace calcined for 4 h. The obtained samples were subjected to photocatalytic tests according to the previous test conditions.

## 5. Conclusions

By varying the amount of  $\text{Zn}(\text{NO}_3)_2$  precursor, Zn-ZSM-5 zeolite photocatalysts with different Zn/Si ratio were synthesized by a one-step hydrothermal synthesis method. It was shown that the Zn/Si ratio has a significant impact on the crystal structure, surface morphology, photo-response activity and texture characteristics. The Zn/Si ratio exhibits an optimal value of 1:100, where the basic framework and the Zn-ZSM-5 composite display an MFI-type topology. The pore structure was found to be rather regular with a uniform pore size distribution.

The  $\text{Zn}(\text{NO}_3)_2$  precursor is transformed into sub-nanometer ZnO clusters during synthesis, where the clusters are assembled on the surface and inside of the hierarchical ZSM-5 zeolite. The synthesized Zn-ZSM-5 zeolite then contains more photocatalytic active site, which improves the enrichment efficiency of MB, facilitates the photocatalytic reactions, which leads to a synergistic effect of enhanced adsorption on the composite surface and improved photocatalytic activity. However, excessive addition of zinc leads to a blocking of the pores and the zeolite framework structure collapses, resulting in an insignificant photocatalytic degradation rate.

**Author Contributions:** Investigation, M.Q.; Methodology, J.D. and Z.C.; Validation, M.Q.; Writing—original draft, H.L. and Y.Z.; Writing—review & editing, H.L. All authors have read and agreed to the published version of the manuscript.

**Funding:** This work was supported by the National Natural Science Foundation of China (No. 21573171), Shanxi Province Key Research and Development Plan of China (2021SF-438), the Shanxi Provincial Natural Science Foundation of China (No. 17JK0327), the Ph.D. Research Initiation Fund of Xi'an Polytechnic University (BS201932), and the Research and Innovation Training Project for Graduate in General Universities of China (201910709028), and thanks eceshi ([www.eceshi.com](http://www.eceshi.com), accessed on 29 June 2021) for the XPS analysis.

## References

1. Zhu, Q.-R.; He, S.-Y.; Zhao, X.-L.; Tang, W.-Y.; Song, X.-B.; Xue, L.-H.; Yang, L.-Z. Photocatalytic degradation of methyl orange by  $\text{AgCl}/\text{ZnO}/\text{GO}$ . *Res. Environ. Sci.* **2020**, *33*, 969–977.
2. Shang, J.-P.; Liu, R.; Qin, X.-P.; Zhao, B. Modified attapulgite clay with copper and rare earth catalytic oxidation printing and dyeing wastewater. *Chem. Ind. Eng. Prog.* **2020**, *39*, 439–444.
3. Gu, L.; Yu, H.-X.; Wang, Y.; Wang, T.; Yang, W.-H.; Wen, H.-F.; Tao, H. Preparation of  $\text{TiO}_2$ /river sediment composite and its visible light photocatalytic performance. *Acta Mater. Compos. Sin.* **2019**, *36*, 2665–2673.
4. Dong, M.-R.; Yu, X.-J.; Yu, J.; Lin, W.-S. Preparation and photocatalytic performance of  $\text{g-C}_3\text{N}_4/\text{ZnO}$  composite. *J. Synth. Cryst.* **2019**, *48*, 1314–1319.
5. Salazar, H.; Martins, P.M.; Santos, B.; Fernandes, M.M.; Reizabal, A.; Sebastián, V.; Botelho, G.; Tavares, C.J.; Vilas-Vilela, J.L.; Lanceros-Mendez, S. Photocatalytic and antimicrobial multifunctional nanocomposite membranes for emerging pollutants water treatment applications. *Chemosphere* **2020**, *250*, 126299–126314. [CrossRef]
6. Liu, X.-W.; Chen, Y.-J.; Liu, M.-J.; Zhang, X. Preparation and photocatalytic properties of  $\text{ZnS}/\text{ZnO}/\text{rGO}$  composite. *Min. Metall. Eng.* **2020**, *40*, 131–135.
7. Hung, F.-P.; Zou, Z.-B.; Zhou, X.-M.; Li, C.-H.; Liu, B.-X.; Ding, L. Preparation of  $\text{ZnO}/\text{Cu}_2\text{O}$  composite photocatalyst and study on its photocatalytic performance. *J. Funct. Mater.* **2020**, *51*, 12113–12119.
8. Zhou, X.-B.; Chen, J.-L.; Hu, Y.-Y.; Liu, Q.; Chen, C. Research progress on modification of nano-ZnO and its photocatalytic degradation performance. *New Chem. Mater.* **2019**, *47*, 47–52.
9. Cheng, T.; Hu, X.-B.; Xu, Y.-Q.; Wang, L.-J.; Jiang, W.; Jiang, W.H.; Xie, Z.X. Hydrothermal synthesis and fluorescence properties of  $\text{AgInS}_2/\text{ZnS}$  Core/Shell quantum dots. *Chin. J. Inorg. Chem.* **2020**, *6*, 69–78.
10. Tang, C.; Li, Y.-Y.; Liu, H.; Li, J.-S.; Xia, Z.; Zuo, J.-L.; Zhao, L.  $\text{AgBr}/\text{ZnO}$  composite photocatalyst and Its photocatalytic performance. *J. Chin. Ceram. Soc.* **2021**, *49*, 202–210.
11. Kumaresan, N.; Ramamurthi, K.; Babu, R.R.; Sethuraman, K.; Babu, S.M. Hydrothermally grown ZnO nanoparticles for effective photocatalytic activity. *Appl. Surf. Sci.* **2017**, *418*, 138–146. [CrossRef]
12. Chai, B.; Song, F.-K.; Chen, W.-J.; Zhou, H.; Zhang, F.; Zhu, Y.-C. Preparation and photocatalytic properties of flake-like  $\text{C}_{60}/\text{ZnO}$  nanocomposites. *J. Funct. Mater.* **2013**, *44*, 1816–1820.
13. Yan, B.; Cheng, W.; Ma, J.-Z. Morphology control of ZnO microstructures by varying hexamethylenetetramine and trisodium citrate concentration and their photocatalytic activity. *Mater. Des.* **2016**, *101*, 7–15.
14. Wu, X.; Sun, Y.-Z.; Wang, Y.; Deng, X.-Y.; Ma, C.; Li, L.-H. Research progress on zinc-based nano photocatalyst in wastewater treatment. *New Chem. Mater.* **2019**, *47*, 35–39.

15. Liu, W.; Zhan, W.-T.; Li, Y.; Chen, R.-S.; Ni, H.-W. Synthesis of ZnO/graphene oxide nanocomposite by microwave hydrothermal method and its photoelectrochemical property. *J. Wuhan Univ. Sci. Technol.* **2019**, *42*, 22–27.
16. Lu, Y.-H.; Xu, Y.-H.; Zhang, S.-L.; Bai, X.-J.; Huang, Y.; Chen, Y.-S. Visible-light photocatalytic activity of ZnO enhanced by single-walled carbon nanotubes. *CIESC J.* **2014**, *65*, 2855–2860.
17. Wang, Z.-Q.; Liang, X.-R.; Zhu, Y.-Y.; Zouhu, X.-Z.; Zhu, R.-J. Ag and Cu<sub>2</sub>O modified 3D flower-like ZnO nanocomposites and evaluated by photocatalysis oxidation activity regulation. *Ceram. Int.* **2019**, *45*, 23310–23319. [CrossRef]
18. Vijaya, K.; Suprabha, Y.; Anuj, M.; Kavitha, K.; Bernabe, M.; Naveen, K. Surface plasmon response of Pd deposited ZnO/CuO nanostructures with enhanced photocatalytic efficacy towards the degradation of organic pollutants. *Inorg. Chem. Commun.* **2020**, *121*, 108241–108250.
19. Haris-Mahyuddin, M.; Tanaka, S.; Shiota, Y.; Yoshizawa, K. Room-Temperature activation of methane and direct formations of acetic acid and methanol on Zn-ZSM-5 zeolite: A mechanistic DFT study. *Bull. Chem. Soc. Jpn.* **2020**, *93*, 345–354. [CrossRef]
20. Zhang, J.-M.; Liu, Y.-Q.; Li, H.-J.; Li, K.L. Study on Photocatalytic Performance of Natural Attapulgite and Optimization Of response Surface method. *J. Funct. Mater.* **2020**, *51*, 6158–6163.
21. Wei, C.-L.; Gao, J.; Wang, K.; Dong, M.; Fan, W.-B.; Qin, Z.-F.; Wang, J.-G. Effect of hydrogen pre-treatment on the catalytic properties of Zn/HZSM-5 zeolite for ethylene aromatization reaction. *Acta Phys. Chim. Sin.* **2017**, *33*, 1483–1491. [CrossRef]
22. Dauda, I.B.; Yusuf, M.; Gbadamasi, S.; Bello, M.; Atta, A.Y.; Aderemi, B.O.; Jibril, B.Y. Highly selective hierarchical ZnO/ZSM-5 catalysts for propane aromatization. *ACS Omega* **2020**, *5*, 2725–2733. [CrossRef]
23. Chen, Y.; Yang, X.-Y.; Zhang, P.; Liu, D.-S.; Gui, J.-Z.; Peng, H.-L.; Liu, D. Noble metal-supported rod-like ZnO with enhanced photocatalytic performance. *Acta Phys. Chim. Sin.* **2017**, *33*, 2082–2091.
24. Yang, Z.-Q.; Yuan, F.; Wang, Y.; Zhao, S.; Sun, Z.-M. Preparation and photocatalytic performance of ZnO/stellerite composite. *Inorg. Chem. Ind.* **2021**, *53*, 100–104.
25. Waez, Z.; Javanbakht, V. Synthesis characterization and photocatalytic activity of ZSM-5/ZnO nanocomposite modified by Ag nanoparticles for methyl orange degradation. *J. Photochem. Photobiol. A Chem.* **2020**, *388*, 112064–112075.
26. Xin, M.; Xing, E.; Ouyang, Y.; Xu, G.-T.; Luo, Y.-B.; Shu, X.-T. Influence of status of Zn species in Zn/ZSM-5 on its catalytic performance. *Pet. Process. Petrochem.* **2019**, *50*, 42–50.
27. Shi, J.; Chen, J.; Feng, Z.; Chen, T.; Wang, X.; Ying, P.; Li, C. Time-Resolved Photoluminescence Characteristics of Subnanometer ZnO Clusters Confined in the Micropores of Zeolites. *J. Phys. Chem. B* **2006**, *110*, 25612–25618. [CrossRef]
28. Tang, X.; Gang, R.; Li, J.; Zhang, Z.-Q.; Xiang, C.-X. Extremely efficient and rapidly adsorb methylene blue using porous adsorbent prepared from waste paper: Kinetics and equilibrium studies. *J. Hazard. Mater.* **2021**, *402*, 123579–123592. [CrossRef]
29. Fathi, R.; Mohammadi, P.; Hosseini, S.A.; Yosefvand, F.; Norouzi, H. Modeling of ammonia removal from wastewater using air stripping/modified clinoptilolite: Reusability, optimization, isotherm, kinetic, and equilibrium studies. *Int. J. Environ. Sci. Technol.* **2021**, *170*, 148–157.
30. Kolyagin, Y.G.; Ordonsky, V.V.; Khimyak, Y.Z.; Rebrov, A.I.; Fajula, F.; Ivanova, I.I. Initial stages of propane activation over Zn MFI catalyst studied by in situ NMR and IR spectroscopic techniques. *J. Catal.* **2006**, *238*, 122–133. [CrossRef]
31. Li, H.-J.; Wang, F.-L.; Li, X.; Yang, J.; Song, J.-H.; Li, B. Influence of activated attapulgite on synthesis and pore structure of hierarchical zeolite. *J. Mater. Eng.* **2020**, *48*, 158–164.





## Article

# Experimental and Physico-Chemical Comparison of ZnO Nanoparticles' Activity for Photocatalytic Applications in Wastewater Treatment

Stefano Alberti , Irene Basciu, Marco Vocciante  and Maurizio Ferretti 

Department of Chemistry and Industrial Chemistry, University of Genoa, Via Dodecaneso 31, 16146 Genoa, Italy; irene.basciu55@gmail.com (I.B.); marco.vocciante@unige.it (M.V.); ferretti@chimica.unige.it (M.F.)

\* Correspondence: stefano.alberti@edu.unige.it; Tel.: +39-010-3358737

**Abstract:** In this contribution, the photoactivity upon activation by simulated sunlight of zinc oxide (ZnO) obtained from two different synthetic pathways (Acetate and Nitrate) is investigated for water purification. Different reagents and processes were exploited to obtain ZnO nanoparticles. Products have been characterized by means of X-Ray Diffraction, Scanning Electron Microscopy along with Energy Dispersive Spectrometer, Dynamic Light Scattering, and Diffuse Reflectance Measurements, to highlight the different outcomes ascribable to each synthesis. A comparison of characteristics and performances was also carried out with respect to commercial ZnO. Nanoparticles of this semiconductor can be obtained as aggregates with different degrees of purity, porosity, and shape, and their physical-chemical properties have been addressed to the specific use in wastewater treatment, testing their effectiveness on the photocatalytic degradation of methylene blue (MB) as a model pollutant. Excluding the commercial sample, experimental results evidenced a better photocatalytic behavior for the ZnO Nitrate sample annealed at 500 °C, which was found to be pure and stable in water, suggesting that ZnO could be effectively exploited as a heterogeneous photocatalyst for the degradation of emerging pollutants in water, provided that thermal treatment is included in the synthetic process.

**Keywords:** zinc oxide; nanoparticle synthesis; photocatalysis; wastewater treatment; emerging pollutants removal; advanced oxidation processes

**Citation:** Alberti, S.; Basciu, I.; Vocciante, M.; Ferretti, M. Experimental and Physico-Chemical Comparison of ZnO Nanoparticles' Activity for Photocatalytic Applications in Wastewater Treatment. *Catalysts* **2021**, *11*, 678. <https://doi.org/10.3390/catal11060678>

Academic Editors: Gassan Hodaifa, Rafael Borja and Weilin Dai

Received: 26 February 2021

Accepted: 24 May 2021

Published: 26 May 2021

**Publisher's Note:** MDPI stays neutral with regard to jurisdictional claims in published maps and institutional affiliations.



**Copyright:** © 2021 by the authors. Licensee MDPI, Basel, Switzerland. This article is an open access article distributed under the terms and conditions of the Creative Commons Attribution (CC BY) license (<https://creativecommons.org/licenses/by/4.0/>).

## 1. Introduction

Environmental pollution represents a severe threat to the health of all living beings due to the presence of thousands of hazardous compounds continuously released into the environment as a consequence of various industries, such as pharmaceutical, cosmetic, plastic, leather, and textile [1]. Many of these pollutants are chemically stable, so they can accumulate and spread over a wide variety of processes in water and soil. The presence of such toxic and non-biodegradable molecules has drastically reduced the quality of the environment, causing toxicity to aquatic life, carcinogenicity to humans, and many other insidious side effects [2].

It is well evident that there is an urge to find effective and eco-sustainable methodologies able to counteract the spread of environmental pollution and its related drawbacks. Nowadays, several treatment methods such as biodegradation, adsorption, flocculation, and coagulation can be used to face different types of contamination in a practical way; adsorption-based technologies, in particular, are known to be a simple and cost-effective approach for the removal of various contaminants, both organic [3] and inorganic, such as metals [4] and nitrogen compounds [5], relying on a remarkable variety of adsorbent materials, which also includes the reuse of some industrial waste [6].

However, in most cases, these conventional approaches are not effective enough to achieve complete removal of pollutants from waters [7]. Therefore, in recent years, scientific research focused on innovative and powerful methods known as Advanced

Oxidation Processes (AOPs), to both increase the oxidation of recalcitrant pollutants and allow the simultaneous removal of a large variety of compounds. All AOPs are based on the generation of Reactive Oxygen Species (ROS), which are very reactive radical species that behave as powerful oxidants, and of all ROS, the hydroxyl radical is known to be the most powerful oxidizing agent for degrading non-biodegradable compounds as well as hazardous microorganisms in the aqueous phase. In addition, if AOPs are compared to other commonly used decontamination processes, the formation of the main disinfection by-products is not involved in such methods, making it possible to extend their application to drinking water facilities.

Being an eco-sustainable process, which involves the generation of hydroxyl radicals, heterogeneous semiconductor photocatalysis is considered a promising approach among AOPs. After the absorption of either artificial or natural light (as Grotthuss–Draper law states) by a semiconductor metal oxide, e.g., ZnO and/or TiO<sub>2</sub>, the promotion of an electron within the semiconductor's electronic bands results in the formation of the radical (upon reaction with a water molecule, for instance); subsequently, the total mineralization of refractory organic compounds is promoted [8,9]. Nano-sized semiconductor metal oxides are considered efficient for their large surface area, low cost, long lifespan, excellent chemical as well as thermal stability, and low toxicity. Over the past few decades, nanomaterials have emerged as promising commodities in many fields including cosmetics, healthcare, biomedicine, food and feed, drug-delivery, the environment, catalysis, electronics, the space industry, energy science, optics, and light emitters [10,11]. However, properties and potential applications of nanoparticles vary with their phases, sizes, and morphologies, so the synthesis of such materials plays a fundamental role in the optimization of these metal oxides according to the specific purpose to fulfill.

Among all photocatalysts, ZnO is of great interest due to a plethora of interesting features: it is a semiconductor with a wide direct band gap (3.37 eV) [12] that is also non-toxic, highly photo-sensitive, physicochemically stable, environmentally friendly, and bio-compatible. Therefore, it can be effectively used in many applications such as catalysis, piezoelectric devices, chemical sensors, solar cells, antireflection coatings, sunscreen, antimicrobial agents, and so on [13], with its properties being strongly dependent on the method by which it is prepared [14].

Currently, several synthetic pathways are available: Laser ablation, hydrothermal synthesis, co-precipitation, gas or vapor transport, and pressurized melt-blow [15] are some of the options. Generally, bottom-up and top-down techniques are the two major processes used to synthesize nanoparticles, such as redox practices [16] and sol-gel processing, which guarantee easy, low cost, and homogeneous products, and enhance the control of the chemical composition with good reproducibility [17–20]. However, compared to other approaches, soft chemistry routes give the possibility to investigate the synthesis of new photocatalytic materials by merging different active agents in different steps of the synthesis. Indeed, the coupling of different materials in composite photocatalysts showing increased performances is widely reported in the literature [21–24]. In most cases, this is also a much simpler approach than trying to adapt commercially available products to specific needs. Several zinc precursors may be used for the synthesis: nitrate, chloride, perchlorate, acetylacetonate, propoxide, acetate, but metal salts are reported to be more suitable for large-scale production. The synthesis of ZnO nanoparticles can also be considered taking innovative and green synthetic routes into account: plant extracts [25], green tea leaves [26], honey [27], aloe *bardanensis* leaves, brown marine macroalgae [28], Arabic gum [29] and starch [30] are some examples of chemical's green sources. Unfortunately, the main drawbacks are related to the presence of impurities and disadvantageous microstructures in the final products, which are likely to hinder the photocatalytic activity of the semiconductor [31,32]. Post-treatments improve the crystalline quality without reducing photoactive defects [33,34]; some research papers, for example, report innovative synthetic routes able to lower the post-treatment temperature for the crystalline phase using nanoparticles as nucleation seeds [35,36].

From what has been said, ZnO activity is closely related to the morphology and shape of nanoparticles, including their microstructural and surface features, which is, in turn, the function of the annealing procedure [37]. In particular, the Wurtzite crystalline habitus is widely reported to be the most thermodynamically stable and favorable for photocatalytic processes [38].

Given this, this work aims to experimentally investigate the characteristics and performances of ZnO photocatalysts obtained by employing two distinct synthetic paths retrieved from known literature, in comparison with a commercial ZnO catalyst. Such synthesis paths were selected as they involve chemical reagents of different natures and different post-treatment processes (presence and absence of an annealing treatment), making it possible to correlate the outcomes of the investigated routes with the final physico-chemical and morphological features of Wurtzite ZnO NPs.

The photocatalytic activity of the samples was also preliminarily evaluated over the degradation of methylene blue solutions, to get insights on the applicability in the wider field of wastewater remediation. Indeed, a further key aspect is that synthetic paths considered are suitable for easy self-production, possibly recovering resources from waste materials, which represents added value in terms of environmental sustainability if compared to brand-new commercial products being specifically purchased.

## 2. Results and Discussion

### 2.1. Physico-Chemical Characterization

Figure 1 shows the XRD spectra of the synthesized ZnO samples, compared to the Wurtzite ZnO reference.

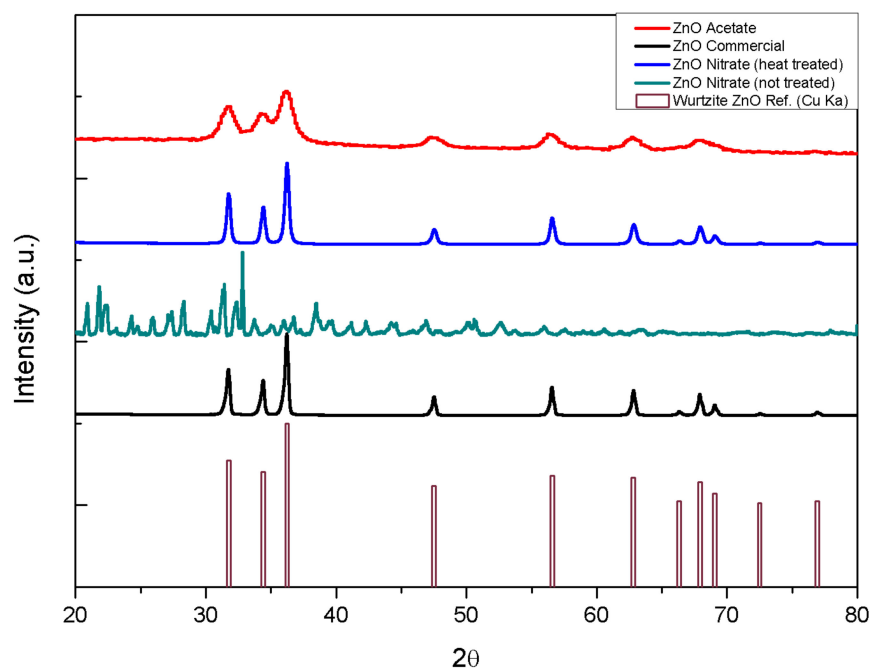


**Figure 1.** XRD experimental spectra obtained from synthesized samples compared to ZnO hexagonal Wurtzite reference spectrum (retrieved from Pearson’s Crystal Data database, n° 1837628).

In Figure 1, as well as throughout the manuscript, the ZnO Acetate label refers to the ZnO sample obtained from the acetate route, while ZnO Nitrate labels refer to the ZnO samples obtained from the Nitrate route, as described in Section 3.1. Based on XRD measurements, it was possible to confirm that the untreated ZnO Nitrate sample is ascribable to unreacted  $\text{Zn}_3(\text{C}_6\text{H}_5\text{O}_7)_2 \cdot 7\text{H}_2\text{O}$ , as typical peaks belonging to the hexagonal Wurtzite phase are completely absent, in favor of a more complicated XRD pattern. As highlighted in Section 3.1.1, the lack of thermal treatment did not allow the finished ZnO product to be obtained (Equation (2)), with the synthesis stopping at the Zinc citrate

intermediate step. For what concerns other synthesized samples, it is possible to state that both the Citrate and Nitrate (heat-treated) synthetic paths led to the same outcome in terms of the crystalline hexagonal Wurtzite phase (reported for reference).

From the Person Crystal Database comparison, it was possible to assign the correct Miller index values to the crystallographic peaks: (100) to 31.73 2 $\theta$ ; (002) to 34.39 2 $\theta$ ; (101) to 36.20 2 $\theta$ ; (102) to 47.49 2 $\theta$ ; (110) to 56.54 2 $\theta$ ; (103) to 62.80 2 $\theta$ ; (200) to 66.34 2 $\theta$ ; (112) to 67.90 2 $\theta$ ; and (201) to 69.04 2 $\theta$ . In this case, the crystalline outcome did not remarkably change according to the different synthetic paths, so it seems that the acetate route could be advantageously used to get Wurtzite nanoparticles at low temperatures. On the other hand, the peak shape can give some hints about the nanometric habitus: the annealing temperature should reasonably have led to bigger particles and an increased crystalline fraction, as suggested by the narrow FWHM reported for ZnO nitrate with respect to ZnO Acetate, where larger FWHM values are reasonably ascribable to small crystallites and amorphous nature. Verification in this sense was carried out by calculating the mean crystallite size according to the Scherrer equation (Equation (5)); results are reported in Table 1:

**Table 1.** Mean crystallite size obtained from the Scherrer equation applied to the first seven crystallographic peaks of investigated samples.

Sample	Mean Crystallite Size
ZnO Acetate route	6.84 $\pm$ 1.18 nm
ZnO Commercial	29.85 $\pm$ 2.59 nm
ZnO Nitrate (heat-treated) route	24.48 $\pm$ 2.09 nm

These data seem to confirm expectations, with the crystallite size of the Acetate sample being about three times lower than the Nitrate (heat-treated) one, which instead has a dimensional range in line with the commercial sample. This is in good agreement with the literature, where other studies report that ZnO dimensions increase proportionally to the increase in annealing temperature [33].

The hydrodynamic behavior of the powdered samples was investigated by means of DLS analysis (Figure 2), in order to evaluate the aggregates' size in an aqueous medium and the colloidal stability of the particles.

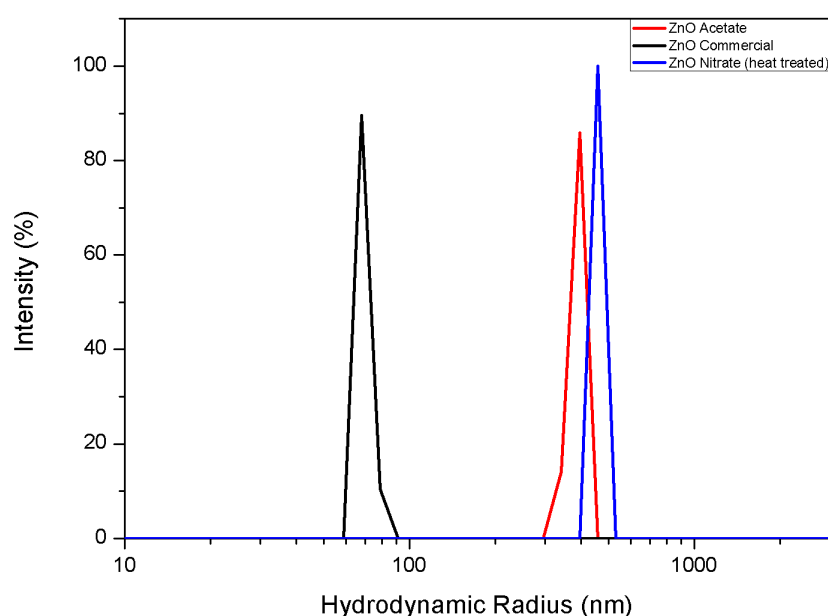


**Figure 2.** DLS results on the hydrodynamic radius of ZnO samples: ZnO Acetate route (red), ZnO commercial (black), and ZnO Nitrate route (blue).

From the comparison with the data in Table 1, the hydrodynamic radius results are much higher than the crystallite size for all synthesized samples. This suggests that synthesized NPs gather together in aqueous media, in aggregates ranging from 400 to 700 nm. A different consideration applies to the ZnO Commercial sample, whose hydrodynamic radius strongly resembles the crystallite size found with the Scherrer equation. This is probably ascribable to the controlled industrial production process, which leads to homogeneously mono-dispersed NPs. As examined samples were not grafted with any capping agent, the global behavior in water suspension resulted similarly in a short-term period, while the longer-term stability, evaluated along 50 min (equal to the photocatalytic experiments' time, described in Section 3.3), without stirring, resulted quite differently. ZnO Commercial and ZnO Nitrate samples were still visibly dispersed (a whitish aspect of the solution) while ZnO acetate completely settled down. The instability of ZnO Acetate in an aqueous medium can be related to the remarks of Sun et al. [31], which report ZnO to be stable in methanol and hexane solutions rather than aqueous ones.

By means of SEM-EDS characterization, it was possible to address the final morphology and the overall dimensions of ZnO samples to the specific synthetic path investigated. Figure 3a–d shows the morphology of the ZnO Nitrate sample and Figure 4a–c displays the outcome of the ZnO Acetate sample. ZnO Commercial and ZnO Nitrate (not treated) were not analyzed.

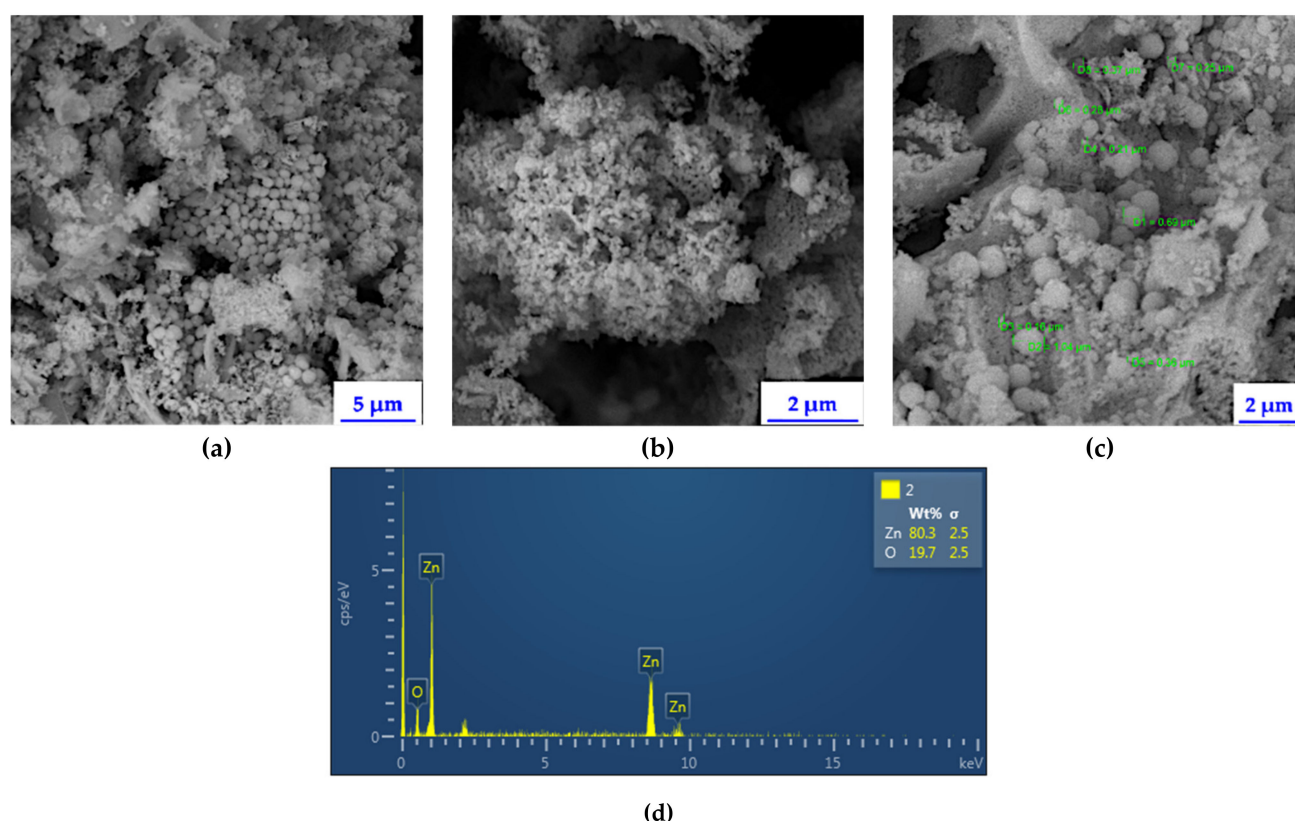


**Figure 3.** SEM images of ZnO Nitrate (heat treated) sample: (a) 10,000 $\times$  magnification (5  $\mu$ m marker); (b) 30,000 $\times$  magnification (2  $\mu$ m marker); (c) 20,000 $\times$  magnification (2  $\mu$ m marker) with particle size markers; (d) EDS elemental composition.

EDS elemental composition confirmed that the Nitrate route led to a homogeneous composition of Zn and O, without the presence of any other moieties, while the product of the Acetate route still shows K impurity, due to the synthetic process, despite the four washing cycles performed on the product, which were supposed to lower the K impurities to ppm levels [31]. The shape of the particles that can be seen from Figures 3 and 4 for the different samples is noteworthy, because the application of the annealing process in the Nitrate sample was specifically directed to particles with spherical shapes and



dimensions of hundreds of nanometers (160 nm–690 nm), and the DLS results are in line with expectations, highlighting the desired morphology with respect to the thermally untreated sample. The ZnO Acetate sample, synthesized without the annealing process, led instead to a peculiar platelet arrangement: randomly distributed, with sharp nanometric edges, a few micrometers long. This morphological outcome could be reasonably ascribed to the particular ultrasonic bath employed during the synthetic process, in concurrence with the low temperature (63 °C) used during the synthesis.

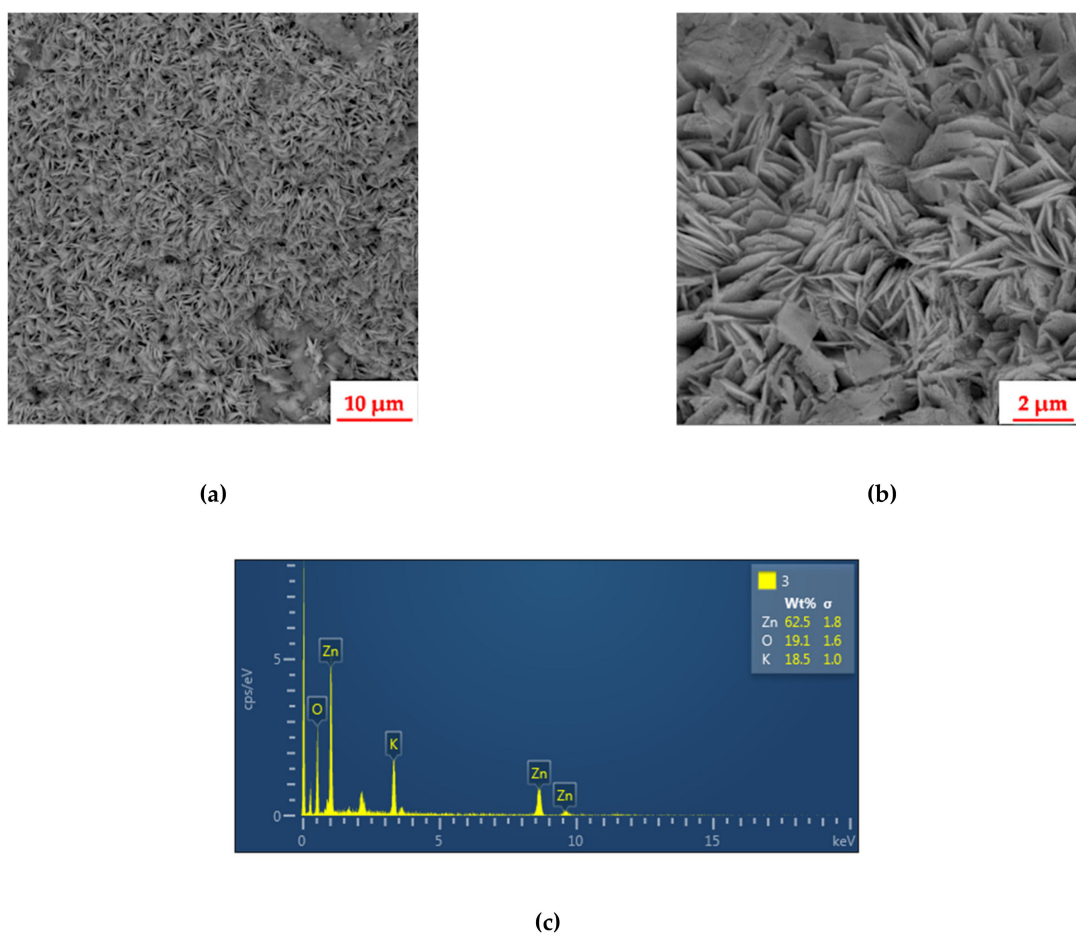


**Figure 4.** SEM images of ZnO Acetate sample: (a) 5000× magnification (10 μm marker); (b) 20,000× magnification (2 μm marker); (c) EDS elemental composition.

In view of the possible use of the synthesized ZnO nanoparticles in wastewater treatment processes, it is more likely for the spherical nanoparticles to be better photocatalysts, as the spherical shape can exhibit a wider surface area with respect to other shapes. In order to prove this scenario and correlate the highlighted physico-chemical features, preliminary photocatalytic experiments under simulated solar light were performed.

## 2.2. Photocatalytic Results

Preliminary methylene blue (MB) degradation experiments allowed us to compare the behavior of the different ZnO samples as heterogeneous photocatalysts to find out the most active sample to be used for real applications. Table 2 reports the percentage MB degradation calculated after 50 min of simulated solar light irradiation, and the computed kinetic constants for MB degradation, calculated assuming a 1st order kinetic, as widely reported in the literature [39]. It has to be noted that the constants are computed according to the whole process and thus they must be considered as averages.

**Table 2.** Photocatalytic results expressed as methylene blue (MB) percentage degradation after 50 min and 1st order kinetic constants.

Samples	MB Dark Absorption (20 min)	MB% Degradation	Dev. st. (n = 3)	k (l)
MB Photolysis	n.c.	8%	2.5	0.002 min <sup>−1</sup>
ZnO Acetate route	0.9%	78%	2.0	0.054 min <sup>−1</sup>
ZnO Commercial	5.2%	100%*	0.5	0.162 min <sup>−1</sup>
ZnO Nitrate (heat treated) route	2.3%	93%	0.9	0.085 min <sup>−1</sup>

\* 100% Degradation is referred to as MB absorbance lower than the detection limit (DL)

According to the experimental results, the ZnO Commercial sample is able to degrade MB dye down to the detection limit (DL), corresponding to zero absorbance (0.1 ppm) and equivalent to 100% degradation, with the highest kinetic constant, while the two synthetic samples fail to achieve such performances, clearly placing both synthesized products below the commercial one in general terms. Indeed, a difference in MB% degradation up to 15% is observed in the worst case (ZnO Acetate), which is slight but still significant.

However, the results obtained are actually fully in line with the most recent investigations, when it comes to homemade synthesized ZnO.

In a recent work by Rambabu et al. [40], where commercial ZnO was not considered, ZnO catalysts self-produced under conditions similar to the present experimentation recorded MB degradation of about 55–65% in 50 min, therefore below the results obtained here. Furthermore, on the closer comparison, it appears that in [40] the initial concentration of MB was actually half of that used in the present study. In view of this, it is evident that there is still room for improvement and the possibility of modifications to be investigated in the synthesis processes considered.

In order to examine the results in depth, the degradation due to only MB photolysis and MB absorption in dark conditions was also considered and reported in Table 2. However, because of the duration of the experiments, MB was degraded at a maximum of 8% in the considered conditions, which is significantly lower than the overall reached percentages; similarly, the dark absorption, performed in order to understand the surface behavior of the samples, did not exceed 5.2%, which was as low as the photolysis percentage.

Based on these results, it is possible to attribute the degradation of the dye to the photocatalytic activity under solar radiation of the synthesized samples, as a consequence of the semiconductor nature of the material and the physico-chemical features given by the investigated syntheses.

The main differences found in the performance of the samples obtained from the two synthesis paths considered are probably to be sought in the enhanced porosity of the ZnO Nitrate sample, as suggested from SEM images, along with its spherical shape, which can ensure better interaction with the dye with respect to other shapes. In addition, the expected presence of vacancies and crystal defects, imparted by the annealing process to the ZnO lattice, is expected to provide the best catalytic performance for oxidizing/reducing reactions, as also reported in the literature [41]; the preliminary experimental evidence obtained from these photocatalytic results seems to confirm this trend.

As a conclusion, in order to understand and justify the exhibited photocatalytic behavior, diffuse reflectance spectra were recorded to obtain the Energy Gap values ( $E_{\text{gap}}$ ) of the investigated samples. By means of the integrating sphere, it was possible to record percentage Reflectance values on powders in a short spectral range, between 400 and 700 nm. Results were modeled according to the Kubelka-Munk method, based on the following equation:

$$F(R) = \frac{(1 - R)^2}{2R} \quad (1)$$

$E_{\text{gap}}$  values were retrieved by the graphical representation of the Tauc Plot, obtained by plotting  $(F(R)h\nu)^n$  vs  $h\nu$ , using  $n = 1/2$  for a direct allowed transition, as reported



in [42]. As a consequence of the short spectral range that the exploited instrument could investigate, only the  $E_{\text{gap}}$  values are reported and shown in Table 3.

**Table 3.**  $E_{\text{gap}}$  values obtained from the graphical representation of the Tauc Plot. Values were extrapolated from the slopes in the flat section to  $y = 0$ .

Samples	$E_{\text{gap}}$ Values	$\lambda$ Absorption
ZnO Nitrate (heat treated) route	3.27 eV	379 nm
ZnO Commercial	3.40 eV	364 nm
ZnO Acetate route	3.31 eV	374 nm

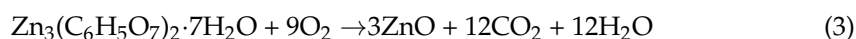
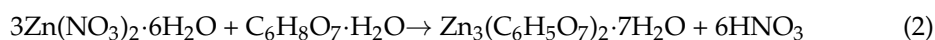
As expected, some differences in the electronic structure were identified: the highest band gap value was recorded for the ZnO Commercial sample, while ZnO Acetate and ZnO Nitrate, differing with the commercial sample, showed a difference of 0.04 eV, equal to a 5 nm difference for photon absorption. These findings are in good agreement with the experimental results highlighted by Zak et al. [34], showing that ZnO  $E_{\text{gap}}$  should decrease as the annealing temperature increases, while the presence of possible impurities may have affected synthesized ZnO microstructures, lowering the  $E_{\text{gap}}$  but affecting their photo-activity.

### 3. Materials and Methods

#### 3.1. ZnO Syntheses

##### 3.1.1. $\text{Zn}(\text{NO}_3)_2 \cdot 6\text{H}_2\text{O}$ Precursor

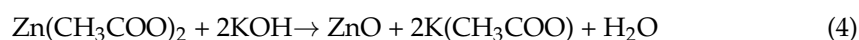
The following synthetic path was retrieved from the work of Acosta-Humánez et al., where a sol-gel synthesis involving zinc nitrate hexahydrate as a precursor and an annealing post-treatment to reach the Wurtzite phase was investigated [20]. A mass of 5.85 g of  $\text{Zn}(\text{NO}_3)_2 \cdot 6\text{H}_2\text{O}$  (98%, Sigma Aldrich, Darmstadt, Germany) was dissolved in 3.4 mL of deionized water (system ARIOSO Water Purification System) while 4.13 g of citric acid monohydrated (99.5+%, Alfa Aesar, Kandel, Germany) was dissolved in 2.5 mL of deionized water. Both solutions were heated up to 70 °C and kept under magnetic stirring for 30 min separately. After this time, zinc nitrate solution was slowly poured into the citric acid solution while kept under stirring, and the reaction mixture was kept in the same stirring and temperature conditions until gel formation. The gel was then transferred into a porcelain capsule and left to dry for 12 h at 100 °C. The resulting xerogel was roughly ground in an agate mortar to obtain the powder of zinc citrate which was eventually heat treated in a muffle furnace at 500 °C for 12 h to obtain the desired crystalline product. The overall reactions can be described as follows:



##### 3.1.2. $\text{Zn}(\text{CH}_3\text{COOH})_2$ Precursor

The following solvothermal route was retrieved from the work of Lova et al. [43] as Wurtzite ZnO without an annealing process was reported to be obtained. A mass of 4.61 g of zinc acetate (99.99%, Sigma Aldrich, Darmstadt, Germany) was dissolved in 200 mL of methanol (99.8%, Scharlab S.L., Sentmenat, Spain), which was in turn placed in a three-neck round-bottom flask and left in a thermostated ultrasonic bath at 63 °C in reflux conditions. Separately, 2.35 g of potassium hydroxide (Merck, p.a., Darmstadt, Germany) was dissolved in 100 mL of methanol and the resulting solution was added dropwise in the first reaction system. After 3 h, a white precipitate was visible at the bottom of the flask; it was left to settle down while the supernatant was removed and the leftover was washed with a methanol/water solution. Settling washing cycles were repeated four times and

eventually the product was dried in an oven at 100 °C for 12 h. The overall reaction can be described as follows:



### 3.2. Characterization Techniques

XRD spectra on synthesized samples were recorded with the powders method, by means of an automatic diffractometer Empyrean (Malvern PANalytical, Malvern, United Kingdom) in Bragg-Brentano ( $\theta$ :2 $\theta$ ) geometry, using a two-axis high-resolution vertical goniometer. A 1.8 kW Cu K $\alpha$  sealed ceramic tube with a Ni filter was used as an X-ray source. Spectra were acquired from 20 to 80 (2 $\theta$ ), using 0.02 (2 $\theta$ ) as the step size and 4 s as the time per step. Crystallite mean size was retrieved on measured XRD spectra using the Scherrer equation:

$$D = \frac{K\lambda}{\beta \cos \theta} \quad (5)$$

where D represents crystallite mean size, K is the Scherrer constant (equal to approximately 0.9),  $\lambda$  is the X-ray wavelength used,  $\beta$  is the full width at half maximum of diffraction peaks, and  $\theta$  is the peak position.

DLS analysis was performed with a zetasizer Nano ZS90 (Malvern Instruments, Malvern, United Kingdom), where 0.01 wt% (10 mg/mL) aqueous suspensions of the synthesized nanoparticle were subjected to the characterization. The wavelength of the laser used was 632.8 nm so that it was possible to put 0.000 as the absorption. Refractive Index (R.I.) for the dispersant medium (water) was set to 1.33 while R.I. for ZnO was set to 2.263. Mild centrifugation followed by sonication with Omni Sonic Ruptor Ultrasonic Homogenizer (tip microprocessor 5/3200, at 40% power) was performed before analysis, to remove bigger aggregates. Measurements were performed at 25 °C thermostated temperature by means of a Peltier thermostated system.

SEM images were acquired with a FeSEM Zeiss SUPRA 40VP microscope (Carl Zeiss AG, Oberkochen, Germany) coupled with an EDS detector (EDXS Oxford “INCA Energie 450 x 3” Oxford Instrument, Abingdon UK) for micro-analysis. The experimental conditions were set at low voltage (5 kV). A second SEM (Tescan Vega3 XML) coupled with an EDS detector (Oxford X-Max) and software (AZtec 2.4) was also employed. Samples were prepared with Au coating.

Diffuse reflectance spectra were collected by means of a CM-2600D spectrophotometer (Konica Minolta, Tokyo, Japan), equipped with an integrating sphere. DRS spectra were recorded in the spectral range between 400 and 700 nm (the instrument does not allow the investigation in a shorter wavelength range) to extrapolate the  $E_{\text{gap}}$  values of investigated samples through graphical extrapolation from the Tauc plot, obtained using the Kubelka-Munk method [42].

### 3.3. Photocatalytic Experiments

Photocatalytic experiments were performed in order to preliminarily investigate the activity of the synthesized nanoparticles and to identify any difference ascribable to the synthesis. A volume of 25 mL of a 0.02 g/L MB aqueous solution, in the presence of suspended ZnO NPs, at a concentration of 0.5 mg/mL, was subjected to solar simulated light irradiation with an OSRAM Ultra-Vitalux lamp (300 W). MB dye was chosen as suggested by the ISO 10678:2010 protocol, for the assessment of heterogeneous photocatalysts activity in aqueous solutions. The lamp's emission spectrum is depicted in Figure 5 while its irradiance is reported in the literature to be: 1.1 W/m<sup>2</sup> for UV-B range, 7.3 W/m<sup>2</sup> for UV-A range, and 29.7 W/m<sup>2</sup> for Vis range (these values take the lifetime of the lamps used into account) [44]. In order to overcome the intensity decrease due to their lifetime, lamps were put at 20 cm distance from the solutions. Suspended samples were kept under magnetic stirring in the dark for 20 min in order to ensure the adsorption/desorption equilibrium between the photocatalyst and the dye, as a result of dark absorption experiments, per-

formed with the same conditions but without irradiation. Eventually, the photocatalytic experiments were left under irradiation for another 50 min (experiments were performed in triplicate). Aliquots withdrawn from the solution were subjected to 13,200 rpm centrifugation and eventually analyzed by means of UV-Vis spectrophotometry (LAMBDA 35 Perkin-Elmer-Whaltam, MA, USA) to calculate the percentage MB abatement. Recovery and recycling experiments were not reported as they are the result of ongoing scientific collaboration and are meant to be delivered successively. The quant mode was used to observe the absorbance value recorded for each aliquot at 664 nm, which corresponds to the maximum absorption value of methylene blue.

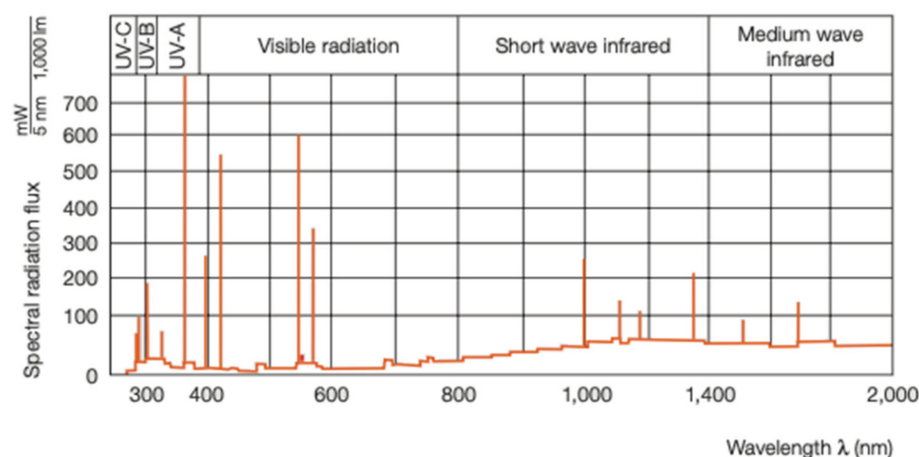


**Figure 5.** Spectral distribution of the OSRAM Ultra-Vitalux 300W lamp used. Reprinted with permission from ref. [45]. Copyright 2019 Elsevier and Copyright Clearance Center.

#### 4. Conclusions

In the present work, two different synthetic paths for the synthesis of ZnO nanoparticles to be addressed for use in the environmental field of wastewater remediation were analyzed and compared. By means of a physico-chemical characterization, along with a preliminary kinetic evaluation of the photocatalytic performances, it was possible to determine the most important parameters that ZnO nanoparticles should possess to exhibit good photocatalytic activity to be used in the pollutants' degradation in water media.

After the experimental investigation, it was shown that the Wurtzite crystalline phase alone is not sufficient to reach the desired photocatalytic activity, but rather the annealing process results in a crucial parameter for the synthesis of efficient zinc oxide. Other studies report that temperature directly affects the electronic behavior and the lattice nature of the semiconductor, and the present experimentation suggests this as a key parameter to get the correct lattice features for photocatalytic water treatment. Indeed, the absence of the annealing procedure for the ZnO Acetate sample, as highlighted by XRD, led to a reduced crystalline fraction and likely led to a reduced lattice arrangement of defects and vacancies (acting as active sites for interaction and charge transfer in the heterogeneous photocatalytic process), resulting in reduced degradation of the target contaminant.

Unfortunately, none of the synthesized samples were able to reach the performance of ZnO Commercial sample: even though it was not the desired outcome, the syntheses prepared proved to be quite efficient, with results in line with or superior to those reported in the literature for other self-produced ZnO NPs. Although further investigation is needed, it's reasonable to attribute this outcome to a sum of influences resulting from the industrial procedure (not fully disclosed), which made the ZnO Commercial sample highly compatible with pollutants.

Regarding this, it is worth noting that, for research purposes, a synthetic route is much more desirable than a commercial product. Especially when dealing with environmental remediation, the perspective of a possible recovery of resources for in-house production, and the sustainability of the remediation materials and processes themselves, are remarkable

aspects in line with all the most recent directives of the European Community on the circular economy and zero waste approaches. In addition, dealing with homemade synthesis simplifies the coupling with other active materials for enhanced activity. Reassessing the results obtained in the light of these considerations, and therefore excluding the commercial ZnO from the comparison, the most suitable synthetic path to obtain ZnO for wastewater application appears to be the Nitrate route, due to the lower  $E_{gap}$ , the spherical shape, and the colloidal stability in water, and also considering the crystallinity and purity of the sample, as shown by the characterizations performed. On the contrary, the Acetate route led to a particular platelet arrangement of ZnO nanoparticles, but their stability resulted unfavorably for aqueous solutions, limiting their use in environmental applications.

Future perspectives could involve the performance of further characterization techniques (e.g., BET measurements) in an attempt to fully identify the synthetic parameters that can confer the ZnO Commercial sample's photocatalytic features while preserving and improving the environmental sustainability of the presented summary. At the same time, tests are planned concerning real applications (such as real pollutants, volume scale-up, recovery, and recycling of the photocatalyst).

**Author Contributions:** conceptualization, S.A., I.B.; methodology S.A.; validation S.A.; investigation, S.A., I.B.; resources, M.F.; data curation, S.A., I.B.; writing—original draft preparation, S.A.; writing—review and editing, S.A., M.V., M.F.; visualization, M.V.; supervision, M.V., M.F.; project administration, M.F.; funding acquisition, M.F. All authors have read and agreed to the published version of the manuscript.

**Funding:** Some of the researchers who worked on the present paper are financed by the Operating Program Por-FSE Regione Liguria 2014-2020 (Grant number RLOF18ASSRIC/32).

**Data Availability Statement:** Data is contained within the article.

**Acknowledgments:** Authors would like to acknowledge Emanuela Sartori (Univ. of. Genoa, Italy) for her precious help in the collection of XRD patterns.

**Conflicts of Interest:** The authors declare no conflict of interest.

## References

- Pietrelli, L.; Ferro, S.; Reverberi, A.P.; Voccianti, M. Removal and recovery of heavy metals from tannery sludge subjected to plasma pyro-gasification process. *J. Clean. Prod.* **2020**, *273*, 123166. [CrossRef]
- Soltani, R.D.C.; Jorfi, S.; Safari, M.; Rajaei, M.S. Enhanced sonocatalysis of textile wastewater using bentonite-supported ZnO nanoparticles: Response surface methodological approach. *J. Environ. Manag.* **2016**, *179*, 47–57. [CrossRef]
- Voccianti, M.; Finocchi, A.; De Folly D'Auris, A.; Conte, A.; Tonziello, J.; Pola, A.; Reverberi, A.P. Enhanced oil spill remediation by adsorption with interlinked multilayered graphene. *Materials* **2019**, *12*, 2231. [CrossRef]
- Fu, F.; Wang, Q. Removal of heavy metal ions from wastewaters: A review. *J. Environ. Manag.* **2011**, *92*, 407–418. [CrossRef] [PubMed]
- Voccianti, M.; De Folly D'Auris, A.; Finocchi, A.; Tagliabue, M.; Bellettato, M.; Ferrucci, A.; Reverberi, A.P.; Ferro, S. Adsorption of ammonium on clinoptilolite in presence of competing cations: Investigation on groundwater remediation. *J. Clean. Prod.* **2018**, *198*, 480–487. [CrossRef]
- Pietrelli, L.; Ippolito, N.M.; Ferro, S.; Dovì, V.G.; Voccianti, M. Removal of Mn and As from drinking water by red mud and pyrolusite. *J. Environ. Manag.* **2019**, *237*, 526–533. [CrossRef]
- Bel Hadjilaiefa, H.; Ben Zina, M.; Galvez, M.E.; Da Costa, P. Photocatalytic degradation of methyl green dye in aqueous solution over natural clay-supported ZnO-TiO<sub>2</sub> catalysts. *J. Photochem. Photobiol. A Chem.* **2016**, *315*, 25–33. [CrossRef]
- Bloh, J.Z.; Dillert, R.; Bahnemann, D.W. Designing Optimal Metal-Doped Photocatalysts: Correlation between Photocatalytic Activity, Doping Ratio, and Particle Size. *J. Phys. Chem. C* **2012**, *116*, 25558–25562. [CrossRef]
- De Franco, M.A.E.; da Silva, W.L.; Bagnara, M.; Lansarin, M.A.; dos Santos, J.H.Z. Photocatalytic degradation of nicotine in an aqueous solution using unconventional supported catalysts and commercial ZnO/TiO<sub>2</sub> under ultraviolet irradiation. *Sci. Total Environ.* **2014**, *494*, 97–103. [CrossRef]
- Toccafondi, C.; Dante, S.; Reverberi, A.P.; Salerno, M. Biomedical Applications of Anodic Porous Alumina. *Curr. Nanosci.* **2015**, *11*, 572–580. [CrossRef]
- Pascariu, V.; Avadanei, O.; Gasner, P.; Stoica, I.; Reverberi, A.P.; Mitoseriu, L. Preparation and characterization of PbTiO<sub>3</sub>-epoxy resin compositionally graded thick films. *Phase Transit.* **2013**, *86*, 715–725. [CrossRef]
- McCluskey, M.; Jokela, S. Sources of n-type conductivity in ZnO. *Phys. B Condens. Matter* **2007**, *401*, 355–357. [CrossRef]

13. Jiang, Y.; O'Neill, A.J.; Ding, Y. Zinc oxide nanoparticle-coated films: Fabrication, characterization, and antibacterial properties. *J. Nanoparticle Res.* **2015**, *17*, 180. [CrossRef]
14. Van de Walle, C.G. Hydrogen as a cause of doping in zinc oxide. *Phys. Rev. Lett.* **2000**, *85*, 1012–1015. [CrossRef] [PubMed]
15. Janotti, A.; Van de Walle, C.G. Fundamentals of zinc oxide as a semiconductor. *Rep. Prog. Phys.* **2009**, *72*, 1–29. [CrossRef]
16. Reverberi, A.P.; Salerno, M.; Lauciello, S.; Fabiano, B. Synthesis of copper nanoparticles in ethylene glycol by chemical reduction with vanadium (+2) salts. *Materials* **2016**, *9*, 809. [CrossRef]
17. Janotti, A.; Van de Walle, C.G. Hydrogen multicentre bonds. *Nat. Mater.* **2007**, *6*, 44–47. [CrossRef] [PubMed]
18. Martinelli, A.; Alberti, S.; Caratto, V.; Lova, P.; Locardi, F.; Pampararo, G.; Villa, S.; Ferretti, M. Structural studies on copper and nitrogen doped nanosized anatase. *Z. Krist. Cryst. Mater.* **2018**, *233*, 867–876. [CrossRef]
19. Caratto, V.; Locardi, F.; Alberti, S.; Villa, S.; Sanguineti, E.; Martinelli, A.; Balbi, T.; Canesi, L.; Ferretti, M. Different sol–gel preparations of iron-doped TiO<sub>2</sub> nanoparticles: Characterization, photocatalytic activity and cytotoxicity. *J. Sol Gel Sci. Technol.* **2016**, *80*, 152–159. [CrossRef]
20. Humánez, M.F.A.; Vides, L.A.M.; Almanza-Montero, O.A. Sol-gel synthesis of zinc oxide nanoparticle at three different temperatures and its characterization via XRD, IR and EPR. *DYNA* **2016**, *83*, 224–228. [CrossRef]
21. Alberti, S.; Ferretti, M.; Vicini, S.; Castellano, M.; Caratto, V. Porous polydimethylsiloxane membranes loaded with low-temperature crystallized TiO<sub>2</sub> NPs for detachable antibacterial films. *J. Mater. Sci.* **2018**, *54*, 1665–1676. [CrossRef]
22. Alberti, S.; Locardi, F.; Sturini, M.; Speltini, A.; Maraschi, F.; Costa, G.A.; Ferretti, M.; Caratto, V. Photocatalysis in darkness: Optimization of sol-gel synthesis of NP-TiO<sub>2</sub> supported on a persistent luminescence material and its application for the removal of ofloxacin from water. *J. Nanomed. Nanotechnol.* **2018**, *9*, 501. [CrossRef]
23. Alberti, S.; Caratto, V.; Peddis, D.; Belviso, C.; Ferretti, M. Synthesis and characterization of a new photocatalyst based on TiO<sub>2</sub> nanoparticles supported on a magnetic zeolite obtained from iron and steel industrial waste. *J. Alloys Compd.* **2019**, *797*, 820–825. [CrossRef]
24. Sampaio, M.J.; Bacsá, R.; Benyounes, A.; Axet, R.; Serp, P.; Silva, C.; Silva, A.; Faria, J. Synergistic effect between carbon nanomaterials and ZnO for photocatalytic water decontamination. *J. Catal.* **2015**, *331*, 172–180. [CrossRef]
25. Kumar, P.P.N.V.; Shameem, U.; Kollu, P.; Kalyani, R.L.; Pammi, S.V.N. Green Synthesis of Copper Oxide Nanoparticles Using Aloe vera Leaf Extract and Its Antibacterial Activity Against Fish Bacterial Pathogens. *BioNanoScience* **2015**, *5*, 135–139. [CrossRef]
26. Senthilkumar, S.R.; Sivakumar, T. Green tea (*Camelia Sinensis*) mediated synthesis of zinc oxide (ZnO) nanoparticles and studies on their antimicrobial activities. *Int. J. Pharm. Pharm. Sci.* **2014**, *6*, 461–465.
27. Balasooriya, E.R.; Jayasinghe, C.D.; Jayawardena, U.A.; Ruwanthika, R.W.D.; Mendis de Silva, R.; Udagama, P.V. Honey mediated green synthesis of nanoparticles: New era of safe technology. *Hindawi J. Nanomater.* **2017**, 5919836. [CrossRef]
28. Azizi, S.; Ahmad, M.B.; Namvar, F.; Mohamad, R. Green biosynthesis and characterization of zinc oxide nanoparticles using brown marine macroalga *Sargassum muticum* aqueous extract. *Mater. Lett.* **2014**, *116*, 275–277. [CrossRef]
29. Fardood, S.T.; Ramazani, A.; Moradi, S.; Asiabi, P.A. Green synthesis of zinc oxide nanoparticles using arabic gum and photocatalytic degradation of direct blue 129 dye under visible light. *J. Mater. Sci. Mater. Electron.* **2017**, *28*, 13596–13601. [CrossRef]
30. Vigneshwaran, N.; Kumar, S.; A Kathe, A.; Varadarajan, P.V.; Prasad, V. Functional finishing of cotton fabrics using zinc oxide–soluble starch nanocomposites. *Nanotechnology* **2006**, *17*, 5087–5095. [CrossRef]
31. Sun, D.; Wong, M.; Sun, L.; Li, Y.; Miyatake, N.; Sue, H.-J. Purification and stabilization of colloidal ZnO nanoparticles in methanol. *J. Sol-Gel Sci. Technol.* **2007**, *43*, 237–243. [CrossRef]
32. Znaidi, L. Sol-gel deposited ZnO thin films: A review. *Mater. Sci. Eng. B* **2010**, *174*, 18–30. [CrossRef]
33. Xu, L.; Gu, F.; Su, J.; Chen, Y.; Li, X.; Wang, X. The evolution behavior of structures and photoluminescence of K-doped ZnO thin films under different annealing temperatures. *J. Alloys Compd.* **2011**, *509*, 2942–2947. [CrossRef]
34. Zak, A.K.; Abrishami, M.E.; Majid, W.A.; Yousefi, R.; Hosseini, S. Effects of annealing temperature on some structural and optical properties of ZnO nanoparticles prepared by a modified sol–gel combustion method. *Ceram. Int.* **2011**, *37*, 393–398. [CrossRef]
35. Villa, S.; Caratto, V.; Locardi, F.; Alberti, S.; Sturini, M.; Speltini, A.; Maraschi, F.; Canepa, F.; Ferretti, M. Enhancement of TiO<sub>2</sub> NPs Activity by Fe<sub>3</sub>O<sub>4</sub> Nano-Seeds for Removal of Organic Pollutants in Water. *Materials* **2016**, *9*, 771. [CrossRef]
36. Alberti, S.; Villa, S.; Singh, G.; Seland, F.; Martinelli, A.; Ferretti, M.; Canepa, F.; Caratto, V. Systematic study on TiO<sub>2</sub> crystallization via hydrothermal synthesis in the presence of different ferrite nanoparticles as nucleation seeds. *J. Nanosci. Nanotechnol.* **2019**, *19*, 4994–4999. [CrossRef] [PubMed]
37. Sofianos, V.; Lee, J.; Silvester, D.; Samanta, P.; Paskevicius, M.; English, N.; Buckley, C. Diverse morphologies of zinc oxide nanoparticles and their electrocatalytic performance in hydrogen production. *J. Energy Chem.* **2021**, *56*, 162–170. [CrossRef]
38. Lee, K.M.; Lai, C.W.; Ngai, K.S.; Juan, J.C. Recent developments of zinc oxide based photocatalyst in water treatment technology: A review. *Water Res.* **2016**, *88*, 428–448. [CrossRef]
39. Xiong, S.F.; Yin, Z.L.; Yuan, Z.F.; Yan, W.B.; Yang, W.Y.; Liu, J.J.; Zhang, F. Dual frequency (20/40 kHz) ultra-sonic assisted photocatalysis for degradation of methylene blue effluent: Synergistic effect and kinetic study. *Ultrason. Sonochem.* **2012**, *19*, 756–761. [CrossRef]
40. Rambabu, K.; Bharath, G.; Banat, F.; Show, P.L. Green synthesis of zinc oxide nanoparticles using *Phoenix dactylifera* waste as bioreductant for effective dye degradation and antibacterial performance in wastewater treatment. *J. Hazard. Mater.* **2021**, *402*, 123560. [CrossRef]

41. Kurbanov, S.; Yang, W.C.; Kang, T.W. Kelvin probe force microscopy of defects in ZnO nanocrystals associated with emission at 3.31 eV. *Appl. Phys. Express* **2011**, *4*, 021101. [CrossRef]
42. López, R.; Gómez, R. Band-gap energy estimation from diffuse reflectance measurements on sol-gel and commercial TiO<sub>2</sub>: A comparative study. *J. Sol. Gel Sci. Technol.* **2012**, *61*, 1–7. [CrossRef]
43. Lova, P.; Manfredi, G.; Boarino, L.; Laus, M.; Urbinati, G.; Losco, T.; Marabelli, F.; Caratto, V.; Ferretti, M.; Castellano, M.; et al. Hybrid ZnO:polystyrene nanocomposite for all-polymer photonic crystals. *Phys. Status Solidi C* **2015**, *12*, 158–162. [CrossRef]
44. Stefan, M. More than just light. Solutions in ultraviolet light. In *100 Years of Innovation Osram*; OSRAM GmbH: Munich, Germany, 2016; p. 24.
45. Mahfoudh, I.; Principi, P.; Fioretti, R.; Safi, M. Experimental studies on the effect of using phase change material in a salinity-gradient solar pond under a solar simulator. *Sol. Energy* **2019**, *186*, 335–346.





## Article

# Visible Light Driven Spherical $\text{CuBi}_2\text{O}_4$ with Surface Oxygen Vacancy Enhanced Photocatalytic Activity: Catalyst Fabrication, Performance, and Reaction Mechanism

Xin Zhong <sup>1,2,\*</sup>, Yihong Cai <sup>1</sup>, Heping Bai <sup>1,2</sup>, Wei Huang <sup>1</sup> and Binxue Zhou <sup>1</sup>

<sup>1</sup> Department of Environmental Engineering and Science, Beijing Normal University, Zhuhai 519000, China; wohehuli@sina.com (Y.C.); baiheping@bnu.edu.cn (H.B.); huangwei@bnu.edu.cn (W.H.); zbxbnuz@bnu.edu.cn (B.Z.)

<sup>2</sup> College of Education for the Future, Beijing Normal University at Zhuhai, Zhuhai 519000, China

\* Correspondence: zhongxin@bnu.edu.cn; Tel.: +86-(0)-756-368-3012

Received: 21 July 2020; Accepted: 14 August 2020; Published: 17 August 2020

**Abstract:** Here, a spherical  $\text{CuBi}_2\text{O}_4$  catalyst with surface oxygen vacancy was fabricated through a facile hydrothermal method, which exhibited remarkable enhanced photocatalytic activity of refractory chemicals in the heterogeneous sulfate radical-based Fenton-like reaction under visible light emitting diode (LED) light irradiation. The property of the catalysts was systematically characterized by scanning electron microscopy (SEM)/high resolution transmission electron microscopy (HRTEM), X-ray diffraction (XRD), X-ray photoelectron spectroscopy (XPS), and UV/vis methods. The effects of parameters of solution pH, potassium peroxymonosulfate (PMS) concentration, catalyst dosage, and catalyst reusability on Rhodamine B (RhB) degradation were investigated. In the interface reaction, the improved photodegradation efficiency could be attributed to the decomposition of PMS, which produced sulfate radicals and hydroxyl radicals owing to the transmission of photo-generated electron/hole pairs. Herein, the introduction of surface oxygen vacancy as well as the cycling of copper valence states ( $\text{Cu(II)/Cu(I)}$  pairs) can facilitate the production of free reactive radicals, leading to the high degradation efficiency. The catalyst showed high removal efficiency and presented good cycle stability in the reaction. Additionally, the free radical quencher experiment and electron spin resonance (EPR) experiments were conducted, and a proposed photocatalytic mechanism was also illustrated.

**Keywords:**  $\text{CuBi}_2\text{O}_4$ ; visible LED light; peroxymonosulfate

## 1. Introduction

Owing to the rapid development of industry and fast growth of the population, the increased water pollution problem has attracted much more attention. To get the solution for these deteriorated water situations, it was really urgent to develop effective and economic technologies to eliminate these problems [1–3]. In recent years, advanced oxidation processes (AOPs) have brought more concern in the degradation of organic pollutants, which was considered really difficult to degrade by traditional methods [4–6]. Among these various AOPs, sulfate radical-based advanced oxidation processes (SR-based AOPs) possessed high removal efficiency of these concomitants, leading to the formation of sulfate radical ( $\text{SO}_4^{\cdot-}$ ), which had similar redox potential with hydroxyl radicals [7–9]. Additionally, heterogeneous catalyst was employed for the activation of persulfate (PS) or potassium peroxymonosulfate (PMS, trade name Oxone) in SR-Fenton like oxidation process to achieve degradation and mineralization of contaminants in the wastewater. By introducing the visible light in the

heterogeneous SR-Fenton like system (i.e., heterogeneous SR-photo-Fenton like process), the reaction rate was improved in the reaction, which was also widely studied.

In the heterogeneous SR-photo-Fenton like process, the heterogeneous catalyst played a great role for the degradation efficiency. Firstly, the heterogeneous catalysts were effective for the PMS activation, leading to the decomposition of PMS and the formation of sulfate radicals [10–12]. On the other hand, the catalyst could also be stimulated by the visible light, while the generated hole/electron pairs could participate in the degradation process. Many kinds of heterogeneous catalysts have been investigated and applied in the heterogeneous SR-photo-Fenton like process, such as hybrid metal-organic framework (MIL53(Fe)) [13], inorganic oxide heterojunction ( $\text{CuBi}_2\text{O}_4/\text{Bi}_2\text{O}_3$ ) [14], metal oxides ( $\text{Co}_3\text{O}_4$ ) [15], and perovskite structure ( $\text{BiFeO}_3$ ) [16]. In the heterogeneous SR-photo-Fenton like process, PMS was not only an oxidant, but also an electron acceptor, which could prevent the recombination of photo-generated holes and electrons [17–19]. The formed holes and electrons could react with PMS, facilitating the generation of sulfate radicals and hydroxyl radicals. Thus, it could improve the reduction between the high valence state and the low valence state of metal ions, facilitating the cycling of transition metal ions. It was considered that the synergistic effect existed between the catalyst/visible light process and heterogeneous SR-Fenton like reaction [20–23]. Unfortunately, the heterogeneous catalyst possessed high efficiency and stability was still rare, and the reaction mechanism needs further exploration in the heterogeneous SR-photo-Fenton like process.

In recent years, Bi-based catalysts, which acted as the photocatalyst for the degradation of contaminants owing to their unique properties and narrow band gap, have received more attention, facilitating the application of visible light.  $\text{CuBi}_2\text{O}_4$ , as one of p-type Bi-based semiconductor, have aroused widespread concern as it took advantage of the low band gap (1.3–3.7 eV) and high stability [24–26]. The low band gap provided much convenience in the absorption of low energy photons and a better response to the visible light, which has shown notable photocatalytic performance in heterogeneous SR-Fenton like systems [27–29]. By the introduction of visible light, the degradation efficiency was enhanced owing to the reduction of transition Cu ions and photo-generated holes/electrons pairs on the surface of catalyst. Moreover, the photocatalytic performance by single usage of  $\text{CuBi}_2\text{O}_4$  was unsatisfied, which suffered quick recombination of photogenerated holes and electrons. The degradation efficiency of the target pollutant was assumed to be further improved by using pure  $\text{CuBi}_2\text{O}_4$  catalyst alone. On the other hand, to achieve better degradation efficiency, a large amount of photocatalyst was utilized in these systems. It was reported that, in the presence of PMS/PS, which acted as the electron acceptor, the photocatalytic activity was much improved, while the comparison between the absence and presence of PMS/PS by the application of Bi-based catalyst is listed in Table S1. Moreover, the photocatalysis performance of  $\text{CuBi}_2\text{O}_4$  could also be improved by coupling with other semiconductors, such as  $\text{Ag}_2\text{S}/\text{CQDs}$  [30],  $\text{Bi}_2\text{MoO}_6$  [31],  $\text{Ag}_3\text{PO}_4$  [32], and  $\text{WO}_3$  [33]. On the other hand, the introduction of surface oxygen vacancies on catalyst was considered an effective way to improve its photocatalytic activity, which can grip the photo-generated holes and electrons and inhibit the recombination of the hole/electron pairs. Many studies investigated the good catalytic activity of catalyst with surface oxygen vacancies, such as  $\text{Fe(III)}/\text{Bi}_2\text{MoO}_6$  [34],  $\text{BiOBr}$  [35], and  $\text{TiO}_2$  [36]. With the presence of surface oxygen vacancy on the catalyst, the results proved that the band gap was narrowed and the separation and migration of photo-generated electron/holes was facilitated, resulting in better degradation efficiency.

In this study,  $\text{CuBi}_2\text{O}_4$  with surface oxygen vacancy ( $\text{CuBi}_2\text{O}_4\text{-OVs}$ ) was synthesized by the one-pot hydrothermal method, which was used in the heterogeneous SR-photo-Fenton like reaction for the removal of RhB. Visible LED light was chosen as the light source instead of the high-power xenon lamp or gold halide/tungsten lamp owing to its long working life, broad emission spectrum, and cost-effectiveness, and was considered as an efficient light source for removal of pollutants in wastewater. The cycling catalytic activity and copper ion leaching was carefully evaluated. The effects of initial pH, PMS concentration, and catalyst dosage were investigated. Therefore, on the basis of the various characterization analyses, a possible catalytic mechanism for the heterogeneous SR-photo-Fenton like

reaction by the usage of  $\text{CuBi}_2\text{O}_4$ -OVs catalyst was proposed. Radical quenching experiments and EPR tests were conducted to evaluate the main reactive free radicals. Overall, these results showed a novel strategy for the heterogeneous SR-photo-Fenton like reactions in wastewater treatment.

## 2. Results

### 2.1. Synthesis of Catalysts

A hydrothermal method was used to synthesize the  $\text{CuBi}_2\text{O}_4$  catalyst with surface oxygen vacancy. Here, 2 mM  $\text{Bi}(\text{NO}_3)_3 \cdot 5\text{H}_2\text{O}$  and 1 mM  $\text{Cu}(\text{NO}_3)_2 \cdot 3\text{H}_2\text{O}$  were dissolved in 10 mL of ethylene glycol, respectively. Then, both solutions were mixed under stirring. Afterward, 30 mL ethanol and 0.3 g of glucose were added to the mixed solution. After being completely dissolved, the mixture was transferred into the 100 mL Teflon-lined stainless-steel autoclave and kept at 160 °C for 12 h. The solid was centrifuged and washed with deionized water and ethanol, which was dried at 70 °C for 24 h, which denoted as  $\text{CuBi}_2\text{O}_4$ -OVs.  $\text{CuBi}_2\text{O}_4$  was also prepared without the addition of glucose. The glucose was used in the synthesis procedure, which played a great role on the morphology of the nanocomposites owing to the reduction effect, thus further improving the photocatalytic performance of the catalyst. Pure CuO and  $\text{Bi}_2\text{O}_3$  were also prepared by the above method with the addition of  $\text{Cu}(\text{NO}_3)_2 \cdot 3\text{H}_2\text{O}$  or  $\text{Bi}(\text{NO}_3)_3 \cdot 5\text{H}_2\text{O}$ , respectively.

### 2.2. Material Characterization

X-ray diffraction (XRD) pattern was performed using a Bruker D8ADVANCE X-ray diffractometer with a graphite monochromatic Cu  $K\alpha$  radiation ( $\lambda = 1.54 \text{ \AA}$ ) at the accelerating voltage 40 kV and the current 30 mA over the  $2\theta$  scanning range of 10–80°. Scanning electron microscopy (SEM) was characterized on a Hitach SU8220 field emission with X-ray energy dispersive spectra (EDS) instrument, which would find out the element distribution. High resolution transmission electron microscopy (TEM) images were obtained using FEI Talos F200S with high-resolution at 200 kV. The X-ray photoelectron spectroscopy (XPS) was carried out on Thermo Fisher ESCALAB250Xi. The diffuse reflectance spectrum (DRS) was operated on ultraviolet visible near infrared spectrophotometer with Shimadzu UV-3600 Plus. The Brunauer-Emmett-Teller (BET) specific surface area, pore size, and volumes were analyzed by  $\text{N}_2$  adsorption–desorption technology using automatic micromeritics instrument corporation TriStar II 3020.

### 2.3. Photocatalytic Performance Experiments

In the experimental setup, a 30 W LED lamp (30 W, 460 nm, Xujia Company, Shanghai, China) was employed as the light source. Further, 0.1 g photocatalyst was added to 200 mL of RhB solution (20 mg/L). Before the light turned on, the mixture was magnetically stirred in the dark for 60 min in order to obtain the absorption–desorption equilibrium. Then, 0.049 g PMS was added in the system and LED lights were turned on. The sample was taken out and filtered through 0.22  $\mu\text{m}$  membrane filters; the concentrations of RhB and total organic carbon (TOC) were measured by UV/vis spectrophotometer (UV 3600 II, Shanghai, China) and TOC (Elementar vario) analyzer, respectively. Each sample was measured three times and the average values are shown in the figures. Electron spin resonance (ESR, JES FA200, JEOL) was used to measure the intensity of free radicals in methanol and deionized water. The copper leaching measurements were performed using the inductively coupled plasma mass spectrometry (ICP-MS) method (Agilent 7000). In the batch experiments, the degradation of RhB was fitted well with the pseudo first order kinetics model, which can be expressed as Equation (1).

$$\ln C/C_0 = -k_{\text{app}} \times t \quad (1)$$

where  $C$  refers to the concentration of RhB at time  $t$ ,  $C_0$  refers to the initial RhB concentration,  $k_{\text{app}}$  refers to the kinetic rate constant, and  $t$  refers to the reaction time.

### 3. Discussion

#### 3.1. Characterization of Prepared Samples

The morphology and microstructure of the as-prepared  $\text{CuBi}_2\text{O}_4$  and  $\text{CuBi}_2\text{O}_4$ -OVs were characterized by SEM and HRTEM. Figure 1 presented that the  $\text{CuBi}_2\text{O}_4$  sample was composed of a sphere-like morphology, which was made of nanocrystals of 20–40 nm thickness. However, it was also observed that large bulks were presented on the surface with agglomeration, owing to the anisotropic growth of crystals on the surface. The diameter of the sphere was in the width of ~400 nm. On the other hand, the morphology of  $\text{CuBi}_2\text{O}_4$ -OVs synthesized after the addition of glucose showed smaller diameter of ~350 nm with a wool-ball like morphology, which was different with the  $\text{CuBi}_2\text{O}_4$ . The results can be attributed to the reductant of glucose, which prevent the growth of crystallization, resulting in the decreased crystallinity of the  $\text{CuBi}_2\text{O}_4$  sample. Furthermore, the elemental distribution of the  $\text{CuBi}_2\text{O}_4$ -OVs composite was determined by energy dispersive spectroscopy (EDS). It was observed that there were three elements detected in the as-prepared samples, that is, Cu, Bi, and O, where the atomic ratio of Cu and Bi was close to 1:2.

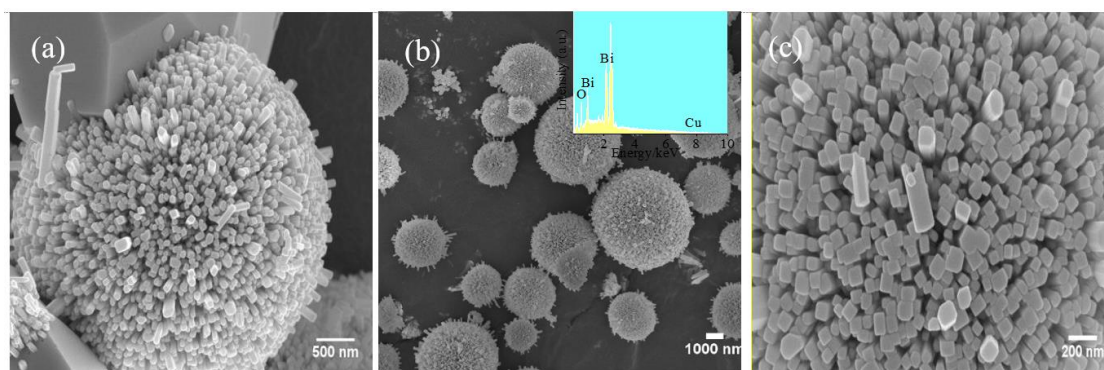


**Figure 1.** Scanning electron microscopy (SEM) images of as-prepared (a)  $\text{CuBi}_2\text{O}_4$  and (b,c)  $\text{CuBi}_2\text{O}_4$ -OVs; the inset is the energy dispersive spectroscopy (EDS) spectra of  $\text{CuBi}_2\text{O}_4$ -OVs.

The HRTEM images clearly showed the lattice spacing of 0.245 nm and 0.253 nm, which was attributed to the (310) plane of the  $\text{CuBi}_2\text{O}_4$  and  $\text{CuBi}_2\text{O}_4$ -OVs samples, respectively, which was shown in Figure 2 [37]. Moreover, the EDS element mapping image of Cu, Bi, and O demonstrated the homogeneous distribution of these elements, which were presented on the surface of catalyst. However, the lattice edges of the  $\text{CuBi}_2\text{O}_4$ -OVs sample were not distinct, found with disordered and blurred boundaries, which could be attributed to the introduction of surface oxygen vacancies. The TEM image of  $\text{CuBi}_2\text{O}_4$ -OVs showed that the average size of the particles was close to 64 nm, where the particles presented partial agglomeration. The results of HRTEM images were consistent with the XRD data.

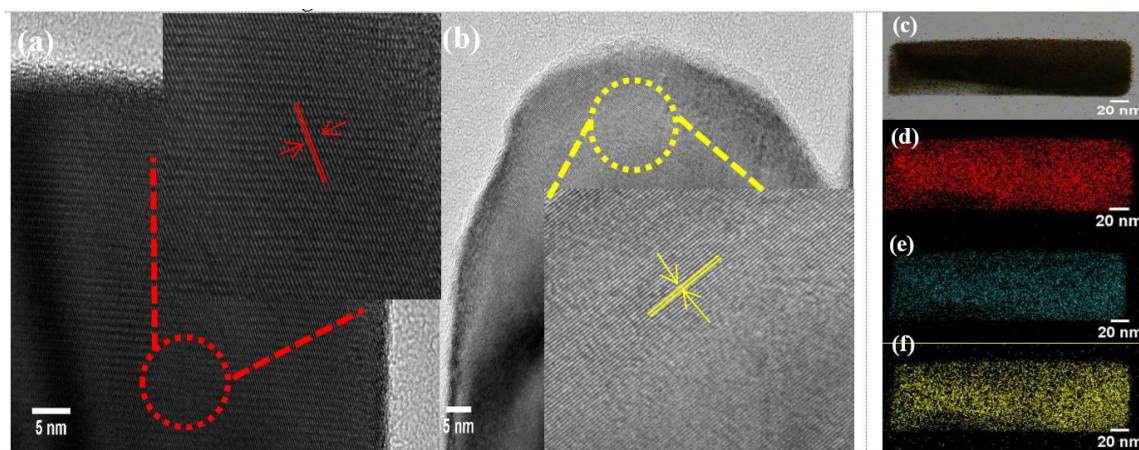


**Figure 2.** Transmission electron microscopy (TEM) images of as-prepared (a)  $\text{CuBi}_2\text{O}_4$  and (b)  $\text{CuBi}_2\text{O}_4$ -OVs, and (c) all elements EDS mapping images of  $\text{CuBi}_2\text{O}_4$ -OVs, (d) Bi 4f, (e) Cu 2p, and (f) O 1s. The inset image is magnified image of the encircled area.

The crystal properties of the prepared  $\text{CuBi}_2\text{O}_4$ -OVs,  $\text{Bi}_2\text{O}_3$ , and  $\text{CuO}$  samples were characterized by XRD, which is shown in Figure 3. All the diffraction peaks of  $\text{CuBi}_2\text{O}_4$ -OVs corresponded well to the phase of  $\text{CuBi}_2\text{O}_4$  (JCPDS No. 48-1886). No impurities were found, indicating the preparation procedure was successful and the crystal structure of  $\text{CuBi}_2\text{O}_4$  was unchanged during the synthesis [38,39]. The diffraction peaks were narrow and strong, which showed the good crystallization of the  $\text{CuBi}_2\text{O}_4$  catalyst. With the introduction of surface oxygen vacancy, the intensity of diffraction peaks was slightly decreased. Diffraction peaks of  $\text{CuO}$  (JCPDS 44-0706) and  $\text{Bi}_2\text{O}_3$  (JCPDS 27-0050) were also identified, demonstrating the pure crystal structure of synthesized catalysts. Moreover, the prepared samples possessed an average size of around 53.2 nm according to the Debye–Scherrer formula, which was in good agreement with SEM and TEM results.

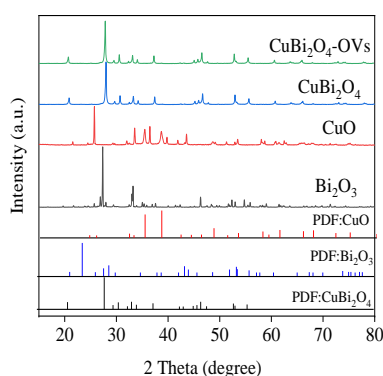


**Figure 3.** X-ray diffraction (XRD) patterns of as-prepared catalysts.

The chemical composition and element state of the prepared samples were carried out by the XPS method. As shown in Figure 4, the peaks of Bi, O, Cu, and trace C were found on the surface of as-prepared samples, which were sharp and clear. The characteristic peaks of Bi 4f were centered at 158.6 eV and 163.9 eV, corresponding to Bi 4f<sub>5/2</sub> and Bi 4f<sub>7/2</sub>, which indicated the existence of  $\text{Bi}^{3+}$  [40]. It was observed that the peaks were slightly shifted to higher binding energy owing to the introduction of surface oxygen vacancy. The peak observed at 955.5 eV with a satellite peak at 964.8 eV in the XPS spectra of Cu 2p was assigned to Cu 2p<sub>1/2</sub>, and the peak of Cu 2p<sub>3/2</sub> centered at 934.3 eV would be deconvoluted to 935.6 eV and 932.8 eV, respectively, which was considered as Cu(II) and reduced copper species [41]. The presence of reduced copper species on the surface of sample could be



attributed to the reduction of Cu(II), which facilitated the heterogeneous SR-photo-Fenton like reaction by the cycling reaction between Cu(II) and Cu(I). The peak centered around 530 eV can be denoted as O 1s, which shifted to a higher binding energy owing to the electron attraction effect of oxygen vacancy. The characteristic peak of O 1s could be deconvoluted into three internal peaks at 529.7 eV, 531.5 eV, and 532.5 eV in the fresh catalyst, representing the lattice oxygen, metal-O bonds (Bi-O, Cu-O), hydroxyl groups, and absorbed H<sub>2</sub>O on the surface, respectively [42]. The peak of hydroxyl groups and absorbed H<sub>2</sub>O in CuBi<sub>2</sub>O<sub>4</sub>-OVs took a much higher proportion than that of the CuBi<sub>2</sub>O<sub>4</sub> samples. Additionally, the metal-O bonds were also different, which further proved the formation of surface oxygen vacancy on the catalyst. The proportion of the three peaks was changed after the heterogeneous SR-photo-Fenton like reaction, demonstrating the participation of the H<sub>2</sub>O and oxygen vacancy in the reactions, leading to the formation of reactive oxygen radicals. The results also proved that there was a redox transition of Cu ions under LED light irradiation.

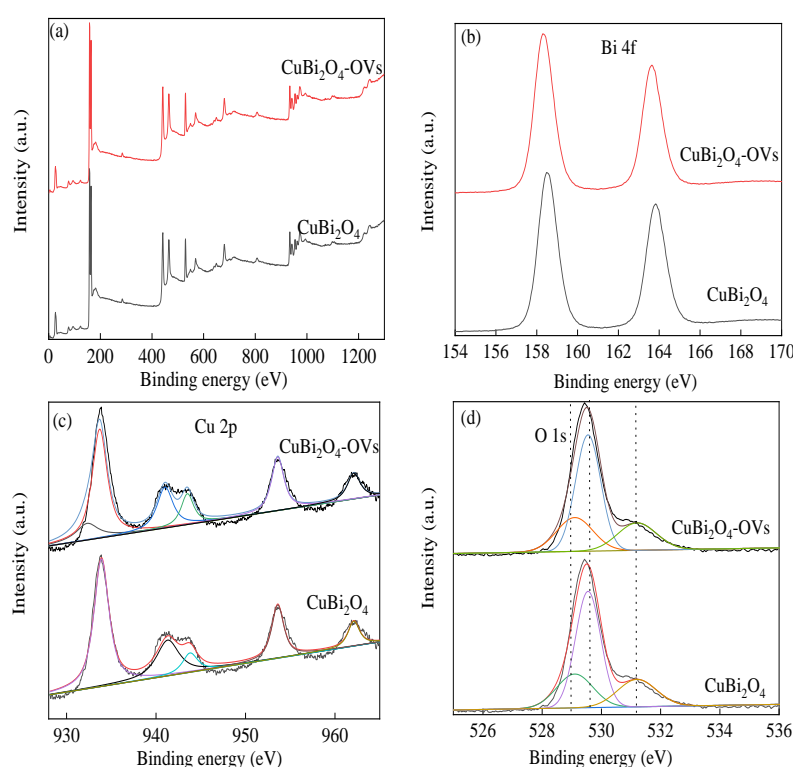


**Figure 4.** X-ray photoelectron spectroscopy (XPS) spectra of as-prepared catalysts. (a) full-scale XPS spectra, (b) Bi 4f, (c) Cu 2p, and (d) O 1s.

The UV/vis diffusion spectra of the CuBi<sub>2</sub>O<sub>4</sub> and CuBi<sub>2</sub>O<sub>4</sub>-OVs catalyst were shown in Figure 5. It was observed that both the CuBi<sub>2</sub>O<sub>4</sub> and CuBi<sub>2</sub>O<sub>4</sub>-OVs catalyst showed a long band absorption in the visible light region, implying good response to the visible light. However, the absorption area in the visible light region was higher in the CuBi<sub>2</sub>O<sub>4</sub>-OVs than in the CuBi<sub>2</sub>O<sub>4</sub> catalyst owing to the introduction of surface oxygen vacancy. The results proved that the enhanced absorption in visible light region would result in better catalytic activity. The band gap energy ( $E_g$ ) of CuBi<sub>2</sub>O<sub>4</sub> and CuBi<sub>2</sub>O<sub>4</sub>-OVs was determined by the Tauc model, which is commonly used in the semiconductor catalyst [43].

$$ah\nu = A(h\nu - E_g)^{n/2} \quad (2)$$

where  $a$ ,  $h\nu$ ,  $A$  and  $E_g$ , are the absorbance, photon energy, a constant, and the band gap, respectively. The band gap energy of the CuBi<sub>2</sub>O<sub>4</sub> and CuBi<sub>2</sub>O<sub>4</sub>-OVs catalyst was calculated to be fixed at 1.83 eV and 1.72 eV, respectively, which was assumed to perform good photocatalytic activity under visible

LED light irradiation. In the presence of surface oxygen vacancy, the narrowed band gap showed enhanced adsorption ability to visible light, promoting the separation of photo-generated holes and electrons pairs, causing the enhancement of photocatalytic activity. The  $N_2$  absorption/desorption isotherms of the  $CuBi_2O_4$  and  $CuBi_2O_4$ -OVs catalyst are shown in Figure S1. The isotherms of both the  $CuBi_2O_4$  and  $CuBi_2O_4$ -OVs catalyst presented type H3 isotherms. The BET surface area of  $CuBi_2O_4$  was  $4.76\text{ m}^2/\text{g}$  and the pore size was around  $10.9\text{ nm}$ , as the BET surface area of  $CuBi_2O_4$ -OVs was  $5.01\text{ m}^2/\text{g}$  and the pore size was  $11.1\text{ nm}$ . With the presence of surface oxygen vacancy, the BET surface area and pore size was slightly increased, which is listed in Table S2.

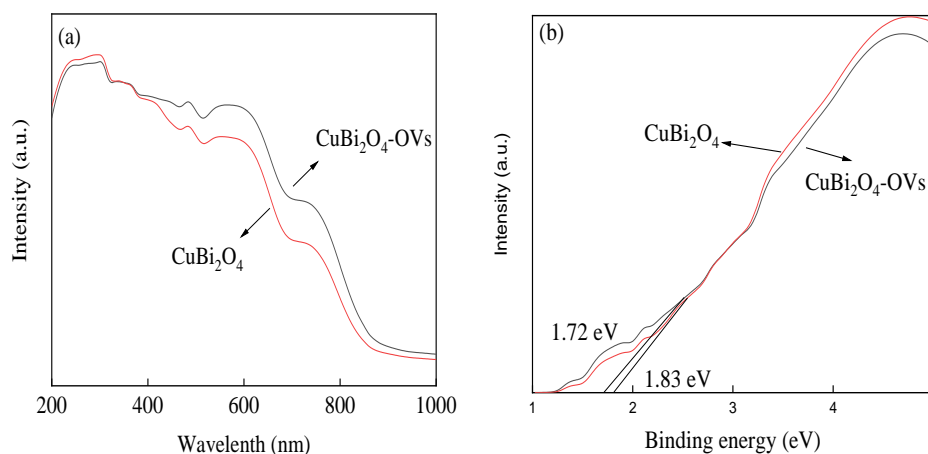


**Figure 5.** (a,b) UV/vis diffusion reflectance spectra of as-prepared catalysts.

### 3.2. Heterogeneous SR-Photo Degradation of RhB

The prepared catalysts have no adsorption removal efficiency on RhB in the reaction time owing to the limited BET surface area. Negligible removal of RhB was obtained by using PMS alone and using LED light alone, owing to hardly any production of reactive free radicals. Figure 6 shows the degradation efficiency of photocatalysis, heterogeneous SR-Fenton reaction, and heterogeneous SR-photo-Fenton like reaction was 29.4%, 56.8%, and 87.9%, respectively. The value of reaction constant  $k_{app}$  for heterogeneous SR-photo-Fenton like process was higher than the sum of photocatalysis and heterogeneous SR-Fenton like reaction, which demonstrated there was a synergistic effect for RhB degradation in heterogeneous SR-photo-Fenton like reaction with  $CuBi_2O_4$ -OVs as catalyst. Herein, compared with the  $CuBi_2O_4$ -OVs catalyst, the removal efficiency of RhB was 100% and 40.9% for  $CuO$  and  $Bi_2O_3$ , respectively. On the other hand, with the introduction of surface oxygen vacancy, the synergistic effect between the heterogeneous SR-Fenton like reaction and photocatalysis could improve the degradation activity of RhB as well as the degradation rate constant [44]. The results might be attributed to the increased hydroxyl group on the surface, which formed more reactive oxygen species in the heterogeneous SR-photo-Fenton like reaction. The separation and transmission of photo-generated holes and electrons was also improved owing to the presence of surface oxygen vacancy, leading to better degradation efficiency. The addition of visible LED light to the heterogeneous SR-Fenton like systems enhanced the RhB removal degradation efficiency and rate constant. Consequently, the heterogeneous SR-photo-Fenton like system showed the highest removal efficiency for RhB by using  $CuBi_2O_4$ -OVs catalyst combined with surface oxygen vacancy [45].



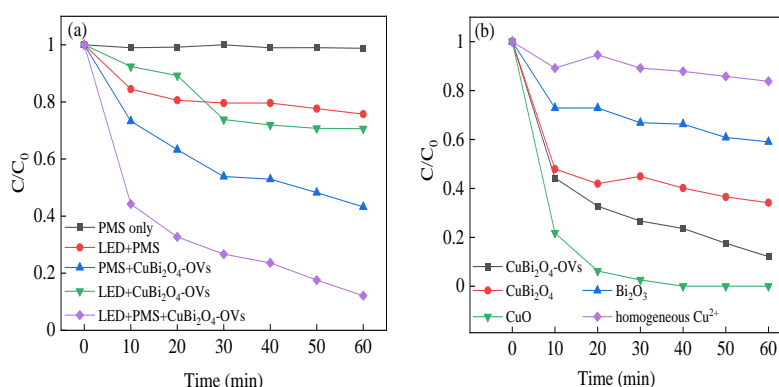


**Figure 6.** (a) Comparison of RhB degradation activity in different systems; (b) effect of different catalyst on RhB degradation. Reaction conditions: RhB (20 mg/L), PMS (0.4 mM), catalyst (0.5 g/L), neutral pH.

The pseudo-first-order kinetic model was applied to calculate the degradation rate constants, which fitted well with the results. The  $k_{app}$  values were 0.0064, 0.0126, and 0.0304 h<sup>−1</sup> for photocatalysis, heterogeneous SR-Fenton like reaction, and heterogeneous SR-photo-Fenton like reaction, respectively, which demonstrated the existence of a synergistic effect. Moreover, the metal leaching problem was very important in the heterogeneous reaction, which directly affected the stability of the heterogeneous catalyst. The leaching copper was very low and ranged from 0.020 to 0.0895 mg/L as the pH value declined from 10.7 to 3.2. The SR-photo-Fenton like reaction with 0.0895 mg/L copper ions in the system was also carried out and showed a poor contribution to PMS activation, evidencing that the catalyst played a significant role in the system. Therefore, photo-generated holes and electrons would participate in the redox transmission of copper ions in the heterogeneous SR-photo-Fenton like reaction, improving the formation of reactive oxygen species, leading to the enhancement of removal efficiency [46].

### 3.3. Effect of Reaction Conditions

Then, the reaction conditions were explored to get the best removal efficiency. As shown in Figure 7a, the removal efficiency of RhB declined from 86.2% to 37.9% as the solution pH climbed from 3.2 to 4.9. When the solution pH further climbed from 4.9 to 8.8, the degradation efficiency and rate constant were almost at the same level. Moreover, the removal efficiency of RhB was enhanced to 96.6% as the solution pH was raised to 10.7. In the acidic solution, the formation of  $SO_5^{2-}$  ions was obtained and showed no catalytic activity [47]. The results showed that PMS possessed more stability rather than decomposed to sulfate radicals, thus retarding the degradation efficiency in highly acidic conditions [48]. When the solution pH came to neutral and basic condition, the hydroxyl radicals formed, which showed similar redox potential with sulfate radicals, resulting in better RhB removal efficiency. The removal rate remained unchanged in the pH range of 4.9–8.8, which proved that the CuBi<sub>2</sub>O<sub>4</sub>-OVs catalyst would be effective in a wide range of pH in the heterogeneous SR-photo-Fenton like process.

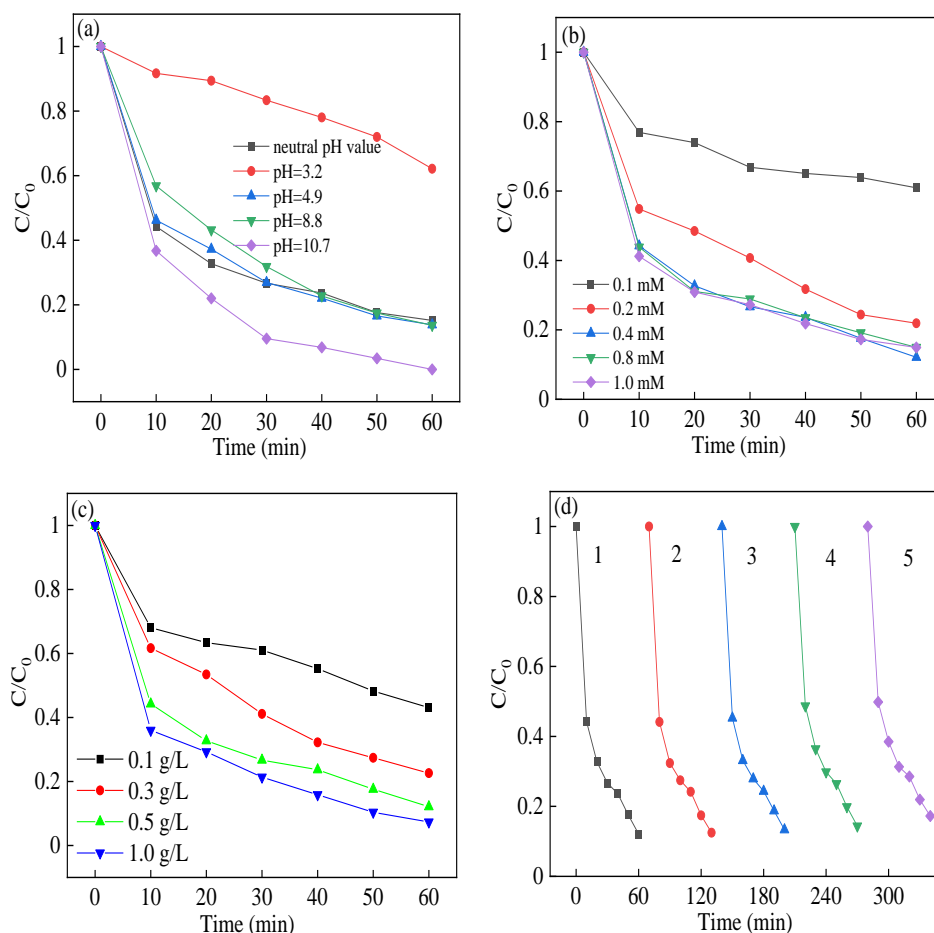


**Figure 7.** Effect of (a) reaction initial pH value; (b) PMS concentration; (c) catalyst dosage; and (d) reuse on RhB degradation in heterogeneous sulfate radical (SR)-photo-Fenton like reaction. Reaction conditions: RhB (20 mg/L), PMS (0.1–1.0 mM), catalyst (0.1–1.0 g/L), pH in the range of 3.2–10.7 in (a–c); PMS (0.4 mM), catalyst (0.5 g/L), neutral pH in (d).



The removal efficiency of RhB with different PMS concentrations in the range of 0.1–1.0 mM in the heterogeneous SR-photo-Fenton like reaction was shown in Figure 7b. The degradation efficiency of RhB increased from 39.1% to 87.9% with the increased PMS concentration, and the degradation rate constant varied from 0.0071 to 0.0304  $\text{h}^{-1}$ . However, the degradation efficiency of RhB was not further increased; as the PMS concentration rose higher than 0.4 mM, the rate constant remained nearly unchanged. The results could be attributed to the reactive sites on the surface of catalyst, which participated in the activation of PMS, leading to greater generation of oxidant species in the increment of PMS concentrations; on the other hand, overdosed oxidants will compete with other reactive radicals, resulting in the consumption of free radicals and declined removal efficiency of RhB [49]. When the PMS concentration was too high, it would inhibit the reaction between the reactive species and the contaminants, resulting in the decreased removal rate constant, which was a waste of PMS.

The removal efficiency of RhB in heterogeneous SR-photo-Fenton like reaction with different catalyst dosages was shown in Figure 7c. When the catalyst dosage increased from 0.1 g/L to 1.0 g/L, the removal efficiency climbed from 57.1% to 92.7% in the reaction time, where the degradation rate

changed from 0.012 to 0.0391 h<sup>-1</sup>. As the catalyst dosage was over 0.5 g/L, the increasing rate of  $k_{app}$  was not fast enough when the catalyst dosage was fixed at 1.0 g/L. Firstly, with the increment of the catalyst addition, more reactive sites were employed to generate more reactive oxygen species, where more surface area was provided in the reaction. Secondly, the excessive catalyst would be an obstacle to the adsorption and transmission of visible light [50]. This phenomenon would give a negative effect on the excitation of electrons and lead to the reduction of activation efficiency. All the above results indicated that the prepared CuBi<sub>2</sub>O<sub>4</sub>-OVs catalyst showed high and effective activity for RhB removal in the heterogeneous SR-photo-Fenton like reaction.

The recycling experiments of CuBi<sub>2</sub>O<sub>4</sub>-OVs were evaluated under the optimized reaction conditions, which are shown in Figure 7d. The RhB degradation efficiency remained high in five successive reactions, and only showed slightly decreased efficiency in the fifth cycling experiment with 82.7% RhB removal. This might be attributed to the occupancy of reactive sites on the surface of catalyst in the successive reactions, where the leaching copper also affected the removal efficiency. Moreover, the rate constant also remained in the range of 0.0304 to 0.0258 h<sup>-1</sup>. The leached copper element was no more than 0.0895 mg/L, demonstrating the stability of synthesized CuBi<sub>2</sub>O<sub>4</sub>-OVs in heterogeneous SR-photo-Fenton like reaction. Compared with the fresh composite, the XRD diffraction peaks of CuBi<sub>2</sub>O<sub>4</sub>-OVs had no obvious change after the reaction, which are shown in Figure S2. The major phase of the CuBi<sub>2</sub>O<sub>4</sub>-OVs catalyst showed no obvious difference between the fresh and used catalyst, indicating the stability of the CuBi<sub>2</sub>O<sub>4</sub>-OVs structure. The XPS peak of O 1s in the used catalyst showed slightly increased owing to the increment of oxygen or the water adsorption on the surface of catalyst. All the above results showed the catalyst had good reusability and stability in the heterogeneous SR-photo-Fenton like reaction.

TOC experiments were also used to evaluate the mineralization of RhB under optimal reaction conditions, which were shown in Figure 8. The TOC degradation was 13.3%, 32.8%, and 63.2% in the photocatalysis reaction, heterogeneous SR-Fenton like reaction, and heterogeneous SR-photo-Fenton like reaction, respectively. The results showed the mineralization of RhB was satisfied owing to the synergism effect, and were in good agreement with the degradation efficiency of RhB. Moreover, the CuBi<sub>2</sub>O<sub>4</sub>-OVs was also employed for the removal of other organic contaminants in the heterogeneous SR-photo-Fenton reaction, such as Orange II, methyl red (MR), ciprofloxacin (CIP), and levofloxacin (LVF). The degradation efficiency of Orange II and MR was 85.1% and 83.7% in the reaction time, whereas the degradation of CIP and LVF was about 10.4% and 16.2%, respectively. The results showed that the heterogeneous SR-photo-Fenton like reaction was effective for mostly common organic pollutants, especially for the removal of dyes.

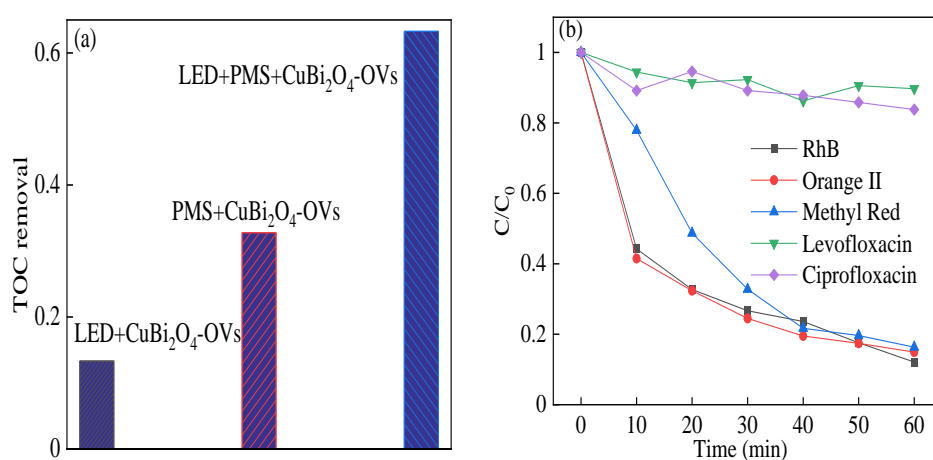


**Figure 8.** (a) Total organic carbon (TOC) removal of RhB; (b) degradation of various contaminants in heterogeneous SR-photo-Fenton like reaction. Reaction conditions: contaminants (20 mg/L), PMS (0.4 mM), catalyst (0.5 g/L), neutral pH.

### 3.4. Reaction Mechanism

It was known that the reactive radical species dominated the reaction rate and efficiency in the heterogeneous SR-photo-Fenton like reaction. In order to identify the reactive radicals, radical quencher chemicals were applied in the system to find the possible free radicals. Compared with the reaction with sulfate radicals, the reaction between tert-Butyl alcohol (TBA) and hydroxyl radicals was really fast. In this case, TBA was usually considered as the trapping agent of  $\cdot\text{OH}$ . Methanol (MeOH) could react with sulfate and hydroxyl radicals in the meantime, which was used as the trapping agent for sulfate radicals and hydroxyl radicals. It can be seen in Figure 9a that the degradation efficiency of RhB was 79.5% and 70.6%, which slightly decreased in the presence of TBA and MeOH compared with the control experiment. Herein, it was proposed that both sulfate radicals and hydroxyl radicals were formed in the reaction. However, the two free radicals took a little contribution for the reaction, implying the two scavenging chemicals took a moderate inhibition in the reaction. Moreover, in order to identify the existence of photogenerated holes and superoxide radicals, p-benzoquinone (BQ) and sodium oxalate (SO,  $\text{Na}_2\text{C}_2\text{O}_4$ ) were used as quenching chemicals for the reactive species. When BQ and SO chemicals were added in the solution, the degradation efficiency of RhB was declined to 15.8% and 40.2%, which demonstrated the superoxide radicals and holes were also generated and dominated in the reaction. It was assumed that the superoxide, photogenerated holes, sulfate radicals, and hydroxyl radicals were all produced in the reaction. The sulfate radicals, holes, and superoxide radicals played a dominant role in the RhB removal process, leading to enhancement of the photocatalytic reaction.

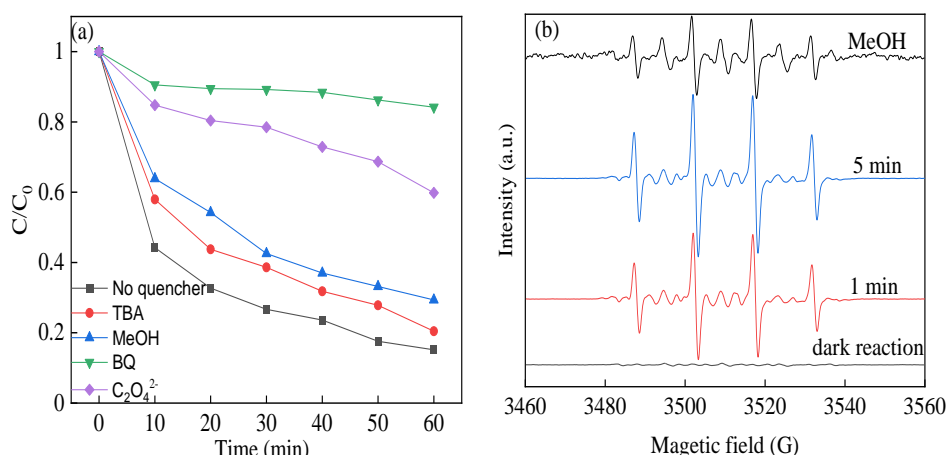
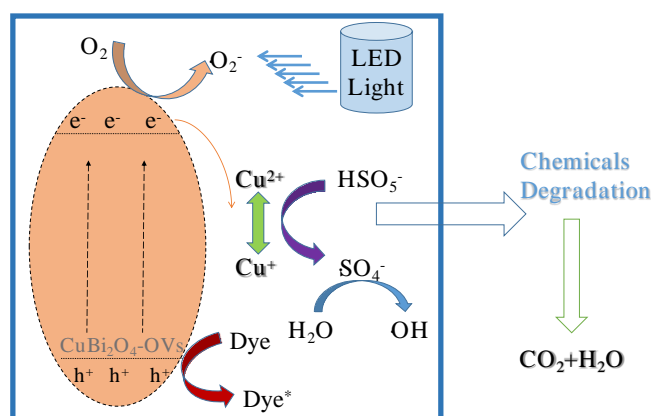


**Figure 9.** (a) Different quenching chemicals to remove RhB; (b) DMPO spin-trapping EPR spectra in heterogeneous SR-photo-Fenton like reaction. BQ, p-benzoquinone.

In order to evidence the existence of free reactive radicals, EPR experiments were also conducted using 5, 5-Dimethyl-1-Pyrrolidine-N-oxide (DMPO) as a spin trapping agent, as shown in Figure 9b. Weak typical peaks of DMPO-OH were identified under dark condition, indicating certain number of radicals were produced as a result of the activation of PMS. However, when the heterogeneous SR-Fenton like system was irradiated by visible LED light, strong signals of DMPO-OH peaks were observed. The EPR signals of DMPO-SO<sub>4</sub> were found with weak intensity owing to the quick reaction with H<sub>2</sub>O, leading to the generation of hydroxyl radicals, which made it difficult to capture the signal in the solution [51]. The signal remained sharp after 5 min reaction, evidencing the persistent production of these free radicals. Moreover, the signal of DMPO-O<sub>2</sub> radicals was also observed, which proved the presence of superoxide radicals in the systems. Thus, the CuBi<sub>2</sub>O<sub>4</sub>-OVs catalyst could produce lots of free reactive radicals in the heterogeneous SR-photo-Fenton like reaction, which agreed well with the results of the quenching experiments.

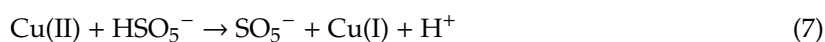
### 3.5. Proposed Reaction Mechanism

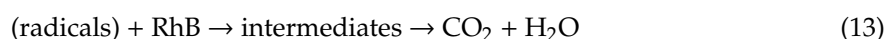
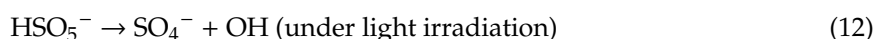
Figure 10 illustrates the mechanism in the heterogeneous SR-photo-Fenton like reaction using the  $\text{CuBi}_2\text{O}_4$ -OVs catalyst under LED light irradiation on the basis of the above results. In the XPS spectra, the peaks for Cu element could be attributed to Cu(II) and Cu(I). The redox pair of Cu(I)/Cu(II) could participate in the decomposition of PMS to generate  $\text{SO}_4^{\cdot -}$  and  $\cdot\text{OH}$ , which was much higher after the reaction than that of fresh catalyst. The continuous redox of Cu(II) occurred through the reduction caused by generated electrons, leading to the production of reduced Cu species. Meanwhile, the electrons could jump from CB to VB on the catalyst surface, which was occupied with rich surface oxygen vacancy, facilitating the rapid conversion of Cu(II)/Cu(I) pairs. With the presence of surface oxygen vacancy, the free radicals were formed more quickly, leading to better degradation efficiency. Moreover, surface oxygen vacancy could be considered as a defect on the catalyst surface, acting as the reactive sites, which was effective to prevent the recombination of photo-generated holes/electrons, leading to better catalytic activity [52]. Additionally, the visible region of catalyst was also extended, which was helpful for the visible light adsorption on the surface.



**Figure 10.** Mechanism of heterogeneous SR-photo-Fenton like degradation of RhB using the  $\text{CuBi}_2\text{O}_4$ -OVs catalyst.

In conclusion, as the  $\text{CuBi}_2\text{O}_4$ -OVs catalyst was irradiated by visible LED light, the production of photo-generated hole and electrons occurred, which would react with PMS to generate free radicals. PMS was applied as the electron acceptor and the oxidant in the heterogeneous SR-photo-Fenton like reaction, which suppressed the recombination of holes and electrons, leading to better degradation efficiency [53]. As the surface oxygen vacancy was presented on the surface of catalyst, the free radicals were quickly formed owing to the quick transmission of photo-generated carriers and good separation efficiency of the pairs. The extended response to the visible light would also be attributed to the introduction of surface oxygen vacancy. Then, with the persistent attack of superoxide, holes, sulfate radicals, and hydroxyl radicals, the target pollutant RhB was gradually degraded in the reaction and mineralized to  $\text{CO}_2$  and  $\text{H}_2\text{O}$ .





#### 4. Conclusions

In this study, the CuBi<sub>2</sub>O<sub>4</sub>-OVs catalyst was prepared and applied in a heterogeneous SR-photo-Fenton like system. The removal of RhB fitted well with the pseudo first-order kinetics model. The optimal experiment condition was obtained such that the catalyst dosage was fixed at 0.5 g/L and PMS concentration was fixed at 0.4 mM under neutral pH, which showed a synergism effect of the photocatalysis and heterogeneous SR-Fenton like reaction. The introduction of surface oxygen vacancy could prevent the recombination of photogenerated holes and electrons and narrow the band gap of CuBi<sub>2</sub>O<sub>4</sub>, leading to higher degradation efficiency. With the increased dosage of PMS and catalyst, the removal efficiency was improved, but retarded with overdosed addition owing to side competitive reactions. The CuBi<sub>2</sub>O<sub>4</sub>-OVs catalyst exhibited good photocatalytic performance. Moreover, the reusability of catalyst was excellent in five successive experiments with low leaching of Cu ions. The roles of superoxide radicals, holes, sulfate radicals, and hydroxyl radicals were identified by quencher chemicals and EPR experiments. The reaction mechanism was also proposed in the heterogeneous SR-photo-Fenton like reaction. Therefore, the heterogeneous SR-photo-Fenton like system has good aspect for the treatment of organic pollutant in wastewater.

**Supplementary Materials:** The following are available online at <http://www.mdpi.com/2073-4344/10/8/945/s1>, Figure S1: N<sub>2</sub> adsorption–desorption isotherm of CuBi<sub>2</sub>O<sub>4</sub> and CuBi<sub>2</sub>O<sub>4</sub>-OVs; Figure S2: XRD patterns of the CuBi<sub>2</sub>O<sub>4</sub>-OVs catalyst before and after the reaction; Table S1: Studies on of Bi-based catalysts in the photocatalytic reactions; Table S2: Surface area, pore volume, pore size of CuBi<sub>2</sub>O<sub>4</sub>, and CuBi<sub>2</sub>O<sub>4</sub>-OVs samples.

**Author Contributions:** Methodology, X.Z.; investigation, Y.C., H.B., and X.Z.; resources, W.H. and B.Z.; writing—original draft preparation, X.Z.; writing—review and editing, X.Z.; project administration, X.Z., W.H., and B.Z. All authors have read and agreed to the published version of the manuscript.

**Funding:** This work is financially supported by the Project of Youth Innovative Foundation of Guangdong Province of China (Grant No. 201912017QX); Provincial undergraduate innovation and Entrepreneurship Project (S202013177014); Promotion Project Funds of Beijing Normal University, Zhuhai (Grant No. 201850001); Quality Engineering Project of Beijing Normal University, Zhuhai (Grant No. 201832); and Plan of Youth Teachers of Guangdong Higher Education Association (Grant No. 19GYB060).

**Acknowledgments:** This work is financially supported by Project of Youth Innovative Foundation of Guangdong Province of China for help in XRD, SEM, TEM, and XPS analysis.

**Conflicts of Interest:** The authors declare that there is no conflict of interests.

#### References

1. Frank, S.N.; Bard, A.J. Heterogeneous photocatalytic oxidation of cyanide and sulfite in aqueous solutions at semiconductor powders. *J. Phys. Chem.* **1977**, *81*, 1484–1488. [CrossRef]
2. Li, R.; Li, T.; Zhou, Q. Impact of titanium Dioxide (TiO<sub>2</sub>) modification on its application to pollution treatment—A Review. *Catalyst* **2020**, *10*, 804. [CrossRef]

3. Karthikeyan, C.; Arunachalam, P.; Ramachandran, K.; Al-Mayouf, A.M.; Karuppuchamy, S. Recent advances in semiconductor metal oxides with enhanced methods for solar photocatalytic applications. *J. Alloy. Compd.* **2020**, *828*, 15. [CrossRef]
4. Gray, H.E.; Powell, T.; Choi, S.; Smith, D.S.; Parker, W.J. Organic phosphorus removal using an integrated advanced oxidation-ultrafiltration process. *Water Res.* **2020**, *1821*, 115968.
5. Gonzalez, T.; Dominguez, J.R.; Correia, S. Neonicotinoids removal by associated binary, tertiary and quaternary advanced oxidation processes: Synergistic effects, kinetics and mineralization. *J. Environ. Manag.* **2020**, *2611*, 110156. [CrossRef]
6. Wang, J.; Zhuan, R. Degradation of antibiotics by advanced oxidation processes: An overview. *Sci. Total Environ.* **2020**, *701*, 135023. [CrossRef]
7. Zhao, Q.; Mao, Q.; Zhou, Y.; Wei, J.; Liu, X.; Yang, J.; Luo, L.; Zhang, J.; Chen, H.; Chen, H.; et al. Metal-free carbon materials-catalyzed sulfate radical-based advanced oxidation processes: A review on heterogeneous catalysts and applications. *Chemosphere* **2017**, *189*, 224–238. [CrossRef]
8. Oh, W.D.; Dong, Z.; Lim, T.T. Generation of sulfate radical through heterogeneous catalysis for organic contaminants removal: Current development, challenges and prospects. *Appl. Catal. B* **2016**, *1945*, 169–201. [CrossRef]
9. Hu, P.; Long, M. Cobalt-catalyzed sulfate radical-based advanced oxidation: A review on heterogeneous catalysts and applications. *Appl. Catal. B* **2016**, *181*, 103–117. [CrossRef]
10. Shukla, P.; Sun, H.; Wang, S.; Ang, H.M.; Tade, M.O. Co-SBA-15 for heterogeneous oxidation of phenol with sulfate radical for wastewater treatment. *Catal. Today* **2011**, *175*, 380–385. [CrossRef]
11. Wang, Y.; Indrawirawan, S.; Duan, X.; Sun, H.; Ang, H.M.; Tade, M.O.; Wang, S. New insights into heterogeneous generation and evolution processes of sulfate radicals for phenol degradation over one-dimensional  $\alpha$ -MnO<sub>2</sub> nanostructures. *Chem. Eng. J.* **2015**, *266*, 12–20. [CrossRef]
12. Wu, C.H.; Yang, M.T.; Lin, K.Y.A. Magnetic Co/Fe nanohybrid supported on carbonaceous marcosphere as a heterogeneous catalyst for sulfate radical-based chemical oxidation. *J. Environ. Chem. Eng.* **2018**, *6*, 426–434. [CrossRef]
13. Zhang, Y.; Zhou, J.; Chen, J.; Feng, X.; Cai, W. Rapid degradation of tetracycline hydrochloride by heterogeneous photocatalysis coupling persulfate oxidation with MIL-53(Fe) under visible light irradiation. *J. Hazard. Mater.* **2020**, *392*, 122315. [CrossRef] [PubMed]
14. Wang, Y.; Liu, C.; Zhang, Y.; Meng, W.; Yu, B.; Pu, S.; Yuan, D.; Qi, F.; Xu, B.; Chu, W. Sulfate radical-based photo-Fenton reaction derived by CuBi<sub>2</sub>O<sub>4</sub> and its composites with  $\alpha$ -Bi<sub>2</sub>O<sub>3</sub> under visible light irradiation: Catalyst fabrication, performance and reaction mechanism. *Appl. Catal. B* **2018**, *235*, 264–273. [CrossRef]
15. Lv, C.; Liang, H.; Chen, H.; Wu, L. Hydroxyapatite supported Co<sub>3</sub>O<sub>4</sub> catalyst for enhanced degradation of organic contaminants in aqueous solution: Synergistic visible-light photo-catalysis and sulfate radical oxidation process. *Microchem. J.* **2019**, *149*, 103959. [CrossRef]
16. Soltani, T.; Lee, B.K. Enhanced formation of sulfate radicals by metal-doped BiFeO<sub>3</sub> under visible light for improving photo-Fenton catalytic degradation of 2-chlorophenol. *Chem. Eng. J.* **2017**, *313*, 1258–1268. [CrossRef]
17. Zhang, M.W.; Lin, K.Y.A.; Huang, C.F.; Tong, S. Enhanced degradation of toxic azo dye, amaranth, in water using Oxone catalyzed by MIL-101-NH<sub>2</sub> under visible light irradiation. *Sep. Purif. Tech.* **2019**, *227*, 115632. [CrossRef]
18. Karbasi, M.; Karimzadeh, F.; Raeissi, K.; Giannakis, S.; Pulgarin, C. Improving visible light photocatalytic inactivation of E. coli by inducing highly efficient radical pathways through peroxymonosulfate activation using 3-D, surface-enhanced, reduced graphene oxide (rGO) aerogels. *Chem. Eng. J.* **2020**, *396*, 125189. [CrossRef]
19. Bi, W.; Wu, Y.; Dong, W. The degradation of oxytetracycline with low concentration of persulfate sodium motivated by copper sulphate under simulated solar light. *Chem. Eng. J.* **2020**, *393*, 122782. [CrossRef]
20. Wang, A.; Chen, Z.; Zheng, Z.; Xu, H.; Yan, K. Remarkably enhanced sulfate radical-based photo-Fenton-like degradation of levofloxacin using the reduced mesoporous MnO@MnO<sub>x</sub> microspheres. *Chem. Eng. J.* **2020**, *379*, 122340. [CrossRef]
21. Feng, Q.; Zhou, J.; Luo, W.; Ding, L.; Cai, W. Photo-Fenton removal of tetracycline hydrochloride using LaFeO<sub>3</sub> as a persulfate activator under visible light. *Ecotoxicol. Environ. Saf.* **2020**, *198*, 110661. [CrossRef] [PubMed]



22. Chen, Q.; Ji, F.; Guo, Q.; Fan, J.; Xu, X. Combination of heterogeneous Fenton-like reaction and photocatalysis using Co-TiO<sub>2</sub> nanocatalyst for activation of KHSO<sub>5</sub> with visible light irradiation at ambient conditions. *J. Environ. Sci.* **2014**, *26*, 2440–2450. [CrossRef] [PubMed]
23. Zhu, B.; Cheng, H.; Ma, J.; Qin, Y.; Kong, Y.; Komarneni, S. Bi<sub>2</sub>MoO<sub>6</sub> microspheres for the degradation of orange II by heterogeneous activation of persulfate under visible light. *Mater. Lett.* **2020**, *261*, 127099. [CrossRef]
24. Li, M.; Tian, X.; Zou, X.; Han, X.; Du, C.; Shan, B. Promoting photoelectrochemical hydrogen evolution activity of CuBi<sub>2</sub>O<sub>4</sub> photocathode through ramping rate control. *Int. J. Hydrogen Energy* **2020**, *45*, 15121–15128. [CrossRef]
25. Ma, C.; Ma, D.K.; Yu, W.; Chen, W.; Huang, S. Ag and N-doped graphene quantum dots co-modified CuBi<sub>2</sub>O<sub>4</sub> submicron rod photocathodes with enhanced photoelectrochemical activity. *Appl. Surf. Sci.* **2019**, *481*, 661–668. [CrossRef]
26. Chen, X.; Dai, Y.; Guo, J. Hydrothermal synthesis of well-distributed spherical CuBi<sub>2</sub>O<sub>4</sub> with enhanced photocatalytic activity under visible light irradiation. *Mater. Lett.* **2015**, *161*, 251–254. [CrossRef]
27. Sabri, M.; Habibi-Yangjeh, A.; Ghosh, S. Novel ZnO/CuBi<sub>2</sub>O<sub>4</sub> heterostructures for persulfate-assisted photocatalytic degradation of dye contaminants under visible light. *J. Photoch. Photobiol. A* **2020**, *391*, 112397. [CrossRef]
28. Zhang, H.; Nengzi, L.; Li, X.; Wang, Z.; Cheng, X. Construction of CuBi<sub>2</sub>O<sub>4</sub>/MnO<sub>2</sub> composite as Z-scheme photoactivator of peroxymonosulfate for degradation of antibiotics. *Chem. Eng. J.* **2020**, *386*, 124011. [CrossRef]
29. Oh, W.D.; Dong, Z.; Lim, T.T. Hierarchically-structured Co-CuBi<sub>2</sub>O<sub>4</sub> and Cu-CuBi<sub>2</sub>O<sub>4</sub> for sulfanilamide removal via peroxymonosulfate activation. *Catal. Today* **2017**, *280*, 2–7. [CrossRef]
30. Gao, H.; Wang, F.; Wang, S.; Wang, X.; Yi, Z.; Yang, H. Photocatalytic activity tuning in a novel Ag<sub>2</sub>S/CQDs/CuBi<sub>2</sub>O<sub>4</sub> composite: Synthesis and photocatalytic mechanism. *Mater. Res. Bull.* **2019**, *115*, 140–149. [CrossRef]
31. Shi, W.; Li, M.; Huang, X.; Ren, H.; Guo, F.; Tang, Y.; Lu, C. Construction of CuBi<sub>2</sub>O<sub>4</sub>/Bi<sub>2</sub>MoO<sub>6</sub> p-n heterojunction with nanosheets-on-microrods structure for improved photocatalytic activity towards broad-spectrum antibiotics degradation. *Chem. Eng. J.* **2020**, *394*, 125009. [CrossRef]
32. Chen, X.; Yu, C.; Zhu, R.; Li, N.; Chen, M.; Lin, Q.; Xu, S.; Chen, X.; Wang, H. Photocatalytic performance and mechanism of Z-Scheme CuBi<sub>2</sub>O<sub>4</sub>/Ag<sub>3</sub>PO<sub>4</sub> in the degradation of diclofenac sodium under visible light irradiation: Effects of pH, H<sub>2</sub>O<sub>2</sub>, and S<sub>2</sub>O<sub>8</sub><sup>2-</sup>. *Sci. Total Environ.* **2020**, *711*, 134643. [CrossRef]
33. Wang, L.; Huang, T.; Yang, G.; Lu, C.; Dong, F.; Li, Y.; Guan, W. The precursor-guided hydrothermal synthesis of CuBi<sub>2</sub>O<sub>4</sub>/WO<sub>3</sub> heterostructure with enhanced photoactivity under simulated solar light irradiation and mechanism insight. *J. Hazard. Mater.* **2020**, *381*, 120956. [CrossRef]
34. Fu, F.; Shen, H.; Sun, X.; Xue, W.; Shoneye, A.; Ma, J.; Luo, L.; Wang, D.; Wang, J.; Tang, J. Synergistic effect of surface oxygen vacancies and interfacial charge transfer on Fe(III)/Bi<sub>2</sub>MoO<sub>6</sub> for efficient photocatalysis. *Appl. Catal. B* **2019**, *247*, 150–162. [CrossRef]
35. Lyu, J.; Hu, Z.; Li, Z.; Ge, M. Removal of tetracycline by BiOBr microspheres with oxygen vacancies: Combination of adsorption and photocatalysis. *J. Phys. Chem. Solids* **2019**, *129*, 61–70. [CrossRef]
36. Li, D.; Haneda, H.; Labhsetwar, N.K.; Hishita, S.; Ohashi, N. Visible-light-driven photocatalysis on fluorine-doped TiO<sub>2</sub> powders by the creation of surface oxygen vacancies. *Chem. Phys. Lett.* **2005**, *401*, 579–584. [CrossRef]
37. Xie, Y.; Zhang, Y.; Yang, G.; Liu, C.; Wang, J. Hydrothermal synthesis of CuBi<sub>2</sub>O<sub>4</sub> nanosheets and their photocatalytic behavior under visible light irradiation. *Mater. Lett.* **2013**, *107*, 291–294. [CrossRef]
38. Shan, W.; Hu, Y.; Bai, Z.; Zheng, M.; Wei, C. In situ preparation of g-C<sub>3</sub>N<sub>4</sub>/bismuth-based oxide nanocomposites with enhanced photocatalytic activity. *Appl. Catal. B* **2016**, *188*, 1–12. [CrossRef]
39. Hossain, M.K.; Samu, G.F.; Gandha, K.; Santhanagopalan, S.; Liu, J.P.; Janaky, C.; Rajeshwar, K. Solution combustion synthesis, characterization, and photocatalytic activity of CuBi<sub>2</sub>O<sub>4</sub> and its nanocomposites with CuO and α-Bi<sub>2</sub>O<sub>3</sub>. *J. Phys. Chem. C* **2017**, *121*, 8252–8261. [CrossRef]
40. Brezesinski, K.; Ostermann, R.; Hartmann, P.; Perlich, J.; Brezesinski, T. Exceptional Photocatalytic Activity of Ordered Mesoporous β-Bi<sub>2</sub>O<sub>3</sub> Thin Films and Electrospun Nanofiber Mats. *Chem. Mater.* **2010**, *22*, 3079–3085. [CrossRef]

41. Zhang, L.; Lyu, L.; Nie, Y.; Hu, C. Cu-doped Bi<sub>2</sub>O<sub>3</sub>/Bi<sup>0</sup> composite as an efficient Fenton-like catalyst for degradation of 2-chlorophenol. *Sep. Purif. Tech.* **2016**, *157*, 203–208. [CrossRef]
42. Zhang, Y.; Liu, C.; Xu, B.; Qi, F.; Chu, W. Degradation of benzotriazole by a novel Fenton-like reaction with mesoporous Cu/MnO<sub>2</sub>: Combination of adsorption and catalysis oxidation. *Appl. Catal. B* **2016**, *199*, 447–457. [CrossRef]
43. Zhang, X.; Wang, X.; Chai, J.; Xue, S.; Wang, R.; Jiang, L.; Wang, J.; Zhang, Z.; Dionysiou, D.D. Construction of novel symmetric double Z-scheme BiFeO<sub>3</sub>/CuBi<sub>2</sub>O<sub>4</sub>/BaTiO<sub>3</sub> photocatalyst with enhanced solar-light-driven photocatalytic performance for degradation of norfloxacin. *Appl. Catal. B* **2020**, *272*, 119017. [CrossRef]
44. Sun, Q.; Wu, S.; Li, K.; Han, B.; Chen, Y.; Pang, B.; Yu, L.; Dong, L. The favourable synergistic operation of photocatalysis and catalytic oxygen reduction reaction by a novel heterogeneous CoFe<sub>2</sub>O<sub>4</sub>-TiO<sub>2</sub> nanocomposite. *Appl. Surf. Sci.* **2020**, *516*, 146142. [CrossRef]
45. Hu, J.; Li, J.; Cui, J.; An, W.; Liu, L.; Liang, Y.; Cui, W. Surface oxygen vacancies enriched FeOOH/Bi<sub>2</sub>MoO<sub>6</sub> photocatalysis-fenton synergy degradation of organic pollutants. *J. Hazard. Mater.* **2020**, *384*, 121399. [CrossRef] [PubMed]
46. Chen, X.; Zhou, J.; Zhang, T.; Ding, L. Enhanced degradation of tetracycline hydrochloride using photocatalysis and sulfate radical-based oxidation processes by Co/BiVO<sub>4</sub> composites. *J. Water Process. Eng.* **2019**, *32*, 100918. [CrossRef]
47. Huang, J.; Zhang, H. Mn-based catalysts for sulfate radical-based advanced oxidation processes: A review. *Environ. Int.* **2019**, *133*, 105141. [CrossRef]
48. Chen, Z.; Bi, S.; Zhao, G.; Chen, Y.; Hu, Y. Enhanced degradation of triclosan by cobalt manganese spinel-type oxide activated peroxymonosulfate oxidation process via sulfate radicals and singlet oxygen: Mechanisms and intermediates identification. *Sci. Total Environ.* **2020**, *711*, 134715. [CrossRef]
49. Hao, S.M.; Yu, M.Y.; Zhang, Y.J.; Abdelkrim, Y.; Qu, J. Hierarchical mesoporous cobalt silicate architectures as high-performance sulfate-radical-based advanced oxidization catalysts. *J. Colloid. Interf. Sci.* **2019**, *545*, 128–137. [CrossRef]
50. Baran, N.Y.; Baran, T.; Menteş, A. Design of highly robust halloysite nanoclay supported palladium complex as a highly active heterogeneous catalyst for construction of biaryls. *Appl. Clay Sci.* **2019**, *18115*, 105225. [CrossRef]
51. Hu, L.; Wang, P.; Shen, T.; Wang, Q.; Zhang, G. The application of microwaves in sulfate radical-based advanced oxidation processes for environmental remediation: A review. *Sci. Total. Environ.* **2020**, *722*, 137831. [CrossRef] [PubMed]
52. You, J.; Sun, W.; Su, S.; Ao, Z.; Liu, C.; Yao, G.; Lai, B. Degradation of bisphenol A by peroxymonosulfate activated with oxygen vacancy modified nano-NiO-ZnO composite oxides: A typical surface-bound radical system. *Chem. Eng. J.* **2020**, *400*, 125915. [CrossRef]
53. Huang, Z.; Wu, P.; Liu, J.; Yang, S.; Chen, M.; Li, Y.; Niu, W.; Ye, Q. Defect-rich carbon based bimetallic oxides with abundant oxygen vacancies as highly active catalysts for enhanced 4-aminobenzoic acid ethyl ester (ABEE) degradation toward peroxymonosulfate activation. *Chem. Eng. J.* **2020**, *395*, 124936. [CrossRef]



© 2020 by the authors. Licensee MDPI, Basel, Switzerland. This article is an open access article distributed under the terms and conditions of the Creative Commons Attribution (CC BY) license (<http://creativecommons.org/licenses/by/4.0/>).

## Article

# Ti<sub>2</sub>O<sub>3</sub>/TiO<sub>2</sub>-Assisted Solar Photocatalytic Degradation of 4-tert-Butylphenol in Water

Saule Mergenbayeva <sup>1</sup>, Timur Sh. Atabaev <sup>2</sup> and Stavros G. Pouloupoulos <sup>1,\*</sup>

<sup>1</sup> Department of Chemical and Materials Engineering, School of Engineering and Digital Sciences, Nazarbayev University, 53 Kabanbay Batyr Ave., Nur-Sultan 010000, Kazakhstan; saule.mergenbayeva@nu.edu.kz

<sup>2</sup> Department of Chemistry, School of Sciences and Humanities, Nazarbayev University, Nur-Sultan 010000, Kazakhstan; timur.atabaev@nu.edu.kz

\* Correspondence: stavros.pouloupoulos@nu.edu.kz; Tel.: +7-7172-694608

**Abstract:** Colored Ti<sub>2</sub>O<sub>3</sub> and Ti<sub>2</sub>O<sub>3</sub>/TiO<sub>2</sub> (mTiO) catalysts were prepared by the thermal treatment method. The effects of treatment temperature on the structure, surface area, morphology and optical properties of the as-prepared samples were investigated by XRD, BET, SEM, TEM, Raman and UV–VIS spectroscopies. Phase transformation from Ti<sub>2</sub>O<sub>3</sub> to TiO<sub>2</sub> rutile and TiO<sub>2</sub> anatase to TiO<sub>2</sub> rutile increased with increasing treatment temperatures. The photocatalytic activities of thermally treated Ti<sub>2</sub>O<sub>3</sub> and mTiO were evaluated in the photodegradation of 4-tert-butylphenol (4-t-BP) under solar light irradiation. mTiO heated at 650 °C exhibited the highest photocatalytic activity for the degradation and mineralization of 4-t-BP, being approximately 89.8% and 52.4%, respectively, after 150 min of irradiation. The effects of various water constituents, including anions (CO<sub>3</sub><sup>2−</sup>, NO<sub>3</sub>, Cl and HCO<sub>3</sub><sup>−</sup>) and humic acid (HA), on the photocatalytic activity of mTiO-650 were evaluated. The results showed that the presence of carbonate and nitrate ions inhibited 4-t-BP photodegradation, while chloride and bicarbonate ions enhanced the photodegradation of 4-t-BP. As for HA, its effect on the degradation of 4-t-BP was dependent on the concentration. A low concentration of HA (1 mg/L) promoted the degradation of 4-t-BP from 89.8% to 92.4% by mTiO-650, but higher concentrations of HA (5 mg/L and 10 mg/L) had a negative effect.

**Keywords:** 4-tert-butylphenol; solar photocatalysis; Ti<sub>2</sub>O<sub>3</sub>/TiO<sub>2</sub>; degradation; mineralization

**Citation:** Mergenbayeva, S.; Sh. Atabaev, T.; Pouloupoulos, S.G. Ti<sub>2</sub>O<sub>3</sub>/TiO<sub>2</sub>-Assisted Solar Photocatalytic Degradation of 4-tert-Butylphenol in Water. *Catalysts* **2021**, *11*, 1379. <https://doi.org/10.3390/catal11111379>

Academic Editors: Gassan Hodaifa and Rafael Borja

Received: 30 September 2021  
Accepted: 11 November 2021  
Published: 16 November 2021

**Publisher's Note:** MDPI stays neutral with regard to jurisdictional claims in published maps and institutional affiliations.



**Copyright:** © 2021 by the authors. Licensee MDPI, Basel, Switzerland. This article is an open access article distributed under the terms and conditions of the Creative Commons Attribution (CC BY) license (<https://creativecommons.org/licenses/by/4.0/>).

## 1. Introduction

Water pollution by a broad category of organic pollutants is a rising issue of worldwide concern [1]. During the last decade, the consumption of personal care products (PPCPs), pharmaceuticals and endocrine-disrupting compounds (EDCs) has increased owing to economic development and population growth [2–5]. Their widespread use has increased their appearance in the aqueous environment, including rivers, lakes and reservoirs, at concentrations starting from several nanograms (ng/L) to several micrograms (μg/L) per liter [6–12]. They can even escape wastewater treatment plants (WWTPs) and drinking water treatment plants (DWTPs), ultimately reaching drinking water sources. These contaminants are termed emerging pollutants (EPs) and can cause severe adverse effects on human health and the aquatic environment [13].

In particular, 4-t-BP is an industrial chemical used as a raw material for the production of synthetic phenol and polycarbonate resins [14,15]. As a representative of EDCs, 4-t-BP has a high estrogenic effect and acute/chronic environmental toxicity [16,17]. Considering its adverse effects on human health and aquatic systems, 4-t-BP, as a highly persistent pollutant, needs to be controlled efficiently.

To date, various methods have been investigated to remove 4-t-BP from water, mainly including advanced oxidation processes (AOPs) and biological processes [16,18–20]. Among them, AOPs have attracted great attention for the removal such contaminants by converting

them into carbon dioxide and water [21,22]. The high efficiency of the process has mostly been associated with the production of hydroxyl radicals (standard potential, 2.8 V) used as oxidants. AOPs may vary in terms of work conditions, used materials and different paths of hydroxyl radical ( $\text{OH}^\cdot$ ) production [23,24]. Heterogeneous photocatalysis may be considered an economically feasible solution to remove 4-t-BP from water due to the competitive cost of the process and the ambient conditions of temperature and pressure [25–27]. Moreover, it is considered an environmentally friendly oxidation process since it allows not only the degradation of the pollutant from the contaminated system but also its total elimination, without generating any undesired by-products, which could be even more toxic compounds than the parent one [28,29].

Although various photoactive materials have been investigated,  $\text{TiO}_2$ -based photocatalysts remain the most studied ones due to their high photocatalytic oxidation activity, chemical stability and availability [30–32]. The P25 form of  $\text{TiO}_2$  is one of the most effective photocatalytic materials, which can be attributed to the combination of anatase and rutile phases [33–35]. However, the high energy band gap of approximately 3.0–3.2 eV limits the application of  $\text{TiO}_2$  under solar light. In this context, numerous strategies have been devoted to extending the absorption wavelength to the visible area for the efficient utilization of sunlight. For example, the introduction of  $\text{Ti}^{3+}$  into  $\text{TiO}_2$  demonstrated the capacity to extend the light response of  $\text{TiO}_2$ . It has been reported that the formation of  $\text{Ti}^{3+}$  species is accompanied by the generation of oxygen vacancies ( $\text{O}_\text{v}$ ), which can favor the separation of electron–hole pairs and thus improve the visible light activity of  $\text{TiO}_2$  [36–38]. Moreover,  $\text{Ti}^{3+}$  and oxygen vacancies can form localized states below the conduction band (CB), which reduces the band gap of  $\text{TiO}_2$  (Figure 1), so that it can distinctly expand the absorption to the visible region [39–43]. The reported methods to prepare structurally defective  $\text{TiO}_2$  with  $\text{Ti}^{3+}$  include the partial oxidation of low-valence Ti species (Ti, Ti (II) and Ti (III)),  $\text{H}_2$  thermal treatment and the reduction of  $\text{Ti}^{4+}$  to  $\text{Ti}^{3+}$  by a chemical reducing agent ( $\text{NaBH}_4$ ), metals (Al, Mg, Li, Zn), etc. [44–49]. Although there are numerous preparation methods available, most of them require high consumption of chemicals, as well as multiple steps using specialized equipment. Therefore, it is of significant importance to develop a facile and feasible method to prepare defective  $\text{TiO}_2$  with  $\text{Ti}^{3+}$ .

### Potential (v) / vs NHE

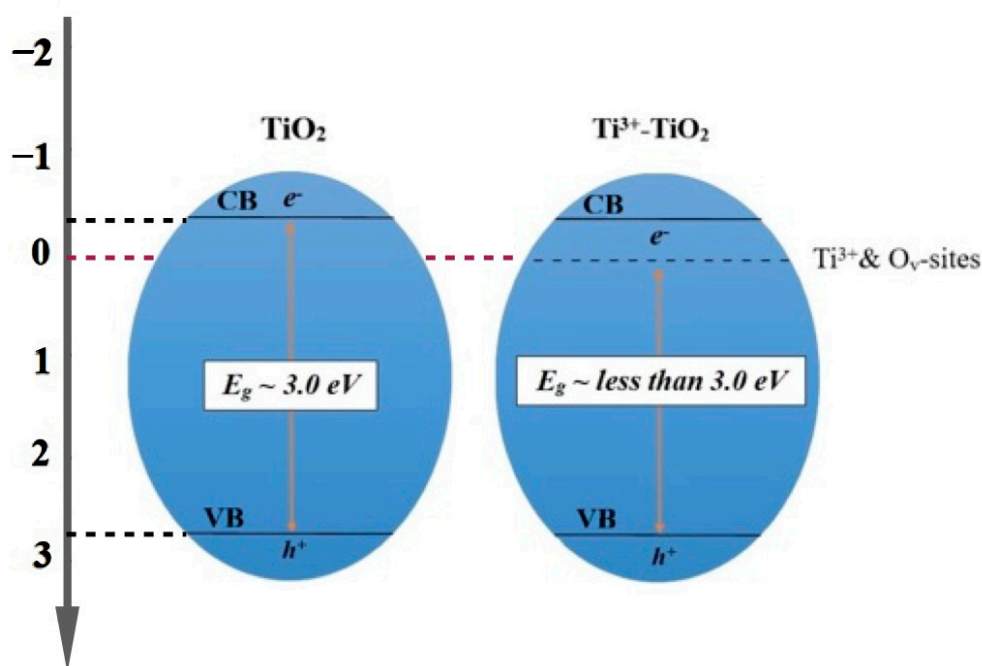


Figure 1. Schematic showing energy levels of  $\text{TiO}_2$  in the presence of  $\text{Ti}^{3+}$  ions.

In the present work,  $\text{Ti}_2\text{O}_3$  alone or in combination with  $\text{TiO}_2$  (P25) was thermally treated through a simple one-step method, and their photocatalytic performance towards 4-t-BP degradation under simulated solar light was tested. The as-prepared samples were characterized by means of SEM, TEM, BET, XRD, Raman and UV–VIS spectroscopies to study their morphology, textural properties, crystal structure and optical properties. The effects of the presence of humic acid (HA) and inorganic ions ( $\text{CO}_3^{2-}$ ,  $\text{NO}_3^-$ ,  $\text{Cl}^-$  and  $\text{HCO}_3^-$ ) on 4-t-BP degradation were also investigated.

## 2. Results and Discussion

### 2.1. Characterization of Photocatalysts

XRD measurements were conducted to identify the phase structures of the thermally treated  $\text{Ti}_2\text{O}_3$  and  $\text{Ti}_2\text{O}_3/\text{TiO}_2$  (hereinafter denoted as mTiO) catalysts (Figures 2 and 3). The diffraction peaks at  $2\theta = 23.823^\circ$  (012),  $33.040^\circ$  (104),  $34.836^\circ$  (110),  $40.219^\circ$  (113),  $48.786^\circ$  (024),  $53.692^\circ$  (116),  $61.42^\circ$  (214) and  $62.64^\circ$  (300) were attributed to  $\text{Ti}_2\text{O}_3$  (JCPDS No. 00-043-1033). With the increase in treatment temperature, the intensity of all characteristic peaks corresponding to  $\text{Ti}_2\text{O}_3$  became weaker in both  $\text{Ti}_2\text{O}_3$  and mTiO samples. As the temperature further increased to  $750^\circ\text{C}$ , no typical peaks of  $\text{Ti}_2\text{O}_3$  were observed, indicating the complete transformation of  $\text{Ti}_2\text{O}_3$  to rutile  $\text{TiO}_2$  (JCPDS No. 00-021-1276) [50,51].

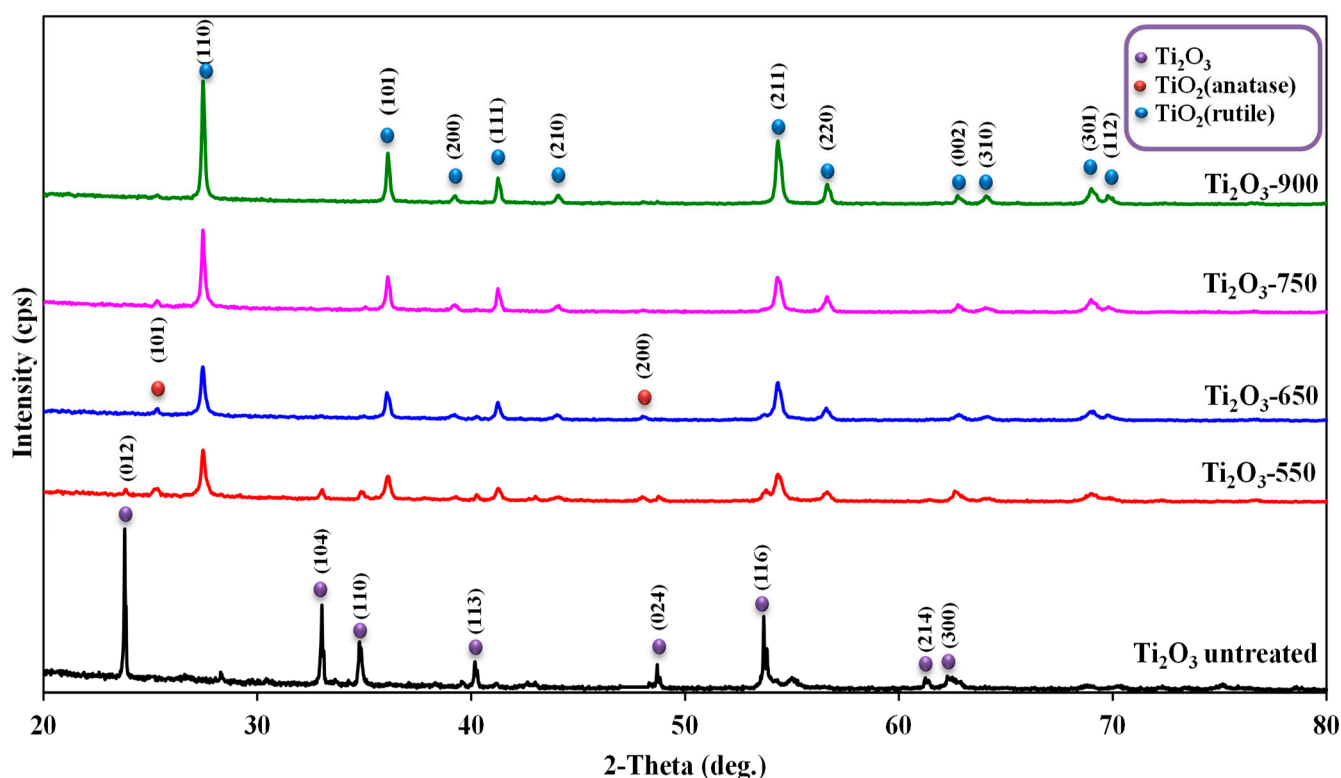


Figure 2. XRD patterns of treated  $\text{Ti}_2\text{O}_3$  catalysts.

In the  $\text{Ti}_2\text{O}_3$ -550 sample (Figure 2), apart from the diffraction peaks of  $\text{TiO}_2$  rutile, peaks attributed to the anatase phase of  $\text{TiO}_2$  (JCPDS No. 00-021-12-72) also appeared at  $2\theta = 25.3^\circ$  (101) and  $48.028^\circ$  (200). These findings reveal that the transformation of  $\text{Ti}_2\text{O}_3$  into  $\text{TiO}_2$  anatase also took place. The results are in good agreement with previously reported ones [52]. These peaks almost completely disappeared at  $900^\circ\text{C}$ , suggesting the transformation of  $\text{TiO}_2$  anatase into  $\text{TiO}_2$  rutile.

The composition of the catalysts was further investigated by Raman spectroscopy (Figures 4 and 5). The Raman peak at around  $143\text{ cm}^{-1}$  justified the existence of the  $\text{TiO}_2$  anatase phase in both types of catalysts. For treated  $\text{Ti}_2\text{O}_3$  (Figure 4), this peak became more intense with the increase in treatment temperature to  $750^\circ\text{C}$ , confirming the successful

transformation of  $\text{Ti}_2\text{O}_3$  into  $\text{TiO}_2$  anatase. In addition, low-intensity peaks corresponding to the  $\text{TiO}_2$  anatase phase were observed at  $196.85\text{ cm}^{-1}$ ,  $399.57\text{ cm}^{-1}$  and  $514.54\text{ cm}^{-1}$  in the spectra of  $\text{Ti}_2\text{O}_3$ -650 and  $\text{Ti}_2\text{O}_3$ -750, while a further increase in temperature to  $900\text{ }^\circ\text{C}$  led to an increase in the  $\text{TiO}_2$  rutile phase. However, no peaks were observed corresponding to  $\text{Ti}_2\text{O}_3$ , which could be attributed to the low intensities of the Raman bands of the  $\text{Ti}_2\text{O}_3$  structure.

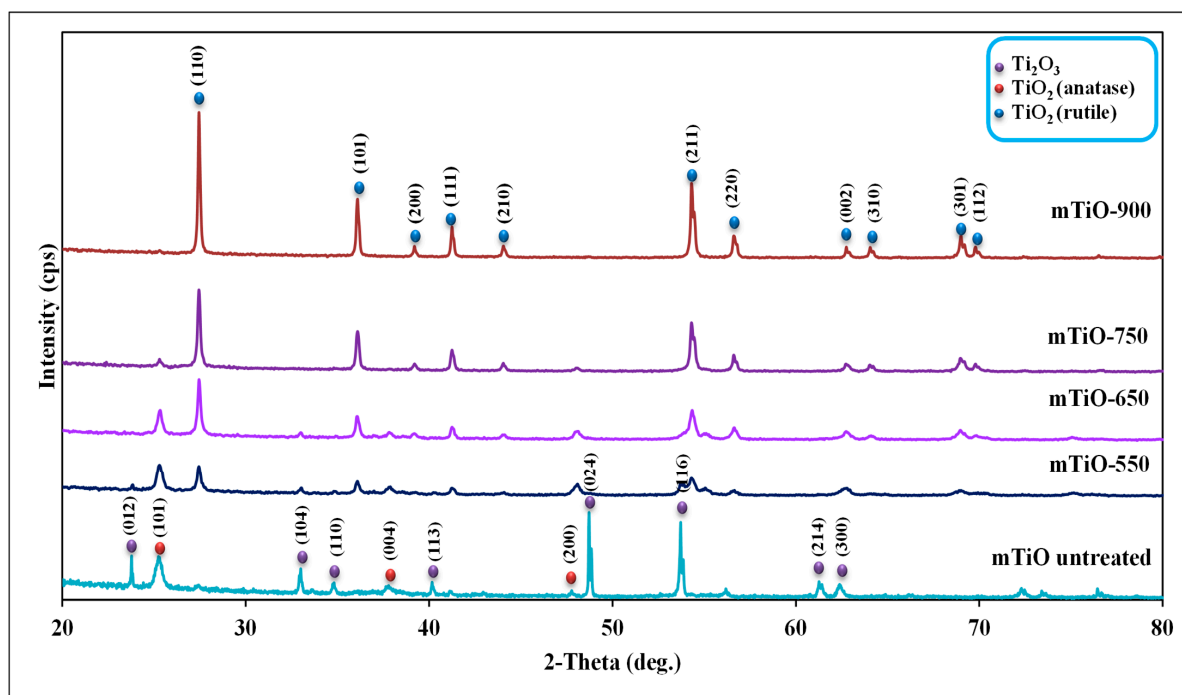


Figure 3. XRD patterns of treated mTiO catalysts.

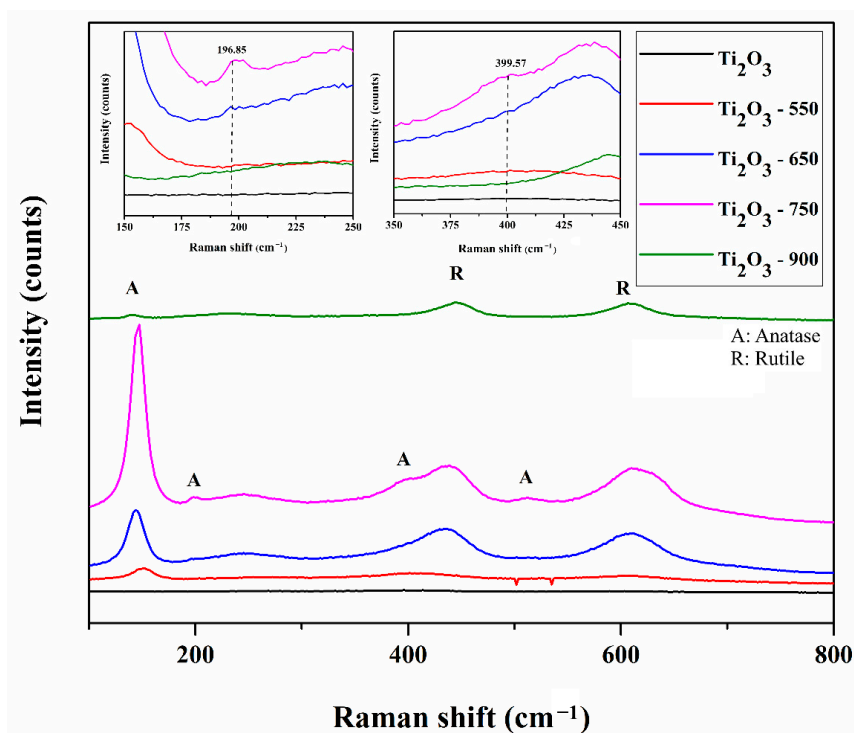
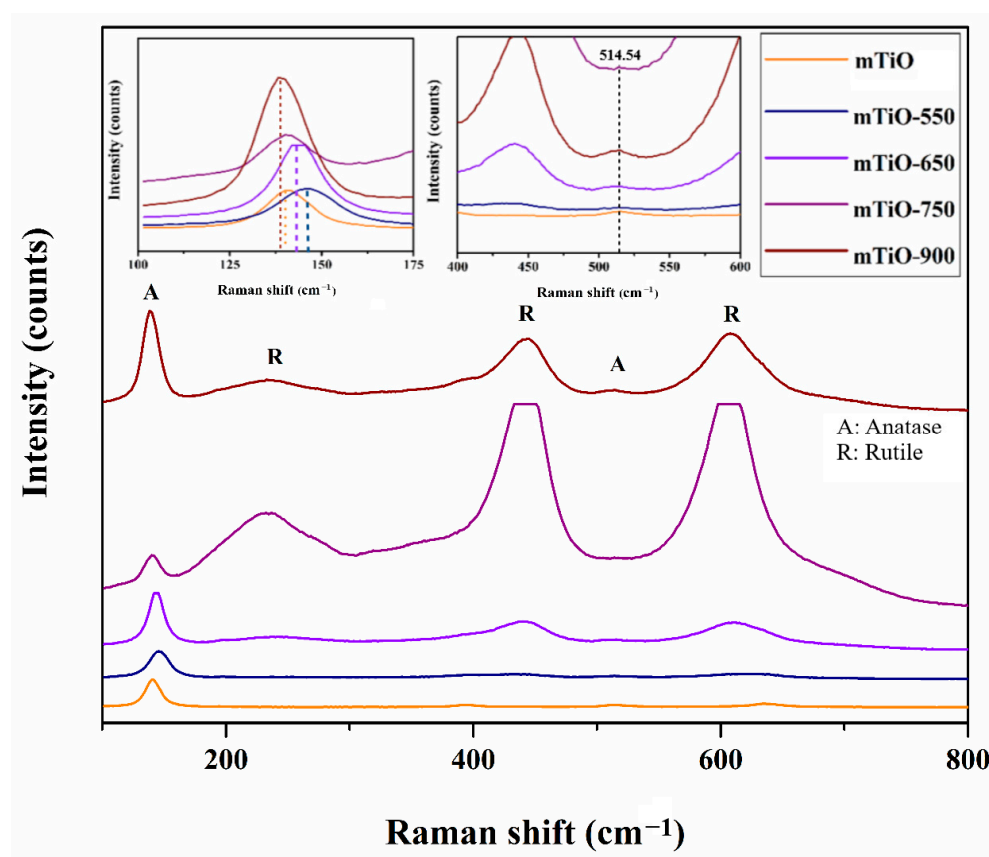


Figure 4. Raman spectra of treated  $\text{Ti}_2\text{O}_3$  catalysts.





**Figure 5.** Raman spectra of treated mTiO catalysts.

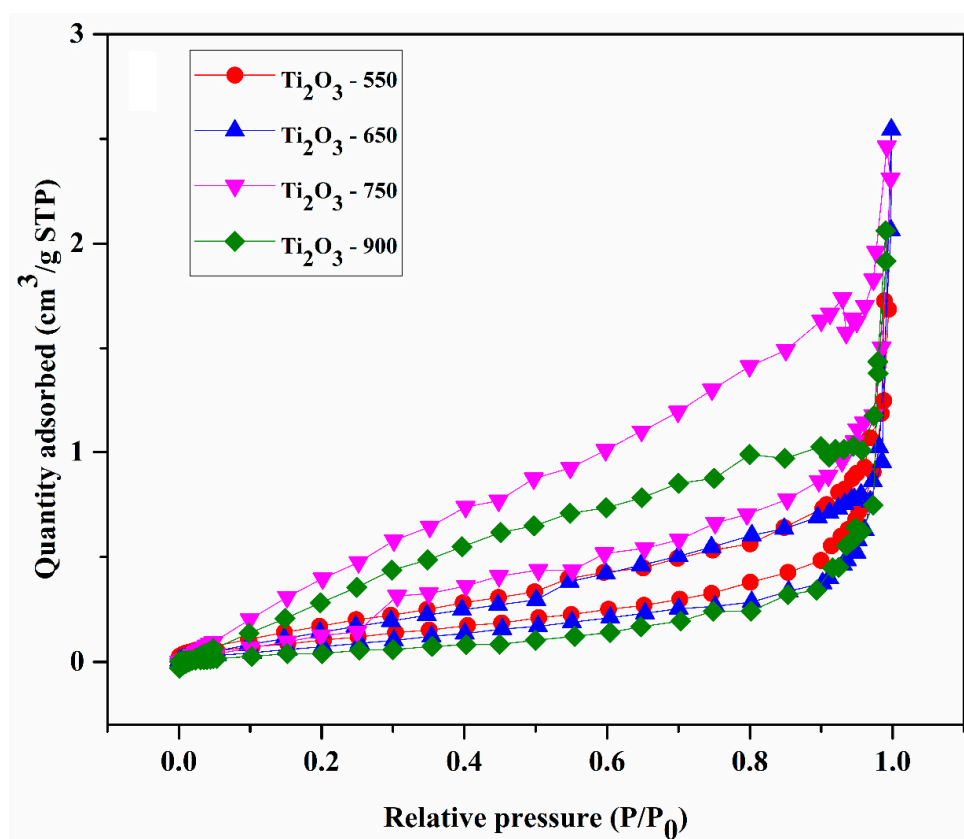
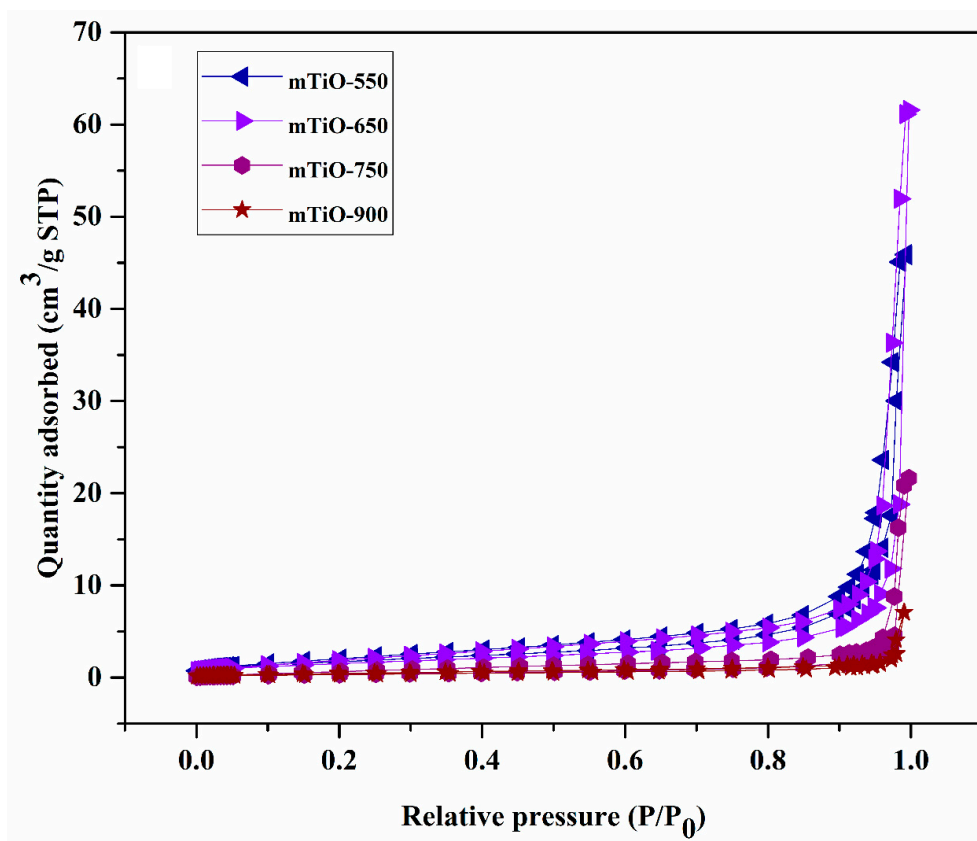
Compared to untreated mTiO, mTiO-900 exhibited a negative shift at  $143\text{ cm}^{-1}$  (Figure 5), indicating the association of  $\text{Ti}_2\text{O}_3$  with  $\text{TiO}_2$ , while, for mTiO-550 and mTiO-650, a positive shift in this peak could possibly be attributed to the introduction of  $\text{Ti}^{3+}$  and oxygen vacancies into the  $\text{TiO}_2$  lattice as a result of the thermal treatment [53]. In the photocatalytic process, the presence of such structural defects in  $\text{TiO}_2$  can inhibit the recombination of charge carriers and thus improve the photocatalytic activity.

The results from Raman spectroscopy are in general agreement with the ones obtained from XRD analysis, with the exception of the  $\text{TiO}_2$  anatase phase, which was detected only with the first technique for the catalysts treated at  $900\text{ }^\circ\text{C}$ .

The textural properties of all catalysts were evaluated by BET  $\text{N}_2$  adsorption/desorption measurements. As presented in Figures 6 and 7, all the catalysts revealed a typical type-III isotherm according to the classification of the international union of pure and applied chemistry (IUPAC). Interestingly,  $\text{Ti}_2\text{O}_3$  and mTiO catalysts heated at  $650\text{ }^\circ\text{C}$  exhibited the highest  $\text{N}_2$  adsorption capacity and pore volume ( $V_p$ ). In general, larger values of  $V_p$  can be beneficial for the photocatalytic reaction through providing ionic diffusion and charge transfer on the surface of the photocatalyst [54].

Some other characteristics obtained from the BET analysis are displayed in Table 1, which shows that the treatment temperature had a significant effect on the microstructure of thermally treated  $\text{Ti}_2\text{O}_3$  and mTiO, particularly on the BET surface area ( $S_{\text{BET}}$ ) and pore volume ( $V_p$ ). It could be noticed that the  $S_{\text{BET}}$  of treated  $\text{Ti}_2\text{O}_3$  was relatively low compared to that of mTiO. The  $S_{\text{BET}}$  of treated  $\text{Ti}_2\text{O}_3$  catalysts increased gradually as the treatment temperature increased from  $550\text{ }^\circ\text{C}$  to  $750\text{ }^\circ\text{C}$ , which could be likely associated with the formation of a better crystalline framework. However, a further increase in the treatment temperature to  $900\text{ }^\circ\text{C}$  caused a drastic decrease in  $S_{\text{BET}}$  due to the phase transformation of  $\text{TiO}_2$  anatase to  $\text{TiO}_2$  rutile [55].



Figure 6.  $N_2$  adsorption/desorption of treated  $Ti_2O_3$  catalysts.Figure 7.  $N_2$  adsorption/desorption of treated  $mTiO$  catalysts.

**Table 1.** BET surface area and pore volume of as-prepared catalysts.

Photocatalyst	$S_{\text{BET}}$ ( $\text{m}^2/\text{g}$ )	$V_p$ ( $\text{cm}^3/\text{g}$ )
Ti <sub>2</sub> O <sub>3</sub> -550	1.629	0.009
Ti <sub>2</sub> O <sub>3</sub> -650	1.985	0.017
Ti <sub>2</sub> O <sub>3</sub> -750	2.733	0.014
Ti <sub>2</sub> O <sub>3</sub> -900	0.974	0.012
mTiO-550	23.012	0.255
mTiO-650	20.894	0.347
mTiO-750	5.593	0.134
mTiO-900	3.443	0.029

The increase in treatment temperature continuously decreased the  $S_{\text{BET}}$  of treated mTiO. The lowering of  $S_{\text{BET}}$  can be attributed to the increase in particle size as a result of aggregation [56].

The morphology of the prepared catalysts was examined by SEM and TEM. As can be seen from Figure 8, untreated Ti<sub>2</sub>O<sub>3</sub> particles exhibited an irregular shape with a smooth continuous morphology. In contrast, heating under different temperatures resulted in the formation of a much rougher surface of Ti<sub>2</sub>O<sub>3</sub>, which could be associated with the phase transformation from Ti<sub>2</sub>O<sub>3</sub> to TiO<sub>2</sub> rutile. Such an increase in surface roughness can increase the surface area of the catalyst and further influence the catalytic activity of the material. These results are consistent with the findings obtained from BET analysis, where the heating of Ti<sub>2</sub>O<sub>3</sub> up to 750 °C was accompanied by an increase in  $S_{\text{BET}}$ .

SEM images of treated mTiO catalysts clearly revealed that thermal treatment caused a particle size growth in TiO<sub>2</sub>, well-distributed on the surface of Ti<sub>2</sub>O<sub>3</sub> (Figure 9). The increase in the size of TiO<sub>2</sub> particles may have resulted in the decrease in  $S_{\text{BET}}$ .

A UV–VIS absorption study was carried out to assess the light-harvesting ability of the prepared samples (Figures 10 and 11). It can be seen that the temperature variation influenced the light absorption properties of all prepared catalysts. The rise in treatment temperature for Ti<sub>2</sub>O<sub>3</sub> catalysts from 550 °C to 650 °C extended the light absorption to the visible region (400–550 nm), while a further increase in the treatment temperature to 900 °C lowered the visible light absorption capacity (Figure 10).

In contrast, all prepared mTiO catalysts demonstrated a good light absorption ability within the wavelength range of 300–400 nm, although to different extents (Figure 11). Specifically, catalysts heated at lower temperatures demonstrated stronger absorption, which is in accordance with the expectations based on the color change of the catalysts. At the same time, mTiO-550 and mTiO-650 were found to be absorbing in the 400–550 nm region. This phenomenon may be attributed to the transformation of Ti<sub>2</sub>O<sub>3</sub> to TiO<sub>2</sub> rutile, containing Ti<sup>3+</sup> (oxygen vacancies) sites [50,56]. It is noteworthy that the light absorption of mTiO-650 in the visible region was substantially enhanced compared with mTiO-550, as a result of the higher concentration of oxygen vacancies in the lattice of TiO<sub>2</sub>. Such an enhancement in the light absorption is favorable for improving the photoactivity of the material. On the other hand, the intensities at wavelengths higher than approximately 550 nm gradually weakened for mTiO-550 and mTiO-650.

Moreover, the band gap values of the prepared catalysts were estimated using the Kubelka–Munk equation and the corresponding Tauc plots. As illustrated in Figure 12, the calculated direct band gap energies were found to be 1.76, 1.75, 1.79 and 2.69 eV for Ti<sub>2</sub>O<sub>3</sub>-550, Ti<sub>2</sub>O<sub>3</sub>-650, Ti<sub>2</sub>O<sub>3</sub>-750 and Ti<sub>2</sub>O<sub>3</sub>-900, respectively. Similar variations in band gap energies were obtained for mTiO catalysts, where mTiO-650 had a lower band gap of 2.01 eV compared to mTiO-550, mTiO-750 and mTiO-900 (Figure 13). These results reveal the possible application of the prepared catalysts in solar-light-driven photocatalytic reactions.

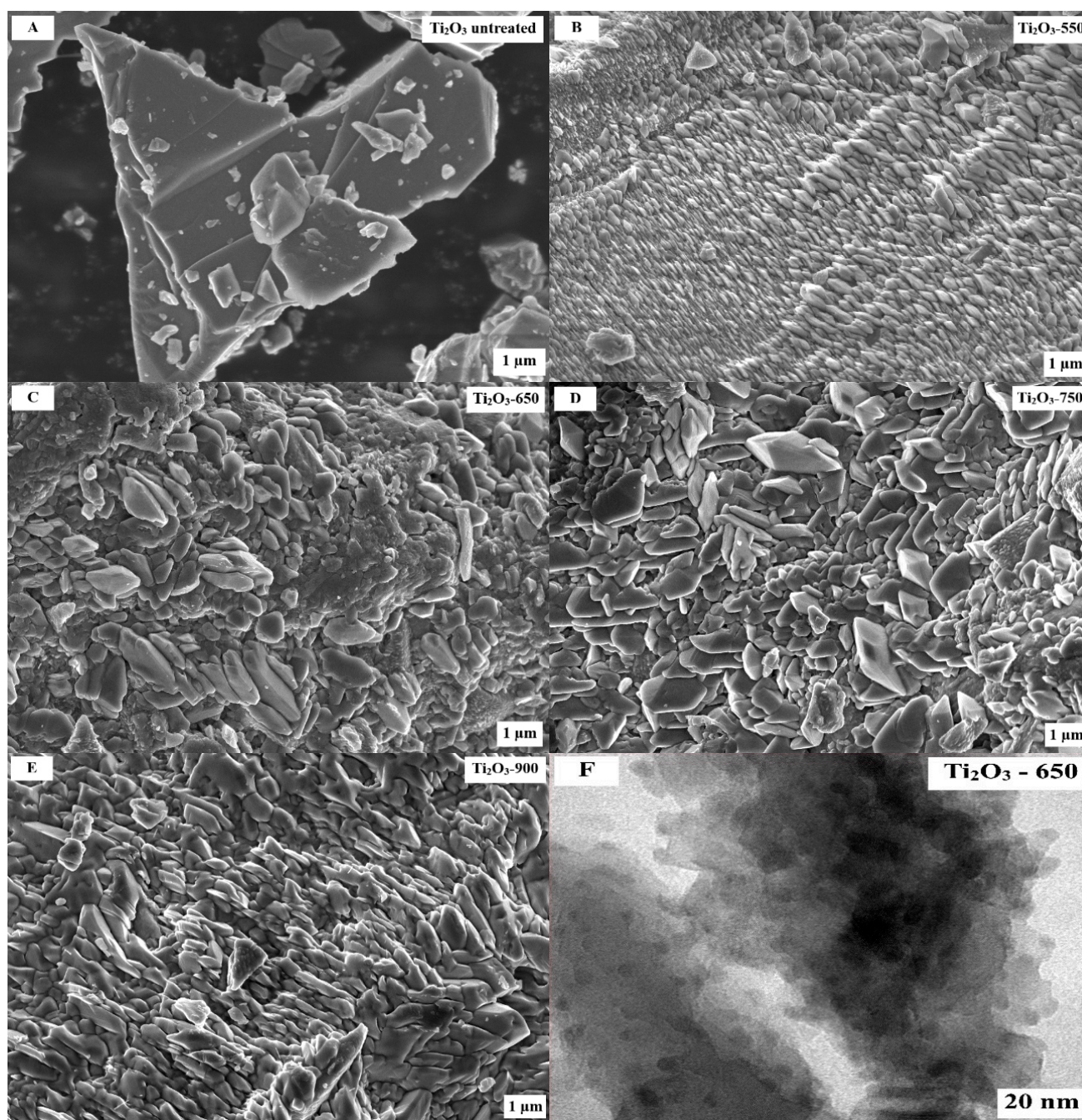


**Figure 8.** SEM images of  $\text{Ti}_2\text{O}_3$  untreated (A),  $\text{Ti}_2\text{O}_3$ -550 (B),  $\text{Ti}_2\text{O}_3$ -650 (C),  $\text{Ti}_2\text{O}_3$ -750 (D),  $\text{Ti}_2\text{O}_3$ -900 (E) and TEM image of  $\text{Ti}_2\text{O}_3$ -650 (F).



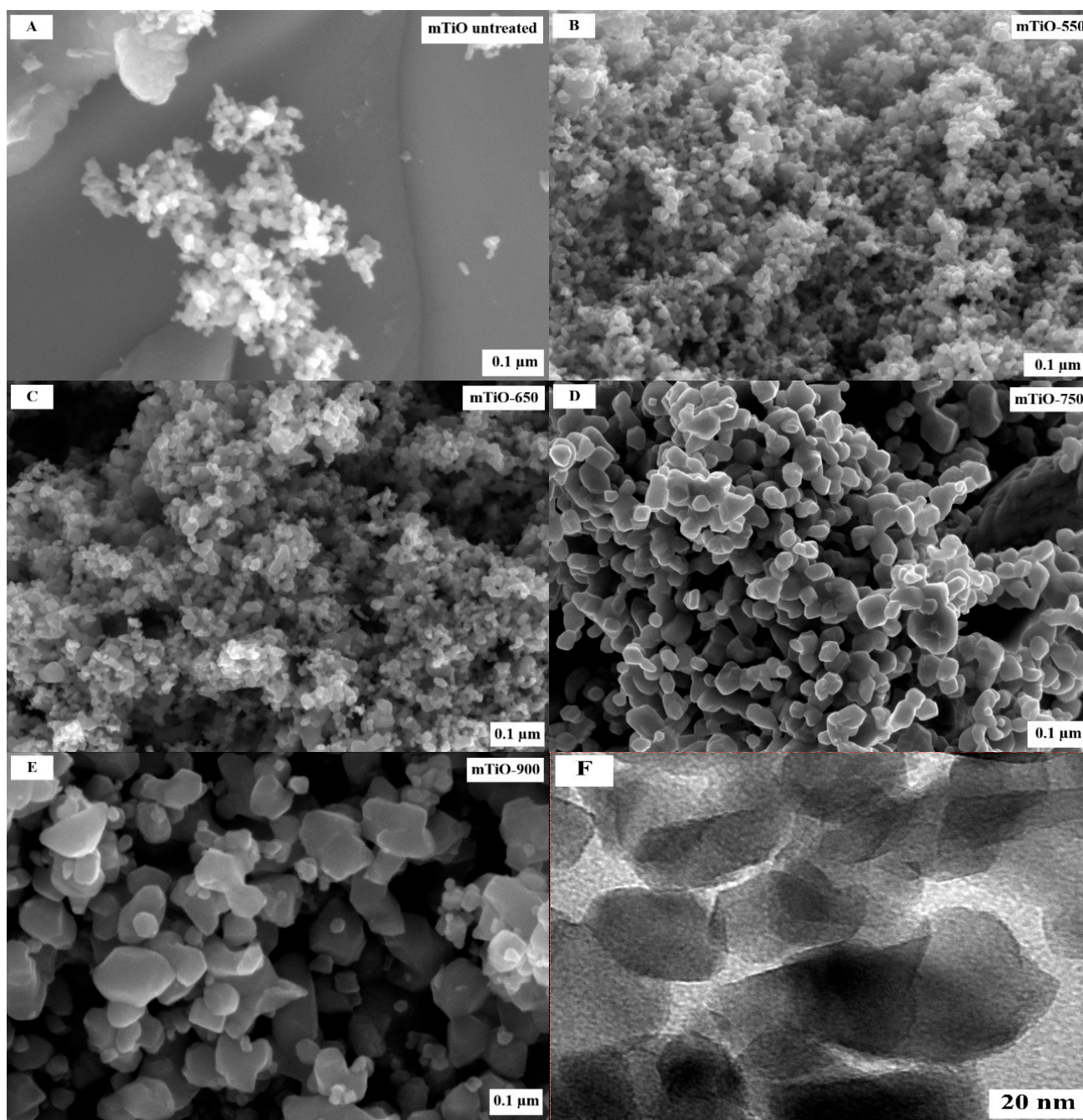


**Figure 9.** SEM images of mTiO untreated (A), mTiO-550 (B), mTiO-650 (C), mTiO-750 (D), mTiO-900 (E) and TEM image of mTiO-650 (F).

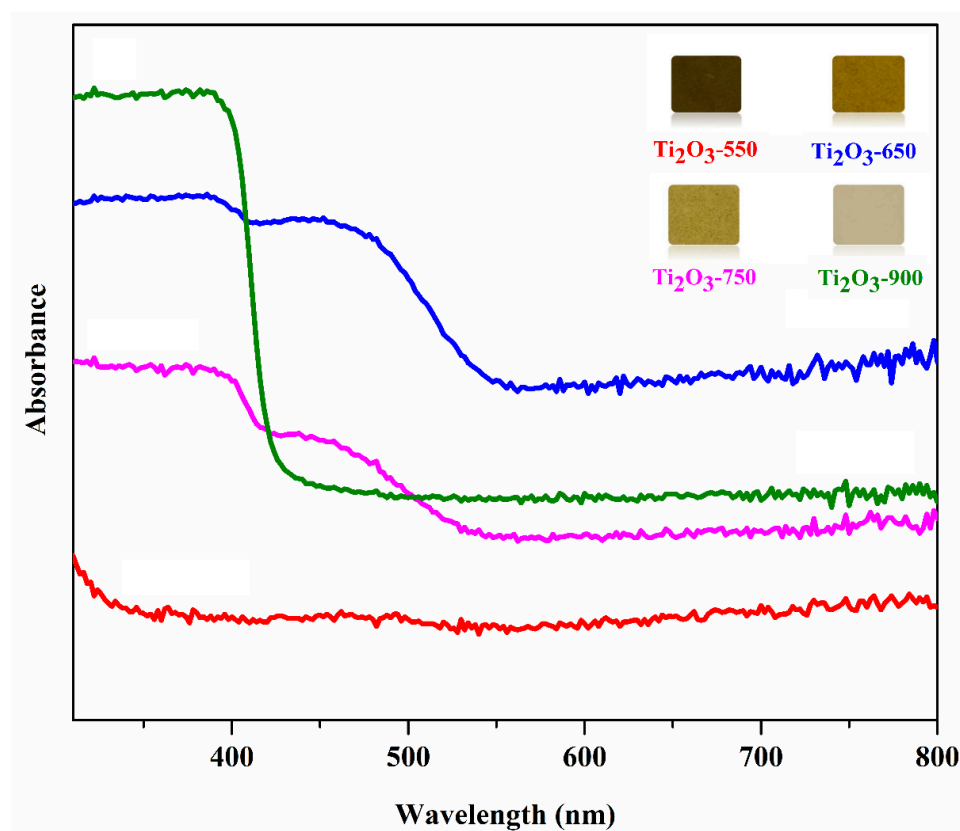


Figure 10. UV–VIS spectra of treated  $\text{Ti}_2\text{O}_3$  catalysts.

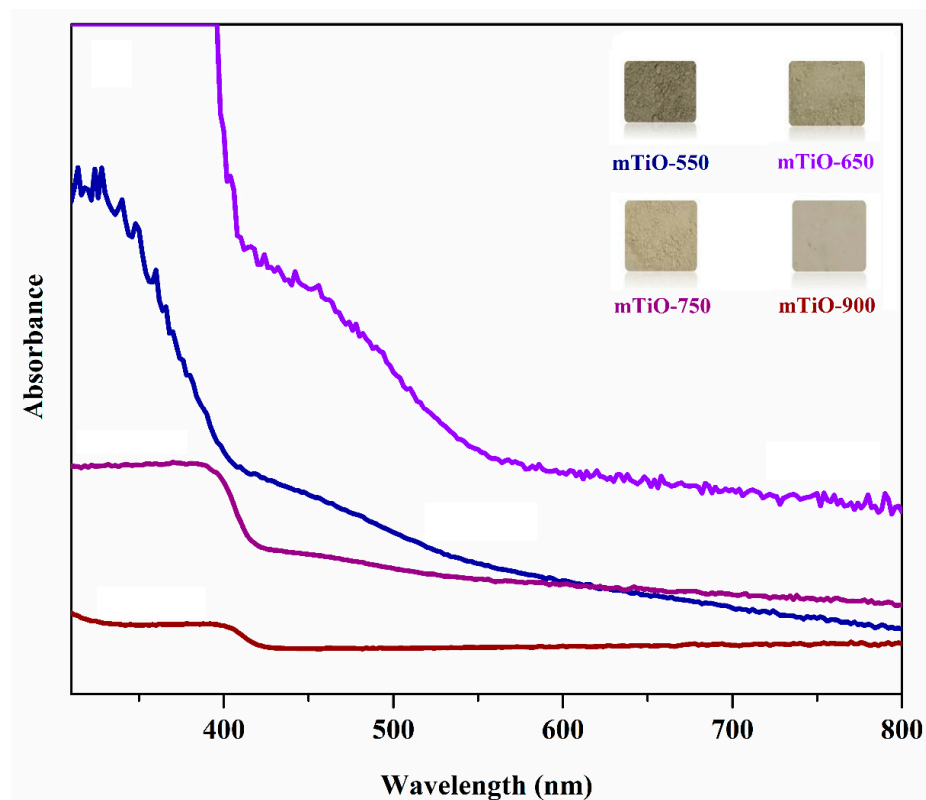


Figure 11. UV–VIS spectra of treated mTiO catalysts.

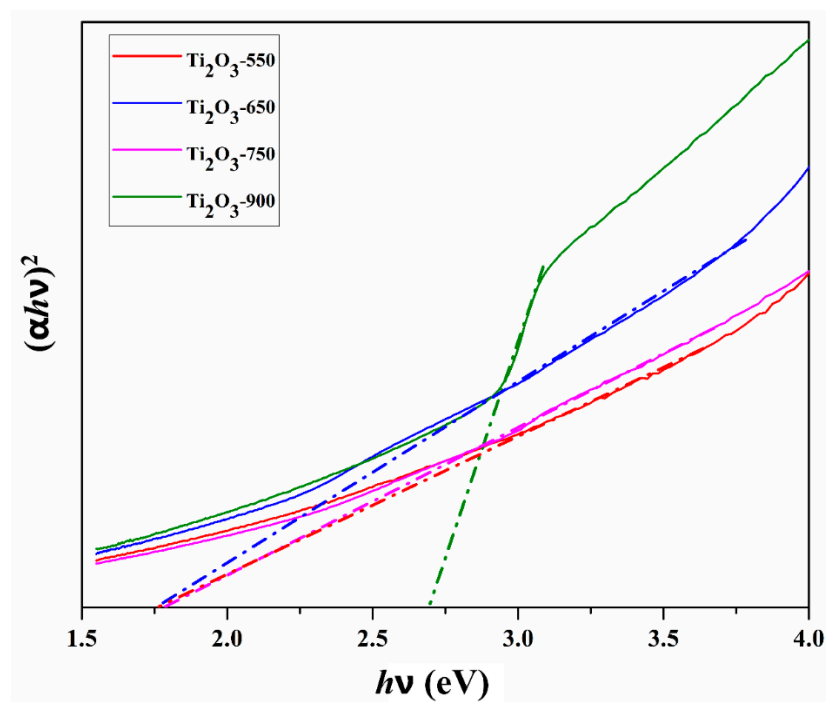


Figure 12. Tauc plot of treated  $\text{Ti}_2\text{O}_3$  catalysts.

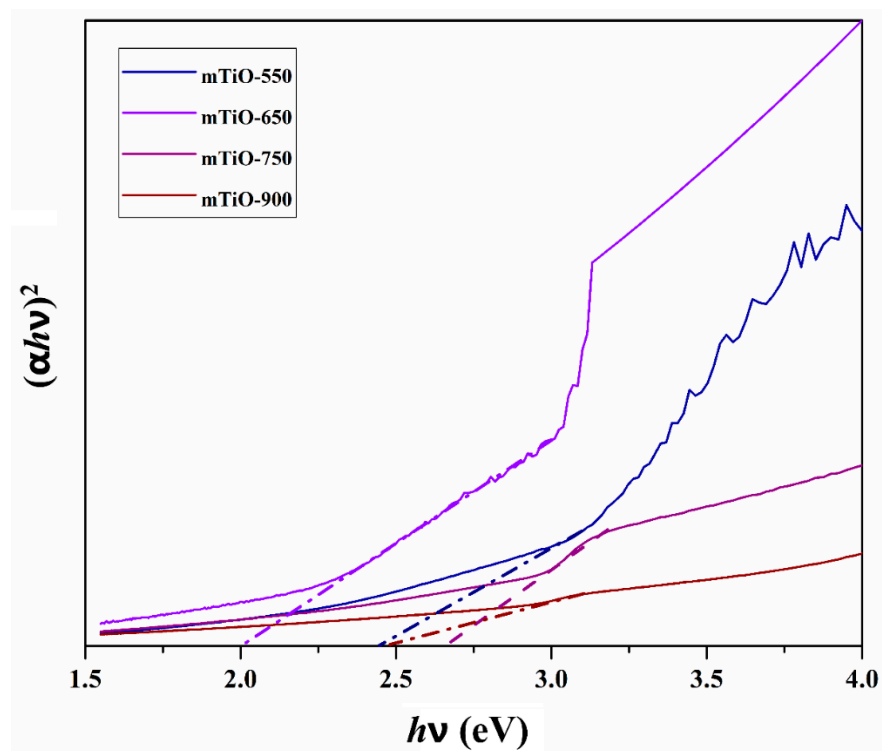
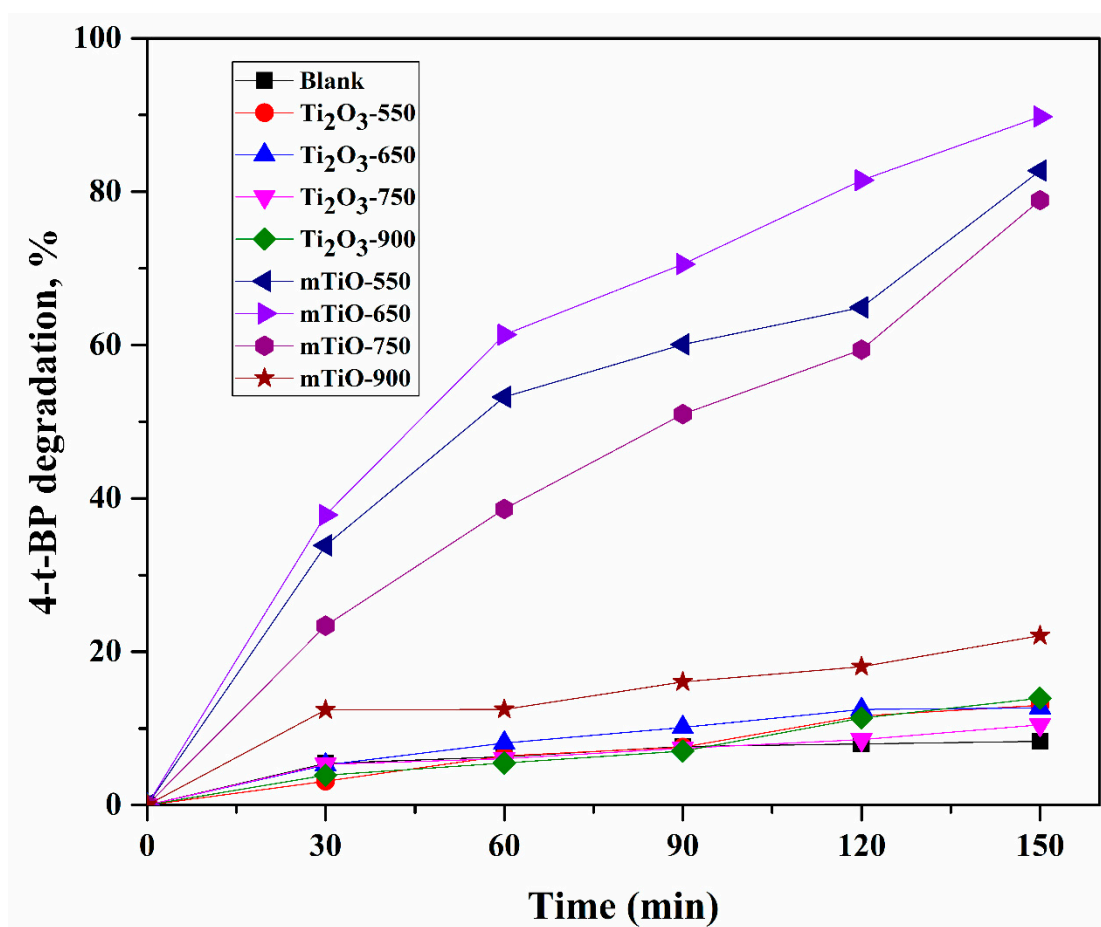


Figure 13. Tauc plot of treated mTiO catalysts.

## 2.2. Photocatalytic Degradation of 4-t-BP in Aqueous Solution

The photocatalytic activity of all the prepared catalysts was evaluated by the photodegradation of 4-t-BP under solar light irradiation, and the results are shown in Figure 14. In the absence of a catalyst, the decomposition of 4-t-BP observed after 150 min of irradiation was only 8.3%.



**Figure 14.** The 4-t-BP degradation under solar light irradiation in the presence of prepared catalysts. Reaction conditions:  $[4\text{-t-BP}]_0 = 5 \text{ mg/L}$ ,  $[\text{photocatalyst}] = 200 \text{ mg/L}$ .

Treated  $\text{Ti}_2\text{O}_3$  showed low photocatalytic activity and approximately 13%, 12.7%, 10.5% and 14% of 4-t-BP was decomposed by  $\text{Ti}_2\text{O}_3$ -550,  $\text{Ti}_2\text{O}_3$ -650,  $\text{Ti}_2\text{O}_3$ -750 and  $\text{Ti}_2\text{O}_3$ -900, respectively, after 150 min of irradiation. In contrast, mTiO exhibited much higher photocatalytic degradation efficiency. Among mTiO catalysts, mTiO-650 showed the highest photocatalytic activity, achieving 89.8% of 4-t-BP degradation. These findings are consistent with the results obtained from physico-chemical characterization, where mTiO-650 exhibited better optical properties and a lower band gap and pore volume as compared to mTiO-550, mTiO-750 and mTiO-900, indicating the importance of the treatment temperature on the optical properties and photocatalytic activity of the catalyst [57].

The mineralization efficiency of a photocatalyst is an important indicator for assessing its practical application. Thus, the mineralization of 4-t-BP was evaluated via total organic carbon (TOC) measurements (Figure 15). As in the case of 4-t-BP photodegradation, the treated mTiO catalysts exhibited higher TOC removal than  $\text{Ti}_2\text{O}_3$  catalysts. In particular, 54.2% of TOC removal was obtained in 150 min using mTiO-650 under solar light irradiation. In the same reaction time, 32.5%, 12.4%, 12.2%, 11.2%, 10%, 7.8% and 5.4% of TOC removal was obtained for mTiO-550, mTiO-900, mTiO-750,  $\text{Ti}_2\text{O}_3$ -750,  $\text{Ti}_2\text{O}_3$ -900,  $\text{Ti}_2\text{O}_3$ -650 and  $\text{Ti}_2\text{O}_3$ -550. The observed photocatalytic efficiency of the catalysts tested for TOC removal was in accordance with the 4-t-BP photodegradation results.



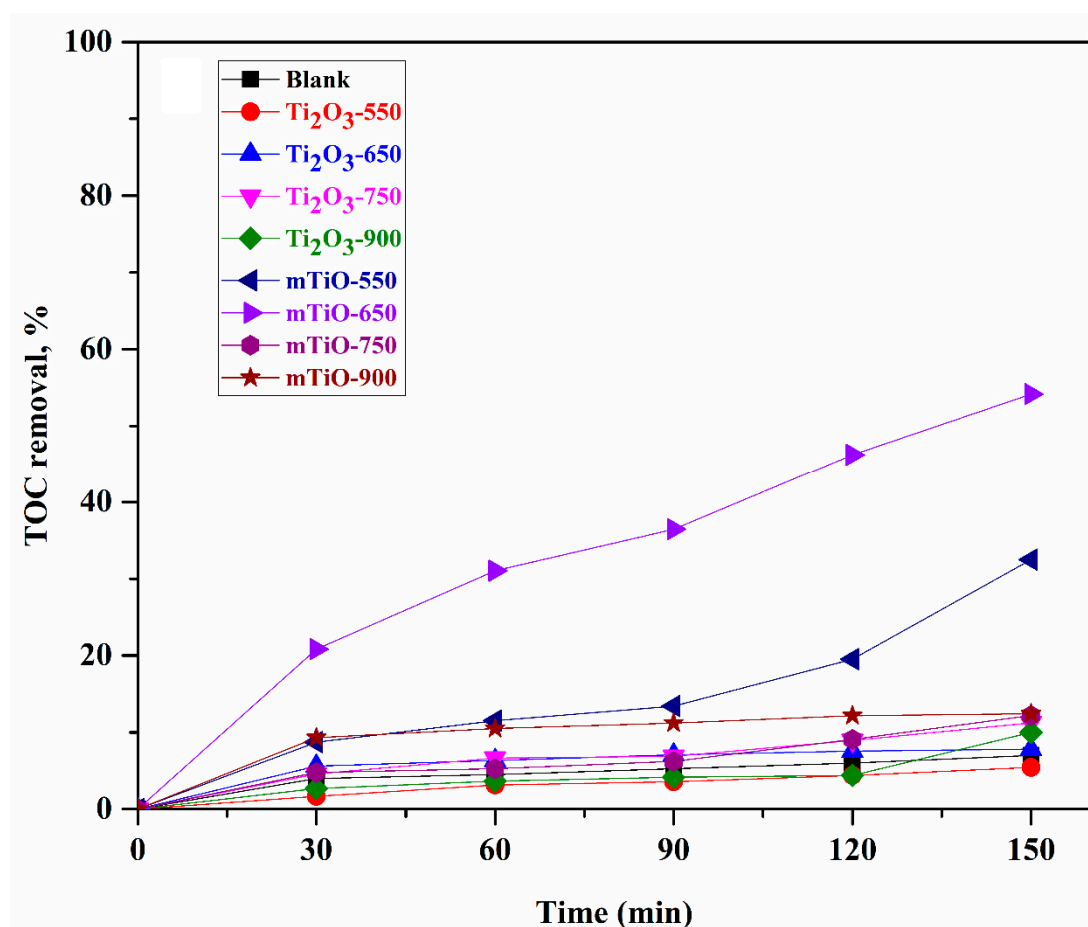


**Figure 15.** TOC removal under solar light irradiation in the presence of prepared catalysts.  $[4\text{-t-BP}]_0 = 5 \text{ mg/L}$ ,  $[\text{photocatalyst}] = 200 \text{ mg/L}$ .

### 2.3. Effect of HA and Coexisting Ions ( $\text{CO}_3^{2-}$ , $\text{NO}_3^-$ , $\text{Cl}^-$ and $\text{HCO}_3^-$ ) on the Degradation of 4-t-BP

The widespread water constituents in wastewater, including natural organic matter (NOM) and inorganic ions ( $\text{CO}_3^{2-}$ ,  $\text{NO}_3^-$ ,  $\text{Cl}^-$  and  $\text{HCO}_3^-$ ), could significantly affect the performance of the reaction system towards the degradation and mineralization of the target pollutants [58,59].

NOM is considered an integral part of natural water bodies and wastewater, and it is mainly composed of humic compounds and proteins [60,61]. In this study, HA was used as a model NOM compound and the effects of different concentrations of HA (1 mg/L, 5 mg/L and 10 mg/L) on the degradation of 4-t-BP were investigated. As shown in Figure 16, the presence of HA in the mTiO-650/solar light system could promote or hinder the degradation of 4-t-BP, depending on its concentration. The presence of a relatively low concentration (1 mg/L) of HA increased the degradation efficiency of 4-t-BP from 89.8% to 92.4%, while higher concentrations (5 mg/L and 10 mg/L) of HA decreased the degradation efficiency of 4-t-BP to 84.6% and 70.8%, respectively. The enhanced degradation of 4-t-BP in the presence of HA was also observed for the degradation of Bisphenol A [62] and dimethoate [63] by  $\text{TiO}_2$  photocatalytic degradation. The positive effect of HA at low concentrations might be ascribed to the photosensitization of HA, which would produce extra electrons, leading to an improvement in the photocatalytic degradation of organic pollutants [62,64,65]. On the other hand, at higher concentrations, HA adsorbed on the surface of the catalyst could compete with 4-t-BP for active sites, resulting in a reduction in degradation efficiency [66,67].

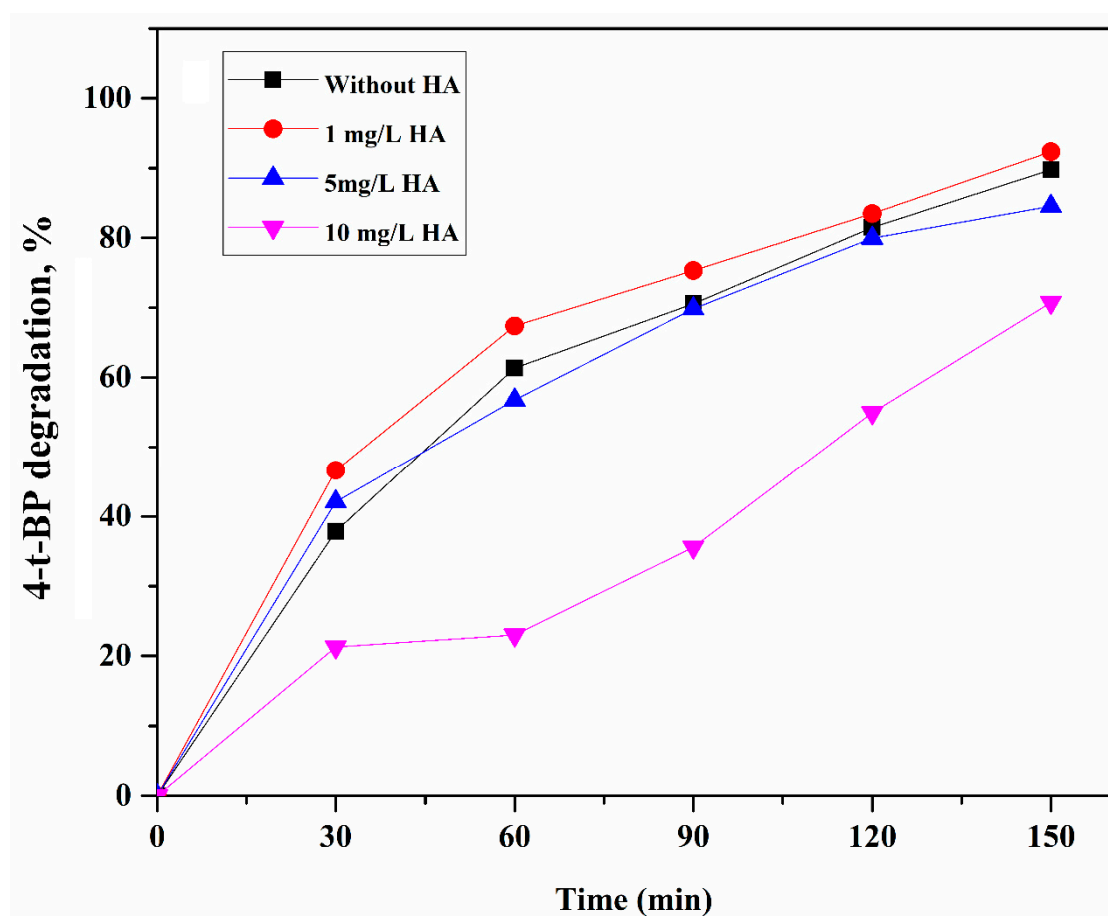
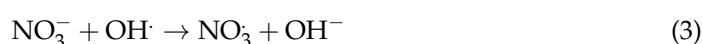
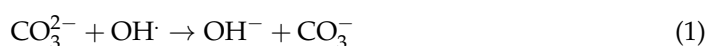


**Figure 16.** Effects of HA on 4-t-BP degradation under solar irradiation in the presence of mTiO-650. Reaction conditions:  $[4\text{-t-BP}]_0 = 5 \text{ mg/L}$ ,  $[\text{photocatalyst}] = 200 \text{ mg/L}$ .

The presence of  $\text{CO}_3^{2-}$ ,  $\text{NO}_3^-$ ,  $\text{Cl}^-$  and  $\text{HCO}_3^-$  anions in the concentration of 100 mg/L had dual effects on the degradation of 4-t-BP over mTiO-650.  $\text{CO}_3^{2-}$  and  $\text{NO}_3^-$  ions resulted in a certain degree of negative effect with respect to the degradation of 4-t-BP. As shown in Figure 17, the 4-t-BP degradation decreased from 89.8% to 87.3% and 70.3% in the presence of nitrate and carbonate, respectively. The inhibition effect of  $\text{CO}_3^{2-}$  and  $\text{NO}_3^-$  was due to: (1) the quenching of oxidizing species, such as hydroxyl radicals ( $\text{OH}^\cdot$ ), and positive holes ( $h^+$ ) by anions (Equations (1)–(3)); (2) anions could compete with 4-t-BP molecules for the available active sites of the catalyst surface, which further affects the degradation process [68–71]. Several studies have highlighted that  $\text{NO}_3^-$  ions are usually weakly adsorbed on the surface of the catalyst and, thus, they slightly inhibit photodegradation reactions [69,72].



It is noteworthy that both  $\text{Cl}^-$  and  $\text{HCO}_3^-$  accelerated the degradation of 4-t-BP by mTiO-650. The addition of  $\text{Cl}^-$  and  $\text{HCO}_3^-$  to the system resulted in 92.5% and 100% degradation after 150 min of solar light irradiation.  $\text{Cl}^-$  anions reacting with hydroxyl radicals can produce  $\text{ClOH}^\cdot$  and subsequently transform into  $\text{Cl}^\cdot$  (Equations (4) and (5)) [73]. The generated active chlorine species can selectively attack electron-rich organic compounds [74]. The complete 4-t-BP degradation in the presence of  $\text{HCO}_3^-$  could be most likely attributed to the generated alkaline condition or the formation of more selective radicals ( $\text{CO}_3^\cdot$ ) by

the reaction of  $\text{HCO}_3^-$  with  $\text{OH}^\cdot$  (Equation (6)), which can promote the degradation of 4-t-BP [69,75].

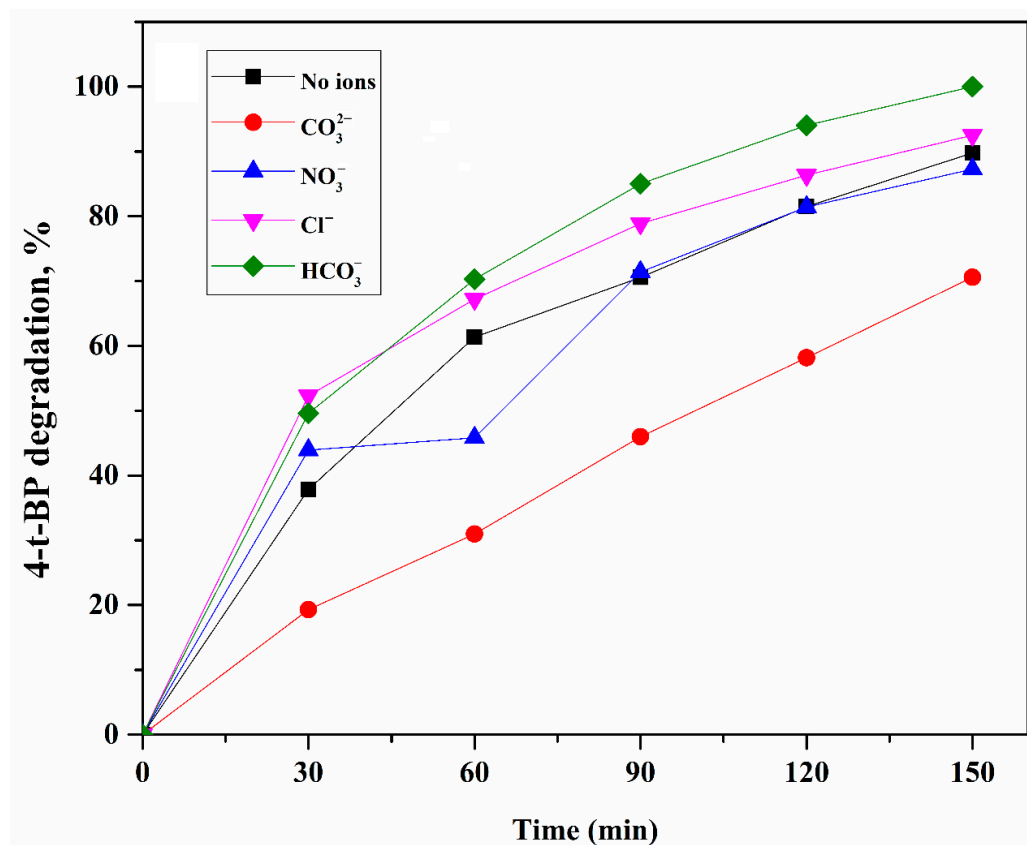
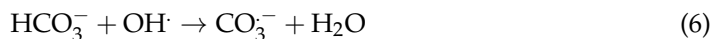
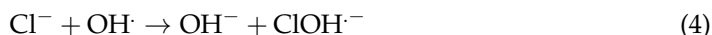


**Figure 17.** Effects of anions ( $\text{CO}_3^{2-}$ ,  $\text{NO}_3^-$ ,  $\text{Cl}^-$  and  $\text{HCO}_3^-$ ) on 4-t-BP degradation under solar light irradiation in the presence of mTiO-650. Reaction conditions:  $[\text{4-t-BP}]_0 = 5 \text{ mg/L}$ ,  $[\text{photocatalyst}] = 200 \text{ mg/L}$ .

### 3. Materials and Methods

#### 3.1. Materials

The 4-t-BP (99%), titanium (IV) oxide ( $\text{TiO}_2$ , nanopowder, 21 nm primary particle size, purity  $\geq 99.5\%$  trace metals basis, P25), titanium (III) oxide ( $\text{Ti}_2\text{O}_3$ , 100 mesh, 99.9% trace metals basis),  $\text{Na}_2\text{CO}_3$ ,  $\text{NaNO}_3$ ,  $\text{NaCl}$ ,  $\text{NaHCO}_3$  and HA were purchased from Sigma Aldrich. All chemicals were of analytical grade and used as purchased. All aqueous solutions were prepared with ultrapure water (UPW) using a Milli-Q System (18.2 M $\Omega$ . cm).

#### 3.2. Preparation of the Photocatalysts

The preparation process was the same for both  $\text{Ti}_2\text{O}_3$  alone and mTiO. At first,  $\text{Ti}_2\text{O}_3$  or a mixture of  $\text{Ti}_2\text{O}_3$  and  $\text{TiO}_2$  was crushed into a fine powder and then heated in a muffle furnace at 550 °C, 650 °C, 750 °C or 900 °C for 3 h in air. For mTiO, the weight ratio between  $\text{Ti}_2\text{O}_3$  and  $\text{TiO}_2$  was 1:1. The final products were denoted as  $\text{Ti}_2\text{O}_3\text{-X}$  and mTiO-X (with X being the temperature of the thermal treatment), respectively. The detailed synthesis process is illustrated in Figure 18.

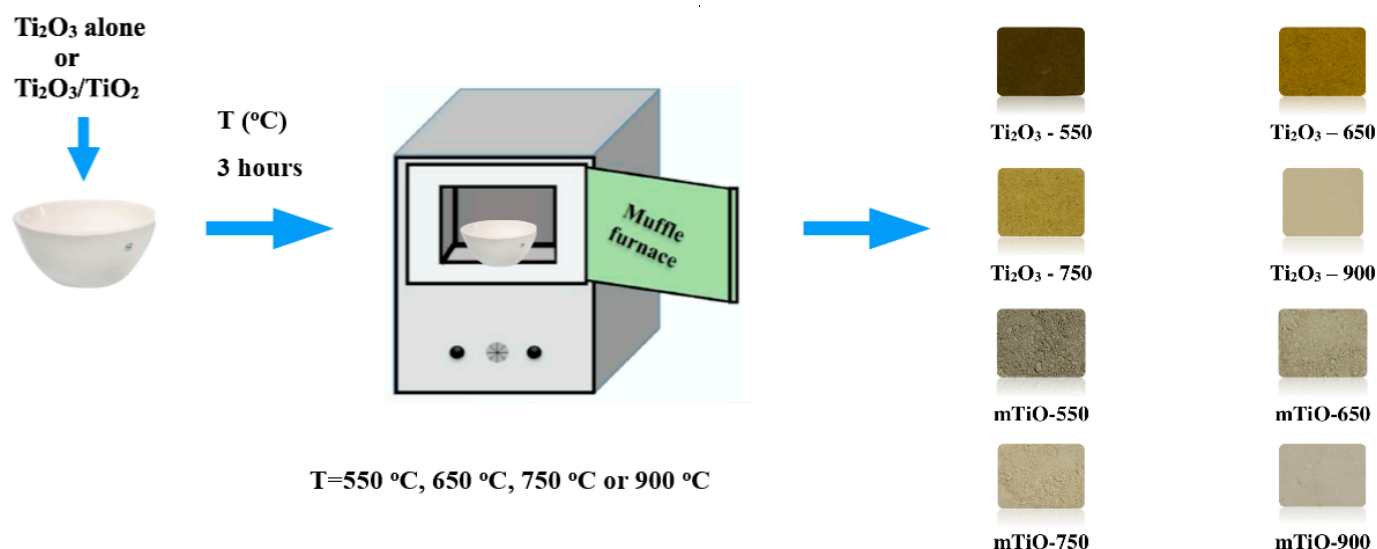


**Figure 18.** Preparation of thermally treated  $\text{Ti}_2\text{O}_3$  and mTiO catalysts.

### 3.3. Characterization of the Photocatalysts

The crystallographic properties and XRD patterns of the prepared catalysts were acquired at  $2\theta$  of  $20\text{--}80^\circ$  on an X-ray diffraction (XRD, Rigaku Smartlab) system. Raman spectra were recorded with the help of a Raman spectrometer (Horiba, LabRam HR evolution) and excitation energy was  $\lambda = 532\text{ nm}$ . Textural properties, including specific surface area ( $S_{\text{BET}}$ ) and pore volume ( $V_p$ ), were measured using an automated gas sorption analyzer (Autosorb iQ, Quantachrome, Boynton Beach, FL, USA) by the Brunauer–Emmett–Teller (BET) and Barrett–Joyner–Halenda (BJH) method, respectively. Surface morphology was observed by a Scanning Electron Microscope (SEM, Auriga CrossBeam 540, Carl Zeiss) and Transmission Electron Microscope (TEM, JEOL JEM-1400 Plus). UV–VIS spectroscopy of samples was implemented on a Thermo Scientific Genesys 150 UV–Visible spectrophotometer.

### 3.4. Photodegradation Tests

The photocatalytic performance of the prepared catalysts was evaluated through the experiments of 4-t-BP degradation under simulated solar light irradiation. First, 100 mg of catalyst was added to 500 mL 4-t-BP (5 mg/L) aqueous solution. Prior to irradiation, the mixture was kept in the dark for 15 min under stirring to reach the adsorption/desorption equilibrium. Then, while stirring, the suspension was exposed to the simulated solar irradiation produced by a 100 W Xenon lamp with an AM1.5G filter (LCS-100 solar simulator). During the experiment, 20 mL of reaction solution was extracted at regular time intervals and filtered by a  $0.22\text{ }\mu\text{m}$  Millex syringe filter to remove the photocatalyst for further analysis.

The concentration of 4-t-BP was analyzed by a high-performance liquid chromatography instrument (HPLC, Agilent 1290 Infinity II, Santa Clara, CA, USA) equipped with an SB-C8 column ( $2.1\text{ mm} \times 100\text{ mm}$ ,  $1.8\text{ }\mu\text{m}$ ). The mobile phase composition was methanol and UPW (50:50,  $v/v$ ), which were mixed to compose the mobile phase. The mineralization of 4-t-BP solution was monitored from the decay of TOC content, measured by a TOC analyzer (Multi N/C 3100, Analytic Jena, Jena, Germany).

## 4. Conclusions

In summary,  $\text{Ti}_2\text{O}_3$  and mTiO photocatalysts were prepared via a one-step synthesis method and further characterized by different tests. The effect of treatment temperature on the physicochemical properties and photocatalytic performance of the prepared catalysts in the degradation of 4-t-BP under simulated solar light irradiation was investigated. Based

on the results obtained, the increase in treatment temperature from 550 °C to 650 °C caused an increase in the pore volume and enhanced light absorbance in the visible region (400–550 nm) for both  $\text{Ti}_2\text{O}_3$  and mTiO photocatalysts. The improved textural and optical properties related to the anatase to rutile ratio and specific surface area contributed to the enhanced performance of mTiO-650, which exhibited the highest photocatalytic activity at the dosage of 0.2 mg/L, achieving 89.8% degradation and 54.2% mineralization of 4-t-BP after 150 min. The effect of treatment temperature on the catalytic performance of the treated  $\text{Ti}_2\text{O}_3$  catalysts was almost negligible and resulted in 13%, 12.7%, 10.5% and 14% 4-t-BP degradation by  $\text{Ti}_2\text{O}_3$ -550,  $\text{Ti}_2\text{O}_3$ -650,  $\text{Ti}_2\text{O}_3$ -750 and  $\text{Ti}_2\text{O}_3$ -900, respectively. In addition, the effects of the presence of HA and various inorganic ions, including  $\text{CO}_3^{2-}$ ,  $\text{NO}_3^-$ ,  $\text{Cl}^-$  and  $\text{HCO}_3^-$  on the photodegradation of 4-t-BP by mTiO-650 were also studied. At relatively low concentrations, HA could act as a photosensitizer and therefore promoted the degradation of 4-t-BP, whereas higher concentrations inhibited the degradation. The presence of  $\text{Cl}^-$  and  $\text{HCO}_3^-$  exhibited a positive influence on 4-t-BP degradation, resulting from the favorable formation of additional reactive species, while the presence of  $\text{NO}_3^-$  and  $\text{CO}_3^{2-}$  slightly inhibited the reaction.

**Author Contributions:** Conceptualization, S.M. and S.G.P.; methodology, S.M. and S.G.P.; validation, T.S.A.; investigation, S.M.; resources, T.S.A. and S.G.P.; writing—original draft preparation, S.M.; writing—review and editing, S.M., T.S.A. and S.G.P.; supervision, T.S.A. and S.G.P.; project administration, S.G.P.; funding acquisition, S.G.P. All authors have read and agreed to the published version of the manuscript.

**Funding:** This research was funded by the Nazarbayev University project “Cost-Effective Photocatalysts for the Treatment of Wastewaters containing Emerging Pollutants”, Faculty Development Competitive Research Grants Program for 2020–2022, Grant Number 240919FD3932, awarded to S.G. Pouloupoulos.

**Data Availability Statement:** Not applicable.

**Acknowledgments:** The authors acknowledge funding support from Nazarbayev University. The technical support of the Core Facilities of Nazarbayev University is greatly acknowledged.

**Conflicts of Interest:** The authors declare no conflict of interest. The funders had no role in the design of the study; in the collection, analyses, or interpretation of data; in the writing of the manuscript, or in the decision to publish the results.

## References

1. Zhang, M.; Dong, H.; Zhao, L.; Wang, D.-X.; Meng, D. A Review on Fenton Process for Organic Wastewater Treatment Based on Optimization Perspective. *Sci. Total Environ.* **2019**, *670*, 110–121. [CrossRef] [PubMed]
2. Yu, X.; Sui, Q.; Lyu, S.; Zhao, W.; Liu, J.; Cai, Z.; Yu, G.; Barcelo, D. Municipal Solid Waste Landfills: An Underestimated Source of PPCPs in the Water Environment. *Environ. Sci. Technol.* **2020**, *54*, 9757–9768. [CrossRef] [PubMed]
3. Yadav, D.; Rangabhashiyam, S.; Verma, P.; Singh, P.; Devi, P.; Kumar, P.; Kumar, K.S. Environmental and Health Impacts of Contaminants of Emerging Sources: Recent Treatment Challenges and Approaches. *Chemosphere* **2021**, *272*, 129492. [CrossRef]
4. Noguera-Oviedo, K.; Aga, D. Lessons Learned from More than Two Decades of Research on Emerging Contaminants in the Environment. *J. Hazard. Mater.* **2016**, *316*, 242–251. [CrossRef]
5. Ferronato, N.; Torretta, V. Waste Mismanagement in Developing Countries: A Review of Global Issues. *Int. J. Environ. Res. Public Health* **2019**, *16*, 1060. [CrossRef] [PubMed]
6. Fobbe, R.; Kuhlmann, B.; Nolte, J.; Preuß, G.; Skark, C.; Zullei-Seibert, N. Organic Pollutants in the Water Cycle: Properties, Occurrence, Analysis and Environmental Relevance of Polar Compounds. In *Organic Pollutants in the Water Cycle: Properties, Occurrence, Analysis and Environmental Relevance of Polar Compounds*; John Wiley & Sons: Hoboken, NJ, USA, 2006; pp. 121–153. [CrossRef]
7. Peck, A.M. Analytical Methods for the Determination of Persistent Ingredients of Personal Care Products in Environmental Matrices. *Anal. Bioanal. Chem.* **2006**, *386*, 907–939. [CrossRef] [PubMed]
8. Giokas, D.L.; Salvador, A.; Chisvert, A. UV Filters: From Sunscreens to Human Body and the Environment. *TrAC Trends Anal. Chem.* **2007**, *26*, 360–374. [CrossRef]
9. Wang, C.; Shi, H.; Adams, C.D.; Gamagedara, S.; Stayton, I.; Timmons, T.; Ma, Y. Investigation of Pharmaceuticals in Missouri Natural and Drinking Water Using High Performance Liquid Chromatography-Tandem Mass Spectrometry. *Water Res.* **2011**, *45*, 1818–1828. [CrossRef] [PubMed]

10. Lai, W.W.-P.; Lin, J.; Tung, H.-H.; Lo, S.-L.; Lin, A. Occurrence of Pharmaceuticals and Perfluorinated Compounds and Evaluation of the Availability of Reclaimed Water in Kinmen. *Emerg. Contam.* **2016**, *2*, 135–144. [CrossRef]
11. Wanda, E.M.M.; Nyoni, H.; Mamba, B.B.; Msagati, T.A.M. Occurrence of Emerging Micropollutants in Water Systems in Gauteng, Mpumalanga, and North West Provinces, South Africa. *Int. J. Environ. Res. Public Health* **2017**, *14*, E79. [CrossRef]
12. Rivera-Jaimes, J.A.; Postigo, C.; Melgoza-Alemán, R.M.; Aceña, J.; Barceló, D.; López de Alda, M. Study of Pharmaceuticals in Surface and Wastewater from Cuernavaca, Morelos, Mexico: Occurrence and Environmental Risk Assessment. *Sci. Total Environ.* **2018**, *613–614*, 1263–1274. [CrossRef]
13. Nikolaou, A. Pharmaceuticals and Related Compounds as Emerging Pollutants in Water: Analytical Aspects. *Glob. Nest J.* **2013**, *15*, 1–12.
14. Seibert, D.; Quesada, H.; Bergamasco, R.; Borba, F.; Pellenz, L. Presence of Endocrine Disrupting Chemicals in Sanitary Landfill Leachate, Its Treatment and Degradation by Fenton Based Processes: A Review. *Process Saf. Environ. Prot.* **2019**, *131*, 255–267. [CrossRef]
15. Reis, B.; Silveira, A.; Tostes, L.; Okuma, A.; Lange, L.; Amaral, M. Organic Compounds Removal and Toxicity Reduction of Landfill Leachate by Commercial Bakers' Yeast and Conventional Bacteria Based Membrane Bioreactor Integrated with Nanofiltration. *Waste Manag.* **2017**, *70*, 170–180. [CrossRef]
16. Dan, A.; Fujii, D.; Soda, S.; Machimura, T.; Ike, M. Removal of Phenol, Bisphenol A, and 4-Tert-Butylphenol from Synthetic Landfill Leachate by Vertical Flow Constructed Wetlands. *Sci. Total Environ.* **2016**, *578*, 566–576. [CrossRef]
17. Barse, A.V.; Chakrabarti, T.; Ghosh, T.; Pal, A.; Jadhao, S. One-Tenth Dose of LC50 of 4-Tert-Butylphenol Causes Endocrine Disruption and Metabolic Changes in Cyprinus Carpio. *Pestic. Biochem. Physiol.* **2006**, *86*, 172–179. [CrossRef]
18. He, G.; Xing, C.; Xiao, X.; Hu, R.; Zuo, X.; Nan, J. Facile Synthesis of Flower-like Bi<sub>12</sub>O<sub>17</sub>C<sub>12</sub>/β-Bi<sub>2</sub>O<sub>3</sub> Composites with Enhanced Visible Light Photocatalytic Performance for the Degradation of 4-Tert-Butylphenol. *Appl. Catal. B Environ.* **2015**, *170*, 1–9. [CrossRef]
19. Xiao, X.; Xing, C.; He, G.; Zuo, X.; Nan, J.; Wang, L. Solvothermal Synthesis of Novel Hierarchical Bi<sub>4</sub>O<sub>5</sub>I<sub>2</sub> Nanoflakes with Highly Visible Light Photocatalytic Performance for the Degradation of 4-Tert-Butylphe. *Appl. Catal. B Environ.* **2014**, *148–149*, 154–163. [CrossRef]
20. Makhatova, A.; Ulykbanova, G.; Sadyk, S.; Sarsenbay, K.; Atabaev, T.; Inglezakis, V.; Pouloupoulos, S. Degradation and Mineralization of 4-Tert-Butylphenol in Water Using Fe-Doped TiO<sub>2</sub> Catalysts. *Sci. Rep.* **2019**, *9*, 1–15. [CrossRef] [PubMed]
21. Black & Veatch Corporation. *White's Handbook of Chlorination and Alternative Disinfectants*; John Wiley & Sons, Inc.: Hoboken, NJ, USA, 2009. [CrossRef]
22. Chong, M.N.; Jin, B.; Chow, C.W.K.; Saint, C. Recent Developments in Photocatalytic Water Treatment Technology: A Review. *Water Res.* **2010**, *44*, 2997–3027. [CrossRef]
23. Paździor, K.; Bilińska, L.; Ledakowicz, S. A Review of the Existing and Emerging Technologies in the Combination of AOPs and Biological Processes in Industrial Textile Wastewater Treatment. *Chem. Eng. J.* **2018**, *376*, 120597. [CrossRef]
24. Wang, J.; XU, L. Advanced Oxidation Processes for Wastewater Treatment: Formation of Hydroxyl Radical and Application. *Crit. Rev. Environ. Sci. Technol.* **2012**, *42*, 251–325. [CrossRef]
25. Palmisano, L.; García-López, E.I.; Marci, G. Inorganic Materials Acting as Heterogeneous Photocatalysts and Catalysts in the Same Reactions. *Dalton Trans.* **2016**, *45*, 11596–11605. [CrossRef]
26. Novak Tusar, N.; Kaucic, V.; Zabukovec Logar, N. Functionalized Porous Silicates as Catalysts for Water and Air Purification. *New Future Dev. Catal. Hybrid Mater. Compos. Organocatalysts* **2013**, 365–383. [CrossRef]
27. Ibhaddon, A.O.; Fitzpatrick, P. Heterogeneous Photocatalysis: Recent Advances and Applications. *Catalysts* **2013**, *3*, 189–218. [CrossRef]
28. Siti nor Hidayah, A.; Mohamed, R.; Al-Gheethi, A.; Lai, C.W.; Yashni, G. Heterogeneous Photocatalysis of Triclocarban and Triclosan in Greywater: A Systematic and Bibliometric Review Analysis. *Int. J. Environ. Anal. Chem.* **2021**, *0*, 1–19. [CrossRef]
29. Younis, S.A.; Kim, K.-H. Heterogeneous Photocatalysis Scalability for Environmental Remediation: Opportunities and Challenges. *Catalysts* **2020**, *10*, 1109. [CrossRef]
30. Chen, D.; Cheng, Y.; Zhou, N.; Chen, P.; Wang, Y.; Li, K.; Huo, S.; Cheng, P.; Peng, P.; Zhang, R.; et al. Photocatalytic Degradation of Organic Pollutants Using TiO<sub>2</sub>-Based Photocatalysts: A Review. *J. Clean. Prod.* **2020**, *268*, 121725. [CrossRef]
31. Luo, C.; Ren, X.; Dai, Z.; Zhang, Y.; Qi, X.; Pan, C. Present Perspectives of Advanced Characterization Techniques in TiO<sub>2</sub>-Based Photocatalysts. *ACS Appl. Mater. Interfaces* **2017**, *9*, 23265–23286. [CrossRef]
32. Chen, J.; Qiu, F.; Xu, W.; Cao, S.; Zhu, H. Recent Progress in Enhancing Photocatalytic Efficiency of TiO<sub>2</sub>-Based Materials. *Appl. Catal. Gen.* **2015**, *495*, 131–140. [CrossRef]
33. Ohno, T.; Sarukawa, K.; Tokieda, K.; Matsumura, M. Morphology of a TiO<sub>2</sub> Photocatalyst (Degussa, P-25) Consisting of Anatase and Rutile Crystalline Phases. *J. Catal.* **2001**, *203*, 82–86. [CrossRef]
34. Sangchay, W.; Sikong, L.; Kooptarnond, K. Comparison of Photocatalytic Reaction of Commercial P25 and Synthetic TiO<sub>2</sub>-AgCl Nanoparticles. *Procedia Eng.* **2012**, *32*, 590–596. [CrossRef]
35. Obaid, D. Bulk TiO<sub>2</sub> vs alternative Ti-based photocatalysts for the mild aerobic oxidation of alcohols. Ph.D. Thesis, Université Pierre et Marie Curie-Paris VI, Paris, France, 2017.
36. Khan, H.; Swati, I.K. Fe<sup>3+</sup>-Doped Anatase TiO<sub>2</sub> with d–d Transition, Oxygen Vacancies and Ti<sup>3+</sup> Centers: Synthesis, Characterization, UV–Vis Photocatalytic and Mechanistic Studies. *Ind. Eng. Chem. Res.* **2016**, *55*, 6619–6633. [CrossRef]



37. Karthik, P.M.; Vinesh, V.; Shaheer, A.R.M.; Neppolian, B. Self-Doping of  $\text{Ti}^{3+}$  in  $\text{TiO}_2$  through Incomplete Hydrolysis of Titanium (IV) Isopropoxide: An Efficient Visible Light Sonophotocatalyst for Organic Pollutants Degradation. *Appl. Catal. Gen.* **2019**, *585*, 117208. [CrossRef]
38. Zhang, Q.; Wang, Y.; Zhu, X.; Liu, X.; Li, H. 1T and 2H Mixed Phase  $\text{MoS}_2$  Nanobelts Coupled with  $\text{Ti}^{3+}$  Self-Doped  $\text{TiO}_2$  Nanosheets for Enhanced Photocatalytic Degradation of RhB under Visible Light. *Appl. Surf. Sci.* **2021**, *556*, 149768. [CrossRef]
39. Wu, C.; Gao, Z.; Gao, S.; Wang, Q.; Xu, H.; Wang, Z.; Huang, B.; Dai, Y.  $\text{Ti}^{3+}$  Self-Doped  $\text{TiO}_2$  Photoelectrodes for Photoelectrochemical Water Splitting and Photoelectrocatalytic Pollutant Degradation. *J. Energy Chem.* **2016**, *25*, 726–733. [CrossRef]
40. Li, G.; Li, J.; Li, G.; Jiang, G. N and  $\text{Ti}^{3+}$  Co-Doped 3D Anatase  $\text{TiO}_2$  Superstructures Composed of Ultrathin Nanosheets with Enhanced Visible Light Photocatalytic Activity. *J. Mater. Chem. A* **2015**, *3*, 22073–22080. [CrossRef]
41. Randorn, C.; Irvine, J.T.S. Synthesis and Visible Light Photoactivity of a High Temperature Stable Yellow  $\text{TiO}_2$  Photocatalyst. *J. Mater. Chem.* **2010**, *20*, 8700–8704. [CrossRef]
42. Xiu, Z.; Guo, M.; Zhao, T.; Pan, K.; Xing, Z.; Li, Z.; Zhou, W. Recent Advances in  $\text{Ti}^{3+}$  Self-Doped Nanostructured  $\text{TiO}_2$  Visible Light Photocatalysts for Environmental and Energy Applications. *Chem. Eng. J.* **2019**, *382*, 123011. [CrossRef]
43. Ghosh, N.G.; Sarkar, A.; Zade, S.S. The Type-II n-n Inorganic/Organic Nano-Heterojunction of  $\text{Ti}^{3+}$  Self-Doped  $\text{TiO}_2$  Nanorods and Conjugated Co-Polymers for Photoelectrochemical Water Splitting and Photocatalytic Dye Degradation. *Chem. Eng. J.* **2021**, *407*, 127227. [CrossRef]
44. Zheng, Z.; Huang, B.; Meng, X.; Wang, J.; Wang, S.; Lou, Z.; Wang, Z.; Qin, X.; Zhang, X.; Dai, Y. Metallic Zinc- Assisted Synthesis of  $\text{Ti}^{3+}$  Self-Doped  $\text{TiO}_2$  with Tunable Phase Composition and Visible-Light Photocatalytic Activity. *Chem. Commun. Camb. Engl.* **2012**, *49*, 868–870. [CrossRef]
45. Fang, W.; Xing, M.; Zhang, J. A New Approach to Prepare  $\text{Ti}^{3+}$  Self-Doped  $\text{TiO}_2$  via  $\text{NaBH}_4$  Reduction and Hydrochloric Acid Treatment. *Appl. Catal. B Environ.* **2014**, *160–161*, 240–246. [CrossRef]
46. Wang, Z.; Yang, C.; Lin, T.; Yin, H.; Chen, P.; Wan, D.; Xu, F.; Huang, F.; Lin, J.; Xie, X.; et al. Visible-Light Photocatalytic, Solar Thermal and Photoelectrochemical Properties of Aluminium-Reduced Black Titania. *Energy Environ. Sci.* **2013**, *6*, 3007–3014. [CrossRef]
47. Sinhamahapatra, A.; Jeon, J.-P.; Yu, J.-S. A New Approach to Prepare Highly Active and Stable Black Titania for Visible Light-Assisted Hydrogen Production. *Energy Environ. Sci.* **2015**, *8*, 3539–3544. [CrossRef]
48. Li, G.; Lian, Z.; Li, X.; Xu, Y.; Wang, W.; Zhang, D.; Tian, F.; Li, H. Ionothermal Synthesis of Black  $\text{Ti}^{3+}$ -Doped Single-Crystal  $\text{TiO}_2$  as an Active Photocatalyst for Pollutant Degradation and  $\text{H}_2$  Generation. *J. Mater. Chem. A* **2015**, *3*, 3748–3756. [CrossRef]
49. Liu, X.; Zhu, G.; Wang, G.; Yuan, X.; Lin, T.; Huang, F. Progress in Black Titania: A New Material for Advanced Photocatalysis. *Adv. Energy Mater.* **2016**, *6*, 1600452. [CrossRef]
50. Kako, T.; Umezawa, N.; Xie, K.; Ye, J. Undoped Visible-Light-Sensitive Titania Photocatalyst. *J. Mater. Sci.* **2013**, *48*, 108–114. [CrossRef]
51. Xu, M.; Zada, A.; Yan, R.; Li, H.; Sun, N.; Qu, Y.  $\text{Ti}_2\text{O}_3/\text{TiO}_2$  Heterophase Junctions with Enhanced Charge Separation and Spatially Separated Active Sites for Photocatalytic  $\text{CO}_2$  Reduction. *Phys. Chem. Chem. Phys.* **2020**, *22*, 4526–4532. [CrossRef] [PubMed]
52. Li, Y.; Yang, Y.; Shu, X.; Wan, D.; Wei, N.; Yu, X.; Breese, M.B.H.; Venkatesan, T.; Xue, J.M.; Liu, Y.; et al. From Titanium Sesquioxide to Titanium Dioxide: Oxidation-Induced Structural, Phase, and Property Evolution. *Chem. Mater.* **2018**, *30*, 4383–4392. [CrossRef]
53. Hardcastle, F.D.; Ishihara, H.; Sharma, R.; Biris, A.S. Photoelectroactivity and Raman Spectroscopy of Anodized Titania ( $\text{TiO}_2$ ) Photoactive Water-Splitting Catalysts as a Function of Oxygen- Annealing Temperature. *J. Mater. Chem.* **2011**, *21*, 6337–6345. [CrossRef]
54. Yahya, N.; Aziz, F.; Jaafar, J.; Lau, W.J.; Yusof, N.; Norharyati, W.; Ismail, A.; Aziz, M. Impacts of Annealing Temperature on Morphological, Optical and Photocatalytic Properties of Gel-Combustion-Derived  $\text{LaFeO}_3$  Nanoparticles. *Arab. J. Sci. Eng.* **2020**, *46*, 6153–6165. [CrossRef]
55. Ji, J.; Xu, Y.; Huang, H.; He, M.; Liu, S.; Liu, G.; Xie, R.; Feng, Q.; Shu, Y.; Zhan, Y.; et al. Mesoporous  $\text{TiO}_2$  under VUV Irradiation: Enhanced Photocatalytic Oxidation for VOCs Degradation at Room Temperature. *Chem. Eng. J.* **2017**, *327*, 490–499. [CrossRef]
56. Hamdy, M.; Saputera, W.; Groenen, E.; Mul, G. A Novel  $\text{TiO}_2$  Composite for Photocatalytic Wastewater Treatment. *J. Catal.* **2014**, *310*, 75–83. [CrossRef]
57. Chen, Q.; Liu, H.; Xin, Y.; Cheng, X.  $\text{TiO}_2$  Nanobelts—Effect of Calcination Temperature on Optical, Photoelectrochemical and Photocatalytic Properties. *Electrochim. Acta* **2013**, *111*, 284–291. [CrossRef]
58. Li, H.; Li, J.; Ai, Z.; Jia, F.; Zhang, L. Oxygen Vacancy-Mediated Photocatalysis of  $\text{BiOCl}$ : Reactivity, Selectivity and Perspective. *Angew. Chem. Int. Ed. Engl.* **2017**, *57*, 122–138. [CrossRef] [PubMed]
59. Wang, Y.; Ao, Z.; Sun, H.; Duan, X.; Wang, S. Activation of Peroxymonosulfate by Carbonaceous Oxygen Groups: Experimental and Density Functional Theory Calculations. *Appl. Catal. B Environ.* **2016**, *198*, 295–302. [CrossRef]
60. Yang, W.; Bradford, S.; Wang, Y.; Sharma, P.; Shang, J.; Baoguo, L. Transport of Biochar Colloids in Saturated Porous Media in the Presence of Humic Substances or Proteins. *Environ. Pollut.* **2018**, *246*, 855–863. [CrossRef] [PubMed]
61. Wang, X.-X.; Liu, B.-M.; Lu, M.-F.; Li, Y.-P.; Jiang, Y.-Y.; Zhao, M.-X.; Huang, Z.-X.; Pan, Y.; Miao, H.-F.; Ruan, W.-Q. Characterization of Algal Organic Matter as Precursors for Carbonaceous and Nitrogenous Disinfection Byproducts Formation: Comparison with Natural Organic Matter. *J. Environ. Manag.* **2021**, *282*, 111951. [CrossRef]



62. Wu, W.; Guoqiang, S.; Wang, S.; Zhu, L.; Yue, L.; Xiang, Q.; Zhang, Y.; Li, Z. Environmentally Relevant Impacts of Nano-TiO<sub>2</sub> on Abiotic Degradation of Bisphenol A under Sunlight Irradiation. *Environ. Pollut.* **2016**, *216*, 166–172. [CrossRef]
63. Chen, J.; Hu, Z.; Wang, D.; Gao, C.; Ji, R. Photocatalytic Mineralization of Dimethoate in Aqueous Solutions Using TiO<sub>2</sub>: Parameters and by-Products Analysis. *Desalination* **2010**, *258*, 28–33. [CrossRef]
64. Cheng, R.; Kang, M.; Shen, Z.-P.; Shi, L.; Zheng, X. Visible-Light-Driven Photocatalytic Inactivation of Bacteriophage F2 by Cu-TiO<sub>2</sub> Nanofibers in the Presence of Humic Acid. *J. Environ. Sci.* **2018**, *77*. [CrossRef]
65. Li, L.; Zheng, X.; Chi, Y.; Wang, Y.; Sun, X.; Yue, Q.; Zhou, W.; Xu, S. Molecularly Imprinted Carbon Nanosheets Supported TiO<sub>2</sub>: Strong Selectivity and Synergic Adsorption-Photocatalysis for Antibiotics Removal. *J. Hazard. Mater.* **2019**, *383*, 121211. [CrossRef]
66. Wang, M.; Zhang, L.; Guilong, Z.; Pang, T.; Zhang, X.; Cai, D.; Wu, Z. In Situ Degradation of Antibiotic Residues in Medical Intravenous Infusion Bottles Using High Energy Electron Beam Irradiation. *Sci. Rep.* **2017**, *7*, 39928. [CrossRef]
67. Guo, Z.; Zhu, S.; Zhao, Y.; Cao, H.; Liu, F. Radiolytic Decomposition of Ciprofloxacin Using  $\gamma$  Irradiation in Aqueous Solution. *Environ. Sci. Pollut. Res.* **2015**, *22*, 15772–15780. [CrossRef] [PubMed]
68. Ma, B.; Yu, N.; Xin, S.; Xin, Y.; Zhang, C.; Ma, X.; Gao, M. Photoelectrocatalytic Degradation of P-Chloronitrobenzene by g-C<sub>3</sub>N<sub>4</sub>/TiO<sub>2</sub> Nanotube Arrays Photoelectrodes under Visible Light Irradiation. *Chemosphere* **2021**, *267*, 129242. [CrossRef] [PubMed]
69. Li, J.; Xia, Z.; Ma, D.; Liu, G.; Song, N.; Xiang, D.; Xin, Y.; Zhang, G.; Chen, Q. Improving Photocatalytic Activity by Construction of Immobilized Z-Scheme CdS/Au/TiO<sub>2</sub> Nanobelt Photocatalyst for Eliminating Norfloxacin from Water. *J. Colloid Interface Sci.* **2021**, *586*, 243–256. [CrossRef]
70. Saleh, R.; Taufik, A.; Prakoso, S.P. Fabrication of Ag<sub>2</sub>O/TiO<sub>2</sub> Composites on Nanographene Platelets for the Removal of Organic Pollutants: Influence of Oxidants and Inorganic Anions. *Appl. Surf. Sci.* **2019**, *480*, 697–708. [CrossRef]
71. Chládková, B.; Evgenidou, E.; Kvitek, L.; Panacek, A.; Zboril, R.; Kovář, P.; Lambropoulou, D. Adsorption and Photocatalysis of Nanocrystalline TiO<sub>2</sub> Particles for Reactive Red 195 Removal: Effect of Humic Acids, Anions and Scavengers. *Environ. Sci. Pollut. Res. Int.* **2015**, *22*, 16514–16524. [CrossRef] [PubMed]
72. Barka, N.; Qourzal, S.; Assabbane, A.; Nounah, A.; Ait-Ichou, Y. Factors Influencing the Photocatalytic Degradation of Rhodamine B by TiO<sub>2</sub>-Coated Non-Woven Paper. *J. Photochem. Photobiol. Chem.* **2008**, *195*, 346–351. [CrossRef]
73. Ziegmann, M.; Doll, T.; Frimmel, F.H. Matrix Effects on the Photocatalytical Degradation of Dichloroacetic Acid and Atrazine in Water. *Acta Hydrochim. Hydrobiol.* **2006**, *34*, 146–154. [CrossRef]
74. Kanakaraju, D.; Motti, C.; Glass, B.; Oelgemöller, M. TiO<sub>2</sub> Photocatalysis of Naproxen: Effect of the Water Matrix, Anions and Diclofenac on Degradation Rates. *Chemosphere* **2015**, *139*, 579–588. [CrossRef] [PubMed]
75. Bekkouche, S.; Merouani, S.; Hamdaoui, O.; Bouhelassa, M. Efficient Photocatalytic Degradation of Safranin O by Integrating Solar-UV/TiO<sub>2</sub>/Persulfate Treatment: Implication of Sulfate Radical in the Oxidation Process and Effect of Various Water Matrix Components. *J. Photochem. Photobiol. Chem.* **2017**, *345*, 80–91. [CrossRef]

## Article

# Preparation of CdS Nanoparticles-TiO<sub>2</sub> Nanorod Heterojunction and Their High-Performance Photocatalytic Activity

Jianhua Song <sup>1,2,†</sup>, Dedong Zeng <sup>1,2,†</sup>, Yu Xie <sup>1,2,\*</sup> , Fayun Zhang <sup>1</sup>, Shenli Rao <sup>1</sup>, Fahui Wang <sup>1</sup>, Jinsheng Zhao <sup>3,\*</sup> , Jinbing Zhang <sup>1</sup> and Lei Wang <sup>4,\*</sup>

<sup>1</sup> School of New Energy Science and Engineering, Xinyu University, Xinyu 338004, China; songjianhua@163.com (J.S.); zengdedong@163.com (D.Z.); zhangfayun@163.com (F.Z.); raoshenli@163.com (S.R.); wangfahui@163.com (F.W.); zhangjingbing@163.com (J.Z.)

<sup>2</sup> College of Environment and Chemical Engineering, Nanchang Hangkong University, Nanchang 330063, China

<sup>3</sup> Shandong Key Laboratory of Chemical Energy Storage and Novel Cell Technology, Liaocheng University, Liaocheng 252059, China

<sup>4</sup> State Key Laboratory of Environmental Criteria and Risk Assessment, Chinese Research Academy of Environmental Sciences, Beijing 100012, China

\* Correspondence: xieyu\_121@163.com (Y.X.); j.s.zhao@163.com (J.Z.); wanglei01@craes.org.cn (L.W.); Tel.: +86-(791)-8395-3408 (Y.X.); Fax: +86-(791)-8395-3373 (Y.X.)

† These authors contributed equally to this work.

Received: 25 March 2020; Accepted: 17 April 2020; Published: 19 April 2020

**Abstract:** As a new and emerging technology, photocatalytic oxidation is widely used in the fields of sewage treatment and organic pollution control. In this study, CdS nanoparticles were prepared at room temperature by an innovative preparation method, then TiO<sub>2</sub> nanorod–CdS nanoparticle heterojunction photocatalysts were prepared using the solvothermal method, with TiCl<sub>3</sub> used as the precursor for TiO<sub>2</sub> nanorods. This study mainly took advantage of the small size of the CdS nanoparticles in combination with TiO<sub>2</sub> nanorods, and the resultant heterojunctions had large specific surface areas, thereby increasing the contact area between the catalysts and the contaminants. In addition, due to the lower band gap energy (2.4 eV) of CdS, the photo response range of the heterojunction photocatalysts was also increased. In an experimental study, through photocatalytic performance tests of the catalysts with different weight ratios, it was found that the TiO<sub>2</sub>(40%)@CdS composite had the best photocatalytic performance and the highest catalytic rate. BET, SEM, and other tests showed that the specific surface area of the TiO<sub>2</sub>(40%)@CdS composite was the largest. TiO<sub>2</sub> nanorods and CdS particles were uniformly distributed in the composite, and the optical response range was extended to the visible light region.

**Keywords:** TiO<sub>2</sub> nanorods; CdS nanoparticles; hydrothermal method; methyl orange; photocatalysis

## 1. Introduction

The photocatalytic activity of titanium dioxide (TiO<sub>2</sub>) was discovered in 1972 [1]; since then, TiO<sub>2</sub> as a novel photocatalytic material has attracted extensive attention. Many excellent characteristics have been discovered by researchers, such as its non-toxicity, non-polluting behavior, low cost, and high catalytic efficiency [2]. Because of these excellent properties, TiO<sub>2</sub> is widely applied in various areas related to environmental protection [3–7]. For example, TiO<sub>2</sub> has been used to treat wastewater that contains organic pollutants such as dyes, pesticides, and petroleum pollutants, and even waters containing heavy metal pollutants. Moreover, if TiO<sub>2</sub> is prepared as a photocatalytic decontamination

coating, the nitric oxide ( $\text{NO}_x$ ) in the atmosphere [8,9], sulfur oxide [10,11] and other pollutants such as halogenated hydrocarbons [12,13], aldehydes [14], and polycyclic aromatic hydrocarbons from automotive exhaust gas can be absorbed and degraded [15,16].  $\text{TiO}_2$  also shows a good performance in light-sensitive solar cells [17] and biomedical devices [18]. In addition, nano- $\text{TiO}_2$  has broad applications in many aspects such as sterilization, degradation, deodorization, self-cleaning and energy storage [19–23]. However,  $\text{TiO}_2$  has a bandgap of 3.2 eV, and can only respond to ultraviolet light, which only accounts for 5% of sunlight. Therefore, the red shift of the wavelength of the absorption wave via the modification of  $\text{TiO}_2$  is an important method for improving the photocatalytic performance of  $\text{TiO}_2$ .

Therefore, many studies have been undertaken to build heterojunctions with specific morphologies and enhanced specific surface areas for extending the visible light absorption and, as a result, the photocatalytic activities of the heterojunctions were usually superior to that of bare  $\text{TiO}_2$ . Kavil et al. fabricated a  $\text{TiO}_2$ –CdS photocatalyst with nano heterostructures via the hydrothermal method and the catalyst  $\text{TiO}_2$ –CdS 10, with 10 wt% CdS content, acquired a higher photocatalytic activity towards the degradation of methyl orange (MO) than that of the bare  $\text{TiO}_2$  [24]. Yang et al. prepared CdS/ $\text{TiO}_2$  heterojunctions with porous structures, which exhibited enhanced catalytic degradation capacity towards organic dyes including Methyl Orange (MO) and Rhodamine B (RhB)—in particular, the degradation rate of MO reached 95% in 120 min [25]. Furthermore, more recently, a hydrolysis–hydrothermal calcined method was proposed for the synthesis of three-dimensional porous CdS/ $\text{TiO}_2$ , which displayed high activity in the degradation process of MO under visible light [26]. The photocatalytic activities of the CdS/ $\text{TiO}_2$  heterojunctions are influenced by many factors including the crystal composition, the micromorphology, the specific surface area, the band gap and the energy levels, etc. However, the catalytic activity of these catalysts is not satisfactory, and there is still a high demand for the improvement of the catalytic activity through the optimization of the synthesis methods [27,28].

This paper describes the preparation of a heterojunction catalyst consisting of  $\text{TiO}_2$  nanorods with CdS nanoparticles. Because of the unstable chemical properties of CdS, it is difficult to prepare nanoparticles at high temperatures. In this study, an innovative preparation method was introduced to successfully prepare CdS nanoparticles by adjusting the rate of CdS precipitation at room temperature. A composite of  $\text{TiO}_2$  nanorods and CdS nanoparticles was prepared in the presence of a surfactant from CdS nanoparticles and  $\text{TiCl}_3$  by the solvothermal method. The CdS nanoparticle has a lower bandgap of 2.4 eV, as well as a smaller size, which has a compatible energy level with that of  $\text{TiO}_2$ . In the present study we prepared the  $\text{TiO}_2$  nanorod/CdS nanoparticle heterojunction photocatalyst with excellent photocatalytic performance. Methyl orange solution could be completely degraded by the prepared catalyst within 40 min. It maintained a high recycling performance with the repeated degradation of methyl orange over 10 times, with the degradation rate remaining at 100%.

## 2. Results and Discussion

### 2.1. Surface Morphology Characterization

SEM images showed that there were connected nanoparticles on the surface of the  $\text{TiO}_2(20\%)\text{@CdS}$  composite material, with a weight content of 20%  $\text{TiO}_2$ . These particles were likely to be  $\text{TiO}_2$  or CdS nanoparticles. No nanorod structure was formed and the accumulation between nanoparticles was strong (Figure 1a), resulting in its low specific surface area. In the composites of  $\text{TiO}_2(30\%)\text{@CdS}$ , nanoparticles were partially attached on the surface of the nanorods and aggregated with each other to form nanoparticle agglomerates (Figure 1b). This showed that there were nanorods in the composite, but with a more obvious accumulation. In Figure 1c, for the  $\text{TiO}_2(40\%)\text{@CdS}$  composite, the rod-like structure and the granular material were uniformly integrated. The configuration of the composite nanorods was symmetrical, the length was homogenous, and the size of the nanoparticles was uniform, and there were good recombinations between  $\text{TiO}_2$  nanorods and CdS nanoparticles. Figure 1d verified that the agglomeration of the  $\text{TiO}_2(50\%)\text{@CdS}$  composite was very obvious, and many large particle agglomerates were observed.

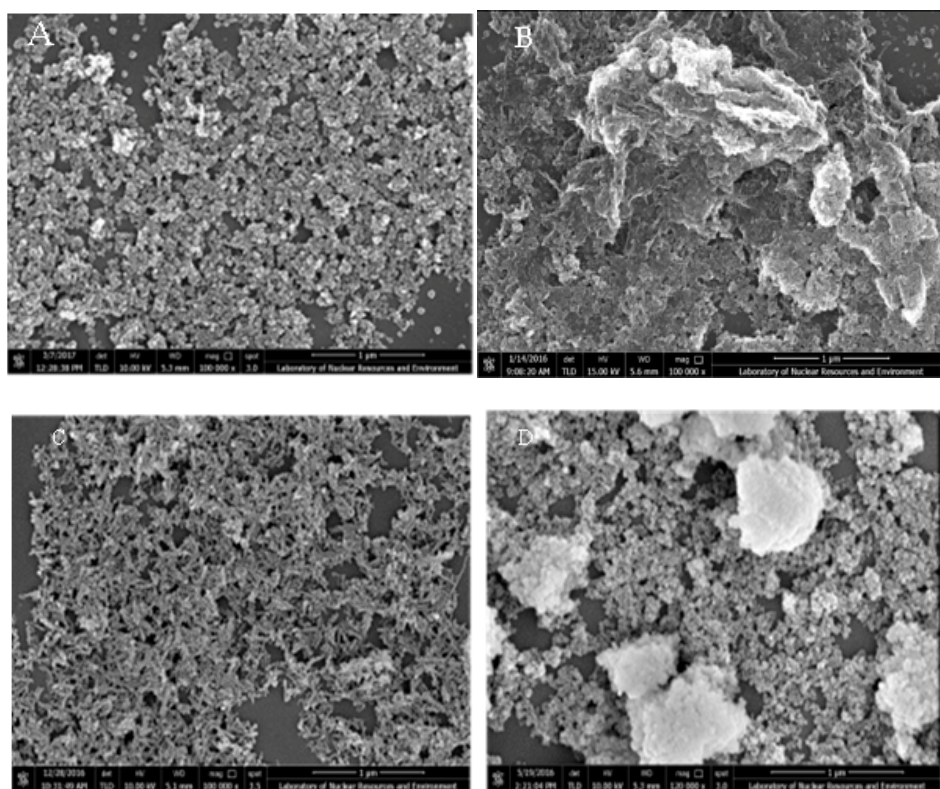


**Figure 1.** SEM image of (A)  $\text{TiO}_2(20\%)\text{@CdS}$  composite; (B)  $\text{TiO}_2(30\%)\text{@CdS}$ ; (C)  $\text{TiO}_2(40\%)\text{@CdS}$ ; (D)  $\text{TiO}_2(50\%)\text{@CdS}$ . Magnification:  $\times 100,000$ , and the samples were sprayed with gold before measurement.

TEM images demonstrated that the coexistence of nanoparticles and nanorods was found on the  $\text{TiO}_2(40\%)\text{@CdS}$  composite (Figure 2a), in which CdS nanoparticles were uniformly distributed on the surface  $\text{TiO}_2$  nanorods (Figure 2b). TEM images clearly showed that the morphology of  $\text{TiO}_2$  is nanorods with a length and width of 200 nm and 20 nm, respectively. The form of CdS is nanoparticles with the length ranging from 10 nm to 30 nm. HRTEM images (Figure 2c–d) indicated that the  $\text{TiO}_2$  nanorods were the anatase type, which can be concluded due to the lattice fringe of the HRTEM image, where a lattice distance of 0.346 nm corresponds with the {001} crystal face of anatase. The CdS nanoparticles were the wurtzite type. The distance between the crystal faces was 0.35 nm, obtained by the lattice fringe of the HRTEM image, which agrees with the {002} crystal face of wurtzite. More importantly, CdS nanoparticles were loaded on the  $\text{TiO}_2$  nanorods, resulting in a structure which is similar to an interface.

In summary, among the as-prepared nano-composites,  $\text{TiO}_2(30\%)\text{@CdS}$  and  $\text{TiO}_2(40\%)\text{@CdS}$  composites were successfully prepared, but there were differences in the shape and size of the composites. The difference could be further confirmed from the diversified performance of the photocatalytic properties of the composites in the following dye degradation experiments.



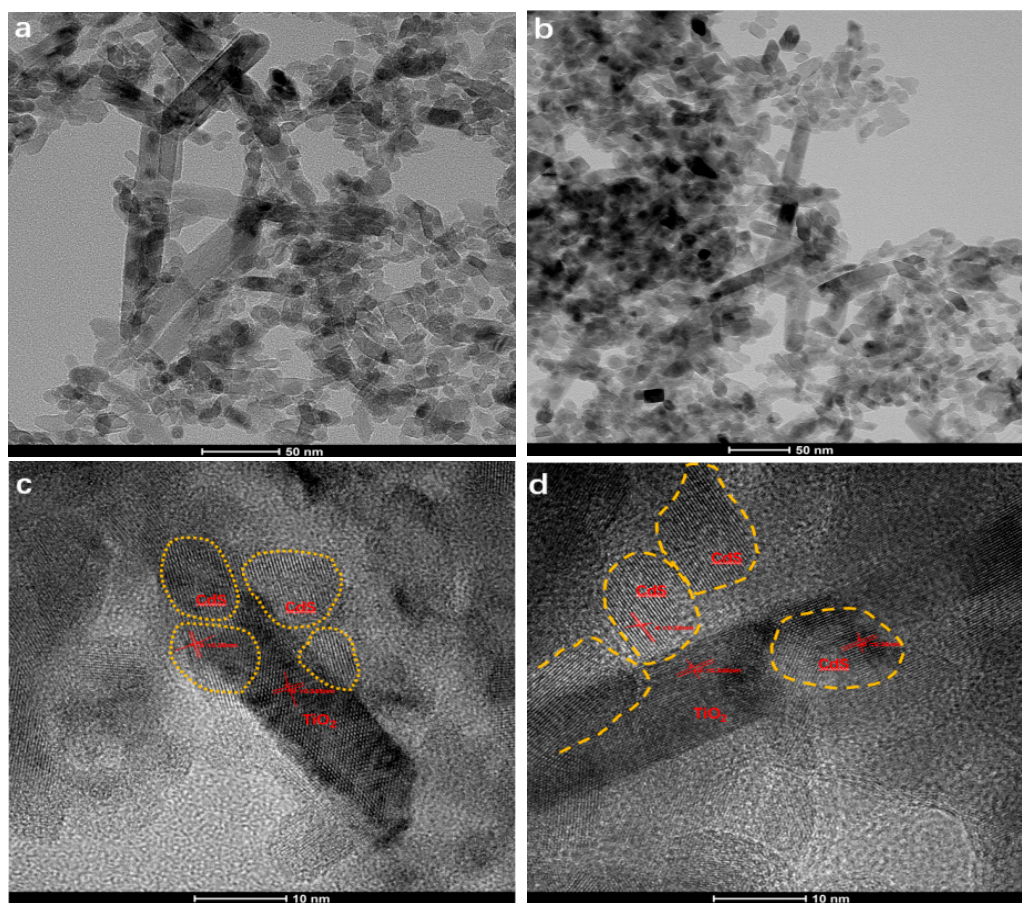


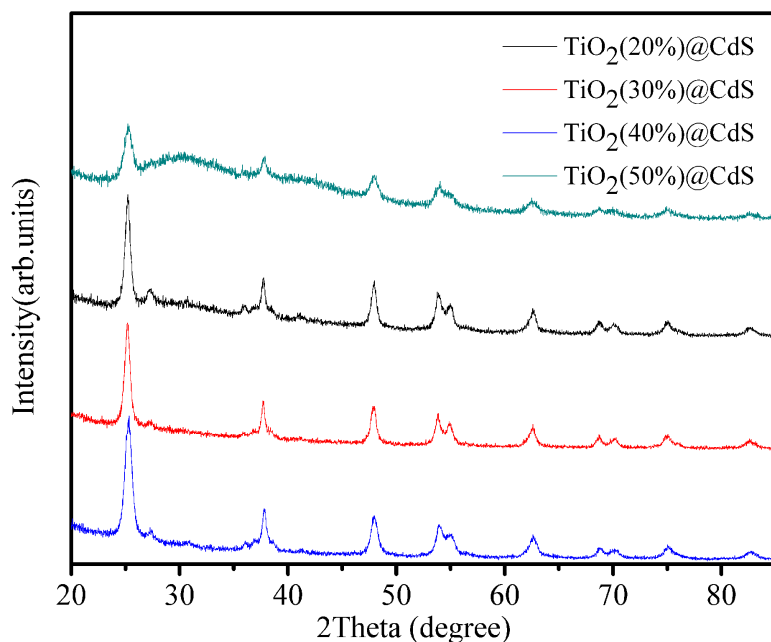
**Figure 2.** TEM patterns of  $\text{TiO}_2(40\%)\text{@CdS}$  composites(a–d).

## 2.2. Crystal Structure Characterization

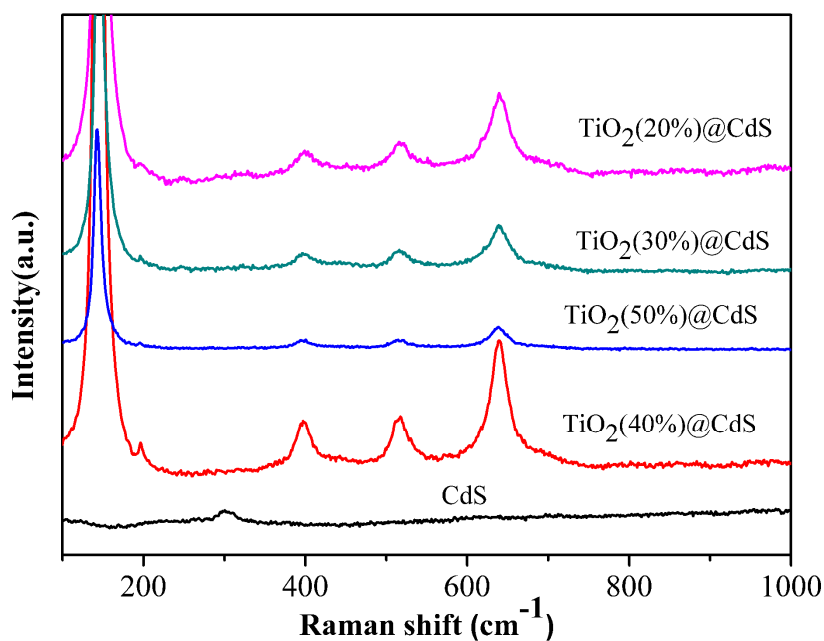
As can be seen from Figure 3, all the composites with different  $\text{TiO}_2$  percentage concentrations have the same series of characteristic peaks corresponding to the two-theta angles  $25.13^\circ$ ,  $25.30^\circ$ ,  $36.05^\circ$ ,  $37.89^\circ$ ,  $40.93^\circ$ ,  $47.82^\circ$ ,  $53.87^\circ$ ,  $55.05^\circ$ ,  $62.61^\circ$ ,  $68.83^\circ$ ,  $70.52^\circ$ , and  $75.00^\circ$ . According to the XRD standard spectrum line of cadmium sulfide crystals [29], there are three characteristic peaks and their respective two-theta angles are  $25.05^\circ$  (100),  $47.98^\circ$  (103) and  $52.13^\circ$  (220), respectively. However, according to the XRD standard spectrum line of titanium dioxide, there are more corresponding peaks. These characteristic peaks have their corresponding two-theta angles at  $27.51^\circ$  (110),  $36.06^\circ$  (101),  $39.23^\circ$  (201),  $54.33^\circ$  (211),  $56.69^\circ$  (220),  $62.77^\circ$  (002),  $69.04^\circ$  (221),  $69.90^\circ$  (307). According to these existing characteristic peaks of  $\text{TiO}_2$ , there are two kinds of crystal types of titanium dioxide, including the anatase crystal form and the rutile crystal form. The anatase crystal form is dominant, and the rutile crystal form is of little importance. The sharpness of the XRD peaks reflects the degree of crystallinity of the crystals, the sharper the XRD peaks are, the better the crystallinity of the material is. Figure 3 shows that the crystallization effect of the  $\text{TiO}_2$  (50%)@CdS was the worst, and the crystal structure was classified as a looser type, which might be unfavorable for photocatalytic activity. The  $\text{TiO}_2(40\%)\text{@CdS}$  composite had a sharp peak in the XRD pattern with few impurity peaks, indicating that the crystalline state was better, which might explain the photocatalytic performance of the catalyst.

Figure 4 shows the FT-Raman spectroscopy of the  $\text{TiO}_2$  nanorod–CdS nanoparticle with different  $\text{TiO}_2$  contents. The peaks with Raman shifts at  $135\text{ cm}^{-1}$ ,  $396\text{ cm}^{-1}$ ,  $515\text{ cm}^{-1}$ , and  $641\text{ cm}^{-1}$  represent the presence of rutile  $\text{TiO}_2$  ( $\text{A1g} + 2\text{B1g} + 3\text{1g}$ ) [30]. The peaks with Raman shifts at  $300\text{ cm}^{-1}$ ,  $600\text{ cm}^{-1}$ , and  $900\text{ cm}^{-1}$  are the characteristic Raman peaks of CdS nanoparticles [31]. It is apparent that the abovementioned peaks are all present and have the most high peak intensities for  $\text{TiO}_2(40\%)\text{@CdS}$  than

that of other composites with other  $\text{TiO}_2$  contents, which suggested that both of the  $\text{TiO}_2$  nanorods and CdS nanoparticles maintained their unique crystal structures and coexisted in the composite, which supports the exertion of their synergistic effect in photocatalytic degradation.



**Figure 3.** XRD pattern of  $\text{TiO}_2$  nanorod–CdS nanoparticles.



**Figure 4.** Raman pattern of  $\text{TiO}_2$  nanorod–CdS nanoparticle composites.

### 2.3. Test of Absorption Performance

For the CdS nanoparticle, the maximum wavelength of the absorption is located at 500 nm in the ultraviolet-visible diffuse reflectance spectrum; after that, the absorption curve drops sharply, and there is almost no absorption. The 2.11 eV of the bandgap energy for the CdS nanoparticle was obtained according to an onset absorption wavelength of 588 nm. Compared to the CdS bulk material (2.4 eV), the bandgap energy of the CdS nanoparticles was reduced due to the reduction in the particle sizes.

However, when the wavelength was increased to more than 500 nm, the absorption effect sharply decreased, which is one of the reasons why it has limited practical applications. The onset absorption wavelengths of the TiO<sub>2</sub> nanorod–CdS nanoparticle composites were 428 nm, 435 nm, 486 nm, and 442 nm, respectively, for the composites with 20%, 30%, 40% and 50% TiO<sub>2</sub> contents. The corresponding bandgap energies were 2.89 eV, 2.85 eV, 2.55 eV and 2.81 eV, respectively. The absorption spectrum of the TiO<sub>2</sub>(40%)@CdS was maintained at a higher level on average, in the range of 400 nm to 780 nm wavelengths, which was better than other composites with 20%, 30%, and 50% TiO<sub>2</sub> contents. Specifically, the above data suggest that the TiO<sub>2</sub> (40%)@CdS composite was efficient as photocatalyst in visible and infrared regions. From the data in Figure 5, it was found that the formation of the composites that recombined with TiO<sub>2</sub> nanorods and CdS nanoparticles enlarged the range for photo-absorption and, among them, the TiO<sub>2</sub>(40%)@CdS composite was the best light absorbent. Based on these results, it is reasonable to suggest that the composite has the best ability for the photocatalytic degradation of pollutants, such as organic dyes.

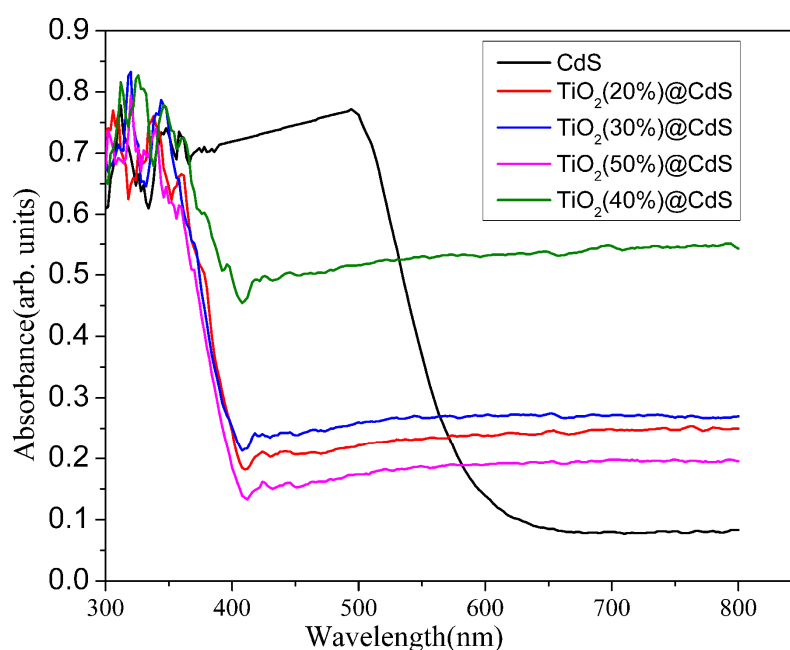


**Figure 5.** UV-visible diffuse reflectance spectra of TiO<sub>2</sub> nanorod–CdS nanoparticle composites and the CdS nanoparticles.

#### 2.4. Photocurrent Test

From Figure 6, it can be seen that the photocurrent intensity of the CdS nanoparticle is the lowest, and the photocurrent is attenuated by more than half after 600 s, which suggests that the photocurrent stability of the CdS particles was the worst. Of all the composites, the TiO<sub>2</sub>(40%)@CdS composite had the highest photocurrent, which was followed by the composites with 30%, 50% and 20% TiO<sub>2</sub> contents, respectively. As the illumination time increased to 400 s or more, the intensities of the photocurrents gradually became stable, then the approximate steady state of the photocurrent began to appear.

The speeds and intensities of the currents generated by the composites varied along with the variance in TiO<sub>2</sub> contents. Figure 6 also shows that both the current generation speed and the magnitude of the photocurrent of the TiO<sub>2</sub>(30%)@CdS composite was slightly inferior to that of the TiO<sub>2</sub>(40%)@CdS composite. The reason for the above fact was that the CdS nanoparticles did not bind tightly with the TiO<sub>2</sub> nanorods. Furthermore, the photocurrent intensities of the TiO<sub>2</sub>(20%)@CdS and TiO<sub>2</sub>(50%)@CdS composites were much weaker than those of the composites of TiO<sub>2</sub>(30%)@CdS, which might be attributed to the lack of TiO<sub>2</sub> nanorods in the structures, which make it difficult to form



a tightly bound  $\text{TiO}_2$  nanorod–CdS nanoparticle [32]. As a result, this limited the further enhancement of the photocurrent performance.

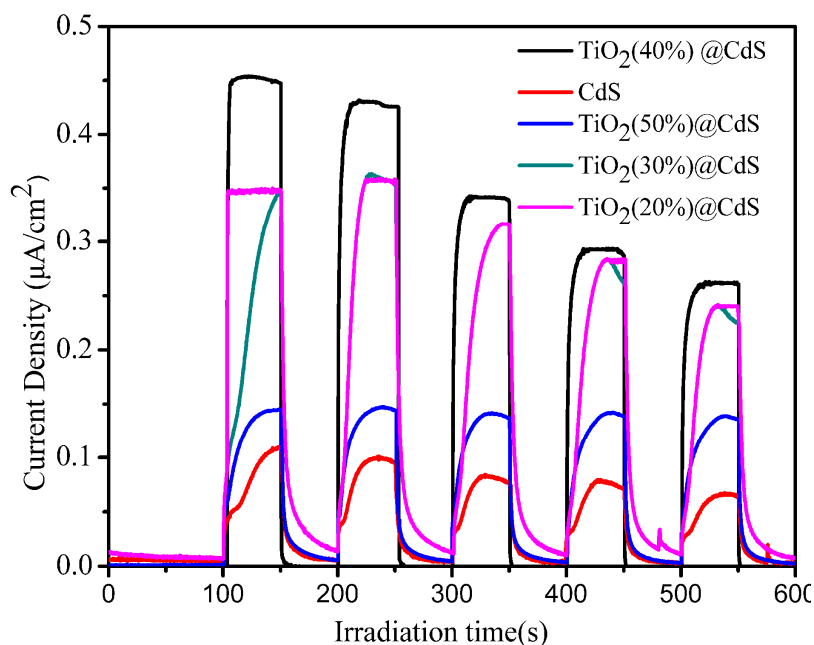


**Figure 6.** Photocurrent response curve of  $\text{TiO}_2$  nanorod–CdS nanoparticle composites.

## 2.5. BET Test

Figure 7 shows the  $\text{N}_2$  adsorption–desorption isothermal curves and pore size distribution of the  $\text{TiO}_2$  nanorod–CdS nanoparticle composites. From Figure 7A, it was observed that the nitrogen adsorption–desorption isotherms of  $\text{TiO}_2(20\%)\text{@CdS}$  and  $\text{TiO}_2(50\%)\text{@CdS}$  composites primarily adapted to the type IV isotherm line, which is often accompanied by the mesoporous capillary condensation phenomenon [33]. An isotherm curve was formed by the mesoporous solid and there were differences between the adsorption curve and the desorption curve, which meant that a hysteresis loop could be observed. According to the International Union of Pure and Applied Chemistry(IUPIC), the isotherm hysteresis loop of the  $\text{TiO}_2(40\%)\text{@CdS}$  composite agreed with the H1-type hysteresis loop, which is relatively parallel and nearly vertical. The H1 hysteresis loop often suggests that a material with this type of curve is composed of holes of a uniform size and regular shape. The adsorption–desorption isotherm of the composite is either a type IV isotherm or a type V isotherm. In particular, at low pressure, the characteristics of the isotherm line conform to the V type isotherm, while, at high pressure, the characteristics of the isotherm line conform to the type IV isotherm. As a result, though there were lots of pores in the rod-like construction of  $\text{TiO}_2(30\%)\text{@CdS}$ , its pore size distribution uniformity and pore–channel connectivity were inferior to that of the  $\text{TiO}_2(40\%)\text{@CdS}$  composite. Among all of four composites, the  $\text{TiO}_2(30\%)\text{@CdS}$  composite had the smallest specific surface area, the largest pore size, and its morphology was less uniform than that of the  $\text{TiO}_2(40\%)\text{@CdS}$  composite. The nitrogen adsorption–desorption isotherms of the  $\text{TiO}_2(20\%)\text{@CdS}$  nanoparticle and  $\text{TiO}_2(50\%)\text{@CdS}$  composites did not fit to both of the type IV or type V isotherms. This type of isotherm was consistent with their irregular morphologies, and also revealed the poor connectivity of the channels, and the inhomogeneous pore size distribution in the two composites with the  $\text{TiO}_2$  contents of 20% and 50% [34]. The low efficiencies of both  $\text{TiO}_2(20\%)\text{@CdS}$  and  $\text{TiO}_2(50\%)\text{@CdS}$  composites are verified by their photocatalytic performance.

Table 1 shows that the  $\text{TiO}_2(40\%)\text{@CdS}$  composite has the maximum specific surface area and the minimum pore volume among the four composites, which might have contributed to the formation of the ideal optimal space configuration of the catalyst between the nanoparticles and the

nanorods. It simultaneously reduced the agglomeration effect between the CdS nanoparticle and the TiO<sub>2</sub> nanorods.

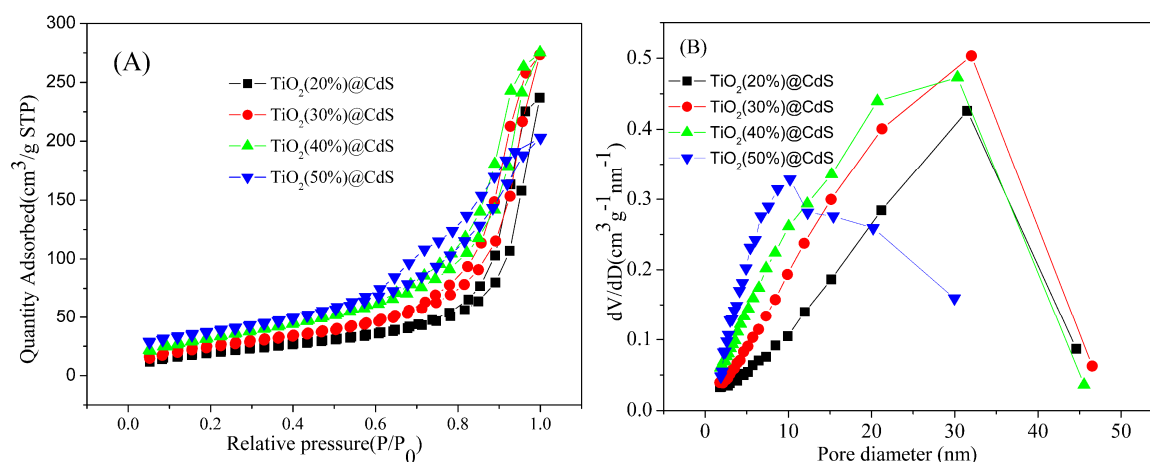


**Figure 7.** N<sub>2</sub> adsorption–desorption isothermal graphs (A) and pore size distribution (B) of TiO<sub>2</sub>(20%)@CdS, TiO<sub>2</sub>(30%)@CdS, TiO<sub>2</sub>(40%)@CdS, and TiO<sub>2</sub>(50%)@CdS composites.

**Table 1.** Specific surface area and pore volume of the sample.

Project Type Size	BET Surface Area (m <sup>2</sup> /g)	Pore Size (nm)
TiO <sub>2</sub> (40%)@CdS	61.4	35.5
TiO <sub>2</sub> (30%)@CdS	53.6	42.7
TiO <sub>2</sub> (40%)@CdS	107.5	14.6
TiO <sub>2</sub> (50%)@CdS	86.5	25.7

## 2.6. Photocatalytic Performance

As is illustrated in Figure 8, the adsorption efficiencies of the as-prepared composites for methyl orange under the darkness condition were essentially the same. In the photodegradation reaction with 50 mg of the catalyst, 50 mg/L of methyl orange solution was completely decolorized by the TiO<sub>2</sub>(40%)@CdS composite after 40 min. The absorption intensities of the dye were monitored by utilizing a UV-vis spectrophotometer. After 30 min, the degradation rate of TiO<sub>2</sub>(40%)@CdS composite proved to be rapid and nearly constant; after that, the degradation rate slowed up slightly due to a decrease in the dye concentration (Figure 8a). For the TiO<sub>2</sub>(50%)@CdS composite, a time interval of about 60 min was required for the complete removal of the dye, and the degradation rate in the first 50 min was slightly faster than that in the last 10 min. The time required for the complete decomposition of the dye was more than 70 min for both of the TiO<sub>2</sub>(30%)@CdS and the TiO<sub>2</sub>(20%)@CdS composite, with the degradation rate of the former composite being slightly higher (Figure 8A). The reaction kinetics of the degradation of the dye by the presence of the catalytic composites could be evaluated from the linear relationship between the  $\ln(C_t/C_0)$  vs. time. Figure 8B showed that there were good linear relationships between the  $\ln(C_t/C_0)$  vs. time [32], revealing the characteristics of the pseudo-first order reaction kinetics. According to the slopes of the above lines, it was apparent that TiO<sub>2</sub>(40%)@CdS possessed the best degradation performance, and it was followed by TiO<sub>2</sub>(50%)@CdS, TiO<sub>2</sub>(30%)@CdS and TiO<sub>2</sub>(20%)@CdS, respectively.

Furthermore, in order to evaluate the stability and retention of the photocatalytic abilities of the catalyst, it was used and reused several times, and the results are recorded in Figure 9. The cycling performance of the TiO<sub>2</sub>(40%)@CdS composite was evaluated in detail. In this experiment, the dye of MO was added in batches, while the catalyst remained unchanged. After the solution became clear, another batch of MO dye was added and the cycle was repeated. Ten cycles of the experiments were conducted to evaluate the persistence of the catalyst.

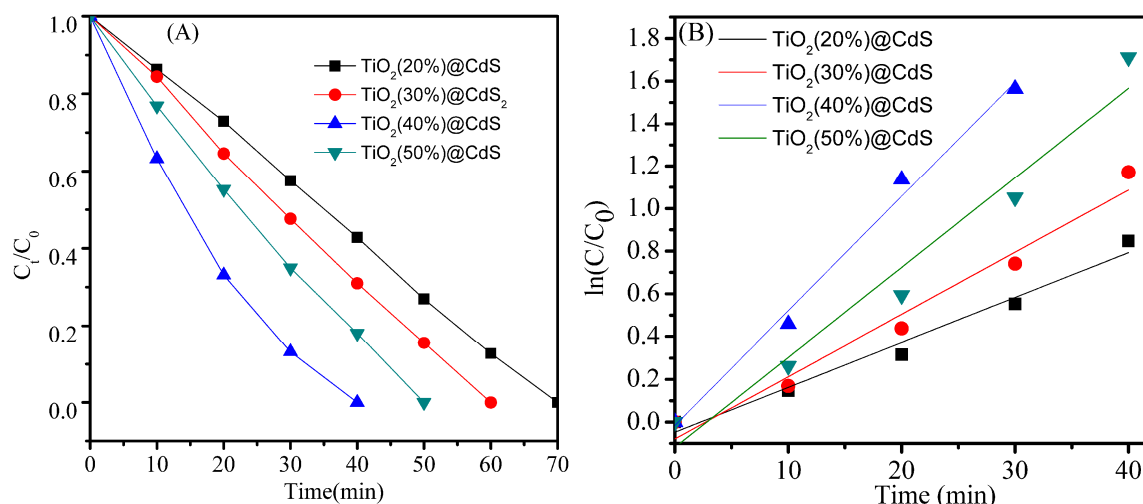


**Figure 8.** (A) Photocatalytic degradation of methyl orange of TiO<sub>2</sub> nanorod–CdS nanoparticle composites; (B) first order kinetic equation of TiO<sub>2</sub> nanorod–CdS nanoparticle composites.

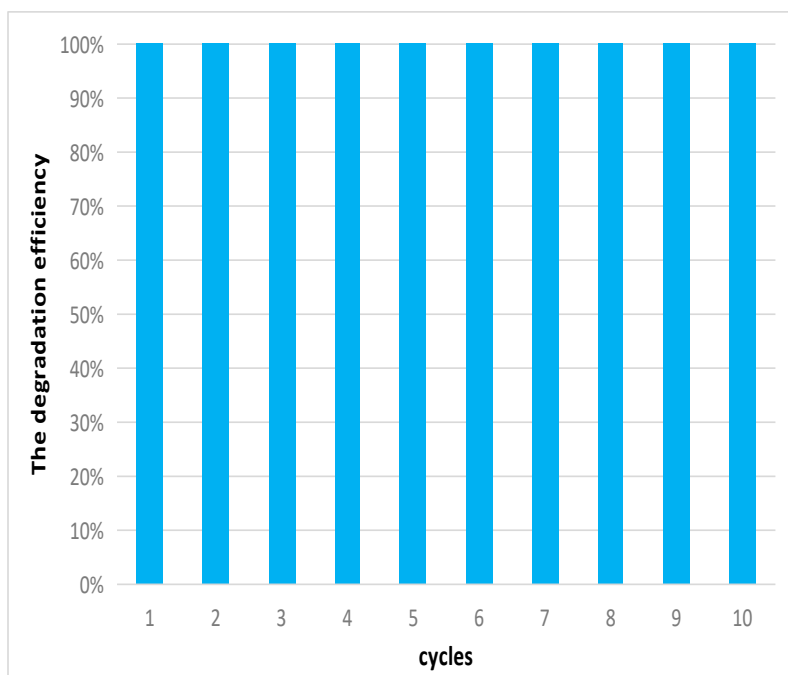


**Figure 9.** Cyclic degradation of MO by the catalyst of TiO<sub>2</sub>(40%)@CdS under light irradiation with a reaction time of 120 min for each cycle.

As shown in Figure 9, the TiO<sub>2</sub>(40%)@CdS showed excellent stability due to the retention of its 100% degradation efficiency, even after 10 cycles. This long-term cycling performance indicates that adsorption of dye on the catalyst surface did not affect its subsequent catalytic degradation ability.

As discussed above, the TiO<sub>2</sub>(40%)@CdS was a mutual complex, which was formed by CdS nanoparticles and TiO<sub>2</sub> nanorod (Figure 10). Moreover, CdS nanoparticles uniformly adhered onto the surface of the TiO<sub>2</sub> nanorods, and a compact structure was formed between the two components [34,35]. Due to the low band gap of the CdS nanoparticles (2.11 eV), the photogenerated electrons could be transferred from the valence band of CdS nanoparticles to the conduction band of the TiO<sub>2</sub> nanorods, and thus the band gap energy of the as-prepared composite was reduced in order to promote the degradation of the dye (Figure 10).

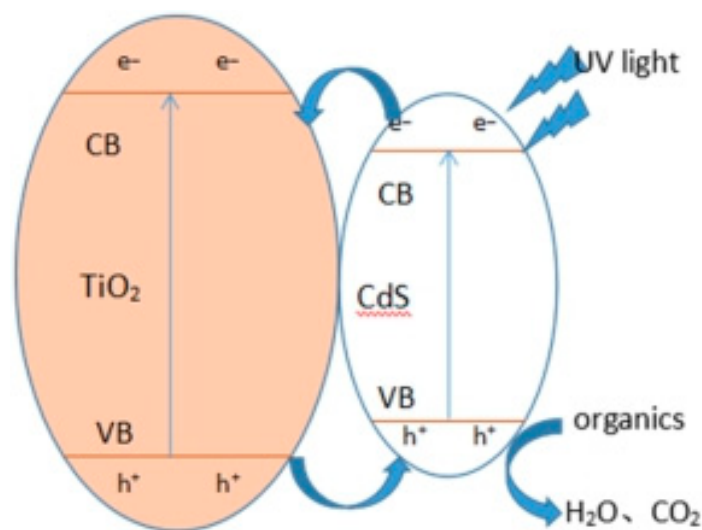


Figure 10. Mechanism of photodegradation.

### 3. Materials and Methods

#### 3.1. Preparation of the Composite of TiO<sub>2</sub> Nanorods and CdS Nanoparticles

##### 3.1.1. Equipment and Reagents

Equipment: Heat collector magnetic stirrer with constant temperature (DF-101S Guang Zheng Medical Instrument Co. Ltd., Shanghai, China), desktop high speed centrifuge (TG16-WS XiangYi Centrifuge Instrument Company, Changsha, China), electronic balance (CP225D Yuhua Instrument Co., Ltd., Gongyi, China), vacuum drying oven (DZF-6050 Shanghai Boxun Industrial Co., Ltd., Shanghai, China), magnetic stirrer (90 Shanghai Huxi Analysis Instrument Factory, Shanghai, China), 300 W xenon lamp power (PLS-SXE300 Beijing Perfect Light Technology Co., Ltd., Beijing, China).

Reagent: Sodium sulfide (Na<sub>2</sub>S·9H<sub>2</sub>O, AR), ammonium hydroxide (NH<sub>3</sub>·H<sub>2</sub>O, AR), sulfuric acid (H<sub>2</sub>SO<sub>4</sub> 98%, AR), potassium permanganate (KMnO<sub>4</sub>, AR), hydrogen peroxide (H<sub>2</sub>O<sub>2</sub>, AR), cetyltrimethylammonium bromide (CTAB, AR), n-amyl alcohol (C<sub>5</sub>H<sub>12</sub>O, AR), n-hexane (C<sub>6</sub>H<sub>14</sub>, AR), titanium trichloride (TiCl<sub>3</sub>, AR), ethanol (C<sub>2</sub>H<sub>6</sub>O, AR, Xilong Scientific Co. LTD., Shantou, China).

##### 3.1.2. Experimental Procedure

Preparation of CdS nanoparticles: an 0.05M CdCl<sub>2</sub> solution was obtained by dissolving 1.1442 g of CdCl<sub>2</sub>·5H<sub>2</sub>O in a 100 mL volumetric flask, which was referred to as solution A. A total of 50 mL of 5% aqueous ammonia solution was obtained by diluting the 10 mL of 25% ammonia water with the additional 40 mL of deionized water, which was designated as solution B. A total of 25 mL of the solution A and 20 mL of solution B were mixed in a beaker and then transferred to a 100 mL volumetric flask. Furthermore, at the same time, a white flocculent precipitate appeared in the volumetric flask; the pH of the solution was determined to be about 11. Then, 0.0752g of Na<sub>2</sub>S·9H<sub>2</sub>O was placed in a beaker, dissolved in a small amount of water, transferred into a 100 mL volumetric flask, and then a 3.13 mM Na<sub>2</sub>S solution was obtained. The white flocculent precipitate and 3.13 mM Na<sub>2</sub>S solution were mixed together and vigorously stirred for 30min, and a yellow precipitate was obtained. It was washed with water and centrifuged (three times), and then the resulting precipitate was dried in a vacuum oven at 60 °C for one day.

Preparation of TiO<sub>2</sub> nanorod–CdS nanoparticle composites: a total of 5.8 g of CTAB was dissolved in a mixture solution of 10 mL of n-pentanol and 60 mL of n-hexane. The beaker was sealed with cling film and the solution was stirred to obtain liquid A. A total of 10 mg of the above CdS nanoparticles and 10 mL of deionized water was mixed to form a dispersion solution, which was liquid B. Liquid B

was slowly added to liquid A and the mixture solution was vigorously stirred at room temperature for 30 min to form liquid C. Then, a certain amount of  $\text{TiCl}_3$  (0.032 mM, 0.054 mM, 0.084 mM and 0.127 mM) solution was added to liquid C solution and magnetically stirred. The resultant liquid was then transferred to a 100 mL Teflon-lined stainless steel autoclave and placed in an oven at 200 °C for 6 h. The resulting product was centrifuged and washed with deionized water and alcohol several times, and was finally placed in a vacuum oven to dry for one day. The final product was named  $\text{TiO}_2(\text{x}\%)\text{@CdS}$  composite,  $\text{x} = 20, 30, 40, 50$ .

### 3.2. Characterization of Physical Performance

X-ray powder diffraction (XRD, Rigaku, RINT 2000,  $\text{CuK}\alpha$  emission line  $\lambda = 0.15418$  nm) was used for the analysis of the phase and textural properties of the sample. The microstructure and lattice structure of the sample were determined using scanning electron microscopy (SEM, JSM-6700F, JEOL, Tokyo, Japan). A UV-visible Diffuse Reflectance Spectrophotometer was used to test the spectral absorption of the samples with an Integrating Sphere (DRS, DUV3700, Shimadzu, Kyoto, Japan), using  $\text{BaSO}_4$  as the background material.

### 3.3. Characterization of the Photocatalytic Activities of the Catalysts

A total of 50 mL of 50 mg/L methyl orange solution was placed in a beaker. Furthermore, 50 mg of the photocatalyst material was added into the beaker, with magnetite stirring in the dark for 30 min in order to maintain the adsorption/desorption balance of methyl orange on the catalyst surface [36]. Furthermore, 3 mL of the solution was sampled from the beaker and then centrifuged, and the concentration of the remaining MO was determined as  $C_0$  by a UV-vis spectrophotometer. After the photocatalytic degradation reaction was initiated, aliquots (3 mL) of the solution were sampled at every 10 min interval, and were centrifuged to remove the photocatalyst particles for UV-vis measurements. The vertical distance between the light source and the beaker was 5 cm, and the temperature of the beaker was kept at 25 °C, with cooling water flowing in a circulating constant temperature jacket. The light intensity was adjusted to 30  $\text{mW}/\text{cm}^2$  during the photocatalytic degradation reaction. The blank test without the presence of the photocatalyst was also conducted to distinguish the degradation of the dye. The remaining concentration of the dye was monitored by measuring the maximum absorbance at 463 nm for MO through a UV-Vis spectrophotometer (UV-2550, Shimadzu, Kyoto, Japan). The sampling operation was repeated until the color of the solution did not change. The solution in the tube was measured with a visible light spectrophotometer for absorbance. Different photocatalysts (different ratios of CdS nanoparticles to  $\text{TiO}_2$  nanorods) were tested according to the above steps. A catalytic degradation map was drawn based on the absorbance, and the performances of the catalysts were compared. The durability of the photocatalyst  $\text{TiO}_2(40\%)\text{CdS}$  was also evaluated in the cyclic degradation of MO by  $\text{TiO}_2(40\%)\text{CdS}$ . The specific operation steps are as follows: a total of 0.05 g of  $\text{TiO}_2(40\%)\text{CdS}$  was added to 50 mL of MO solution (50 mg/L), and the photocatalytic degradation reaction was conducted as the method described above, and the reaction time for each run was set to 120 min. After each run of the degradation reaction, the  $\text{TiO}_2(40\%)\text{CdS}$  sample was recovered from the solution by centrifugation and rinsed with distilled water once. Then, the  $\text{TiO}_2(40\%)\text{CdS}$  was reused in the next round of the experiments, which were conducted under the same conditions.

## 4. Conclusions

In this study, a novel method for preparing CdS nanoparticles was introduced. CdS nanoparticles were prepared at room temperature, and a reaction was then triggered with  $\text{TiCl}_3$ , using a solvothermal treatment to prepare  $\text{TiO}_2(\text{x}\%)\text{@CdS}$ . The contents of  $\text{TiO}_2$  in the composites have a crucial influence on the tuning of the morphologies of the obtained composites. The composite structures in which nanoparticles uniformly grew on nanorods to form composites were mainly attributed to the differences between nanoparticle and nanorod sizes. Nanorods controlled the mutual aggregation of nanoparticles, resulting in a large specific surface area for the as-prepared composites, which was beneficial to

strengthen the contact between the compound and the contaminants and, consequently, improved the decolorization rate due to the utilization of light during the process of photocatalysis. Photocatalytic experiments were designed to meet the need to select an optimal ratio compound. It was found that the  $\text{TiO}_2(40\%)\text{@CdS}$  composites were the ideal candidates with the highest photocatalytic properties. SEM images clearly showed that CdS nanoparticles were uniformly distributed on the  $\text{TiO}_2$  nanorods, a result which could only be obtained nanorods with content of 40%  $\text{TiO}_2$ . The band gap energy of the  $\text{TiO}_2(40\%)\text{@CdS}$  composite was the lowest (2.55 eV) of all the as-prepared composites, which is good for extending the range of the photo response. The cyclic degradation evaluation of methyl orange demonstrated that the  $\text{TiO}_2(40\%)\text{@CdS}$  composite was sufficiently stable, and the photocatalytic properties and cycle performance were excellent. This study produced a good photocatalyst with outstanding photocatalytic properties and provided a feasible solution for the degradation of organic pollutants in water.

**Author Contributions:** Conceptualization, J.S.; methodology, Y.X. and F.Z.; formal analysis, J.S., Y.X. and S.R. Investigation, J.S. and Y.X.; data curation, F.W. and J.Z. (Jinsheng Zhao) ; ; Visualization, D.Z.; writing—original draft preparation, J.S.; writing—review and editing, Y.X., and J.Z. (Jinsheng Zhao); visualization, J.Z. (Jinbing Zhang); supervision, L.W. All authors have read and agreed to the published version of the manuscript.

**Funding:** This research was funded by the National Natural Science Foundation of China (No. 51664047, 21667019), the Key Project of Natural Science Foundation of Jiangxi Province (No. 20171ACB20016), the Jiangxi Province Major Academic and Technical Leaders Cultivating Object Program (No. 20172BCB22014), the Science and Technology Department of Jiangxi Province (No. 20181BCB18003 and 20181ACG70025), the Key Laboratory of Photochemical Conversion and Optoelectronic Materials, TIPC, CSA (No. PCOM201906), and the Key Project of Science and Technology Research of the Jiangxi Provincial Department of Education (No. DA201602063, GJJ191044, GJJ191058), the Aviation Science Foundation of China (No. 2017ZF56020), and Fujian Key Laboratory of Measurement and Control System for of Shore Environment (No. S1-KF1703). Thanks to Edward C. Mignot, Shandong University, for linguistic advice.

**Conflicts of Interest:** The authors declare no conflict of interest.

## References

1. Murgolo, S.; Franz, S.; Arab, H.; Bestetti, M.; Falletta, E.; Mascolo, G. Degradation of emerging organic pollutants in wastewater effluents by electrochemical photocatalysis on nanostructured  $\text{TiO}_2$  meshes. *Water Res.* **2019**, *164*, 114920. [CrossRef] [PubMed]
2. Linsebigler, A.L.; Lu, G.; Yates, J.T. Photocatalysis on  $\text{TiO}_2$  surfaces: Principles, mechanisms, and selected Results. *Chem. Rev.* **1995**, *95*, 735–758. [CrossRef]
3. Cabrera-Rein, A.; Martínez-Piernas, A.B.; Yannis, B.; Xekoukoulotakis, N.P.; Agüera, A.; Pérezbd, J.A.  $\text{TiO}_2$  photocatalysis under natural solar radiation for the degradation of the carbapenem antibiotics imipenem and meropenem in aqueous solutions at pilot plant scale. *Water Res.* **2019**, *166*, 115037. [CrossRef] [PubMed]
4. Tang, H.; Prasad, K.; Sanjines, R.; Schmid, P.E.; Levy, F. Electrical and optical properties of  $\text{TiO}_2$  anatase thin films. *J. Appl. Phys.* **1994**, *75*, 2042–2047. [CrossRef]
5. Burda, C.; Lou, Y.; Chen, X.; Samia, A.C.; Stout, J.; Gole, J.L. Enhanced nitrogen doping in  $\text{TiO}_2$  nanoparticles. *Nano Lett.* **2003**, *3*, 1049–1051. [CrossRef]
6. Antonelli, D.M.; Ying, J.Y. Synthesis of hexagonally packed mesoporous  $\text{TiO}_2$  by a modified sol-gel method. *Angew. Chem. Int. Edit.* **1995**, *34*, 2014–2017. [CrossRef]
7. Kovacic, M.; Papac, J.; Kusic, H.; Karamanis, P.; Bozic, A.L. Degradation of polar and non-polar pharmaceutical pollutants in water by solar assisted photocatalysis using hydrothermal  $\text{TiO}_2\text{-SnS}_2$ . *Chem. Eng. J.* **2020**, *382*, 122826. [CrossRef]
8. Huang, R.; Zhang, S.L.; Ding, J.; Meng, Y.H.; Zhong, Q.; Kong, D.S.; Gu, C.J. Effect of adsorption properties of phosphorus-doped  $\text{TiO}_2$  nanotubes on photocatalytic NO removal. *J. Colloid. Interf. Sci.* **2019**, *553*, 647–654. [CrossRef]
9. Zhang, S.B.; Zhao, Y.C.; Yang, J.P.; Zhang, J.Y.; Zheng, C.G. Fe-modified  $\text{MnOx/TiO}_2$  as the SCR catalyst for simultaneous removal of NO and mercury from coal combustion flue gas. *Chem. Eng. J.* **2018**, *348*, 618–629. [CrossRef]



10. Kazemi, M.L.; Sui, R.H.; Clark, P.D.; Marriott, R.A. Catalytic combustion of Claus tail gas: Oxidation of sulfur species and CO using gold supported on lanthanide-modified TiO<sub>2</sub>. *Appl. Catal. A Gen.* **2019**, *578*, 117256. [CrossRef]
11. Lin, F.; Zhang, Y.N.; Wang, L.; Zhang, Y.L.; Wang, D.G.; Yang, M.; Yang, J.H.; Zhang, B.Y.; Jiang, Z.X.; Li, C. Highly efficient photocatalytic oxidation of sulfur-containing organic compounds and dyes on TiO<sub>2</sub> with dual cocatalysts Pt and RuO<sub>2</sub>. *Appl. Catal. B Environ.* **2012**, *127*, 363–370. [CrossRef]
12. Pei, X.L.; Jiang, C.J.; Chen, W. Enhanced hydrolysis of 1,1,2,2-tetrachloroethane by multi-walled carbon nanotube/TiO<sub>2</sub> nanocomposites: The synergistic effect. *Environ. Pollut.* **2019**, *255*, 113211. [CrossRef] [PubMed]
13. Wang, Y.Y.; Yang, C.Z.; Chen, A.; Pu, W.H.; Gong, J.Y. Influence of yolk-shell Au@TiO<sub>2</sub> structure induced photocatalytic activity towards gaseous pollutant degradation under visible light. *Appl. Catal. B Environ.* **2019**, *251*, 57–65. [CrossRef]
14. Elfalleh, W.; Assadi, A.A.; Bouzaza, A.; Wolbert, D.; Kiwi, J.; Rtimi, S. Innovative and stable TiO<sub>2</sub> supported catalytic surfaces removing aldehydes under UV-light irradiation. *J. Photoch. Photobio A Chem.* **2017**, *343*, 96–102. [CrossRef]
15. Zhang, G.; Gao, M.; Tian, M.; Zhao, W.F. In situ hydrothermal preparation and photocatalytic desulfurization performance of graphene wrapped TiO<sub>2</sub> composites. *J. Solid. State. Chem.* **2019**, *279*, 120953. [CrossRef]
16. Pozo-Antonio, J.S.; Dionísio, A. Self-cleaning property of mortars with TiO<sub>2</sub> addition using real diesel exhaust soot. *J. Clean. Prod.* **2017**, *161*, 850–859. [CrossRef]
17. Chai, W.M.; Zhu, W.D.; Chen, D.D.; Chen, D.Z.; Xi, H.; Chang, J.J.; Zhang, J.C.; Zhang, C.F.; Hao, Y. Combustion-processed NiO/ALD TiO<sub>2</sub> bilayer as a novel low-temperature electron transporting material for efficient all-inorganic CsPbIBr<sub>2</sub> solar cell. *Sol. Energy* **2020**, *203*, 10–18. [CrossRef]
18. Wang, J.M.; Zhang, C.; Yang, Y.Q.; Fan, A.L.; Chi, R.F.; Shi, J.; Zhang, X.Y. Poly (vinyl alcohol) (PVA) hydrogel incorporated with Ag/TiO<sub>2</sub> for rapid sterilization by photoinspired radical oxygen species and promotion of wound healing. *Appl. Surf. Sci.* **2019**, *494*, 708–720. [CrossRef]
19. Yu, Z.C.; Wang, S.; Han, L.; Niu, Y.L. Photocatalytic property of nanostructured S doped TiO<sub>2</sub> films prepared by the micro plasma method. *Rare. Metal. Mat. Eng.* **2015**, *44*, 1629–1632.
20. Xie, Y.; Wu, J.; Sun, C.Y.; Ling, Y.; Li, S.Q.; Li, X.; Zhao, J.S.; Yang, K. La<sub>2</sub>O<sub>3</sub>-modified graphite carbon nitride achieving the enhanced photocatalytic degradation of different organic pollutants under visible light irradiation. *Mater. Chem. Phys.* **2020**, *246*, 122846. [CrossRef]
21. Ren, Y.F.; Li, W.T.; Cao, Z.H.; Jiao, Y.P.; Xu, J.J.; Liu, P.; Li, S.; Li, X. Robust TiO<sub>2</sub> nanorods-SiO<sub>2</sub> core-shell coating with high-performance self-cleaning properties under visible light. *Appl. Surf. Sci.* **2020**, *509*, 145377. [CrossRef]
22. Baena-Moreno, F.M.; Rodriguez-Galán, M.; Vega, F.; Alonso-Farinás, Vilches Arenas, L.F.; Navarrete, B. Carbon capture and utilization technologies: A literature review and recent advances. *Energy Source Part A* **2019**, *41*, 1403–1433. [CrossRef]
23. Ibrahim, H.; Ilinca, A.; Perron, J. Energy storage systems-characteristics and comparisons. *Renew. Sust. Energy. Rev.* **2008**, *12*, 1221–1250. [CrossRef]
24. Kavil, J.; Alshahrie, A.; Periyat, P. CdS sensitized TiO<sub>2</sub> nano heterostructures as sunlight driven photocatalyst. *Nano Struct. Nano Objects* **2018**, *16*, 24–30. [CrossRef]
25. Yang, G.D.; Yang, B.L.; Xiao, T.C.; Yan, Z.F. One-step solvothermal synthesis of hierarchically porous nanostructured CdS/TiO<sub>2</sub> heterojunction with higher light photocatalytic activity. *Appl. Surf. Sci.* **2013**, *283*, 402–410. [CrossRef]
26. Du, Y.B.; Zhang, L.; Ruan, M.; Niu, C.G.; Wen, X.J.; Liang, C.; Zhang, X.G.; Zeng, G.M. Template-free synthesis of three-dimensional porous CdS/TiO<sub>2</sub> with high stability and excellent visible photocatalytic activity. *Mater. Chem. Phys.* **2018**, *212*, 69–77. [CrossRef]
27. Liu, Y.Y.; Xie, Y.; Ling, Y.; Jiao, J.L.; Li, X.; Zhao, J.S. Facile construction of a molybdenum disulphide/zinc oxide nanosheet hybrid for an advanced photocatalyst. *J. Alloys Compd.* **2019**, *778*, 761–767. [CrossRef]
28. Zeng, D.D.; Yang, L.M.; Zhou, P.P.; Hu, D.S.; Xie, Y.; Li, S.Q.; Jiang, L.S.; Ling, Y.; Zhao, J.S. Au-Cu alloys deposited on titanium dioxide nanosheets for efficient photocatalytic hydrogen evolution. *Int. J. Hydrogen Energy* **2018**, *43*, 15155–15163. [CrossRef]
29. Han, J.; Su, H.L.; Dong, Q.; Zhang, D.; Ma, X.X.; Zhang, C.F. Patterning and photoluminescence of CdS nanocrystallites on silk fibroin fiber. *J. Nanopart. Res.* **2010**, *12*, 347–356. [CrossRef]

30. Wang, H.H.; Zhang, N.; Cheng, G.; Guo, H.; Shen, Z.W.; Yang, L.; Zhao, Y.S.; Alsaedi, A.; Hayat, T.; Wang, X.K. Preparing a photocatalytic Fe doped TiO<sub>2</sub>/rGO for enhanced bisphenol A and its analogues degradation in water sample. *Appl. Surf. Sci.* **2020**, *505*, 144640. [CrossRef]
31. Shkir, M.; Ashraf, I.M.; Alfaify, S.; El-Toni, A.M.; Ahmed, M.; Khan, A. A noticeable effect of Pr doping on key optoelectrical properties of CdS thin films prepared using spray pyrolysis technique for high-performance photodetector applications. *Ceram. Int.* **2020**, *46*, 4652–4663. [CrossRef]
32. Sun, C.Y.; Xu, Q.H.; Xie, Y.; Ling, Y.; Jiao, J.L.; Zhu, H.H.; Zhao, J.S.; Liu, X.M.; Hu, B.; Zhou, D. High-efficient one-pot synthesis of carbon quantum dots decorating Bi<sub>2</sub>MoO<sub>6</sub> nanosheets heterostructure with enhanced visible-light photocatalytic properties. *J. Alloys Compd.* **2017**, *723*, 333–344. [CrossRef]
33. Fu, H.H.; Yang, L.M.; Hu, D.S.; Yu, c.; Ling, Y.; Xie, Y.; Li, S.Q.; Zhao, J.S. Titanium dioxide nano-heterostructure with nanoparticles decorating nanowires for high-performance photocatalysis. *Int. J. Hydrogen Energ.* **2018**, *43*, 10359–10367. [CrossRef]
34. Tu, H.; Li, D.; Yi, Y.; Liu, R.; Wu, Y.; Dong, X.Y.; Shi, X.W.; Deng, H.B. Incorporation of rectorite into porous polycaprolactone/TiO<sub>2</sub> nanofibrous mats for enhancing photocatalysis properties towards organic dye pollution. *Compos. Commun.* **2019**, *15*, 58–63. [CrossRef]
35. Wu, J.; Xie, Y.; Ling, Y.; Dong, Y.Y.; Li, J.; Li, S.Q.; Zhao, J.S. Synthesis of flower-like g-C<sub>3</sub>N<sub>4</sub>/BiOBr and enhancement of the activity for the degradation of bisphenol A under visible light irradiation. *Front. Chem.* **2019**, *7*, 649. [CrossRef] [PubMed]
36. Zhu, H.Y.; Jiang, R.; Xiao, L.; Liu, L.; Cao, C.H.; Zeng, G.M. CdS nanocrystals/TiO<sub>2</sub>/crosslinked chitosan composite: Facile preparation, characterization and adsorption-photocatalytic properties. *Appl. Surf. Sci.* **2013**, *273*, 661–669. [CrossRef]



© 2020 by the authors. Licensee MDPI, Basel, Switzerland. This article is an open access article distributed under the terms and conditions of the Creative Commons Attribution (CC BY) license (<http://creativecommons.org/licenses/by/4.0/>).

## Article

# Enhanced Visible-Light Driven Photocatalytic Activity of Ag@TiO<sub>2</sub> Photocatalyst Prepared in Chitosan Matrix

Ivana Grčić <sup>1,\*</sup> , Andreja Gajović <sup>2</sup>, Milivoj Plodinec <sup>3</sup>, Kristina Šimunković <sup>1</sup>, Hrvoje Ivanković <sup>4</sup> and Marc-Georg Willinger <sup>5</sup> 

<sup>1</sup> Faculty of Geotechnical Engineering, University of Zagreb, Hallerova aleja 7, HR-42000 Varaždin, Croatia; kristina.simunkovic@gfv.hr

<sup>2</sup> Center of Excellence for Advanced Materials and Sensing Devices, Ruđer Bošković Institute, Bijenička 54, HR-10000 Zagreb, Croatia; andreja.gajovic@irb.hr

<sup>3</sup> Fritz-Haber-Institut der Max-Planck-Gesellschaft, Faradayweg 4-6, 14195 Berlin, Germany; mplodinec@fhi-berlin.mpg.de

<sup>4</sup> Faculty of Chemical Engineering and Technology, University of Zagreb, Marulićev trg 19, HR-10000 Zagreb, Croatia; hivan@fkit.hr

<sup>5</sup> ETH Zürich, Auguste-Piccard-Hof 1, 8093 Zürich, Switzerland; marc.willinger@scopem.ethz.ch

\* Correspondence: igrcic@gfv.hr

Received: 7 June 2020; Accepted: 4 July 2020; Published: 8 July 2020

**Abstract:** Ag doped TiO<sub>2</sub> photocatalysts (Ag@TiO<sub>2</sub>) were prepared with an aim to extend the absorption range of TiO<sub>2</sub> into the visible region, for tentative application under solar irradiation. Photocatalyst synthesized by the novel method using chitosan for reduction of Ag<sup>+</sup> to Ag<sup>0</sup> nanoparticles was compared to similar catalysts previously reported. The photocatalytic activity of Ag@TiO<sub>2</sub> obtained by a simple novel method was evaluated based on degradation of salicylic acid as a model compound. The higher activity under visible irradiation can be attributed to the surface plasmon resonance and suppression of the electron-hole recombination when deposition of Ag nanoparticles on TiO<sub>2</sub> was achieved using chitosan. The photocatalysts were characterized by X-ray diffraction (XRD), Raman spectroscopy, transmission electron microscopy (TEM), high resolution TEM (HRTEM), energy dispersive X-ray spectroscopy (EDXS), selected area diffraction (SAED), and diffuse reflectance spectroscopy (DRS). The photochromism of Ag was observed and explained.

**Keywords:** Ag-doped TiO<sub>2</sub>; chitosan; solar photocatalysis; photochromism

## 1. Introduction

Advanced oxidation processes (AOPs) which involve the generation of highly reactive hydroxyl radicals (HO<sup>•</sup>), have emerged as a promising water and wastewater treatment technology for the degradation of a wide range of organic contaminants [1–3]. High toxicity and resistivity to biodegradation of organic compounds like pharmaceuticals, pesticides, and hormones present in municipal and industrial wastewater pose a threat to the environment and human and animal health and may also affect aquatic organisms in an unpredictable way. In recent years, semiconductor photocatalysis has shown a great potential as a low-cost, environmental friendly and sustainable treatment technology to align with the “zero” waste scheme in the water/wastewater treatment. The ability of this advanced oxidation technology to achieve partial or complete mineralization of persistent organic compounds has been widely demonstrated [4–6]. Application of solar photocatalysis is particularly interesting [7].

The mechanism of a semiconductor photocatalysis has been thoroughly explained in the literature [8,9]. A large number of semiconductor oxides showed good photocatalytic activity. Among these, nanosized  $\text{TiO}_2$  is one of the most promising photocatalysts due to its many advantages, such as high photosensitivity, chemical stability, nontoxicity, easy availability, environmental acceptability, and low cost [10–12].

Still, there are also some shortcomings appearing during the practical application of  $\text{TiO}_2$ . The band gap energy, e.g., is 3.2 eV for anatase and 3.0 eV for rutile and the light wavelength for such photon energy corresponds to  $\lambda < 400$  nm. Therefore,  $\text{TiO}_2$  absorbs radiation of wavelength below the visible range of light spectrum. Thus, in wastewater treatment by  $\text{TiO}_2$  photocatalysis only UV light could be used. The overall efficiency is significantly reduced under sunlight, which consists of 43% visible and only a 5% UV fraction. Furthermore, the charge carrier recombination rate is high and photogenerated electron–hole pairs easily recombine in femtoseconds, which reduces photocatalytic efficiency [4,6,13].

To overcome these limitations of  $\text{TiO}_2$ , many studies have been carried out to increase the lifetime of the charge carrier and to extend the absorption range of  $\text{TiO}_2$  into the visible region. These studies involved the addition of various dopants to  $\text{TiO}_2$  nanoparticles or  $\text{TiO}_2$  nanocomposites such as metals or metal ions (Fe, Mn, Cu, Zn, Zr, Sb, and Ce), non-metals (B, C, N, P, and S) [14–17], noble metals (Ag, Pt, and Pd), [11,17–19] and photosensitization of  $\text{TiO}_2$  with organic dyes, most often phthalocyanine dyes [20]. Among the noble metals used as electron traps, Ag is extremely suitable for industrial application due to its low cost and easy preparation.  $\text{TiO}_2$  doped with Ag has been a feasible approach to narrow the band gap of  $\text{TiO}_2$ , thereby enhancing its visible light photocatalytic activity. The quantum-sized behavior of Ag nanoparticles has prompted considerable research interest in general. The Ag-doped  $\text{TiO}_2$  particles has therefore attracted much interest and the different methods of preparation are used, commonly the following methods: sol–gel, deposition–precipitation, photocatalytic deposition, and deposition–precipitation with photoreduction. In [12], the Ag-doped  $\text{TiO}_2$  photocatalyst was prepared by a sol–gel process. Degradation of organic dye Indigo carmine under visible irradiation indicated that prepared catalyst has the satisfactory photocatalytic efficiency. In [13], Ag/AgCl@ $\text{TiO}_2$  photocatalyst was prepared by the deposition–precipitation with photoreduction. The photocatalyst exhibited efficient photocatalytic activity for the degradation of 4-chlorophenol and photoreduction of Cr (VI) under visible light irradiation. In [21] Ag/AgBr@ $\text{TiO}_2$  photocatalyst was prepared by the deposition–precipitation method and photocatalytic deposition method. The catalyst showed high efficiency for the degradation of azo dyes and the destruction of bacteria under visible light irradiation.

This study demonstrates a new simple method for preparing Ag@ $\text{TiO}_2$  photocatalyst which is more efficient under solar irradiation than widely used commercial  $\text{TiO}_2$ . The reported preparation methods [13,21] were repeated in the frame of this work with the aim to compare the respective efficiencies of above mentioned photocatalysts (hereby marked as S1a–c and S2) with the newly prepared Ag@ $\text{TiO}_2$  via method involving chitosan (marked as S3). The idea was to evaluate the possible application of different Ag doped catalysts in the photocatalytic wastewater treatment under visible and solar irradiation. A novel method for preparation of Ag@ $\text{TiO}_2$  from commercial titania was presented. The method was developed according to the preparation of silver composites with chitosan studied by Twu et al. [22]. The advantage of the presented method is the simplicity per se. Ag nanoparticles were prepared on  $\text{TiO}_2$  surface using basic chitosan suspension as both stabilizer and reductant without any additional chemicals (such as  $\text{NaBH}_4$ ) or irradiation. This kind of synthesis presents a facile green method of photocatalysts applicable for large scale production. The method does not require pre-synthesis of  $\text{TiO}_2$ , since it uses commercially available  $\text{TiO}_2$  (P25) with confirmed photocatalytic activity. The use of toxic solvent is omitted thus presenting an environmentally acceptable solution. The synthesized photocatalysts were characterized and used for the degradation of salicylic acid under visible and simulated solar irradiation. The respective photocatalytic activities were compared with that of commercial non-doped  $\text{TiO}_2$  (P25). Salicylic acid (SA) was chosen as a model pollutant since it has been identified as a water pollutant which arises from a number

of sources including paper milling, cosmetic industries, and landfill leachate. The destruction of SA is of considerable interest. The SA was listed as a pollutant in precipitation, surface waters (approx.  $0.1 \mu\text{g L}^{-1}$ ) and as a constituent of humic material in drinking waters. It may be released to the aquatic environment in wastewater discharges from industry and even sewage treatment facilities [5,23]. In the light of presented results, newly prepared Ag@TiO<sub>2</sub> (S3) deserves further research of the surface phenomena applicable in the field of solar photocatalysis and application on a larger scale.

## 2. Results and Discussion

### 2.1. X-ray Diffraction (XRD) Analysis

Data of performed XRD analysis is given in Figure 1. As it can be observed, all samples contain almost the same proportion of anatase to rutile phase. Photocatalysts prepared by synthesis 1 (S1a, S1b, and S1c), i.e., by deposition–precipitation and photoreduction method using surfactant, contains a certain portion of AgCl on the surface (Figure 1b). Sample S2 contains a negligible portion of AgCl on the surface (Figure 1c). Having in mind unsuccessful reduction to Ag, samples S1a and b were completely excluded from detailed analysis, while photocatalytic activity was checked for S1c (for comparison), S2, and S3 only.

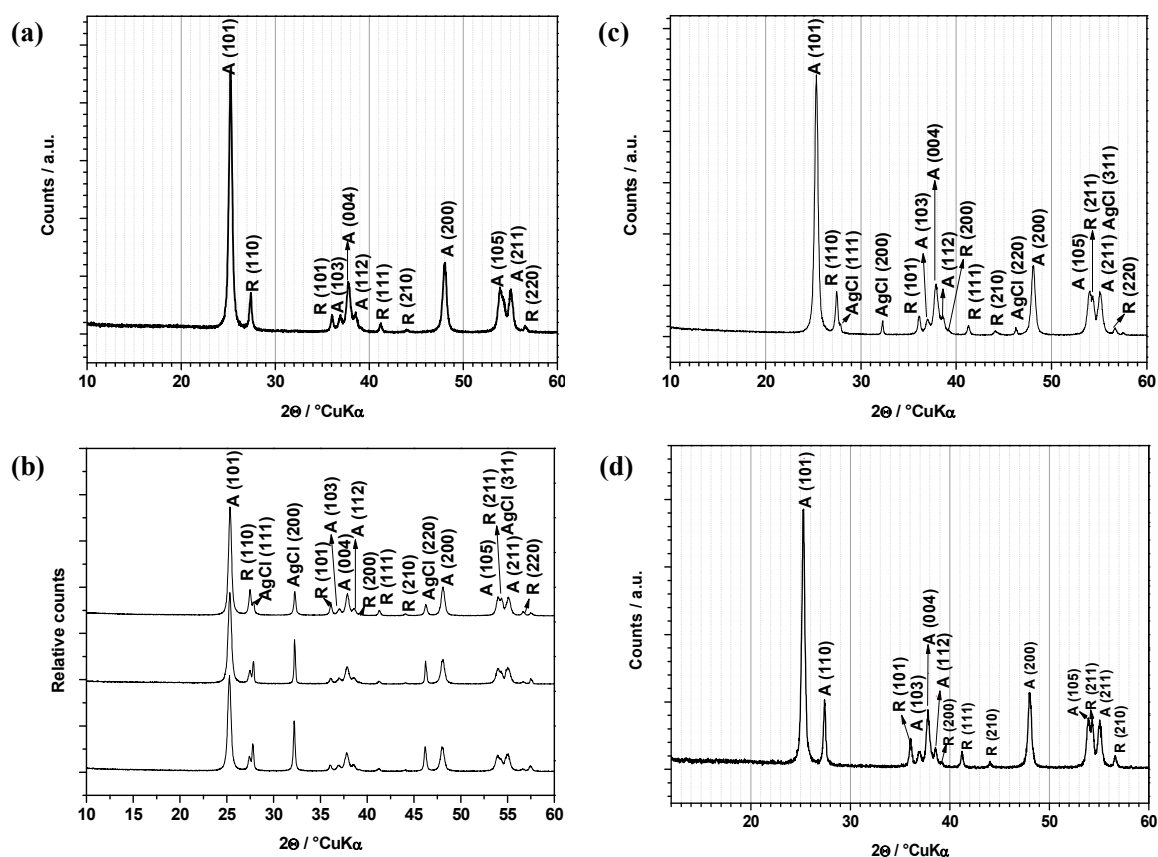


**Figure 1.** X-ray diffraction (XRD) powder patterns of prepared Ag modified TiO<sub>2</sub> photocatalysts compared to original TiO<sub>2</sub> P25 (a): S1a–c from bottom to top (b), S2 (c), and S3 (d).

According to the Scherrer equation (Equation (1)), the average crystallite size ( $D_p$ ) of the anatase and rutile in the powder was calculated from XRD data. Note that  $\beta$  stands for line broadening in radians,  $\theta$  denotes Bragg angle and  $\lambda$  is an X-ray wavelength.

$$D_p = \frac{0,94 \lambda}{\beta_{1/2} \cos \theta} \quad (1)$$

In all XRD patterns, the peaks with highest intensities of anatase (101), (004), and (200) were used to evaluate the size of nanoparticles. For size of rutile nanoparticles we used intensities of (110), (101), and (111) peaks. Calculated  $D_p$  were 20.2(6), 22.8(7), and 22(1) nm for anatase and 30(1), 30(1), and 33.8(5) for rutile, in S1c, S2, and S3, respectively, which corresponds well with the average crystallite size calculated for pure TiO<sub>2</sub> P25 (20.4(7) nm anatase and 31.6(6) nm rutile). Figure 1 indicate that amount of rutile in sample S3 (Figure 1d) is higher than in sample S2 or TiO<sub>2</sub> P25. Since only the calcination above 915 °C would lead to definite transformation of anatase to rutile phase, and the highest calcination temperature in this work was 600 °C (sample S3), the peak differences were attributed to the uncertainty of quantitative determination of crystalline phases by XRD.

## 2.2. Raman Spectroscopy Measurements

Raman spectroscopy results for samples S2 and S3 before photocatalytic reactions indicates that all the samples are dominantly in anatase form of TiO<sub>2</sub>, since all the bands characteristic to anatase (at around 145, 198, 395, 514, and 635 cm<sup>-1</sup>) were observed in the spectra (Figure 2a). Some small amount of rutile can exist in the sample S2 indicated by band at 440 cm<sup>-1</sup> having low intensity (denoted by the arrow). Anatase dominated at least at the surface of the particles since Raman spectroscopy is more sensitive to the surface than to the bulk of the particles [24]. Raman scattering cross section of the anatase phase is larger than that of the rutile. Therefore, in the case of the small amount of rutile in comparison to the anatase in the TiO<sub>2</sub> sample it is hard or impossible to observe bands characteristic for rutile.

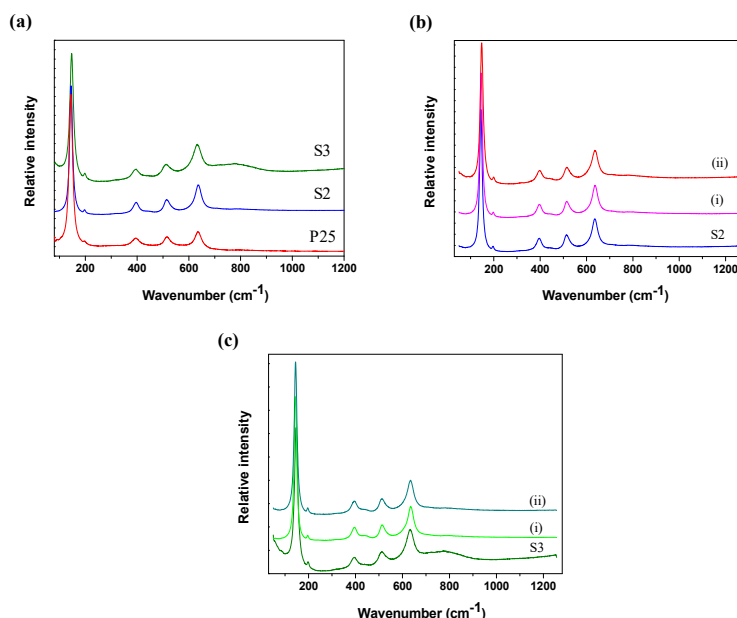


**Figure 2.** (a) Raman spectra of the starting samples before photocatalytic reactions: sample S2, and sample S3 compared to TiO<sub>2</sub> P25. (b) Comparison of Raman spectra of the sample S2 before photo-catalytic reaction (denoted by S2), after the reactions using simulated sunlight (i) and after reaction using only visible part of the spectrum (ii). (c) Comparison of Raman spectra of the sample S3 before photo-catalytic reaction (denoted by S3), after the reactions using simulated sunlight (i) and after reaction using only visible part of the spectrum (ii).

Sample S2 is recorded by Raman spectroscopy after the photocatalytic reactions that have been performed: (i) using simulated sunlight and (ii) using only visible part of the spectrum (Figure 2b). Raman spectroscopy results indicates that before and after reaction anatase form of  $\text{TiO}_2$  dominates, since all the bands characteristic to anatase (at around 144, 198, 395, 514, and  $635\text{ cm}^{-1}$ ) were observed in the spectra while the band of rutile (at  $438\text{ cm}^{-1}$ ) is hardly visible. The small shift of the anatase band at the  $144\text{ cm}^{-1}$  to the higher wavenumbers in the samples recorded after reactions: to  $145\text{ cm}^{-1}$  for the usage of sunlight (Figure 2b(i)), or to the  $147\text{ cm}^{-1}$  for visible light (Figure 2b(ii)) indicated the decrease of the order in the crystal lattice of the anatase (nano)particles, or the possible formation of the defects.

Starting sample S3 show only anatase Raman bands, while after photocatalytic reaction using sunlight of the spectrum, rutile band of very low intensity at  $438\text{ cm}^{-1}$  was observed (Figure 2c(i)). In the case of using visible part, anatase structure with only a small amount of rutile was observed as well (Figure 2c(ii)).

These results were in contradiction with the XRD results that suggested the highest ratio of rutile in S3 samples. Moreover, the Raman spectra of S3 showed certain baseline fluctuations that could cover the already weak rutile signals. Our findings showed the importance of combination of various methods for evaluation of material properties of a catalysts. In this case, one can conclude that the crystalline composition of  $\text{TiO}_2$  have not been changed during sample preparation or application.

### 2.3. Study by TEM Techniques

The structural and morphological characterizations of samples S2 and S3 by TEM methods are shown in Figures 3 and 4. TEM images show that the nanocrystals of both S2 and S3 samples are spherical, cubic-like or truncated tetragonal, and the particle size varies from less than 20 nm to about 50 nm in S2, while in S3 somewhat larger particles are also visible. The faces of the crystallites were not well defined, but the lattice fringes observed by HRTEM clearly indicated both anatase and rutile phase of the crystallites. The observed size of the rutile and anatase nanoparticles (Figures 3 and 4) are in good agreement with crystallite sizes of calculated from XRD patterns (Figure 1) for both samples. SAED patterns (Figures 3h and 4h) also consist of anatase and rutile diffraction points connected in the rings characteristic for monocrystalline materials. The number of the reflexes characteristic for the rutile phase is considerably smaller indicated smaller amount of the rutile phase in the sample.

The presence of Ag in small amounts is observed in all analyzed samples before and after photocatalytic reaction by EDXS measurements (Figures 3g and 4g). The average atomic percentage of Ag indicated by multiple EDXS measurements in S2 was  $(0.5 \pm 0.1)\%$ , while S3 contained somewhat larger amount of silver,  $(0.7 \pm 0.2)\%$ . However, the nanoparticles of pure Ag were not observed, thus indicating that Ag atoms were inbuilt in crystal lattice of  $\text{TiO}_2$ .

There are considerable differences in TEM images after photocatalytic reaction under sunlight and visible irradiation. After photocatalytic reaction, in the case of S2 samples, an amorphous layer of about one nanometer was observed on the surface of the catalyst after photocatalytic reaction using only visible irradiation (Figure 3d). The formation of this amorphous layer indicates that the products of catalytic reaction were accumulated on the surface of the catalysts. The reason for that accumulation could be incomplete degradation of the model pollutant (SA) under the visible light, so the formation of this amorphous layer could induce the decrease of the catalytic activity in time under only visible part of the irradiation spectrum. Moreover, the crystal structure of the  $\text{TiO}_2$  particles could be also affected at the surface, which could be inferred from comparison with the Raman spectroscopy measurements. In the Raman spectrum  $144\text{ cm}^{-1}$  band shifting to higher wavenumbers was observed indicating disorder of  $\text{TiO}_2$  anatase crystal lattice, as was mentioned before.



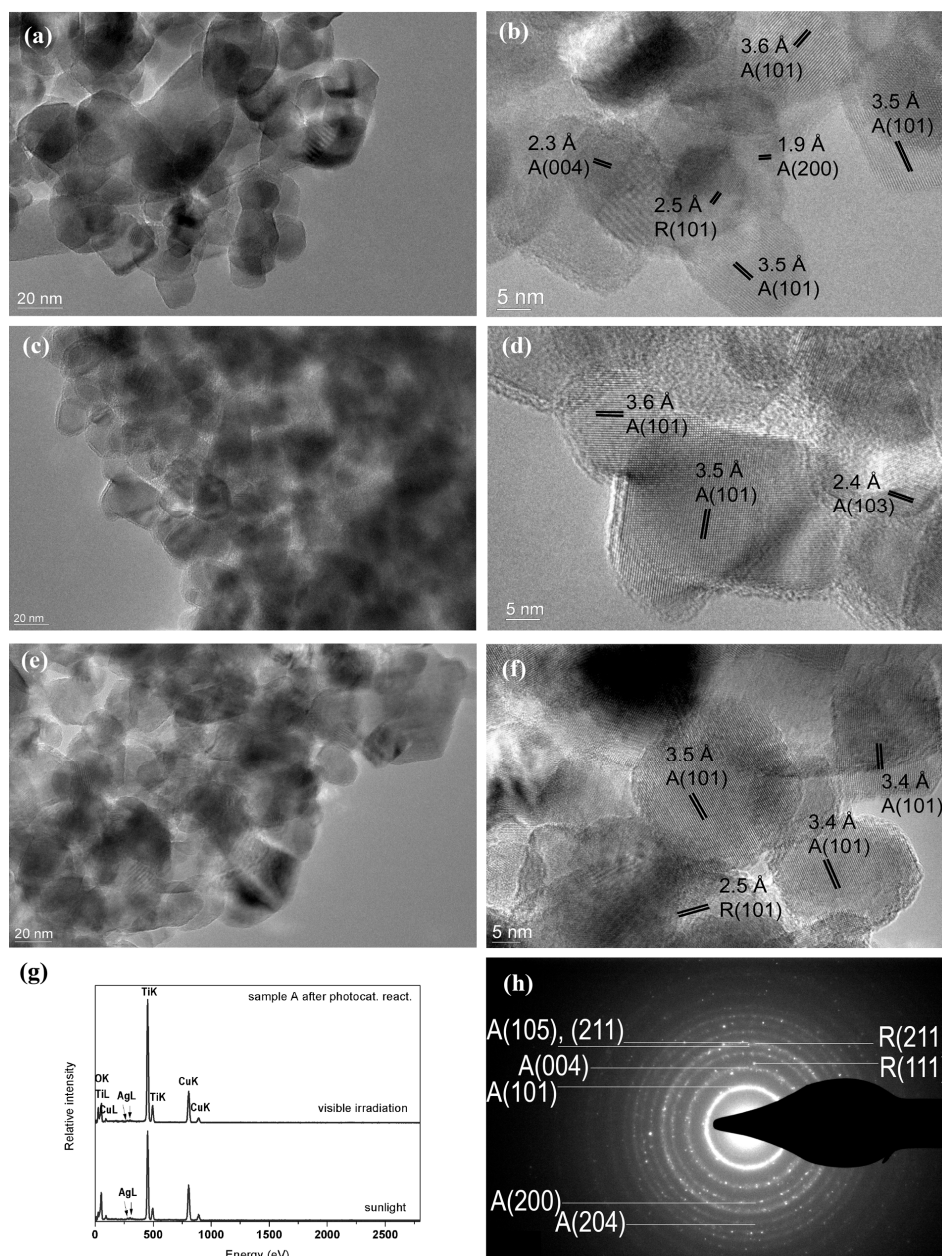


**Figure 3.** Sample S2: TEM (a) and high resolution transmission electron microscopy (HRTEM) (b) images before photo-catalytic reaction, TEM (c) and HRTEM (d) images after photo-catalytic reaction using only visible part of the spectra, TEM (e) and HRTEM (f) images after photo-catalytic reaction using sun light, energy dispersive X-ray spectroscopy (EDXS) of the sample after photo-catalytic reaction using both visible irradiation and sun light (g) SAED of the sample after photo-catalytic reaction using sun light (h).

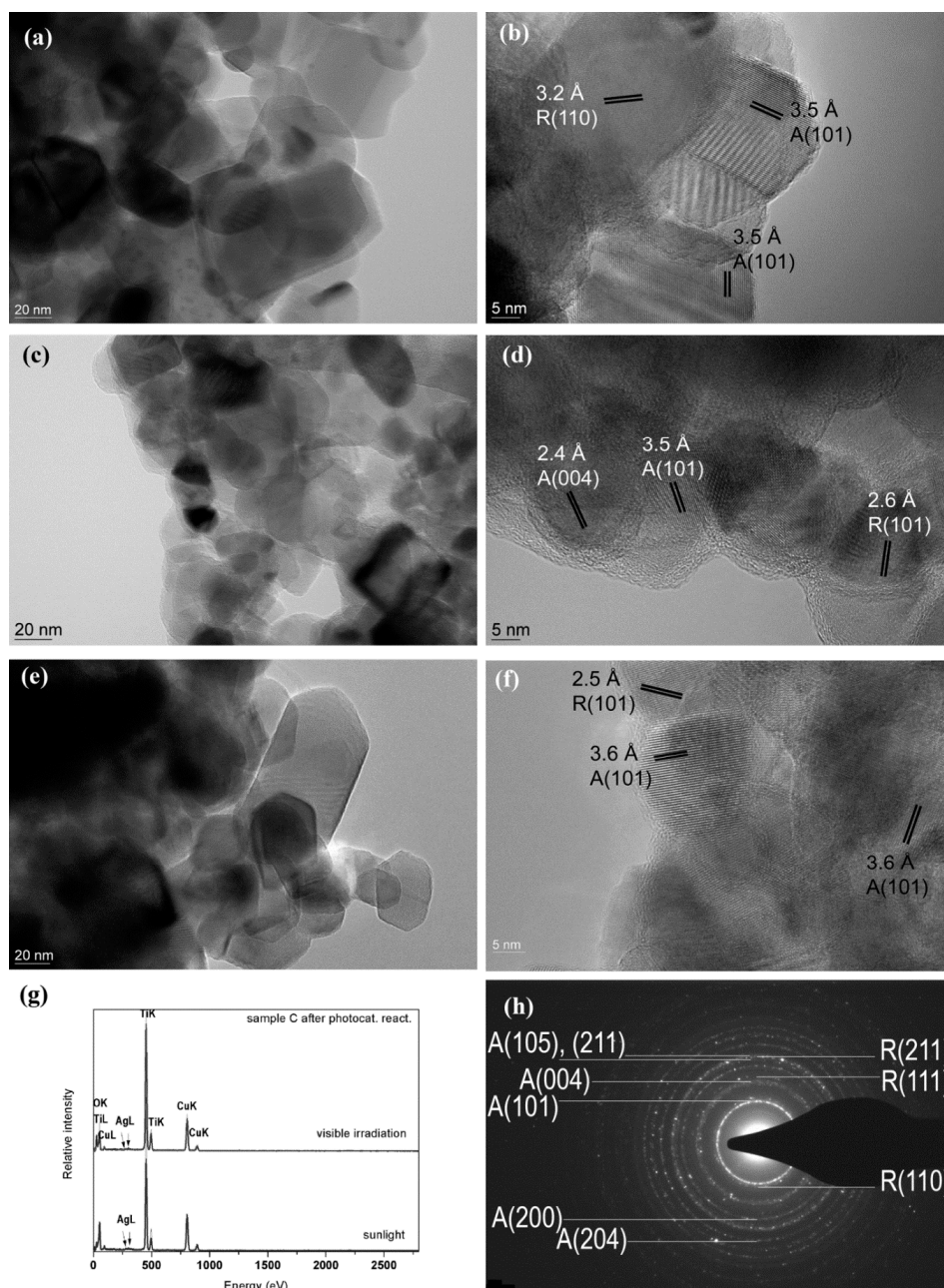


**Figure 4.** Sample S3: TEM (a) and HRTEM (b) images before photo-catalytic reaction, TEM (c) and HRTEM (d) images after photo-catalytic reaction using only visible part of the spectra, TEM (e) and HRTEM (f) images after photo-catalytic reaction using sun light, EDXS of the sample after photo-catalytic reaction using sun light (g), SAED of the sample before photo-catalytic reaction (h).

In the case of catalytic reaction using complete sunlight, the amorphous layer was not formed (or is considerably thinner) at the surface of the S2 catalyst (Figure 3e,f) thus indicating that the reaction was completed when both visible and UV part of the simulate sunlight spectrum were used for photocatalysis.

The formation of the thick amorphous layer is also observed in the case of photocatalysis with only visible irradiation in sample S3 (Figure 4c,d) which points to the accumulation of organics on the surface due to slower degradation as well. However, in the case of S3 sample when simulated sunlight was used for photocatalysis, there were not observed any amorphous layer on the sample surface (Figure 4e,f), thus the best catalytic performance was expected from this sample.

EDXS measurements of both samples after the reactions (Figures 3g and 4g) indicate that the Ag is still present in the samples after catalytic reaction no matter which irradiation was used. Moreover, the crystal structure of TiO<sub>2</sub> nanoparticles is also preserved, so still the mixture of anatase and rutile crystallites was observed by SAED after the reactions, which is in accordance with the Raman spectroscopy measurements of the samples after catalytic reactions.

#### 2.4. UV-Vis Diffuse-Reflectance Spectral Analysis

Figure 5 shows the UV-Vis diffuse-reflectance spectra of the as-prepared catalysts. These materials show a strong absorption in the UV region, a characteristic typical of semiconductors. Therefore, strong absorption below 350 nm corresponds with the band gap for TiO<sub>2</sub> which comes from difference in position of valence and conductive band in prepared samples (Eg<sub>1</sub> in Table 1). The series of Ag@TiO<sub>2</sub> photocatalysts also exhibited broad absorption in the region of visible light. The absorption in the visible part should be assigned to surface plasmon resonance of silver nanoparticles, centered at 490–530 nm [12,22]. However, in case of S2 and S3, no nanoparticles were observed by HRTEM. Therefore, the band gap lowering might be due to Ag inbuilt in the crystal structure of TiO<sub>2</sub> nanoparticles acting as a dopant in TiO<sub>2</sub> semiconductor crystal that form additional energy levels in band gap region of TiO<sub>2</sub>. The samples S1c, S2, and S3 exhibit a visible light absorption, so corresponding band gaps (Eg<sub>2</sub>) can be calculated, as denoted in Table 1.

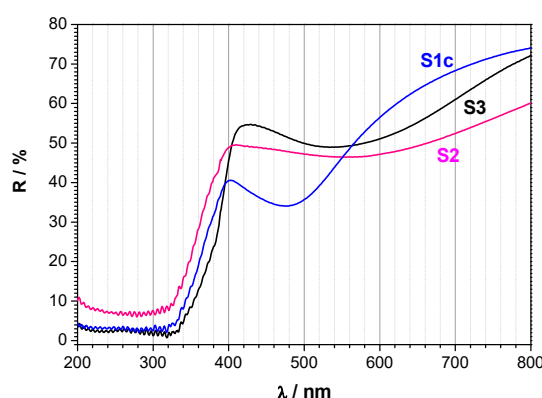


**Figure 5.** UV-Vis diffuse-reflectance spectra of prepared Ag@TiO<sub>2</sub> photocatalysts S1c, S2, and S3.

The band gaps are calculated by known procedure [25,26]. According to the Kubelka–Monk theory of diffuse reflectance, the data were transformed using the function Equation (2) versus energy where R<sub>∞</sub> is diffuse reflectance.

$$F(R_{\infty}) = (1 - R_{\infty})^2 / (2R_{\infty}) \quad (2)$$

**Table 1.** Band gaps of investigated samples calculated from UV-Vis measurements using formula  $[F(R) \times h\nu]^{1/2}$  [26].

Sample	Eg <sub>1</sub> (eV)	Eg <sub>2</sub> (eV)
S1c	2.86	1.19
S2	2.86	1.18
S3	2.98	1.19

The data were plotted in the form of Tauc plots as  $[F(R) \times h\nu]^n$  versus  $h\nu$ , where  $n = 2$  for direct transitions and  $n = \frac{1}{2}$  for indirect transitions. The value of  $n = 1/2$  was used since both anatase and rutile phase of TiO<sub>2</sub> have indirect band gap. The optical band gap sizes were estimated from the onset of absorption, as extrapolated from the line arising section of the curve that intersects with the baseline [25,26] and is listed in Table 1.

All three samples (S1c, S2, and S3) show similar values for band gap transitions in TiO<sub>2</sub>: 2.86, 2.86, and 2.98 eV, respectively (Table 1). These are the band gaps of TiO<sub>2</sub> that were shifted to visible region due to the presence of Ag. The red-shift of the band-gap absorption was expected since it is noticed with metal and non-metal loading of TiO<sub>2</sub> [14]. Another transition which was occurred around 1.2 eV could be attributed to the additional energy levels in band gap region of TiO<sub>2</sub> due to the Ag that acts as dopant.

### 2.5. Detection of Ag Nanoparticles

In TEM images of S3, Ag is not identified as individual crystals, which indicates that Ag might be substituted in TiO<sub>2</sub> crystal network. However, cell parameters (calculation not presented) did not show much difference from an undoped TiO<sub>2</sub>. In literature [27] was reported that only a small number of Ag nanoparticles were found by TEM, and the majority of them were recessed in the TiO<sub>2</sub> nanopores. Applied preparation method must have resulted in Ag nanoparticles finely dispersed on TiO<sub>2</sub> surface. Growth of Ag nanoparticles in chitosan matrix ensures development of small nanoparticles [22] which can easily enter the TiO<sub>2</sub> pores. The latter was expected since only S3 sample retain white color and other Ag doped catalysts were colored from pinkish to grey. It was observed that the color of S3 sample that was kept refrigerated in dark did not change. In contrary, sample that was kept indoor under ambient conditions (room temperature, ambient light, no UV) changed color to greyish-purple after few weeks. However, it was impossible to keep the observed color for possible analysis since it immediately turned back to white after the sample was shaken (Figure 6). The explanation for the observed phenomena, which resembles to photochromism [28] and clearly indicates the presence of Ag in S3 sample, was found in similarity with the two-photon luminescence experiments [29]. Under ambient conditions, only low-intensity visible-NIR irradiation can reach the surface of the sample which after a longer period of exposure corresponds to visible-NIR excitations regularly used in two-photon luminescence experiments. Ag nanoparticle is then excited with “two-photons” and fluorescence emission is observed when return to ground state. On the other hand, TiO<sub>2</sub> plays important role in rapid color retrieval. If we assume that excited Ag loses electron (Equation (3)), and that electron freely circle in the TiO<sub>2</sub> conduction band, when air rapidly flows through the sample (“shaking” of the sample), oxygen adsorbs on the TiO<sub>2</sub> surface and captures the excess electron (Equation (4)). Eventually, superoxide anions recombine rapidly with Ag<sup>+</sup> and the white color is observed again.

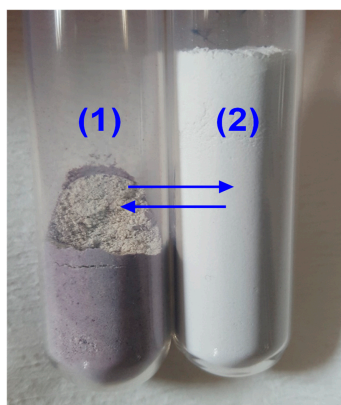


**Figure 6.** S3 sample after few weeks under ambient conditions (1), initial white color of S3 sample return after shaking (2).

Justification for a tentative mechanism explaining the observed spontaneous photochromism of S3 sample is found in related researches. In [28], it was reported that interconversion between plasmonic Ag nanoparticles and Ag<sup>+</sup> is responsible for reversible color changes in case of multicolor photochromism, and electrons from small Ag nanoparticles are easily injected into TiO<sub>2</sub>, while O<sub>2</sub> acts as electron acceptor for excited nanoparticles [27].

To estimate the emission wavelength from excited particles, observed color was associated with colors from Pantone® color chart and British Standard BS4800 colors. Observed greyish-purple color (Figure 7) matches Pantone PMS 5275 and PMS 5285 and BS4800 22-C-37, all described as blue-magenta shades with approximated corresponding wavelengths ( $\lambda_{\text{approx}}$ ) from 455 to 469 nm. Obtained  $\lambda_{\text{approx}}$  correspond with the reported values absorption of Ag deposited on TiO<sub>2</sub> [27,30,31].

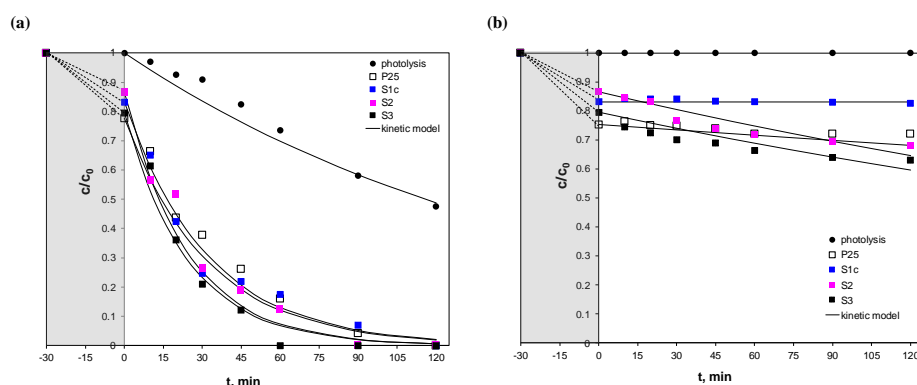


**Figure 7.** Kinetics and efficiency of photocatalytic degradation of salicylic acid (SA) under full-spectrum solar irradiation (a) and visible irradiation (b) using TiO<sub>2</sub> P25 and Ag@TiO<sub>2</sub> photocatalysts under given conditions. The grey areas represent the dark period prior reaction, i.e., time necessary to achieve sorption equilibrium.

## 2.6. Photocatalytic Activity

The visible and full solar light driven photocatalytic activity of prepared Ag@TiO<sub>2</sub> samples were investigated for the degradation of SA. Figure 7a,b show the kinetics and efficiency of photocatalytic degradation of SA. Commercial TiO<sub>2</sub> P25 was tested as a reference. It can be seen that TiO<sub>2</sub> did not show photocatalytic activity under visible irradiation and also photocatalyst S1c appeared as inactive, possibly due to residual AgCl on TiO<sub>2</sub> surface that absorbed the useful irradiation and block active sites necessary for generation of HO• radicals. The photocatalytic activities were observed as follows: S3 ≈ S2 under visible irradiation and S3 > TiO<sub>2</sub> P25 ≈ S2 ≈ S1c under solar irradiation. As it can be seen, S3 seemed to be an efficient photocatalyst under both solar and visible irradiation. The complete degradation of SA was achieved for 60 min of irradiation while its activity is increased by about 20% compared to TiO<sub>2</sub> P25. Therefore, the best photocatalytic performance of this sample was shown, although the S3 sample has the largest band gap  $E_{g1}$ . The main reason for better performance could be explained by modification made using chitosan. The method is not only facile and environmentally friendly, but the use of the viscous gel-like medium provided an even distribution of Ag throughout the sample. During photocatalytic processes, electrons and holes are excited in TiO<sub>2</sub>. These electrons and holes can recombine and result in the reduction in the photocatalytic efficiency, if TiO<sub>2</sub> is used alone without any modification of it. Since TiO<sub>2</sub> is modified, it is expected that presence of Ag could suppress the electron–hole recombination and increase efficiency [32] apart from surface plasmon resonance.

Confirmation for the given explanation on enhanced activity is found in [33,34]. The loading of noble metal nanoparticles on TiO<sub>2</sub> surface is one of possible approaches to reduce the high recombination rate process. After the light absorption, the promoted electrons from the valence band into conduction band of semiconductor is subsequently captured by noble metal which have a lower Fermi energy level than the semiconductor, leading to the separation of electron–hole pairs and an increase of the photocatalytic efficiency, particularly under UV irradiation. Instead, under visible light irradiation,

the charge carriers in noble metal are injected from the excited plasmonic metal nanostructure into the semiconductor thus reducing the recombination rate process and simultaneously increasing the photocatalytic activity.

The photodegradability of SA was also investigated in the absence of photocatalyst. The SA did not undergo any degradation under visible light (Figure 7b) while under solar light was degraded even around 50% after 2 h as shown in Figure 7a.

The photocatalytic degradation of SA follows the Langmuir–Hinshelwood kinetics model that is typically used for describing degradation kinetics over irradiated photocatalytic films [35]. As the initial concentration of SA is a millimolar solution ( $0.2 \text{ mmol L}^{-1}$ ) and its concentration in comparison with the suspended catalysts loading ( $1 \text{ g L}^{-1}$ ) is small, the model can be simplified to give a first-order equation (Equation (5)).

$$\frac{dc_{SA}}{dt} = -k_{SA, obs} c_{SA} \quad (5)$$

In the case of full-spectrum solar irradiation with an enhanced UV-B irradiation, the equation accounted rate of photolysis as shown in (Equation (6)).

$$\frac{dc_{SA}}{dt} = -(k_{photolysis} + k_{SA, obs}) c_{SA} \quad (6)$$

The  $k_{photolysis}$  and  $k_{SA, obs}$  are pseudo-first order rate constants for photolysis and photocatalysis of SA in investigated system, respectively, both given in  $\text{min}^{-1}$ . Under given conditions, the observed rate constant for photolysis,  $k_{photolysis}$  was  $6 \times 10^{-3} \text{ min}^{-1}$ .

Rate constants were evaluated from Equations (7) and (8) through the linear regression of  $\ln(c_{SA}/c_{SA,0})$  vs. Time where  $c_{SA}$  is the SA concentration ( $\text{mg L}^{-1}$ ) at a time  $t$  (min) and  $c_{SA,0}$  is the initial SA concentration after adsorption ( $\text{mg L}^{-1}$ ).

$$\ln \frac{c_{SA}}{c_{SA,0}} = -k_{SA, obs} t \quad (7)$$

$$\ln \frac{c_{SA}}{c_{SA,0}} = -(k_{photolysis} + k_{SA, obs}) t \quad (8)$$

The corresponding values of the pseudo-first order rate constant  $k_{SA, obs}$  as well as the degradation half-time,  $t_{1/2}$  and the determination coefficient  $R^2$  are given in Table 2. The comparison of photocatalytic activity using the simple kinetic model disregarding the catalysts surface area was justified since all catalysts have very similar specific surface areas. Namely, compared to commercial  $\text{TiO}_2$  P25 whose  $S_{BET}$  was  $56 \text{ m}^2 \text{ g}^{-1}$ , the surface areas of  $S_{BET}$  of S1c, S2, and S3 were 45, 47, and  $52 \text{ m}^2 \text{ g}^{-1}$ , respectively.

**Table 2.** The pseudo-first order rate constant ( $k_{SA, obs}$ ) for the degradation of SA in the flow cell irradiated with simulated solar and visible irradiation.

Sample	Full-Spectrum Solar Irradiation			Visible Irradiation		
	$k_{SA, obs} (\times 10^3 \text{ min}^{-1})$	$t_{1/2} (\text{min})$	$R^2$	$k_{SA, obs} (\times 10^3 \text{ min}^{-1})$	$t_{1/2} (\text{min})$	$R^2$
$\text{TiO}_2$ P25	22.2	15–30	0.9718	0.83	835	0.9680
S1c	25.3		0.9646	0.003	231049	0.9168
S2	33.4		0.9125	2.43	285	0.9568
S3	35.0		0.9330	2.41	287	0.9127

The rate of photocatalytic degradation of SA with all used photocatalysts is quite high when artificial solar light was applied and less than half an hour is needed for its half-degradation.

The photocatalytic activity of S2 and S3 was almost the same under visible irradiation. This can be explained by the insignificant difference in net contribution of Ag in the  $\text{TiO}_2$  lattice. Moreover, both S2 and S3 have an absorption band at 400–700 nm (Figure 5.) that could be assigned to surface plasmon absorption of silver, typically centered at 490–530 nm [21]. The broader band of S2 suggested

the larger Ag particles than those in S3. The small particle size and electron sharing phenomena are well described and incorporated in the explanation of the observed spontaneous photochromism (Section 2.5).

### 3. Materials and Methods

#### 3.1. Preparation of Ag/TiO<sub>2</sub> Photocatalysts

The photocatalysts were prepared by the known methods (S1a–c and S2) similar to those described in the literature [13,21], and by a novel method (S3) developed using literature on the preparation of Ag/chitosan composites [22]. The Ag@TiO<sub>2</sub> photocatalysts marked as S1a and S1b were prepared by deposition precipitation with photoreduction, S1c was prepared by deposition precipitation and S2 by photocatalytic deposition. Photocatalyst marked as S3 was prepared by a novel method including deposition precipitation and reduction by chitosan. Detailed preparation routes are described in following subsections. In all procedures, TiO<sub>2</sub>P25 (Evonik, AEROXIDE®) was used as starting titania material.

##### 3.1.1. Preparation of S1a

TiO<sub>2</sub> (0.20 g) and cationic surfactant N, N-Dodecyl-N, and N-dimethylammoniumchloride (hereafter: BARDAC) manufactured by Lonza, Switzerland (0.34 mL) were suspended in Milli-Q water (100 mL) and stirred for 60 min, followed by the addition of AgNO<sub>3</sub> (0.1 M, 2.00 mL). The resulting suspension was stirred at room temperature for 60 min and then placed in UV chamber for 20 min. UV chamber consist of four 8 W lamps with emission output at  $\lambda = 300$  nm. The suspension was filtered and washed with Milli-Q water. The obtained grey powder was dried at 80 °C for 12 h and then calcined at 300 °C for 3 h.

##### 3.1.2. Preparation of S1b

TiO<sub>2</sub> (0.20 g) and BARDAC (0.75 mL) were suspended in Milli-Q water (100 mL) and stirred for 60 min, followed by the addition of AgNO<sub>3</sub> (0.1 M, 2.00 mL). The resulting suspension was stirred at room temperature for 60 min and then irradiated with ultraviolet lamp ( $\lambda = 254$  nm, 8 W) for 20 min. The suspension was filtered and washed with Milli-Q water. The obtained greyish-pink powder was dried at 80 °C for 12 h and then calcined at 300 °C for 3 h.

##### 3.1.3. Preparation of S1c

TiO<sub>2</sub> (1.00 g) was suspended in Milli-Q water (100 mL) and sonicated for 30 min. After sonication, BARDAC (1.20 mL) was added and suspension was stirred for 30 min, followed by the addition of AgNO<sub>3</sub> (0.21 g) and NH<sub>4</sub>OH (2.30 mL, 25 wt.% NH<sub>3</sub>). The resulting suspension was stirred at room temperature for 12 h. The product was filtered, washed with distilled water, and dried at 70 °C for 12 h. Finally, the grey powder was calcined under air at 500 °C for 3 h.

##### 3.1.4. Preparation of S2

TiO<sub>2</sub> (2.00 g) was suspended in aqueous solution of methanol (4 mL), AgNO<sub>3</sub> (0.1 M, 3.80 mL) and NaCl (0.0018 M, 200 mL) in the round-bottom flask of 400 mL. The suspension was purged with a stream of nitrogen and irradiated with UV lamp ( $\lambda = 365$  nm, 4 W) for 3 h. The product was filtered, washed with distilled water, and dried at 100 °C for 12 h.

##### 3.1.5. Preparation of S3

Chitosan (Aldrich) (0.055 g) was dissolved in acetic acid (0.15 M, 25 mL) and the resulting biogel was added to NaOH aqueous solution (0.13 M, 100 mL). After a short mixing, TiO<sub>2</sub> (6.00 g) and AgNO<sub>3</sub> (0.13 M, 2.50 mL) were added simultaneously. Stirring was continued for 24 h in the dark. Finally, the suspension was filtered and then calcined at 600 °C for 3 h to eliminate chitosan.



### 3.2. Catalysts Characterization

The samples were studied by X-ray diffraction (XRD) analysis using a Shimadzu XRD 6000 diffractometer with  $\text{CuK}\alpha$  radiation. Data were collected over a  $2\theta$  range between 10 and  $70^\circ$   $2\theta$  in step scan mode with steps of  $0.02^\circ$  and counting time 4 s per step. The identification of crystal phases was done using Joint Committee on Powder Diffraction Standards (JCPDS) card catalogue.

Raman spectroscopy measurements were performed using a Horiba Jobin-Yvon T64000 Raman system (Villeneuve d'Ascq, France) working in micro-Raman configuration. Coherent, Innova 400 (Santa Clara, CA, USA) argon ion laser operating at 514.5 nm was used for excitation. The Raman data were collected in a true backscattering geometry with the aid of a liquid nitrogen-cooled multi-channel charge-coupled device (CCD) detector. Nominal laser power of 20 or 7 mW (depending of the sample) was focused on the samples using a long working distance 50 $\times$  objective lens with numerical aperture NA = 0.5 (Olympus, Tokyo, Japan).

High resolution transmission electron microscopy (HRTEM) was performed using Philips CM200-FEG transmission electron microscope operated at 200 kV, equipped with energy dispersive X-ray spectroscopy (EDXS) detector Genesis 4000. For the TEM measurements, the samples were first suspended in chloroform by sonication; then, a small drop of the suspension was transferred onto the carbon-coated copper grid. Finally, the grid was dried in air.

The UV-Vis spectra of the prepared samples were obtained using DRS (Shimadzu UV-3101PC) equipped with an integrating sphere. The spectra were recorded at room temperature in the wavelength range of 200–800 nm.  $\text{BaSO}_4$  was used as a reference. The diffuse reflectance spectra were presented with the reflectance of the “infinitely thick” layer of the solid,  $R(\%)$ .

The BET surface areas were estimated from nitrogen adsorption and desorption isotherm data using an ASAP 2000 apparatus (Micromeritics Corporation). Prior to analysis, samples were degassed (6.6 Pa) at  $400^\circ\text{C}$  to remove any physically adsorbed gases.

### 3.3. Photocatalytic Experiments

The photocatalytic activities of the prepared Ag-doped  $\text{TiO}_2$  photocatalysts were evaluated in terms of degradation of salicylic acid (SA) under solar and visible light. Salicylic acid (p.a. grade) was obtained as a free-of-charge sample from pharmaceutical industry Pliva in Croatia and used without further purification. The aqueous solution of  $0.2\text{ mmol L}^{-1}$  of SA was prepared with distilled water and pH 4 of the solution was measured. Photocatalytic experiments were performed in a flow cell (Figure 8) using a peristaltic pump set at a constant flow rate of  $67\text{ mL min}^{-1}$ . Prior to irradiation, photocatalysts ( $1\text{ g L}^{-1}$ ) were suspended in 40 mL of SA solution and homogenized in ultrasonic bath for 5 min and then recirculated in flow cell in the dark for 25 min to get an adsorption/desorption equilibrium. Total sorption time in dark was presented with grey area in Figure 7a,b. During photocatalytic experiments the flow cell was directly irradiated. The sources of irradiation were: (i) full-spectrum compact fluorescent bulb simulating solar spectra with enhanced UV-B irradiation (Exo Terra, 26 W) and (ii) incandescent bulb emitting only visible light (Osram Daylight, 100 W,  $I_{\text{UV-B}} = I_{\text{UV-A}} = 0.0\text{ mW cm}^{-2}$ ). All experiment were done under ambient conditions:  $T = 25 \pm 2^\circ\text{C}$ .

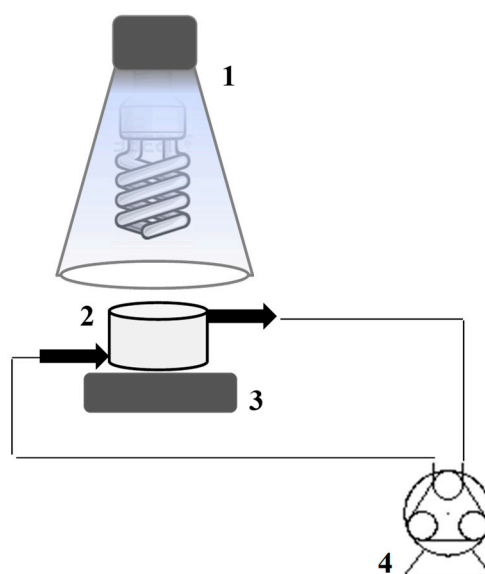


**Figure 8.** Scheme of the experimental set-up used for the photocatalytic degradation experiments; 1—irradiation source with reflective surface, 2—photocatalytic cell (dcell = 45 mm, reaction mixture level = 24 mm), 3—magnetic stirrer, and 4—peristaltic pump.

The full-spectrum solar bulbs were used to simulate the solar irradiation. Relative intensities over a range of wavelengths from 340 to 640 nm corresponded to the intensities of natural sunlight averaged around in year on northern hemisphere ( $\sim 45^\circ$  N). The UV-B intensity of a lamp was slightly higher, mimicking the desert sunlight. In the case of full-spectrum solar bulb, the overall intensities in UV-B and UV-A region were measured by UVP UVX radiometer, fitted with the corresponding sensors. Given intensities on the cell top (suspension level) were:  $I_{\text{UV-B}} = 2.9 \text{ mW cm}^{-2}$  and  $I_{\text{UV-A}} = 3.4 \text{ mW cm}^{-2}$ . At given time intervals the SA concentration was analyzed using HPLC, Shimadzu, with SUPELCO C18 column, length 250 mm, internal diameter 4.6 mm and UV (diode array) detection (DAD) at 303 nm. The analyses were carried out by binary flow elution with mobile phase solvents A and B at a flow rate of 0.6 and  $0.4 \text{ mL min}^{-1}$ , respectively. Solvent A consisted of 0.5:99.5 (*v/v*) methanol: 0.1 M phosphoric acid and solvent B was 100% methanol. Experiments were done in triplicated and average results were reported.

#### 4. Conclusions

In this work, a series of Ag@TiO<sub>2</sub> photocatalysts were prepared by five different synthetic pathways based on deposition–precipitation, photoreduction, photochemical deposition, and reduction in chitosan biogel. The synthesized photocatalysts were characterized by the means of XRD, Raman spectroscopy, TEM, HRTEM, EDXS, SAED, and UV-vis DRS and their photocatalytic activity was determined using salicylic acid as a model pollutant, chosen due to its persistent presence in the environment.

It was observed that the solar and visible photocatalytic activity of obtained photocatalysts strongly depends on the preparation methods. The rate of photocatalytic degradation of salicylic acid with all used photocatalyst is quite high when solar light was applied and less than half an hour is needed for its half-degradation. Ag@TiO<sub>2</sub> prepared by a simple novel method based on reduction of Ag on TiO<sub>2</sub> surface in chitosan biogel (sample S3) seems to be the most promising photocatalyst under solar irradiation (about 20% more efficient than TiO<sub>2</sub>) and deserves further attention. Although the activity under visible irradiation was the same for samples S2 and S3, the synthesis of S3 via chitosan is simple one-pot green synthesis readily available for large-scale production of photocatalysts.

Observed photocatalytic behavior of S3 could be explained by the fact that TiO<sub>2</sub> lattice of this photocatalyst contains somewhat higher atomic percentage of silver that form additional energy level in band gap region of TiO<sub>2</sub>. On the other hand, the presence of Ag nanoparticle on TiO<sub>2</sub> surface and inside the pores enhances the absorption in visible part of spectra and suppresses the electron–hole recombination and increase photoactivity. The contribution of Ag in the surface redox reaction was confirmed by spontaneous photochromism of a sample. The study confirmed that only visible part of solar spectra could alone induce the photocatalytic reaction, which is promising from the practical point of view: such catalysts could be used for outdoor applications in areas with lower daily solar irradiance.

**Author Contributions:** Conceptualization, I.G. and A.G.; validation, A.G. and H.I.; investigation, K.Š., I.G., M.P., and A.G.; resources, I.G., H.I., and A.G.; data curation, I.G., K.Š., and M.-G.W.; writing—original draft preparation, I.G. and A.G.; writing—review and editing, I.G. and A.G.; visualization, I.G.; supervision, A.G. and M.-G.W.; funding acquisition, I.G., A.G. All authors have read and agreed to the published version of the manuscript.

**Funding:** This research was supported by European Regional Development Fund (ERDF) under the project “Waste & Sun for photocatalytic degradation of micropollutants in water” (OS-Mi), KK.01.1.1.04.0006., and by the Ministry of science and education of Croatia under the project HrZZ-IP-2018-01-5246. Authors acknowledge the Centre of Excellence for Advanced Materials and Sensing Devices, Ruđer Bošković Institute, Zagreb, Croatia, KK.01.1.1.01.0001 and partial support by European Regional Development Fund (ERDF) under the (IRI) project “Improvement of solar cells and modules through research and development” (KK.01.2.1.01.0115).

**Conflicts of Interest:** The authors declare no conflict of interest. The funders had no role in the design of the study; in the collection, analyses, or interpretation of data; in the writing of the manuscript, or in the decision to publish the results.

## References

- Horáková, M.; Klementová, Š.; Kříž, P.; Balakrishna, S.K.; Špatenka, P.; Golovko, O.; Hájková, P.; Exnar, P. The synergistic effect of advanced oxidation processes to eliminate resistant chemical compounds. *Surf. Coat. Technol.* **2014**, *241*, 154–158. [CrossRef]
- Thiruvengatathari, R.; Vigneswaran, S.; Moon, I.S. A review on UV/TiO<sub>2</sub> photocatalytic oxidation process. *Korean J. Chem. Eng.* **2008**, *25*, 64–72. [CrossRef]
- Wols, B.A.; Hofman-Caris, C.H.M. Review of photochemical reaction constants of organic micropollutants required for UV advanced oxidation processes in water. *Water Res.* **2012**, *46*, 2815–2827. [CrossRef] [PubMed]
- Chong, M.N.; Jin, B.; Chow, C.W.; Saint, C. Recent developments in photocatalytic water treatment technology: A review. *Water Res.* **2010**, *44*, 2997–3027. [CrossRef]
- Nageswara Rao, A.; Sivasankar, B.; Sadasivam, V. Kinetic study on the photocatalytic degradation of salicylic acid using ZnO catalyst. *J. Hazard. Mater.* **2009**, *166*, 1357–1361. [CrossRef]
- Lu, S.; Wu, D.; Wang, Q.L.; Yan, J.; Buekens, A.G.; Cen, K.F. Photocatalytic decomposition on nano-TiO<sub>2</sub>: Destruction of chloroaromatic compounds. *Chemosphere* **2011**, *82*, 1215–1224. [CrossRef]
- Malato, S.; Fernández-Ibáñez, P.; Maldonado, M.I.; Blanco, J.; Gernjak, W. Decontamination and disinfection of water by solar photocatalysis: Recent overview and trends. *Catal. Today* **2009**, *147*, 1–59. [CrossRef]
- Parsons, S. *Advanced Oxidation Processes for Water and Wastewater Treatment*; IWA Publishing: London, UK, 2005. [CrossRef]
- Nakata, K.; Fujishima, A. TiO<sub>2</sub> photocatalysis: Design and applications. *J. Photochem. Photobiol. C Photochem. Rev.* **2012**, *13*, 169–189. [CrossRef]
- Aazam, E.S. Visible light photocatalytic degradation of thiophene using Ag–TiO<sub>2</sub>/multi-walled carbon nanotubes nanocomposite. *Ceram. Int.* **2014**, *40*, 6705–6711. [CrossRef]
- Mohamed, R.M.; Baeissa, E.S. Preparation and characterisation of Pd–TiO<sub>2</sub>–hydroxyapatite nanoparticles for the photocatalytic degradation of cyanide under visible light. *Appl. Catal. A Gen.* **2013**, *464–465*, 218–224. [CrossRef]
- Suwanchawalit, C.; Wongnawa, S.; Sriprang, P.; Meanha, P. Enhancement of the photocatalytic performance of Ag-modified TiO<sub>2</sub> photocatalyst under visible light. *Ceram. Int.* **2012**, *38*, 5201–5207. [CrossRef]
- Guo, J.-F.; Ma, B.; Yin, A.; Fan, K.; Dai, W.L. Highly stable and efficient Ag/AgCl@TiO<sub>2</sub> photocatalyst: Preparation, characterization, and application in the treatment of aqueous hazardous pollutants. *J. Hazard. Mater.* **2012**, *211–212*, 77–82. [CrossRef] [PubMed]

14. Bhosale, R.R.; Pujari, S.R.; Muley, G.G.; Patil, S.H.; Patil, K.R.; Shaikh, M.F.; Gambhire, A.B. Solar photocatalytic degradation of methylene blue using doped TiO<sub>2</sub> nanoparticles. *Solar Energy* **2014**, *103*, 473–479. [CrossRef]
15. Deng, Q.R.; Xia, X.H.; Guo, M.L.; Gao, Y.; Shao, G. Mn-doped TiO<sub>2</sub> nanopowders with remarkable visible light photocatalytic activity. *Mater. Lett.* **2011**, *65*, 2051–2054. [CrossRef]
16. Chang, S.; Liu, W. The roles of surface-doped metal ions (V, Mn, Fe, Cu, Ce, and W) in the interfacial behavior of TiO<sub>2</sub> photocatalysts. *Appl. Catal. B Environ.* **2014**, *156–157*, 466–475. [CrossRef]
17. McManamon, C.; Delaney, P.; Morris, M.A. Photocatalytic properties of metal and non-metal doped novel sub 10nm titanium dioxide nanoparticles on methyl orange. *J. Colloid Interface Sci.* **2013**, *411*, 169–172. [CrossRef]
18. Ghasemi, S.; Esfandiar, A.; Setayesh, S.R.; Habibi-Yangjeh, A.; Gholami, M.R. Synthesis and characterization of TiO<sub>2</sub>-graphene nanocomposites modified with noble metals as a photocatalyst for degradation of pollutants. *Appl. Catal. A Gen.* **2013**, *462–463*, 82–90. [CrossRef]
19. Suwarnkar, M.B.; Dhabbe, R.S.; Kadam, A.N.; Garadkar, K.M. Enhanced photocatalytic activity of Ag doped TiO<sub>2</sub> nanoparticles synthesized by a microwave assisted method. *Ceram. Int.* **2014**, *40*, 5489–5496. [CrossRef]
20. Vargas, E.; Vargas, R.; Núñez, O. A TiO<sub>2</sub> surface modified with copper(II) phthalocyanine-tetrasulfonic acid tetrasodium salt as a catalyst during photoinduced dichlorvos mineralization by visible solar light. *Appl. Catal. B Environ.* **2014**, *156–157*, 8–14. [CrossRef]
21. Hu, C.; Lan, Y.; Qu, J.; Hu, X.; Wang, A. Ag/AgBr/TiO<sub>2</sub> Visible Light Photocatalyst for Destruction of Azodyes and Bacteria. *J. Phys. Chem. B* **2006**, *110*, 4066–4072. [CrossRef]
22. Twu, Y.-K.; Chen, Y.-W.; Shih, C.-M. Preparation of silver nanoparticles using chitosan suspensions. *Powder Technol.* **2008**, *185*, 251–257. [CrossRef]
23. PubChem. Available online: <https://pubchem.ncbi.nlm.nih.gov/compound/Salicylic-acid> (accessed on 15 May 2020).
24. Gajović, A.; Furić, K.; Tomašić, N.; Popović, S.; Skoko, Ž.; Musić, S. Mechanochemical preparation of nanocrystalline TiO<sub>2</sub> powders and their behavior at high temperatures. *J. Alloys Compd.* **2005**, *398*, 188–199. [CrossRef]
25. Kortüm, G. *Reflectance Spectroscopy*; Springer: Berlin, Germany, 1969.
26. Yu, J.; Kudo, A. Effects of Structural Variation on the Photocatalytic Performance of Hydrothermally Synthesized BiVO<sub>4</sub>. *Adv. Funct. Mater.* **2006**, *16*, 2163–2169. [CrossRef]
27. Ohko, Y.; Tatsuma, T.; Fujii, T.; Naoi, K.; Niwa, C.; Kubota, Y.; Fujishima, A. Multicolour photochromism of TiO<sub>2</sub> films loaded with silver nanoparticles. *Nat. Mater.* **2003**, *2*, 29–31. [CrossRef]
28. Kazuma, E.; Tatsuma, T. Photoinduced reversible changes in morphology of plasmonic Ag nanorods on TiO<sub>2</sub> and application to versatile photochromism. *Chem. Commun. R. Soc. Chem.* **2012**, *48*, 1733–1735. [CrossRef]
29. Gong, H.M.; Xiao, S.; Su, X.R.; Han, J.B.; Wang, Q.Q. Photochromism and two-photon luminescence of Ag-TiO<sub>2</sub> granular composite films activated by near infrared ps/fs pulses. *Opt. Express* **2007**, *15*, 13924–13929. [CrossRef]
30. Herrmann, J.-M.; Tahiri, H.; Ait-Ichou, Y.; Lassaletta, G.; Gonzalez-Elipe, A.R.; Fernandez, A. Characterization and photocatalytic activity in aqueous medium of TiO<sub>2</sub> and Ag-TiO<sub>2</sub> coatings on quartz. *Appl. Catal. B Environ.* **1997**, *13*, 219–228. [CrossRef]
31. Temgire, M.K.; Joshi, S.S. Optical and structural studies of silver nanoparticles. *Radiat. Phys. Chem.* **2004**, *71*, 1039–1044. [CrossRef]
32. Hasmath Farzana, M.; Meenakshi, S. Photocatalytic aptitude of titanium dioxide impregnated chitosan beads for the reduction of Cr(VI). *Int. J. Biol. Macromol.* **2015**, *72*, 1265–1271. [CrossRef]
33. Kochuveedu, S.T.; Jang, Y.H.; Kim, D.H. A study on the mechanism for the interaction of light with noble metal-metal oxide semiconductor nanostructures for various photophysical applications. *Chem. Soc. Rev.* **2013**, *42*, 8467–8493. [CrossRef]

34. DAmato, C.A.; Giovannetti, R.; Zannotti, M.; Rommozzi, E.; Ferraro, S.; Seghetti, C.; Minicucci, M.; Gunnella, R.; Di Cicco, A. Enhancement of visible-light photoactivity by polypropylene coated plasmonic Au/TiO<sub>2</sub> for dye degradation in water solution. *Appl. Surf. Sci.* **2018**, *441*, 575–587. [CrossRef]
35. Grčić, I.; Papić, S.; Brnardić, I. Photocatalytic Activity of TiO<sub>2</sub> Thin Films: Kinetic and Efficiency Study. *Int. J. Chem. React. Eng.* **2017**, *16*, 20160153. [CrossRef]






© 2020 by the authors. Licensee MDPI, Basel, Switzerland. This article is an open access article distributed under the terms and conditions of the Creative Commons Attribution (CC BY) license (<http://creativecommons.org/licenses/by/4.0/>).



## Article

# Photocatalytic Nanocomposite Polymer-TiO<sub>2</sub> Membranes for Pollutant Removal from Wastewater

Khelil Bouziane Errahmani <sup>1</sup>, Ouassila Benhabiles <sup>2</sup> , Sohbi Bellebia <sup>1</sup>, Zohra Bengharez <sup>1</sup> , Mattheus Goosen <sup>3</sup>  and Hacene Mahmoudi <sup>4,\*</sup>

- <sup>1</sup> Laboratory of Advanced Materials and Physicochemistry for Environment and Health, Faculty of Exact Sciences, Djillali Liabes University Sidi Bel Abbas, P.O. Box 89, Sidi Bel Abbas 22000, Algeria; be.khelil@gmail.com (K.B.E.); bellebia\_sohbi@yahoo.fr (S.B.); dzbengharez@yahoo.fr (Z.B.)
- <sup>2</sup> Unité de Développement des Equipements Solaires, UDES/Centre de Développement des Energies Renouvelables, CDER, Bou Ismail, Tipaza 42004, Algeria; benhabiles.ouassila@gmail.com
- <sup>3</sup> Office of Research & Graduate Studies, Alfaisal University, P.O. Box 50927, Riyadh 11533, Saudi Arabia; mgoosen@alfaisal.edu
- <sup>4</sup> Faculty of Technology, University Hassiba Benbouali of Chlef, Chlef 02000, Algeria
- \* Correspondence: h.mahmoudi@univ-chlef.dz; Tel.: +213-777170833

**Citation:** Bouziane Errahmani, K.; Benhabiles, O.; Bellebia, S.; Bengharez, Z.; Goosen, M.; Mahmoudi, H. Photocatalytic Nanocomposite Polymer-TiO<sub>2</sub> Membranes for Pollutant Removal from Wastewater. *Catalysts* **2021**, *11*, 402. <https://doi.org/10.3390/catal11030402>

Academic Editors: Gassan Hodaifa and Rafael Borja

Received: 8 February 2021

Accepted: 17 March 2021

Published: 23 March 2021

**Publisher's Note:** MDPI stays neutral with regard to jurisdictional claims in published maps and institutional affiliations.



**Copyright:** © 2021 by the authors. Licensee MDPI, Basel, Switzerland. This article is an open access article distributed under the terms and conditions of the Creative Commons Attribution (CC BY) license (<https://creativecommons.org/licenses/by/4.0/>).

**Abstract:** Photocatalytic TiO<sub>2</sub>-PVDF/PMMA nano-composites flat sheet membranes were fabricated by phase inversion and then employed in a crossflow filtration pilot to remove model pollutants of various sizes and charge from aqueous solution. The dope solution contained a mixture of PVDF and PMMA as polymers, polyethylene glycol (PEG) and polyvinylpyrrolidone (PVP) as additives, triethyl phosphate (TEP) as green solvent and TiO<sub>2</sub> as immobilized photo catalyst. After undergoing characterization tests such as SEM morphology thickness, porosity, contact angle and water permeability, the membranes were used to eliminate the model pollutants from synthetic aqueous solution. The impact of the operating conditions (i.e., pH, pressure and initial pollutant concentration) and composition of the doping solution on the performance and photocatalytic and antifouling activity of the membranes was investigated. The results showed that Congo Red and Tartrazine despite their small size were rejected at 99% and 81%, respectively, because of their negative charge, while Ciprofloxacin, which is larger than Tartrazine but of neutral charge, crossed the membrane. The permeability did not decrease with a decline in pollutant concentration but diminished when the pressure increased and was reduced by more than half for wastewater.

**Keywords:** wastewater treatment; photo catalytic micro ultra-filtration; PVDF/PMMA/TiO<sub>2</sub> nano composite membranes; MWCO

## 1. Introduction

Efficient techniques for wastewater treatment are critical not only to limit the release of pollutants into the natural environment, but also to produce safe potable water for human consumption. Organic compound contaminants for example are found in the effluents from the textile, food, and pharmaceutical industries [1]. Furthermore, the water produced by conventional purification processes can still contain micropollutants such as pharmaceuticals, pesticides and chemicals which are harmful to the ecosystem and human health, especially for young children, infants, and pregnant women [2]. The incidence of a variety of recently recognized compounds of anthropogenic or natural origin in the marine environment has also turned out to be a worldwide environmental concern. These pollutants are mainly organic in nature and usually occur in trace concentrations in the range from parts per trillion (ppt or ng/L) to parts per billion (ppb or µg/L) [1,3]. There is thus an urgent need for developing efficient effluent treatment practices.

Advanced oxidation techniques for the treatment of water and wastewater have been the subject of several research projects aimed at the selection of materials such as



semiconductors and their composites as well as optimal process treatment operating conditions [4–9]. Among the numerous photocatalysts assessed titanium dioxide ( $\text{TiO}_2$ ) was found to be the best due to its ready availability and low cost [10]. The effectiveness of  $\text{TiO}_2$ , as a heterogeneous catalyst for photo-degradation of aqueous pollutants and disinfection, was found to depend predominantly on the initial concentration of pollutants as well as on the light intensity on the  $\text{TiO}_2$  surface.

As well, membrane filtration technology has been extensively utilized not only in desalination but also in wastewater treatment, the food industry, pharmaceuticals manufacturing, and fermentation reactions [11,12]. Several researches on the application of membranes for wastewater treatment were investigated. For example, A.M. Khalil et al. [13] developed a cross-linked  $\beta$ -cyclodextrin nanofiber composite membrane for steroid hormone micropollutant removal. Similarly, L. Cseri et al. [14] suggest that nanofibrous polyimide membranes enhanced with ion exchange properties are promising candidates for the treatment of dye-laden textile wastewater.

As a real-world example of the application of nanocomposite materials, Ahdab and Rehman [15] studied brackish water desalination for greenhouses by employing monovalent selective electrodialysis reversal (MSED-R) for improving groundwater quality for irrigation. Experimentally determined membrane selectivities were used to evaluate the nutrient and fertilizer cost savings of MSED-R relative to Reverse Osmosis (RO).

For environmental remediation, A. Alammari et al. [16] prepared nanocomposite hydrogels based on sustainable cellulose acetate and demonstrated their robustness and practicality in continuous environmental remediation by using the hydrogels to treat contaminated groundwater from the Adyar River in India.

However, a major drawback of membrane processes is fouling. This phenomenon is due to the deposition of minerals, as well as colloidal and organic substances on the membrane surface [10,17]. The deposition process can be complex. Quantitative analysis for example has been done of membrane fouling mechanisms involved in microfiltration of humic acid–protein mixtures [17]. Clogging decreases the filtration flow, which considerably increases energy requirements, the rate at which membranes must be changed, the washing frequency and consequently the overall cost of the operation.

Furthermore, in the case of photocatalytic membranes which are a hybrid technology, as with all new processes, there are challenges that need to be overcome. Progress has been made for instance in photocatalytic membrane reactors (PMR) for water treatment. Such reactors exhibit enormous potential in the field of water treatment and in the cleansing of the environment [18–22]. In this photocatalysis-membrane system the benefits of two systems are combined [23].

A variety of studies have been reported on hybrid ultrafiltration/photocatalytic membranes for water treatment [3,24–26]. These include flat micro ultrafiltration membranes [24]. Among recent studies on photocatalytic membranes, Polyethersulfone (PES)/sulfonated polysulfone (SPSf)/ $\text{TiO}_2$  mixed matrix membranes (MMMs) were fabricated for oil-in-water emulsion separation. Results show that small concentrations of  $\text{TiO}_2$  NPs can be used to successfully modify morphology and separation performance of membranes according to C. N. Matindi et al. [27]. Jie Yu et al. [28] report that membranes fabricated using a solvothermal-induced assembly of a 2D-2D reduced graphene oxide (rGO)- $\text{TiO}_2$  mesoporous material with a laminar structure have an impressive self-cleaning ability and thus exhibit great potential application in the field of membrane separation.

Polyvinylidene fluoride (PVDF) membranes have great potential since a negative charge on the surface of the membrane prevents the adhesion of bacteria, thus limiting biofouling [23,25,26]. Furthermore, PVDF is a highly crystalline linear polymer with chemical and mechanical thermal stability. In addition, PMMA (polymethyl methacrylate) is a polymer with a higher transparency index than the mineral glass allowing for enhanced penetration of light and thus improved photocatalytic activity [24]. However, according to Benhabiles et al. [20], membranes prepared using PMMA have a low mechanical resistance.

It can be argued that owing to the strong compatibility of PVDF and PMMA, the combination of both polymers in a membrane may be employed to give enhanced overall properties such as improved mechanical resistance, hydrophilicity, processability, and ionic conductivity. Furthermore, membranes have recently been fabricated using triethyl phosphate (TEP) as the polymer solvent. Substituting hazardous solvents with TEP represents an attractive alternative for membrane fabrication. The solvent which has a high boiling point (215 °C) and has complete miscibility with water and alcohols, has been investigated by several authors [20,29–31].

In the current study, the application of photocatalytic nanocomposite polymer-TiO<sub>2</sub> membranes fabricated by phase inversion was assessed for pollutant removal from aqueous solutions including wastewater. TiO<sub>2</sub>-PVDF/PMMA nano-composites flat sheet membranes were prepared by NIPS (Non-Solvent Induced Phase Separation). Scanning electron microscopy (SEM) was employed to characterize the surface and the cross-section morphology of the membranes. Pore size, pure water permeability (PWP), porosity, and contact angle measurements were also carried out. The fabricated membranes were assessed in a crossflow filtration cell on their effectiveness in removing pollutants with diverse molecular weights, shapes, and charges. Filtration tests for gram- and gram + bacterial suspensions were also performed. The final part of this study focused on membrane filtration performance including the effect of different operating conditions such as pH, operating pressure, and initial pollutant concentration. Antifouling and antibiofouling properties were also investigated.

## 2. Results and Discussion

### 2.1. Membrane Morphology

Morphology plays a fundamental role in membrane behavior and filtration performance. Membrane permeability and selectivity are both affected by membrane morphology [32]. SEM analysis of the surface (top and bottom) and cross-section of the membranes indicated that the morphology of PVDF/PMMA nanocomposites is homogeneous and has a sponge-like symmetric formation (Figure 1).

The structure of the M1 membrane was homogeneous, with small pores of the same size distributed on the upper surface. The membrane showed a porous structure with interconnected pores and an absence of macro voids. This arrangement can be due to the higher polymer content in the M1 casting solution, which would have increased the viscosity [33]. It is generally recognized that a rise in solution viscosity strongly limits water passage through the polymer chains, thus hindering the formation of macro voids in the membrane. The presence of PVP and PEG additives in the dope solutions would also have contributed to the formation of membranes with a discontinuous cross-section structure. Furthermore, it can be argued that the presence of triethyl phosphate (TEP) as an alternative non-toxic solvent would have slowed down the phase separation rate, leading to a porous spongy membrane [34].

Membrane M2 was observed to contain visible macro voids according to the cross-section image (Figure 1). This structure can be induced by a lower polymer concentration which would have resulted in membranes with larger pores. The presence of 5% photocatalyst titanium dioxide (TiO<sub>2</sub>) particles in the membrane matrix would have led to an increase in the hydrophobicity of the dope solution and therefore affected the exchanges between the solvent and the non-solvent in the coagulation bath [35]. Additionally, TiO<sub>2</sub> particles were evenly well distributed in the membrane, as seen in Figure 2. There was more TiO<sub>2</sub> in M2 (5%) than in M1 (2.5%). The size of the nanoparticles of TiO<sub>2</sub> appeared to be greater than 21 nm because the dispersion was not complete by simple agitation.

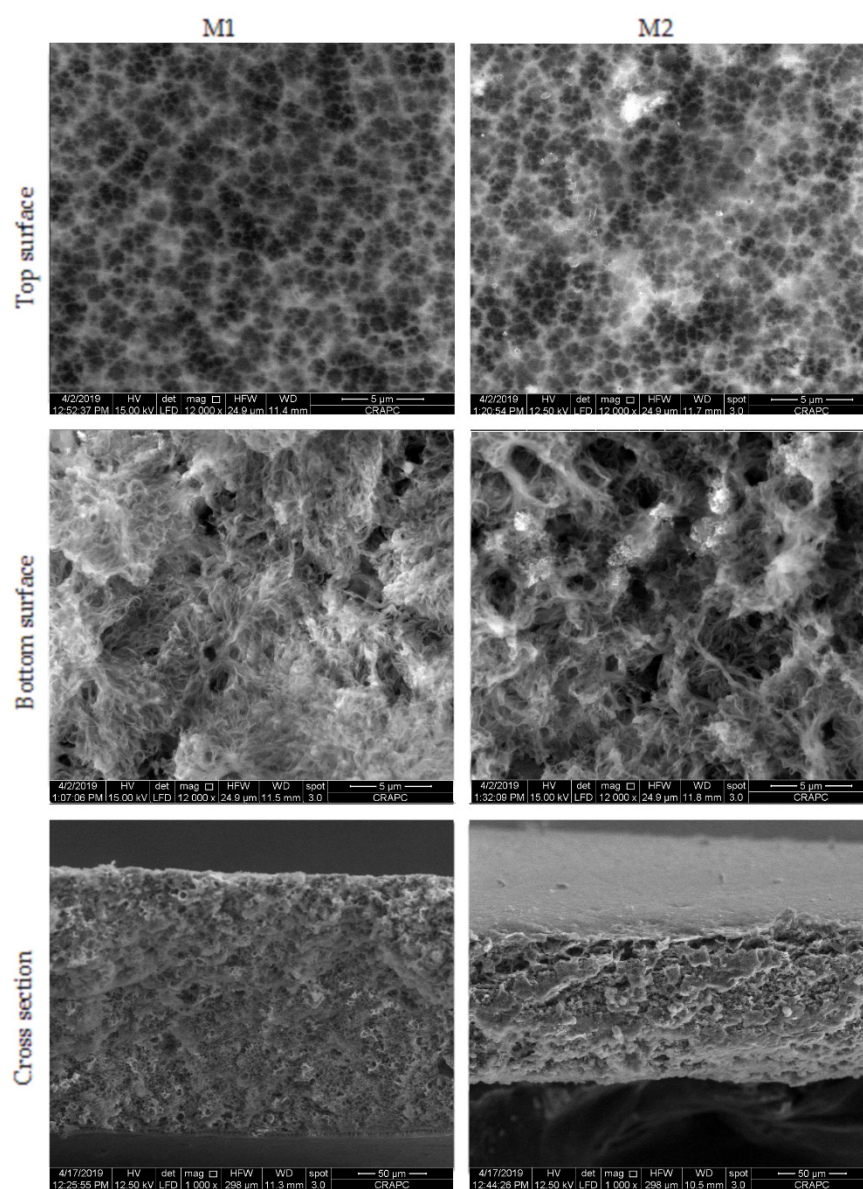


Figure 1. SEM images: top surface, bottom surface, and cross-sections of membranes M1 and M2.

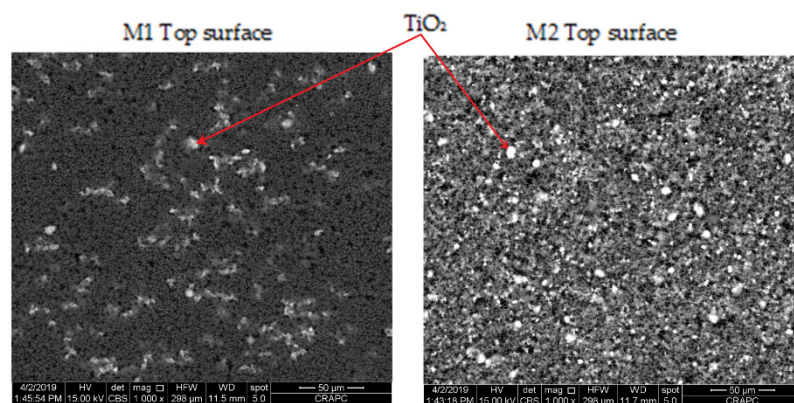


Figure 2. Top surface of membranes M1 and M2 collected on the concentric backscatter (CBS) detector from the FEI company.

## 2.2. Membrane Characterization

Fabricated membranes were characterized by measuring thickness, porosity, pure water permeability, pore size and contact angle (Table 1). The thickness of M1 was estimated at 0.159 mm which was greater than M2 at 0.099 mm. Membrane thickness increased concomitantly with an increase in polymer content. For example, the concentrations of PVDF and PMMA was 7 wt % compared to 6 wt % in M1 and M2 respectively (Figures 1 and 2). In a related study, Ortiz de Zarate et al. [36] also found that membrane thickness, with a sponge-like structure across the membrane and free of macro voids, increased with a higher polymer content, which presumably delayed separation during phase inversion. Moreover, it was observed that the porosity of M1 decreased (36.44%) compared to M2 (76.76%). A less-porous surface was detected when the polymer concentration increased (Figures 1 and 2). The reduction in cavities is presumably a consequence of an increasing polymer concentration. This is a very well documented phenomenon [18,24]. High polymer concentrations, in fact, slow down the precipitation process leading to the formation of a membrane with a lower pore size and therefore a lower porosity.

**Table 1.** Characteristics of the fabricated membranes.

Membrane	Membrane Thickness (mm)	Contact Angle (Degrees)	Pure Water Permeability (L/hm <sup>2</sup> bar)	Porosity (%)	Pore Size-Average Value (nm)
M1	0.156	90 ± 2.60	158	36.44	150
M2	0.099	85 ± 2.51	226	76.76	300

All membranes exhibited a hydrophilic nature because of the presence of PVDF and TiO<sub>2</sub>, which increased the wettability characteristics [32]. This is supported by the low contact angle measurements which gave values of 90° and 85° for M1 and M2 respectively.

One of the most important indicators in assessing the structure and morphology of membranes is the pure water permeability (PWP). The PWPs of the fabricated PVDF/PMMA/TiO<sub>2</sub> membranes are illustrated in Figure 3. The membrane prepared with a high polymer content (i.e., M1) led to a low PWP, which is associated with porosity and pore size. For example, for membranes M1 and M2 at a pressure of 1 bar the PWP was 125 and 275 L/h.m<sup>2</sup>.bar respectively. The PWP of membranes decreased with the pressure. For membrane M2 the PWP decreased from 300 to 225 L/h.m<sup>2</sup>.bar as the cross-membrane pressure increased from 0.5 to 1.5 bar. The reason for this could be two-fold. Firstly, for polymeric UF/MF membranes, compaction increases at high pressures which may alter/decrease the pore size, thus decreasing the water passage through the membrane. Secondly, there may have been membrane deformation caused by the metallic support. As the pressure increased, the membrane surface is compressed against the support, and thus exerts an additional resistance to water permeation. These experimental results are similar to those reported in the literature [37].

## 2.3. Filtration Tests

### 2.3.1. Impact of Pollutants

Figure 4 shows the changes in the permeate concentrations of Congo Red, Tartrazine, and Ciprofloxacin as a function of time for the same initial dye concentration. The results showed a good elimination of Congo Red, achieving 99% removal, and for Tartrazine 81% elimination despite a molecular weight smaller than the molecular weight cut-off (MWCO) of the membranes. The initial concentration of all pollutant models was 20 mg/L; after 10 min of filtration, the concentration of Congo Red and Tartrazine in the permeate decreased to 0.5 mg/L; while a concentration of 18 mg/L was noticed for Ciprofloxacin, even though the differences in molecular weights between the three pollutants were small (i.e., 697, 534, and 331 g/mol, respectively). The slight increase in Tartrazine concentration in the permeate as a function of time suggests that the separation process for molecules such as Tartrazine also depends on factors other than the MWCO, such as charge.

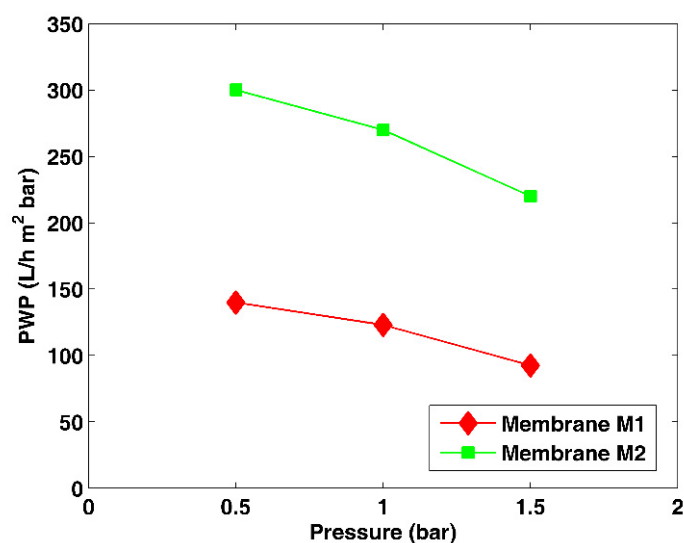


Figure 3. Pure water permeability (PWP) as a function of transmembrane pressure through the membranes M1 and M2.

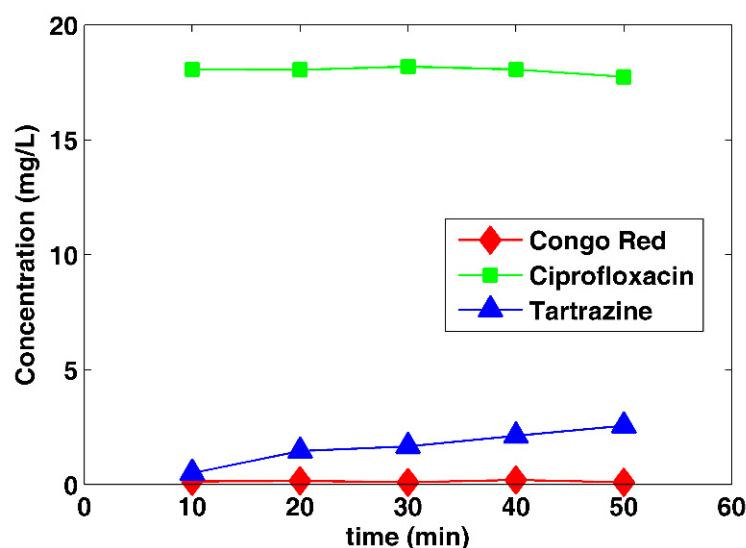
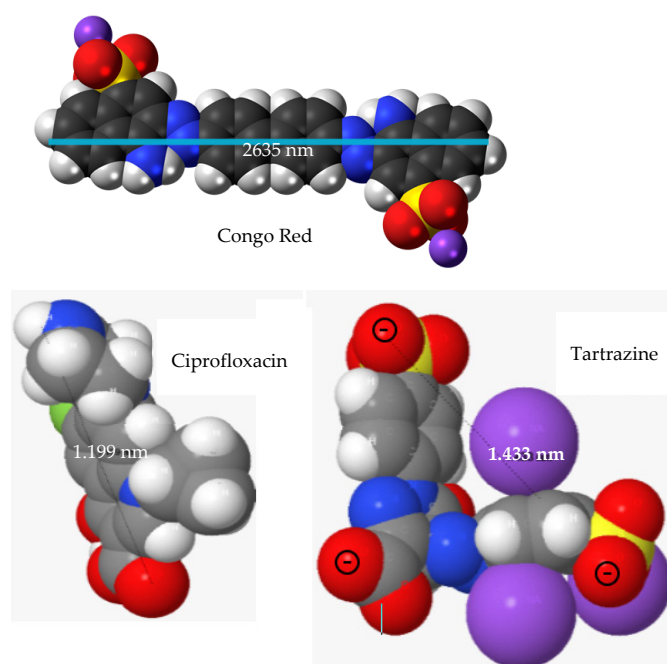


Figure 4. Pollutant concentration in permeate as a function of time for membrane M1.

Recent studies have shown the importance of the charge and shape of the molecules in the ultrafiltration process [38,39]. In Figure 5 it can be seen that Congo Red and Tartrazine have a linear structure with negative charges making it easier for their rejection by membranes with a negative surface charge. On the other hand, the globular structure and neutral charge of Ciprofloxacin reduces its rejection as shown by the higher permeate concentration (Figure 4). These results are similar to those reported by others [38,39].

The elimination rate was higher for the Congo Red (99%) and for Tartrazine molecule (81%) than for the Ciprofloxacin molecule (15%). This can be explained with the steric and electrostatic effect between these molecules and the negative charge of the membrane (Figure 5).

Uncharged molecules were able to pass through pores, while small, charged molecules could not pass. For pollutants with low or neutral charge, shape becomes an important factor, with globular being favored over a linear structure.



**Figure 5.** Steric configuration of pollutants models.

### 2.3.2. Impact of Operating Conditions

The concentration of Congo Red in the permeate decreased from 20 mg/L to 0.2 mg/L and remained stable throughout the filtration time. The Figure 6 shows that the pressure does not have a visible effect on the membrane retention of the Congo Red.

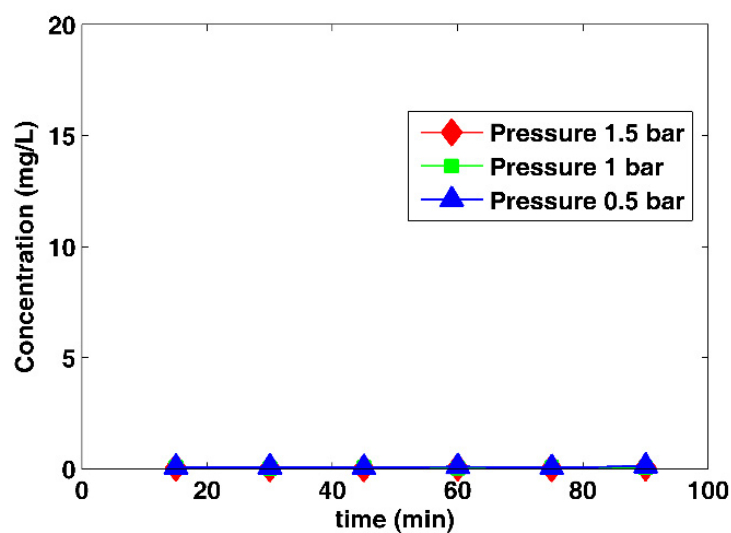


**Figure 6.** Effect of pressure on permeate concentration of Congo Red solution versus time.

As shown in Figure 7, the pressure applied does not affect the retention rate of Congo Red, unlike the retention rate of Tartrazine, which decreases with pressure. For example, with Tartrazine at 40 mg/L, as the pressure increased from 0.5 to 1.5 bar, retention decreased from 80% to 38%, respectively. This is presumably due to the smaller size of Tartrazine (slightly lower than MWCO) which allows it to be forced through the pores of the membrane at height pressures.

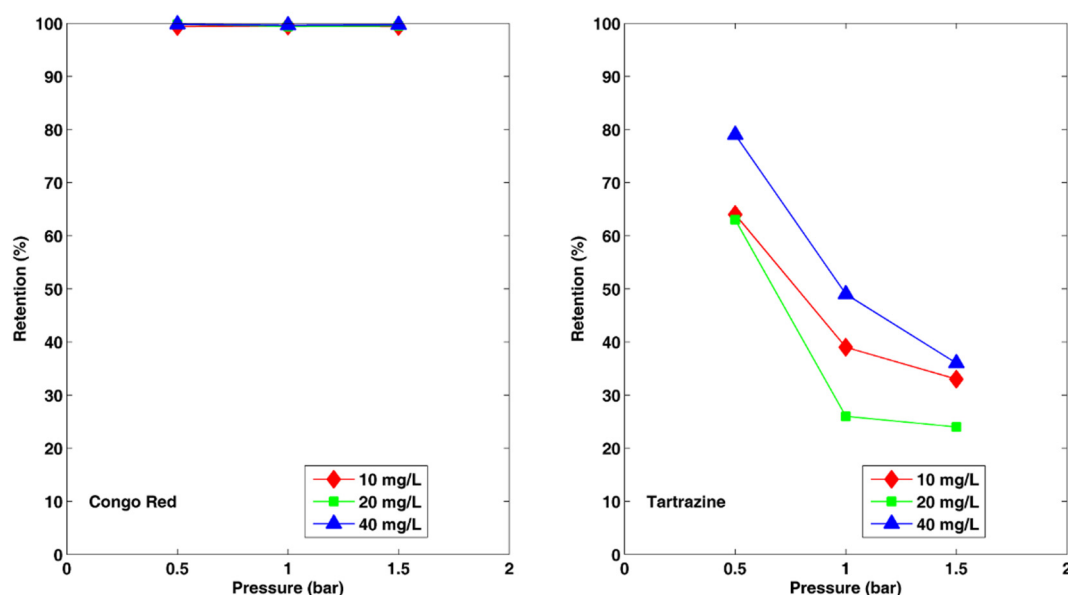


Figure 7. Effect of transmembrane pressure on retention of Congo Red and Tartrazine for the membrane.

In Figure 8, it was observed that the total volume flux linearly increased as the applied pressure increased. On the other hand, it was not greatly affected by the pH. This behavior has also been observed by Bandini et al. [40]. One can speculate that this could be due to the presence of pollutant molecules close to the membrane surface resulting in pore clogging. Consequently, the fluid had difficulty in passing through the pores. In the case of Tartrazine at 20 mg/L the highest permeate flux (188 L/m<sup>2</sup>.h) was achieved at 1.5 bar and the lowest flux value (88 L/m<sup>2</sup>.h) at 0.5 bar at 90 min of operation. These results are better than that reported by Waeger et al. [41] who showed that the permeate flux did not increase beyond a 0.5 bar. The improved fluxes in the current study may be due to the charged membrane which helps to repel the pollutant molecules from the surface.

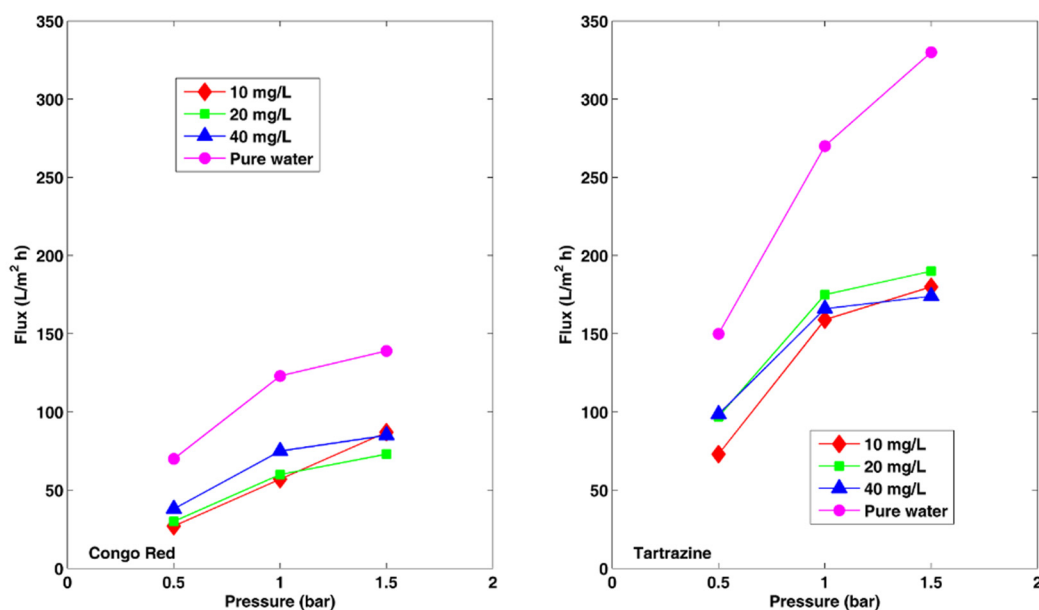


Figure 8. Effect of pressure on permeate flux of pure water and aqueous solutions of Congo Red and Tartrazine through the photocatalytic membrane.

To access the impact of pollutant concentration on the performance of the photocatalytic membrane and on its antifouling properties, a solution of Congo Red was filtered



at different concentrations. There were no significant differences in pollutant effluent concentrations between low and high feed concentrations of Congo Red (i.e., 10, 20, and 40 mg/L) (Figure 9). It can be argued that this was due to the antifouling properties of the negatively charged photocatalytic membrane. Similar results were found by Molinari et al. [42]. Figure 10 shows a difference between Tartrazine and Congo Red. Tartrazine retention increased at higher concentration. For example, from 10 to 20 mg/L, retention was about 65%, while at 40 mg/L, retention increased to 80%. At a higher dye concentration, the dye accumulation on membrane surface probably increased, thus reducing the flux [43].

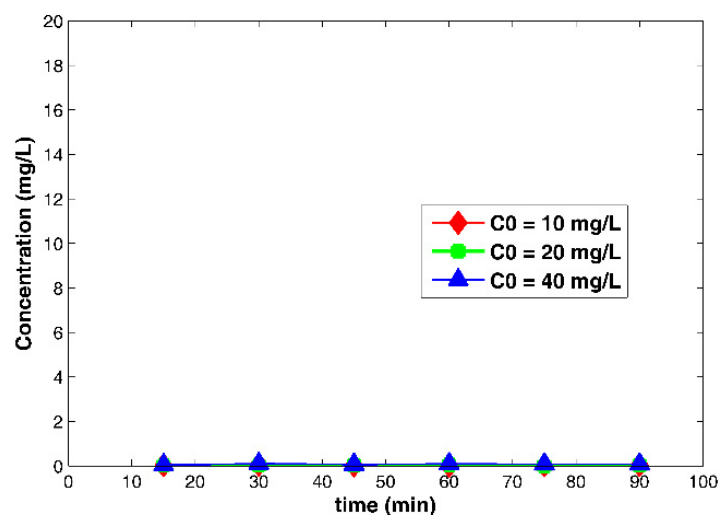


Figure 9. Effect of initial concentration on elimination of Congo Red by filtration using photocatalytic membrane.

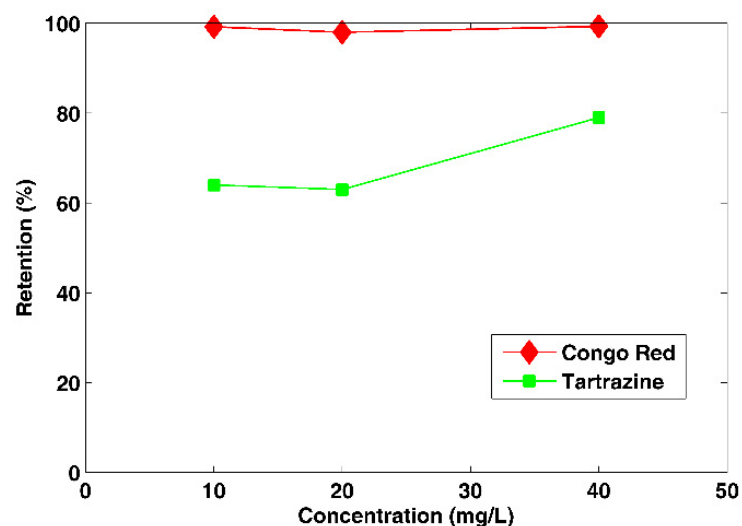
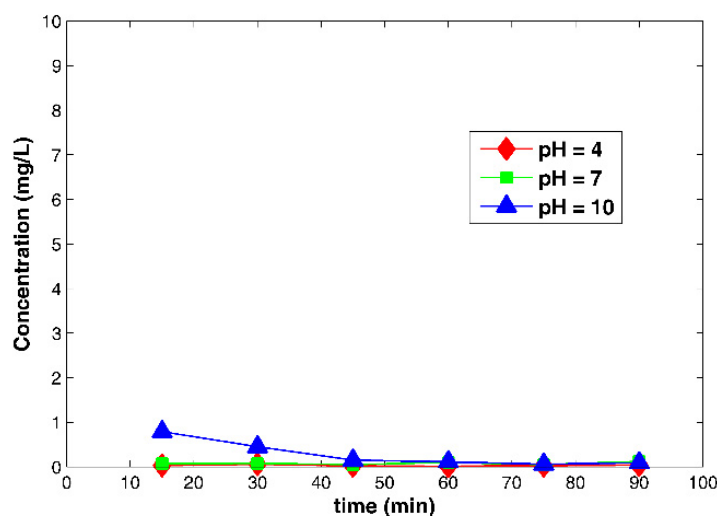


Figure 10. Effect of initial concentration on retention of Congo Red and Tartrazine.

Figure 11 illustrates the changes in Congo Red concentration in the permeate with time using the photocatalytic membrane M1. There was a significant effect at pH = 10 during the first 45 min. However, there was little apparent effect at pH 4 to 7. All three pollutants behaved the same after 45 min. Thus, the retention of Congo Red by the membrane M1 was not significantly affected by pH variation after an initial contact time, unlike pollutants of a monovalent and divalent ion nature, where the rejection rate is affected by the pH value [44].



**Figure 11.** Effect of pH on concentration of Congo Red in permeate during filtration with photocatalytic membrane M1 ( $C_0 = 10$  mg/L,  $P = 0.5$  bar).

### 2.3.3. Application of Photocatalytic Membranes for Removal of Bacteria from Wastewater

In preliminary photocatalytic membrane experiments with wastewater, there was a significant reduction in the bacterial (i.e., *Escherichia coli* and *Streptococcus* sp.) concentration due to the treatment. Water taken from a drainage effluent (conductivity = 11.18 ms/cm) gave a turbidity of 9.61 NTU (Nephelometric Turbidity Unit) before filtration and 0.17 NTU in the permeate after filtration using the M1 membrane. The conductivity, however, decreased very little because of filtration. The conductivity before and after filtration was 11.18 and 10.21 ms/cm, respectively. The lack of change was due presumably to the retention of organic matter and the presence of bivalent or monovalent cations which were retained. However, the pure water permeability (PWP) of the membrane decreased more than half from 140 to 67 L/h.m<sup>2</sup> and was due likely to the phenomenon of clogging by algae and microorganisms which are resistant to photo catalytic degradation. Removal of algae and microorganisms will require pretreatment.

A rich solution of two bacterial species, *Escherichia coli* and *Streptococcus* sp. was filtered through the M1 membrane. After counting on nutrient agar, by the MPN method (Most Probable Number), the results obtained showed a decrease in the two cultures in the permeate to approximately 240 cfu/mL. In addition, it was noted that the microbial populations in the retentate were uncountable.

## 3. Experimental

### 3.1. Chemicals

The polymers polyvinylidene fluoride (PVDF CAS 24937-79-9, Mw = 275 kg/mol) and poly methyl methacrylate (PMMA CAS 9011-14-7, Mw = 350 kg/mol) were supplied by Sigma-Aldrich (82024 Taufkirchen, Germany). Triethyl phosphate (Purity  $\geq 99.8\%$ ) 538728 Sigma Aldrich, Germany) was used as a solvent without further purification. Polyvinylpyrrolidone (PVP10 CAS 9003-39-8 Sigma-Aldrich, 82024 Taufkirchen, Germany, Mw = 10 kg/mol) and Polyethylene glycol (PEG-200, CAS 25322-68-3 Sigma Aldrich, 82024 Taufkirchen Germany, Mw = 200 g/mol) were added to the polymeric solution, as pore-forming agents. TiO<sub>2</sub> (Aeroxide-Degussa P25) photocatalyst was dispersed in the dope solution. As reported by the supplier, the TiO<sub>2</sub> nanoparticles have a primary mean diameter of 21 nm, with a density of 4 g/cm<sup>3</sup> with a predominance of the anatase form. Bi-distilled water was employed as a non-solvent for polymer precipitation.

### 3.2. Membrane Fabrication

Membranes were prepared as described by Benhabiles et al. [45] via the phase inversion technique. A non-solvent induced phase separation (NIPS) was used to fabricate

flat-sheet membranes using a dope solution containing PMMA, PVDF, PVP, PEG, TiO<sub>2</sub> and triethyl phosphate (TEP) as an alternative non-toxic solvent. TiO<sub>2</sub> particles are incorporated in the polymer matrix. The dope solution was cast on a glass plate to a predetermined thickness of 350 µm using a manual Casting knife (Elcometer 3700 Film Applicator Blade with Tank, Elcometer Instrument GmbH, Aalen, Germany). Two types of membranes were fabricated (Table 2). For example, membranes M1 & M2 contained 2.5 wt % and 5 wt % TiO<sub>2</sub> respectively. The produced membranes (60 cm × 16 cm) are washed three times with water at 60 °C, then dried in open air for 12 h.

**Table 2.** TiO<sub>2</sub>-PVDF/PMMA photocatalytic membranes produced by varying casting solution composition.

Membrane Code	TiO <sub>2</sub> /wt %	PVDF/wt %	PMMA/wt%	PVP/wt %	PEG/wt %	TEP/wt %
M1	2.5%	7%	7%	5%	5%	73.5%
M2	5%	6%	6%	5%	5%	73%

### 3.3. Membrane Characterization

#### 3.3.1. Membrane Morphology

Scanning electron microscopy (SEM) was performed to assess the structure, porosity, and thickness of the membrane. A Quanta 250 from the FEI Company was employed for the SEM. Cross sections of the membranes were prepared by fracturing the membranes in liquid nitrogen. Membranes were observed at a magnification ranging from 500× to 24,000×.

#### 3.3.2. Membrane Porosity

Porosity, defined as the pore volume divided by the total volume of the membrane, was calculated by the following equation:

$$Porosity(\%) = \frac{\frac{Wt_w - Wt_d}{\rho_k}}{\frac{Wt_w - Wt_d}{\rho_k} + \frac{Wt_d}{\rho_p}} \times 100 \quad (1)$$

where  $Wt_w$  is the wet membrane weight,  $Wt_d$  is the dry membrane weight,  $\rho_k$  is the isopropanol density and  $\rho_p$  is the polymer density. Each membrane sample was weighed and subsequently submerged in a container filled with isopropanol and stored for 24 h. The test was performed three times and the porosity value was calculated.

#### 3.3.3. Contact Angle

The contact angle  $\theta$  for the membrane surface was measured by an optical tensiometer (CAM100 Instrument, Nordtest srl, GI, Serravalle Scrivia (AL), Italy) via the drop method. The contact angle determines the wettability and hydrophobicity of the membrane.

#### 3.3.4. Pure Water Permeability

A laboratory crossflow cell (DeltaE srl, Italy), operating at 25 °C, was employed to carry out pure water permeability (PWP) experiments. Pure water was passed across the membrane by means of a peristaltic pump (Tuthill Pump Co., Concord, CA, USA). Stability of the permeate flow was achieved before running the permeability tests. PWP was calculated by applying the following equation:

$$PWP = \frac{Q}{At\rho} \quad (2)$$

where  $A$  is the membrane area expressed in m<sup>2</sup>,  
 $\rho$  is the pressure expressed in bar,  
 $Q$  is the permeate volume in liters,  
and  $t$  is the time expressed in hours.

One of the most important indicators in assessing the structure and morphology of membranes is the pure water permeability (PWP). It was carried out by measuring the flow of permeate at different working pressures in the range 0.5–1.5 bars.

### 3.3.5. Permeate Flux and Retention

The permeate flux was calculated by dividing the permeate volume by the membrane effective area and a specified time (Equation (3)):

$$\text{Permeate flux} = \frac{\text{permeate volume collected}}{\text{effective area} \times \text{time}} \quad (3)$$

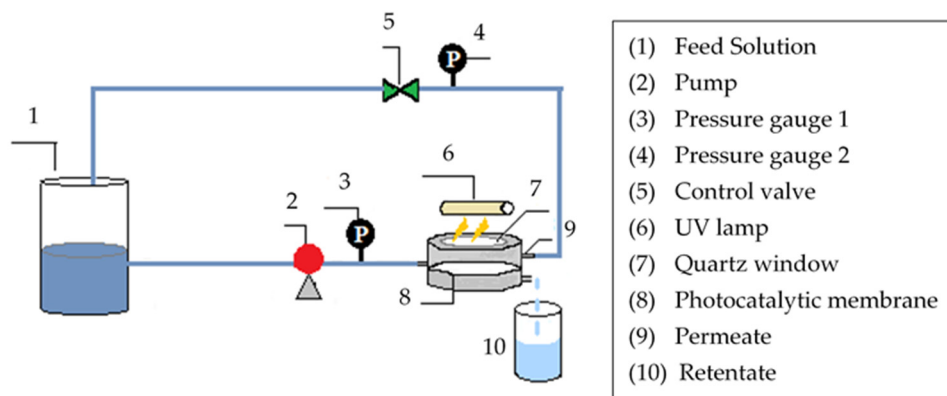
The retention indicates pollutant removal by the membrane and was calculated as follows:

$$\text{Retention}(\%) = \left(1 - \frac{C_p}{C_f}\right) \times 100 \quad (4)$$

where  $C_p$  and  $C_f$  are the concentrations in the permeate and in the feed respectively.

### 3.4. Experimental Setup

Figure 12 represents the experimental setup for membrane performance evaluation by a crossflow filtration cell, also known as tangential flow filtration. All experiments were carried out at room temperature. The system consisted of a reservoir, pump, valves, pressure regulators, and filtration cell with viewport for photocatalytic application designed by DeltaE SRL (Rende (CS) Italy). The peristaltic pump (ESMATEC-IDEX Corporation) was employed to circulate the feed and supply the operating pressure, manometers, and feed tank linked together with polymeric flexible pipes.



#### Process parameters

Feed Volume 1 L    Concentration range: 10–40 mg/L    Flow rate  $\approx$  2 L/min    Pressure: 0.5–2 bars

**Figure 12.** Schematic of the crossflow system.

The filtration cell was circular with an effective membrane area of 0.0013 m<sup>2</sup>. The applied feed was formed from dissolving various amounts of model pollutant powder in purified water (i.e., 10 mg/L, 20 mg/L and 40 mg/L). The retentate was recirculated to the reservoir and the permeate was collected and measured. The volume of the feed solution was 1 L for all experiments.

### 3.5. Filtration Experiments

The filtration experiments were carried out using the pilot crossflow system shown in Figure 12 at the Waste Water Treatment and Valorization laboratory (EVER) of the

Solar Equipment Development Unit (UDES). A flat sheet membrane with 47 mm diameter ( $0.0013 \text{ m}^2$  effective surface) is supported by a stainless-steel grid integrated in the cell (PMR). Before each filtration test the membrane was washed with purified water for 30 min in recirculation mode.

The pollutants assessed were chosen according to their physico-chemical properties (e.g., Molecular Weight, pKa, charge) and the size of the pores of the membranes. Three model pollutant compounds were tested, Congo Red (MW = 696.66 Da, pKa = 4), Tartrazine (MW = 534.3 Da, pKa = 9.2), and Ciprofloxacin (MW = 331.3 Da, pKa = 6.09). The separation efficiency of the membranes was evaluated by filtration of molecules from different families: Congo Red (697 g/mol); textile dye with the empirical formula ( $\text{C}_{32}\text{H}_{22}\text{N}_6\text{Na}_2\text{O}_6\text{S}_2$ ), Tartrazine (534 g/mol) which is a food color with formula ( $\text{C}_{16}\text{H}_9\text{N}_4\text{Na}_3\text{O}_9\text{S}_2$ ), and a pharmaceutical product Ciprofloxacin (331 g/mol) with the molecular formula ( $\text{C}_{17}\text{H}_{18}\text{FN}_3\text{O}_3$ ).

A volume of 1 L at 20 mg/L of each pollutant was filtered through the membrane M1 under a pressure of 0.5 bar. The filtration tests were carried out at room temperature under a transmembrane pressure varying from 0.5 bar to 1.5 bar, with recirculation of the retentate and permeation to the feed tank.

The concentration of pollutants in the permeate and the retentate were quantitatively determined using a spectrophotometer Shimadzu UV-VIS 18000, at a wavelength of 497 nm for Congo Red, 427 nm for Tartrazine, and 273 nm for Ciprofloxacin. The determined concentrations were used for calculation of the retention rate. The impact of operating conditions: pH, pressure, and pollutant concentration in the feed were studied. The evolution of concentration in the permeate and retentate solution was assessed by spectroscopy UV for the chemical pollutants. The flux and the retention values for each pollutant was measured and compared.

### 3.6. Application of Photocatalytic Membranes for Bacteria Removal from Wastewater

The use of filtration with a photocatalytic membrane to eliminate bacteria (*Escherichia coli* and *Streptococcus* sp.) present in a wastewater solution containing a mixture of the two strains was assessed. The conductivity of water taken from a drainage effluent before and after filtration by the M1 membrane was evaluated. A culture was performed on nutritive agar for the retentate and for the permeate. These results were analyzed to determine how well the photocatalytic membrane retained bacteria.

## 4. Conclusions

The resulting  $\text{TiO}_2$ -PVDF/PMMA nano-composites flat sheet membranes had a high permeability and porosity that could retain organic molecules such as Congo Red (MW 696.66 g/mol), and thus is an excellent candidate for use in the treatment of wastewater from the pharmaceutical industry.

The results revealed an excellent elimination of Congo Red with 99% removal and 81% for Tartrazine. However, a decrease of only 15% was observed for Ciprofloxacin. This behavior suggests that the separation process depends on factors other than the molecular weight cut-off of the membrane (MWCO), such as charge. Results suggest that negative charge on the hydrophilic membrane plays a significant role in the rejection process. In addition to filtration performance, the  $\text{TiO}_2$  in the polymer matrix has anti-fouling properties.

In experiments with wastewater, there was a significant reduction in the bacterial (*Escherichia coli* and *Streptococcus* sp.) concentration observed.

Operating pressures (0.5–1.5 bar) do not have a significant effect on the retention of pollutants. In all cases, permeate flux was increased by raising the operating pressure and decreased by increasing the organic concentration. Under similar operating conditions, pH showed a variable influence on the retention of the model pollutant molecules with no significant influence observed for Tartrazine, Ciprofloxacin, and Red Congo.

Additional studies are still needed to take advantage of photocatalytic membrane potential and develop their anti-clogging performance.

**Author Contributions:** Conceptualization, K.B.E., O.B. and H.M.; Methodology, O.B. and H.M.; Validation, K.B.E., O.B., S.B. and Z.B.; Formal Analysis, O.B. and K.B.E.; Investigation, K.B.E., O.B.; Data Curation, M.G. and H.M.; All authors have read and agreed to the published version of the manuscript.

**Funding:** This research received no external funding.

**Conflicts of Interest:** The authors declare no conflict of interest.

## References

1. Rout, P.R.; Zhang, T.C.; Bhunia, P.; Surampalli, R.Y. Treatment technologies for emerging contaminants in wastewater treatment plants: A review. *Sci. Total Environ.* **2020**, *753*, 141990. [CrossRef] [PubMed]
2. Margot, J.; Rossi, L.; Barry, D.A.; Holliger, C. A review of the fate of micropollutants in wastewater treatment plants. *Wiley Interdiscip. Rev. Water* **2015**, *2*, 457–487. [CrossRef]
3. Rodriguez-Narvaez, O.M.; Peralta-Hernandez, J.M.; Goonetilleke, A.; Bandala, E.R. Treatment technologies for emerging contaminants in water: A review. *Chem. Eng. J.* **2017**, *323*, 361–380. [CrossRef]
4. Deng, Y.; Zhao, R. Advanced oxidation processes (AOPs) in wastewater treatment. *Curr. Pollut. Rep.* **2015**, *1*, 167–176. [CrossRef]
5. Malato, S.; Fernández-Ibáñez, P.; Maldonado, M.I.; Blanco, J.; Gernjak, W. Decontamination and disinfection of water by solar photocatalysis: Recent overview and trends. *Catal. Today* **2009**, *147*, 1–59. [CrossRef]
6. Al-Dawery, S.K. Photo-catalyst degradation of tartrazine compound in wastewater using TiO<sub>2</sub> and UV light. *J. Eng. Sci. Technol.* **2013**, *8*, 683–691.
7. da Silva, S.W.; Klauck, C.R.; Siqueira, M.A.; Bernardes, A.M. Degradation of the commercial surfactant nonylphenol ethoxylate by advanced oxidation processes. *J. Hazard. Mater.* **2015**, *282*, 241–248. [CrossRef]
8. Mierzwa, J.C.; Rodrigues, R.; Teixeira, A.C.S.C.; Ameta, I.S.C.; Ameta, R. *Advanced Oxidation Processes for Wastewater Treatment: Emerging Green Chemical Technology*; Academic Press: Cambridge, MA, USA, 2018; pp. 13–48.
9. Amor, C.; Marchão, L.; Lucas, M.S.; Peres, J.A. Application of advanced oxidation processes for the treatment of recalcitrant agro-industrial wastewater: A review. *Water* **2019**, *11*, 205. [CrossRef]
10. Fernandes, A.; Makoš, P.; Wang, Z.; Boczkaj, G. Synergistic effect of TiO<sub>2</sub> photocatalytic advanced oxidation processes in the treatment of refinery effluents. *Chem. Eng. J.* **2020**, *391*, 123488. [CrossRef]
11. Norman, N.; Anthony, L.; Fane, G.; Ho, W.S.W.; Matsuura, T. *Advanced Membrane Technology and Applications*; John Wiley & Sons, Inc.: Hoboken, NJ, USA, 2008.
12. Goh, P.S.; Wong, T.W.; Lim, J.W.; Ismail, A.F.; Hilal, N. Chapter 9-Innovative and sustainable membrane technology for wastewater treatment and desalination application. *Innov. Strateg. Environ. Sci.* **2020**, 291–319.
13. Khalil, A.M.; Schäfer, A.I. Cross-linked  $\beta$ -cyclodextrin nanofiber composite membrane for steroid hormone micropollutant removal from water. *J. Membr. Sci.* **2021**, *618*, 118228. [CrossRef]
14. Cseri, L.; Topuz, F.; Abdulhamid, M.A.; Alammari, A.; Budd, P.M.; Szekely, G. Electrospun Adsorptive Nanofibrous Membranes from Ion Exchange Polymers to Snare Textile Dyes from Wastewater. *Adv. Mater. Technol.* **2021**, 2000955. [CrossRef]
15. Ahdab, Y.D.; Rehman, D. Brackish water desalination for greenhouses: Improving groundwater quality for irrigation using monovalent selective electrodialysis reversal. *J. Membr. Sci.* **2020**, *610*, 118072. [CrossRef]
16. Abdulaziz, A.; Sang-Hee, P.; Izwaharyanie, I.; Deepak, A.; Tibor, H.; Ludovic, F.D.; Hong Ngee, L.; Gyorgy, S. Architecting neonicotinoid-scavenging nanocomposite hydrogels for environmental remediation. *Appl. Mater. Today* **2020**, *21*, 100878.
17. Sun, C.; Zhang, N.; Li, F.; Ke, G.; Song, L.; Liu, X.; Liang, S. Quantitative analysis of membrane fouling mechanisms involved in microfiltration of humic acid–protein mixtures at different solution conditions. *Water* **2018**, *10*, 1306. [CrossRef]
18. Galiano, F.; Figoli, A.; Deowan, S.A.; Johnson, D.; Altinkaya, S.A.; Veltri, L.; De Luca, G.; Mancuso, R.; Hilal, N.; Gabriele, B.; et al. A step forward to a more efficient wastewater treatment by membrane surface modification via polymerizable bicontinuous microemulsion. *J. Membr. Sci.* **2015**, *482*, 103–114. [CrossRef]
19. Molinari, R.; Lavorato, C.; Argurio, P. Recent progress of photocatalytic membrane reactors in water treatment and in synthesis of organic compounds. A review. *Catal. Today* **2017**, *281*, 144–164. [CrossRef]
20. Benhabiles, O.; Mahmoudi, H.; Lounici, H.; Goosen, M.F.A. Effectiveness of a photocatalytic organic membrane for solar degradation of methylene blue pollutant. *Desalin. Water Treat.* **2016**, *57*, 14067–14076. [CrossRef]
21. Choi, H.; Stathatos, E.; Dionysiou, D.D. Photocatalytic TiO<sub>2</sub> films and membranes for the development of efficient wastewater treatment and reuse systems. *Desalination* **2007**, *202*, 199–206. [CrossRef]
22. Figoli, A.; Ursino, C.; Galiano, F.; Di Nicolò, E.D.; Campanelli, P.; Carnevale, M.C.; Criscuoli, A. Innovative hydrophobic coating of perfluoropolyether (PFPE) on commercial hydrophilic membranes for DCMD application. *J. Membr. Sci.* **2017**, *522*, 192–201. [CrossRef]
23. Hsu, C.H.; Venault, A.; Huang, Y.T.; Wu, B.W.; Chou, C.J.; Ishihara, K.; Chang, Y. Toward antibiofouling PVDF membranes. *Langmuir* **2019**, *35*, 6782–6792. [CrossRef]
24. Romanos, G.E.; Athanasekou, C.P.; Likodimos, V.; Aloupogiannis, P.; Falaras, P. Hybrid Ultrafiltration/Photocatalytic Membranes for Efficient Water Treatment. *Ind. Eng. Chem.* **2013**, *52*, 13938–13947. [CrossRef]

25. Li, X.; Lu, X. Morphology of polyvinylidene fluoride and its blend in thermally induced phase separation process. *J. Appl. Polym. Sci.* **2006**, *101*, 2944–2952. [CrossRef]
26. Gnanou, Y.; Fontanille, M. *Organic and Physical Chemistry of Polymers*; Wiley Blackwell: Hoboken, NJ, USA, 2008.
27. Matindi, C.N.; Hu, M.; Kadanyo, S.; Ly, Q.V.; Gumbi, N.N.; Dlamini, D.S.; Li, J.; Hu, Y.; Cui, Z.; Li, J. Tailoring the morphology of polyethersulfone/sulfonated polysulfone ultrafiltration membranes for highly efficient separation of oil-in-water emulsions using TiO<sub>2</sub> nanoparticles. *J. Membr. Sci.* **2021**, *620*, 118868. [CrossRef]
28. Yu, J.; Zhang, Y.; Chen, J.; Cui, L.; Jing, W. Solvothermal-induced assembly of 2D-2D rGO-TiO<sub>2</sub> nanocomposite for the construction of nanochannel membrane. *J. Membr. Sci.* **2020**, *600*, 117870. [CrossRef]
29. Figoli, A.; Simone, S.; Drioli, E.; Hilal, I.N.; Ismail, A.F.; Wright, C. *Membrane Fabrication*; Taylor & Francis Group: Boca Raton, FL, USA, 2015; pp. 1–42.
30. Marino, T.; Blefari, S.; di Nicolò, E.; Figoli, A. A more sustainable membrane preparation using triethyl phosphate as solvent. *Green Process. Synth.* **2017**, *6*, 295–300. [CrossRef]
31. Mozia, S.; Darowna, D.; Przepiórski, J.; Morawski, A.W. Evaluation of performance of hybrid photolysis-DCMD and photocatalysis-DCMD systems utilizing UV-C radiation for removal of diclofenac sodium salt from water. *Pol. J. Chem. Technol.* **2013**, *15*, 51–60. [CrossRef]
32. Said, M.; Nasir, S.; Priadi, D.P. The Effect of Pressure and Time Operation of Gasing River Water Treasure on Pollutant Concentration by Using Ceramic Membrane Separation. *Sriwij. J. Environ.* **2018**, *3*, 47–54. [CrossRef]
33. Marino, T.; Russo, F.; Figoli, A. The Formation of polyvinylidene fluoride membranes with tailored properties via vapour/non-solvent induced phase separation. *Membranes* **2018**, *8*, 71. [CrossRef] [PubMed]
34. Wang, L.; Yong, W.F.; Yu, L.E.; Chung, T. Design of high efficiency PVDF-PEG hollow fibers for air filtration of ultrafine particles. *J. Membr. Sci.* **2017**, *535*, 342–349. [CrossRef]
35. Drelich, J.; Chibowski, E. Superhydrophilic and superwetting surfaces: Definition and mechanisms of control. *Langmuir* **2010**, *26*, 18621–18623. [CrossRef]
36. de Zárate, J.M.O.; Pen˜a, L.; Mengual, J.I. Characterization of membrane distillation membranes prepared by phase inversion. *Desalination* **1995**, *100*, 139–148. [CrossRef]
37. Kim, Y.C.; Elimelech, M. Adverse impact of feed channel spacers on the performance of pressure retarded osmosis. *Environ. Sci. Technol.* **2012**, *46*, 4673–4681. [CrossRef]
38. Arsuaga, J.M.; Sotto, A.; López-Muñoz, M.J.; Braeken, L. Influence of type and position of functional groups of phenolic compounds on NF/RO performance. *J. Membr. Sci.* **2011**, *372*, 380–386. [CrossRef]
39. Revchuk, A.D.; Suffet, I.N. Ultrafiltration separation of aquatic natural organic matter: Chemical probes for quality assurance. *Water Res.* **2009**, *43*, 3685–3692. [CrossRef] [PubMed]
40. Bandini, S.; Drei, J.; Vezzani, D. The role of pH and concentration on the ion rejection in polyamide nanofiltration membranes. *J. Membr. Sci.* **2005**, *264*, 65–74. [CrossRef]
41. Waeger, F.; Delhay, T.; Fuchs, W. The use of ceramic microfiltration and ultrafiltration membranes for particle removal from anaerobic digester effluents. *Sep. Purif. Technol.* **2010**, *73*, 271–278. [CrossRef]
42. Molinari, R.; Pirillo, F.; Falco, M.; Loddò, V.; Palmisano, L. Photocatalytic degradation of dyes by using a membrane reactor. *Chem. Eng. Process.* **2004**, *43*, 1103–1114. [CrossRef]
43. Koyuncu, I. Reactive dye removal in dye/salt mixtures by nanofiltration membranes containing vinylsulphone dyes: Effect of feed concentration and cross flow velocity. *Desalination* **2002**, *143*, 243–253. [CrossRef]
44. Qin, J.-J.; Oo, M.H.; Lee, H.; Coniglio, B. Effect of feed pH on permeate pH and ion rejection under acidic conditions in NF process. *J. Membr. Sci.* **2004**, *232*, 153–159. [CrossRef]
45. Benhabiles, O.; Galiano, F.; Marino, T.; Mahmoudi, H.; Lounici, H.; Figoli, A. Preparation and characterization of TiO<sub>2</sub>-PVDF/PMMA blend membranes using an alternative non-toxic solvent for UF/MF and photocatalytic application. *Molecules* **2019**, *24*, 724. [CrossRef] [PubMed]





## Article

# Study of Catalysts' Influence on Photocatalysis/ Photodegradation of Olive Oil Mill Wastewater. Determination of the Optimum Working Conditions

Gassan Hodaifa <sup>1,\*</sup> , Cristina Agabo García <sup>1,2</sup>  and Rafael Borja <sup>3</sup> 

<sup>1</sup> Molecular Biology and Biochemical Engineering Department, Chemical Engineering Area, Faculty of Experimental Sciences, University of Pablo de Olavide, ES-41013 Seville, Spain; cristina.agabo@uca.es

<sup>2</sup> Department of Environmental Technologies, University of Cadiz, Campus de Puerto Real, ES-11500 Puerto Real, Cadiz, Spain

<sup>3</sup> Instituto de la Grasa (CSIC), Campus Universitario Pablo de Olavide, Carretera de Utrera km 1, Building 46, ES-41013 Seville, Spain; rborja@cica.es

\* Correspondence: ghodaifa@upo.es; Tel.: +34-954-978-206

Received: 22 April 2020; Accepted: 15 May 2020; Published: 17 May 2020

**Abstract:** The high production of raw olive oil mill wastewater (OMW) is a current environmental problem due to its high organic load and phenol compounds. In this work, photo-Fenton reaction as an advanced oxidation process has been chosen for OMW treatment. In this sense, different iron salts ( $\text{FeCl}_3$ ,  $\text{Fe}_2(\text{SO}_4)_3$ ,  $\text{FeSO}_4 \cdot 7\text{H}_2\text{O}$ , and  $\text{Fe}(\text{ClO}_4)_3$ ) as catalysts were used in order to compare their effects on treatment. For each catalyst, different  $\text{H}_2\text{O}_2$  concentrations (2.5, 5.0, 7.5, 10.0, 15.0, 20.0, and 30.0%, w/v) as oxidizing agents were tested. The common experimental conditions were temperature 20 °C, the catalyst/ $\text{H}_2\text{O}_2$  ratio = 0.03, pH = 3, and ultraviolet light. The Lagergren kinetic model, in cases of total organic carbon removal, for the best  $\text{H}_2\text{O}_2$  concentration per catalyst was used. During the experiments, the water quality was determined by measuring the removal percentages on chemical oxygen demand, total carbon, total organic carbon, total nitrogen, total phenolic compounds, total iron, turbidity and electric conductivity. The best catalyst was  $\text{FeCl}_3$  and the optimum  $\text{H}_2\text{O}_2$  concentration was 7.5% (w/v). At these optimal conditions, the removal percentages for chemical oxygen demand, total phenolic compounds, total carbon, total organic carbon and total nitrogen were 60.3%, 88.4%, 70.1%, 63.2% and 51.5%, respectively.

**Keywords:** olive oil mill wastewater; degradation; photo-Fenton; UV light; iron salts

## 1. Introduction

Global olive oil production is about 3 millions of tons per year. European Union is the most olive oil producing region representing around 73% of world production, and Spanish olive oil industry produces 45% of total world production [1]. This high production brings a considerable amount of wastewater. In the two-phase process, the wastewater generated come from olives and olive oil washing.

The physicochemical characterization of olive mill wastewater (OMW) depends on the process in which it has been generated. For the press and three-phase continuous centrifugation processes, chemical oxygen demand (COD) and biological oxygen demand ( $\text{BOD}_5$ ) values of wastewater vary in the range of 40–220 g  $\text{O}_2/\text{L}$  and 35–110 g  $\text{O}_2/\text{L}$ , respectively [2,3]. Nevertheless, for the two-phase continuous centrifugation process, the COD and  $\text{BOD}_5$  values of wastewater vary from 0.5 to 65 g  $\text{O}_2/\text{L}$  and 0.5 to 19 g  $\text{O}_2/\text{L}$ , respectively [4–6]. In general, total phenolic compounds (TPCs) are in the range of 0.044–1 g/L [7,8]. The high organic load present in OMW requires more dissolved oxygen for its degradation by aerobic microorganisms, which implies its consumption causing low dissolved oxygen

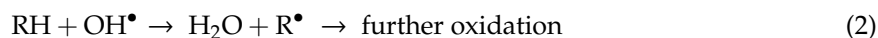
levels. In addition, the phenolic compounds it contains have inhibitory/toxic effects on microbial growth. The solubility of phenolic compounds in water and its relative stability in the environment make them resistance to natural biodegradation. In fact, the US Environmental Protection Agency reported that the degradation of phenol compounds in wastewater is a priority [9]. In addition, this kind of component produces a negative environmental impact on rivers, other natural surface and underground waters, making them unsuitable for use. For this reason, it is necessary to treat these wastewaters before discharging them to natural streams.

Due to the lack of consensus on European legislation for OMW treatment, different possibilities have arisen [10]. In some countries, such as Spain, the main management method is based on the accumulation of these wastewaters in evaporation ponds (large reservoirs) in order to its biological auto-depuration and its elimination during the summer months. This solution requires a low economic investment due to its simplicity of operation. In any case, the auto-depuration of OMW needs large expanses of land with 1 m<sup>2</sup> of area and 1.5 m of deep per each 2.5 m<sup>3</sup> of OMW [11]. Besides, the management method is commonly uncontrolled (having different operational conditions in each season), slow (complete evaporation needs approximately 8–9 months) and has some environmental risks related to atmospheric pollution, clogging, insect plague and aquifer infiltration [12,13].

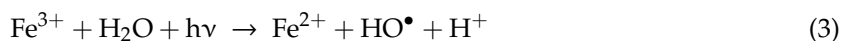
In this context, advanced oxidation processes (AOPs) have considerable potential for the treatment of different polluted wastewaters, due to the formation of hydroxyl radicals, which oxidize a wide range of compounds [14–17]. In addition, chemical oxidation not only has a high efficiency and simplicity but also it produces no residues [18]. Advanced oxidation processes include normally a transition metal (Fe<sup>3+</sup>, Cu<sup>2+</sup>, Mn<sup>2+</sup>, Co<sup>2+</sup> and Ag<sup>+</sup>) as a catalyst, an oxidizing agent (O<sub>3</sub>, H<sub>2</sub>O<sub>2</sub> and KMnO<sub>4</sub>) and/or an energy source (artificial UV-light or solar light) [19]. The combination of H<sub>2</sub>O<sub>2</sub> as an oxidizing agent and iron salt without any energy source (dark conditions) is named as the Fenton reagent [20,21]. It is known that the Fenton reaction has a high potential to treat wastewater with a high load of organic matter due to its high effectivity in removing a wide range of hazardous organic pollutants from wastewater. Its main benefit is the complete degradation of the contaminants to harmless compounds, e.g., CO<sub>2</sub>, water and inorganic salts [18,22–24]. Fenton's reagent generates hydroxyl radicals according to the following reaction [25]:



The generation of hydroxyl radicals involves a complex reaction sequence in an aqueous solution. Hydroxyl radicals can oxidize organics (RH) by abstraction of protons producing organic radicals (R<sup>•</sup>), which are highly reactive and can be further oxidized [26]:



Recent studies claim the benefits of combined Fenton process with ultraviolet/solar light irradiation (H<sub>2</sub>O<sub>2</sub>/catalyst/UV or Visible) due to the reaction time being shorter and the removal rate being higher, which makes it possible to work with smaller equipment and reduce operating costs [14,27–29]. In addition, in these conditions, the Fenton reaction increases its oxidizing capacity due to the decomposition of the photoactive Fe(OH)<sub>2</sub><sup>+</sup> species by UV/visible light, promoting an additional generation of OH<sup>•</sup> radicals (Equation (3)) in the solution [30,31].



Reaction 3 shows that UV/Visible irradiation leads not only to the formation of additional hydroxyl radicals but also to the recycling of the iron catalyst. The resulting product of organic matter after the photo-Fenton reaction is carbon dioxide as the final product. If the organic matter contains heteroatoms, oxidation often leads to the formation of inorganic acids (HCl, HNO<sub>3</sub>, H<sub>2</sub>SO<sub>4</sub>, etc.). [29]. The organic

bonded nitrogen can be released in ionic and gaseous forms, for example as nitrate, nitrite, ammonia, molecular nitrogen, dinitrogen monoxide and nitrogen monoxide [32].

The implementation of these treatment processes in olive oil mills is clearly beneficial, taking into account: (i) the mild operational conditions (room temperature, atmospheric pressure), (ii) the lack of high investments (economic equipment), (iii) the simplicity of the technology and (iv) the eco-friendly character of the process (harmless oxidizing agents and recoverable catalysts) [33]. In previous works,  $\text{Fe}^{3+}$  salts (coming mainly from ferric chloride,  $\text{FeCl}_3$ ) were as effective as  $\text{Fe}^{2+}$  ones, in spite of producing an initial slower rate of  $\text{H}_2\text{O}_2$  decomposition [30]. In this sense, Nieto et al. [18] studied OMW treatment through a homogeneous Fenton-like reaction. Furthermore, Esteves et al. [33] tested  $\text{Fe}^{3+}/\text{H}_2\text{O}_2$  and  $\text{Fe}^{3+}/\text{H}_2\text{O}_2/\text{UV}$  systems for OMW treatment. In the second system, the UV/visible light generated from a high-pressure mercury vapor, Heraeus TQ (TQ is the lightest of the permissible cap lamps) 150 with 150 W, was used. The comparison between Fenton and photo-Fenton reactions for OMW treatment was developed achieving 34.9% vs. 41.8% on total organic carbon (TOC) removal, 55.7% vs. 63.2% on COD removal and 81.4% vs. 83.8% of total phenolic compounds (TPCs) removal. Esteves et al. [33], also tested two different iron salts  $\text{FeSO}_4 \cdot 7\text{H}_2\text{O}$  and  $\text{FeCl}_3 \cdot 6\text{H}_2\text{O}$  at only  $[\text{Fe}^{2+}$  or  $\text{Fe}^{3+}] = 1 \text{ g/L}$ , obtaining that TOC removal was higher in the case of  $\text{FeCl}_3 \cdot 6\text{H}_2\text{O}$  in comparison with applying  $\text{FeSO}_4 \cdot 7\text{H}_2\text{O}$  as the catalyst.

In this research work, the treatment of olives and olive oil washing wastewaters using a homogeneous photo-Fenton reaction for the photodegradation of the organic matter was studied. The effect of four iron salts ( $\text{Fe}^{2+}$  or  $\text{Fe}^{3+}$ ) at different hydrogen peroxide concentrations (2.5, 5.0, 7.5, 10.0, 15.0, 20.0, and 30.0%, w/v) in the photodegradation of industrial OMWs were studied (data not found in the literature). In addition, the photolysis effect on OMW (UV/OMW) at different initial organic matters were studied as control experiments. The best catalyst for OMWs treatment was chosen based on the evaluation of the photodegradation efficacy in terms of total carbon (TC), total organic carbon (TOC), total nitrogen (TN), COD, phenolic compounds (PCs), and turbidity in the final treated wastewater. In addition, the best % $\text{H}_2\text{O}_2$  (w/v) to use was selected according to the kinetic modelling in base of TOC removal.

## 2. Results and Discussion

### 2.1. Analysis of OMW Characterization Parameters

Table 1 shows the characterization of raw OMWs collected from different evaporation ponds. In general, high values for all parameter were registered. However, low values ( $\text{COD} = 501 \text{ mg O}_2/\text{L}$ ,  $\text{TOC} = 177 \text{ mg/L}$ ,  $\text{TN} = 12.6 \text{ mg/L}$ , electric conductivity ( $\text{EC} = 1.51 \text{ mS/cm}$  and  $\text{pH} = 7.04$ ) were registered in the case of OMW accumulated in the pond of Seville 2. This pond only accumulated olives washing wastewater, which normal COD value is below  $1000 \text{ mg O}_2/\text{L}$  [22]. According to the literature [17,22,23,27,28], COD values of olive oil washing wastewater from the two-phase process normally vary from 4000 to 16,000  $\text{mg O}_2/\text{L}$ . In this sense, only COD of Seville 1 ( $6187 \text{ mg O}_2/\text{L}$ ) was found in the range. Samples of Seville 3 and 4 have high organic matter ( $\text{COD} = 18,981 \text{ mg O}_2/\text{L}$  and  $38,139 \text{ mg O}_2/\text{L}$ , respectively) in comparison with the literature, due to the evaporation effect in the ponds during spring and summer seasons in this region. Similar effect was observed on the other OMWs parameters as  $\text{pH} (>7.04)$  and electric conductivity ( $>30.7 \text{ mS/cm}$ ) values registered. Besides, other wastewaters (as that coming from washing of machines and tanks or brine wastewater) can be mixed in the ponds since some of these ponds collected also wastewaters from table olive processing.

On the other hand, the great variation among the different parameters of these wastewaters was not only due to the mixture of wastewaters in each pond but also because of the way each industry operates (Table 1). In this sense, the variation may be also due to (1) the regeneration cycles of the water used in the olives machines, (2) the chemicals and dirt contained in the olives, (3) the chemicals used for OMW treatment by sedimentation such as aluminum sulfate or ferric chloride before its discharge in the evaporation ponds, etc.

**Table 1.** Characterization of raw olive oil mill wastewater (OMW) from different evaporation ponds.

Parameters	Seville 1	Seville 2	Seville 3	Seville 4
pH	8.6	7.04	8.6	8.63
Electric Conductivity (mS/cm)	30.7	1.51	116	142
Turbidity (FTU)	149	134	997	724
Total Solids (% w/w)	2.32	0.0935	11.4	26.2
Suspended Solids (% w/w)	0.518	0.0625	-	25.06
Organic matter (% w/w)	0.316	0.0501	1.90	0.177
Ash (% w/w)	2.01	0.0434	9.56	25.9
Chemical oxygen demand, COD, (mg O <sub>2</sub> /L)	6187	511	18,981	38,139
Total phenolic compounds, TPCs, (mg/L)	20.0	7.2	189.6	84.9
Total carbon, TC, (mg/L)	3710	207	14,212	29,981
Total organic carbon, TOC, (mg/L)	2903	177	11,684	25,006
Inorganic carbon, IC, (mg/L)	807	119	2528	4875
Total nitrogen, TN, (mg/L)	87	12.6	391.7	928
Total iron (mg/L)	48.2	9.0	42.3	107.6
Chloride (mg/L)	8756	-	11,544	10,637
Sulfates (mg/L)	545	631	1299	21,270

## 2.2. Effect of Photo-Fenton Reaction on Organic Matter Degradation

Considering the characterization determined of the raw wastewaters (Table 1) and the mean initial COD values showed in the bibliography (3000–4000 mg O<sub>2</sub>/L, Nieto et al. [18]). In this work, it was chosen to use a wastewater with a relatively high initial COD value equal to  $6454 \pm 307$  mg O<sub>2</sub>/L for the performance of the experiments. Therefore, mixtures of these real raw wastewaters were performed to eliminate the factor of the uniqueness of the mill and to achieve a real representative OMW sample, as shown in Table 2.

**Table 2.** Characterization of the representative initial wastewater used in the photocatalyzed experiments.

Parameter	Value $\pm$ Standard Deviation
pH	$9.0 \pm 0.4$
Electric conductivity (mS/cm)	$37 \pm 3$
COD (mg O <sub>2</sub> /L)	$6454 \pm 307$
TOC (mg/L)	$3245 \pm 683$
TC (mg/L)	$4060 \pm 718$
IC (mg/L)	$814 \pm 113$
TN (mg/L)	$104 \pm 12$
Turbidity (FTU)	$278 \pm 220$
Total Phenolic compounds (mg/L)	$30 \pm 9$
Total iron, (mg/L)	$39 \pm 55$
SO <sub>4</sub> <sup>2-</sup> , (mg/L)	$441 \pm 219$
Chlorine, mg/L	$10,295 \pm 1907$

Figure 1A shows how the TOC values of OMW decreased throughout the experiment time. For both OMW loads, an instantaneous reaction was detected in the first 3 min. Then, a slowly reaction was observed towards the end of the experiment. Figure 1B shows the removal percentages registered for nitrogen and carbon species. In this sense, depreciated variation was determined in the cases of TOC (average value =  $33.7 \pm 0.7$  mg/L and CV = 2.1%), TC (average value =  $42.5 \pm 1.0$  mg/L and CV = 2.4%) and TN (average value =  $40.6 \pm 0.4$  mg/L and CV = 0.1%). Only, in the case of inorganic carbon (IC) slightly higher CV = 8.3% was registered (IC =  $81.9 \pm 6.8$  mg/L). In addition, similar results were obtained in the case of the COD values (average value =  $15.6 \pm 0.5$  mg O<sub>2</sub>/L and CV = 3.5%). These results allow the conclusion that, in the OMW photolysis experiments, the removal percentages of TOC, TC, IC, TN and COD are virtually independent of the initial organic matter of OMWs.

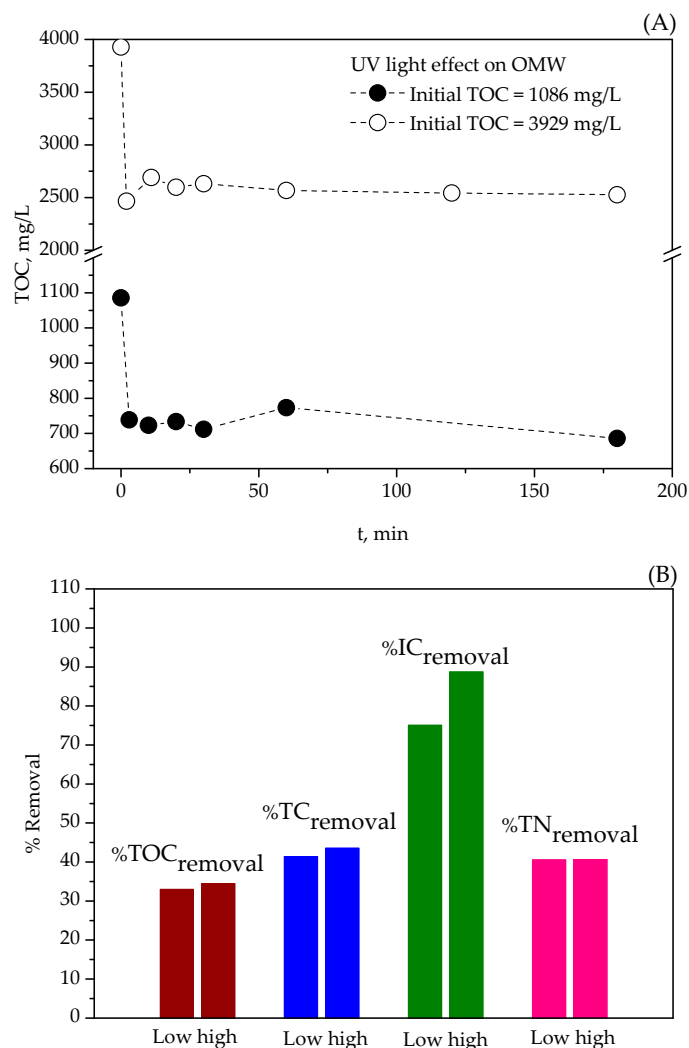


**Figure 1.** Effect of artificial ultraviolet light on the photodegradation of OMW (photolysis). **(A)** Variation of TOC value of two different OMW with high (Initial TOC = 3929 mg/L) and low (Initial TOC = 1086 mg/L) organic loads throughout the photodegradation. **(B)** Variation of the global removal percentages of TOC, TC, IC and TN parameters for OMW with different organic loads. Common operating conditions: pH = 3, T = 20 °C and stirring speed = 150 rpm.

Figure 2 shows the variation of the TC content of the wastewater versus the operating time when the  $\text{FeCl}_3$  is used as a catalyst in the system (Catalyst/UV/ $\text{H}_2\text{O}_2$ ). A similar behavior has been recorded in the rest of the iron catalysts used (Figure S1). As it can be observed, photo-oxidation of OMW occurs in two stages: the first is an instantaneous reduction (instantaneous reaction) of total carbon in the first 5 min, and the second is a gradual reduction (slower reaction) where the degradation occurs more slowly (Figure 2). This mechanism of reaction is similar to that observed in the reaction recorded during OMW photolysis (Figure 1A). In this sense, the complexity of the chemical compounds formed as intermediates in the photo-Fenton oxidation of OMW makes it virtually impossible to carry out a detailed kinetic study with the different individual reactions that take place during the photochemical oxidation. The instantaneous decrease at the beginning of the reaction can be explained considering the high power of the UV-lamp used in this research up to 150 W and its emission over a wide range (UV-visible). Not to mention that the photo-reactor configuration has 8 cm internal diameter and immersion UV-lamp with a diameter 4 cm, which means the thickness of the OMW liquid exposed to UV-light is only 2 cm. In addition,  $\text{Fe(III)}$  hydroxy complexes present in a mildly acidic solution, such as  $\text{Fe(OH)}^{2+}$  and  $\text{Fe}_2(\text{OH})_2^{4+}$ , absorb light appreciably in the UV and into the visible region.

These complexes undergo photo-reduction to give  $\text{HO}^\bullet$  and  $\text{Fe(II)}$ . The most important species is  $\text{Fe(OH)}^{2+}$  due to a combination of its relatively high absorption coefficient and concentration relative to other  $\text{Fe(III)}$  species under typical conditions [34–36].

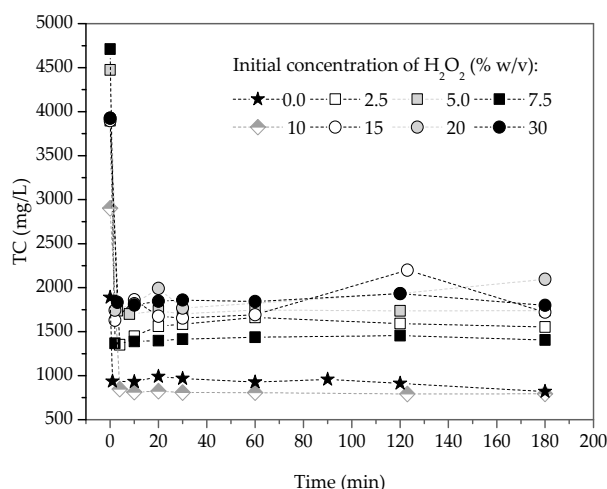


**Figure 2.** Variation of the TC content of OMW with respect to operating time for different concentrations of  $\text{H}_2\text{O}_2$  in the system (Catalyst/UV/ $\text{H}_2\text{O}_2$ ). Common operating conditions: pH = 3,  $T = 20^\circ\text{C}$ , stirring speed = 150 rpm and the ratio  $[\text{FeCl}_3]/[\text{H}_2\text{O}_2] = 0.03$ .

The difference in the initial TC values at the beginning of each experiment is due to the variation obtained after crude OMWs mixtures. For this reason and for the correct interpretation of the experimental results, the parameters TC, TOC and TN have been normalized as follows:

$$\text{TC}_{\text{norm}} = \frac{\text{TC}}{\text{TC}_0}; \text{TOC}_{\text{norm}} = \frac{\text{TOC}}{\text{TOC}_0}; \text{IC}_{\text{norm}} = \frac{\text{IC}}{\text{IC}_0}; \text{TN}_{\text{norm}} = \frac{\text{TN}}{\text{TN}_0} \quad (4)$$

where  $\text{TC}_{\text{norm}}$ ,  $\text{TOC}_{\text{norm}}$  and  $\text{TN}_{\text{norm}}$  represent the normalized values of each parameter and  $\text{TC}_0$ ,  $\text{TOC}_0$  and  $\text{TN}_0$  correspond to the values of each parameter at the beginning of the experiment ( $t = 0$  min).

Figure 3 shows the variation in the normalized total organic carbon values of OMW throughout the photo-oxidation reaction time, when  $\text{FeCl}_3$  was used as catalyst.

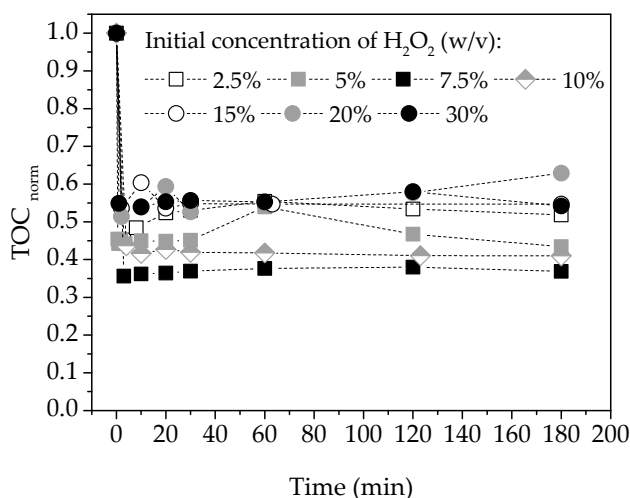


**Figure 3.** Normalized TOC values variation throughout the experiment time for different initial  $\text{H}_2\text{O}_2$  concentrations in the system (Catalyst/UV/ $\text{H}_2\text{O}_2$ ). Operating conditions: Catalyst used:  $\text{FeCl}_3$ , initial TOC =  $3113 \pm 573$  mg/L, pH = 3,  $T = 20^\circ\text{C}$ , stirring speed = 150 rpm, and  $[\text{Catalyst}]/[\text{H}_2\text{O}_2]$  ratio = 0.03.



The lowest value of  $\text{TOC}_{\text{norm}}$  at the end of the experiments ( $0.368 \pm 0.008$ ) was obtained when 7.5% of initial  $\text{H}_2\text{O}_2$  concentration was used. The best range of initial  $\text{H}_2\text{O}_2$  concentrations to use for OMWs photodegradation was from 5% to 10% (w/v). In the same way, similar behaviors were obtained for  $\text{TC}_{\text{norm}}$ ,  $\text{IC}_{\text{norm}}$  and  $\text{TN}_{\text{norm}}$ .

Table 3 shows the average removal percentages of the main characterization parameters of treated OMWs by the photo-Fenton reaction at different oxidant concentrations. As it can be seen, all catalysts used the highest percentage reductions values: 52.0–72.1% in TC, 45.3–80.6% in TOC, 46.0–69.5% in TN, 25.8–74.3% in COD and 34.1–72.1% in total phenolic compounds (TPCs) parameters were recorded using hydrogen peroxide in the range of 5 to 10% (w/v), with the exception of  $\text{Fe}(\text{ClO}_4)_3 \cdot \text{H}_2\text{O}$ .

**Table 3.** Average TC, TOC, TN, COD, TPCs removal percentages determined after OMWs treatment by photo-Fenton at different oxidant concentrations. Operating conditions: pH = 3, T = 20 °C, Agitation rate = 150 rpm, and  $[\text{Catalyst}]/[\text{H}_2\text{O}_2]$  ratio = 0.03.

Parameter	% $\text{H}_2\text{O}_2$ (w/v)	$\text{FeCl}_3$	$\text{Fe}_2(\text{SO}_4)_3 \cdot \text{H}_2\text{O}$	$\text{FeSO}_4 \cdot 7\text{H}_2\text{O}$	$\text{Fe}(\text{ClO}_4)_3 \cdot \text{H}_2\text{O}$
%TC	2.5	61.8	65.3	65.0	59.1
	5	61.2	69.3	72.1	70.8
	7.5	70.1	69.9	57.9	69.5
	10	71.8	72.5	71.1	52.0
	15	52.5	40.0	32.4	48.8
	20	52.0	44.2	51.0	49.5
	30	53.4	54.0	53.4	52.5
%TOC	2.5	46.4	55.1	66.4	51.6
	5	54.2	54.7	69.2	56.8
	7.5	63.2	62.7	57.9	63.3
	10	57.9	52.0	68.3	44.5
	15	45.5	26.5	38.6	38.1
	20	46.1	34.2	55.8	41.6
	30	43.9	46.1	55.0	47.8
%TN	2.5	57.6	60.6	63.8	60.5
	5.0	59.1	69.5	50.9	52.5
	7.5	51.5	44.5	59.4	46.9
	10	67.9	65.1	69.4	46.0
	15	57.6	50.5	61.0	58.6
	20	98.7	52.8	60.0	59.3
	30	65.0	62.3	59.5	62.2
%COD	2.5	30.8	40.9	54.0	48.5
	5	56.5	66.0	52.7	70.0
	7.5	60.3	57.0	58.0	38.3
	10	74.3	64.2	61.4	25.8
	15	36.7	47.6	41.8	21.4
	20	20.0	14.6	23.4	16.1
	30	40.0	17.6	14.9	17.6
%TPCs	2.5	55.3	39.7	25.7	56.8
	5	68.3	48.7	36.1	44.8
	7.5	88.4	56.3	52.2	-
	10	72.1	34.1	46.1	45.1
	15	68.3	33.4	-	51.0
	20	63.5	31.7	51.2	20.0
	30	41.6	24.6	46.0	24.6
%Turbidity	2.5	80.8	91.8	87.5	87.5
	5	87.8	90.9	92.9	75.0
	7.5	94.8	99.9	81.8	52.9
	10	83.1	80.2	81.2	51.7
	15	90.0	99.8	95.7	65.4
	20	92.8	94.2	90.9	79.2
	30	94.4	90.0	94.4	66.0

In this exceptional case, optimal TOC degradation percentages (47–80%) were reached when oxidant concentrations were 2.5–5.0% (w/v)  $\text{H}_2\text{O}_2$ . Comparing the degree of organic matter removal it can be seen that in the case of the TC and TOC parameters, the best concentration of hydrogen peroxide was 7.5% (w/v), and for COD, the best concentration was 10% (w/v). Concentration of hydrogen peroxide is the operating parameter that more significantly affects the photodegradation. The rise in initial hydrogen peroxide concentration entails an increase in the photodegradation efficiency until achieving the optimal concentration. Then, further increases in the initial hydrogen peroxide concentration cause a decrease in the photodegradation efficiency due to the “scavenging nature” of OH radicals at high  $\text{H}_2\text{O}_2$  concentrations. The result is the formation of perhydroxyl radicals, which are significantly less reactive than hydroxyl radicals, which directly affect the final efficiency of wastewater photodegradation [37]. This fact permits more options in the selection of the initial hydrogen peroxide concentration to use at the industrial treatment level.

In the case of total phenolic compounds, removal percentages higher than 36.1% or next to 72.1% were registered at optimal hydrogen peroxide concentrations (5–10%) for all the tested catalysts. In general, the percentages of total nitrogen removal (Table 3) were not greatly affected by the concentration of hydrogen peroxide registering values of  $65.3\% \pm 14.5\%$ ,  $57.9\% \pm 8.2\%$ ,  $60.6\% \pm 5.1\%$  and  $55.1\% \pm 6.2\%$  for  $\text{FeCl}_3$ ,  $\text{Fe}_2(\text{SO}_4)_3 \cdot \text{H}_2\text{O}$ ,  $\text{FeSO}_4 \cdot 7\text{H}_2\text{O}$  and  $\text{Fe}(\text{ClO}_4)_3 \cdot \text{H}_2\text{O}$  catalysts, respectively. The high standard deviation ( $>10\%$ ) observed in the case of  $\text{FeCl}_3$  is due to the high nitrogen removal percentage (98.7%) achieved in the experiment that operated at an initial hydrogen peroxide concentration of 20% (w/v), which is approximately double than that reached for the 7.5% of  $\text{FeCl}_3$ . A possible reason for this behavior is that nitrogen is generated in specific conditions (abiotic  $\text{N}_2$  fixation in presence of  $\text{CO}_2$  abundance conditions [38,39]), which was not examined.

Considering the selectivity of the TOC parameter compared with the COD parameter, as well as the rest of removal results, 7.5% (w/v) of hydrogen peroxide concentration as the optimal concentration has been chosen to be used in the photocatalysis system. This is in concordance with previous studies, where low concentrations of  $\text{H}_2\text{O}_2$  were used in order to avoid “scavenging effect” to  $\text{OH}^\bullet$  radicals [23].

Figure 4 shows the discoloration of OMW samples during and after the photo-Fenton treatment, indicating the gradual degradation of color with the course of the photo-oxidation reaction.

It is important to note that the amount of final iron determined (residual iron) in the treated water throughout the experiment (all catalysts) was about 95% lower than the initial amount of iron (Figure 5). This is because centrifugation allows the removal of  $\text{MnO}_2$  and a large part of the iron ions that form sedimentary complexes with the organic matter and the OH molecules.

Different researchers have postulated that the degradation of organic matter using different iron salts varies depending on the nature of the salt used (iron II or III). In this sense, in a study conducted by Franch et al. [31], photo-catalyzed degradation of maleic acid was studied using Fe(III) salt of different natures:  $\text{Fe}_2(\text{SO}_4)_3$ ,  $\text{FeCl}_3$ ,  $\text{Fe}(\text{ClO}_4)_3$ , among others. The values of the constant of lower “K” reactions were obtained when using the  $\text{Fe}(\text{ClO}_4)_3$  salt since  $\text{ClO}_4^-$  did not form complexes with Fe(III) or Fe(II) [40]. In this work and as an example, the time needed by the photodegradation reaction to achieve the highest removal percentage of TC was 7 min in the case of  $\text{Fe}(\text{ClO}_4)_3$  in comparison with 2 to 4 min for the other catalysts used at 5% of  $\text{H}_2\text{O}_2$  (w/v). In addition, it was observed that when using iron-chloride, complexes gave a small water absorption band at 350 nm that did not appear when using iron-sulfate complexes, so that could affect the degradation kinetics.

The photodegradation of OMW leads to photo-reduction of dissolved ferric iron to ferrous iron (Equation (3)). The first step is a ligand-to-metal charge-transfer (LMCT) reaction. Secondly, intermediate complexes dissociate formation. The ligand can be any Lewis base able to form a complex with ferric iron ( $\text{OH}^-$ ,  $\text{H}_2\text{O}$ ,  $\text{HO}_2^-$ ,  $\text{Cl}^-$ ,  $\text{R-COO}^-$ ,  $\text{R-OH}$ ,  $\text{R-NH}_2$ , etc.). Depending on the reacting ligand, the product may be a hydroxyl radical ( $\text{OH}^\bullet$ ) or another radical derivate from the ligand ( $\text{R}^\bullet$ ). Depending on the ligand, the ferric iron complex has different light absorption properties and a reaction takes place. Therefore, the pH plays a crucial role in the efficiency of the photo-Fenton reaction, because it strongly influences which complexes are formed. Hence, pH 2.8 was frequently

indicated as an optimum pH for the photo-Fenton treatment, because at this pH, precipitation does not take place yet and the dominant iron species in solution is  $[\text{Fe}(\text{OH})]^{2+}$ , the most photoactive ferric iron–water complex [35,36].

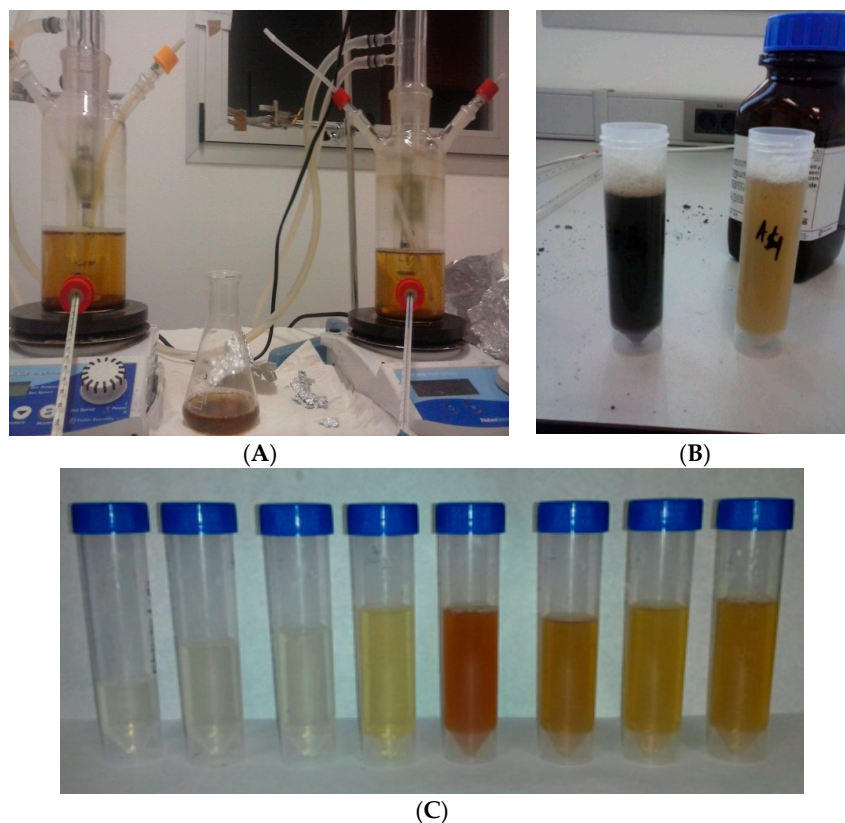


**Figure 4.** (A) Experimental device used for the treatment of OMWs by the photo-Fenton system (Catalyst/UV/ $\text{H}_2\text{O}_2$ ) after natural sedimentation. (B) Stopping the photo-Fenton reaction with  $\text{MnO}_2$ . (C) Samples taken along the photodegradation of OMWs. Operating conditions: COD = 6670 mg  $\text{O}_2/\text{L}$ ;  $\text{H}_2\text{O}_2$  concentration used = 10% w/v; pH = 3; T = 20 °C; Agitation rate = 150 rpm and  $[\text{Fe}(\text{ClO}_4)_3 \cdot \text{H}_2\text{O}]/[\text{H}_2\text{O}_2]$  ratio = 0.03; operating time = 180 min.

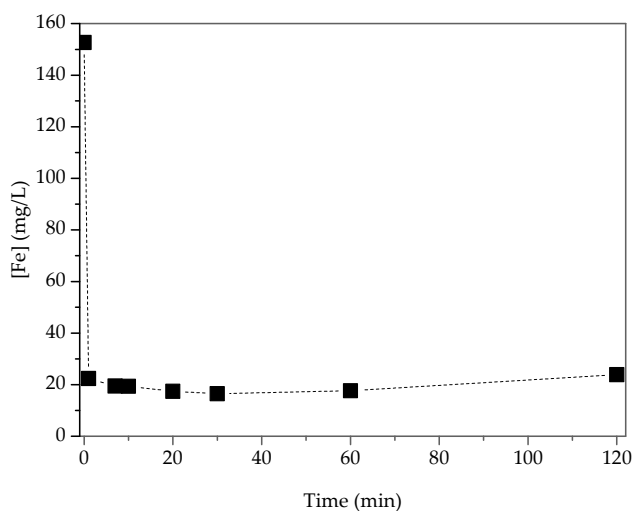


**Figure 5.** Behavior of iron during OMWs treatment by the photo-Fenton reaction. Operating conditions: Initial concentration of the  $\text{H}_2\text{O}_2$  solution used = 5.0% (w/v); pH = 3.0; T = 20 °C; agitation rate = 600 rpm and  $[\text{Fe}_2(\text{SO}_4)_3 \cdot \text{H}_2\text{O}]/[\text{H}_2\text{O}_2]$  ratio = 0.03.

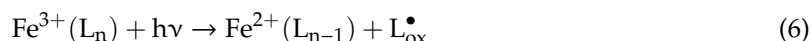
Bamwenda et al., [41] studied the formation of O<sub>2</sub> and H<sub>2</sub> from water using different iron salts coupled to a tungsten salt. They concluded that the solution of Fe<sub>2</sub>(SO<sub>4</sub>)<sub>3</sub> had much higher absorption in near UV-light than FeSO<sub>4</sub>, indicating that, in this region, iron III ions had a higher coefficient of light absorption than iron II species. However, in the present study, quite similar percentages of degradation in terms of TOC have been obtained when using any of the catalysts where the highest percentages of TOC removal have been registered when using concentrations of H<sub>2</sub>O<sub>2</sub> in the range 5–10% (w/v) (Table 3).

### Selection of Catalyst

Results showed that catalyst application promotes higher removal percentages than without a catalyst. In this sense, when only photolysis (UV-light) was applied (Figure 1B), the initial organic load is independent of the final removal percentages registered. In addition, Hodaifa et al. [5] developed photo-oxidation of OMW using UV/H<sub>2</sub>O<sub>2</sub> system at similar conditions to that used in this work but without a catalyst (initial COD = 1944.2 mg O<sub>2</sub>/L, initial H<sub>2</sub>O<sub>2</sub> concentration = 10% (w/v), stirring speed = 150 rpm, T = 20 °C and pH = 3). In this sense, and in order to define the effect of the combination or not among UV light, oxidant and catalyst in the same system, it could be indicated that the removal percentages were increased according to the following sequence UV < UV/H<sub>2</sub>O<sub>2</sub> < UV/FeCl<sub>3</sub>/H<sub>2</sub>O<sub>2</sub>. The final percentages reached for the parameters TC, TOC and TN have been for only UV-light 43.3%, 34.3% and 40.0%, for UV/H<sub>2</sub>O<sub>2</sub> system 42.9%, 38.4% and 45.3% [5] and for the system UV/FeCl<sub>3</sub>/H<sub>2</sub>O<sub>2</sub>, 71.8%, 57.9% and 67.9%, respectively. These results were obtained using OMW with similar initial TOC value = 3929 mg/L. Irradiation of OMW with ultraviolet light (UV) leads to faster rates and higher yields of inorganic products. This degradation is due mainly to the photochemistry of Fe(III) present in the OMW, as in Equation (5) [36].



Fe<sup>3+</sup> complexes go through ligand-to-metal charge transfer (LMCT) excitation, dissociating to give Fe(II) and an oxidized ligand, L<sub>ox</sub>, [29],



The photochemistry of Fe(III) is advantageous to Fenton AOPs because the reduced iron can then react with H<sub>2</sub>O<sub>2</sub> to produce HO• (Equation (1)) and because oxidation of the ligand may lead to further degradation of the target pollutant [29,34–36]. UV-light can also photolysis H<sub>2</sub>O<sub>2</sub> as in Equation (7):



In the photo-oxidation system of UV/catalyst/H<sub>2</sub>O<sub>2</sub>, the removal percentages of the other water quality parameters were determined, such as TN, TPCs and Turbidity (Table 3). TN and Turbidity were not highly affected by the type of catalyst used. In all cases, the removal percentages of TN were in the range of 50% to 70% and the removal percentages of turbidity were in the range of 80% to 90%. An exception was observed in the case of the catalyst Fe(ClO<sub>4</sub>)<sub>3</sub>·H<sub>2</sub>O, where the range registered was from 52% to 88%. However, for TPCs, a clear difference in the efficiency when FeCl<sub>3</sub> was used as catalyst was shown. In this case, removal percentages were from 41.6% to 88.4% against 25.0% to 58.0% for the rest of the catalysts used. In the same way, FeCl<sub>3</sub> as the catalyst used in the range of 5% to 10% (w/v) registered higher removal percentages for TOC (55.0% and 80.1%) and COD (56.5% and 74.3%), respectively.

Table 4 shows the commercial prices and the application of the different catalysts used in this work. The economic advantage of the use of ferric chloride as a catalyst is an additional benefit.

**Table 4.** Oxidation state and commercial price of the iron use as catalysts.

Catalyst	Oxidation State	Price/Supplier	Applications
FeCl <sub>3</sub>	Fe <sup>+3</sup>	38.9 €/kg Sigma-Aldrich	Wastewater coagulation [42]; reduces membrane fouling in MBRs [43]; removes heavy metals in soils [44]; removes phosphates and heavy metals in water [45]; advanced immobilized oxidation [46].
Fe <sub>2</sub> (SO <sub>4</sub> ) <sub>3</sub> ·H <sub>2</sub> O	Fe <sup>+3</sup>	176.3 €/kg Honeywell Fluka	Homo and heterogeneous catalysis of wastewater oxidation [47].
FeSO <sub>4</sub> ·7H <sub>2</sub> O	Fe <sup>+2</sup>	60 €/kg Sigma-Aldrich	Advanced chemical oxidation [48]; coagulant [42].
Fe(ClO <sub>4</sub> ) <sub>3</sub> ·H <sub>2</sub> O	Fe <sup>+3</sup>	394 €/kg Sigma-Aldrich	Advanced chemical oxidation in OMWs [49]. Synthesis of furans and indoles by photodegradation [50].

Taking into account the results obtained (all parameters determined) as well as the economic viewpoint, the best catalyst to be used on the OMWs degradation is FeCl<sub>3</sub>. In addition, this catalyst is widely used because its different capacities as a coagulant [42], for fouling mitigation in anaerobic membrane reactors [31], for reduction of phosphates and heavy metals in wastewater [45,46], etc.

### 2.3. Kinetic Study

Figure 6 shows the variation of TOC conversion values of OMW throughout the photodegradation reaction time for the best initial concentration of the hydrogen peroxide (7.5%, w/v) and for other H<sub>2</sub>O<sub>2</sub> concentration (5%, w/v). In previous work [5], it has been demonstrated the effective adjustment of TOC conversion data to the integrated equation of the Lagergren model [51],

$$X_{\text{TOC}, t} = X_{\text{TOC}, \max} (1 - \exp(-k t)) \quad (8)$$

where ‘*k*’ is the rate constant of pseudo-first order reaction (1/min), ‘*X*<sub>TOC, max</sub>’ is the maximum conversion achieved when *t* = *t*<sub>∞</sub> and ‘*X*<sub>TOC, *t*</sub>’ is the conversion obtained at any time during the photoreaction.

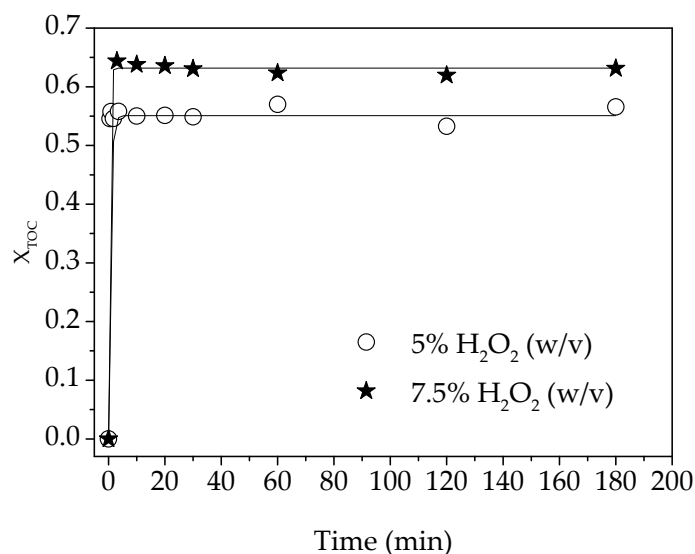


**Figure 6.** Variation of TOC conversion values of OMW throughout the photodegradation reaction time. Operating conditions: Initial concentration of the H<sub>2</sub>O<sub>2</sub> solution used = 5.0% and 7.5% (w/v); pH = 3.0; T = 20 °C; agitation rate = 600 rpm and [FeCl<sub>3</sub>]/[H<sub>2</sub>O<sub>2</sub>] ratio = 0.03. Solid line corresponding to the model adjustment.

Table 5 shows the kinetic parameters determined by fitting experimental data to Equation (8). The kinetic parameters were determined for the optimal conditions obtained for each catalyst.

**Table 5.** Kinetic parameters determined for the best operational conditions of each catalyst used. Operational conditions: pH = 3, T = 20 °C, agitation rate = 150 rpm and [Catalyst]/[H<sub>2</sub>O<sub>2</sub>] ratio = 0.03.

Catalyst	%H <sub>2</sub> O <sub>2</sub>	X <sub>TOC, max</sub>	k (min <sup>-1</sup> )	RSS *	R <sup>2</sup>
FeCl <sub>3</sub>	7.5	0.632	3.00	4.17 × 10 <sup>-4</sup>	0.999
FeCl <sub>3</sub>	10	0.583	0.841	2.01 × 10 <sup>-4</sup>	0.999
Fe <sub>2</sub> (SO <sub>4</sub> ) <sub>3</sub> ·H <sub>2</sub> O	5	0.549	2.00	7.92 × 10 <sup>-4</sup>	0.996
Fe <sub>2</sub> (SO <sub>4</sub> ) <sub>3</sub> ·H <sub>2</sub> O	7.5	0.628	1.13	3.61 × 10 <sup>-5</sup>	0.999
FeSO <sub>4</sub> ·7H <sub>2</sub> O	5	0.693	2.00	1.16 × 10 <sup>-3</sup>	0.997
FeSO <sub>4</sub> ·7H <sub>2</sub> O	10	0.687	1.50	2.36 × 10 <sup>-3</sup>	0.993
Fe(ClO <sub>4</sub> ) <sub>3</sub> ·H <sub>2</sub> O	5	0.578	1.00	4.55 × 10 <sup>-3</sup>	0.983
Fe(ClO <sub>4</sub> ) <sub>3</sub> ·H <sub>2</sub> O	7.5	0.636	1.20	4.33 × 10 <sup>-3</sup>	0.985

\* Residual sum of squares.

As it can be seen, in general and for all the catalysts, the average value of the maximum conversion values achieved was  $0.623 \pm 0.047$ . This fact together with the efficiency of FeCl<sub>3</sub> in remove TPCs (72%), COD (74.3%) as well as its low price, demonstrate that FeCl<sub>3</sub> is the best catalyst for the photo-Fenton treatment of OMW.

Finally, it is important to mention that photo-oxidation represents only one-step in a more complete process for OMW treating. After photo-oxidation, a neutralization unit would be necessary to raise the pH (pH = 6–9) by using a base solution (such as NaOH). Then, a natural sedimentation or assisted sedimentation by flocculation unit would be required to separate and recover the catalyst in Fe(OH)<sub>3</sub> form, which could be reused through its recirculation to the oxidation reactor. To remove turbidity after sedimentation unit a filtration through a sand filter or any other filtering body allows the obtaining of treated water for irrigation. In the case that the target of the OMW treatment process is to achieve a treated water for reuse, the addition of an ultrafiltration by using a membrane unit or reverse osmosis unit would be necessary.

### 3. Materials and Methods

#### 3.1. Chemicals

For the photo-Fenton oxidation, the catalysts used in this study were: Iron (III) chloride (FeCl<sub>3</sub>) 30% (w/w), Iron (III) sulfate hydrate (Fe<sub>2</sub>(SO<sub>4</sub>)<sub>3</sub>·H<sub>2</sub>O), Iron (II) sulfate heptahydrate (FeSO<sub>4</sub>·7H<sub>2</sub>O), and Iron(III) perchlorate hydrate (Fe(ClO<sub>4</sub>)<sub>3</sub>·H<sub>2</sub>O). All chemicals were purchased from Sigma-Aldrich (Madrid, Spain), except FeCl<sub>3</sub>, purchased from PanReac S.A (Barcelona, Spain).

Hydrogen peroxide solution (30% w/v) in stable form, Manganese IV oxide and potassium dichromate, 99.5% were purchased from Fisher Scientific (Madrid, Spain). Hydrochloric acid 37% was purchased from Acro organics (Barcelona, Spain). Titanium (IV) oxysulfate-sulfuric acid solution 27–31% H<sub>2</sub>SO<sub>4</sub> was supplied by Fluka Analytical (Madrid, Spain).

#### 3.2. Sampling and Comparative Analysis of OMW

The raw wastewaters used in this work were directly collected during spring months (April–June) from accumulation rafts of four different mills in Seville province (Spain), all of them operating with a two-phase continuous centrifugation process. These wastewaters were the result of mixing olives and olive oil washing wastewaters with all the other wastewaters generated in the mill.

#### 3.3. Methodology

The oxidation reaction was performed in a photo-reactor (1L capacity). In this sense, the catalyst was dissolved in 600 mL of OMW sample and the pH value was adjusted to 3.0 by 1 M HCl [18].

Subsequently,  $\text{H}_2\text{O}_2$  solution (at the studied concentration) was added and the immersion ultraviolet lamp was switched on.

The UV-lamp in the photo-reactor was covered by a quartz immersion tube and a quartz cooling jacket. A magnetic stirrer inside the photo-reactor to increase the degree of mixing of the OMW was used, which allows greater access to the UV-light. The UV-lamp used was an immersion lamp, model TQ 150 (standard), N° 5600 1725, brand HNG Germany G4 (Hanau, Germany). The dimensions of the UV-lamp were total immersion 384 mm, luminous part 303 mm, the emission center at 44 mm and with a power of 150W. The power of the UV-lamp per surface unit was  $10,000 \text{ W/m}^2$ , which is higher than the maximum power of the sun for an average day ( $146 \text{ W/m}^2$ ), [52]. The inner photo-reactor temperature was controlled through a quartz-cooling jacket located around the UV-lamp. A portable chiller (Mod. PolyScience, Niles, Illinois, USA) pumped the cooled water through the quartz jacket of the lamp.

The common operating conditions were  $\text{pH} = 3$ , temperature =  $20^\circ\text{C}$ , stirring rate = 150 rpm and the  $[\text{Catalyst}]/[\text{H}_2\text{O}_2]$  ratio = 0.03. This low ratio used ensures the sensibility of the catalyst to degrade OMW and to avoid false results. In other words, to detect the maximum capacity of each catalyst to degrade the organic matter of OMW. The initial hydrogen peroxide amount necessary for the complete degradation of the organic matter (COD) of OMW was calculated according to the reaction stoichiometry.

For the photoreaction monitoring, 40 mL of effluent were sampled at 3, 10, 20, 30, 60, 120 and 180 min. Four sets of experiments, one set for each catalyst used, were performed. In each experimental set by catalyst, experiments at different  $\text{H}_2\text{O}_2$  concentrations (2.5%, 5.0%, 7.5%, 10.0%, 15.0%, 20.0%, and 30.0%, w/v) were performed.

### 3.4. Analytical Methods

Real OMWs were characterized by measuring the following parameters: pH value, electric conductivity, turbidity, moisture and volatile materials, total solids, organic matter, ashes, chemical oxygen demand (COD), total carbon (TC), total organic carbon (TOC), inorganic carbon (IC), total nitrogen (TN), total phenolic compounds (TPCs), total iron, chloride and sulfates.

The value of pH was measured using a CRISON pH meter, mod. LPG 22.

Electric conductivity was determined directly by a CRISON conductivity meter, GLP31 model.

Turbidity was measured by a Turbidimeter Hanna, mod. HI93703.

The total solids and moisture and volatile materials were determined according to the weight loss of the sample after being placed in an oven, type Memmert UF110 at  $105 \pm 1^\circ\text{C}$ .

Ashes were determined by using an oven, type ELF14 of CARBOLITE at  $575 \pm 5^\circ\text{C}$ .

The percentage of organic matter was calculated as percentage of total solid minus the percentage of ashes.

Chemical oxygen demand (COD) was measured by the photometric determination (620 nm) of the concentration of chromium (III) after 2 h of oxidation with potassium dichromate/sulfuric acid/silver sulfate at  $148^\circ\text{C}$  [53].

Total carbon (TC) represents all the carbon contained in the sample; this includes organic and inorganic carbon ( $\text{TC} = \text{TOC} + \text{IC}$ ), total organic carbon (TOC) is the organic carbon that is converted into carbon dioxide after oxidation ( $\text{TOC} = \text{TC} - \text{IC}$ ), inorganic carbon (IC) is the inorganic carbon in a sample that after acidification, turns into carbon dioxide. IC includes all carbonates, bicarbonate and dissolved carbon dioxide ( $\text{IC} = \text{TC} - \text{TOC}$ ) and total nitrogen (TN) is all nitrogen in the sample, and this includes organic and inorganic nitrogen. Total Carbon and Nitrogen were determined using an analyzer provided by Skalar Company (mod. Formacs<sup>HT</sup> and Formacs<sup>TN</sup>, Breda, Netherlands).

Total phenolic compounds (TPCs) was determined by making it react with a derivative thiazol, giving a purple azo dye, which was measured photometrically at 475 nm [54,55].



Total iron ions was determined by reduction of all iron ions to iron ion (II) in a thioglycolate medium with a derivative of triazine. This reaction resulted in a reddish-purple complex that was determined photometrically at 565 nm [54,55].

Sulfates and chloride were determined photometrically at 420 nm and 450 nm, respectively [54,55].

### 3.5. Calculations and Kinetics

Removal percentages for each parameter were calculated as follows:

$$\% \text{Removal of the parameter} = \frac{(\text{Parameter}_0 - \text{Parameter}_i)}{\text{Parameter}_0} \quad (9)$$

where 'Parameter<sub>0</sub>' is the value of the parameter at time equal to 0 (at the beginning of the experiment), and 'Parameter<sub>i</sub>' corresponds to the value of the parameter at any time during the experiment.

For the kinetic study of the organic matter degradation by the photo-Fenton reaction, the TOC parameter was selected due to its high selectivity and sensibility to any change in the organic matter [56]. In this sense, taking into account that the reaction was developed in a batch stirred tank reactor and considering a constant density of the mixture, TOC conversion can be calculated as follows:

$$X_{\text{TOC}} = \frac{(\text{TOC}_0 - \text{TOC}_i)}{\text{TOC}_0} \quad (10)$$

where 'TOC<sub>0</sub>' is the TOC value at t = 0 h (at the beginning of the experiment), 'TOC<sub>i</sub>' is the TOC value at any time during the photoreaction and 'X<sub>TOC</sub>' is the degree of conversion of the organic matter represented on TOC base.

The mathematical models used in this work were adjusted by using OriginPro 8 Program.

## 4. Conclusions

The photo-Fenton reaction is proposed as a very effective method for treating high-polluted OMW (without dilution) due to its capacity on the degradation of a wide range of compounds. The photoreaction occurs in two stages: first, an instantaneous stage (<4 min), and a second slower stage. This method has a high degradation capacity and high treated wastewater productivity (due to short time for photoreaction), which means small and compact equipment at industrial scale.

On the other hand, among different iron salts tested, FeCl<sub>3</sub> was selected as the best catalyst due to its effectiveness, economic price and availability standpoint. This catalyst registered high removal values for COD (60.3%), TOC (63.2%), TN (51.5%), and total phenolic compounds (88.4%), when hydrogen peroxide concentration was used at 7.5% (w/v).

The photodegradation of OMW by photo-Fenton would only be an operating unit integrated in a complete process for the treatment of OMW. In fact, this photo-oxidation unit can be integrated in a treatment process based on physicochemical treatments or in a combination of physicochemical and biological treatments. In the first process, the process sequence can be formed by (1) OMW natural sedimentation by gravity, (2) photo-oxidation, (3) neutralization, (4) sedimentation-flocculation, (5) conventional filtration by sand filters with or without membrane filtration (ultrafiltration or reverse osmosis). In the second process, photo-oxidation can be used to reduce initial organic load and remove microbial growth inhibitory/toxic compounds before the biological treatment or after the biological treatment in order to remove the residual organic load obtained.

## 5. Patents

Hodaifa, G.; Agabo-García, C. Method for wastewater treatment based on photo-oxidation by ultraviolet light. Patent ES-2673673-B1, 2019.

**Supplementary Materials:** The following are available online at <http://www.mdpi.com/2073-4344/10/5/554/s1>, Figure S1: Variation of the TC content of OMW with respect to operating time for different concentrations of H<sub>2</sub>O<sub>2</sub>

(• 2.5%, • 5%, • 10%, • 15%, • 20% and • 30%) in the system (Catalyst/UV/H<sub>2</sub>O<sub>2</sub>). Common operating conditions: pH = 3, T = 20 °C, stirring speed = 150 rpm and the ratio [FeCl<sub>3</sub>]/[H<sub>2</sub>O<sub>2</sub>] = 0.03.

**Author Contributions:** Conceptualization, G.H.; methodology, G.H. and C.A.G.; software, G.H. and C.A.G.; validation, G.H., C.A.G. and R.B.; formal analysis, G.H. and C.A.G.; investigation, C.A.G. and G.H.; resources, G.H.; data curation, G.H., C.A.G. and R.B.; writing—original draft preparation, C.A.G.; R.B. and G.H.; writing—review and editing, G.H.; visualization, G.H. and R.B.; supervision, G.H.; project administration, G.H.; funding acquisition, G.H. All authors have read and agreed to the published version of the manuscript.

**Funding:** This research was funded by Junta of Andalusia and Ministry of Economy and Competitiveness (Spain) “Project: Application of advanced oxidation technologies for treating of washing wastewaters of olive oil and olives, grant number AGR-7092”.

**Conflicts of Interest:** The authors declare no conflict of interest.

## References

1. International Olive Oil Council. Available online: <https://www.internationaloliveoil.org/wp-content/uploads/2020/04/HO-W901-29-11-2019-P.pdf> (accessed on 15 May 2020).
2. Niaounakis, M.; Halvadakis, C.P. *Olive Processing Waste Management, Volume 5 Pergamon*, 2nd ed.; Elsevier Science: Amsterdam, The Netherlands, 2006; pp. 23–64.
3. Hodaifa, G.; Sanchez, S.; Martínez, M.E.; Orpez, R. Biomass production of *Scenedesmus obliquus* from mixtures of urban and olive-oil mill wastewaters used as culture medium. *Appl. Energy* **2013**, *104*, 345–352. [CrossRef]
4. Hodaifa, G.; Martínez, M.E.; Sanchez, S. Use of industrial wastewater from olive-oil extraction for biomass production of *Scenedesmus obliquus*. *Bioresour. Technol.* **2008**, *99*, 1111–1117. [CrossRef]
5. Hodaifa, G.; Agabo, C.; Moya, A.J.; Pacheco, R.; Mateo, S. Treatment of olive oil mill wastewater by UV-light and UV/H<sub>2</sub>O<sub>2</sub>. *Int. J. Green Technol.* **2015**, *1*, 46–53. [CrossRef]
6. Bouknana, D.; Hammouti, B.; Salghi, R.; Jodeh, S.; Zarrouk, A.; Warad, I.; Aouniti, A.; Sbaa, M. Physicochemical characterization of olive oil mill wastewaters in the eastern region of Morocco. *J. Mater. Environ. Sci.* **2014**, *5*, 1039–1058.
7. Borja, R.; Martin, A.; Alonso, V.; Garcia, I.; Banks, C.J. Influence of different aerobic pretreatments on the kinetics of anaerobic digestion of olive mill wastewater. *Water Res.* **1995**, *29*, 489–495. [CrossRef]
8. Caputo, A.C.; Scacchia, F.; Pelagagge, P.M. Disposal of by-products in olive oil industry: Waste-to-energy solutions. *Appl. Therm. Eng.* **2003**, *23*, 197–214. [CrossRef]
9. Nickheslat, A.; Mehdi-Amin, M.; Izanloo, H.; Fatehizadeh, A.; Mousavi, S.M. Phenol photocatalytic degradation by advanced oxidation process under ultraviolet radiation using titanium dioxide. *J. Environ. Public Health* **2013**, *2013*, 1–9. [CrossRef]
10. Spanish Law 22/2011. Wastes and Polluted Soils. Available online: <https://www.boe.es/eli/es/l/2011/07/28/22/con> (accessed on 16 May 2020).
11. Israilides, C.; Vlyssides, A.; Galiatsatou, P.; Iconomou, D.; Arapoglou, D.; Christopoulou, N.; Bocari, M. Methods of integrated management of olive oil mill wastewater (OMW) in the framework of the EU Environmental Quality Standards (EQS). In Proceedings of the VIII International Conference “Protection and Restoration of the Environment”, Chania, Greece, 28 June–1 July 2006; pp. 291–292.
12. Jarboui, R.; Sellami, F.; Kharroubi, A.; Gharsallah, N.; Ammar, E. Olive mill wastewater stabilization in open-air ponds: Impact on clay–sandy soil. *Bioresour. Technol.* **2008**, *99*, 7699–7708. [CrossRef]
13. Fernández-Santos Ortiz-Yribas, F.X.; Rodríguez Padilla, L.M.; Cárdenas Fernández, J.; Capítulo, V. *Sector de Almazaras de Aceitunas. Incidencias Ambientales y Medidas Correctoras en Sectores Agroalimentarios*; Junta Andalucía Conserjería de medio Ambiente: Córdoba, Spain, 1997.
14. Petrovic, M.; Radjenovic, J.; Barcelo, D. Advanced oxidation processes (AOPs) applied for wastewater and drinking water treatment: Elimination of pharmaceuticals. *Holist. Approach Environ.* **2011**, *1*, 63–74.
15. Sekine, M.; Salehi, Z.; Tokumura, M.; Kawase, Y. Solar photo-Fenton process for the treatment of colored soft drink wastewater: Decolorization, mineralization and COD removal of oolong tea effluent. *J. Environ. Sci. Health A* **2012**, *47*, 2181–2189. [CrossRef]
16. Ebrahiem, E.E.; Al-Maghrabi, M.N.; Mobarki, A.R. Removal of organic pollutants from industrial wastewater by applying photo-Fenton oxidation technology. *Arab. J. Chem.* **2017**, *10*, S1674–S1679. [CrossRef]
17. Khoufi, S.; Aloui, F.; Sayadi, S. Treatment of olive oil mill wastewater by combined process electro-Fenton reaction and anaerobic digestion. *Water Res.* **2006**, *40*, 2007–2016. [CrossRef] [PubMed]

18. Nieto, M.L.; Hodaifa, G.; Rodríguez, S.; Giménez, J.A.; Ochando, J.M. Degradation of organic matter in olive-oil mill wastewater through homogeneous Fenton-like reaction. *Chem. Eng. J.* **2011**, *173*, 503–510. [CrossRef]
19. Chong, M.N.; Sharma, A.K.; Burn, S.; Saint, C.P. Feasibility study on the application of advanced oxidation technologies for decentralised wastewater treatment. *J. Clean. Prod.* **2012**, *35*, 230–238. [CrossRef]
20. Kalajdzic, B.B.; Habuda-stanić, M.; Romić, Ž.; Trossmayer, J.J.; Kuleš, M. Removal of natural organic matter from groundwater using Fenton's process. *Glob. NEST J.* **2013**, *15*, 13–20.
21. Wang, N.N.; Zheng, T.; Zhang, G.S.; Wang, P. A review on Fenton-like processes for organic wastewater treatment. *J. Environ. Chem. Eng.* **2016**, *4*, 762–787. [CrossRef]
22. Nieto, L.M.; Hodaifa, G.; Vives, S.; Casares, J.A.; Driss, S.B.; Grueso, R. Treatment of olive-mill wastewater from a two-phase process by chemical oxidation on an industrial scale. *Water Sci. Technol.* **2009**, *59*, 2017–2027. [CrossRef]
23. Hodaifa, G.; Ochando, J.M.; Vives, S.R.; Ferez, M.A. Optimization of continuous reactor at pilot scale for olive-oil mill wastewater treatment by Fenton-like process. *Chem. Eng. J.* **2013**, *220*, 117–124. [CrossRef]
24. Huang, C.P.; Dong, C.; Tang, Z. Advanced chemical oxidation: Its present role and potential future in hazardous waste treatment. *Waste Mgmt.* **1993**, *13*, 361–377. [CrossRef]
25. Lu, M.C.; Lin, C.J.; Liao, C.H.; Ting, W.P.; Huang, R.Y. Influence of pH on the dewatering of activated sludge by Fenton's reagent. *Water Sci. Technol.* **2001**, *44*, 327–332. [CrossRef]
26. Lin, S.H.; Lo, C.C. Fenton process for treatment of desizing wastewater. *Water Res.* **1997**, *31*, 2050–2056. [CrossRef]
27. Agabo-García, C.; Hodaifa, G. Real olive oil mill wastewater treatment by photo-Fenton system using artificial ultraviolet light lamps. *J. Clean. Prod.* **2017**, *162*, 743–753. [CrossRef]
28. García-Ballesteros, S.; Grimalt, J.; Berto, S.; Minella, M.; Laurenti, E.; Vicente, R.; López-Pérez, M.F.; Amat, A.M.; Prevot, A.B.; Arques, A. New route for valorization of oil mill wastes: Isolation of humic-like substances to be employed in solar-driven processes for pollutants removal. *ACS Omega* **2018**, *3*, 13073–13080. [CrossRef] [PubMed]
29. Pignatello, J.J.; Oliveros, E.; MacKay, A. Advanced oxidation processes for organic contaminant destruction based on the Fenton reaction and related Chemistry. *Crit. Rev. Environ. Sci. Technol.* **2006**, *36*, 1–84. [CrossRef]
30. Gallard, H.; De Laat, J. Kinetic modelling of Fe (III)/H<sub>2</sub>O<sub>2</sub> oxidation reactions in dilute aqueous solution using atrazine as a model organic compound. *Water Res.* **2000**, *34*, 3107–3116. [CrossRef]
31. Franch, M.I.; Ayllón, J.A.; Xavier Domènech, J.P. Fe(III) photocatalyzed degradation of low chain carboxylic acids: Implications of the iron salt. *Appl. Catal. B Environ.* **2004**, *50*, 89–99. [CrossRef]
32. Maletzky, P.; Bauer, R. The photo-Fenton method-degradation of nitrogen containing organic compounds. *Chemosphere* **1998**, *37*, 899–909. [CrossRef]
33. Esteves, B.M.; Rodrigues, C.S.D.; Maldonado-Hódar, F.J.; Madeira, L.M. Treatment of high-strength olive mill wastewater by combined Fenton-like oxidation and coagulation/flocculation. *J. Environ. Chem. Eng.* **2019**, *7*, 103252. [CrossRef]
34. Safarzadeh-Amiri, A.; Bolton, J.R.; Cater, S.R. The use of iron in advanced oxidation processes. *J. Adv. Oxid. Technol.* **1996**, *1*, 18–26. [CrossRef]
35. Pignatello, J.J. Dark and photoassisted Fe<sup>3+</sup>-Catalyzed Degradation of chlorophenoxy herbicides by hydrogen peroxide. *Environ. Sci. Technol.* **1992**, *26*, 944–951. [CrossRef]
36. Faust, B.C.; Hoigne, J. Photolysis of Fe(III)-hydroxy complexes as sources of OH radicals in clouds, fog and rain. *Atmos. Environ.* **1990**, *24A*, 79–89. [CrossRef]
37. Bergendahl, J.A.; Thies, T.P. Fenton's oxidation of MTBE with zero-valent iron. *Water Res.* **2004**, *38*, 327–334. [CrossRef] [PubMed]
38. Mancinelli, R.L.; McKay, C. The evolution of nitrogen cycling. *Orig. Life Evol. Biosph.* **1988**, *18*, 311–325.
39. Trigo-Rodríguez, J.M.; Raulin, F.; Muller, C.; Nixon, C. *The Early Evolution of the Atmospheres of Terrestrial Planets*; Springer: New York, NY, USA, 2013.
40. Hermanson, M.H.; Hites, R.A. Polychlorinated biphenyls in tree bark. *Environ. Sci. Technol.* **1990**, *24*, 666–671. [CrossRef]
41. Bamwenda, G.R.; Sayama, K.; Arakawa, H. The effect of selected reaction parameters on the photoproduction of oxygen and hydrogen from a WO<sub>3</sub>-Fe<sup>2+</sup>-Fe<sup>3+</sup> aqueous suspension. *J. Photochem. Photobiol. A* **1999**, *122*, 175–183. [CrossRef]

42. Rana, S.; Suresh, S. Comparison of different Coagulants for Reduction of COD from Textile industry wastewater. *Mater. Today Proceed* **2017**, *4*, 567–574. [CrossRef]
43. Dong, Q.; Parker, W.; Dagnew, M. Impact of FeCl<sub>3</sub> dosing on AnMBR treatment of municipal wastewater. *Water Res.* **2015**, *80*, 281–293. [CrossRef]
44. Guo, X.; Wei, Z.; Wu, Q.; Li, C.; Qian, T.; Zheng, W. Effect of soil washing with only chelators or combining with ferric chloride on soil heavy metal removal and phytoavailability: Field experiments. *Chemosphere* **2016**, *147*, 412–419. [CrossRef]
45. Balamane-Zizi, O.; Ait-Amara, H. Study of the simultaneous elimination of phosphates and heavy metals contained in dairy wastewater by a physical-chemical and biological mixed process; consequences on the biodegradability. *Energy Procedia* **2012**, *18*, 1341–1360. [CrossRef]
46. Bedia, J.; Monsalvo, V.M.; Rodriguez, J.J.; Mohedano, A.F. Iron catalysts by chemical activation of sewage sludge with FeCl<sub>3</sub> for CWPO. *Chem. Eng. J.* **2017**, *318*, 224–230. [CrossRef]
47. Sreeja, P.H.; Sosamony, K.J. A comparative study of homogeneous and heterogeneous photo-Fenton process for textile wastewater treatment. *Proc. Technol.* **2016**, *24*, 217–223. [CrossRef]
48. Lofrano, G.; Meriç, S.; Belgiorio, V.; Napoli, R.M. Fenton's oxidation of various-based tanning materials. *Desalination* **2007**, *211*, 10–21. [CrossRef]
49. Andreozzi, R.; Longo, G.; Majone, M.; Modesti, G. Integrated treatment of olive oil mill effluents (OME): Study of ozonation coupled with anaerobic digestion. *Water Res.* **1998**, *32*, 2357–2364. [CrossRef]
50. Krýsová, H.; Jirkovský, J.; Krýsa, J.; Mailhot, G.; Bolte, M. Comparative kinetic study of atrazine photodegradation in aqueous Fe (ClO<sub>4</sub>)<sub>3</sub> solutions and TiO<sub>2</sub> suspensions. *Appl. Catal. B Environ.* **2003**, *40*, 1–12. [CrossRef]
51. Lagergren, S.Y. Zur Theorie der sogenannten Adsorption gelöster Stoffe. *Kungliga Sven. Vetensk. Handl.* **1898**, *24*, 1–39.
52. Patila, S.; Kumara, N. Sun light transmission through silica optical fibers for lighting: An experimental study. *Mater. Today Proc.* **2018**, *5*, 22943–22949. [CrossRef]
53. DIN 38409-41. *German Standard Methods for Examination of Water, Waste Water and Sludge; Summary Action and Material Characteristic Parameters (group H); Determination of the Chemical Oxygen Demand (COD) in the Range over 15 mg/L (H41)*; German Institute for Standardisation (Deutsches Institut für Normung): Berlin, Germany, 1980.
54. ISO 8466-1. *Water Quality-Calibration and Evaluation of Analytical Methods and Estimation of Performance Characteristics—Part 1: Statistical Evaluation of the Linear Calibration Function*; International Organization for Standardization: Genève, Switzerland, 1990.
55. DIN 38402 A51. *German Standard Methods for the Examination of Water, Waste Water and Sludge; General Information (Group A); Calibration of Analytical Methods, Evaluation of Analytical Results and Linear Calibration Functions Used to Determine the Performance Characteristics of Analytical Methods (A 51)*; German Institute for Standardisation (Deutsches Institut für Normung): Berlin, Germany, 1986.
56. Dubber, D.; Gray, N.F. Replacement of chemical oxygen demand (COD) with total organic carbon (TOC) for monitoring wastewater treatment performance to minimize disposal of toxic analytical waste. *J. Environ. Sci. Health A Tox. Hazard. Subst. Environ. Eng.* **2010**, *45*, 1595–1600. [CrossRef]






© 2020 by the authors. Licensee MDPI, Basel, Switzerland. This article is an open access article distributed under the terms and conditions of the Creative Commons Attribution (CC BY) license (<http://creativecommons.org/licenses/by/4.0/>).



## Article

# Colour Changes during the Carbamazepine Oxidation by Photo-Fenton

Natalia Villota <sup>1,\*</sup>, Cristian Ferreiro <sup>2</sup> , Hussein Ahmad Qulatein <sup>3</sup> , Jose María Lomas <sup>1</sup>, Luis Miguel Camarero <sup>1</sup> and José Ignacio Lombrana <sup>2</sup> 

<sup>1</sup> Department of Chemical and Environmental Engineering, Faculty of Engineering of Vitoria-Gasteiz, University of the Basque Country UPV/EHU, Nieves Cano 12, 01006 Vitoria-Gasteiz, Spain; josemaria.lomas@ehu.es (J.M.L.); luismiguel.camarero@ehu.es (L.M.C.)

<sup>2</sup> Department of Chemical Engineering, Faculty of Science and Technology, University of the Basque Country UPV/EHU, Barrio Sarriena s/n, 48940 Leioa, Spain; cristian.ferreiro@ehu.es (C.F.); ji.lombrana@ehu.es (J.I.L.)

<sup>3</sup> Department of Chemical Engineering, Faculty of Engineering, Anadolu University, 26555 Eskisehir, Turkey; husseinqulatein@gmail.com

\* Correspondence: natalia.villota@ehu.es; Tel.: +34-9450-13248

**Abstract:** The oxidation of aqueous solutions of carbamazepine is conducted using the Fenton reagent, combined with the photolytic action of a 150 W medium pressure UV lamp, operating at T = 40 °C. The effect of acidity is analysed at an interval pH = 2.0–5.0, verifying that operating at pH = 5.0 promotes colour formation (Colour = 0.15 AU). The effect of iron is studied, finding that the colour of the water increases in a linear way, Colour = 0.05 + 0.0075 [Fe]<sub>0</sub>. The oxidising action of hydrogen peroxide is tested, confirming that when operating with [H<sub>2</sub>O<sub>2</sub>]<sub>0</sub> = 2.0 mM, the maximum colour is generated (Colour<sub>max</sub> = 0.381 AU). The tint would be generated by the degradation of by-products of carbamazepine, which have chromophoric groups in their internal structure, such as oxo and dioxocarbazepines, which would produce tint along the first minutes of oxidation, while the formation of acridones would slowly induce colour in the water.

**Keywords:** acridone; carbamazepine; colour; oxo-carbamazepine; photo-Fenton

**Citation:** Villota, N.; Ferreiro, C.; Qulatein, H.A.; Lomas, J.M.; Camarero, L.M.; Lombrana, J.I. Colour Changes during the Carbamazepine Oxidation by Photo-Fenton. *Catalysts* **2021**, *11*, 386. <https://doi.org/10.3390/catal11030386>

Academic Editors: Gassan Hodaifa and Rafael Borja

Received: 24 February 2021

Accepted: 16 March 2021

Published: 18 March 2021

**Publisher's Note:** MDPI stays neutral with regard to jurisdictional claims in published maps and institutional affiliations.



**Copyright:** © 2021 by the authors. Licensee MDPI, Basel, Switzerland. This article is an open access article distributed under the terms and conditions of the Creative Commons Attribution (CC BY) license (<https://creativecommons.org/licenses/by/4.0/>).

## 1. Introduction

The study of emerging pollutants in wastewater, as well as its treatment and elimination, are receiving great attention in recent times due to their presence in many kinds of waters and their possible repercussions on the environment [1]. In almost all wastewater of both urban and industrial origin, different emerging pollutants have been detected in variable concentrations, depending on the activities conducted in the original areas of such waters. Recently, several governments are beginning to limit the presence of some of them, based on the Directive 2013/39/EU of the European Parliament, as well as the Council of 12 August 2013 Amending Directives 2000/60/EC and 2008/105/EC [2], although the effects that they cause or their content in the environment are largely unknown.

The main source of entry into the environment for these pollutants is through unprocessed wastewater and effluents from wastewater treatment plants (WWTPs). Conventional plants are not designed for the elimination of this type of micro-pollutants, so their removal in many cases is not complete. Based on this approach, a need arises for these studies, which seek to know the behaviour of emerging pollutants, which are selected based on European guidelines to be analysed in WWTPs. In this way, the aim of this work is to establish indicators of contamination throughout the different phases that form the treatment systems of these plants, being a key aspect to consider the degree of elimination of these contaminants in the different treatment processes currently used.

Among these priority substances, pharmaceutical products, being active biological substances, can affect living organisms in water even in small concentration. Pharmaceu-

tics such as hormones, pain relievers, and antidepressants can have adverse influence on fish, crustaceans, and algae, because they have a similar kind of receptors as humans. The consequences on animals and plants can be very different from the pharmacological effects expected in humans. For this reason, there is a current need to develop new analysis methods that ensure the effectiveness of the AOPs, in order to conduct a correct design of the new processes [3].

Following the indications of Directive 2013/39/EU of the European Parliament, this work is part of a central line of research that is focussed on the development of techniques that allow the degradation of drugs, because there are resistant micro-pollutants contained in wastewater. The purpose is to prevent their transmission to water distribution networks based on the Commission Implementing Rule (EU) 2018/840 of 5 June 2018 [4].

This work focusses on the study of the degradation of the drug carbamazepine. This drug has been selected as a model pollutant of the study, due to its persistence in conventional treatment plants, as well as its wide presence in urban water [5]. Carbamazepine (CBZ) is a medicine utilised to treat neurological conditions such as epilepsy, depression, or bipolar disorder. In humans, around 72% is absorbed and metabolised in the liver, and 28% is excreted in feces. CBZ is one of the most frequently detected pharmaceutical compounds in urban aqueous systems [6,7]. On the other hand, the main metabolites detected in urine are BBZ-epoxide, CBZ-diol, CBZ-acridan, 2-OH-CBZ, and 3-OH-CBZ [5,8,9]. CBZ is a recalcitrant pollutant identified in the effluents of sewage treatment plants and in superficial waters, which has a potential impact on the environment due to its physico-chemical properties, since it is seldom eliminated in conventional water treatments [10].

Due to its potential effect on aquatic microorganisms and human health, there is a notable concern about its removal from water. Studies performed in the presence of CBZ in relevant concentrations show that it can induce disorders in lipid metabolism, as well as damage to mitochondria and DNA in fish [11,12]. Moreover, research published by Faisal et al. [5] shows that CBZ residues in drinking water could cause congenital malformations and/or neurological development problems after long-term intrauterine exposure or breastfeeding. On the other hand, analysis of UV-irradiated aqueous CBZ solutions reveals that acridine, a compound known to be carcinogenic, is one of the by-products formed [13].

Within this context, Advanced Oxidation Processes (AOPs) are presented as an alternative with great potential to effectively eliminate emerging pollutants. To perform the industrial implementation of AOPs, it is necessary to evaluate the different technologies to minimise toxic risks to human health [14], and to solve problems regarding technical feasibility, cost-effectiveness, and their own sustainability [15]. On the other hand, the low concentration levels in which these micro-pollutants are found in the waters limit the effectiveness of these treatments [16]. Assessing the effects induced by the discharge of these wastewaters into natural channels is a challenge, since it presents the difficulty of identifying numerous pollutants, metabolites, and transformation products in very low concentrations.

Among these technologies, this work tries to test the use of hydrogen peroxide combined with iron salts and ultraviolet (UV) light, called photo-Fenton Technology, in order to study the degradation of carbamazepine in aqueous solution. Ultraviolet light is a germicide emission that does not present any residual or secondary effects. Therefore, this technique has a great potential to become a useful tool with high viability. Nevertheless, it is necessary to develop a solid foundation of knowledge in the design of feasible processes for the degradation of emerging pollutants, which requires exhaustive research on the laboratory scale and in pilot plants.

## 2. Results

### 2.1. Colour Changes during Carbamazepine Oxidation

Figure 1 displays the colour changes that occur in the aqueous solution during the degradation of carbamazepine using the photo-Fenton process. The operating conditions in



the tests shown in Figure 1a lead to the formation of a tinted aqueous residue recalcitrant to oxidation. For this reason, it is chosen as a representative essay to analyse this phenomenon. The degradation of carbamazepine occurs during the first two hours of reaction following second-order kinetic guidelines. The generation of tint in the water occurs during the first 40 min of reaction until it reaches a maximum value that remains stable over time.

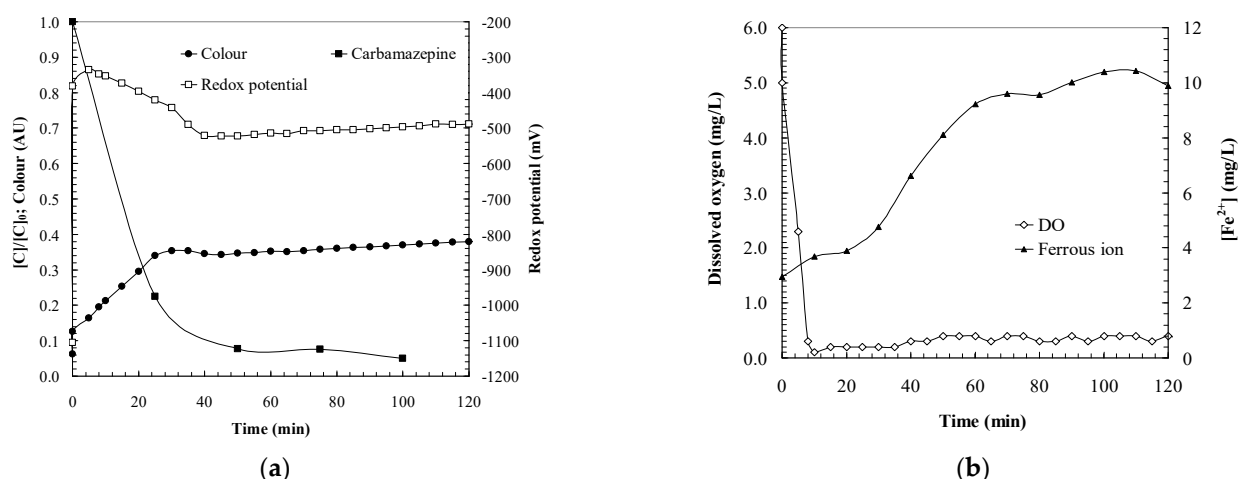


**Figure 1.** Water quality parameters analysed during carbamazepine oxidation by photo-Fenton: (a) Carbamazepine concentration, colour and redox potential. (b) Dissolved oxygen and ferrous ion. Experimental conditions:  $[CBZ]_0 = 50.0$  mg/L; pH = 3.0;  $[H_2O_2]_0 = 2.0$  mM;  $[Fe]_0 = 10.0$  mg/L;  $[UV] = 150$  W;  $T = 40$  °C.

Analysing the redox potential values, an intense increase is observed during the first 5 min of the reaction until reaching a maximum value that decreases, arriving to a steady state after 40 min. This similar evolution between the colour and the redox potential changes makes it possible to associate the species that produce the hue changes in the water with the degradation intermediates of carbamazepine, which cause the redox potential values considered in the solution.

It should be noted that the increase in the redox potential during the first minutes of the reaction may be due to the oxidation of the ferrous ions to ferric, which is presented in Figure 1b. This allows verifying that approximately 70% of iron added to the reaction mixture in the form of ferrous ions is oxidised through the Fenton mechanism to ferric ions. Furthermore, during the course of the reaction, it is found that under the conditions tested, complete regeneration of the catalyst to ferrous ions occurs.

These results allow proposing a direct relationship between the redox potential and the reaction intermediates generated in the different stages of the carbamazepine oxidation mechanism. The substitution of groups of different nature (hydroxyl, oxo) in the aromatic rings affect the redox potential of the molecule, enlarging or reducing its value depending on the inducing effect of the substituent groups to accept or reject electrons in such a way that if the substitution in the ring is favored, they decrease the redox potential. In the case of hydroxylated carbamazepine molecules, when the aromatic ring loses the proton of the substituted hydroxyl group, electron delocalisation increases, thereby enlarging stability and causing the redox potential to decline [17]. Based on this hypothesis, it could be considered that the diminishment in redox potential would be related to the maximum concentration of dihydroxylated carbamazepines in the reaction medium, which would be contemplated as the precursor species of colour formation in water.

On the other hand, Figure 1b shows the evolution of dissolved oxygen (DO, mg  $O_2$ /L). During the first 10 min of the reaction, there is a high consumption of oxygen dissolved in water, until reaching levels around (DO = 0.1 mg  $O_2$ /L). This utilisation can be related to the oxidation process through the formation of strongly oxidising radical species. In this way, a highly oxidising environment is created that requires a large consumption of oxidising species. In addition, it is found that the moment when almost all the DO is

exhausted corresponds to the highest redox potential. This aspect can be associated to the maximum concentration of ferric ions generated in the Fenton reaction.

Next, the DO concentration begins to increase slightly until reaching levels of about 0.4 mg O<sub>2</sub>/L after two hours of reaction. This behaviour is similar to that observed in studies reported in the bibliography during the oxidation of other organic pollutants [18], where this second stage of DO production presents a clear dependence on the nature of the oxidised species. In general, it is found that DO release is higher during the oxidation of organic matter that does not form organometallic complexes with iron, due to their molecular structure configuration. When the release of DO in the water is very slow, it is attributed to the fact that the degradation intermediates can form supramolecular structures with the ferric ions, preventing the iron regeneration.

In the case of the oxidation of carbamazepine shown in Figure 1b, it is observed that the DO release rate in water is very low ( $k_{DO} = 0.0017$  mg O<sub>2</sub>/L min), although the ferric ions are completely regenerated to ferrous. This result could be attributed to oxygen evolution reactions, where free radicals participate. The conditions that facilitate the formation of tint in the water are related to the use of scarce oxidant with respect to the contaminant load. This leads to partial oxidation of carbamazepine towards the formation of colour precursor intermediates. By conducting the reaction with a shortage of oxidant, it causes the generated radical load to be consumed through the processes of oxidation of organic matter and iron regeneration. As a result, the interrational reactions producing oxygen release in the water are relegated.

## 2.2. pH Effect

Figure 2 presents the effect of pH on water colour changes during the oxidation of aqueous carbamazepine solutions, operating between pH = 2.0 and 5.0. It should be noted that the acidity has remained stable throughout the reaction at the initial established value. In the tests conducted, it was found that during the first 5 min of the oxidation, tint was generated in the water until it reached a maximum value and then decreases to a stable value, around 30 min of reaction time. PH determines the value of the colour area as well as the residual hue of the oxidised water. On the other hand, it is observed that operating between pH = 2.0 and 3.5, the maximum colour formation occurs at around 5 min of reaction. However, at pH = 4.0 and 5.0 the maximum colour formation occurs between 10 and 15 min.

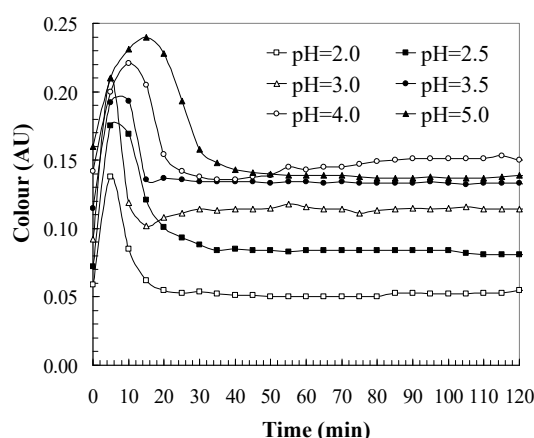


**Figure 2.** pH effect on colour changes in a photo-Fenton system during the carbamazepine oxidation. Experimental conditions: [CBZ]<sub>0</sub> = 50.0 mg/L; [H<sub>2</sub>O<sub>2</sub>]<sub>0</sub> = 15.0 mM; [Fe]<sub>0</sub> = 10.0 mg/L; [UV] = 150 W; T = 40 °C.

To analyse this result in more detail, Figure 3a represents the colour of the treated water once it has reached a steady state, together with the redox potential values. It is observed that both variables show a similar evolution regarding pH effect. By increasing the value from pH = 2.0 to 5.0, the intensity of the colour and the redox potential increases,

showing a maximum when carrying out the tests at pH = 5.0. As this pH increases, the colour and redox potential of the water decrease.

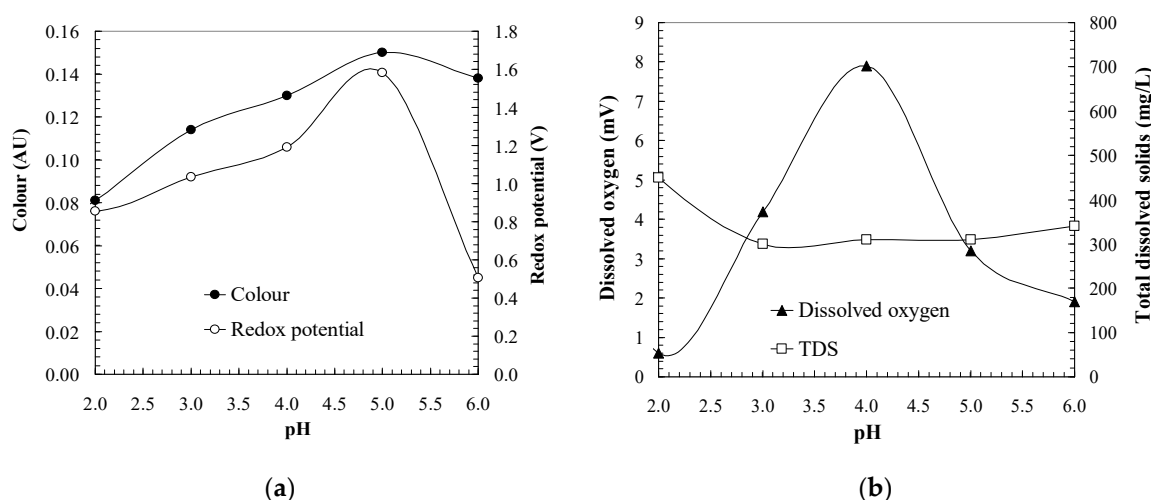


**Figure 3.** Indicator parameters of water quality analysed at the steady state: (a) Colour and redox potential. (b) Dissolved oxygen and total dissolved solids. Experimental conditions:  $[CBZ]_0 = 50.0$  mg/L;  $[H_2O_2]_0 = 15.0$  mM;  $[Fe]_0 = 10.0$  mg/L;  $[UV] = 150$  W;  $T = 40$  °C.

To explain this effect, the speciation diagram of Fe (III) species as pH function in a photo-Fenton system [19] has been analysed. Then, it is found that the formation of the  $Fe(OH)_2^-$  species in a photo-Fenton system potentially increases from pH = 2.0 until reaching its maximum at pH = 5.5. Thus, the effect of pH on colour formation could be associated with the presence of ferric hydroxide in the aqueous medium. The colour reduction operating at values higher than pH = 5.5 may be due to the fact that from this value, the formation of ferric hydroxide takes place, which would precipitate. This could cause a decrease in the concentration of iron dissolved, diminishing the aqueous tint.

Figure 3b displays the effect of pH on the concentration of DO in the water, which leads to verify a strong increase from pH = 2.0 to pH = 4.0, where the maximum concentration of DO occurs ( $[DO] = 7.9$  mg  $O_2$ /L), and then, it decreases from pH = 4.0 to 6.0. This effect could be explained with the Pourbaix diagram for iron, which presents the predominance of the various chemical species in water for an element. Analysing the redox potential diagram of the medium as a function of pH, it can be verified that the experimental redox potential values measured for each pH (see Figure 3a) indicate that within the interval between pH = 2.0 and 4.0, the iron would be in the  $Fe^{3+}$  form. Meanwhile, the values analysed at pH = 5.0 would indicate that iron would be in the  $FeO_4^{2-}$  form and at pH = 6.0 in the  $Fe_2O_3$  form. This change in the nature of the iron species that would coexist in the system could be related with the reactions of oxygen release.

### 2.3. Effect of Hydrogen Peroxide Dosage

During the oxidation treatment of aqueous carbamazepine samples, it is found that the water acquires colour during the first 20 min of reaction (Figure 4a). It is verified that the intensity of the tint depends on the dose of oxidant used. The results present two clear trends in the kinetics of colour formation. On the one hand, operating with low concentrations of oxidant, around  $[H_2O_2]_0 = 2.0$  mM, corresponding to stoichiometric ratios of 1 mol CBZ: 10 mol  $H_2O_2$ , tint is generated in the water according to a ratio of 0.0086 AU/min, until reaching its maximum intensity ( $Colour_{max} = 0.353$  AU) at 30 min of reaction. Subsequently, the hue continues increasing but much more slowly, following ratios of 0.0005 AU/min, until it arrives at the steady state ( $Colour_{\infty} = 0.381$  AU).

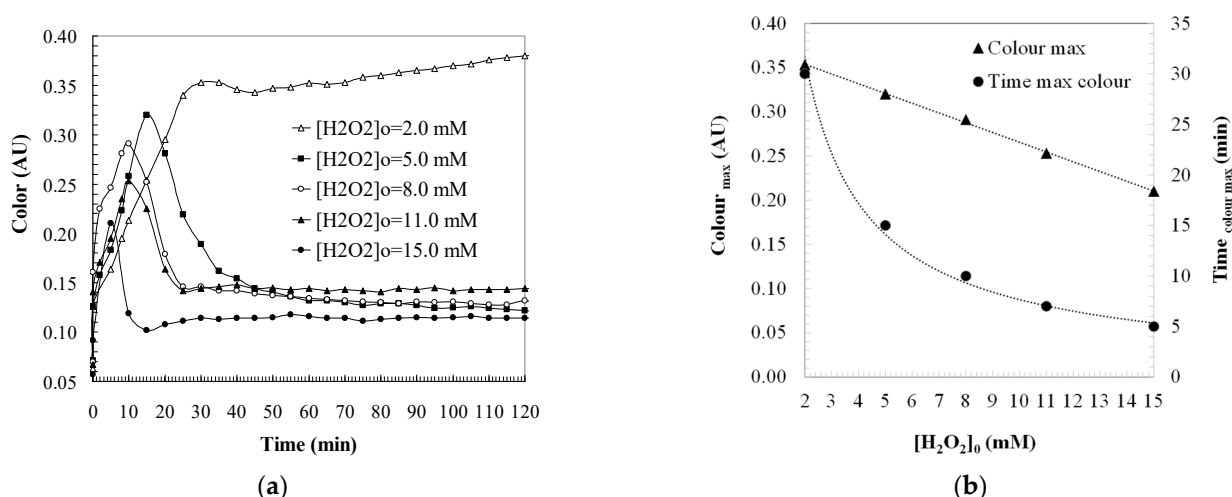


**Figure 4.** (a) Effect of hydrogen peroxide on colour changes in a photo-Fenton system during the carbamazepine oxidation. (b) Maximum colour formation (Colour<sub>max</sub>, AU) and time corresponding to the maximum colour formation (Time<sub>colour max</sub>, min) as a function of the oxidant dosage. Experimental conditions: [CBZ]<sub>0</sub> = 50.0 mg/L; pH = 3.0; [Fe]<sub>0</sub> = 10.0 mg/L; [UV] = 150 W; T = 40 °C

Performing with oxidant concentrations greater than [H<sub>2</sub>O<sub>2</sub>]<sub>0</sub> = 5.0 mM, corresponding to stoichiometric ratios greater than 1 mol CBZ: 25 mol H<sub>2</sub>O<sub>2</sub>, the colour formation follows the evolution of a reaction intermediate, with rapid colour formation during the first minutes of oxidation, until reaching a maximum value, and decreasing until obtaining a colourless solution. The oxidant dosage determines both the maximum colour generated (Equation (1)) and the time in which the formation of the highest colour intensity occurs (Equation (2)), as it is shown in Figure 4b. This result indicates that the stoichiometric ratio of oxidant utilised determines the degree of oxidation achieved—that is, the stage of the carbamazepine degradation mechanism reached and, consequently, the nature of the intermediates that coexist in solution. As a result, the higher the molar ratio of oxidant, the lower the intensity of the tint generated, so that the formation of coloured species is reduced. The fact that under these conditions, a colourless oxidised residue is obtained shows that operating in all conditions, the dose of oxidant is sufficient to degrade the intermediates that provide tint to colourless species.

$$\text{Colour}_{\text{max}} = 0.3759 - 0.011 [\text{H}_2\text{O}_2]_0 \quad (r^2 = 0.9988) \quad (1)$$

$$t_{\text{colour max}} = 58.31 \times [\text{H}_2\text{O}_2]_0^{-0.8813} \quad (r^2 = 0.9916) \quad (2)$$

The results shown indicate the existence of two stages in colour formation based on the carbamazepine degradation mechanism proposed in Figure 5. The first step takes place during the first stages of decomposition and leads to the formation of highly tinted species. This stage would involve hydroxylation reactions through the electrophilic attack of the hydroxyl radicals to the olefinic double bond in the central and lateral heterocyclic rings of carbamazepine, conducting to the formation of the corresponding hydroxylated carbamazepines. The action of hydroxyl radicals can generate a new hydroxylation of the molecule, leading to the creation of cis and trans-dihydroxy-carbamazepine [20]. The formation of the rare cis isomer appears to be less than that of trans [21]. Finally, the oxidation of these species would produce colour precursors, oxo and dioxo-carbazepines (10-OH-CBZ, 9-OH-CBZ, EP-CBZ, OX-CBZ), due to the presence of chromophore groups in their molecular structure.

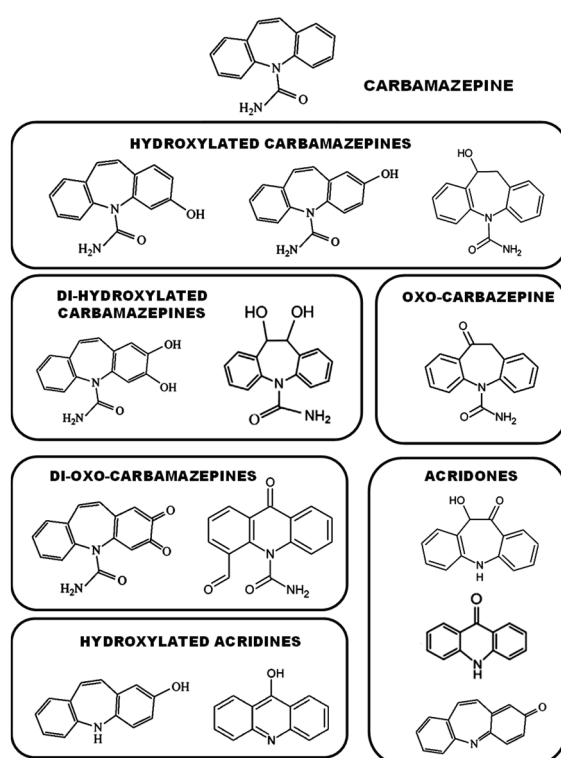


**Figure 5.** Reaction intermediates causing colour in oxidised carbamazepine solutions.

During the second stage, there would be the creation of additional species that coexist with those generated in the previous stage, which provide less intensity of tint to the water. In this case, it is possible to consider the formation of degradation by-products of the carbamazepine species, generating hydroxylated molecules of acridine (9-OH-acridine) and the corresponding acridones that cause the additional contribution of colour.

Figure 6 shows the effect of the oxidant concentration used on several parameters that indicate the quality of the water once it is treated. Analysing the tint of the oxidised water, it is found that operating with concentrations  $[H_2O_2]_0 = 2.0$  mM, the oxidation of carbamazepine leads to the formation of highly coloured species. On the other hand, working with concentrations higher than  $[H_2O_2]_0 = 5.0$  mM, a colourless water is obtained. Simultaneously, the redox potential shows an evolution characterised by a slight decrease until reaching a minimum value ( $[Redox]_{min} = -0.489$  V) in  $[H_2O_2]_0 = 2.0$  mM, when the maximum colour formation take place ( $Colour_{max} = 0.381$  AU). Subsequently, it increases practically linear with respect to the concentration of oxidant applied.

To explain this minimum value of redox potential, a relationship can be established between the evolution of the potential and the reaction intermediates generated in the different stages of the oxidation mechanism. Studies carried out on the effect of the substitution of groups of different nature in aromatic rings indicate that they affect the value of the redox potential of the molecule, increasing or decreasing depending on the inducing effect of the substituent groups to accept or transfer electrons [17]. Therefore, if ring substitution is favored, the redox potential value diminishes.

In the case of carbamazepine, there is a small stabilisation by resonance, which is attributable to electronic delocalisation. When the ring loses the proton of the substituted hydroxyl group, electron delocalisation increases, thus favoring stability and reducing the redox potential. Therefore, based on these hypotheses, the minimum value observed would be related to the maximum concentration of hydroxylated and dihydroxylated carbamazepines in the reaction medium, which would be the precursors of the tint that the solution acquires. By increasing the oxidant ratio, these intermediates are degraded, increasing the degree of oxidation, and it is found that the redox potential of the system evolves to positive values, which would indicate the formation of quinones and acridines.

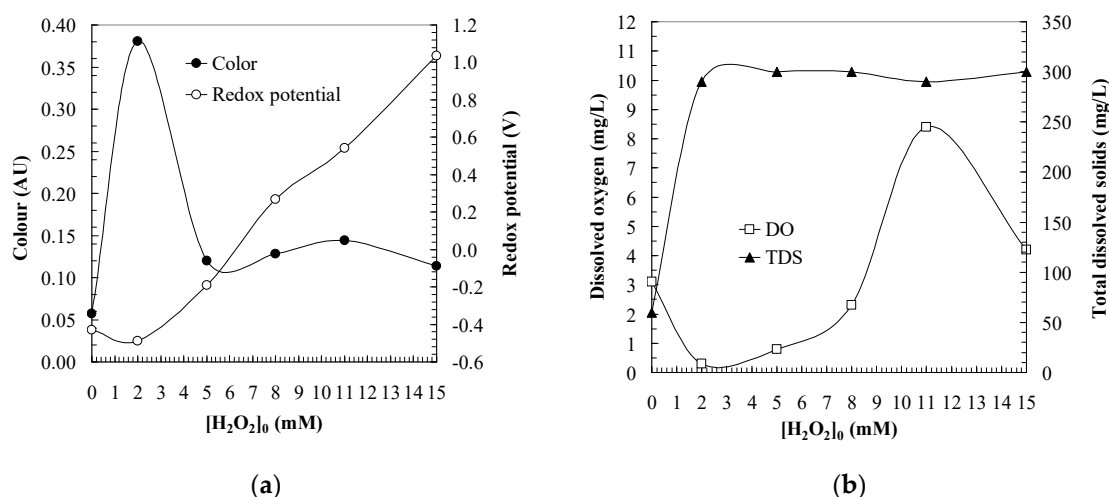


**Figure 6.** Indicator parameters of water quality analysed at the steady state: (a) Colour and redox potential. (b) Dissolved oxygen and total dissolved solids. Experimental conditions:  $[CBZ]_0 = 50.0$  mg/L;  $pH = 3.0$ ;  $[Fe]_0 = 10.0$  mg/L;  $[UV] = 150$  W;  $T = 40$  °C.

The dissolved oxygen analysed in treated samples is consistent with their redox potential values. It is observed that the DO concentration in water increases as the treatment is conducted with higher concentrations of oxidant, up to a maximum operating point, which corresponds to  $[H_2O_2]_0 = 11.0$  mM, with a  $DO = 8.4$  mg  $O_2$ /L. However, in the test carried out using  $[H_2O_2]_0 = 15.0$  mM, the DO experienced a big decrease until values of  $DO = 4.2$  mg  $O_2$ /L. These lower levels of DO are observed throughout the course of the reaction, which could be due to operating with excess of oxidant with respect to the iron concentration. On the other hand, the concentration of Total Dissolved Solids (TDS, mg/L) remains constant in all the tests performed.

#### 2.4. Effect of Iron Dosage

Figures 7 and 8 show the effect of catalyst concentration on the colour acquired by oxidised carbamazepine solutions. Operating with different iron concentrations (Figure 7a), it is observed that adding the iron dose established for each experiment increases tint to the initial carbamazepine solution ( $Colour_0$ , AU). The colour that the water gains shows a second degree polynomial increase (Equation (3)) with respect to the concentration of total iron supplied ( $[Fe]_0$ , mg/L). The initial iron added to the solution in the form of ferrous sulfate undergoes a series of equilibrium reactions between species, because the pH of the sample is adjusted to  $pH = 3.0$  (Figure 7b). For this reason, one part of the iron ions is in a reduced state and the other is oxidised, being the ferric ions the providers of the tint to the water.

When the oxidant is added and the oxidation of the carbamazepine begins, the hue generated in the water increases until reaching a maximum value ( $Colour_{max}$ , AU) at 5 min after oxidation in all the tests conducted. This fact indicates that when using the same concentration of oxidant, the degradation intermediates of carbamazepine formed in water are similar species. Therefore, the colour peaks occur simultaneously, and following identical kinetics, they are displaced in parallel. This linear displacement is established by the iron concentration (Equation (4)).

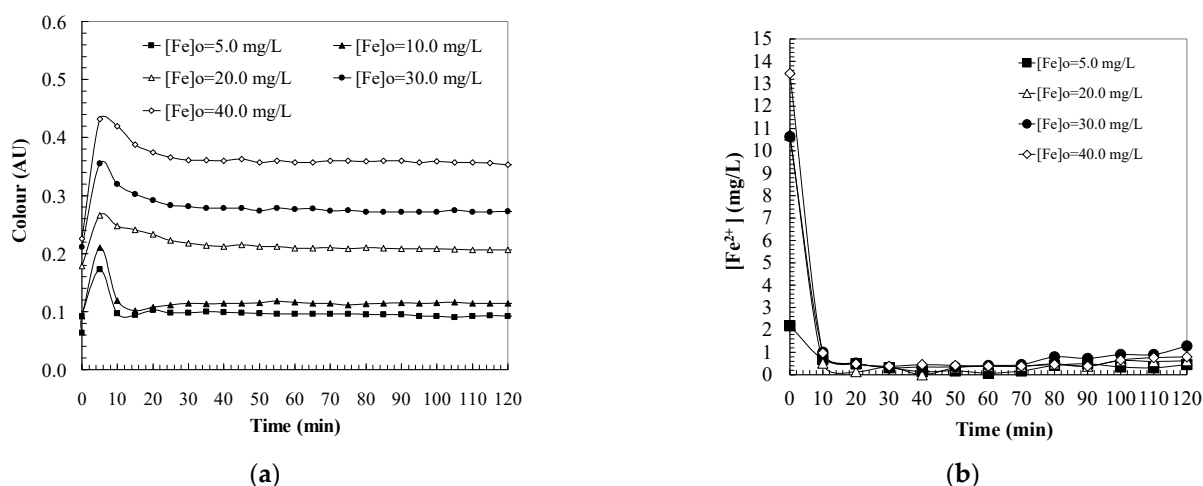


**Figure 7.** (a) Effect of iron on colour changes in a photo-Fenton system during the carbamazepine oxidation. (b) Ferrous ions concentration in water solution during carbamazepine oxidation. Experimental conditions: [CBZ]<sub>0</sub> = 50.0 mg/L; pH = 3.0; [H<sub>2</sub>O<sub>2</sub>]<sub>0</sub> = 15.0 mM; [UV] = 150 W; T = 40 °C.

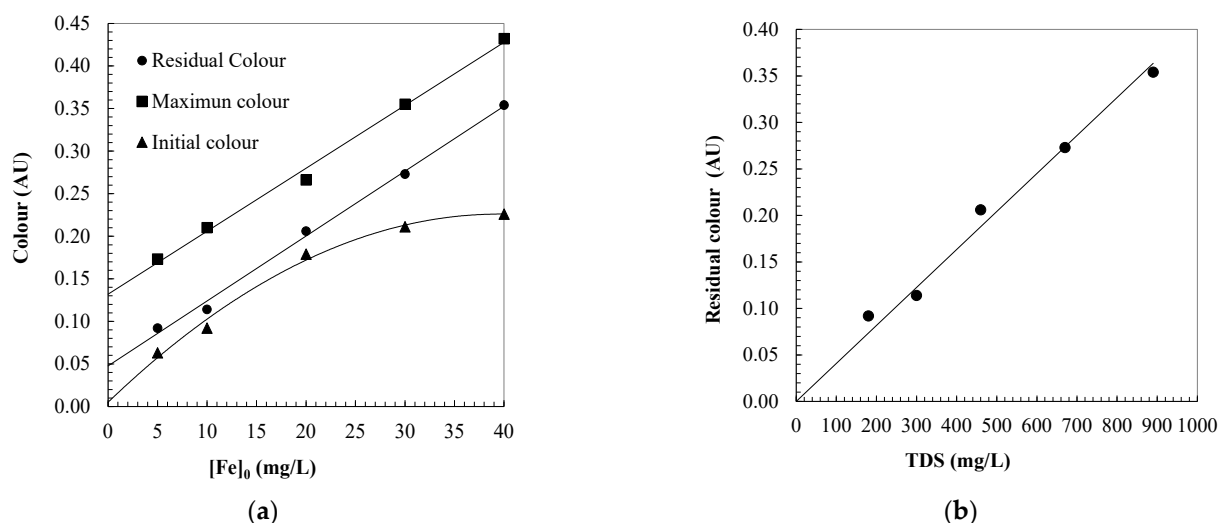


**Figure 8.** (a) Effect of iron dosage on water colour levels observed during the carbamazepine oxidation. (b) Relation-ship between total dissolved solids and the residual colour of water oxidized. Experimental conditions: [CBZ]<sub>0</sub> = 50.0 mg/L; pH = 3.0; [H<sub>2</sub>O<sub>2</sub>]<sub>0</sub> = 15.0 mM; [UV] = 150 W; T = 40 °C.

On the other hand, the persistent colour that lasts in the oxidised sample (Colour<sub>∞</sub>, AU) increases linearly with the iron concentration (Equation (5)). It is observed that both the maximum colour and the residual increase linearly with the total iron concentration, according to an average ratio of  $k_{Fe} = 0.0075$  AU L/mg Fe. Furthermore, it is found that they remain constant in all the tests: a difference between the maximum colour and the residual of 0.0843 AU. This tint value is explained by the contribution of iron species that can interact with the organic load of the water, forming metallic complexes, which are degraded during oxidation. As shown in Figure 8b, the lasting residual colour is provided by the iron species in suspension, which contribute linearly (Equation (7)) to the total suspended solids (TDS, mg/L).

$$\text{Colour}_0 = 0.0117 [\text{Fe}]_0 - 0.0002 [\text{Fe}]_0^2 \quad (r^2 = 0.9901) \quad (3)$$

$$\text{Colour}_{\text{max}} = 0.132 + 0.0074 [\text{Fe}]_0 \quad (r^2 = 0.9946) \quad (4)$$

$$\text{Colour}_{\infty} = 0.0477 + 0.0076 [\text{Fe}]_0 \quad (r^2 = 0.9961) \quad (5)$$



$$[\text{TDS}] = 72.982 + 20.211 [\text{Fe}]_0 \quad (r^2 = 0.9974) \quad (6)$$

$$\text{Colour}_\infty = 0.0004 [\text{TDS}] \quad (r^2 = 0.9826) \quad (7)$$

### 3. Materials and Methods

#### 3.1. Experimental Methods

Samples of carbamazepine aqueous solutions ( $[\text{CBZ}]_0 = 50.0 \text{ mg/L}$ , Fagron 99.1%) were studied in a photocatalytic 1.0 L reactor provided with an UV-150 W mercury lamp of medium pressure (Heraeus, 95%, transmission between 300 and 570 nm). Reactions started adding the iron catalyst as ferrous ion ( $[\text{Fe}]_0$ , mg/L), operating between  $[\text{Fe}]_0 = 5.0\text{--}40.0 \text{ mg/L}$  ( $\text{FeSO}_4 \cdot 7 \text{ H}_2\text{O}$ , Panreac 99.0%) and the oxidant dosage for each set of experiments, which varied between  $[\text{H}_2\text{O}_2]_0 = 0\text{--}15.0 \text{ mM}$  (Panreac, 30% *w/v*). All the experiments were conducted at around 40 °C in order to simulate real working conditions, considering the heat absorbed by the water that is in direct contact with the UV lamp. Assays were performed under different initial pH conditions (pH between 2.0 and 5.0) in order to assess the effect of this parameter on colour formation during the oxidation of carbamazepine aqueous solutions. Acidity was kept constant adding NaOH and HCl.

#### 3.2. Analytical Methods

Carbamazepine concentration (CBZ, mg/L) was assessed along the reaction at  $\lambda = 210 \text{ nm}$  by a High-Performance Liquid Chromatograph attached to a spectrophotometer UV/Vis (HPLC Agilent 1200). Analysis was performed by injecting manually 20.0  $\mu\text{L}$  samples, which were dragged by a carrier of 1.0 mL/min flow, consisting of a mixture of methanol and distilled water MeOH/ $\text{H}_2\text{O}$ : 80/20, through a Column C<sub>18</sub>, XBridge Phenyl 5  $\mu\text{m}$  4.6  $\times$  250 mm (Bridge Waters), with limit of detection 0.1 mg/L.

Colour expressed in Absorbance Units (AU) was quantified by the absorbance of the aqueous solution analysed at  $\lambda = 455 \text{ nm}$  and ferrous ion ( $[\text{Fe}^{2+}]$ , mg/L) at  $\lambda = 510 \text{ nm}$  by the phenanthroline method using an UV/Vis Spectrophotometer 930-Uvikon [22]. Dissolved oxygen (DO, mg/L) was measured by a DO-meter HI9142. Total dissolved solids (TDS, mg/L) were analysed by a TDS Metter Digital and Redox potential (V) by a conductimeter (Basic 20 Crison).

#### 3.3. Liquid Chromatography-Mass Spectrometry to Elucidate the Intermediates of Carbamazepine Degradation

Samples were analysed by Liquid Chromatography-Mass Spectrometry to find the carbamazepine degradation pathways that induce high levels of colour in the water during the oxidation process. Analysis was performed with an LC/Q-TOF provided with an ionisation source ESI + Agilent Jet Stream, with the following conditions: Kinetex column EVO C18 (100  $\times$  3 mm) 2.6  $\mu\text{m}$ . Moving phase 0.1% Formic Acid (A): Acetonitrile 0.1% Formic Acid (B). Gradient, %B: time (min): 20:0; 20:2; 100:24; 100:28; 20:30. Flow 0.3 mL/min. Column Temperature 35 °C. Injection volume 5  $\mu\text{L}$ . Ionisation: Gas temperature 300 °C, drying gas 10 L/min, nebuliser 20 psig, shelf gas temperature 350 °C, shelf gas flow 11 L/min, frag 125 V.  $V_{\text{cap}}$  3500 V.

A screening method was developed, allowing the elution and ionisation of the majority of compounds in the sample. Before starting the analysis, the stabilisation of the system, the reproduction in the signals, and the correction of the exact masses were checked. With the aforementioned conditions, the chronogram shown in Figure 9 was attained.

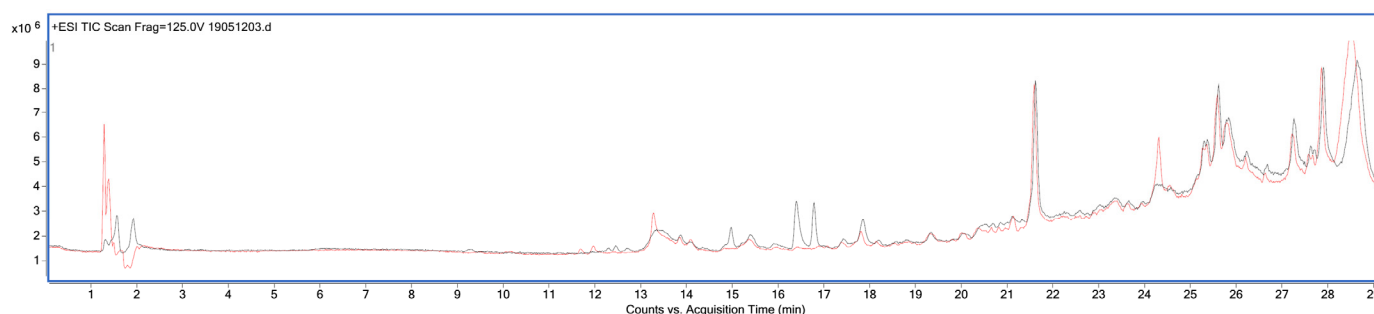


**Figure 9.** Chromatographic profile of a methanol blank (grey line) and of the sample (red line).

The search for compounds was performed using the Find deconvolution algorithm by molecular features and a subsequent screening of the proposed compounds, based on compounds detected in the blank, background noise, and minimum abundance of the compound (Figure 10). Appendix A summarises the major ions ( $m/z$ ) and the experimental masses calculated for each of the compounds.

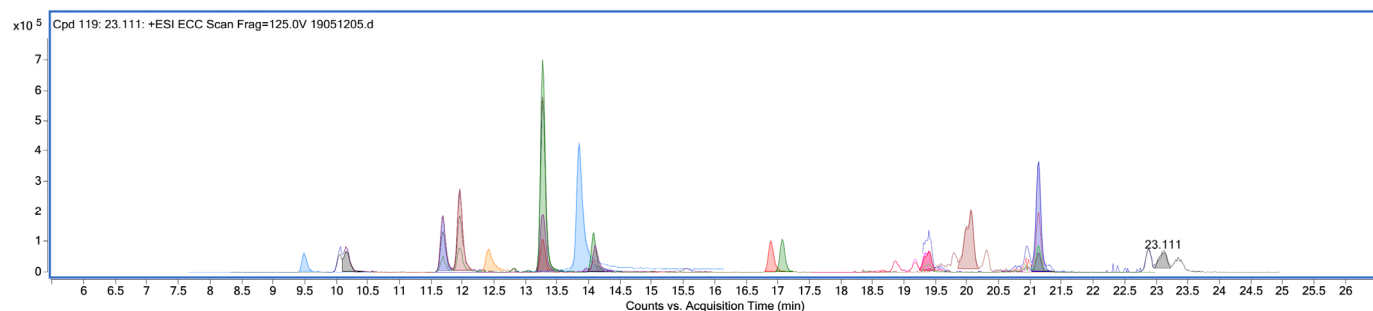


**Figure 10.** Chromatographic profile of the major compounds in the oxidised carbamazepine sample.

#### 4. Conclusions

The stoichiometric ratio of oxidant determines the degree of oxidation achieved, that is, the nature of the intermediates that coexist in solution. Performing with low concentrations of oxidant, corresponding to stoichiometric ratios of 1 mol CBZ: 10 mol  $H_2O_2$ , colour is generated in the water until it reaches its maximum intensity (oxo and dioxo-carbazepines). Subsequently, the tint continues to increase more slowly, until arriving at the steady state, remaining a coloured aqueous residue that would contain hydroxylated acridines and acridones. Applying concentrations higher than 1 mol CBZ: 25 mol  $H_2O_2$ , the colour formation follows the evolution of a reaction intermediate, obtaining a colourless solution.

The initial iron added to the solution, in the form of ferrous sulfate, undergoes a series of equilibrium reactions between species. This is due to the fact that the acidity of the sample is adjusted to pH = 3.0. Therefore, a part of the iron ions are found in a reduced state and the another in its oxidised, being the ferric ions that provide tint to the water. Both the maximum colour and the persistent colour increase with the concentration of iron used in the treatment, according to an average ratio of  $k_{Fe} = 0.0075 \text{ AU L/mg Fe}$ . The maximum tint would be generated by the iron species that interact with the organic load, forming metallic complexes, while the lasting colour would be generated by the iron species in suspension.

**Author Contributions:** Conceptualization, N.V. and J.M.L.; methodology, L.M.C. and H.A.Q.; software, J.M.L.; validation, C.F., J.I.L. and N.V.; formal analysis, J.I.L.; investigation, N.V., H.A.Q. and C.F.; resources, C.F.; data curation, N.V.; writing—original draft preparation, N.V., C.F. and H.A.Q.; writing—review and editing, J.M.L., L.M.C. and J.I.L.; visualization, N.V. and C.F.; supervision, L.M.C.; project administration, N.V. and J.I.L. and J.I.L. acquired the funding. All authors have read and agreed to the published version of the manuscript.

**Funding:** Authors are grateful to the University of the Basque Country UPV/EHU the financial support to carry out this research study through the scholarship Student Movility for Traineeships in the Erasmus + Programme between the Anadolu University in Eskisehir (Turkey) and the Faculty of Engineering Vitoria-Gasteiz (Spain), and the research Project PPGA20/33.

**Acknowledgments:** The authors thank for technical and human support provided by Central Service of Analysis from Álava—SGIker—UPV/EHU.

**Conflicts of Interest:** The authors declare no conflict of interest.

## Appendix A

Label	RT	m/z	Mass	Height	Name	Score	Diff (DB, ppm)	Ions
Cpd 31: carbamazepine	13.276	237.1029	236.0956	500597	carbamazepine	96.87	-2.51	7
Cpd 76: 13.857	13.857	274.2747	273.2674	352024				3
Cpd 112: 21.134	21.134	320.2563	297.2671	162272				8
Cpd 14: 10-OH-CBZ	11.961	255.1133	254.106	157787	10-OH-CBZ	97.82	-2	5
Cpd 33: 13.277	13.277	377.2089	376.2018	147084				3
Cpd 12: 10-OH-CBZ	11.893	255.113	254.1057	117504	10-OH-CBZ	99.74	-0.69	4
Cpd 104: 20.044	20.044	318.2412	295.2519	104589				5
Cpd 81: 14.083	14.083	237.1027	236.0954	93089				3
Cpd 30: 13.276	13.276	275.0584	274.0511	85219				3
Cpd 90: 16.894	16.894	238.111	237.1027	75562				3
Cpd 83: 14.110	14.11	318.2306	317.2733	69324				3
Cpd 115: 21.135	21.135	336.2303	335.223	65581				3
Cpd 17: 9-OH-acridine	12.421	196.0759	195.0686	63672	9-OH-acridine	99.55	-1.06	2
Cpd 91: 17.075	17.075	226.0865	225.0793	63218				5
Cpd 9: 10-OH-CBZ	10.167	255.1132	254.1059	56756	10-OH-CBZ	98.81	-1.47	2
Cpd 98: 19.375	19.375	280.2641	279.2568	55466				2
Cpd 6: 9.494	9.494	234.2067	233.1995	55020				2
Cpd 100: 19.384	19.384	320.2569	319.2497	54644				2
Cpd 119: 23.111	23.111	280.2638	279.2566	53960				2
Cpd 113: 21.134	21.134	356.3274	355.3201	50339				2
Cpd 86: 14.340	14.34	288.2895	287.2823	45626				2
Cpd 85: 14.155	14.155	210.0915	209.0842	42403				2
Cpd 35: 13.278	13.278	295.1557	294.1484	40689				2
Cpd 19: 12.963	12.963	267.1861	266.1788	36857				2
Cpd 111: 20.951	20.951	320.2565	297.2671	37049				6
Cpd 49: EP-CBZ	13.392	255.0975	252.0902	36822	EP-CBZ	99.19	-1.22	2
Cpd 105: 20.049	20.049	334.215	333.2077	35819				3
Cpd 78: 14.068	14.068	290.2698	289.2625	35753				2
Cpd 18: 12.147	12.147	264.2324	263.2251	35155				2
Cpd 99: 19.177	19.177	280.264	279.2568	34356				2
Cpd 15: 12.028	12.028	248.2431	245.2358	33414				2
Cpd 107: 20.311	20.311	318.2406	295.2511	32304				4
Cpd 80: 14.082	14.082	275.0585	274.0513	30799				3
Cpd 29: 13.275	13.275	617.1398	1232.2651	30685				3
Cpd 27: 13.239	13.239	606.1349	1210.2552	30129				3
Cpd 106: 20.056	20.056	354.3127	353.3054	29989				2
Cpd 94: 18.871	18.871	280.2638	279.2568	29484				2
Cpd 25: 13.202	13.202	595.1377	1188.2408	28766				3
Cpd 10: OX-CBZ	11.455	253.0974	252.0902	28240	OX-CBZ	99.39	-1.06	2
Cpd 79: 14.082	14.082	220.0761	219.0688	27418				2
Cpd 92: 18.868	18.868	320.2569	319.2496	27350				2
Cpd 38: 13.311	13.311	628.147	1254.2795	26627				2
Cpd 103: 19.794	19.794	318.2408	295.2515	26475				4
Cpd 28: 13.240	13.24	605.8839	1209.7633	26362				3
Cpd 60: 13.472	13.472	550.151	549.1437	26184				2
Cpd 26: 13.203	13.203	594.8776	1187.7406	26183				3
Cpd 89: 15.304	15.304	158.1537	157.1464	25035				2
Cpd 50: 13.409	13.409	532.5398	531.5325	24788				2
Cpd 82: 14.089	14.089	301.2856	300.2783	24337				2
Cpd 84: 14.126	14.126	239.118	238.1107	24171				2
Cpd 57: 13.443	13.443	541.3456	540.3383	24099				2
Cpd 75: EP-CBZ	13.706	253.097	252.0898	23905	EP-CBZ	99.85	0.53	2
Cpd 24: 13.164	13.164	584.1215	1166.2284	23833				3
Cpd 63: 13.503	13.503	558.9567	557.9494	23484				2
Cpd 87: 14.414	14.414	244.2638	243.2565	23324				2
Cpd 67: 13.533	13.533	567.762	566.7547	23093				2
Cpd 32: 13.277	13.277	616.8904	1231.7663	22863				3
Cpd 39: 13.312	13.312	627.8961	1253.7777	22613				3
Cpd 99: 19.383	19.383	336.2311	335.2238	22451				3
Cpd 41: 13.343	13.343	639.1532	1276.2919	22192				3
Cpd 8: 10.079	10.079	237.1025	236.0952	22176				2
Cpd 108: 20.338	20.338	293.2085	292.2012	22094				3
Cpd 47: 13.377	13.377	523.7354	522.7282	21838				2
Cpd 23: 13.163	13.163	583.871	1165.7274	21569				3
Cpd 18: 12.606	12.606	356.2799	355.2726	21417				2
Cpd 69: 13.562	13.562	576.5671	575.5598	21292				2
Cpd 4: 8.489	8.489	218.2118	217.2045	19862				2
Cpd 59: 13.471	13.471	550.3513	549.344	19427				2
Cpd 43: 13.361	13.361	263.0799	240.0905	19233				4
Cpd 48: 13.378	13.378	650.1607	1296.3068	19170				3
Cpd 110: 20.949	20.949	336.2306	335.2233	18835				2
Cpd 101: 19.382	19.382	316.2255	293.2362	18690				2
Cpd 70: 13.590	13.59	585.3719	584.3646	18102				2
Cpd 52: 13.410	13.41	532.7411	531.7338	17844				2
Cpd 61: 13.473	13.473	549.9508	548.9435	17777				2
Cpd 66: 13.531	13.531	567.9614	566.9542	17321				2
Cpd 22: 13.126	13.126	573.1151	1144.2156	17313				2
Cpd 42: 13.345	13.345	638.9041	1275.7937	17090				3
Cpd 55: 13.440	13.44	541.5456	540.5383	16747				2
Cpd 64: 13.503	13.503	559.1561	558.1488	16712				2
Cpd 62: 13.502	13.502	558.7568	557.7495	16674				2
Cpd 58: 13.444	13.444	541.1454	540.1382	16651				2
Cpd 7: 9.927	9.927	278.2338	277.2265	16503				2
Cpd 51: 13.410	13.41	661.1668	1320.319	16386				2
Cpd 53: 13.411	13.411	532.3405	531.3332	16342				2
Cpd 5: 9.370	9.37	282.2383	261.231	16255				2
Cpd 37: 13.309	13.309	505.923	504.9157	15944				2
Cpd 72: 13.615	13.615	594.1771	593.1699	15851				2
Cpd 36: 13.309	13.309	506.1242	505.1169	15539				2
Cpd 77: 14.042	14.042	288.2899	287.2826	15366				2
Cpd 46: 13.377	13.377	523.9355	522.9282	15261				2
Cpd 65: 13.530	13.53	567.5607	566.5534	14913				2
Cpd 44: 13.376	13.376	523.5355	522.5282	14899				2
Cpd 21: 13.125	13.125	572.8649	1143.7152	14659				2
Cpd 3: 5.852	5.852	120.0436	137.0473	14406				2
Cpd 2: 5.222	5.222	170.1176	187.1208	14396				2
Cpd 118: 22.908	22.908	336.3235	335.3163	14080				2
Cpd 45: 13.377	13.377	649.9099	1297.8052	13910				3
Cpd 73: 13.619	13.619	594.376	593.3687	13878				2
Cpd 68: 13.562	13.562	576.3662	575.3589	13754				2
Cpd 40: 13.343	13.343	514.7299	513.7226	13575				2
Cpd 34: 13.278	13.278	281.1401	280.1329	13193				2
Cpd 88: 14.862	14.862	224.1433	223.1361	13078				2
Cpd 102: 19.782	19.782	214.2174	213.2101	13071				2
Cpd 54: 13.412	13.412	660.9158	1319.8171	12993				3
Cpd 11: 11.546	11.546	239.0822	238.0749	12912				2
Cpd 1: 12.841	12.841	156.1018	173.1052	12774				2
Cpd 93: 18.869	18.869	336.2303	335.223	12673				2
Cpd 56: 13.443	13.443	672.1734	1342.3323	12590				2
Cpd 13: 11.958	11.958	220.0759	219.0686	12462				2
Cpd 97: 19.182	19.182	336.2305	335.2232	11979				2
Cpd 116: 21.404	21.404	431.1659	430.1586	11763				2
Cpd 71: 13.591	13.591	585.1719	584.1647	11328				2
Cpd 117: 22.123	22.123	429.3195	428.3122	11051				2
Cpd 74: 13.620	13.62	593.9763	592.969	10811				2
Cpd 95: 18.968	18.968	316.2252	293.2355	10142				3
Cpd 109: 20.479	20.479	486.3842	487.3769	10113				2
Cpd 20: 13.085	13.085	561.8572	1121.6999	10112				2
Cpd 114: 21.135	21.135	339.2996	338.2923	10052				2

**Figure A1.** Major ions ( $m/z$ ) and experimental masses calculated for each of the intermediate compounds detected in a sample of carbamazepine oxidized by photo-Fenton treatment under operating conditions that lead to the formation of coloured solution.

## References


- Adedara, I.A.; Ajayi, B.O.; Afolabi, B.A.; Awogbindin, I.O.; Rocha, J.B.T.; Farombi, E.O. Toxicological Outcome of Exposure to Psychoactive Drugs Carbamazepine and Diazepam on Non-Target Insect Nauphoeta Cinerea. *Chemosphere* **2021**, *264*, 128449. [CrossRef] [PubMed]
- Ribeiro, A.R.; Nunes, O.C.; Pereira, M.F.R.; Silva, A.M.T. An Overview on the Advanced Oxidation Processes Applied for the Treatment of Water Pollutants Defined in the Recently Launched Directive 2013/39/EU. *Environ. Int.* **2015**, *75*, 33–51. [CrossRef] [PubMed]
- Giribabu, N.; Reddy, S. Protection of Male Reproductive Toxicity in Rats Exposed to Di-n-Butyl Phthalate during Embryonic Development by Testosterone. *Biomed. Pharmacother.* **2017**, *87*, 355–365. [CrossRef] [PubMed]
- European Commission Commission Implementing Decision (EU) 2018/840 of 5 June 2018. Available online: [https://eur-lex.europa.eu/eli/dec\\_impl/2018/840/oj](https://eur-lex.europa.eu/eli/dec_impl/2018/840/oj) (accessed on 22 February 2021).

5. Hai, F.I.; Yang, S.; Asif, M.B.; Sencadas, V.; Shawkat, S.; Sanderson-Smith, M.; Gorman, J.; Xu, Z.-Q.; Yamamoto, K. Carbamazepine as a Possible Anthropogenic Marker in Water: Occurrences, Toxicological Effects, Regulations and Removal by Wastewater Treatment Technologies. *Water* **2018**, *10*, 107. [CrossRef]
6. Arye, G.; Dror, I.; Berkowitz, B. Fate and Transport of Carbamazepine in Soil Aquifer Treatment (SAT) Infiltration Basin Soils. *Chemosphere* **2011**, *82*, 244–252. [CrossRef] [PubMed]
7. Al Aukidy, M.; Verlicchi, P.; Jelic, A.; Petrovic, M.; Barcelò, D. Monitoring Release of Pharmaceutical Compounds: Occurrence and Environmental Risk Assessment of Two WWTP Effluents and Their Receiving Bodies in the Po Valley, Italy. *Sci. Total Environ.* **2012**, *438*, 15–25. [CrossRef] [PubMed]
8. Badia-Fabregat, M.; Lucas, D.; Pereira, M.A.; Alves, M.; Pennanen, T.; Fritze, H.; Rodríguez-Mozaz, S.; Barceló, D.; Vicent, T.; Caminal, G. Continuous Fungal Treatment of Non-Sterile Veterinary Hospital Effluent: Pharmaceuticals Removal and Microbial Community Assessment. *Appl. Microbiol. Biotechnol.* **2016**, *100*, 2401–2415. [CrossRef] [PubMed]
9. Behera, S.K.; Kim, H.W.; Oh, J.-E.; Park, H.-S. Occurrence and Removal of Antibiotics, Hormones and Several Other Pharmaceuticals in Wastewater Treatment Plants of the Largest Industrial City of Korea. *Sci. Total Environ.* **2011**, *409*, 4351–4360. [CrossRef] [PubMed]
10. Tian, Y.; Xia, X.; Wang, J.; Zhu, L.; Wang, J.; Zhang, F.; Ahmad, Z. Chronic Toxicological Effects of Carbamazepine on *Daphnia Magna* Straus: Effects on Reproduction Traits, Body Length, and Intrinsic Growth. *Bull. Environ. Contam. Toxicol.* **2019**, *103*, 723–728. [CrossRef] [PubMed]
11. Xin, J.; Yan, S.; Hong, X.; Zhang, H.; Zha, J. Environmentally Relevant Concentrations of Carbamazepine Induced Lipid Metabolism Disorder of Chinese Rare Minnow (*Gobiocypris Rarus*) in a Gender-Specific Pattern. *Chemosphere* **2021**, *265*, 129080. [CrossRef] [PubMed]
12. Yan, S.; Chen, R.; Wang, M.; Zha, J. Carbamazepine at Environmentally Relevant Concentrations Caused DNA Damage and Apoptosis in the Liver of Chinese Rare Minnows (*Gobiocypris Rarus*) by the Ras/Raf/ERK/P53 Signaling Pathway. *Environ. Pollut.* **2021**, *270*, 116245. [CrossRef] [PubMed]
13. Almeida, Â.; Calisto, V.; Domingues, M.R.M.; Esteves, V.I.; Schneider, R.J.; Soares, A.M.V.M.; Figueira, E.; Freitas, R. Comparison of the Toxicological Impacts of Carbamazepine and a Mixture of Its Photodegradation Products in *Scrobicularia Plana*. *J. Hazard Mater.* **2017**, *323*, 220–232. [CrossRef] [PubMed]
14. Prasse, C.; Stalter, D.; Schulte-Oehlmann, U.; Oehlmann, J.; Ternes, T.A. Spoilt for Choice: A Critical Review on the Chemical and Biological Assessment of Current Wastewater Treatment Technologies. *Water Res.* **2015**, *87*, 237–270. [CrossRef] [PubMed]
15. Benner, J.; Helbling, D.E.; Kohler, H.-P.E.; Wittebol, J.; Kaiser, E.; Prasse, C.; Ternes, T.A.; Albers, C.N.; Aamand, J.; Horemans, B.; et al. Is Biological Treatment a Viable Alternative for Micropollutant Removal in Drinking Water Treatment Processes? *Water Res.* **2013**, *47*, 5955–5976. [CrossRef] [PubMed]
16. Magi, A.; Semeraro, R.; Mingrino, A.; Giusti, B.; D'Aurizio, R. Nanopore Sequencing Data Analysis: State of the Art, Applications and Challenges. *Brief. Bioinform.* **2018**, *19*, 1256–1272. [CrossRef] [PubMed]
17. Fieser, L.F.; Fieser, M. *Química Orgánica Superior*; Grijalbo: Barcelona, Mexico, 1966; Volume 2.
18. Villota, N.; Lomas, J.; Camarero, L. Changes of Turbidity during the Oxidation of Dihydroxylated Benzenes by Fenton Reagent and Effect on Dissolved Oxygen. *Desalination Water Treat.* **2018**, *127*, 2–7. [CrossRef]
19. De Luis, A. *Degradación de Compuestos Fenólicos En Disolución Acuosa Con Peróxido de Hidrógeno: Modelización de Los Sistemas de Generación de Radicales*; University of the Basque Country: Leioa, Spain, 1999.
20. Zhang, L.; Zhao, X.; Niu, C.; Tang, N.; Guo, H.; Wen, X.; Liang, C.; Zeng, G. Enhanced Activation of Peroxymonosulfate by Magnetic Co<sub>3</sub>MnFeO<sub>6</sub> Nanoparticles for Removal of Carbamazepine: Efficiency, Synergetic Mechanism and Stability. *Chem. Eng. J.* **2019**, *362*, 851–864. [CrossRef]
21. Golan-Rozen, N.; Seiwert, B.; Riemenschneider, C.; Reemtsma, T.; Chefetz, B.; Hadar, Y. Transformation Pathways of the Recalcitrant Pharmaceutical Compound Carbamazepine by the White-Rot Fungus *Pleurotus Ostreatus*: Effects of Growth Conditions. *Environ. Sci. Technol.* **2015**, *49*, 12351–12362. [CrossRef] [PubMed]
22. Mijangos, F.; Varona, F.; Villota, N. Changes in Solution Color During Phenol Oxidation by Fenton Reagent. *Environ. Sci. Technol.* **2006**, *40*, 5538–5543. [CrossRef] [PubMed]



## Article

# Quarry Residue: Treatment of Industrial Effluent Containing Dye

Lariana Negrão Beraldo de Almeida <sup>1,\*</sup>, Tatiana Gulminie Josué <sup>2</sup>, Othavio Henrique Lupepsa Nogueira <sup>2</sup>, Daniele Toniolo Dias <sup>3</sup> , Angelo Marcelo Tusset <sup>4</sup>, Onélia Aparecida Andreo dos Santos <sup>1</sup> and Giane Gonçalves Lenzi <sup>2</sup>

<sup>1</sup> Departamento de Engenharia Química, Universidade Estadual de Maringá, 5790, Maringá 87020-900, Brazil; oaasantos@uem.br

<sup>2</sup> Departamento de Engenharia Química, Universidade Tecnológica Federal do Paraná, Rua Doutor Washington Subtil Chueire, 330, Ponta Grossa 84016-210, Brazil; tatianajosue@alunos.utfpr.edu.br (T.G.J.); othavionogueira@alunos.utfpr.edu.br (O.H.L.N.); gianeg@utfpr.edu.br (G.G.L.)

<sup>3</sup> Departamento Acadêmico de Física, Universidade Tecnológica Federal do Paraná, Rua Doutor Washington Subtil Chueire, 330, Ponta Grossa 84016-210, Brazil; danielletdias@utfpr.edu.br

<sup>4</sup> Departamento de Engenharia, Universidade Tecnológica Federal do Paraná, Rua Doutor Washington Subtil Chueire, 330, Ponta Grossa 84016-210, Brazil; tusset@utfpr.edu.br

\* Correspondence: pg53631@uem.br or beraldolariana@gmail.com

**Citation:** Almeida, L.N.B.d.; Josué, T.G.; Nogueira, O.H.L.; Dias, D.T.; Tusset, A.M.; Santos, O.A.A.d.; Lenzi, G.G. Quarry Residue: Treatment of Industrial Effluent Containing Dye. *Catalysts* **2021**, *11*, 852. <https://doi.org/10.3390/catal11070852>

Academic Editors: Gassan Hodaifa and Rafael Borja

Received: 10 June 2021

Accepted: 12 July 2021

Published: 16 July 2021

**Publisher's Note:** MDPI stays neutral with regard to jurisdictional claims in published maps and institutional affiliations.



**Copyright:** © 2021 by the authors. Licensee MDPI, Basel, Switzerland. This article is an open access article distributed under the terms and conditions of the Creative Commons Attribution (CC BY) license (<https://creativecommons.org/licenses/by/4.0/>).

**Abstract:** This work is devoted to the investigation of the discoloration of the synthetic and industrial effluent, using a quarry residue (MbP), which is a material naturally composed of mixed oxides, compared to zinc oxide (ZnO), acting as photocatalysts and adsorbents. The optimization of the pH and catalyst concentration parameters was carried out, and the industrial effluent was then treated by photocatalytic reactions, adsorption, and photolysis. Industrial effluent was supplied by a packaging company and was collected for a period of seven consecutive days, showing the oscillation of the parameters in the process. The material characterizations were obtained by scanning electron microscopy (SEM-EDS), X-Ray diffraction (XRD), and photoacoustic spectroscopy (PAS). The results indicated that the composition of the quarry waste is mainly silica and has  $E_{gap}$  2.16 eV. The quarry residue as photocatalyst was active for the artificial effluent (synthetic dye solution), with a maximum of 98% discoloration, and as an adsorbent for industrial effluent, with a maximum of 57% of discoloration. Although the quarry residue has shown results lower than ZnO, it is considered a promising material in adsorption processes and photocatalytic reactions for discoloration of aqueous solutions.

**Keywords:** adsorption; photolysis; photocatalysis; quarry residue; discoloration; packaging industry

## 1. Introduction

Dyes are chemical compounds that have the ability to color the surface of materials such as fabric fibers, packaging, and food. Industrial processes that use water and dyes in the production stages probably will present dye residual concentrations in effluent. Effluents, before being released into the environment or even reused, will need to undergo treatments to remove, among other compounds, their coloring.

Different techniques are performed to promote discoloration, including ultrafiltration, coagulation, flocculation, sonochemical decomposition, adsorption, biological treatments, heterogeneous photocatalysis, Fenton and photo-Fenton processes, advanced oxidation electrochemical processes, etc. [1–4].

Heterogeneous photocatalysis is classified as an advanced oxidative process [5] and has been widely studied due to its diversified application, such as the reduction of chromium VI to chromium III [6], mercury reduction [7], degradation of emerging pollutants such as caffeine [8], drugs [9,10], dyes [11], and reduction of bromate in water intended for human consumption [12].

In photocatalytic reactions, there are many variables that must be considered in order, such as the radiation source, pH of the reaction medium, temperature, and material used as a semiconductor material. The main materials used in the photoreactions are  $\text{TiO}_2$  and  $\text{ZnO}$  as they are nontoxic and have good photochemical properties [13–16]; however, researchers commonly describe improvements in the catalysts' properties through new syntheses [17], the addition of metals [18,19], mixed oxides, etc.

In this direction, the search for new catalytic materials is also a very interesting and encouraging subject, particularly if this new material is a by-product in large quantities or a waste product without the exact destination of any industrial process.

The rice husk can be mentioned as an example; as agro-industrial residue, it has already been used as a source of silica for the synthesis of catalysts applied in the degradation of terephthalate acid [20] and discoloration of methyl violet dye [21].

Some quarries generate, in excess volumes, a by-product called stone powder or rock powder. This material has characteristics and chemical composition that varies and depends on the type of rock to be explored. In intrusive igneous rocks, silicon dioxide ( $\text{SiO}_2$ ) is one of the most significant components and the classification of the rock occurs according to the  $\text{SiO}_2$  present amount: above 63% are acid igneous rocks, 52–63% are intermediate or neutral igneous rocks, 45–52% are mafic or basic igneous rocks, and <45% are ultramafic or ultrabasic igneous rocks [22]. Using this type of in-water treatment waste is a recent and promising proposal.

In this context, the present work contributes with a new material catalytic/adsorbent material, giving value a residue, as an alternative to traditional catalysts/adsorbent (mineral by-product). In addition, tests with industrial effluent, from the packaging industry, samples were collected for a period of seven consecutive days, considering the industrial process dynamics. The photocatalytic and adsorptive capacity of the stone powder was evaluated in the discoloration, applied both to the synthetic effluent and to the industrial effluent.

## 2. Results and Discussion

### 2.1. Catalysts Characterizations

Figure 1 shows the results for SEM-EDS, PAS, and XRD for  $\text{ZnO}$  and the mineral by-product (MbP).

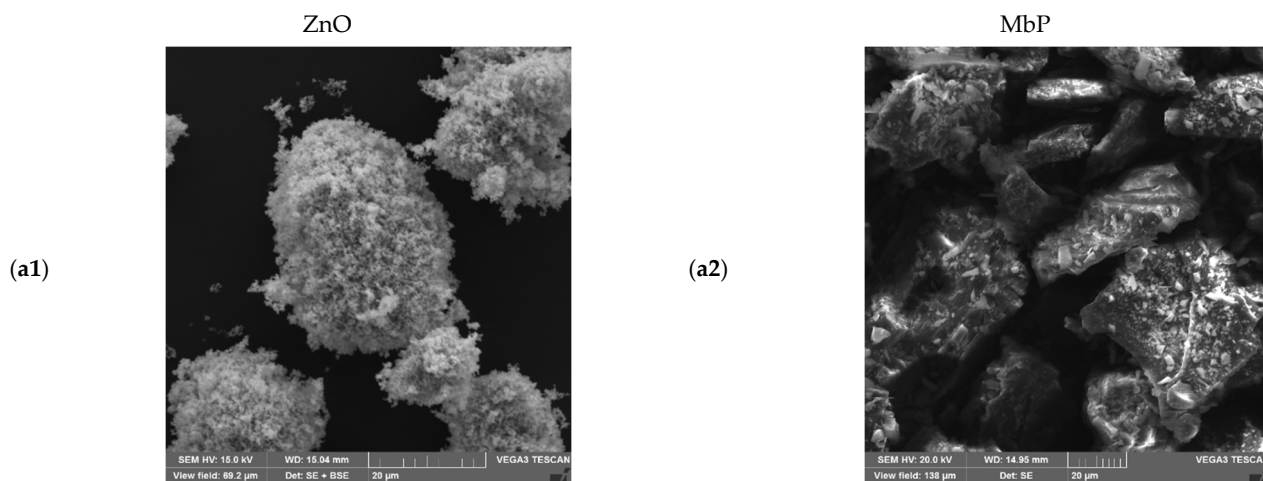
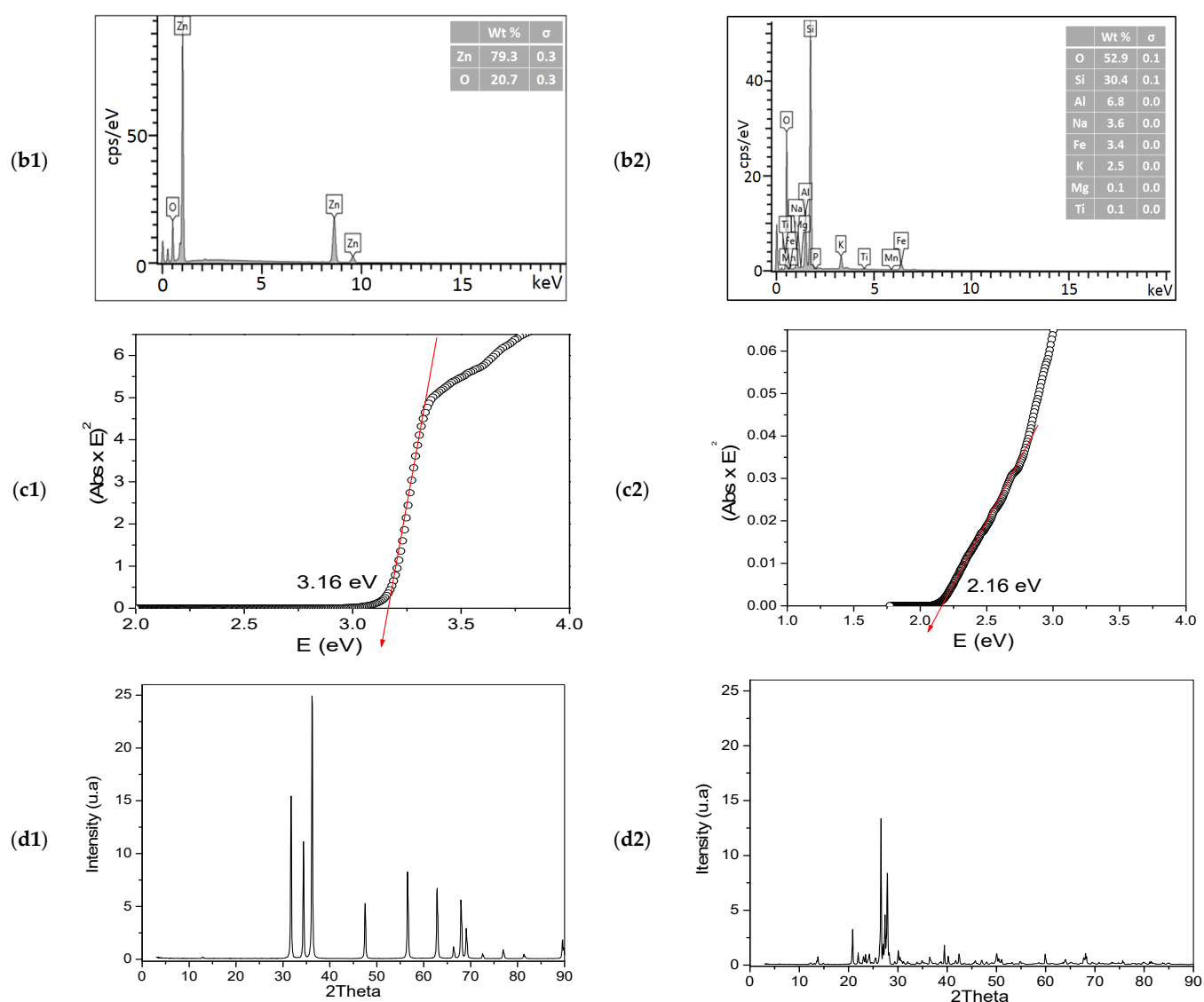


Figure 1. *Conts.*





**Figure 1.** Characterizations of ZnO and mineral by-product (MbP): (a1,b1,c1) and (d1) correspond to SEM, EDS, PAS and XRD to ZnO, respectively. And (a2,b2,c2) and (d2) correspond to SEM, EDS, PAS and XRD to MbP, respectively.

The ZnO composition is defined by approximately 80% zinc and 20% oxygen (Figure 1), the material bandgap energy is 3.16 eV, and a crystalline definition in hexagonal wurtzite, which is the most common for this material. Such characteristics are similar to those already described in the literature [23–25].

For the MbP, there is a large number of elements in its structure; however, the elements O, Si, and Al correspond to approximately 90% of the material. In this way, is possible to compare the quarry residue used with quartz sand, which is also naturally composed of silica and other impurities such as  $\text{Fe}_2\text{O}_3$ ,  $\text{Al}_2\text{O}_3$ ,  $\text{TiO}_2$ ,  $\text{CaO}$ ,  $\text{MgO}$ , and  $\text{K}_2\text{O}$  [24]. Materials containing silica ( $\text{SiO}_2$ ) and alumina ( $\text{Al}_2\text{O}_3$ ) can be found in the literature as supporting materials for catalysts [26,27]. Regarding the MbP crystallinity, the peaks identified in  $2\theta$  between 20 and 30° is characteristic of the hexagonal mesoporous silicate [28]; in addition, the MbP  $E_{\text{gap}}$  value was close to 2.16 eV, being very close to  $E_{\text{gap}}$  of Si nanoparticles from quartz sand, defined at 2.22 eV [29].

## 2.2. Experimental Tests

### PH and Catalyst Concentration

The experimental tests first carried out were aimed at identifying the optimal parameters, pH, and catalyst/adsorbent concentration for both industrial and synthetic effluents. Figures 2 and 3 indicate the results obtained for synthetic and industrial effluent and material used. All graphs referring to the experimental tests are presented as  $C/C_0$  versus time (min), where  $C$  ( $\text{mg L}^{-1}$ ) is the concentration at any time  $t$  (min), and  $C_0$  is the initial concentration ( $t = 0$ ).

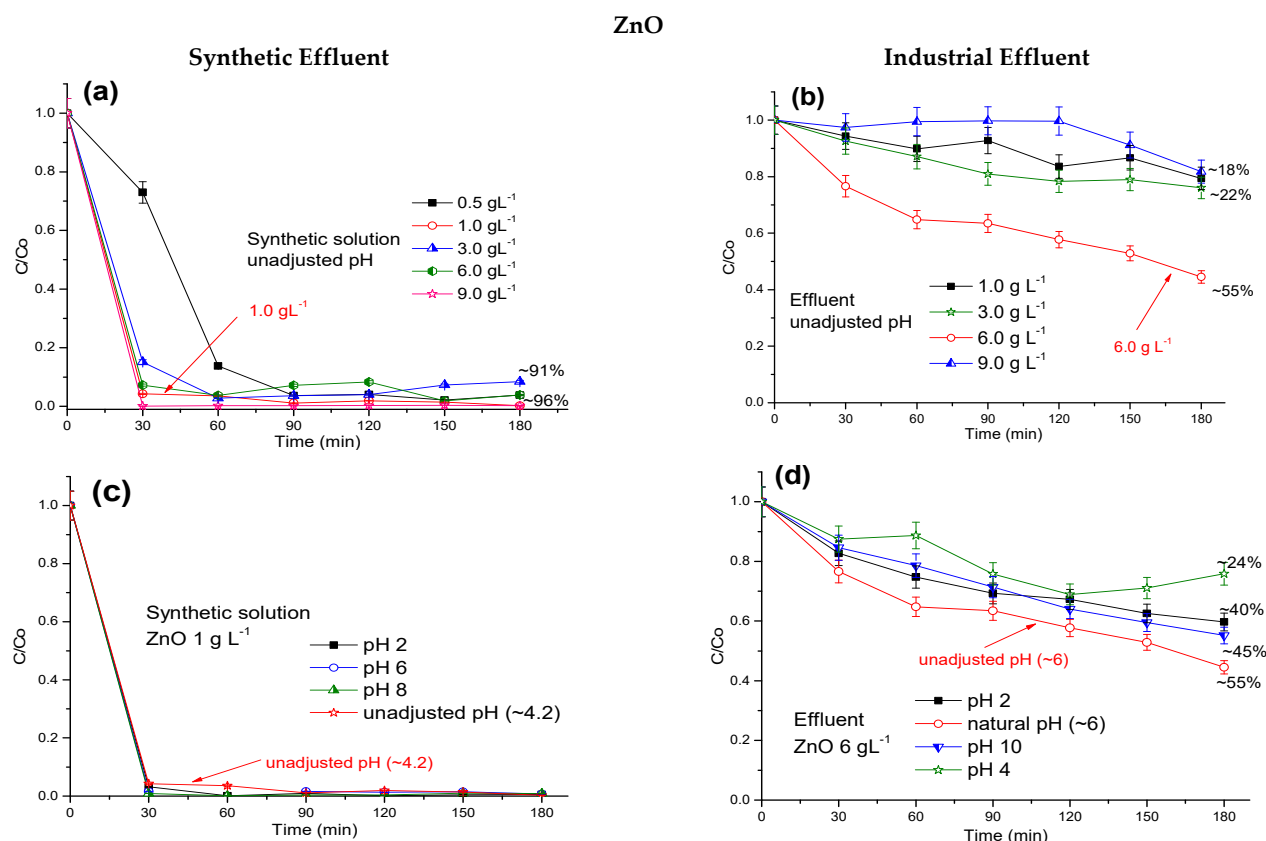


**Figure 2.** Catalyst concentration (a,b) and pH (c,d) tests for ZnO with synthetic and industrial effluent.

Figures 2 and 3 have some aspects in common that can be highlighted; for example, when the industrial effluent was treated, there was a greater and faster solution discoloration. This fact is related to the effluent composition, that is, while the synthetic effluent contained only dye and distilled water, the industrial effluent had a large organic load. Figure 7 indicated that the presence of organic compounds can impair photocatalytic reactions since such compounds will compete for surface adsorption with the material's active sites.

Another aspect that can be highlighted is that the catalyst concentration has also been changed independently of the used material. When the photocatalytic process was applied in the synthetic effluent, 1.0  $\text{g L}^{-1}$  was the solution was satisfactorily discolored; on the other hand, for the industrial effluent, 6.0  $\text{g L}^{-1}$  was needed so that greater percentages of discoloration were achieved.

Although with MbP in the 9.0  $\text{g L}^{-1}$  concentration, at the beginning of the reaction, it had a quick discoloration, the difference for when 6.0  $\text{g L}^{-1}$  was used was small; thus, this would not justify an increase of 50% in catalyst concentration for the reaction.

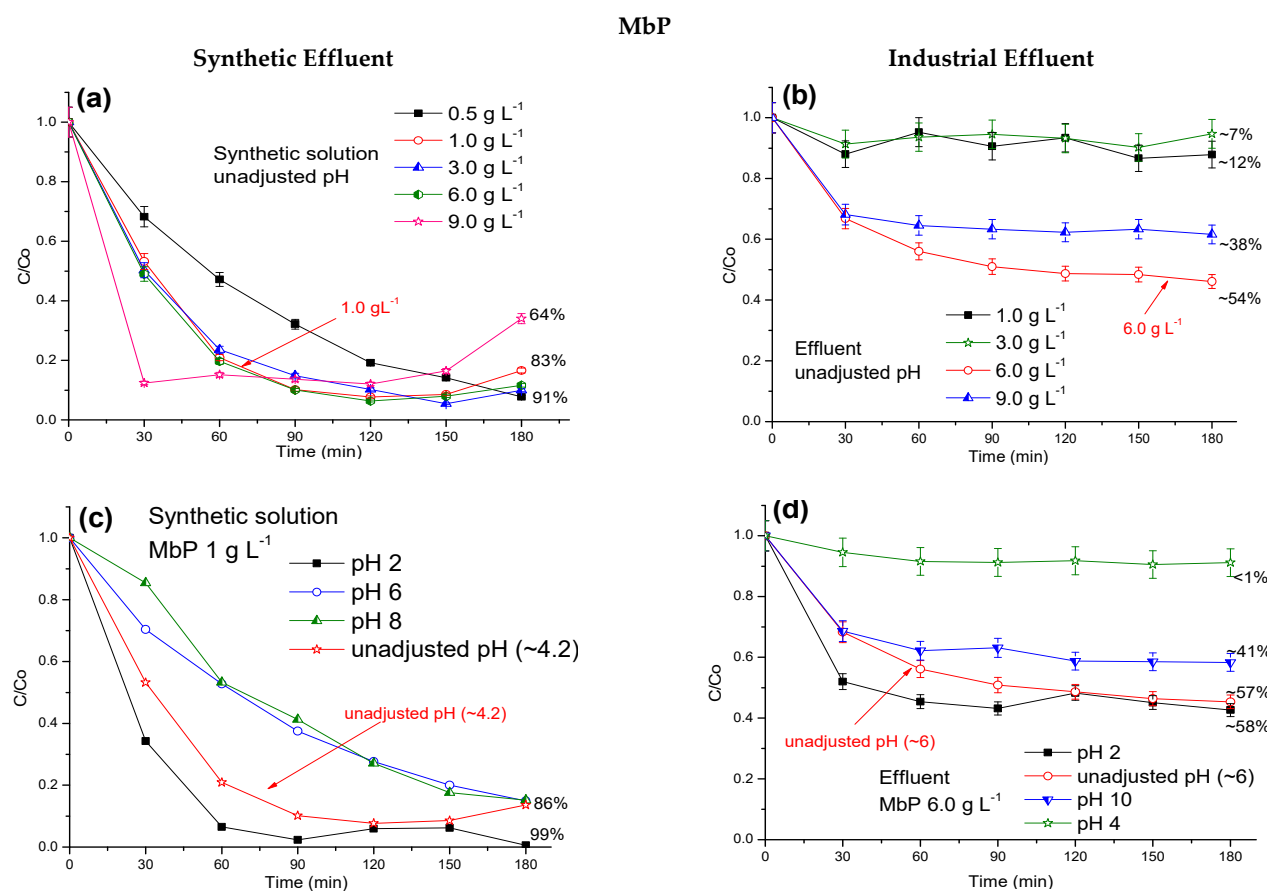


**Figure 3.** Catalyst concentration (a,b) and pH (c,d) tests for MbP with synthetic and industrial effluent.

The reaction speed is related to the photocatalyst concentration. As the concentration of catalysts increases, reaction speed is increased, as more active sites will be available. However, when this concentration reaches an optimum point, if more photocatalyst is added, the reaction may be impaired, and therefore, radiation penetration tends to decrease with the light screening effect, a factor often observed by different authors with different pollutants [30–32].

Regarding the pH of the reaction medium, for both cases, it appears that the pH without adjustment, that is, the unadjusted pH proper to the effluent (synthetic ~4.2 or industrial ~6.2) were identified as ideal for photoreaction.

The working advantage with the solution itself, that is, without adjustments, is the time that is saved in the adjustment steps before and after reactions. Figure 4 shows the results obtained for photolysis and adsorption tests (synthetic solution).

Both photolysis and adsorption results demonstrate the need for a photocatalyst-radiation combination for greater discoloration of the synthetic solution.

After defining the pH and catalyst concentration conditions, i.e., pH without adjustment (unadjusted pH) and 6.0 g L<sup>-1</sup> of ZnO or MbP, the experimental tests were realized for samples collected from the industrial effluent during seven consecutive days.

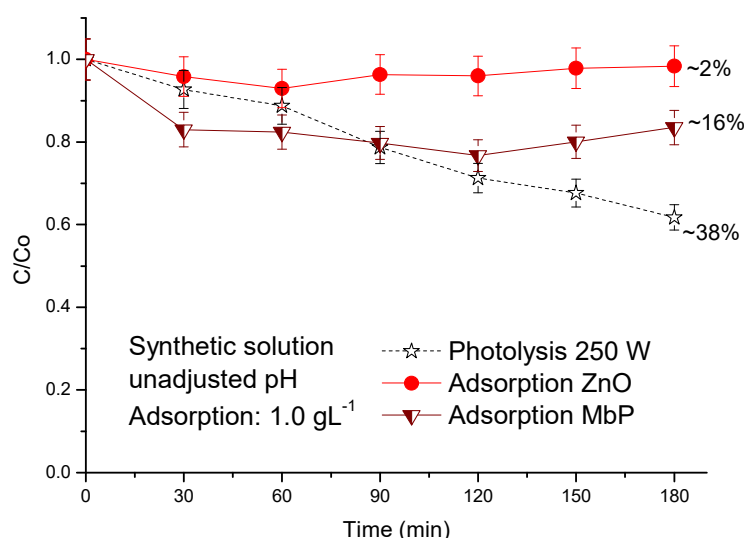


**Figure 4.** Photolysis and adsorption with synthetic solution, unadjusted pH, and concentration of  $1 \text{ gL}^{-1}$  of ZnO or MbP.

### 2.3. Industrial Effluent

Molded pulp packaging, which is the product manufactured in the company where the industrial effluent was collected, is basically made of paper, water, and additives, and follows a process, as described in Figure 5.

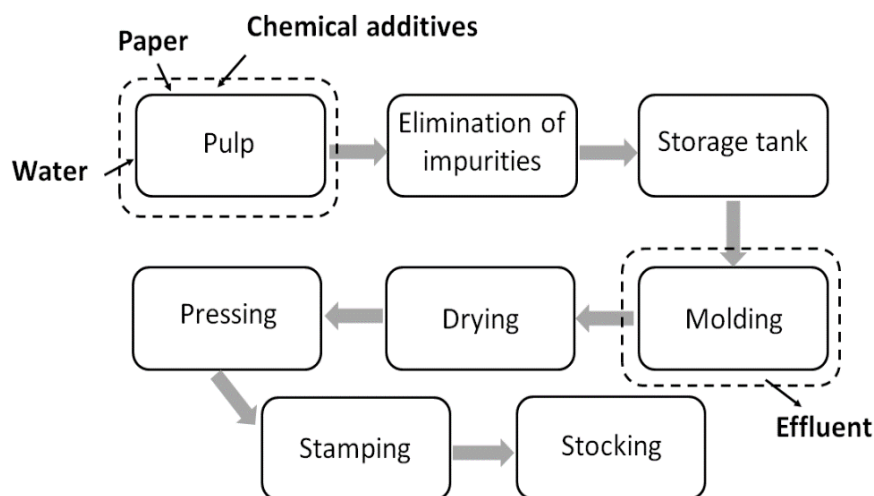


**Figure 5.** The manufacturing process of molded pulp packaging.

The first stage of the process is the formation of the pulp, which consists of water, chemical additives, and paper of different types; then, this pulp undergoes a process in which the gross impurities are removed. Subsequently, the mass proceeds to a storage tank that feeds the equipment used for molding, which basically consists of pressure and suction operations of excess water. Then, the ready packages are processed, by means of mats, for drying which, depending on the moisture conditions of the material, are heated from 180 to 240 °C for approximately 10 to 15 min and, finally, before advancing to the printing (the step in which it adds images and writings according to what was established by the client), the packages undergo a pressing process in which the objective is to provide a better finish and resistance [33].

Currently, the effluent that leaves the molding stage is reused without being subjected to any treatment at the inputs entrance for the pulp manufacture. However, it is very difficult to adjust the color of the next batch of packaging, since in some cases, other dyes are also used. This situation causes dissatisfaction among customers, as there is no color standardization. Therefore, based on the results we had in item 2.2, the effluent treatment was realized, aiming to identify the parameter variation and how the reactions would be conducted. Figure 6 shows the results.

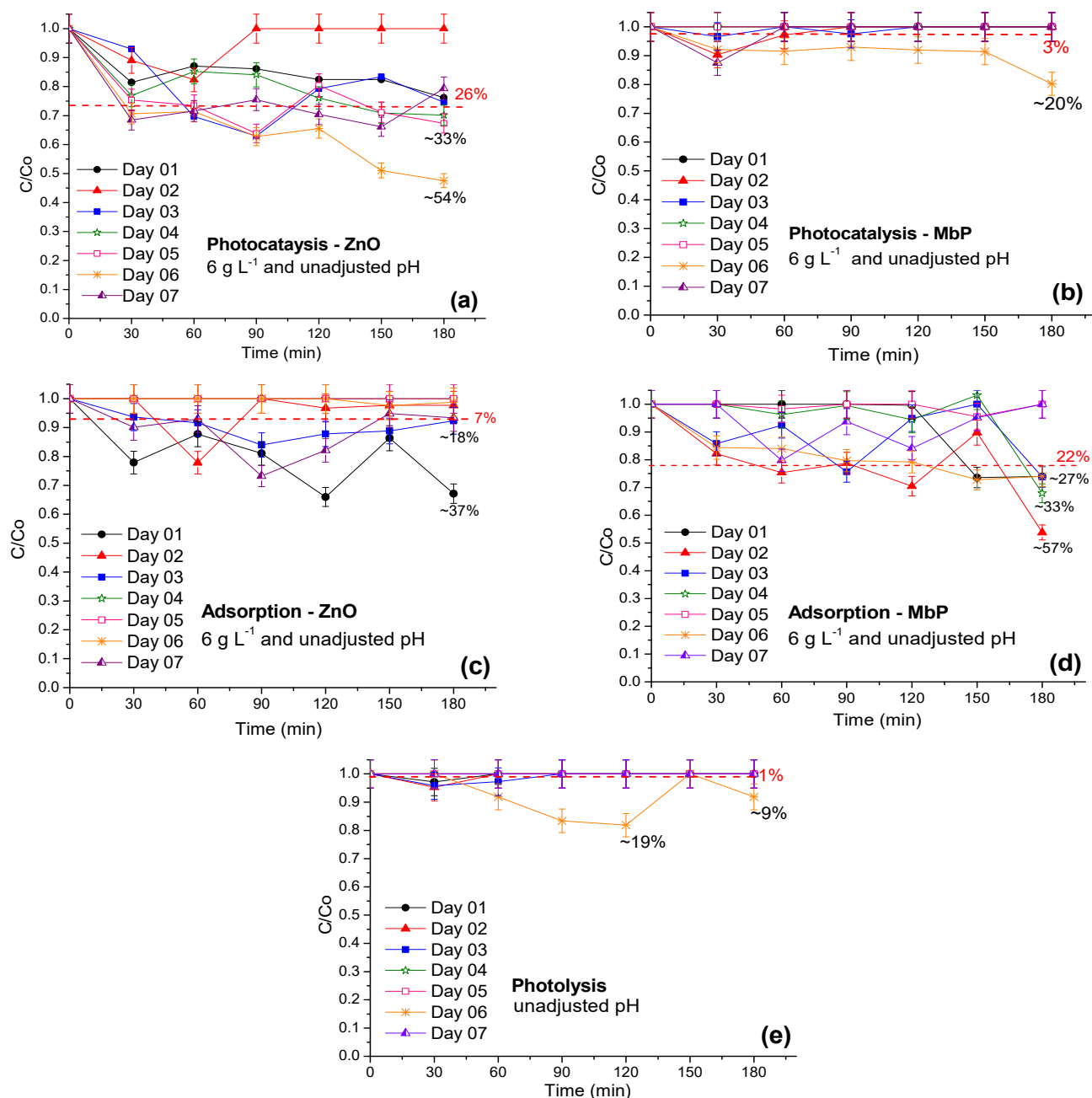


**Figure 6.** Tests of heterogeneous photocatalysis (a,b), adsorption (c,d), and photolysis (e) of industrial effluents.

Figure 7 shows the initial composition of each collected effluent sample and its subsequent composition after the reactions used. The variables total soluble solids and N (NO<sub>3</sub>); surfactants are not quantified in the graph since they always presented the same values of <100, <10, and <10, respectively.

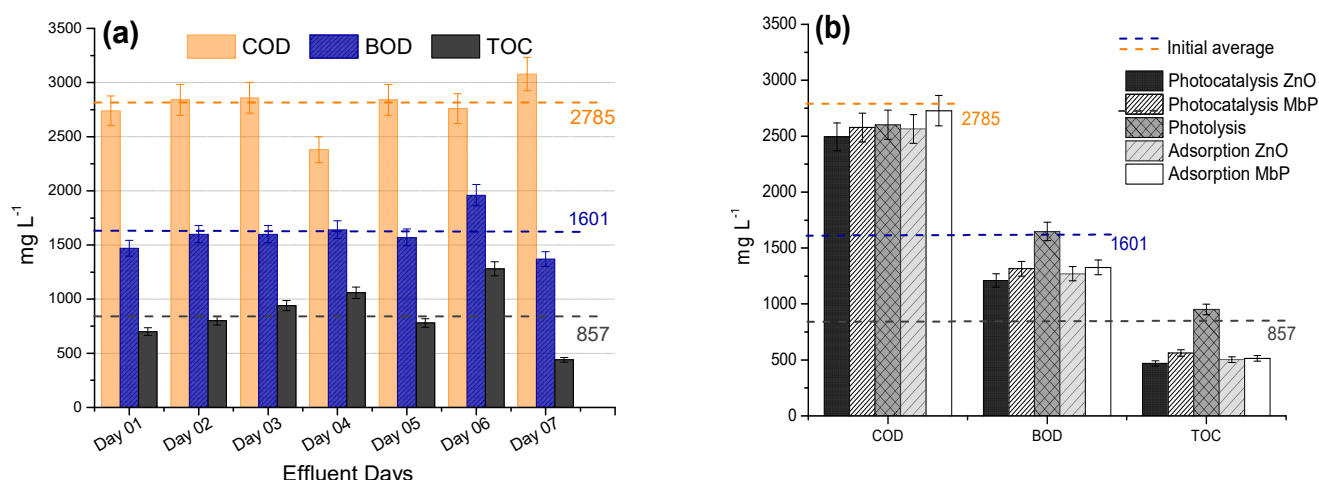


**Figure 7.** Organic load (a) initially and (b) after reactions with industrial effluents. The dashed lines indicate the initial average of COD, BOD, and TOC ( $\text{mg L}^{-1}$ ) of the 7 days from the collected effluent.

There was great variation in the efficiency of the tests performed, beginning with the photocatalytic tests that showed an average of 26% and 3% discoloration when used ZnO and MbP, respectively, which is a significant drop when compared to the results shown in Figures 3 and 4. Photolysis had unfavorable performance, both in the discoloration of the dye (Figure 6e) and in the organic load reduction (Figure 7b). Regarding adsorption, it appears that MbP was, generally, a good adsorbent of the present dye in the industrial effluent, presenting on average 22%.

All this unstable behavior observed during the reactions is related to the variation in the industrial effluent composition observed in Figure 7a. Changes in the reactions kinetic behavior when using a synthetic dye solution and when using an industrial effluent have already been observed in the literature [34] in which the authors evaluated the discoloration of synthetic effluent containing blue dye and industrial textile effluent and verified a decrease in the efficiency of the process when industrial textile effluent was used. In the literature [35], they also verified superior results when they treated a synthetic effluent containing dye rather than real industrial effluent. Both authors justified this behavior due to the effluent's composition, such as the presence of interfering ions and organic load.

Organic compounds, when present in the solution, can compete for the photogenerated hydroxyl radical and the active sites available on the catalyst surface with the target pollutant, which, in the present research, was the dye CI basic yellow 96, which can decrease the efficiency of photocatalysis [36].

When comparing the initial composition of this effluent with other effluents already studied, it can be highlighted that the effluent from the molded pulp packaging industry has a high organic load with high values of COD, BOD, and TOC when compared with other effluents, as reported in the literature [37,38].

In addition to the concentration reduction of dye present in the effluent, it is necessary to evaluate the organic load decrease. It is noted that for all reactions, except for the photolysis reactions, a decrease in the organic load occurs, mainly in terms of TOC. This parameter (TOC) is related to the pollutant mineralization; in the present study, it is possible to notice that the dye degradation and the mineralization of the same occurred simultaneously [39,40]. It is important to note that adsorption has also been shown to be effective in reducing organic matter. The decrease in organic load in the industrial effluent brings benefits to the water quality since the organic load has less capacity to pollute the effluent.

In the present work, it is possible to affirm that MbP has catalytic properties; however, it also presented an adsorbent behavior in some experimental tests. MbP is a low-cost material available in large quantities, which can bring financial benefits to the companies involved. Quartz sand, which is a material very similar to the by-product studied in the present work, has also been applied as an adsorbent and has shown promising results such

as the methylene blue dye adsorption [41], together with graphene in the adsorption of  $\text{Hg}^{2+}$  e  $\text{Pb}^{2+}$  [42] and the adsorption of Ciprofloxacin [43].

Using waste or by-products as catalysts is a recent proposal and involves numerous challenges. Some authors have already described the performance of residues as catalysts and adsorbents in the most diverse degradations and adsorption, such as, for example, the study [44], in which they studied the use of depleted acacia bark (agro-industrial waste) as support for photocatalysts used in the degradation of organic phenolic pollutants, and the study [45], in which they used bauxite residue from the aluminum industry as a new photocatalyst for hydrogen generation. However, in most research studies, the photocatalytic reactions use the residues only as a support for catalysts such as  $\text{TiO}_2$  or else as a source of some metal to be impregnated in the semiconductor. Studies are carried out with pollutants present in synthetic solutions, which facilitate the reproducibility of the results and applicability favor the new catalyst.

### 3. Materials and Methods

#### 3.1. Chemicals

The used dye in the synthetic solution reactions was supplied by the same company that supplied the real effluent; this dye is known as CI Basic Yellow 96 (BASF–Solenis), is used to dye the molded pulp packaging in industrial processes, has a yellow color, and liquid form.

The materials used as catalysts and adsorbents were (i) zinc oxide ( $\text{ZnO}$ ) as a reference material, supplied by Dinâmica Química Ltd.a (Sao Paulo, Brazil) and (ii) quarry residue, in this work defined as a mineral by-product (MbP).

The MbP was supplied by a company located in the region of Campos Gerais in the state of Paraná—Brazil. This company operates in the sale of stones and gravel, asphalt, providing services in the area of earthworks and paving. The rock explored is classified as intrusive igneous granite. Both  $\text{ZnO}$  and MbP were used without previous treatment; however, their grain size was standardized. Both were sieved in order to obtain particles smaller than 0.3 mm. This characteristic is observed in the  $\text{ZnO}$  (used as a reference).

#### 3.2. Catalysts Characterizations

##### 3.2.1. Scanning Electron Microscopy (SEM) Associated with Dispersive Energy Spectroscopy (EDS)

Samples were metalized with gold using IC-50 ION COATER (Shimadzu) for 10 min. The topographic surface images were obtained using a scanning electron microscope model VEGA 3 LMU brand TESCAN, complete with, 30 kV W filament, 3.0 nm resolution, retractable SE and BSE detectors, low-vacuum mode (500 Pa) chamber with an internal diameter of 230 mm, and a CCD camera for viewing the sample chamber. The microscope is also equipped with EDS Detector, model AZTec Energy X-Act, resolution 130 eV, brand Oxford.

##### 3.2.2. X-ray Diffraction (XRD)

A Bruker D8 Advance X-ray diffractometer, 2 from 5 to  $80^\circ$ , with  $2^\circ/\text{min}$  in the scan, 40 kV and 35 mA was used. The result obtained was then analyzed using standards published by the International Center for Diffraction Data (ICDD).

##### 3.2.3. Photoacoustic Spectroscopy (PAS)

A source with Xenon lamp emitted a light that passed through a monochromator, (Oriel, model 66,936 (1/4 m), with inlet and outlet slits adjusted to 3.00 mm. The frequency of light modulation was controlled by a mechanical modulator (Stanford Research Systems, model SR 540) which, with a photodiode, provided a reference signal for the amplifier (lock-in). The microphone attached to the photoacoustic cell (Brüel & Kjaer, model BK 4953) was connected to a power source and a preamplifier. The microphone signal was transferred to a synchronized amplifier (EG & G Instruments, model 5110), and the amplifier provided intensity, and the phase of the photoacoustic signal was transferred to a personal computer;



the spectra (modulation frequency 23 Hz) were normalized with respect to the carbon signal. Direct bandgap energy ( $E_{\text{gap}}$ ) was acquired from a linear fit in the graph obtained from the square of the absorption coefficient ( $(\text{Abs} \times (1240/\lambda))^2$ ) as a function of photon energy ( $E$ ) ( $1240/\lambda$ ) [25,41].

### 3.3. Experimental Tests

The synthetic effluents were prepared with distilled water with a dye concentration of  $10 \mu\text{L L}^{-1}$ , and industrial effluents were supplied by the molded pulp packaging.

The experimental tests were carried out in a jacketed borosilicate reactor (cooling water temperature  $13^\circ\text{C}$ ) to maintain the effluent temperature at approximately  $25^\circ\text{C}$ ; the nominal volume was 600 mL, and 500 mL of effluent (artificial or industrial) was used for the reactions. The system contained a mercury vapor lamp (250 W), coupled just above the reactor, that was open to the environment. Magnetic stirring and air bubbling ( $0.5 \text{ L min}^{-1}$ ) into the reaction medium were used. During the reaction, samples were collected, centrifuged, and the dye residual concentration was analyzed in a UV-Vis spectrophotometer (Femto-800 XI) with a wavelength of 429 nm, dye characteristic.

The photolysis tests followed the same reaction system, but without the presence of airflow and catalyst, to verify only the radiation action under the discoloration reaction. The adsorption tests were realized without radiation and airflow to verify the adsorptive capacity of the studied materials.

#### 3.3.1. PH and Catalyst Concentration Influence

For the pH tests, NaOH and HCl solutions were used for the adjustments, and the values were adjusted between 2 and 10; in addition, tests were also carried out without pH adjustment (unadjusted pH): synthetic effluent  $\sim 4.2$  and industrial effluent  $\sim 6.2$ . For the catalyst concentration optimization, values between  $0.5$  and  $9 \text{ g L}^{-1}$  were evaluated. Both tests were carried out with artificial and industrial effluent preceding the tests carried out for one week.

#### 3.3.2. Industrial Effluent—Treatment for One Week

After the conditions (pH and catalyst concentration) were defined, adsorption, photolysis, and photocatalytic tests were carried out for one week (seven days) to treat the industrial effluent provided by the molded pulp packaging industry. Every day, the effluent was collected immediately at the molded outlet and then transported to the laboratory where the tests were carried out in parallel, following the same conditions described in item 2.3. Industrial effluents were subjected to experimental tests as they were received, without previous treatment.

### 3.4. Characterization of Industrial Effluent

The effluent was characterized quantitatively, identifying and comparing the parameters before and after each reaction. The analyzed parameters were biological oxygen demand (BOD), chemical oxygen demand (COD), total organic carbon (TOC), total soluble solids (TSS), surfactants, and nitrogen–nitrate  $\text{N}(\text{NO}_3)$ . The characterization was performed on the Pastel UV–Secomam equipment, with all analyses performed in duplicates.

This equipment determines the quality of the water and effluents. The method is based on spectral deconvolution where the ultraviolet spectrum hypothesis of effluents can be mostly modeled by a limited number of stable spectrums called the reference spectrum. Many studies have already used it to determine the quality of the effluents [42–45].

## 4. Conclusions

The use of photocatalysts resulting from industrial waste in the effluents' treatment is favorable. However, factors such as the composition variation of the material and the pollutant should be considered, mainly because when it comes to industrial effluents, it is difficult to identify a pattern. In this research, it was found that a quarry by-product

has similar characteristics quartz sand, which is a material already used as a catalyst support and also as an adsorbent for organic pollutants. It was noted that the material has catalytic activity when used as a photocatalyst, showing behavior favorable for synthetic dye solutions. However, when applied to the industrial effluent discoloration from the packaging industry, with a high organic load, it presented better behavior, in most tests, as an adsorbent. Although it has shown lower results than ZnO, MbP can be considered a promising material in the treatment of aqueous solutions.

**Author Contributions:** Conceptualization, L.N.B.d.A.; T.G.J. and G.G.L., methodology, L.N.B.d.A.; T.G.J.; O.H.L.N. and G.G.L. validation, L.N.B.d.A.; T.G.J.; A.M.T. and G.G.L., formal analysis, G.G.L.; A.M.T.; O.A.A.d.S. and D.T.D., investigation L.N.B.d.A.; T.G.J.; O.H.L.N.; A.M.T. and G.G.L., data curation, L.N.B.d.A.; G.G.L. and A.M.T., writing—original draft preparation, L.N.B.d.A.; T.G.J. and G.G.L., writing—review and editing, L.N.B.d.A.; T.G.J., D.T.D. and G.G.L., visualization, L.N.B.d.A.; T.G.J. and G.G.L., supervision, G.G.L. and O.A.A.d.S., project administration, L.N.B.d.A.; G.G.L. and O.A.A.d.S. All authors have read and agreed to the published version of the manuscript.

**Funding:** This research received no external funding.

**Acknowledgments:** The authors would like to thank the CNPq and CAPES for the financial support, UEM, and Multi-User Characterization Center in Materials Research and Development (C2MMA) for analyzes carried. This research did not receive any specific grant from funding agencies in the public, commercial, or not-for-profit sectors.

**Conflicts of Interest:** The authors declare no conflict of interest.

## References

1. Santos, D.H.; Duarte, J.L.; Tavares, M.G.; Tavares, M.G.; Friedrich, L.C.; Meili, L.; Pimentel, W.R.; Tonholo, J.; Zanta, C.L. Electrochemical degradation and toxicity evaluation of reactive dyes mixture and real textile effluent over DSA<sup>®</sup> electrodes. *Chem. Eng. Process. Process. Intensif.* **2020**, *153*, 107940. [CrossRef]
2. Ismail, M.; Wu, Z.; Zhang, L.; Ma, J.; Jia, Y.; Hu, Y.; Wang, Y. High—Efficient synergy of piezocatalysis and photocatalysis in bismuth oxychloride nanomaterial for dye decomposition. *Chemosphere* **2019**, *228*, 212–218. [CrossRef] [PubMed]
3. Dil, E.A.; Ghaedi, M.; Asfaram, A.; Mehrabi, F.; Sadeghfar, F. Efficient adsorption of Azure B onto CNTs/Zn:ZnO@Ni<sub>2</sub>P-NCs from aqueous solution in the presence of ultrasound wave based on multivariate optimization. *J. Ind. Eng. Chem.* **2019**, *74*, 55–62. [CrossRef]
4. Wu, S.; Xie, Y.; Zhang, X.; Huang, Z.; Liu, Y.; Fang, M.; Wu, X.; Min, X. In situ synthesis of adsorptive  $\beta$ -Bi<sub>2</sub>O<sub>3</sub>/BiOBr photocatalyst with enhanced degradation efficiency. *J. Mater. Res.* **2019**, *34*, 3450–3461. [CrossRef]
5. Riaz, S.; Park, S.-J. An overview of TiO<sub>2</sub>-based photocatalytic membrane reactors for water and wastewater treatments. *J. Ind. Eng. Chem.* **2020**, *84*, 23–41. [CrossRef]
6. Josué, T.; Almeida, L.; Lopes, M.; Santos, O.; Lenzi, G. Cr (VI) reduction by photocatalytic process: Nb<sub>2</sub>O<sub>5</sub> an alternative catalyst. *J. Environ. Manag.* **2020**, *268*, 110711. [CrossRef]
7. Lenzi, G.; Favero, C.V.B.; Colpini, L.; Bernabe, H.; Baesso, M.; Specchia, S.; Santos, O. Photocatalytic reduction of Hg(II) on TiO<sub>2</sub> and Ag/TiO<sub>2</sub> prepared by the sol-gel and impregnation methods. *Desalination* **2011**, *270*, 241–247. [CrossRef]
8. Almeida, L.; Lenzi, G.; Pietrobelli, J.; Santos, O. Caffeine degradation using ZnO and Ag/ZnO under UV and solar radiation. *Desalination Water Treat.* **2019**, *153*, 85–94. [CrossRef]
9. Sornalingam, K.; McDonagh, A.; Canning, J.; Cook, K.; Jhir, A.H.; Zhou, J.L.; Ahmed, M.B. Photocatalysis of 17 $\alpha$ -ethynylestradiol and estriol in water using engineered immersible optical fibres and light emitting diodes. *J. Water Process. Eng.* **2020**, *33*, 101075. [CrossRef]
10. Chen, P.; Blaney, L.; Cagnetta, G.; Huang, J.; Wang, B.; Wang, Y.; Deng, S.; Yu, G. Degradation of Ofloxacin by Perylene Diimide Supramolecular Nanofiber Sunlight-Driven Photocatalysis. *Environ. Sci. Technol.* **2019**, *53*, 1564–1575. [CrossRef]
11. Tiwari, D.; Tiwari, A.; Shukla, A.; Kim, D.J.; Yoon, Y.Y.; Lee, S.M. Facile synthesis and characterization of nanocomposite Au<sub>0</sub>(NPs)/titanium dioxide: Photocatalytic degradation of Alizarin Yellow. *J. Ind. Eng. Chem.* **2020**, *82*, 153–163. [CrossRef]
12. Morais, D.F.; Boaventura, R.A.; Moreira, F.C.; Vilar, V.J. Bromate removal from water intended for human consumption by heterogeneous photocatalysis: Effect of major dissolved water constituents. *Chemosphere* **2021**, *263*, 128111. [CrossRef]
13. Litter, M. *Treatment of Chromium, Mercury, Lead, Uranium, and Arsenic in Water by Heterogeneous Photocatalysis*, 1st ed.; Elsevier BV: Amsterdam, The Netherlands, 2009. [CrossRef]
14. Zhao, T.; Qian, R.; Zhou, G.; Wang, Y.; Lee, W.I.; Pan, J.H. Mesoporous WO<sub>3</sub>/TiO<sub>2</sub> spheres with tailored surface properties for concurrent solar photocatalysis and membrane filtration. *Chemosphere* **2021**, *263*, 128344. [CrossRef] [PubMed]
15. Chen, D.; Cheng, Y.; Zhou, N.; Chen, P.; Wang, Y.; Li, K.; Huo, S.; Cheng, P.; Peng, P.; Zhang, R.; et al. Photocatalytic degradation of organic pollutants using TiO<sub>2</sub>-based photocatalysts: A review. *J. Clean. Prod.* **2020**, *268*, 121725. [CrossRef]

16. Gonçalves, B.S.; Silva, L.M.; de Souza, T.C.; de Castro, V.G.; Silva, G.G.; Silva, B.C.; Krambrock, K.; Soares, R.B.; Lins, V.F.; Houmard, M.; et al. Solvent effect on the structure and photocatalytic behavior of TiO<sub>2</sub>-RGO nanocomposites. *J. Mater. Res.* **2019**, *34*, 3918–3930. [CrossRef]
17. Liu, S.; Wang, Y.; Ma, L.; Zhang, H. Ni<sub>2</sub>P/ZnS (CdS) core/shell composites with their photocatalytic performance. *J. Mater. Res.* **2018**, *33*, 3580–3588. [CrossRef]
18. Kako, T.; Yao, W.; Ye, J. Preparation and characterization of visible light sensitive Fe- and Ta-codoped TiO<sub>2</sub> photocatalyst. *J. Mater. Res.* **2010**, *25*, 110–116. [CrossRef]
19. Fu, Y.P.; Chang, W.K.; Wang, H.C.; Liu, C.W.; Lin, C.H. Synthesis and characterization of anatase TiO<sub>2</sub> nanolayer coating on Ni–Cu–Zn ferrite powders for magnetic photocatalyst. *J. Mater. Res.* **2010**, *25*, 134–140. [CrossRef]
20. Yener, H.B.; Helvacı, Ş.Ş. Effect of synthesis temperature on the structural properties and photocatalytic activity of TiO<sub>2</sub>/SiO<sub>2</sub> composites synthesized using rice husk ash as a SiO<sub>2</sub> source. *Sep. Purif. Technol.* **2015**, *140*, 84–93. [CrossRef]
21. Fatimah, I.; Said, A.; Hasanah, U.A. Preparation of TiO<sub>2</sub>-SiO<sub>2</sub> using Rice Husk Ash as Silica Source and The Kinetics Study as Photocatalyst in Methyl Violet Decolorization. *Bull. Chem. React. Eng. Catal.* **2015**, *10*, 43–49. [CrossRef]
22. Haldar, S.K. Igneous rocks. In *Introduction to Mineralogy and Petrology*, 2nd ed.; Elsevier: Amsterdam, The Netherlands, 2014; pp. 159–186. [CrossRef]
23. Mills, A.; Davies, R.H.; Worsley, D. Water Purification by Semiconductor Photocatalysis. *Chem. Soc. Rev.* **2010**, *25*, 417–425. [CrossRef]
24. Abebe, B.; Murthy, H.A.; Amare, E. Enhancing the photocatalytic efficiency of ZnO: Defects, heterojunction, and optimization. *Environ. Nanotechnol. Monit. Manag.* **2020**, *14*, 100336. [CrossRef]
25. Sa-Nguanprang, S.; Phuruangrat, A.; Thongtem, T.; Thongtem, S. Characterization and photocatalysis of visible-light-driven Dy-doped ZnO nanoparticles synthesized by tartaric acid-assisted combustion method. *Inorg. Chem. Commun.* **2020**, *117*, 107944. [CrossRef]
26. Garbarino, G.; Phung, T.K.; Pampararo, G.; Riani, P.; Busca, G. Modification of the properties of  $\gamma$ -Alumina as a support for nickel and molybdate catalysts by addition of silica. *Catal. Today* **2021**. [CrossRef]
27. Park, J.L.; Canizales, K.A.; Argyle, M.D.; Woodfield, B.F.; Stowers, K.J. The effects of doping alumina with silica in alumina-supported NiO catalysts for oxidative dehydrogenation of ethane. *Microporous Mesoporous Mater.* **2020**, *293*, 109799. [CrossRef]
28. Farjadian, F.; Azadi, S.; Mohammadi-Samani, S.; Ashrafi, H.; Azadi, A. A novel approach to the application of hexagonal mesoporous silica in solid-phase extraction of drugs. *Heliyon* **2018**, *4*, e00930. [CrossRef]
29. Arunmetha, S.; Vinoth, M.; Srither, S.R.; Karthik, A.; Sridharpanday, M.; Suriyaprabha, P.; Manivasakan, R.; Rajendran, V. Study on Production of Silicon Nanoparticles from Quartz Sand for Hybrid Solar Cell Applications. *J. Electron. Mater.* **2017**, *47*, 493–502. [CrossRef]
30. Mangrulkar, P.A.; Kamble, S.P.; Joshi, M.M.; Meshram, J.S.; Labhsetwar, N.K.; Rayalu, S.S. Photocatalytic Degradation of Phenolics by N-Doped Mesoporous Titania under Solar Radiation. *Int. J. Photoenergy* **2011**, *2012*, 1–10. [CrossRef]
31. Taffarel, S.R.; Lansarin, M.A.; Moro, C. Styrene photocatalytic degradation reaction kinetics. *J. Braz. Chem. Soc.* **2011**, *22*, 1872–1879. [CrossRef]
32. Wetchakun, K.; Wetchakun, N.; Sakulsermsuk, S. An overview of solar/visible Light—Driven heterogeneous photocatalysis for water purification: TiO<sub>2</sub>- and ZnO-based photocatalysts used in suspension photoreactors. *J. Ind. Eng. Chem.* **2019**, *71*, 19–49. [CrossRef]
33. Martínez, K.Y.P.; Toso, E.A.V. Planejamento da produção na indústria de embalagens de polpa moldada. *Gestão Produção* **2014**, *23*, 649–660. [CrossRef]
34. Jada, A.; Akbour, R.A. Adsorption and Removal of Organic Dye at Quartz Sand-Water Interface. *Oil Gas Sci. Technol.* **2014**, *69*, 405–413. [CrossRef]
35. Ceretta, M.B.; Vieira, Y.; Wolski, E.A.; Foletto, E.L.; Silvestri, S. Biological degradation coupled to photocatalysis by ZnO/polypyrrole composite for the treatment of real textile wastewater. *J. Water Process. Eng.* **2020**, *35*, 101230. [CrossRef]
36. Garcia, V.S.; Rosa, J.M.; Borrelly, S.I. Toxicity and color reduction of a textile effluent containing reactive red 239 dye by electron beam irradiation. *Radiat. Phys. Chem.* **2020**, *172*, 108765. [CrossRef]
37. Nguyen, C.H.; Juang, R.-S. Efficient removal of cationic dyes from water by a combined adsorption-photocatalysis process using Platinum—Doped titanate nanomaterials. *J. Taiwan Inst. Chem. Eng.* **2019**, *99*, 166–179. [CrossRef]
38. Ma, J.; Wang, K.; Wang, C.; Chen, X.; Zhu, W.; Zhu, G.; Yao, W.; Zhu, Y. Photocatalysis-self-Fenton system with high-fluent degradation and high mineralization ability. *Appl. Catal. B Environ.* **2020**, *276*, 119150. [CrossRef]
39. Mohammad-Rezaei, R.; Jaymand, M. Graphene quantum dots coated on quartz sand as efficient and low-cost adsorbent for removal of Hg<sup>2+</sup> and Pb<sup>2+</sup> from aqueous solutions. *Environ. Prog. Sustain. Energy* **2018**, *38*, S24–S31. [CrossRef]
40. Xu, X.; He, J.; Li, Y.; Fang, Z.; Xu, S. Adsorption and Transport of Ciprofloxacin in Quartz Sand at Different pH and Ionic Strength. *Open J. Soil Sci.* **2014**, *04*, 407–416. [CrossRef]
41. Astrath, N.G.C.; Sato, F.; Pedrochi, F.; Medina, A.N.; Bento, A.C.; Baesso, M.L.; Persson, C.; Da Silva, A.F. Band gap energy determination by photoacoustic spectroscopy under continuous light excitation. *Appl. Phys. Lett.* **2006**, *89*, 231926. [CrossRef]
42. Ito, T.; Shimada, Y.; Suto, T. Potential use of bacteria collected from human hands for textile dye decolorization. *Water Resour. Ind.* **2018**, *20*, 46–53. [CrossRef]

43. Methneni, N.; Morales-González, J.A.; Jaziri, A.; Ben Mansour, H.; Fernandez-Serrano, M. Persistent organic and inorganic pollutants in the effluents from the textile dyeing industries: Ecotoxicology appraisal via a battery of biotests. *Environ. Res.* **2021**, *196*, 110956. [CrossRef] [PubMed]
44. Adamczuk, M.; Pawlik-Skowrońska, B.; Solis, M. Do anthropogenic hydrological alterations in shallow lakes affect the dynamics of plankton? *Ecol. Indic.* **2020**, *114*, 106312. [CrossRef]
45. Mieczan, T.; Rudyk-Leuska, N. Seasonal dynamics of the epibiont food web on *Unio tumidus* (Philipsson, 1788) in a eutrophic reservoir. *Eur. J. Protistol.* **2019**, *69*, 138–150. [CrossRef] [PubMed]



## Article

# Enhanced Photocatalytic Activity of ZnO-Graphene Oxide Nanocomposite by Electron Scavenging

Syed Nabeel Ahmed and Waseem Haider \*

School of Engineering & Technology, Central Michigan University, Mt. Pleasant, MI 48859, USA; ahmed1sn@cmich.edu

\* Correspondence: haide1w@cmich.edu

**Abstract:** Advances in nanotechnology have opened new doors to overcome the problems related to contaminated water by introducing photocatalytic nanomaterials. These materials can effectively degrade toxic contaminants, such as dyes and other organic pollutants, into harmless by-products such as carbon dioxide and water. Consequently, these photocatalytic nanomaterials have the potential to provide low-cost and environment-friendly alternatives to conventional water and wastewater treatment techniques. In this study, a nanocomposite of zinc oxide and graphene oxide was developed and evaluated for photocatalysis. This nanocomposite was characterized by XRD, FTIR, FESEM, Diffuse Reflectance Spectroscopy (DRS), TEM and UV-Vis spectrophotometer. The photocatalytic behavior of the nanocomposite was studied through the degradation of methyl orange under ultraviolet light. It is reported that the weight ratios of zinc oxide and graphene oxide do not considerably affect the photocatalytic performance, which gives this process more compositional flexibility. Moreover, hydrogen peroxide was used as an electron scavenger to increase the time-efficiency of the process. The photodegradation rate can be significantly improved (up to 24 times) with the addition of hydrogen peroxide, which increases the number of trapped electrons and generates more oxidizing species, consequently increasing the reaction rate.

**Citation:** Ahmed, S.N.; Haider, W. Enhanced Photocatalytic Activity of ZnO-Graphene Oxide Nanocomposite by Electron Scavenging. *Catalysts* **2021**, *11*, 187. <https://doi.org/10.3390/catal11020187>

Received: 15 October 2020

Accepted: 20 January 2021

Published: 31 January 2021

**Keywords:** nanocomposite; photocatalysis; wastewater treatment

## 1. Introduction

Unavailability of clean water is one of the fastest growing problems in today's world. It is estimated that about 3.6 billion people live in areas that are potentially water-scarce at least one month per year [1]. Due to a 1% increase in the global water demand every year [1], efforts are being made to find low-cost [2] and environmentally friendly [3] ways of reclaiming wastewater. These efforts have introduced heterogeneous photocatalysis as a potential alternative to conventional wastewater treatment techniques [4–6]. However, in real world applications, photocatalytic processes still face challenges due to higher reaction times for batch-type processes, and lower efficiencies and recyclability for continuous type processes. Therefore, efforts are being made to improve the efficiency and to reduce the reaction time of the process. These efforts include better photocatalytic reactor design, modification of photocatalysts by doping and heterojunction, and the use of electron scavengers [6].

Among the most widely studied photocatalysts, zinc oxide is a wide band-gap photocatalytic semiconductor which has gained significant attention during the past years, particularly due to the fact that some researchers have reported ZnO demonstrating a better photocatalytic efficiency than the most widely studied TiO<sub>2</sub> [7,8]. The wide bandgap of ZnO not only makes it highly sensitive to ultra-violet light, but also causes the emission of the blue as well as green light post-irradiation. This emission corresponds to the exciton and defect recombination, which is extremely helpful for photocatalytic applications [9]. However, due to the wide bandgap of ZnO, it is difficult to photoexcite electrons under visible light irradiation [10].

**Publisher's Note:** MDPI stays neutral with regard to jurisdictional claims in published maps and institutional affiliations.



**Copyright:** © 2021 by the authors. Licensee MDPI, Basel, Switzerland. This article is an open access article distributed under the terms and conditions of the Creative Commons Attribution (CC BY) license (<https://creativecommons.org/licenses/by/4.0/>).

It has been reported that hybridizing ZnO with graphene oxide (GO) enhances its photocatalytic activity by providing spatial separation of the photogenerated electrons and holes and preventing electron-hole recombination. Additionally, the large specific surface area of graphene increases the reaction rate by providing more active sites for adsorption. Furthermore, the lower potential of graphene/graphene<sup>−</sup> enables the rapid electron migration from the semiconductor to the graphene [11]. Consequently, many researchers have demonstrated excellent tendency of graphene based ZnO nanocomposites for the degradation of harmful organic compounds, which include methylene blue [12,13], rhodamine B [14], and deoxynivalenol [15]. Moreover, ZnO based nanocomposites have also been reported to have excellent tendency towards the degradation of bacteria [16,17] as well as toxic metal ions [18,19]. Despite all these advantages and decades of research, photocatalysis is still limited to the laboratories and still not feasible for commercial scale, particularly due to very high reaction times. This study aims to solve this issue by accelerating the reaction rate through electron scavengers.

In this study, we have developed a series of ZnO-GO nanocomposites by decorating ZnO nano-powder on graphene oxide sheets in four different ratios of GO:ZnO by weight. The photocatalytic behavior of the resulting nanocomposites has been assessed by studying the degradation of methyl orange in aqueous medium, which is one of the most hazardous chemicals in industrial wastewater. One of the best ways to enhance the photodegradation rate is adding an electron-hole scavenger to increase the number of trapped electrons [20]. Therefore, in this study, we have used hydrogen peroxide (H<sub>2</sub>O<sub>2</sub>) as an electron scavenger to increase the time-efficiency of the process.

## 2. Results and Discussion

Figure 1a demonstrates the TEM images of the graphene oxide sheets, with the inset showing the selected area diffraction pattern of graphene oxide. The morphology of as-synthesized GO exhibited the stacking of graphene layers. The FESEM image of the prepared nanocomposite (sample 1:10) is shown in Figure 1b. Figure 1c,d illustrates the TEM images of ZnO-GO nanocomposite. It can be seen that ZnO nanoparticles were exhibiting irregular powder-like morphology and were attached to GO sheets. Some ZnO particles were agglomerated on the GO sheets.

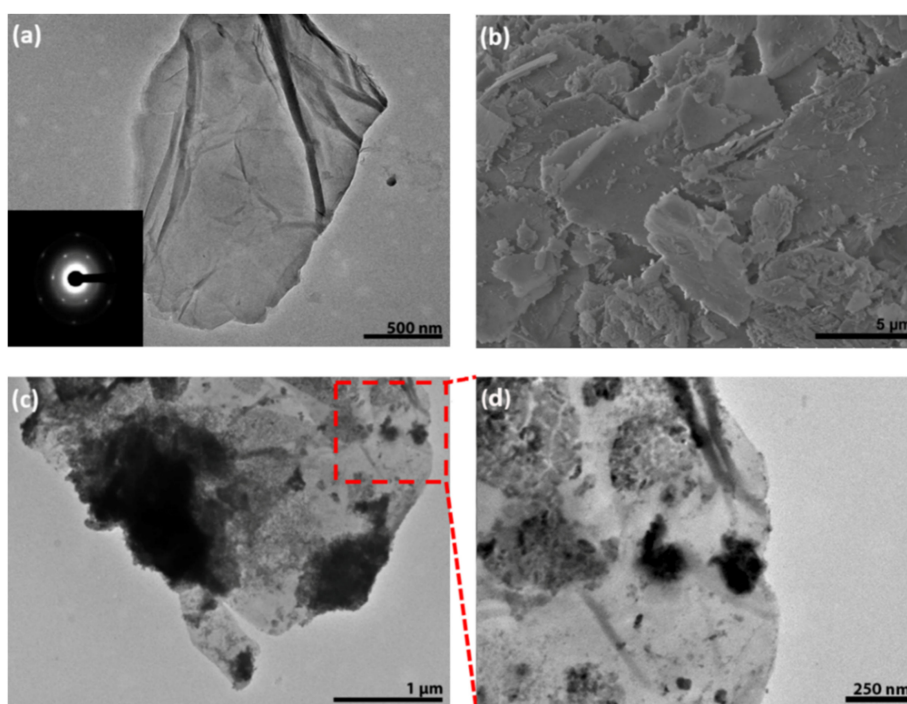


**Figure 1.** (a) TEM image of undecorated graphene oxide (GO), inset shows the diffraction pattern, (b) FESEM image of graphene oxide decorated with ZnO nano-powder (1:10) (c) TEM image of graphene oxide decorated with ZnO nanopowder (1:15) and (d) High magnification TEM view of GO-ZnO nanocomposite.



For studying the composition and crystallographic planes, the prepared nanocomposites have been characterized by XRD and infrared spectroscopy. Figure 2a shows the XRD plot of ZnO-GO nanocomposites with all four weight ratios, indicating the crystallographic planes of ZnO. The peaks at  $31.7^\circ$ ,  $34.4^\circ$ ,  $36.2^\circ$ ,  $47.5^\circ$ ,  $56.5^\circ$ ,  $63.0^\circ$ ,  $68.0^\circ$ ,  $69.0^\circ$ ,  $72.1^\circ$  and  $76.7^\circ$  can be indexed to the (100), (002), (101), (102), (110), (103), (112), (201), (004) and (202) planes of Wurtzite ZnO, respectively.

To further confirm the interaction between ZnO and GO, FTIR spectrum has been recorded. Figure 2b demonstrates the infrared spectra of pure GO, commercial ZnO powder, as well as one of the prepared GO-ZnO nanocomposites (1:10). The bending and stretching of zinc oxygen double bonds generate an absorption peak at a very low wavenumber which even goes below  $400\text{ cm}^{-1}$ , whereas the hydroxyl group bending and stretching peaks can be seen in the GO and ZnO-GO samples at  $1572\text{ cm}^{-1}$  and  $3350\text{ cm}^{-1}$ , respectively. The C-O stretching vibration can be observed at  $1072\text{ cm}^{-1}$ , whereas the noise at around  $2000\text{ cm}^{-1}$  in all three of the infrared spectra is due to the diamond tip of the equipment that comes in contact with the sample.

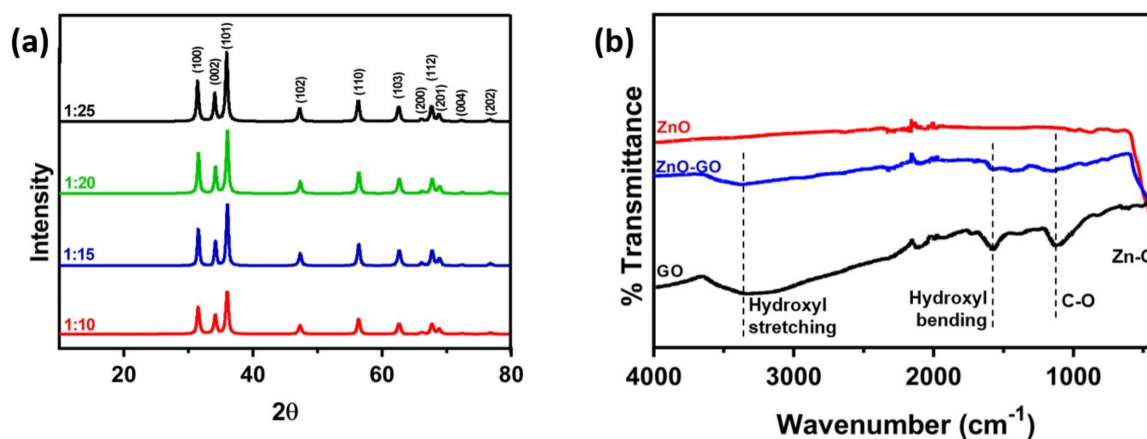


**Figure 2.** (a) XRD of the ZnO-GO nanocomposites with different ratios showing the crystallographic planes of ZnO and (b) FTIR of commercial ZnO powder, pure GO and the ZnO-GO nanocomposite (1:10).

The photocatalytic performance of the nanocomposites is illustrated in Figure 3a–d. All four samples show a complete degradation of dye after 9 h of irradiation. It should be noted that the weight ratios of GO and ZnO do not have a significant effect on the photocatalytic efficiency, since all four samples show almost the same degradation rate. Upon irradiation, the electrons in the valence band of ZnO are first photoexcited, and transferred into the conduction band. These transferred electrons produce negative and positive charge carriers called electrons and holes, respectively. The work function of ZnO (5.2–5.3 eV) is different from that of GO (4.5 eV), so photoexcited electrons transfer readily from ZnO to GO [21,22]. Subsequently,  $\bullet\text{OOH}$  radicals and the trapped electrons combine to produce  $\text{H}_2\text{O}_2$ , finally forming  $\bullet\text{OH}$  radicals. These radicals are mainly responsible for the degradation of methyl orange.

In order to enhance the photocatalytic performance,  $\text{H}_2\text{O}_2$  (0.4 mol/L) was added in the reaction solution. Figure 4a–d indicates that the addition of  $\text{H}_2\text{O}_2$  has significantly enhanced the photocatalytic performance by almost 24 times. This can be explained by the ability of  $\text{H}_2\text{O}_2$  to prevent electron-hole recombination by adding electron acceptors to the reaction, which increases the number of trapped electrons. Another way that explains the significant enhancement in the photocatalytic activity is that  $\text{H}_2\text{O}_2$  generates more  $\bullet\text{OH}$  radicals and other oxidizing species. Additionally, problems caused by  $\text{O}_2$  starvation are also overcome and the oxidation rate of intermediate compounds is also increased by the addition of  $\text{H}_2\text{O}_2$  [23]. All these factors, which include the added electrons,  $\bullet\text{OH}$  radicals and the availability of oxygen, act synergistically and explain the decrease in the photocatalytic degradation time to almost 4% of the original time, after the addition of

0.4 mol/L of hydrogen peroxide, as shown in Figure 4a–d. It should be highlighted that the concentration of hydrogen peroxide should be carefully controlled since it can render the water toxic at higher concentrations. However, 0.4 mol/L of hydrogen peroxide is much lower than its concentration typically used in households (3–10%). Table 1 summarizes the photocatalytic performance of pure ZnO and ZnO-GO nanocomposites from recent studies in various heterojunctions. It can be observed that the ZnO-rGO photocatalysts show a significant improvement in photocatalytic performance compared to past studies.

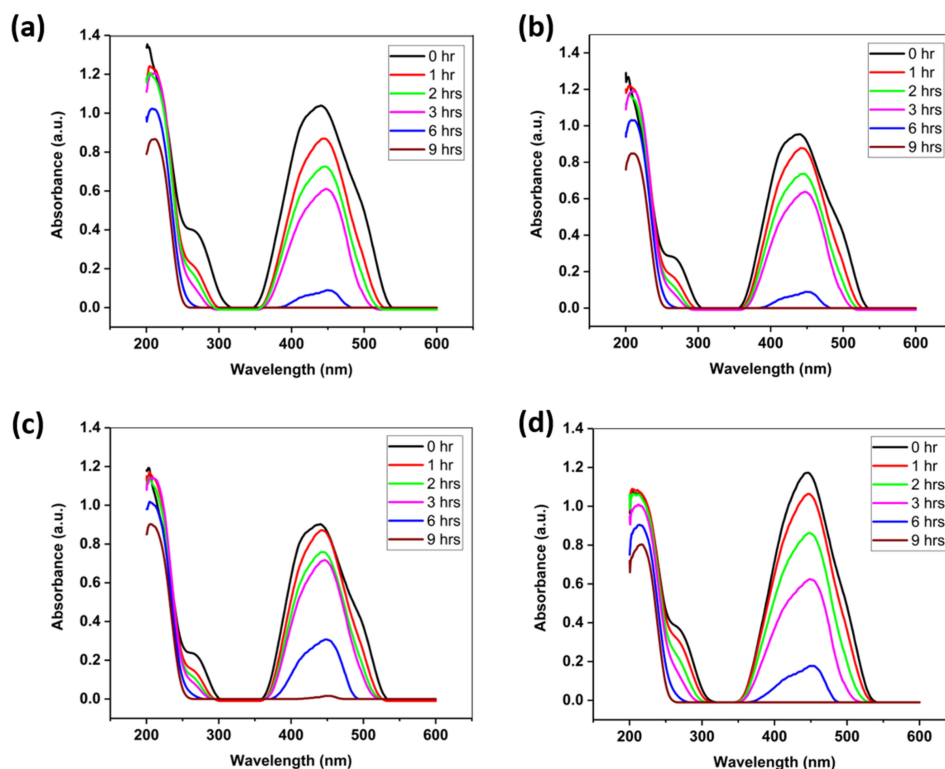


**Figure 3.** Photocatalytic activity of the prepared nanocomposites of ZnO-GO with (a) 1:10 ratio (b) 1:15 ratio (c) 1:20 ratio and (d) 1:25 ratio.

**Table 1.** Photocatalytic performance of ZnO-GO based nanocomposites.

Composition	Light Source	Pollutant	Experimental Conditions	Photocatalytic Efficiency (Pollutant Removal)	Reference
ZnO	100 W UV	Methylene Blue (15g/L)	CL = 1.25 g/L $t_r$ = 80 min	76%	[24]
ZnO-rGO	Sunlight	Methylene Blue (15g/L)	CL = 1.25 g/L $t_r$ = 150 min	97%	[24]
ZnO-rGO	300 W UV	Methylene Blue (0.01g/L)	CL = 0.5 g/L $t_r$ = 120 min ID = 10 cm	99%	[25]
ZnO-graphene	UV (365 nm)	Deoxynivalenol (15 mg/L)	CL = 0.5 mg/L $t_r$ = 30 min	~99%	[15]
ZnO-GO	300 W visible	Methylene Blue (0.03126 mM/L)	CL = 0.1 g/L $t_r$ = 120 min ID = 10 cm	12%	[10]
ZnO-GO	250 W UV	Methylene Blue (960 mg/L)	CL = 0.25 g/L $t_r$ = 450 min	~75%	[13]
Au-ZnO-rGO	UV and Visible	Rhodamine B (94%)	CL = IM $t_r$ = 180 min ID = 1 cm	94%	[14]
ZnO-rGO	20 W UV	Methylene Blue (25 mg/L)	CL = 0.1 g/L $t_r$ = 30 min ID = 10 cm	~86%	[26]

$t_r$  = Irradiation time. CL = Catalyst Loading. ID = Irradiation distance.

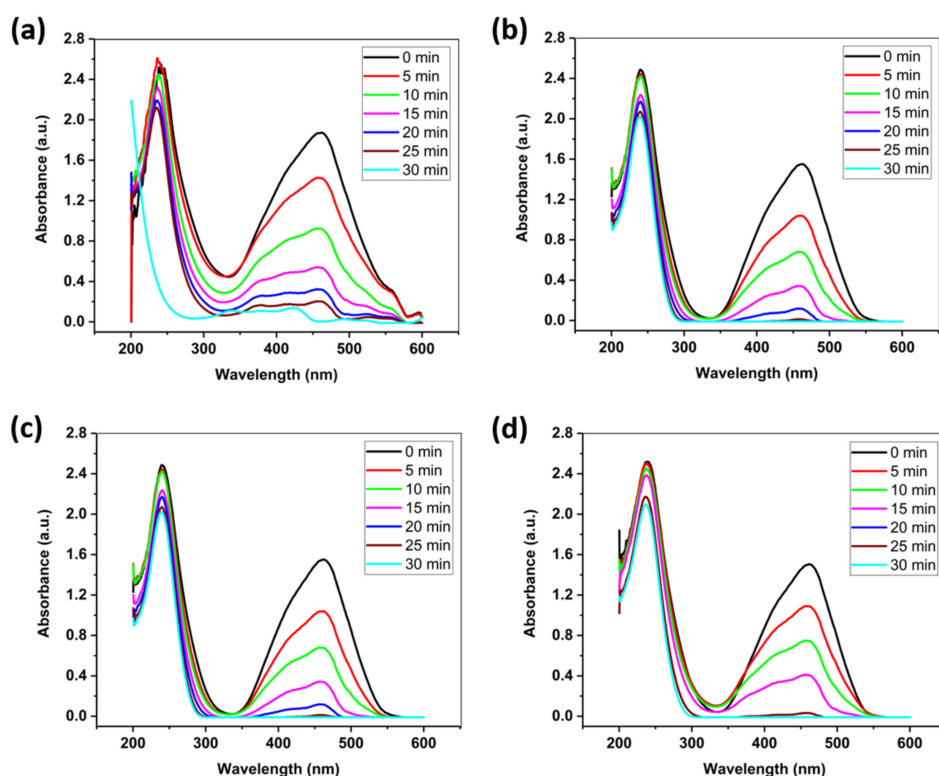


**Figure 4.** Photocatalytic activity of the prepared nanocomposites of ZnO-GO with (a) 1:10 ratio (b) 1:15 ratio (c) 1:20 ratio and (d) 1:25 ratio after adding  $\text{H}_2\text{O}_2$ .

For studying the effect of graphene hybridization on the bandgap of the nanocomposite, UV-Vis Diffuse Reflectance Spectroscopy (DRS) has been performed (Figure 5a). Figure 5b shows the Tauc plots obtained from UV-Vis DRS and from these plots, the bandgap of the nanocomposites has been found to be 3.3 eV. These results indicate that the bandgap of the nanocomposite is independent of the weight percentage of GO in the GO-ZnO nanocomposites, thereby confirming their somewhat similar photocatalytic behavior. The presence of GO provides a higher surface area and the addition of hydrogen peroxide significantly improved the photodegradation reaction rate (upto 24 times), thus improving the photocatalytic efficiency or pollutant removal. Moreover, the addition of  $\text{H}_2\text{O}_2$  significantly reduces the reaction time to about 4% of the original time by increasing the number of trapped electrons and generating more oxidizing species. As far as the durability is concerned, the photocatalysts have to be separated from the solution for reuse, which adds up to the cost and time of the process. Therefore, in terms of durability, a batch type photocatalytic process still needs more improvement than its less efficient continuous type counterpart.

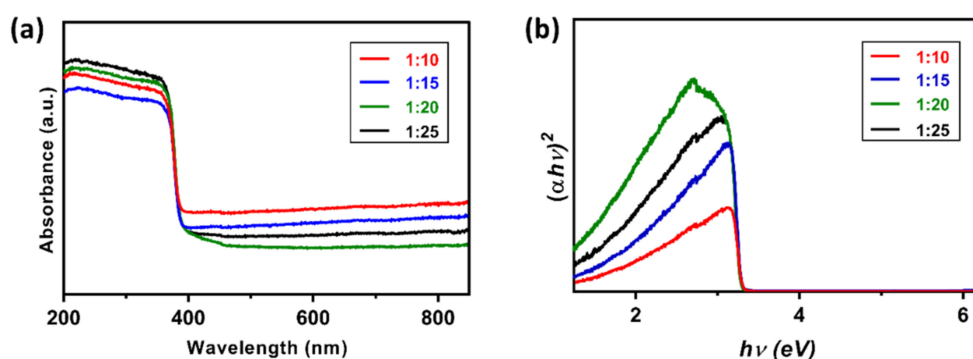


**Figure 5.** (a) UV-Vis Diffuse Reflectance Spectroscopy (DRS) spectra of ZnO-GO nanocomposites with different weight percentages, and (b) Tauc plot obtained from DRS.

### 3. Experimental Methods

#### 3.1. Preparation of Graphene Oxide

For the preparation of graphene oxide, improved Hummers' method has been employed [20]. Briefly, concentrated sulfuric acid (69 mL) was first added to a mixture of 2 g of graphite flakes and 1.5 g of sodium nitrate and the mixture was cooled using the water circulation bath to 5 °C. A total of 9 g of potassium permanganate was then added slowly in portions to keep the reaction mixture temperature below 20 °C. The temperature was then raised to 35 °C and the solution was magnetically stirred for 7 h. A total of 9 g of potassium permanganate was then added again in one portion, and the reaction mixture was stirred continuously for 12 h at the same temperature. The reaction mixture was then cooled to room temperature, followed by the addition of cold Deionized (DI) water (2–5 °C) and 3 mL of 30% H<sub>2</sub>O<sub>2</sub>. The mixture was then purified using the same protocol of filtering/centrifugation as before, decanting with multiple washes by 30% HCl and ethanol. The product was then dried under vacuum overnight at 40 °C [27].

#### 3.2. Decoration of ZnO Nanopowder

For the decoration of ZnO powder, 0.02 moles of Zn(NO<sub>3</sub>)<sub>2</sub> were dissolved in 100 mL of DI water at 5 °C. Separately, graphene oxide was dispersed in 200 mL of DI water and ultrasonicated for 60 min, and then mixed with the Zn(NO<sub>3</sub>)<sub>2</sub> solution under vigorous stirring. The pH was adjusted to 8 by adding 1 M KOH dropwise, and the solution was magnetically stirred for 12 h. Finally, the product was centrifuged for 12 h in vacuum and dried at 60 °C, and then heat treated at 200 °C in air for two hours. Using this method, the GO-ZnO nanocomposites were prepared in four different weight ratios, which are 1:10, 1:15, 1:20 and 1:25. The reason for selecting this range of composition is that at higher percentages of graphene composites, the photocatalytic efficiency decreases due to the shielding effect caused by graphene [9], whereas at narrower percentages, the effect of graphene hybridization is negligible. All the photocatalytic experiments were performed at room temperature.

### 4. Characterization

X-ray diffraction (XRD) analysis for the prepared nanocomposites was performed in the range of  $2\theta = 10\text{--}90^\circ$  at the rate of  $1^\circ/\text{min}$ , by using Rigaku Miniflex II X-ray diffractometer (Rigaku, Tokyo, Japan). The composition/functional property of the nanocomposites was studied with FTIR spectroscopy at room temperature in an acquired range of  $500\text{--}4000\text{ cm}^{-1}$ . For the FTIR, the Thermo scientific Nicolet iS50 FT-IR (Thermo Scientific, Waltham, MA USA) was used. The structure and morphology of the nanocomposites were studied with Transmission Electron Microscopy (TEM), Selected Area Electron Diffraction (SAED) and Field Emission Scanning Electron Microscopy (FESEM). TEM and SAED were carried out using Hitachi Model HT7700 (Hitachi, Tokyo, Japan) using high resolution mode at 120kV.

#### Photocatalytic Studies

For the photocatalytic studies, 3 mL of methyl orange solution (20 mg/L) was mixed with 3 mg of the GO-ZnO nanocomposite. Prior to irradiation, the sample was kept in the dark for 60 min for the adsorption-desorption equilibrium, and then irradiated with ultra-violet (UV) light of wavelength 253 nm (UVC). The measurements were taken through an Ocean Optics UV-Vis spectrophotometer (Ocean Optics, Orlando, FL, USA), at different time intervals (0, 1, 2, 3, 9 h). The photocatalytic studies have also been performed in the presence of 0.4 mol/L of hydrogen peroxide. For band-gap measurements, UV-Vis Diffuse Reflectance Spectroscopy (DRS) was performed and the band gap energies were calculated from a plot  $(\alpha h\nu)^2$  versus photo-energy ( $h\nu$ ) using the Kubelka–Munk function, which shows the relationship between the band gap and the absorption coefficient.

## 5. Conclusions

In this study, GO-ZnO nanocomposites have been prepared with four different weight ratios, which are 1:10, 1:15, 1:20 and 1:25, respectively. These nanocomposites have been characterized by using TEM, SAED, FESEM, XRD and FTIR. The photocatalytic behavior of these nanocomposites has been studied with and without H<sub>2</sub>O<sub>2</sub> as an electron scavenger. It has been concluded that varying the compositions does not show a considerable difference in the photocatalytic activity of the nanocomposites, which has been further confirmed by their bandgaps (3.3 eV). Therefore, such nanocomposites can be prepared and utilized on large scales, without paying attention to compositional variations. Consequently, problems related to localized heterogeneities and segregations can also be avoided. Furthermore, the addition of H<sub>2</sub>O<sub>2</sub> significantly reduces the reaction time to about 4% of the original time by increasing the number of trapped electrons and generating more oxidizing species. Hence, H<sub>2</sub>O<sub>2</sub> as an electron scavenger can be very useful in actual water treatment applications and can significantly improve the time efficiency of the process.

**Author Contributions:** Conceptualization, S.N.A. and W.H.; methodology, S.N.A.; writing—original draft preparation, S.N.A.; writing—review and editing, W.H.; supervision, W.H.; project administration, W.H. All authors have read and agreed to the published version of the manuscript.

**Funding:** This research received no external funding.

**Data Availability Statement:** All the data generated during this study is reported in this article.

**Conflicts of Interest:** The authors declare no conflict of interest.

## References

1. United Nations. The United Nations World Water Development Report 2018: Nature-Based Solutions for Water. 2018. Available online: <http://unesdoc.unesco.org/images/0026/002614/261424e.pdf> (accessed on 1 January 2020).
2. Bouazizi, A.; Breida, M.; Achiou, B.; Ouammou, M.; Calvo, J.I.; Aaddane, A.; Younssi, S.A. Removal of dyes by a new nano-TiO<sub>2</sub> ultrafiltration membrane deposited on low-cost support prepared from natural Moroccan bentonite. *Appl. Clay Sci.* **2017**, *149*, 127–135. [CrossRef]
3. Friedmann, D.; Hakki, A.; Kim, H.; Choi, W.; Bahnemann, D. Heterogeneous photocatalytic organic synthesis: State-of-the-art and future perspectives. *Green Chem.* **2016**, *18*, 5391–5411. [CrossRef]
4. Ayekoe, C.Y.P.; Robert, D.; Lancine, D.G. Combination of coagulation-flocculation and heterogeneous photocatalysis for improving the removal of humic substances in real treated water from Agbo River (Ivory-Coast). *Catal. Today* **2017**, *281*, 2–13. [CrossRef]
5. Wong, W.; Wong, H.Y.; Badruzzaman, A.B.M.; Goh, H.H.; Zaman, M. Recent advances in exploitation of nanomaterial for arsenic removal from water: A review. *Nanotechnology* **2017**, *28*, 042001. [CrossRef] [PubMed]
6. Ahmed, N.; Haider, W. Heterogeneous photocatalysis and its potential applications in water and wastewater treatment: A review. *Nanotechnology* **2018**, *29*, 342001. [CrossRef] [PubMed]
7. McLaren, A.; Valdes-Solis, T.; Li, G.; Tsang, S.C. Shape and size effects of ZnO nanocrystals on photocatalytic activity. *J. Am. Chem. Soc.* **2009**, *131*, 12540–12541. [CrossRef]
8. Xu, T.; Zhang, L.; Cheng, H.; Zhu, Y. Significantly enhanced photocatalytic performance of ZnO via graphene hybridization and the mechanism study. *Appl. Catal. B Environ.* **2011**, *101*, 382–387. [CrossRef]
9. Gröttrup, J.; Schütt, F.; Smazna, D.; Lupan, O.; Adelung, R.; Mishra, Y.K. Porous ceramics based on hybrid inorganic tetrapodal networks for efficient photocatalysis and water purification. *Ceram. Int.* **2017**, *43*, 14915–14922. [CrossRef]
10. Ahmed, G.; Hanif, M.; Zhao, L.; Hussain, M.; Khan, J.; Liu, Z. Journal of Molecular Catalysis A: Chemical Defect engineering of ZnO nanoparticles by graphene oxide leading to enhanced visible light photocatalysis. *J. Mol. Catal. A Chem.* **2016**, *425*, 310–321. [CrossRef]
11. Low, J.; Yu, J.; Jaroniec, M.; Wageh, S.; Al-Ghamdi, A.A. Heterojunction Photocatalysts. *Adv. Mater.* **2017**, *29*, 1601694. [CrossRef]
12. Lv, T.; Pan, L.; Liu, X.; Sun, Z. Enhanced photocatalytic degradation of methylene blue by ZnO-reduced graphene oxide-carbon nanotube composites synthesized via microwave-assisted reaction. *Catal. Sci. Technol.* **2012**, *2*, 2297–2301. [CrossRef]
13. Rokhsat, E.; Akhavan, O. Improving the photocatalytic activity of graphene oxide/ZnO nanorod films by UV irradiation. *Appl. Surf. Sci.* **2016**, *371*, 592–595. [CrossRef]
14. She, P.; Yin, S.; He, Q.; Zhang, X.; Xu, K.; Shang, Y.; Men, X.; Zeng, S.; Sun, H.; Liu, Z. A self-standing macroporous Au/ZnO/reduced graphene oxide foam for recyclable photocatalysis and photocurrent generation. *Electrochim. Acta* **2017**, *246*, 35–42. [CrossRef]
15. Bai, X.; Sun, C.; Liu, D.; Luo, X.; Li, D.; Wang, J.; Wang, N.; Chang, X.; Zong, R.; Zhu, Y. Photocatalytic degradation of deoxynivalenol using graphene/ZnO hybrids in aqueous suspension. *Appl. Catal. B Environ.* **2017**, *204*, 11–20. [CrossRef]

16. Khalil, A.; Gondal, M.A.; Dastageer, M.A. Augmented photocatalytic activity of palladium incorporated ZnO nanoparticles in the disinfection of Escherichia coli microorganism from water. *Appl. Catal. A Gen.* **2011**, *402*, 162–167. [CrossRef]
17. Adhikari, S.; Gupta, R.; Surin, A.; Kumar, T.S.; Chakraborty, S.; Sarkar, D.; Madras, G. Visible light assisted improved photocatalytic activity of combustion synthesized spongy-ZnO towards dye degradation and bacterial inactivation. *RSC Adv.* **2016**, *6*, 80086–80098. [CrossRef]
18. Liu, X.; Pan, L.; Lv, T.; Lu, T.; Zhu, G.; Sun, Z.; Sun, C. Microwave-assisted synthesis of ZnO-graphene composite for photocatalytic reduction of Cr(vi). *Catal. Sci. Technol.* **2011**, *1*, 1189–1193. [CrossRef]
19. Singh, S.; Barick, K.C.; Bahadur, D. Fe<sub>3</sub>O<sub>4</sub> embedded ZnO nanocomposites for the removal of toxic metal ions, organic dyes and bacterial pathogens. *J. Mater. Chem. A* **2013**, *1*, 3325. [CrossRef]
20. Chong, M.N.; Jin, B.; Chow, C.W.K.; Saint, C. Recent developments in photocatalytic water treatment technology: A review. *Water Res.* **2010**, *44*, 2997–3027. [CrossRef]
21. Giovannetti, G.; Khomyakov, P.A.; Brocks, G.; Karpan, V.M.; van den Brink, J.; Kelly, P.J. Doping graphene with metal contacts. *Phys. Rev. Lett.* **2008**, *101*, 4–7. [CrossRef]
22. Roy, P.; Periasamy, A.P.; Liang, C.T.; Chang, H.T. Synthesis of graphene-ZnO-Au nanocomposites for efficient photocatalytic reduction of nitrobenzene. *Environ. Sci. Technol.* **2013**, *47*, 6688–6695. [CrossRef] [PubMed]
23. Malato, S.; Fernandez-Ibanez, P.; Maldonado, M.I.; Blanco, J.; Gernjak, W. Decontamination and disinfection of water by solar photocatalysis: Recent overview and trends. *Catal. Today* **2009**, *147*, 1–59. [CrossRef]
24. Xu, S.; Fu, L.; Pham, T.S.; Yu, A.; Han, F.; Chen, L. Preparation of ZnO flower/reduced graphene oxide composite with enhanced photocatalytic performance under sunlight. *Ceram. Int.* **2015**, *41*, 4007–4013. [CrossRef]
25. Xue, B.; Zou, Y. High photocatalytic activity of ZnO—Graphene composite. *J. Colloid Interface Sci.* **2018**, *529*, 306–313. [CrossRef] [PubMed]
26. Luan, V.H.; Tien, H.N.; Hur, S.H. Fabrication of 3D structured ZnO nanorod/reduced graphene oxide hydrogels and their use for photo-enhanced organic dye removal. *J. Colloid Interface Sci.* **2015**, *437*, 181–186. [CrossRef] [PubMed]
27. Marcano, D.C.; Kosynkin, D.V.; Berlin, J.M.; Sinitskii, A.; Sun, Z.; Slesarev, A.; Alemany, L.B.; Lu, W.; Tour, J.M. Improved Synthesis of Graphene Oxide. *ACS Nano* **2010**, *4*, 4806–4814. [CrossRef]

MDPI  
St. Alban-Anlage 66  
4052 Basel  
Switzerland  
Tel. +41 61 683 77 34  
Fax +41 61 302 89 18  
[www.mdpi.com](http://www.mdpi.com)

*Catalysts* Editorial Office  
E-mail: [catalysts@mdpi.com](mailto:catalysts@mdpi.com)  
[www.mdpi.com/journal/catalysts](http://www.mdpi.com/journal/catalysts)







MDPI  
St. Alban-Anlage 66  
4052 Basel  
Switzerland  
Tel: +41 61 683 77 34  
[www.mdpi.com](http://www.mdpi.com)



ISBN 978-3-0365-6392-3